Ollscoil na hÉireann, Corcaigh

National University of Ireland, Cork

Design of Material for Solar Fuel Production

Thesis presented by

Stephen Rhatigan, MSc

https://orcid.org/0000-0002-9652-468X

for the degree of

Doctor of Philosophy

University College Cork

School of Chemistry

Head of School/Department: Dr. Humphrey Moynihan

Supervisor(s): Dr. Michael Nolan, Prof. Colm O'Dwyer

2020

Table of Contents

Declaration

This is to certify that the work I am submitting is my own and has not been submitted for another degree, at either University College Cork or elsewhere. All external references and sources are clearly acknowledged and identified within the contents. I have read and understood the regulations of University College Cork concerning plagiarism.

Author Contributions

My contribution to the work described in this thesis was to perform the DFT calculations, analyse and present results, prepare manuscripts and respond to reviewers. For study in Chapter 8, I performed the VASP calculations and our collaborator performed the FHI-aims calculations. For those chapters with experimental work, all materials preparation and characterisation were performed by our experimental collaborators.

Acknowledgements

First, I would like to thank my supervisor, Dr. Michael Nolan, for the initial opportunity and all the opportunities since. His guidance, mentorship and support were immense and are very much appreciated.

I would like to thank my thesis committee, Prof. Colm O'Dwyer and Prof. Paul Hurley for their feedback and discussions. Thanks also to my collaborators and co-authors, in particular, but in no particular order, Dr. Suresh Pillai, Dr. Vignesh Kumaravel, Dr. Ciara Byrne, Dr. Gerardo Colón, Prof. Francesc Illas and Dr. Ángel Morales-García.

I acknowledge support from Science Foundation Ireland through the US-Ireland R&D Partnership program, Grant number SFI/US/14/E2915 and the ERA.Net for Materials Research and Innovation (M-ERA.Net 2), Horizon 2020 grant agreement number 685451, SFI Grant Number SFI/16/M-ERA/3418 (RATOCAT). I acknowledge access to SFI funded computing resources at Tyndall National Institute and the SFI/HEA funded Irish Centre for High End Computing.

Massive thanks to my grandparents and parents, for their love and support; I wouldn't be here, literally or figuratively, without them. Thanks to my brothers, Jack and James, for their feigned interest, and Tom, for his honesty in not feigning interest. Thanks to Maggie, for the video calls and the joy they bring. Thanks also to my friends and extended family.

Finally, thanks to Serena, who's always got my back.

List of Publications

Journal Articles

1. CO_2 and water activation on ceria nanocluster modified TiO_2 rutile (110), **Rhatigan, S.**; Nolan, M. *Journal of Materials Chemistry A* **2018,** *6* (19), 9139-9152, https://doi.org/10.1039/C8TA01270A.

2. Impact of surface hydroxylation in MgO-/SnO-nanocluster modified TiO_2 anatase (101) composites on visible light absorption, charge separation and reducibility, **Rhatigan, S.**; Nolan, M. *Chinese Chemical Letters* **2018,** *29* (6), 757-764, https://doi.org/10.1016/j.cclet.2017.11.036.

3. Activation of Water on MnO_x-Nanocluster-Modified Rutile (110) and Anatase (101) TiO_2 and the Role of Cation Reduction, **Rhatigan, S.**; Nolan, M. *Frontiers in Chemistry* **2019,** *7* (67), https://doi.org/10.3389/fchem.2019.00067.

4. Modification of TiO_2 with hBN: High temperature anatase phase stabilisation and photocatalytic degradation of 1,4-dioxane, Byrne, C.; **Rhatigan, S.**; Hermosilla, D.; Merayo, N.; Blanco, Á.; Michel, M. C.; Hinder, S.; Nolan, M.; Pillai, S. *Journal of Physics: Materials* **2019**, https://doi.org/10.1088/2515-7639/ab5a31.

5. Indium-Doped TiO_2 Photocatalysts with High-Temperature Anatase Stability, Kumaravel, V.; **Rhatigan, S.**; Mathew, S.; Bartlett, J.; Nolan, M.; Hinder, S. J.; Sharma, P. K.; Singh, A.; Byrne, J. A.; Harrison, J.; Pillai, S. C. *The Journal of Physical Chemistry C* **2019,** *123* (34), 21083-21096, https://doi.org/10.1021/acs.jpcc.9b06811.

6. Effect of Cu Doping on the Anatase-to-Rutile Phase Transition in TiO_2 Photocatalysts: Theory and Experiments, Byrne, C.; Moran, L.; Hermosilla, D.; Merayo, N.; Blanco, Á.; **Rhatigan, S.**; Hinder, S.; Ganguly, P.; Nolan, M.; Pillai, S. C. *Applied Catalysis B: Environmental* **2019**, https://doi.org/10.1016/j.apcatb.2019.01.058.

7. Surface Modification of Rutile TiO_2 with Alkaline-Earth Oxide Nanoclusters for Enhanced Oxygen Evolution, **Rhatigan, S.**; Sokalu, E.; Nolan, M.; Colón, G. *ACS Applied Nano Materials* **2020,** *3* (6), 6017-6033, https://doi.org/10.1021/acsanm.0c01237.

8. Hydrogen evolution on non-metal oxide catalysts, **Rhatigan, S.**; Michel, M. C.; Nolan, M. *Journal of Physics: Energy* **2020**, https://doi.org/10.1088/2515-7655/aba3bc.

9. Mo doped TiO_2: impact on oxygen vacancies, anatase phase stability and photocatalytic activity, Kumaravel, V.; **Rhatigan, S.**; Mathew, S.; Michel, M. C.;

Bartlett, J.; Nolan, M.; Hinder, S. J.; Gascó, A.; Ruiz-Palomar, C.; Hermosilla, D.; Pillai, S. C. *Journal of Physics: Materials* **2020,** *3* (2), 025008, https://doi.org/10.1088/2515-7639/ab749c.

10. On the use of DFT+U to describe the electronic structure of TiO_2 nanoparticles: $(TiO_2)_{35}$ as a case study, Morales-García, Á.; **Rhatigan, S.**; Nolan, M.; Illas, F. *The Journal of Chemical Physics* **2020,** *152* (24), 244107, https://doi.org/10.1063/5.0012271.

11. Modification of TiO_2 with Metal Chalcogenide Nanoclusters for Hydrogen Evolution, **Rhatigan, S.**; Niemitz, L.; Nolan, M. *ChemRxiv. Preprint* **2020**, https://doi.org/10.26434/chemrxiv.13176773.v1.

Book Chapters

Insights into Photocatalysis from Computational Chemistry, **Rhatigan, S.**; Nolan M. *Heterogeneous Photocatalysis*, Wiley (in print).

Abstract

To harness even a fraction of the solar energy incident at Earth's surface would meet global demands for clean, environmentally friendly electricity and fuel. Sunlight is an intermittent energy source and a mismatch exists between the peaks of supply and demand. A strategy to overcome this drawback is to convert the solar energy to chemical energy (stored in the bonds of chemical fuels), which allows for storage, transport, and reintroduction to the grid as and where required. Solar-to-fuel technologies will also reduce carbon emissions by providing alternatives to fossil fuels. One avenue for the storage of solar energy in fuel is water splitting, where solar energy is used to decompose water into gases of its constituent elements, O_2 and H_2 gases. Solar driven water splitting can proceed at the surface of a semiconductor photocatalyst. The most widely studied, and to date the benchmark, photocatalyst material is titanium dioxide (TiO_2). TiO_2 is abundant, cheap, non-toxic and stable under operating conditions. However, its large band gap means that TiO_2 is only activated by UV light, which constitutes just 4% of the incident solar energy. Thus, the focus of this thesis is the modification of TiO_2, through rational design, to enhance its photocatalytic properties. First principles density functional theory (DFT) simulations of modified TiO_2 are performed to assess the performance of the novel materials as photocatalysts for the water splitting half reactions: the oxygen and hydrogen evolution reactions. We adopt a materials descriptor approach, wherein we compute key performance indicators that can be compared across materials to evaluate the impact of the modification on the photocatalytic properties. Our results inform and explain the experimental results from collaborators in Ireland, the Netherlands and Spain.

1 Introduction

1.1 Solar Fuel Production

Two major societal challenges are (1) climate change as a result of carbon emissions and (2) the increasing global demand for energy, which simply cannot be met by continuing to exploit the available reserves of fossil fuels. Combustion of fossil fuels releases carbon into the atmosphere as CO_2, which is a major contributor to climate change, and reserves of oil and gas are diminishing, while the environmental impact of their increasingly difficult extraction becomes more and more severe.

More energy from the sun hits the earth in two hours than is consumed in one year; yet, we harness only a tiny fraction of this energy source that could alleviate the two issues outlined above. The strategy to confront these challenges will be multi-faceted, as no single technology will provide a panacea. While huge progress continues to be made in the fields of wind energy and photovoltaics, in which sunlight is converted directly to electricity, these technologies do not fully address the mismatch between supply and demand inherent in the use of intermittent renewable sources. In addition, storage of excess electricity produced by wind and solar cells is required. To this end, the efficient conversion and storage of energy in chemicals, for reintroduction to the grid as required, will play a significant role in the transition from fossil fuels to renewable energy.

Water splitting, to produce hydrogen gas (H_2), is an attractive prospect for a variety of reasons. H_2, produced from water using renewably produced electricity, *via* electrocatalysis, or by direct conversion of solar energy, *via* photocatalysis or photoelectrochemistry, offers a zero emissions fuel. H_2 has a lower heating value (LHV) (120 MJ/kg) almost three times that of gasoline (44 MJ/kg)[1] and the only by-product of

its combustion, or recombination with oxygen in a fuel cell, is water. While hydrogen is a gas, it can be stored in liquids such as methanol.

The *photocatalytic* or *photothermal* conversion of radiant energy to chemical energy stored in a fuel are two game-changing strategies to make use of the sun's energy to produce fuels in a sustainable fashion, thus addressing the supply side problem. Technology based on water splitting also tackles the emissions problem, since water is both the feedstock for the process and the only by-product of H_2 combustion.

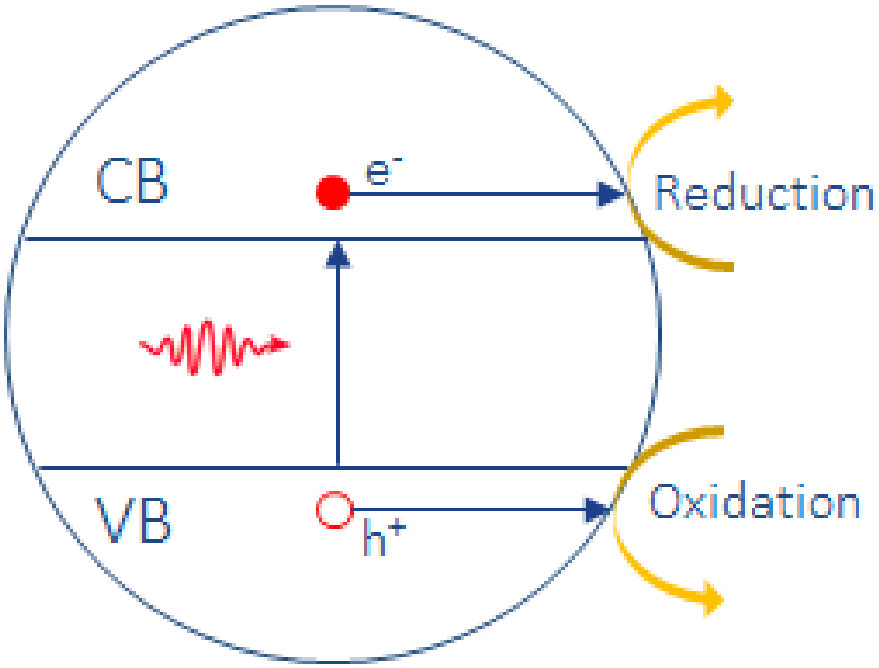

Figure 1.1 Schematic representation of the processes involved in photocatalysis. A semiconductor catalyst (circle) is illuminated by a photon (red arrow). If the photon is of sufficient energy, it can be absorbed by an electron (e^-), which is promoted from the valence band (VB) to the conduction band (CB). A hole (h^+) is left in the VB. These charge carriers separate and migrate to the surface to drive reduction and oxidation reactions.

Photocatalysts are semiconductor materials which absorb photons of energies in excess of the bandgap to produce electron-hole pairs, as shown in the schematic in **Figure 1.1**. These charge carriers separate and migrate to the surface of the catalyst where they drive

chemical reactions *via* reduction and oxidation of adsorbed species. Photocatalysis has a variety of applications, in addition to the solar production of hydrogen from water splitting; these include antimicrobial surfaces, self-cleaning surfaces and pollutant removal.[2-5] In a photothermal process,[6] a metal oxide catalyst is illuminated by concentrated sunlight to produce oxygen vacancies; these active oxygen vacancy sites are potential H_2O activation sites, whereby oxygen fills this vacancy and electrons transfer from the defective catalyst to H_2O.

To make H_2 fuel competitive, it must be produced at a cost of less than \$4/kg of H_2.[7-8] If we consider using solar to produce hydrogen, the US Department of Energy reported that their solar to hydrogen (STH) efficiency target for realistic application of hydrogen production from photocatalytic water splitting is 5%, which would allow a cost of \$4.6/kg for hydrogen generation and this is very close to the \$4/kg target. Improvements in the efficiency of photo-driven water splitting will substantially drive down the cost. In addition, the European Strategic Energy Technologies (SET) Roadmap points out that new and enhanced catalysts are required in the renewable energy generation sector.[9]

However, H_2O is very stable, and significant energy is required to break H-O bonds, which is a pre-requisite for transforming H_2O into a fuel. There is a complex series of reactions involved in splitting H_2O to hydrogen (H_2) and oxygen (O_2) gas, which necessitates a fundamental understanding of the processes and energetics involved to design viable photocatalytic water splitting materials. First principles density functional theory (DFT) simulations are crucial for the development of new multifunctional architectures that incorporate light absorbers, to produce electrons and defects, and provide active sites where reactions can take place, along with control over the reaction pathway to the desired product.

There are currently no useful materials systems that can produce hydrogen from water either photocatalytically or photothermally with adequate efficiency or outside the laboratory. There is a significant effort underway to develop materials that can be deployed to use visible light to split water, and the concept of coupling photochemistry (electron generation) and thermal catalysis (oxygen vacancy formation) is one that is of interest in the community.

1.2 Water Splitting

Water splitting, as the name suggests, is the decomposition of liquid water (H_2O) into gases of its component elements: hydrogen (H_2) and oxygen (O_2) gas. The reaction may be expressed stoichiometrically as follows:[10]

$$2H_2O \rightarrow 2H_2 + O_2 \qquad 1.2.1$$

Water is a stable molecule and water splitting is an uphill (endothermic) reaction. To compute the energy required to decompose H_2O, consider the reverse reaction and the enthalpy (H) of formation of a mole of H_2O from a mole of H_2 and half a mole of O_2. The enthalpy is the sum of the internal energy of the system (U) and the work exerted by the system on its surroundings at constant pressure, P, to occupy a volume, V:

$$H \equiv U + PV \qquad 1.2.2$$

The enthalpy of formation of one mole of H_2O, from its constituent elements in their standard form, is -285.83 kJ,[11] at standard temperature and pressure (STP: T = 298.15 K; P = 1 atm). Thus, in order to form H_2 and O_2 gas from water, an energy of 285.83 kJ mol^{-1} must be introduced into the system, some of which will be taken from the environment in the form of heat. The Gibbs free energy (G) accounts for this heat exchange; for a system in an environment with constant pressure and temperature, G is defined as:

$$G \equiv H - TS \qquad 1.2.3$$

This quantity is the enthalpy minus the heat energy exchanged between the system and its environment, which is expressed as TS, where T is the temperature and S is the entropy. For water splitting, the difference in Gibbs free energy between the initial system (liquid H_2O) and the final system (H_2 and O_2 gases) is:

$$\Delta G = \Delta H - T\Delta S = 285.83 \text{ kJ mol}^{-1} - T\Delta S \quad (1.2.4)$$

The standard entropies (J mol^{-1} K^{-1}) for liquid water and hydrogen and oxygen gases are:[12]

$$S_{\mathrm{H_2O}} = 69.9; S_{\mathrm{H_2}} = 130.7;\ S_{\mathrm{O_2}} = 205.1 \quad (1.2.5)$$

so that in STP conditions, the entropic contribution ($T\Delta S$) to the Gibbs free energy is:

$$T\Delta S = 298.15 \text{ K} \times \left(S_{\mathrm{H_2}} + \frac{1}{2}S_{\mathrm{O_2}} - S_{\mathrm{H_2O}}\right) = 48.72 \text{ kJ mol}^{-1} \quad (1.2.6)$$

Thus, the free energy input required to achieve water splitting at STP is 237.11 kJ mol^{-1} (2.46 eV per water molecule).

1.3 Electrolysis

The free energy input required to split water can be supplied by an electrical current, in a process called water electrolysis. Overall water splitting, described above in equation 1.2.1, can be divided into two half reactions: the oxygen evolution reaction (OER) and the hydrogen evolution reaction (HER), which are oxidation and reduction reactions, respectively. In water electrolysis, the redox reactions occur at the electrodes (anode and cathode) of an electrochemical cell.

The expressions which describe the two half reactions, OER and HER, depend on the conditions under which the reaction takes place. In neutral or alkaline conditions, the half reactions are[10, 13]:

OER, anode $$4OH^- \rightarrow O_2 + 2H_2O + 4e^-$$ 1.3.1.a

HER, cathode $$4H_2O + 4e^- \rightarrow 2H_2 + 4OH^-$$ 1.3.1.b

While in acidic conditions, the oxidation and reduction reactions may be expressed as[10, 13]:

OER, anode $$2H_2O \rightarrow O_2 + 4H^+ + 4e^-$$ 1.3.2.a

HER, cathode $$4H^+ + 4e^- \rightarrow 2H_2$$ 1.3.2.b

In this way, the impetus for the water splitting reaction is provided by the potential bias between the electrodes. The electrochemical cell potential (E_{cell}), is the difference between the anode and cathode potentials.

$$E_{cell} = E_{cathode} - E_{anode}$$ 1.3.3

The electrode potentials are measured relative to the Standard Hydrogen Electrode (SHE) potential, which by convention is set to 0 V at all temperatures.[14] The SHE is based on

the reduction reaction described in equation 1.3.2.b, so in this case, the cell potential is simply given by the oxidation potential: $E_{cell} = -E_{anode}$.

From equation 1.3.2.a, two molecules of H_2O are required to produce O_2; hence, ΔG is 474.22 kJ mol^{-1} for the production of O_2. This quantity is related to the cell potential *via* the following equation[14]:

$$\Delta G = -nFE_{cell} = nF\,E_{anode} \qquad 1.3.4$$

where n is the molar ratio of electrons to product ($e^-: O_2 = 4:1$) and F is the Faraday constant (~96,485 C mol^{-1}). This indicates that an anode potential of +1.23 V, vs. the SHE, is necessary for water oxidation to proceed.

Thus, the ideal thermodynamic voltage required to drive water splitting is -1.23 V at STP. However, in practice, due to losses, kinetic barriers and non-idealities in the catalysts, larger voltages are required. The difference between the thermodynamic and the applied potential is known as the overpotential and it has contributions arising from activation barriers at the anode and cathode surfaces, among other considerations. This renders the HER and, particularly, the OER sluggish and necessitates catalysts to reduce the anodic and cathodic activation barriers and increase reaction rates.

1.4 Photocatalysis

A photocatalyst is a semiconductor material that is activated upon illumination with light with energies (E_λ) in excess of its energy gap (E_g). Photoexcitation promotes electrons from the valence band (VB) of the material to the conduction band (CB), leaving holes in the VB. Should the energy gap be in excess of 1.23 eV and the redox potentials of water splitting lie within the energy gap of the photocatalyst, then photogenerated electrons and holes, in principle, will have sufficient energy to drive the HER and OER, respectively.

A successful photocatalytic reaction can be considered to consist of three steps. First, the photocatalyst absorbs a photon, with energy ($E_\lambda > E_g$) to produce photoexcited electrons and holes. Second, the charge carriers must separate and migrate to the catalyst surface where, third, they take part in reduction and oxidation reactions involving adsorbed species. Each of these processes can be optimised to enhance the overall reaction.

For a photocatalyst to achieve overall water splitting, the (ideal) lower bound for the energy gap, as mentioned, is 1.23 eV. Of the solar energy incident at earth's surface, only *ca.* 4% is in the UV range, whereas *ca.* 43% is in the visible range (VIS). Thus, a practical photocatalyst must also utilise visible light and this sets an upper bound for the energy gap of ~3 eV.[15-16] Strategies to enhance the photocatalytic activity will incorporate materials that maximise absorption of visible light while maintaining band positions which straddle the water splitting redox potentials.

A practical photocatalyst must also exhibit efficient charge carrier separation. This process competes with charge carrier recombination, which is detrimental to the photocatalytic activity. Optimisation of photocatalyst materials will include strategies to promote the separation of photoexcited electrons and holes and their migration to active

surface sites. This can be achieved by establishing an internal electric field[16] or by the introduction of charge trapping states at the catalyst surface.[17]

Finally, an efficient photocatalyst will possess an abundance of active sites at its surface. The identification of what constitutes an active site must precede approaches to engineering photocatalysts with maximal exposure of such sites. As photocatalysis is a surface phenomenon, its optimisation will typically involve structures with high surface areas

These avenues for the enhancement of the photocatalytic activity will be discussed in greater detail in subsequent chapters.

1.5 Titanium Dioxide

Titanium dioxide (TiO_2) based materials represent the most widely studied class of photocatalysts due to favourable properties such as abundance, low-cost, non-toxicity and stability under operating conditions. However, the wide band gap of TiO_2 inhibits the use of these materials as visible light active photocatalysts and much scientific endeavour focuses on inducing a red-shift in the light absorption edge *via* doping, surface modification and nanostructuring strategies.

While the thermodynamically stable rutile phase of TiO_2 exhibits a smaller band gap (3.05 eV) than the metastable anatase phase (3.20 eV), the latter polymorph has been shown to be more photocatalytically active. Thus, preserving the anatase phase under a variety of preparatory and applicatory conditions, including elevated temperatures, is of considerable interest and this is discussed in the following chapters.

TiO_2 was first demonstrated as a photoanode for water splitting by Fujishima and Honda in 1972[18] and has remained at the forefront of photocatalytic research. Indeed the benchmark material, P25, consists of interfaced rutile and anatase TiO_2 interfaces. The main focus of this thesis is the enhancement of the photocatalytic activity of TiO_2 by means of surface modification with dispersed nanoclusters of other materials. The goal is to extend the light absorption edge to longer wavelengths, suppress charge carrier recombination and increase the abundance of active surface sites. These concepts are described in more detail in **Chapter 3**.

1.6 This Thesis

All computational work and the analysis and discussion thereof, described in this thesis, were performed by the author. Some of the studies described herein were undertaken in collaboration with experimental colleagues and all experimental results were obtained by our collaborators. This thesis is constructed as follows:

In **Chapter 2**, the formalism of the Hartree and Hartree-Fock approaches to solutions of the many-body Schrodinger equation will be introduced as a prelude to a discussion of density functional theory (DFT), which is the computational method used for the work described in this thesis. **Chapter 2** also contains more practical considerations for the application of DFT and describes the details of the computational set-ups implemented in this thesis.

A literature review is provided in **Chapter 3**. This review is separated into three sections. The first section deals with computational approaches to the study of photocatalytic materials and introduces the concept of materials descriptors – key performance indicators, which can be computed to assess the viability of a candidate photocatalyst material. The following two sections provide an overview of the state-of-the-art as it pertains to catalysts for the OER and HER, respectively.

Chapter 4 describes the results of three combined experimental and computational studies of doped TiO_2. These studies were undertaken in collaboration with experimental colleagues and focus on the impact of copper (Cu), molybdenum (Mo), and Indium (In) doping on the anatase-to-rutile phase transition and the photocatalytic activity of the titania host. Each section of **Chapter 4** will first describe selected experimental results, which were performed by our collaborators, before describing the complementary

computational work, which was performed by the author, and a comparison of the experimental and DFT results.

Chapter 5 describes four studies regarding surface modified TiO_2. Three of these studies involve metal oxide modifiers: SnO and MgO; CeO_2; and MnO_x. The fourth study, which was performed in combination with experiment, involves hexagonal BN at the anatase TiO_2 surface and selected experimental results are provided before an in-depth discussion of the computational work. In each study, the composite surfaces are characterised in terms of modifier adsorption energies, local atomic structure at the interface, cation and anion oxidation states, light absorption properties, and charge carrier separation and localisation. For the metal oxide modified surfaces, additional analysis includes calculations of oxygen vacancy formation energies, as the reducibility of the surfaces has consequences for the photocatalytic activity.

Chapter 6 describes studies of water adsorption and the water oxidation process at titania surfaces modified with metal oxide nanoclusters. This chapter contains results for water adsorption at the CeO_x- and MnO_x-modified titania surfaces, which were characterised in detail in **Chapter 5**. **Chapter 6** also contains the results of a combined experimental and computational study of rutile TiO_2 modified with alkaline earth oxide (AEO) modifiers. In this description, the results of experimental characterisation, performed by our collaborators, are discussed together with the computational results to facilitate direct comparison between experiment and complementary computational models.

In **Chapter 7**, the TiO_2 rutile (110) surface is modified with nanoclusters of composition Sn_4S_4, Sn_4Se_4, Zn_4S_4 and Zn_4Se_4. The goal of modification with sulphide and selenide nanoclusters is to endow the titania surface with active sites for the hydrogen evolution reaction. These composite materials are assessed in terms of their light absorption

properties, charge carrier separation and localisation, and the free energies of H adsorption at various coverages. This latter quantity is a descriptor for the HER activity, as will be discussed in detail in **Chapter 3**.

The study described in **Chapter 8** was conducted in collaboration with colleagues in University of Barcelona. The goal of this work was to compare two different implementations of DFT+U in their description of the material properties of a titania nanoparticle. The codes used in this study were FHI-aims and VASP, which are based on atom-centred and plane wave potentials, respectively. Hence, they differ in their application of the +U correction. FHI-aims calculations were performed in Barcelona and VASP calculations were performed by the author. We choose a TiO_2 nanoparticle as our model system as this presents with unique features not seen in bulk or surface calculations, such as under-coordinated ions and edge and corner sites. The results in **Chapter 8** represent a systematic study of variations in the material properties, in particular, the geometry and energy gap, with changes in the value of the +U correction. These trends are compared between the FHI-aims and VASP solutions.

Chapter 9 contains a perspective on the results of this thesis and provides an outlook for ongoing work and future directions. This chapter is concluded with considerations for the expansion and refinement of our computational models and other approaches to the modelling of photocatalyst materials.

1.7 Chapter References

1. Wallace, J. S.; Ward, C. A., Hydrogen as a fuel. *International Journal of Hydrogen Energy* **1983,** *8* (4), 255-268.
2. Jiang, C.; Moniz, S. J. A.; Wang, A.; Zhang, T.; Tang, J., Photoelectrochemical devices for solar water splitting - materials and challenges. *Chem. Soc. Rev.* **2017,** *46* (15), 4645-4660.
3. Fujishima, A.; Zhang, X.; Tryk, D. A., TiO_2 photocatalysis and related surface phenomena. *Surface Science Reports* **2008,** *63* (12), 515-582.
4. Ni, M.; Leung, M. K. H.; Leung, D. Y. C.; Sumathy, K., A review and recent developments in photocatalytic water-splitting using TiO_2 for hydrogen production. *Renewable and Sustainable Energy Reviews* **2007,** *11* (3), 401-425.
5. Maeda, K.; Domen, K., Photocatalytic Water Splitting: Recent Progress and Future Challenges. *The Journal of Physical Chemistry Letters* **2010,** *1* (18), 2655-2661.
6. Muhich, C. L.; Ehrhart, B. D.; Al-Shankiti, I.; Ward, B. J.; Musgrave, C. B.; Weimer, A. W., A review and perspective of efficient hydrogen generation via solar thermal water splitting. *Wiley Interdisciplinary Reviews: Energy and Environment* **2016,** *5* (3), 261-287.
7. Pinaud, B. A.; Benck, J. D.; Seitz, L. C.; Forman, A. J.; Chen, Z.; Deutsch, T. G.; James, B. D.; Baum, K. N.; Baum, G. N.; Ardo, S.; Wang, H.; Miller, E.; Jaramillo, T. F., Technical and economic feasibility of centralized facilities for solar hydrogen production via photocatalysis and photoelectrochemistry. *Energy & Environmental Science* **2013,** *6* (7), 1983-2002.
8. Man, I. C.; Su, H.-Y.; Calle-Vallejo, F.; Hansen, H. A.; Martínez, J. I.; Inoglu, N. G.; Kitchin, J.; Jaramillo, T. F.; Nørskov, J. K.; Rossmeisl, J., Universality in Oxygen Evolution Electrocatalysis on Oxide Surfaces. *ChemCatChem* **2011,** *3* (7), 1159-1165.
9. Luttrell, T.; Halpegamage, S.; Tao, J.; Kramer, A.; Sutter, E.; Batzill, M., Why is anatase a better photocatalyst than rutile? - Model studies on epitaxial TiO_2 films. *Scientific Reports* **2014,** *4* (1), 4043.
10. Yan, Y.; Xia, B. Y.; Zhao, B.; Wang, X., A review on noble-metal-free bifunctional heterogeneous catalysts for overall electrochemical water splitting. *Journal of Materials Chemistry A* **2016,** *4* (45), 17587-17603.
11. Chase, M. W., Jr., NIST-JANAF Themochemical Tables, Fourth Edition. *J. Phys. Chem. Ref. Data, Monograph 9* **1998**, 1-1951.
12. Alberty, R. A., Standard molar entropies, standard entropies of formation, and standard transformed entropies of formation in the thermodynamics of enzyme-catalyzed reactions. *The Journal of Chemical Thermodynamics* **2006,** *38* (4), 396-404.
13. Zou, X.; Zhang, Y., Noble metal-free hydrogen evolution catalysts for water splitting. *Chemical Society Reviews* **2015,** *44* (15), 5148-5180.
14. Bratsch, S. G., Standard Electrode Potentials and Temperature Coefficients in Water at 298.15 K. *Journal of Physical and Chemical Reference Data* **1989,** *18* (1), 1-21.
15. Zou, Z.; Ye, J.; Sayama, K.; Arakawa, H., Direct splitting of water under visible light irradiation with an oxide semiconductor photocatalyst. *Nature* **2001,** *414* (6864), 625-627.
16. Chen, X.; Shen, S.; Guo, L.; Mao, S. S., Semiconductor-based Photocatalytic Hydrogen Generation. *Chemical Reviews* **2010,** *110* (11), 6503-6570.
17. Linsebigler, A. L.; Lu, G.; Yates, J. T., Photocatalysis on TiO_2 Surfaces: Principles, Mechanisms, and Selected Results. *Chemical Reviews* **1995,** *95* (3), 735-758.

18. Fujishima, A.; Honda, K., Electrochemical photolysis of water at a semiconductor electrode. *Nature* **1972,** *238* (5358), 37-8.

2 Density Functional Theory and Computational Methodology

2.1 Introduction – the many-body problem

Density Functional Theory (DFT) is often dubbed "the workhorse of computational chemistry" and this is certainly true of the work described in this thesis. This chapter introduces the motivation and formalism of DFT, from the point of view of quantum chemistry and solutions of the time-independent many-body Schrodinger equation. Practical considerations for the implementation of DFT and the computational set up adopted in this thesis are also introduced and discussed.

The motivation and grand challenge of computational quantum chemistry is the solution of the time-independent many-body Schrodinger equation. Consider a system of N electrons, with coordinates $\{\boldsymbol{r}_1 \dots \boldsymbol{r}_N\}$, and M nuclei, with coordinates $\{\boldsymbol{R}_1 \dots \boldsymbol{R}_M\}$. All information about this system is contained in the wave function, whose variables depend on the degrees of freedom of the system. For example, the variables corresponding to the i[th] electron consist of three spatial coordinates, encapsulated by $\boldsymbol{r}_i (\in \mathbb{R}^3)$, and its spin, σ_i. However, for simplicity, we can neglect spin considerations and denote the wave function as $\Psi(\boldsymbol{r}_1 \dots \boldsymbol{r}_N; \boldsymbol{R}_1 \dots \boldsymbol{R}_M) = \Psi(\boldsymbol{r}; \boldsymbol{R})$. The time-independent Schrodinger equation has the form[1]:

$$\mathcal{H}\,\Psi(\boldsymbol{r}; \boldsymbol{R}) = E\,\Psi(\boldsymbol{r}; \boldsymbol{R}) \qquad 2.1$$

where $\mathcal{H}$ is the Hamiltonian operator and E is the total energy of the system. In the absence of magnetic or electric fields, the Hamiltonian has the form[1]:

$$\mathcal{H} = \mathcal{T}_e + \mathcal{T}_n + \mathcal{V}_{en} + \mathcal{V}_{ee} + \mathcal{V}_{nn} \qquad 2.2$$

The first two terms, $\mathcal{T}_e$ and $\mathcal{T}_n$, relate to the kinetic energy of the electrons and nuclei, respectively. The terms $\mathcal{V}_{en}$, $\mathcal{V}_{ee}$ and $\mathcal{V}_{nn}$ describe the potential energy and derive from the electron-nucleus, electron-electron and nucleus-nucleus Coulomb interactions. Adopting atomic units, where the reduced Planck's constant, $\hbar$, the electron mass and charge, m_e and e, and $4\pi\epsilon_0$, where ϵ_0 is the vacuum permittivity, are all set to unity, the Hamiltonian in 2.2 can be expressed, more explicitly, as follows[1]:

$$\mathcal{H} = -\sum_i \frac{1}{2}\nabla_i^2 - \sum_P \frac{1}{2M_P}\nabla_P^2 - \sum_{i,P} \frac{Z_p}{|\boldsymbol{r}_i - \boldsymbol{R}_P|} + \frac{1}{2}\sum_{i,j\neq i} \frac{1}{|\boldsymbol{r}_i - \boldsymbol{r}_j|} + \frac{1}{2}\sum_{P,Q\neq P} \frac{Z_p Z_q}{|\boldsymbol{R}_P - \boldsymbol{R}_Q|} \qquad 2.3$$

In the above, M_p and Z_p are the mass and atomic number of the pth nucleus, respectively, and ∇^2 is the Laplacian operator, which in Cartesian coordinates ($\boldsymbol{r} = (x, y, z)$) has the form[1]:

$$\nabla^2 = \frac{\partial^2}{\partial x^2} + \frac{\partial^2}{\partial y^2} + \frac{\partial^2}{\partial z^2} \qquad 2.4$$

The Hamiltonian may be simplified by introducing the Born-Oppenheimer approximation,[2] which, in essence, fixes the nuclei in space. This approximation means that the kinetic energy term for the nuclei is zero and the nucleus-nucleus Coulomb term is a constant. Under the Born-Oppenheimer approximation the new Hamiltonian can be considered as an electronic Hamiltonian, $\mathcal{H}_{elec}$, and takes the form:

$$\mathcal{H}_{elec} = -\sum_i \frac{1}{2}\nabla_i^2 - \sum_{i,P} \frac{Z_p}{|\boldsymbol{r}_i - \boldsymbol{R}_P|} + \frac{1}{2}\sum_{i,j\neq i} \frac{1}{|\boldsymbol{r}_i - \boldsymbol{r}_j|} \qquad 2.5$$
$$= \mathcal{T}_e + \mathcal{V}_{en} + \mathcal{V}_{ee}$$

In equation 2.5 the nuclei represent an external potential with which the electrons interact. A further consequence of the Born-Oppenheimer approximation is that the wave function now depends only on the electronic degrees of freedom and is parameterised by the nuclear coordinates: $\Psi(\boldsymbol{r}_1 \dots \boldsymbol{r}_N; \boldsymbol{R_1} \dots \boldsymbol{R_M}) \rightarrow \Psi_{elec}(\boldsymbol{r}_1 \dots \boldsymbol{r}_N)$. Even after the simplification of fixing the nuclear positions, the wave function still depends on $3N$ variables. In computational terms, to represent the wave function at each point of a $10 \times 10 \times 10$ grid would require the storage of $(10^3)^N$ numbers – this is prohibitively large, even for moderately sized systems.

Equation 2.5 can be restated in terms of one- and two-electron contributions to the energy as follows[1]:

$$\mathcal{H}_{elec} = \sum_i \left(-\frac{1}{2}\nabla_i^2 - \sum_P \frac{Z_p}{\boldsymbol{r}_{i,P}} \right) + \frac{1}{2}\sum_{i,j\neq i} \left(\frac{1}{\boldsymbol{r}_{i,j}} \right) \qquad 2.6$$
$$= \sum_i \hbar_i + \frac{1}{2}\sum_{i,j\neq i} \mathcal{V}_{i,j}$$

Where $\boldsymbol{r}_{i,P}$ and $\boldsymbol{r}_{i,j}$ denote $|\boldsymbol{r}_i - \boldsymbol{R}_P|$ and $|\boldsymbol{r}_i - \boldsymbol{r}_j|$, respectively. The terms $\hbar_i$ are one-electron operators and extract the kinetic energy of the electrons and their Coulomb potential energy due to interaction with the external potential of the nuclei. The terms $\mathcal{V}_{i,j}$ are two-electron operators and account for the electron-electron interaction.

In summary, the goal of computational quantum chemistry is the solution of the time-independent Schrodinger equation, which, after application of the Born-Oppenheimer approximation, has the form[1]:

$$\mathcal{H}_{elec}\Psi_{\text{elec}}(\boldsymbol{r}) = \left(\sum_i \hbar_i + \frac{1}{2}\sum_{i,j\neq i} \mathcal{V}_{i,j}\right)\Psi_{elec}(\boldsymbol{r}) = E_{elec}\Psi_{elec}(\boldsymbol{r}) \qquad 2.7$$

Adopting *bra-ket* notation and dropping the "elec" subscript, equation 2.7 can also be expressed as:

$$\mathcal{H}|\Psi\rangle = \left(\sum_i \hbar_i + \frac{1}{2}\sum_{i,j\neq i} \mathcal{V}_{i,j}\right)|\Psi\rangle = E|\Psi\rangle \qquad 2.8$$

The total energy of the system, with normalised wave function $|\Psi\rangle$ (i.e., $\langle\Psi|\Psi\rangle = 1$) can be extracted from equation 2.8 as follows:

$$E = \langle\Psi|\mathcal{H}|\Psi\rangle = \langle\Psi|\left(\sum_i \hbar_i + \frac{1}{2}\sum_{i,j\neq i} \mathcal{V}_{i,j}\right)|\Psi\rangle \qquad 2.9$$

Where $\langle\Psi|\mathcal{O}|\Psi\rangle$ represents the expectation value of the operator $\mathcal{O}$. In particular, equation 2.9 is minimised for the ground state wave function, yielding the ground state energy.

2.2 Hartree and Hartree-Fock Approximations

2.2.1 Hartree Approximation

In the Hartree (H) approximation, the N-electron wave function is approximated by the product of N orthonormal single-particle wave functions[3]:

$$\Psi_{\mathrm{H}}(\boldsymbol{r}_1 \ldots \boldsymbol{r}_N) = \prod_i^N \phi_i(\boldsymbol{r}_i) \qquad 2.10$$

This scheme treats the electrons as independent particles and incorporates the electron-electron Coulomb potential energy *via* a mean-field approach. Inserting the wave function in 2.10 into equation 2.9 yields the Hartree approximation to the total energy:

$$E_H = \sum_i \langle \phi_i | \hbar_i | \phi_i \rangle + \frac{1}{2} \sum_{i,j \neq i} \langle \phi_i \phi_j | \mathcal{V}_{i,j} | \phi_i \phi_j \rangle \qquad 2.11$$

By applying the variational principle and implementing Lagrange multipliers, it is possible to derive the single-particle Hartree equations[3]:

$$\left(\hbar_i + \sum_{j \neq i} \langle \phi_j | \mathcal{V}_{i,j} | \phi_j \rangle \right) | \phi_i \rangle = (\hbar_i + \mathcal{V}_H) | \phi_i \rangle = \epsilon_i | \phi_i \rangle \qquad 2.12$$

The single electron operator, $\hbar_i$, extracts the kinetic energy of the electrons and the potential energy due to their Coulomb interaction with the nuclei. The operator $\mathcal{V}_H$ is the Hartree or Coulomb term and accounts for the Coulomb interaction between the i^{th} electron and the charge density due to the remaining $N - 1$ electrons.

2.2.2 Hartree-Fock Approximation

The Hartree wave function does not satisfy the axiom of anti-symmetry of fermionic wave functions. The anti-symmetry requirement arises from the indistinguishability of electrons and the Pauli exclusion principle and states that the wave function must be anti-symmetric under the exchange of particles:

$$\Psi(\dots \boldsymbol{r}_i \dots \boldsymbol{r}_j \dots) = -\Psi(\dots \boldsymbol{r}_j \dots \boldsymbol{r}_i \dots) \tag{2.13}$$

In the Hartree-Fock (HF) scheme, the wave function is approximated as belonging to a subset of anti-symmetric many-body wave functions known as Slater determinants. The Hartree-Fock wave function takes the form[3]:

$$\Psi_{HF}(\boldsymbol{r}_1 \dots \boldsymbol{r}_N) = \frac{1}{\sqrt{N!}} \begin{vmatrix} \phi_1(\boldsymbol{r}_1) & \dots & \phi_1(\boldsymbol{r}_N) \\ \vdots & \ddots & \vdots \\ \phi_N(\boldsymbol{r}_1) & \dots & \phi_N(\boldsymbol{r}_N) \end{vmatrix} \tag{2.14}$$

Using a wave function of this form in equation 2.14 gives the following expression for the energy of the system:

$$E_{HF} = \sum_i \langle \phi_i | \hbar_i | \phi_i \rangle + \frac{1}{2} \sum_{i,j \neq i} \langle \phi_i \phi_j | \mathcal{V}_{i,j} | \phi_i \phi_j \rangle - \frac{1}{2} \sum_{i,j \neq i} \langle \phi_i \phi_j | \mathcal{V}_{i,j} | \phi_j \phi_i \rangle \tag{2.15}$$

The first two terms are equivalent to the Hartree approximation to the total energy; the last term is the so-called Fock exchange energy. By again applying the variational method, the single particle Hartree-Fock equations can be derived. An artefact of describing the wave function as a Slater determinant is the introduction of a term that exchanges the electron orbitals and so, in this instance, it is better to forego the use of *bra-ket* notation[1, 3]:

$$\left(\hbar_i + \sum_{j \neq i} \int d\boldsymbol{r_j}\, \phi_j^*(\boldsymbol{r}_j) \mathcal{V}_{i,j} \phi_j(\boldsymbol{r}_j) \right) \phi_i(\boldsymbol{r}_i)$$

$$- \sum_{j \neq i} \int d\boldsymbol{r_j}\, \phi_j^*(\boldsymbol{r}_j) \mathcal{V}_{i,j} \phi_i(\boldsymbol{r}_j) \phi_j(\boldsymbol{r}_i) \qquad 2.16$$

$$= (\hbar_i + \mathcal{V}_H + \mathcal{V}_F) \phi_i(\boldsymbol{r_i}) = \epsilon_i \phi_i(\boldsymbol{r}_i)$$

Note that in equation 2.16, one can remove the $(j \neq i)$ condition in the summations as the instances of $(j = i)$ cancel out in the Hartree and Fock terms; i.e. in the HF scheme there is no self-interaction. In the HF approximation, the electron energy has contributions due to its kinetics and its interaction with the external potential of the nuclei, which are represented by the single-electron operator, $\hbar_i$. The Hartree term describes the Coulomb interaction of the electron with the mean field due to all other electrons. The Fock term has no intuitive physical meaning and is quantum mechanical in nature – with the inclusion of spin, the Fock term is only non-zero for orbitals with like spin and is the manifestation of the Pauli exclusion principle. In this scheme, electron correlation is only accounted for insofar as electrons of like spin avoid each other.

2.3 Density Functional Theory

Rather than dealing with the mysterious and unobservable wave function, another approach to the many-body problem is to consider the electron density, which is observable and can be measured experimentally. The electron density is[4]:

$$n(\boldsymbol{r}) = N \int d\boldsymbol{r}_2 \ldots \int d\boldsymbol{r}_N \, \Psi^*(\boldsymbol{r}, \boldsymbol{r}_2 \ldots \boldsymbol{r}_N)\Psi((\boldsymbol{r}, \boldsymbol{r}_2 \ldots \boldsymbol{r}_N)) \qquad 2.17$$

This quantity describes the probability of finding an electron in a volume element $d\boldsymbol{r}$ given $N-1$ electrons at arbitrary positions defined by the wave function Ψ. However, such an approach must be justified; it must be shown that no information is lost and that all properties of the system are uniquely determined by the electron density. Such justification was provided Hohenberg and Kohn, whose theorems underpin Density Functional Theory (DFT).

The functional in DFT is similar to a function, but rather than taking a number or set of numbers as its argument, a functional maps a function to a number. This is best expressed as follows for a function $f(\mathrm{x})$ and a functional $F[f]$:

$$x \xrightarrow{f(x)} y$$

$$f(x) \xrightarrow{F[f]} y \qquad 2.18$$

2.3.1 Hohenberg-Kohn Theorems

The Hamiltonian in equation 2.5 can be restated such that the electron-nucleus interaction is relabelled as an external potential:

$$\mathcal{H} = \mathcal{T}_{\mathrm{e}} + \mathcal{V}_{ee} + \mathcal{V}_{ext} \qquad 2.19$$

The first Hohenberg-Kohn theorem[4-6] states that the external potential, $\mathcal{V}_{ext}$, is uniquely determined, up to a constant, by the electron density; i.e. two external potentials, differing by more than a constant, cannot yield the same electron density. Stated in the language of Density Functional Theory (DFT): the external potential is a functional of the electron density.

The first two terms of the Hamiltonian, $\mathcal{T}_e$ and $\mathcal{V}_{ee}$, are universal operators and are not specific to any particular system or arrangement of the nuclei; i.e. their form does not depend on the system.[4] Thus, one can deduce that the ground state properties of the system are determined by the external potential and therefore by the ground state electron density, $n_0(\boldsymbol{r})$. In the words of Hohenberg and Kohn[5]: "[*The external potential*] $v_{ext}(\boldsymbol{r})$ *is (to within a constant) a unique functional of* $n_0(\boldsymbol{r})$*; since, in turn,* $v_{ext}(\boldsymbol{r})$ *fixes* $\mathcal{H}$ *we see that the full many-particle ground state is a unique functional of* $n_0(\boldsymbol{r})$".

The second Hohenberg-Kohn theorem[4-6] states that there exists a density functional, $E_{HK}[n]$, such that, for a given external potential, its minimum is the ground state energy and this is attained at the ground state electron density:

$$E_{GS} = \min(E_{HK}[\mathrm{n}]) = E_{HK}(n_0) \qquad 2.20$$

Equation 2.9, which extracts the total energy of a system based on its wave function, can be restated in functional terms – the total energy is a functional of the wave function:

$$E[\Psi] = \langle\Psi|\mathcal{H}|\Psi\rangle = \langle\Psi|\mathcal{T}_{\mathrm{e}} + \mathcal{V}_{ee}|\Psi\rangle + \langle\Psi|\mathcal{V}_{ext}|\Psi\rangle \qquad 2.21$$

According to the first HK theorem, the Hamiltonian is uniquely determined as a functional of the electron density and so equation 2.21 can be equivalently framed in terms of density functionals:

$$\begin{aligned} E_{HK}[n(\boldsymbol{r})] &= T_e[n(\boldsymbol{r})] + V_{ee}[n(\boldsymbol{r})] + V_{ext}[n(\boldsymbol{r})] \\ &= F_{HK}[n(\boldsymbol{r})] + \int \mathcal{v}_{ext}(\boldsymbol{r}) n(\boldsymbol{r}) d\boldsymbol{r} \end{aligned} \qquad 2.22$$

In the second line of equation 2.22, the energy functional is expressed as the sum of a universally valid functional, $F_{HK}[n]$, which accounts for the kinetic energy ($T_e[n]$) and electron-electron interaction energy ($V_{ee}[n]$), and a system-dependent term, which accounts for the electron-nucleus interaction energy, $\int \mathcal{v}_{ext}(\boldsymbol{r}) n(\boldsymbol{r}) d\boldsymbol{r}$.

Should the form of the functional $F_{HK}[n]$ be known, then it would be possible to minimise equation 2.22 to determine the exact ground state electron density and energy of any system, which would yield all properties of the system.[6] Unfortunately, no expression for $F_{HK}[n]$ is known, but nevertheless knowledge of its existence has spawned the field of DFT-based computational chemistry. Recalling the Hartree term from the HF approximation, the functional $F_{HK}[n]$ can be rewritten:

$$\begin{aligned} F_{HK}[n(\boldsymbol{r})] &= T_e[n(\boldsymbol{r})] + \frac{1}{2}\iint \frac{n(\boldsymbol{r}) n(\boldsymbol{r}')}{|\boldsymbol{r} - \boldsymbol{r}'|} d\boldsymbol{r} d\boldsymbol{r}' + E_{XC}[n(\boldsymbol{r})] \\ &= T_e[n(\boldsymbol{r})] + E_H[n(\boldsymbol{r})] + E_{XC}[n(\boldsymbol{r})] \end{aligned} \qquad 2.23$$

The first two terms on the right hand side of equation 2.23 represent the kinetic ($T_e[n]$) and Coulomb ($E_H[n]$) energies. The final term is the exchange-correlation functional, $E_{XC}[n]$.

In summary, the Hohenberg-Kohn theorems state that for a system with a given external potential, its properties are determined by the ground state electron density. Moreover, the ground state density can be derived through the minimisation of the total energy functional, which takes the form of equation 2.22; the total energy functional attains its minimum at the ground state density. Thus, the many body problem can be approached in terms of the 3-dimensional electron density, rather than the 3N-dimensional wave function. Up to this point, there are no approximations in DFT; however, application of DFT requires an approximation of the functional, $F_{HK}[n]$. In this way, DFT differs from the HF approach: DFT searches for approximate solutions to an exact theory, whereas HF involves exact solutions to an approximate theory.

2.3.2 Kohn-Sham Ansatz

While the Hohenberg-Kohn theorems validate the electron density as the variable from which all system properties can be determined, the Kohn-Sham approach yields a practicable framework for the implementation of DFT.[7-8] In the Kohn-Sham scheme, electrons are replaced with fictitious, non-interacting particles with the same density, $n(\boldsymbol{r})$:

$$n(\boldsymbol{r}) = \sum_i |\phi_i(\boldsymbol{r})|^2 \qquad 2.24$$

In this scheme, the particles occupy the orthonormal Kohn-Sham (KS) orbitals, ϕ_i; this facilitates computation of the kinetic energy, for which the density functional expression is not known. For this system of non-interacting particles, the energy functional in equation 2.22 can be rewritten as the Kohn-Sham functional:

$$E_{KS}[n(\boldsymbol{r})] = \sum_i \left\langle \phi_i \left| -\frac{1}{2}\nabla_{\boldsymbol{r}}^2 \right| \phi_i \right\rangle + \frac{1}{2}\iint \frac{n(\boldsymbol{r})n(\boldsymbol{r}')}{|\boldsymbol{r}-\boldsymbol{r}'|} d\boldsymbol{r}d\boldsymbol{r}' + E_{XC}[n(\boldsymbol{r})] + \int \upsilon_{ext}(\boldsymbol{r})n(\boldsymbol{r})d\boldsymbol{r} \quad 2.25$$

The first term on the right hand side returns the kinetic energy of the non-interacting system; the remainder of the kinetic energy contribution, arising from differences between the interacting and non-interacting systems, is incorporated into the exchange-correlation functional, $E_{XC}[n]$. By applying the variational principle to equation 2.25, one can derive the Kohn-Sham equations[7-8]:

$$\left(-\frac{1}{2}\nabla_{\boldsymbol{r}}^2 + \int \frac{n(\boldsymbol{r}')}{|\boldsymbol{r}-\boldsymbol{r}'|} d\boldsymbol{r}' + \frac{\delta E_{XC}[n(\boldsymbol{r})]}{\delta n(\boldsymbol{r})} + \upsilon_{ext}(\boldsymbol{r})\right)\phi_i(\boldsymbol{r}) = \epsilon_i \phi_i(\boldsymbol{r}) \quad 2.26$$

In the Kohn-Sham approach, all unknowns are funnelled into the E_{XC} term and its functional derivative, $\mathcal{V}_{XC} = \delta E_{XC}/\delta n$. If the exact forms of E_{XC} and V_{XC} were known, then the Kohn-Sham scheme would be exact; i.e. the ground state energy and density, for a given external potential, could be determined exactly *via* the Kohn-Sham equations. However, the form of these functionals is not known and so practical implementations of DFT involve approximations of these quantities. More practical considerations will be presented in the next section.

2.4 Implementation of DFT

The previous section showed that the Kohn-Sham approach to DFT involves solutions to single particle Schrodinger-like equations of the form:

$$\left(-\frac{1}{2}\nabla_{\boldsymbol{r}}^2 + \mathcal{V}_{eff}(\boldsymbol{r})\right)\phi_i(\boldsymbol{r}) = \epsilon_i\phi_i(\boldsymbol{r}) \qquad 2.27$$

Equation 2.27 is a restatement of the Kohn-Sham equations (2.26), where the effective potential term, $\mathcal{V}_{eff}$, encapsulates the attractive and repulsive Coulomb potentials, due to the nuclei and electrons, respectively, and the exchange and correlation potential, $\mathcal{V}_{XC}$.

The following sections describe practical approaches to solving the Kohn-Sham equations from a plane-wave perspective, as the work conducted in this thesis was performed with a plane-wave code. Moreover, the following discussion is limited to periodic crystals, but the arguments can be extended to include surfaces and isolated molecules.

2.4.1 Basis Set

The Kohn-Sham orbitals, $\{\phi_n\}$, can be expressed as linear combinations of appropriately chosen basis set functions, $\alpha_j(\boldsymbol{r})$[9]:

$$\phi_n(\boldsymbol{r}) = \sum_j^{\infty} c_j^n\, \alpha_j(\boldsymbol{r}) \qquad 2.28$$

In a periodic crystal, electrons move under the influence of a periodic potential; i.e., $V(\boldsymbol{r}) = V(\boldsymbol{r} + \boldsymbol{L})$, for some characteristic distance $\boldsymbol{L}$ of the crystal lattice. The Bloch theorem[10] states that the wave function for an electron in a periodic crystal can be expressed as the product of a plane wave and a function with the periodicity of the lattice.

This is also true for the Kohn-Sham quasi-particles and thus, the Kohn-Sham orbitals can be expressed as:

$$\phi_n(\boldsymbol{r}) = \mathrm{e}^{\mathrm{i}\boldsymbol{q}\cdot\boldsymbol{r}} u(\boldsymbol{r}) \qquad 2.29$$

Where $u(\boldsymbol{r}) = u(\boldsymbol{r} + \boldsymbol{L})$. Because the function $u(\boldsymbol{r})$ has the same periodicity as the lattice, it can be expressed as a linear combination of plane waves with wave vectors belonging to the reciprocal lattice (denoted $\boldsymbol{K}$):

$$u(\boldsymbol{r}) = \sum_{\boldsymbol{k}\in\boldsymbol{K}} c_{\boldsymbol{k}}\, \mathrm{e}^{\mathrm{i}\boldsymbol{k}\cdot\boldsymbol{r}} \qquad 2.30$$

Where $\{c_{\boldsymbol{k}}\}$ is the set of expansion coefficients. Combining equations 2.29 and 2.30 shows that the single particle wave function can be expressed in terms of a plane wave basis set:

$$\phi_n(\boldsymbol{r}) = \sum_{\boldsymbol{k}\in\boldsymbol{K}} c_{\boldsymbol{k}}^{\boldsymbol{n}}\, \mathrm{e}^{\mathrm{i}(\boldsymbol{q}+\boldsymbol{k})\cdot\boldsymbol{r}} \qquad 2.31$$

In equation 2.31, the wave vector $\boldsymbol{q}$ belongs to the first Brillouin zone and the reciprocal lattice vectors, $\boldsymbol{k} \in \boldsymbol{K}$, are an infinite set. However, in practice, the basis set of plane waves, indexed by their reciprocal lattice vectors, is truncated for $\boldsymbol{k} > \boldsymbol{k}_{\boldsymbol{max}}$, where the cut-off is chosen such that the wave function is described with adequate accuracy by the finite basis set.

Equipped with a finite basis set, the solution of the Kohn-Sham equations reduces to a matrix equation of the form:

$$\mathrm{HC} = \mathrm{SCE} \qquad 2.32$$

Where H is the Hamiltonian matrix, constructed from the single-particle Hamiltonian operators, C is a square matrix constructed from columns of the expansion coefficients, S is the overlap matrix of basis functions and E is a diagonal matrix with energy eigenvalues on the diagonal.

2.4.2 Pseudopotentials

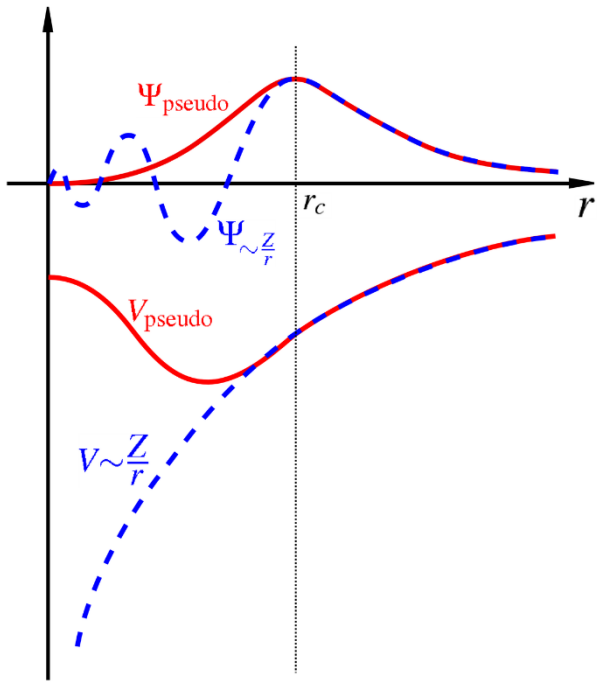

Figure 2.1 Graphical depiction of the pseudo potential approach, where the real potential and wave function are replaced by smoothly varying functions for $\boldsymbol{r < r_c}$ to minimise the number of basis set functions required to describe the wave function.

In plane-wave implementations, the nuclei are replaced with ions consisting of the nuclei and their core electrons. The core electrons are those that are strongly bound and localised at their parent nuclei; thus, they do not take part in bonding, nor contribute to the material properties, to the same extent as the valence electrons. This is known as the frozen core approximation and reduces the degrees of freedom considerably, so that only the valence electrons must be solved for.

The valence wave functions vary rapidly in the vicinity of the ions to maintain orthonormality with the core wave functions and to describe this behaviour a large number of basis set functions would be required. In practice, for distances shorter than some "core" radius, $\boldsymbol{r}_c$, from the nucleus, the ion potential is replaced by a pseudopotential. In this scheme, the potential and wave function are described exactly for $\boldsymbol{r} > \boldsymbol{r}_c$, and replaced with pseudo-descriptions for $\boldsymbol{r} < \boldsymbol{r}_c$, as shown in **Figure 2.1**. The smoother behaviour of the wave functions under the influence of the pseudopotential in the vicinity of the ions means that fewer basis functions are required.

2.4.3 Projector Augmented Waves (PAW)

In the projector augmented wave (PAW) approach,[11] space is partitioned into regions close to ($\boldsymbol{r} < \boldsymbol{r}_c$) and far from the ions ($\boldsymbol{r} > \boldsymbol{r}_c$), which are denoted the core and interstitial regions, respectively. In the PAW method, the Kohn-Sham orbital is written as the sum of three contributions:

$$\phi_n(\boldsymbol{r}) = \tilde{\phi}_n(\boldsymbol{r}) + \sum_a \phi_n^a(\boldsymbol{r}) - \sum_a \tilde{\phi}_n^a(\boldsymbol{r}) \qquad 2.33$$

In equation 2.33, $\tilde{\phi}_n(\boldsymbol{r})$ denotes the pseudo-wave function, which is defined everywhere, is smooth and permits expression with a plane wave basis. Moreover, $\tilde{\phi}_n(\boldsymbol{r})$ matches $\phi_n(\boldsymbol{r})$ exactly in the interstitial region. For the second two terms on the right hand side, the summations run over the ions in the system. Each of the functions in the summations are defined for the core regions; the terms $\phi_n^a(\boldsymbol{r})$ and $\tilde{\phi}_n^a(\boldsymbol{r})$ represent all-electron and pseudo-one-centre wave functions, respectively. The all electron functions $\phi_n^a(\boldsymbol{r})$ account for the rapid oscillations in the core region and the pseudo functions $\tilde{\phi}_n^a(\boldsymbol{r})$ are smooth in

this region. The quantities $\phi_n^a(\boldsymbol{r})$ and $\tilde{\phi}_n^a(\boldsymbol{r})$ can be expressed in terms of partial and pseudo partial wave basis sets, $\{\alpha_i\}$ and $\{\tilde{\alpha}_i\}$, so that equation 2.33 can be rewritten:

$$|\phi_n\rangle = |\tilde{\phi}_n\rangle + \sum_a \sum_i (|\alpha_i^a\rangle - |\tilde{\alpha}_i^a\rangle)\langle p_i^a|\tilde{\phi}_n\rangle \qquad 2.34$$

Where the terms $\{p_i^a\}$ are the species-specific projector functions. Thus, solving the modified Kohn-Sham equations for the pseudo wave functions $\tilde{\phi}_n(\boldsymbol{r})$, and knowing the transformation described in equation 2.34, allows one to derive the wave functions $\phi_n(\boldsymbol{r})$.

2.4.4 Approximations for the exchange-correlation functional

2.4.4.1 Local Density Approximation (LDA)

In the local density approximation (LDA) the exchange and correlation contributions to the energy are approximated to those arising from a homogeneous electron gas[12]:

$$E_{XC}^{LDA}[n(\boldsymbol{r})] = \int n(\boldsymbol{r})\epsilon_{XC}(n(\boldsymbol{r}))\, d\boldsymbol{r} \qquad 2.35$$

The quantity $\epsilon_{XC}(n(\boldsymbol{r}))$ is the exchange-correlation energy per particle of a uniform electron gas of density $n(\boldsymbol{r})$. This is weighted by $n(\boldsymbol{r})$ in the integral; i.e., the probability of finding an electron at position $\boldsymbol{r}$. The ϵ_{XC} term can be expressed as the sum of exchange and correlation contributions:

$$\epsilon_{XC} = \epsilon_X + \epsilon_C \qquad 2.36$$

The exchange term, ϵ_X, is known analytically; the correlation term, ϵ_C, is known analytically in the limits of high and low density; and between these limits, numerical expressions have been determined through quantum Monte Carlo (QMC) simulations.

LDA functionals perform reasonably well in their description of extended systems, where there is moderate variation in the electron density, but yield poor descriptions of atoms and molecules, where a feature of the charge density is its inhomogeneity. Thus, while LDA was the *de facto* functional, the implementation of DFT was restricted to realm of solid-state physics.

2.4.4.2 Generalised Gradient Approximation (GGA)

The generalised gradient approximation (GGA) contains the local density approximation and extends upon it by including the density gradient to account for the non-homogeneity of the true electron density.[12] The general form of the GGA approximation is given by:

$$E_{XC}^{GGA} = \int f(n, \nabla n)\, d\boldsymbol{r} \qquad 2.37$$

In the GGA class of approximations, the exchange-correlation energy is a functional of the density and its gradient, with constraints imposed on the exchange and correlation holes.

There are a number of functionals that fall under the GGA banner, including PW91,[13] PBE[14] and LYP,[15] and these are the staples of what is termed standard DFT. However, GGA functionals also have their limitations. Of relevance to the work of this thesis, standard DFT underestimates semiconductor band gaps and favours delocalisation of charge, particularly for the *d*-orbitals of the transition metals and their oxides. These deficiencies arise due to the so-called self-interaction error and there exist a number of strategies for their circumvention, which will be described in the following sections.

2.5 Beyond DFT

2.5.1 Hybrid DFT

In Hybrid DFT, the XC functional is replaced by an admixture of weighted contributions from GGA, LDA and the exact Fock exchange term. One of the simpler expressions for a Hybrid functional is given in the PBE0 scheme[12]:

$$E_{XC}^{Hyb} = E_{XC}^{GGA} + \alpha(E_X^{HF} - E_X^{GGA}) \qquad 2.38$$

Where the single parameter, α, can be tailored to the system under study.[16] Typically, the default value for α is 0.25. Hybrid functionals provide improved descriptions of structural properties and band gaps and yield solutions with a higher degree of spatial localisation, which addresses the shortcomings of standard-DFT with regard to transition metal oxide systems. However, inclusion of the Fock exchange makes Hybrid DFT computationally heavy, and until recent improvements in computing power, Hybrid calculations were not suitable for large systems.

2.5.2 DFT+U

Another approach to resolve the delocalisation issue is to incorporate on-site Coulomb interactions *via* the introduction of a Hubbard-like U parameter. This approach, known as DFT+U, is a combination of standard DFT and a Hubbard Hamiltonian for the Coulomb repulsion and exchange interaction. On-site Coulomb repulsion is particularly important for *d*- and *f*-electrons, owing to the narrow band-width, and the Hubbard correction is applied only to those orbitals that require it, with other electrons described by standard DFT. In the Dudarev method,[17] the DFT+U energy functional has the form:

$$E_{DFT+U} = E_{DFT} + \frac{(U-J)}{2}\sum_{m,\sigma}\left[n_{m,\sigma} - n_{m,\sigma}^2\right] \qquad 2.39$$

Where U and J are the Coulomb and exchange parameters and $n_{m.\sigma}$ represents the orbital occupancy for magnetic quantum number m and spin σ. This functional penalises partial occupation of the localised orbitals and thereby promotes levels that are completely filled or completely empty.

In the Dudarev model, the U and J parameters are combined into a single parameter, denoted $U_{eff} = U - J$. The value for U_{eff} is system and species dependent and can be determined from first principles, through linear response calculations, or semi-empirically, through comparisons with experiment.

2.6 Computational Methodology

The computational work described in this thesis was performed with the Vienna *ab initio* Simulation Package (VASP)[18-19] using PAW potentials.[11, 20] The PAW potentials separate the electrons into core and valence electrons, with the latter category described explicitly; **Table 2.1** presents the number of valence electrons considered explicitly for each atomic species.

Table 2.1 Data for the number of valence electrons (VE) treated explicitly in the PAW potentials for each species included in this thesis. The superscripts "a" and "b" refer to studies [21-23] (sections 5.2, 5.4, 5.5, 6.2 of this thesis) and [23] (section 5.2), respectively.

Species	#VE	Species	#VE
Ti	4[a] or 12	**O**	6
Cu	11	**S**	6
Mo	12	**Se**	6
In	13	**N**	5
Mg	2[b] or 8	**H**	1
Ca	8		
Sn	4[b] or 14		
Zn	12		
B	3		
Mn	13		
Ce	12		

The exchange correlation functional was approximated by the Perdew-Wang (PW91) functional,[13] which is consistent with previous work carried out in the group and thereby facilitates comparison. The DFT calculations include on-site Coulomb interactions (DFT+U) according to the Dudarev method.[17] Consequently, aspherical gradient corrections were applied throughout. All calculations were spin-polarised and no symmetry constraints were imposed.

The energy cut-off was set to $\mathrm{ENCUT} = \max[\mathrm{ENMAX}_\alpha]$, where ENMAX_α is the cut-off energy recommended in the potential for atomic species α. Typically, the energy cut-off

was 396-400 eV. However, for structural optimisation calculations, a higher value ($\times 1.3$) was selected. Threshold values of 10^{-4} eV and 0.01/0.02 eV Å^{-2} determine convergence for the energy and forces respectively. Further, study-specific details are provided in the following sections.

2.6.1 DFT+U

Table 2.2 Details, including references, for the +U values applied to each species.

Species	Orbital	+U (eV)	REF.
Ti	3*d*	4.5	24-27
Cu	3*d*	7.0	28-29
Mo	4*d*	4.0	30
Ce	4*f*	5.0	31-32
Mn	3*d*	4.0	33-34
Zn	3*d*	7.8	35

To consistently describe the partially filled *d*-states of the transition metals and the *f*-state of Ce, a Hubbard +U correction is applied. The value of the +U correction is informed by a multitude of previous work on metal oxide systems with the same VASP computational set-up. These studies are referenced throughout the thesis. While it is possible to tune the value of +U to reproduce the experimental band gap, this can have a detrimental impact on the accuracy of other material properties and is not advised. Moreover, as we shall see in **Chapter 8**, DFT+U is not a black box – the choice of +U is not transferable between codes as its impact varies depending on the basis set and the DFT+U implementation. **Table 2.2** summarises the DFT+U set-ups employed in this thesis.

An additional +U correction is applied to anion *p*-states in the photoexcitation model, as discussed in **Section 2.6.6**. Moreover, a +U correction, with U = 7 eV, is applied to O 2*p*

states in our study of Cu-doped TiO_2; this set-up is implemented to account for hole localisation at O sites in the stoichiometric Cu-doped system.

2.6.2 Model Constructions

2.6.2.1 Doping

For the doped-TiO_2 studies, the models were constructed by first computing the bulk lattice parameters for the rutile and anatase phases, within the computational set-up. These calculations were performed with a Monkhorst-Pack k-point grid of $(8 \times 8 \times 8)$ and the computed lattice parameters for rutile were: $a = b = 4.613$ Å and $c = 2.961$ Å; for anatase the lattice parameters were: $a = b = 3.791$ Å and $c = 9.583$ Å.

From these bulk unit cells, supercells were constructed such that, upon substituting a Ti ion for the dopant, the modelled dopant concentration would fall within the range considered in the experiments. The data for each study is summarised in **Table 2.3**; note that for the indium-doped TiO_2 study,[36] the higher dopant concentration is due to the presence of 2 dopants in the supercell.

Table 2.3 Details of the doped-TiO_2 models, described in **Chapter 4**. A = anatase and R = rutile.

Dopant	Phase	Supercell	Dopant %	K-points
Cu[37]	**A**	$2 \times 2 \times 2$	3.1	$4 \times 4 \times 2$
	R	$2 \times 2 \times 3$	4.2	$4 \times 4 \times 2$
Mo[38]	**A**	$3 \times 3 \times 1$	2.8	$3 \times 3 \times 4$
In[36]	**A**	$2 \times 2 \times 1$	12.5	$4 \times 4 \times 4$

2.6.2.2 Surface modification models

In modelling surface modification of a titania surface, the first step is to construct the bare surface slab. This is achieved by cleaving the bulk TiO_2 phase in the plane perpendicular to the Miller indices, (*h k l*), which specify the surface. For these slab models, the surface plane is perpendicular to the z-direction. The slab is then placed in a supercell with a vacuum gap along the z-direction, with this gap large enough so that the periodic images of the surfaces do not interact with each other. The vacuum gap and surface expansion must also be large enough such that the modifier does not interact with itself across the periodic boundaries. The energy of this bare surface model is then computed and denoted E_{surf}.

The next step in the construction is to fully relax the nanocluster modifier in the gas phase, which yields the gas-phase energy, E_{NC}. The nanocluster is then adsorbed in different configurations at the titania surface and allowed to relax. The energy of the most stable of the considered configurations is denoted $E_{NC+surf}$. The adsorption energy of the nanocluster at the surface is then calculated using:

$$E_{ads} = E_{NC+surf} - (E_{NC} + E_{surf}) \qquad 2.40$$

If the nanocluster-surface interaction is favourable, E_{ads} will be a negative number; large, negative values of E_{ads} indicate that the modifiers are strongly adsorbed at the surface and will be stable against desorption and migration at the surface to form aggregates. Our work on modified metal oxide surfaces shows that key material properties do not depend on the precise orientation of the modifiers at the surface, so long as the nanocluster modifier binds with the surface through new interfacial bonds.[39]

Oxygen ions of the cluster and surface are denoted O_C and O_S, respectively, and O_S ions are further distinguished according to their position in bridging (O_{br}) or in-plane (O_{ip}) surface sites. Interfacial bonds are identified through a combination of VASP outputs and bond-lengths. For the large supercells in the studies of surface-modified titania, the k-points are sampled at the Γ-point. For the study of metal chalcogenide nanoclusters modifying the rutile (110) surface, presented in **Chapter 7**, the k-points are sampled with a $(4 \times 4 \times 1)$ grid. Further details regarding the surface modification models are provided in **Table 2.4**.

Table 2.4 Details of the surface models described in this thesis. The three surface expansions listed for the *h*BN modifier correspond to the three different models described in **Chapter 5**. The notation ML denotes the number of monolayers in the slab. A = anatase; R = rutile.

Modifier	Phase	Surface	Expansion	ML	Vacuum Gap (Å)
MgO/SnO[23]	**A**	(101)	2×4	12	20
***h*BN**[39]	**A**	(101)	1×4	12	20
	A	(101)	1×6	12	20
	A	(101)	3×2	12	20
CeO_2[22]	**R**	(110)	2×4	18	20
MnO_x[21]	**A**	(101)	1×4	12	20
	R	(110)	2×4	18	20
MgO/CaO[40]	**R**	(110)	3×5	12	15
SnS/ZnS/SnSe/ZnSe[41]	**R**	(110)	2×4	12	10

2.6.3 Oxygen vacancy formation

To model oxygen vacancy (O_V) formation in the doped TiO_2 models, a single O ion is removed from the supercell and the formation energy is calculated using:

$$E_{vac} = E\left(\mathrm{M_xTi_{1-x}O_{2-y}}\right) + \frac{1}{2}E(\mathrm{O_2}) - E\left(\mathrm{M_xTi_{1-x}O_2}\right) \qquad 2.41$$

where $E\left(\mathrm{M_xTi_{1-x}O_{2-y}}\right)$ is the total energy of M-doped TiO_2 with a single oxygen vacancy and $E\left(\mathrm{M_xTi_{1-x}O_2}\right)$ is the total energy of M-doped TiO_2. The formation energy

is referenced to half the total energy of O_2 in the gas phase. This computation is performed for various O sites of the supercell, to identify the most stable site for vacancy formation. A similar process and formula are used to compute the formation energy of subsequent oxygen vacancies.

To model oxygen vacancy formation in surface modified TiO_2, a single O ion is removed from the metal oxide modifier and the formation energy is computed using:

$$E_{vac} = E(\mathrm{M_xO_{x-1}\text{-}TiO_2}) + \frac{1}{2}E(\mathrm{O_2}) - E(\mathrm{M_xO_x\text{-}TiO_2}) \qquad 2.42$$

This is repeated for each cluster O site. Having identified the most stable structure with a single O_V, the calculation is repeated for each of the remaining cluster O sites to determine the most stable structure with two O_V, and so on.

2.6.4 Oxidation States

Oxidation states are assessed through Bader charge analysis[42] and computed spin magnetisations. A Bader charge in the range 9.6-9.7 electrons for Ti ions is attributed to Ti^{4+}. For the case where Ti is described with 4 valence electrons, a Bader charge of 1.2-1.3 electrons corresponds to Ti^{4+}. For O^{2-} sites, the computed Bader charge is in the range 7.1-7.2 electrons. For hydroxylated surfaces, Bader charges for those oxygen atoms of the surface to which H atoms are adsorbed increase to values in the range 7.6-7.7 electrons.

Further details about the computed Bader charges and their corresponding formal charge for each of the species studied in this thesis are provided in **Table 2.5**. These values are a guide only and the interpretation of Bader charges with regard to the formal charge of

a species depends on its environment, coordination and the nature of the bond formed to its neighbouring ions. Thus, when assigning an oxidation state to an ion based on its Bader charge, it is best to also conduct an assessment of the aforementioned considerations. In particular, for oxidation or reduction of species it is important to examine the computed Bader charges before and after the charge localisation.

Table 2.5 Bader charges and the corresponding formal charges for the atomic species studied in this thesis.

Species	Formal Charge	Bader charge	Species	Formal Charge	Bader charge
Ti	4+	9.6-9.7 (1.2-1.3)	O	2-	7.1-8.0
	3+	9.8-10.0 (1.6-1.7)		1-	6.7-6.9
Cu	2+	9.6-9.8	N	3-	7.4-8.0
	1+	10.4-10.5		2-	6.8-7.1
Mo	6+	9.1	S	2-	6.8-7.0
	5+	9.9		1-	6.5-6.7
In	3+	11.0-11.4	Se	2-	6.6-6.9
Mg	2+	6.2-6.3 (0.0)		1-	6.4-6.5
Ca	2+	6.4			
Sn	2+	12.6-13.2			
	3+	12.3-12.4			
Zn	2+	11.0-11.4			
B	3+	0.0			
Mn	3+	11.2-11.3			
	2+	11.5-11.7			
Ce	4+	9.6-9.8			
	3+	9.9-10.0			

2.6.5 Projected Electronic Density of States

To examine the impact of doping/modification on the electronic and light absorption properties of the titania host/support, it is insightful to compute the projected electronic density of states (PEDOS). A PEDOS plot allows one to identify which species and orbitals contribute to features of the total DOS. For example, the total DOS can be decomposed into contributions from the nanocluster modifier and the titania support to

see how the modification impacts the band gap. For calculations of the PEDOS, Gaussian smearing, with $\sigma = 0.1$ eV, is applied. In the PEDOS plots, the titania-derived valence band maximum (VBM) is set to 0 eV and the Fermi level is represented with a vertical dashed line.

2.6.6 Photoexcitation Model

Photoexcitation is modelled by imposing a triplet electronic state on the system. This promotes an electron to the CB with a corresponding hole in the VB and enables an evaluation of the energetics and charge localisation associated with photoexcitation. The following energies are computed:

- The ground state energy of the system, yielding $E^{singlet}$.
- A single point energy calculation at the ground state geometry with the triplet state imposed, yielding $E^{unrelaxed}$.
- An ionic relaxation of the triplet electronic state, which gives $E^{relaxed}$.

From the results of these calculations we compute:

1. The singlet-triplet vertical excitation energy: $E^{vertical} = E^{unrelaxed} - E^{singlet}$.

This is the difference in energy between the ground (singlet) state and the imposed triplet state at the singlet geometry and corresponds to the simple VB-CB energy gap from the computed density of states; i.e., the optical gap.

2. The singlet-triplet excitation energy: $E^{excite} = E^{relaxed} - E^{singlet}$.

This is the difference in energy between the relaxed triplet state and the relaxed singlet state and gives an approximation of the excitation energy.

3. The triplet relaxation (carrier trapping) energy: $E^{relax} = E^{unrelaxed} - E^{relaxed}$.

This difference in energy between the unrelaxed and relaxed triplet states is the energy gained when the electron and hole are trapped at their metal and oxygen sites upon structural relaxation. This energy relates to the stability of the trapped electron and hole. These quantities are summarised schematically in **Figure 2.2**.

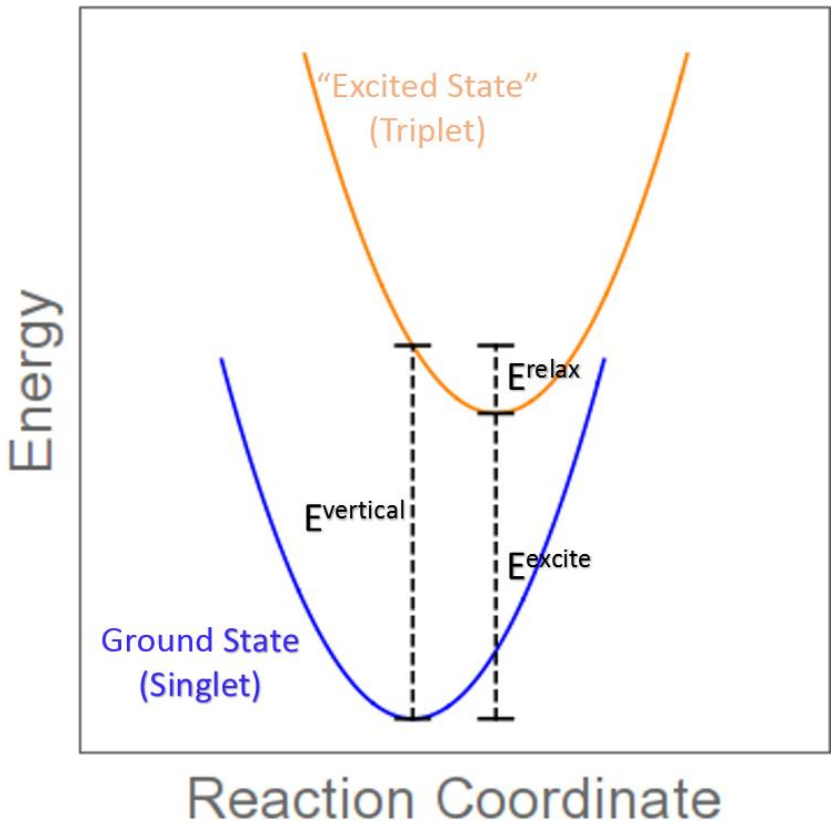

Figure 2.2 Schematic diagram of the relationship between the energies computed in the photoexcited model.

This simple model only captures transitions to a triplet excited state and excited states with a singlet configuration are not accounted for. As will be discussed further in **Chapter 3**, descriptions of excited states within a ground state theory presents challenges and this model is pragmatic in its approach. For the case of TiO_2: in the ground state, the TiO_2 VB is full and occupied by electron pairs (one spin up and one spin down). This is the singlet ground state and in VASP terms, corresponds to NUPDOWN = 0. As the VB is full, if

we impose a triplet state condition, NUPDOWN = 2, an electron is forced to the CB. This is due to the Pauli exclusion principle; i.e. no orbital can be occupied by two electrons of like-spin. This leaves a hole in the valence band. Singlet excited states cannot be probed with this model as such configurations will relax to the singlet ground state.

For calculations involving the model excited state and valence band hole formation, an additional +U correction is applied to the O 2*p*-states with U(O) = 5.5 eV. This computational set-up is used for calculations of the singlet ground state, triplet state at the ground state geometry and the fully relaxed triplet state to facilitate comparisons within the photoexcitation model. Previous work has highlighted the necessity for such a correction in obtaining a correctly localised oxygen hole state in metal oxides.[24, 26, 43-45] This is only required in the photoexcitation model; implementing +U on O 2*p* states for other calculations would make comparisons with computational studies in the literature difficult. The goal of this model is to obtain a qualitative description of the localisation and stability of photoexcited charges. In the studies of BN and metal chalcogenide modification (**Chapters 5** and **7**), +U corrections are applied to the *p*-states of N, S and Se in the photoexcitation models, with U = 5.5 eV.

Typically, analysis of the photoexcitation model corroborates predictions made from the computed PEDOS. In general, electrons are excited from the highest lying VB states, which for modified TiO_2 are derived from low-coordinated anion sites of the modifiers. The excited electrons localise in states at the bottom of the CB. The identity of these states depend on the material combination under study. For the case where the CBM is dominated by Ti 3*d* states, a Ti ion will be reduced to Ti^{3+} in the excited state. However, should the modifier contain a more reducible cation, as is the case for CeO_x-modified TiO_2 (see **Chapter 5**), then the photoexcited electron will localise at these ions in preference to Ti.

2.6.7 Water adsorption

We investigate the adsorption and activation of H_2O at various sites of the nanocluster-modified titania surfaces, taking into particular account the presence of oxygen vacancies. Adsorption energies for molecules adsorbed at the nanocluster-modified surface are calculated as:

$$E_{ads} = E_{surf+mol} - E_{surf} - E_{mol} \qquad 2.43$$

where $E_{surf+mol}$, E_{surf} and E_{mol} refer to the energies of the molecule and modified surface in interaction, the modified surface, and the gas phase H_2O molecule, respectively.

2.6.8 Water oxidation steps

After the initial water adsorption, we consider the proton-coupled electron transfer (PCET) steps proposed in a widely accepted[46-49] water oxidation pathway:

(A) $$H_2O + (*) \rightarrow {}^*OH + (H^+ + e^-)$$

(B) $$^*OH \rightarrow {}^*O + (H^+ + e^-)$$

(C) $$H_2O + {}^*O \rightarrow {}^*OOH + (H^+ + e^-)$$

(D) $$^*OOH \rightarrow O_2 + (*) + (H^+ + e^-)$$

In the above, (*) denotes the adsorption site and (*Z) denotes species Z adsorbed at a surface site. The Gibb's free energy, (ΔG), of each reaction step is computed with the inclusion of zero-point energy and entropic corrections. In this way the free energy of reaction "X" is calculated as:

$$\Delta G_X = \Delta E_X + \Delta ZPE - T\Delta S \quad (2.44)$$

In the above, ΔE_X is the difference in total energy, computed *via* DFT, between the products and reactants. The difference in zero-point energies, ΔZPE, is derived from vibrational frequencies, computed with DFT, according to the method prescribed in the work of Liao *et al*.[48] The entropic contribution, TΔS, is taken from tabulated values for the gas phase molecules and neglected for adsorbed species.

See **Table 2.6** for a comparison of values for ZPE and TS from the literature and computed in the current work. As a benchmark, we refer to the work of Valdés *et al*,[47] in which the authors examined the energies involved in water oxidation at the rutile (110) surface. The highest free energy step in this study was 2.20 eV and we use this value to decide on the favourability of the water oxidation process at the different systems under study in the current work.

Table 2.6 Entropic and zero-point energy contributions to free energies. Superscripts [a], [b] and [c] refer to computations performed in references [47], [48] and the current work, respectively.

Species	TS (eV)	ZPE (eV)[a]	ZPE (eV)[b]	ZPE (eV)[c]
H_2O	0.67	0.56	0.57	0.59
H_2	0.41	0.27	0.27	0.27
O_2	0.63	0.10	0.10	0.10
***OH**	0.00	0.35	0.37	0.32
***O**	0.00	0.05	0.04	0.07
***OOH**	0.00	0.41	0.48	0.44
***H**	0.00	---	---	0.28

Steps A and C each describe water adsorption events; however, water dissociation upon adsorption and the first dehydrogenation are dealt with implicitly as a single step. For an

explicit description, we may consider these steps as consisting of sub-steps, which for water adsorption in dissociated form may be expressed as follows:

(A1) $$H_2O + (*) \rightarrow {}^*OH + {}^*H$$

(A2) $${}^*OH + {}^*H \rightarrow {}^*OH + (H^+ + e^-)$$

And

(C1) $$H_2O + {}^*O \rightarrow {}^*OOH + {}^*H$$

(C2) $${}^*OOH + {}^*H \rightarrow {}^*OOH + (H^+ + e^-)$$

The overall free energy of a given step is then the sum of the free energies of the sub-steps, so that: $\Delta G_X = \Delta G_{X1} + \Delta G_{X2}$. Should a PCET step be thermodynamically unfavourable, this breakdown can prove insightful in identifying the underlying cause. The entropic and zero-point energy corrections to free energies of reaction steps A-D are included in **Table 2.6** and compared with values from the literature.

Table 2.6 Entropic and zero-point energy corrections to free energies of reaction steps A-D. Superscripts [a], [b] and [c] refer to computations performed in references [47], [48] and the current work, respectively.

Reaction Step	ΔZPE - TΔS (eV)[a]	ΔZPE - TΔS (eV)[b]	ΔZPE - TΔS (eV)[c]
A1	---	0.77	0.68
A2	---	-0.37	-0.32
A	0.40	0.40	0.36
B	-0.37	-0.39	-0.32
C1	---	---	0.73
C2	---	---	-0.35
C	0.39	0.47	0.38
D	-0.42	-1.08	-0.75

2.6.9 Hydrogen adsorption and Hydrogen Evolution Reaction

To assess the hydrogen evolution reaction (HER) activity of a titania surface modified with an appropriate nanocluster (e.g. metal chalcogenide/metal phosphide), we examine H adsorption at sites of both the support and the modifier. For computational studies of the HER activity of a catalyst surface it is important to consider coverage effects, particularly for metal oxide surfaces, as H binds strongly to O sites to form hydroxyls. The adsorption energy of the n^{th} H atom at the most stable surface with an existing coverage of $(n-1)$ H atoms is computed *via*:

$$\Delta E_H = E_{nH@surf} - E_{(n-1)H@surf} - \frac{1}{2}\left(E_{H_2}\right) \qquad 2.45$$

Where $E_{nH@surf}$, $E_{(n-1)surf}$, and E_{H_2} are the computed energies of the surface with n H atoms adsorbed, the surface with $(n-1)$ H atoms, and an isolated, gas phase H_2 molecule. From the chemisorption energies (ΔE_H), we compute the free energy of adsorption using:

$$\Delta G_H = \Delta E_H + \Delta E_{ZPE} - T\Delta S_H \qquad 2.46$$

Where ΔE_{ZPE} is the difference in zero point energy (ZPE) between the H atom adsorbed at the surface and in the gas phase; and $T\Delta S_H$ accounts for the difference in entropy between the final and initial state. The zero point energies, for the gas phase H_2 molecule and for H adsorbed at a surface site, are derived from computations of the vibrational frequencies, according to the method prescribed in the work of Liao *et al*.[48] For adsorption, only the vibrations of the H ion and the surface/cluster site to which it is adsorbed are considered; the ZPE for the adsorption site is then subtracted from this value. As is typical in such studies, the entropic contributions for H adsorbed at the surface are

omitted, and so the value for $-T\Delta S_H$ is taken as half the value for molecular H_2. Thus, the ZPE and entropic contributions to the free energy are obtained from:

$$\Delta E_{ZPE} - T\Delta S_H = \left(ZPE_{H*} - \frac{1}{2}ZPE_{H_2}\right) - \left(0 - \frac{1}{2}T\Delta S_{H_2}\right) \qquad 2.47$$

Chapter 7 provides further details of this model as it pertains to a specific surface.

2.6.10 van der Waals

A study of anatase TiO_2 modified with hexagonal boron nitride (*h*BN) is presented in **Section 5.3**. *h*BN has a layered structure wherein layers interact *via* van der Waals forces. Thus, it is important to account for van der Waals forces in the computational description. Two approaches for modelling the van der Waals interaction are implemented and compared. The first is the DFT-D2 method developed by Grimme.[50] This scheme involves computation of a dispersion energy correction, E_{dsip}. The second scheme, vdW-DF, was developed by Dion and colleagues[51] and implements a non-local functional that accounts for dispersion interactions in an approximate way.

Both approaches to accounting for the van der Waals interaction yield qualitatively similar results, as is discussed in more detail in **Section 5.3**.

2.7 Chapter References

1. Koch, W.; Holthausen, M. C., Elementary Quantum Chemistry. In *A Chemist's Guide to Density Functional Theory*, 2001; pp 3-18.
2. Born, M.; Oppenheimer, R., Zur Quantentheorie der Molekeln. *Annalen der Physik* **1927,** *389* (20), 457-484.
3. Misra, P. K., Chapter 7 - Electron–Electron Interaction. In *Physics of Condensed Matter*, Misra, P. K., Ed. Academic Press: Boston, 2012; pp 199-242.
4. Jones, R. O.; Gunnarsson, O., The density functional formalism, its applications and prospects. *Reviews of Modern Physics* **1989,** *61* (3), 689-746.
5. Hohenberg, P.; Kohn, W., Inhomogeneous Electron Gas. *Physical Review* **1964,** *136* (3B), B864-B871.
6. Koch, W.; Holthausen, M. C., The Hohenberg-Kohn Theorems. In *A Chemist's Guide to Density Functional Theory*, 2001; pp 33-40.
7. Koch, W.; Holthausen, M. C., The Kohn-Sham Approach. In *A Chemist's Guide to Density Functional Theory*, 2001; pp 41-64.
8. Kohn, W.; Sham, L. J., Self-Consistent Equations Including Exchange and Correlation Effects. *Physical Review* **1965,** *140* (4A), A1133-A1138.
9. Koch, W.; Holthausen, M. C., The Basic Machinery of Density Functional Programs. In *A Chemist's Guide to Density Functional Theory*, 2001; pp 93-116.
10. Bloch, F., Über die Quantenmechanik der Elektronen in Kristallgittern. *Zeitschrift für Physik* **1929,** *52* (7), 555-600.
11. Blöchl, P. E., Projector augmented-wave method. *Physical Review B* **1994,** *50* (24), 17953-17979.
12. Koch, W.; Holthausen, M. C., The Quest for Approximate Exchange-Correlation Functionals. In *A Chemist's Guide to Density Functional Theory*, 2001; pp 65-91.
13. Perdew, J. P.; Wang, Y., Accurate and simple analytic representation of the electron-gas correlation energy. *Physical Review B* **1992,** *45* (23), 13244-13249.
14. Perdew, J. P.; Burke, K.; Ernzerhof, M., Generalized Gradient Approximation Made Simple. *Physical Review Letters* **1996,** *77* (18), 3865-3868.
15. Lee, C.; Yang, W.; Parr, R. G., Development of the Colle-Salvetti correlation-energy formula into a functional of the electron density. *Physical Review B* **1988,** *37* (2), 785-789.
16. Ko, K. C.; Lamiel-García, O.; Lee, J. Y.; Illas, F., Performance of a modified hybrid functional in the simultaneous description of stoichiometric and reduced TiO_2 polymorphs. *Physical Chemistry Chemical Physics* **2016,** *18* (17), 12357-12367.
17. Dudarev, S. L.; Botton, G. A.; Savrasov, S. Y.; Humphreys, C. J.; Sutton, A. P., Electron-energy-loss spectra and the structural stability of nickel oxide: An LSDA+U study. *Physical Review B* **1998,** *57* (3), 1505-1509.
18. Kresse, G.; Furthmüller, J., Efficiency of Ab-initio Total Energy Calculations for Metals and Semiconductors using a Plane-wave Basis Set. *Computational Materials Science* **1996,** *6* (1), 15-50.
19. Kresse, G.; Furthmüller, J., Efficient Iterative Schemes for Ab-initio Total-energy Calculations using a Plane-wave Basis Set. *Physical Review B* **1996,** *54* (16), 11169.
20. Kresse, G.; Joubert, D., From ultrasoft pseudopotentials to the projector augmented-wave method. *Physical Review B* **1999,** *59* (3), 1758-1775.

21. Rhatigan, S.; Nolan, M., Activation of Water on MnO_x-Nanocluster-Modified Rutile (110) and Anatase (101) TiO_2 and the Role of Cation Reduction. *Frontiers in Chemistry* **2019,** *7* (67).
22. Rhatigan, S.; Nolan, M., CO_2 and water activation on ceria nanocluster modified TiO_2 rutile (110). *Journal of Materials Chemistry A* **2018,** *6* (19), 9139-9152.
23. Rhatigan, S.; Nolan, M., Impact of surface hydroxylation in MgO-/SnO-nanocluster modified TiO_2 anatase (101) composites on visible light absorption, charge separation and reducibility. *Chinese Chemical Letters* **2018,** *29* (6), 757-764.
24. Iwaszuk, A.; Nolan, M., SnO-nanocluster modified anatase TiO_2 photocatalyst: exploiting the Sn(ii) lone pair for a new photocatalyst material with visible light absorption and charge carrier separation. *Journal of Materials Chemistry A* **2013,** *1* (22), 6670-6677.
25. Iwaszuk, A.; Mulheran, P. A.; Nolan, M., TiO_2 nanocluster modified-rutile TiO_2 photocatalyst: a first principles investigation. *J. Mater. Chem. A* **2013,** *1* (7), 2515-2525.
26. Nolan, M., First-principles prediction of new photocatalyst materials with visible-light absorption and improved charge separation: surface modification of rutile TiO_2 with nanoclusters of MgO and Ga_2O_3. *ACS Applied Materials & Interfaces* **2012,** *4* (11), 5863-5871.
27. Morgan, B. J.; Watson, G. W., A DFT + U description of oxygen vacancies at the TiO_2 rutile (110) surface. *Surface Science* **2007,** *601* (21), 5034-5041.
28. Nolan, M.; Watson, G. W., Hole localization in Al doped silica: a DFT+ U description. *The Journal of chemical physics* **2006,** *125* (14), 144701.
29. Nolan, M.; Watson, G. W., The electronic structure of alkali doped alkaline earth metal oxides: Li doping of MgO studied with DFT-GGA and GGA+U. *Surface science* **2005,** *586* (1), 25-37.
30. Wu, M.; Yao, X.; Hao, Y.; Dong, H.; Cheng, Y.; Liu, H.; Lu, F.; Wang, W.; Cho, K.; Wang, W.-H., Electronic structures, magnetic properties and band alignments of 3*d* transition metal atoms doped monolayer MoS_2. *Physics Letters A* **2018,** *382* (2), 111-115.
31. Graciani, J.; Plata, J. J.; Sanz, J. F.; Liu, P.; Rodriguez, J. A., A theoretical insight into the catalytic effect of a mixed-metal oxide at the nanometer level: The case of the highly active metal/CeO_x/TiO_2(110) catalysts. *The Journal of Chemical Physics* **2010,** *132* (10), 104703.
32. Andersson, D. A.; Simak, S. I.; Johansson, B.; Abrikosov, I. A.; Skorodumova, N. V., Modeling of CeO_2, Ce_2O_3, and CeO_{2-x} in the LDA+U formalism. *Phys. Rev. B.* **2007,** *75* (3), 035109.
33. Franchini, C.; Podloucky, R.; Paier, J.; Marsman, M.; Kresse, G., Ground-state properties of multivalent manganese oxides: Density functional and hybrid density functional calculations. *Phys. Rev. B.* **2007,** *75* (19), 195128.
34. Kitchaev, D. A.; Peng, H.; Liu, Y.; Sun, J.; Perdew, J. P.; Ceder, G., Energetics of MnO_2 polymorphs in density functional theory. *Phys. Rev. B.* **2016,** *93* (4), 045132.
35. Iwaszuk, A.; Lucid, A. K.; Razeeb, K. M.; Nolan, M., First principles investigation of anion-controlled red shift in light absorption in ZnX (X = O, S, Se) nanocluster modified rutile TiO_2. *Journal of Materials Chemistry A* **2014,** *2* (44), 18796-18805.
36. Kumaravel, V.; Rhatigan, S.; Mathew, S.; Bartlett, J.; Nolan, M.; Hinder, S. J.; Sharma, P. K.; Singh, A.; Byrne, J. A.; Harrison, J., Indium Doped TiO_2 Photocatalysts with High Temperature Anatase Stability. *The Journal of Physical Chemistry C* **2019**.
37. Byrne, C.; Moran, L.; Hermosilla, D.; Merayo, N.; Blanco, Á.; Rhatigan, S.; Hinder, S.; Ganguly, P.; Nolan, M.; Pillai, S. C., Effect of Cu Doping on the Anatase-to-

Rutile Phase Transition in TiO_2 Photocatalysts: Theory and Experiments. *Applied Catalysis B: Environmental* **2019**.
38. Kumaravel, V.; Rhatigan, S.; Mathew, S.; Michel, M. C.; Bartlett, J.; Nolan, M.; Hinder, S. J.; Gascó, A.; Ruiz-Palomar, C.; Hermosilla, D.; Pillai, S. C., Mo doped TiO_2: impact on oxygen vacancies, anatase phase stability and photocatalytic activity. *Journal of Physics: Materials* **2020,** *3* (2), 025008.
39. Byrne, C.; Rhatigan, S.; Hermosilla, D.; Merayo, N.; Blanco, Á.; Michel, M. C.; Hinder, S.; Nolan, M.; Pillai, S. C., Modification of TiO_2 with *h*BN: high temperature anatase phase stabilisation and photocatalytic degradation of 1,4-dioxane. *Journal of Physics: Materials* **2019,** *3* (1), 015009.
40. Rhatigan, S.; Sokalu, E.; Nolan, M.; Colón, G., Surface Modification of Rutile TiO_2 with Alkaline-Earth Oxide Nanoclusters for Enhanced Oxygen Evolution. *ACS Applied Nano Materials* **2020,** *3* (6), 6017-6033.
41. Rhatigan, S.; Niemitz, L.; Nolan, M., Modification of TiO_2 with Metal Chalcogenide Nanoclusters for Hydrogen Evolution. *ChemRxiv. Preprint* **2020**.
42. Henkelman, G.; Arnaldsson, A.; Jónsson, H., A fast and robust algorithm for Bader decomposition of charge density. *Computational Materials Science* **2006,** *36* (3), 354-360.
43. Fronzi, M.; Iwaszuk, A.; Lucid, A.; Nolan, M., Metal oxide nanocluster-modified TiO_2 as solar activated photocatalyst materials. *Journal of Physics: Condensed Matter* **2016,** *28* (7), 074006.
44. Lucid, A.; Iwaszuk, A.; Nolan, M., A first principles investigation of Bi_2O_3-modified TiO_2 for visible light Activated photocatalysis: The role of TiO_2 crystal form and the Bi^{3+} stereochemical lone pair. *Materials Science in Semiconductor Processing* **2014,** *25*, 59-67.
45. Iwaszuk, A.; Nolan, M., Lead oxide-modified TiO_2 photocatalyst: tuning light absorption and charge carrier separation by lead oxidation state. *Catalysis Science & Technology* **2013,** *3* (8), 2000-2008.
46. Dahan, M. H.; Caspary Toroker, M., Water Oxidation Catalysis with Fe_2O_3 Constrained at the Nanoscale. *The Journal of Physical Chemistry C* **2017,** *121* (11), 6120-6125.
47. Valdés, Á.; Qu, Z. W.; Kroes, G. J.; Rossmeisl, J.; Nørskov, J. K., Oxidation and Photo-Oxidation of Water on TiO_2 Surface. *The Journal of Physical Chemistry C* **2008,** *112* (26), 9872-9879.
48. Liao, P.; Keith, J. A.; Carter, E. A., Water Oxidation on Pure and Doped Hematite (0001) Surfaces: Prediction of Co and Ni as Effective Dopants for Electrocatalysis. *Journal of the American Chemical Society* **2012,** *134* (32), 13296-13309.
49. Tymińska, N.; Wu, G.; Dupuis, M., Water Oxidation on Oxygen-Deficient Barium Titanate: A First-Principles Study. *The Journal of Physical Chemistry C* **2017,** *121* (15), 8378-8389.
50. Grimme, S., Semiempirical GGA-type density functional constructed with a long-range dispersion correction. *Journal of Computational Chemistry* **2006,** *27* (15), 1787-1799.
51. Dion, M.; Rydberg, H.; Schröder, E.; Langreth, D. C.; Lundqvist, B. I., Van der Waals Density Functional for General Geometries. *Physical Review Letters* **2004,** *92* (24), 246401.

3 Literature Review

3.1 Insights into Photocatalysis from Computational Chemistry

3.1.1 Introduction

Computational quantum chemistry is a powerful tool in the development of new photocatalyst materials. Models of photocatalyst materials, and the insight they provide, can be used in the rational design and screening of candidate materials or to shed light on experimental observations. Key to the performance of computational models in predicting the viability of a material for the photocatalysis of a given reaction is the definition of appropriate descriptors. In adopting a descriptor approach, we consider three key processes in photocatalysis:

(1) Light absorption to produce photoexcited electrons and holes.

(2) Separation of photoexcited electrons and holes and their migration to active surface sites.

(3) The interaction of feedstock species with active sites at the catalyst surface.

To each of these steps we can ascribe a descriptor, or set of descriptors, which we may evaluate in a computationally efficient manner to assess the material performance. In describing a photocatalyst *via* computational methods, it is important to consider each of the aforementioned processes; high performance in one step, e.g. visible light absorption, does not guarantee high efficiency. For example, a material may have optimal light

absorption properties but suffer from fast charge carrier recombination, as is commonly seen with metal-doped TiO_2.

In this section, we discuss modelling of photocatalysis from these perspectives, first in terms of the computational descriptors and then with regard to approaches for their optimisation through rational design of new materials. Further consideration will be given to other important material properties, such as stability, cost, toxicity, abundance and synthesis.

3.1.2 Computational descriptors

3.1.2.1 Light Absorption

For light absorption, the goal is to develop materials that absorb the maximum range of wavelengths of light, while maintaining appropriate valence and conduction band edge positions relative to the redox potentials of the reactants. As an example, we consider the case of hydrogen production from water splitting, which proceeds according to the two half reactions:

$$H_2O + 2h^+ \rightarrow 2H^+ + \frac{1}{2}O_2 \qquad 3.1.1$$

$$2H^+ + 2e^- \rightarrow H_2 \qquad 3.1.2$$

For the overall reaction, the change in Gibb's free energy, ΔG, is 1.23 eV per OH bond and, neglecting overpotentials, this specifies the minimum band gap for a water splitting photocatalyst. By convention, the redox potentials are measured relative to the Standard Hydrogen Electrode (SHE), for which the hydrogen evolution reaction (HER), described

by equation 3.1.2, has a reduction potential of 0 V. To catalyse the HER, the conduction band edge (CBE) of the material must be more negative than this potential.

Similarly, for the water oxidation/oxygen evolution reaction (OER), described in equation 3.1.1, to proceed, the valence band edge (VBE) of the photocatalyst must be more positive than the oxidation potential of 1.23 V (vs. SHE) for water. By convention, and for the remainder of this chapter, the band edges will be considered as ascending in energy from the valence band max (VBM), through the band gap, to the conduction band minimum (CBM). Thus, to satisfy the redox criteria, the VBM must be lower in energy than the oxidation potential and the CBM higher in energy than the reduction potential.

An obvious measure in assessing the light absorption properties of a material is the band gap, which determines the spectral range of light absorption. However, an accurate, quantitative computation of band gaps presents challenges. First principles density functional theory (DFT) calculations,[1-3] the workhorse of computational chemistry, inherently underestimate the band gap. This underestimation arises both from the approximations which are necessary to implement DFT[1-3] and, more profoundly, from the Kohn-Sham formulation[4] of the theory wherein non-interacting single-particle Kohn-Sham orbitals substitute for the many-bodied wave function. Eigenvalues of the Kohn-Sham equation are interpreted as single-particle excitation energies despite a fundamental lack of physical significance.[5-6]

To circumvent what has become known as the band gap problem, various strategies are implemented. For molecules and finite systems the band gap can be calculated, with reasonable accuracy in the ΔSCF scheme, as the difference between ionisation potential and electron affinity.[7] For a system of N electrons with ground state energy E(N) this entails calculations of energies E(N+1) and E(N-1), which is unfeasible for extended

systems with periodic boundary conditions (PBC). However, this approach can be extended to bulk systems through consideration of electron screening in the Δ-sol approach in which *N* is specified by material-specific screened volumes.[8]

The local density approximation (LDA) and generalised gradient approximation (GGA) formulations of DFT can be improved to achieve better agreement between computed band gaps and those reported from experiment (see **Figure 3.1.1**). Incorporating on-site Coulomb interactions through the introduction of a Hubbard-like U parameter is a semi-empirical approach that addresses the charge delocalisation (self-interaction) error.[9] Inclusion of the U term in the DFT+U scheme is necessary to describe localised electron and hole states and is particularly important for the partially filled *d*-states of the transition metals.[10] The value of the U correction can be tuned to reproduce the experimental band gap, although one must accept that this is detrimental to the description of other important material parameters.[11]

Another approach is to use hybrid density functionals, wherein the exchange-correlation term contains a portion of the exact Fock exchange from Hartree-Fock (HF) theory.[12] Screened hybrid schemes incorporate a screened Coulomb potential to truncate long-range HF exchange.[13] While these approaches yield better results for a variety of material properties, including the band gap, they are computationally more expensive than standard DFT and DFT+U approaches.[14] Additionally, the percentage of Fock exchange and the screening length are tuneable parameters, which are material specific,[15-17] and this complicates the application of hybrid DFT to heterostructures, which are of interest in the development of new photocatalyst materials.

The final approach we mention derives from many-body perturbation theory implementing the GW approximation.[18] In the GW approach, electrons and the Coulomb

hole that forms about them constitute quasiparticles, which interact *via* a screened interaction, W. The weak interaction between quasiparticles permits their approximation as independent particles whose propagation is described by Green functions. While the GW method provides a rigorously grounded description of accurate excitation energies it is immensely computationally expensive,[14] (see **Figure 3.1.1.b**) which prohibits its use in high-throughput applications.

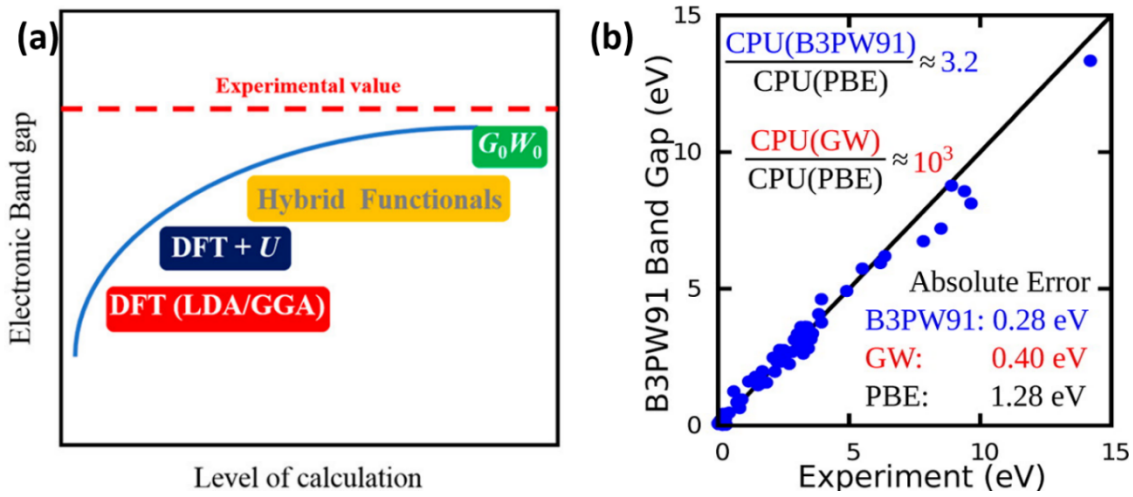

Figure 3.1.1 Schematic diagrams illustrating **(a)** accuracy of standard DFT, DFT+U, Hybrid DFT and GW-based methods in describing band gaps[5] and **(b)** the relative computational costs for standard DFT, Hybrid DFT and GW-methods weighed against their accuracy.[14]

In the context of photocatalysis, many studies take a pragmatic approach. Standard DFT and DFT+U, with appropriate choice of the U parameter, yield useful qualitative information about the atomic structure and nature of the band gap. Hybrid DFT can be run on top of the DFT+U geometry to obtain more accurate band gaps for moderately sized structures (*ca.* 100 atoms). The search for practical and efficient photocatalyst materials often builds on existing materials through a variety of modifications, nanostructuring and interfacing, which will be discussed in **Section 3.1.3**. In this way, computed density of states (DOS) plots, absorption spectra or other means of assessing

the band gap, can be compared within the computational set-up to provide information about the impact of the means of optimisation under study.

3.1.2.2 Charge Carrier Separation

The fate of photoexcited electrons and holes is of crucial importance in the performance of photocatalyst materials and their recombination must be suppressed. To assess the performance of a material in this respect computationally, it is necessary to develop models and descriptors that examine charge separation and localisation. Once again, an efficient and practical description of (photo)excited states in the confines of a ground state theory presents challenges.

A simple yet powerful approach, applicable within the DFT+U level of the theory and beyond, is to impose a triplet electronic state on the system.[19] This promotes an electron from the filled valence band to the previously empty conduction band, leaving a valence band hole. From this model, it is possible to examine the energies and charge separation/localisation relevant to photoexcitation. Three energies are computed, as described in **Chapter 2**: that of the singlet ground state, E_S; the triplet state at the ground state geometry, $E_{T\text{-}S}$; and the fully relaxed triplet state, E_T. The value of $E_S - E_{T\text{-}S}$ is analogous to the computed optical band gap, while $E_T - E_{T\text{-}S}$ reflects the energy gained by the system after geometry relaxations in response to photoexcitation and relates to the stability of the trapped electron and hole. Analysis of computed Bader charges,[20] spin magnetisations and spin density plots for the fully relaxed triplet state indicates the location of the photoexcited electron and hole and the degree of their spatial separation.

In addition to the modelling of photoexcitation *via* imposition of a triplet state, as just described, there are other strategies for investigating charge localisation computationally.

In bulk materials, an electron can be introduced into the system, which populates a conduction band state; similarly, removing one electron creates a valence band hole. In a surface, this is not possible using periodic boundary conditions. To model addition of an electron, a H atom can be added, producing a surface –OH species, which then transfers its electron to the metal oxide. To model a hole, water is adsorbed and a neutral hydrogen atom (which is an electron and a proton) is removed to leave behind a hole.

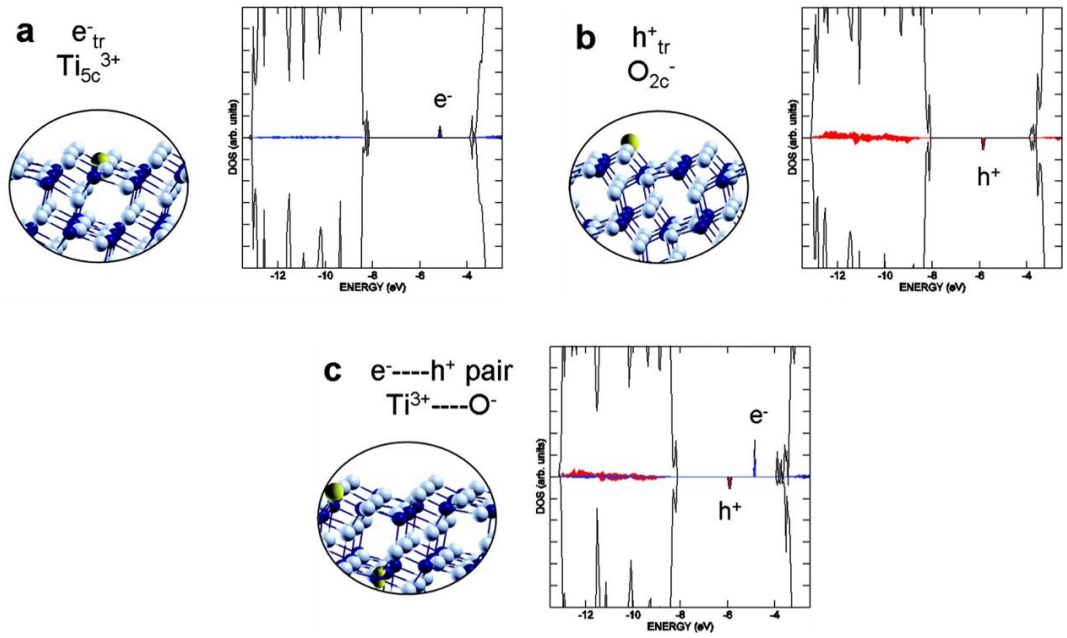

Figure 3.1.2 Computed spin density and electronic density of states for **(a)** excess electron **(b)** excess hole and **(c)** electron-hole pair in anatase (101); the yellow isosurfaces show the location of the spins.[19]

Di Valentin and Selloni have used the triplet electronic state model for electron and hole localisation in anatase (101).[19] **Figure 3.1.2** shows the location of electrons and holes for the following situations: (a) adding an electron, (b) adding a hole and (c) an excited electron and hole. In all cases, using hybrid DFT, the electron and hole localise. The preference is for localisation on one Ti or O site, for electrons and holes, respectively. This gives Ti^{3+} and O^{-} species in anatase. The electronic DOS shows localised states consistent with the formation of these species, which are key in photocatalysis. Later work

from Di Valentin showed that this model captures key aspects of the oxidation of molecules such as CH_3OH on TiO_2 surfaces.[21] This simple model has also been used to characterise electron and hole localisation in more complex photocatalyst surfaces.[22]

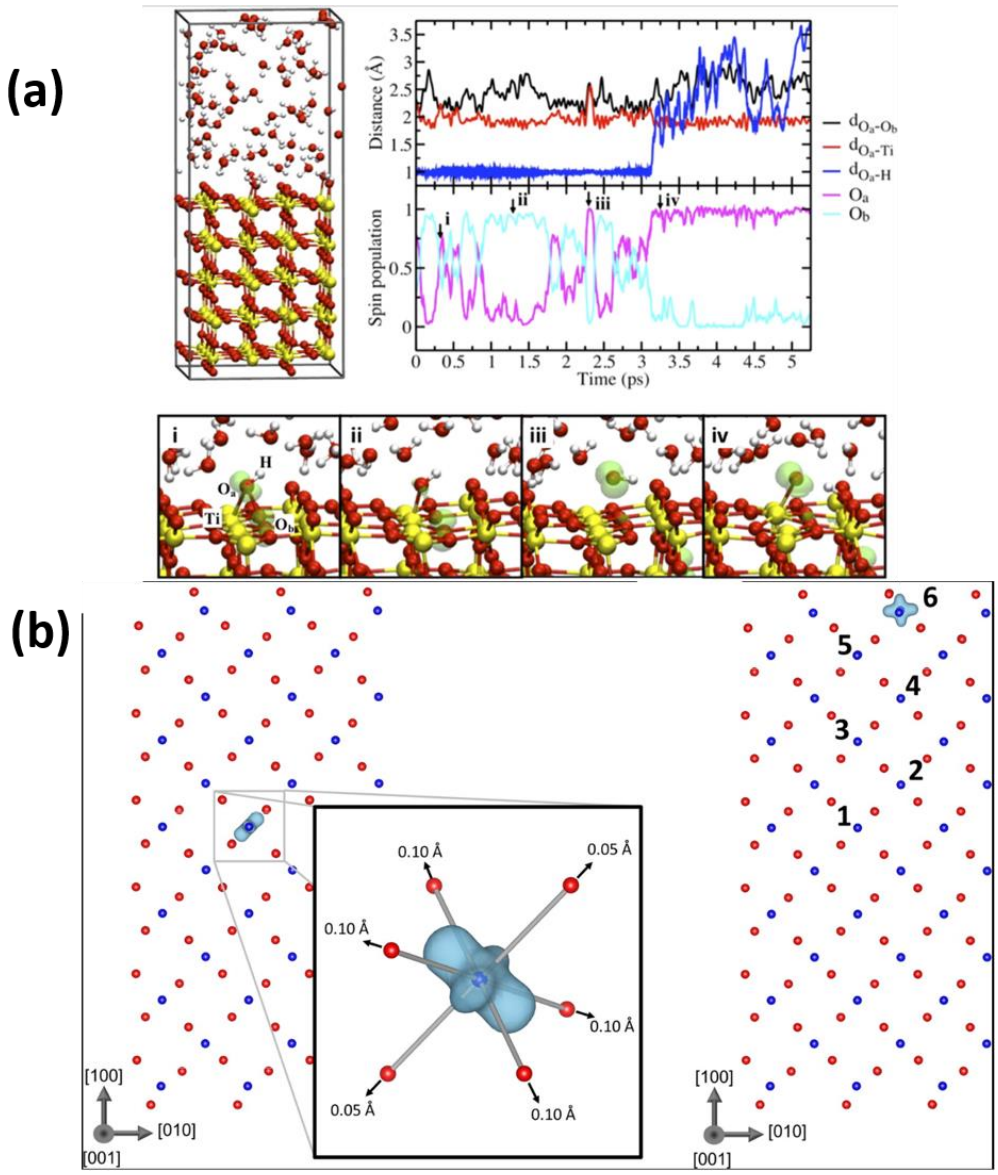

Figure 3.1.3 (a) Location of the hole state in rutile (110) immersed in water from ab initio molecular dynamics simulation at 330 K. The green isosurfaces show the location of the hole on oxygen. The graph shows the spin population on different oxygen atoms during the first 5 ps of the simulation.[23] **(b)** Electron localisation on different Ti sites (blue spin isosurfaces) of a rutile (110) slab. The left image shows localisation in the centre of the slab while the right image shows localisation on a surface Ti atom (indicated as Ti 6). The inset shows the local geometry around the electron.[24]

Direct investigation of electrons or holes produced by excitation or defects can also be probed using Molecular Dynamics schemes, e.g. for the oxygen hole in a system modelled by a water layer on rutile TiO_2[23] (**Figure 3.1.3.a**) or electron trapping on Ti sites in TiO_2 nanocrystals, **Figure 3.1.3.b**.[24]

Figure 3.1.3.a shows results from an ab initio molecular dynamics (MD) (using hybrid DFT) simulation of a water layer on rutile (110). The hole is formed by removing a proton and an electron and the MD is at a temperature of 330 K.[23] This shows the atomic structure of the water-TiO_2 system (top left panel) and the spin on particular oxygen atoms (cyan, purple curves) as the simulation processed over a 5 ps timeframe. These results show that the hole localises on one of two oxygen atoms in the first 3 ps. These are the terminal hydroxyl (O_a) and a nearby surface oxygen atom (O_b). Hole localisation fluctuates over these oxygen atoms, which correlates with changes in geometry around the oxygen atoms involved. After 3 ps, there is a breaking of the OH bond and transfer of the proton to the surface. This leaves behind an O^- species on the surface. These results suggest this process will be fast.

To understand electron trapping in TiO_2 nanocrystals, which have different TiO_2 surfaces exposed, Wallace and McKenna[24] studied electron trapping at low index rutile surfaces, namely (110), (100), (101), (001) and (111), with DFT+U calculations. **Figure 3.1.3.b** shows examples of electron trapping at rutile (100). The sites for Ti localisation are indicated by numbers 1-6, with site 1 in the centre of the slab and number 6 at the surface. The electron localisation induces structural distortions around the localisation site, which are characterised by elongated Ti-O distances around reduced Ti^{3+} cations. From the electron trapping energies, the most stable site in this surface is in the bulk (site 1 in **Figure 3.1.3.b**), with the surface site (site 6) the least stable. The authors found that the surfaces with the most favourable non-bulk trapping sites for electrons are (110) and

(001), in which (110) traps an electron in a subsurface site. Thus, crystal morphologies that expose predominantly (110) and (001) are proposed to enhance electron trapping at non-bulk sites.

Another approach is to compute the electric dipole moment, which measures the separation of positive and negative electric charges.[25] For finite systems, this is defined as $d = \int e \cdot n(\boldsymbol{r})\boldsymbol{r}d\boldsymbol{r}$, where e is the electron charge and $n(\boldsymbol{r})$ is the number density at position $\boldsymbol{r}$. For periodic systems, the dipole moment can be computed as $d = \sum q_i \boldsymbol{r}_i + \sum \boldsymbol{d_i}$, where $\boldsymbol{r}_i$ is the position of atom i relative to the origin of the periodic cell, chosen for convenience as the centre of mass. The net atomic charge, q_i, and the atomic dipole, $\boldsymbol{d}_i$, of atom i are computed with appropriate choice of charge partitioning scheme. Charge partitioning methods include the aforementioned Bader scheme and the Density Derived Electrostatic and Chemical (DDEC) scheme[26] and its refinement, DDEC6,[27-28] among others.[25]

Semiconductor-metal and semiconductor-semiconductor interfaces are of considerable interest in the field of photocatalysis. The rational design of such heterostructures can extend light absorption to longer wavelengths and promote separation of photogenerated charge carriers. Understanding the direction of charge flow at the interface is necessary to predict the behaviour of these systems. The interface of a semiconductor and a metal in intimate contact is described by a Schottky junction.[29] In order to achieve thermal equilibrium, in which the Fermi levels of the semiconductor and metal are aligned, charge must transfer across the interface. The direction of the charge flow is dictated by the relative work functions of the materials, with the work function defined as the difference in energy between the vacuum level and the Fermi level, $W = E_{vac} - E_F$. In general, electrons flow from the material with the lower work function (higher E_F) to that with the higher work function (lower E_F). This results in the depletion of electrons or holes in a

region of the semiconductor near the interface, known as the space charge region, and establishes an electric field.

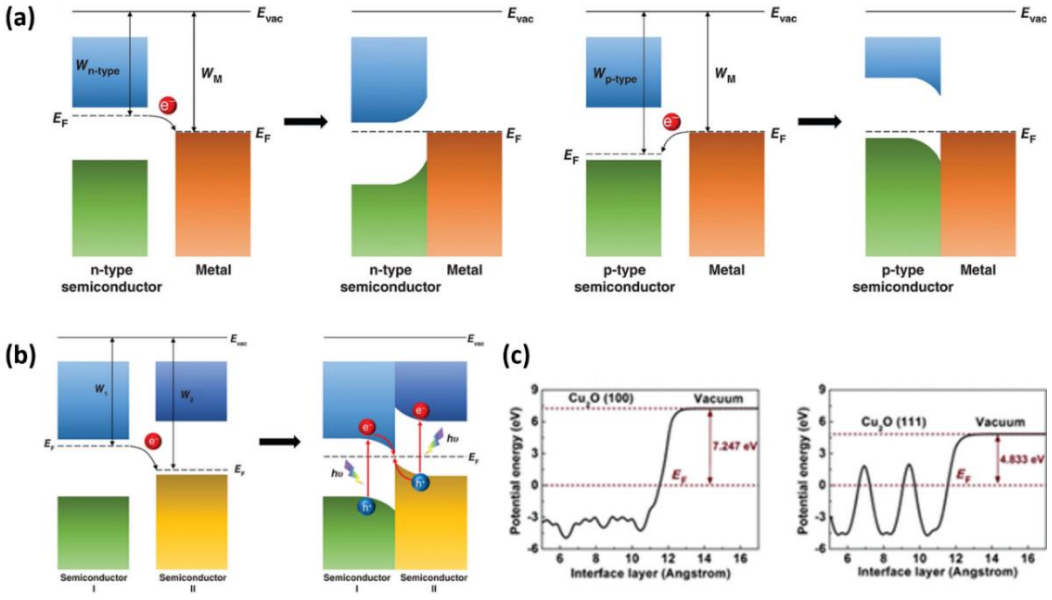

Figure 3.1.4 (a) Band bending at the interface between an n-type (left) and p-type (right) semiconductor in contact with a metal.[25] **(b)** Band bending and transfer of photoexcited charge at the interface of a Z-scheme heterostructure.[25] **(c)** Local potential profiles along the direction perpendicular to the Cu_2O (100) surface (left) and Cu_2O (111) surface (right) showing the difference in work function between the two facets.[30]

If the work function of the metal (W_M) is greater than that of an n-type semiconductor (W_S), the bands in this region bend upwards and a Schottky barrier is formed, which, if large enough, prevents backflow and promotes separation of charges (see **Figure 3.1.4**). If the barrier is low or in the case where $W_M < W_S$, this is an Ohmic contact. The opposite arguments apply to a metal in contact with a p-type semiconductor. To ascertain the nature of the Schottky contact it is therefore necessary to compute the work function of the materials.

The work function is also a useful descriptor for semiconductor-semiconductor heterostructures, for example in the Z-scheme shown in **Figure 3.1.4.b**. New materials

based on such interfaces capitalise on the staggered band edges between semiconductors of different compositions. Once again, the relative work functions determine the direction of band bending and charge flow at the interface. One can conceive of favourable configurations in which photoexcitation of an electron from the valence band of one material to the conduction band of another is achievable at longer wavelengths than would be possible for the respective materials in isolation.

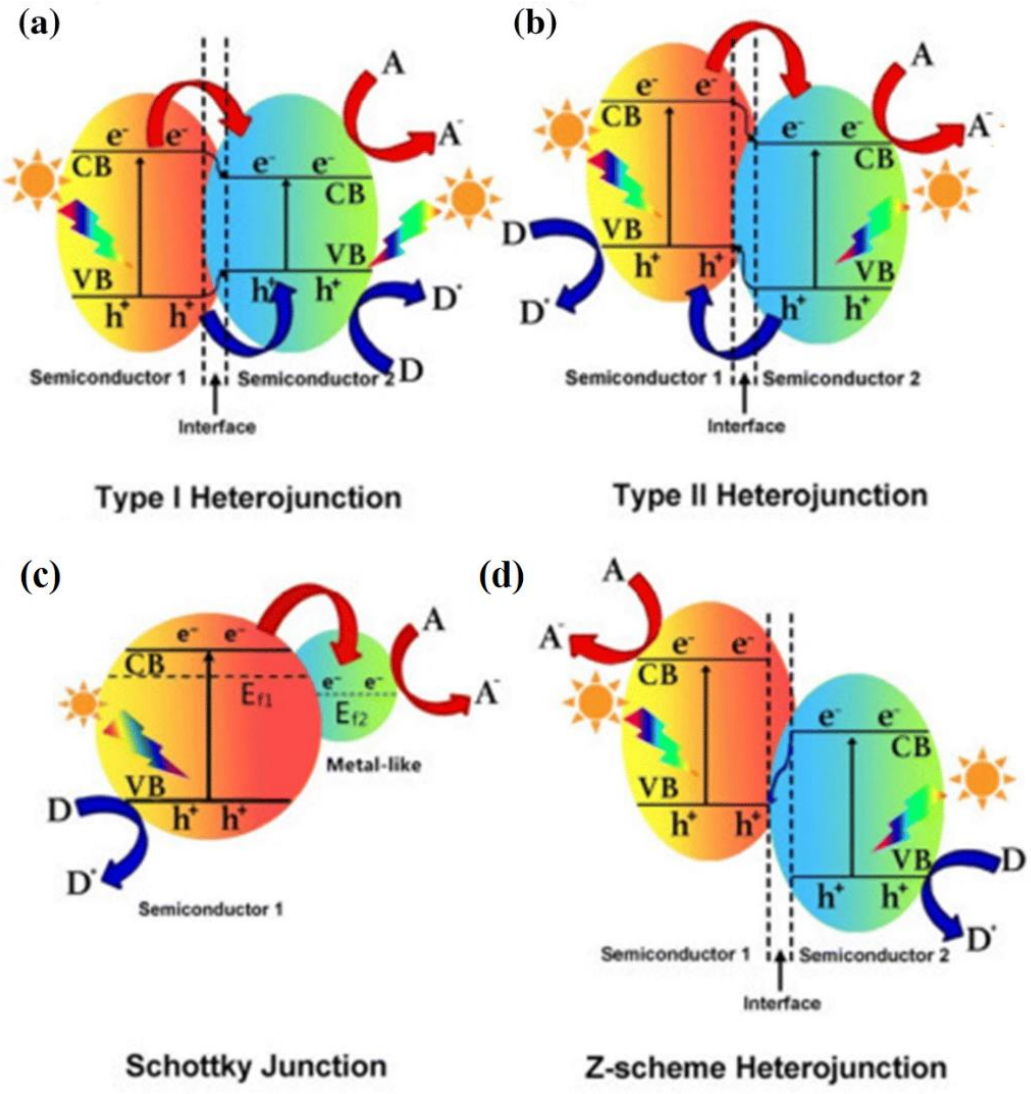

Figure 3.1.5 Different types of heterojunction: **(a)** Type I, **(b)** Type II, **(c)** Schottky and **(d)** Z-scheme heterojunction. Notation: A, D and E_F represent electron acceptor, electron donor and Fermi level respectively). Taken from ref. [32].

Additionally, heterostructuring can circumvent the necessity for the band edges of an individual phase to straddle the redox potentials of the overall reaction; the reduction and oxidation half reactions can be driven at the phases separately. In this way, interfacing two narrow-band gap semiconductors can drive the same reaction as a single wide-band gap material, while utilising a broader spectrum of light. The schematic in **Figure 3.1.5** shows the working principle of some commonly studied heterostructures in photocatalysis.

To compute the work function of a given surface it is necessary to construct a symmetric periodic slab model and generate a local potential profile along the direction perpendicular to the surface as shown in **Figure 3.1.4.c**.[30] For these calculations, the slab must be sufficiently thick such that at its centre it is bulk-like and the vacuum gap between periodic images must be sufficiently large such that the one-electron potential becomes constant in an interval at the mid-point.[31]

3.1.2.3 Surface Reactivity

Light absorption and efficient charge carrier separation count for very little if feedstock species do not interact with the surface of the catalyst, or interact too strongly. To probe the surface reactivity computationally there are a number of descriptors and their implementation and interpretation must take into account the context of the material and reaction under study.

The adsorption energy can be calculated as follows:

$$\Delta E_{ads} = E_{surf+mol} - (E_{surf} + E_{mol}) \qquad 3.1.3$$

where the first, second and third terms on the right hand side are the computed total energy of the surface-adsorbate system, the bare surface and the gas-phase molecule, respectively. Defined in this way, ΔE_{ads} corresponds to the change in enthalpy and negative values indicate an exothermic interaction.

Adsorption energies can be compared across various adsorption sites to elucidate the most active sites at the surface of the catalyst. Activation of adsorbed species is determined by geometry distortions, dissociation and charge transfer. The adsorption energy can be extended to the Gibbs free energy of adsorption by including zero point energy (ZPE) and entropic contributions:

$$\Delta G_{ads} = \Delta E_{ads} + (\Delta ZPE - T\Delta S) \qquad 3.1.4$$

The ZPE of molecules in the gas phase and adsorbed at the surface can be computed using DFT calculations of vibrational frequencies and entropies of molecules are taken from standard tables for the gas phase and neglected for adsorbed species.[33-34] Computing and comparing ΔG among likely intermediates of a given reaction can be used to generate an energy profile and identify the rate limiting step and hence the overpotential required to drive the reaction (see **Figure 3.1.6**).[33-35] If this step is consistent across different catalyst surfaces, ΔG of this step can be used as a descriptor for the performance of the catalyst for the overall reaction.[36-37]

Activation energies can be computed using nudged elastic band (NEB) methods,[38-39] wherein the minimum energy pathway of a transition is computed *via* calculating the energy of a number of intermediate structures between fixed initial and final states.

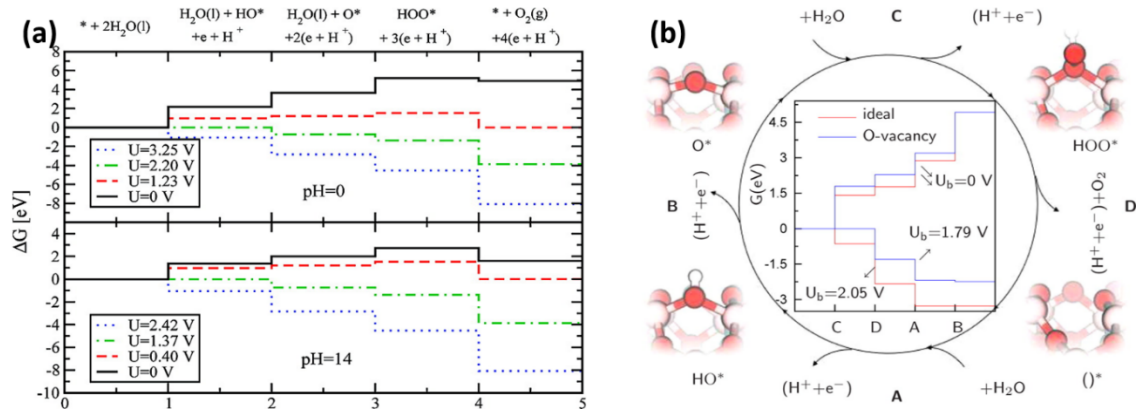

Figure 3.1.6 (a) Gibb's free energy profile computed for intermediates in the water oxidation reaction at rutile (110) with applied potentials of U = 0, 1.23, 2.20 and 3.25 V for pH = 0 (top) and U = 0, 0.40, 1.37 and 2.42 V for pH = 14 (bottom).[33] **(b)** Gibb's free energies of intermediates in the water oxidation reaction at hematite (0001) with overpotentials of U = 0 and 2.05 V for the pristine surface and U = 0 and 1.79 V for the oxygen deficient surface.[35]

For transition metal surfaces, another descriptor of the surface reactivity is provided by the *d*-band centre model, developed by Nørskov and colleagues.[40-41] In this model, insight into the strength of binding between an adsorbate and the transition metal surface is given by a single quantity, the *d*-band centre, which is defined as:[25]

$$\epsilon_d = \frac{\int E \cdot D(E - E_F) dE}{\int D(E - E_F) dE} \qquad 3.1.5$$

where $D(E)$ is the density of states projected on the *d*-orbitals and E_F is the Fermi energy. The adsorption energy is correlated with the shift of ϵ_d relative to E_F. The *d*-band centre is a measure of the degree of filling of anti-bonding states. Upward shifts in the *d*-band centre result in more empty anti-bonding states above the Fermi level, hence indicating increased binding strength.[42-43] Conversely, lower values of ϵ_d correspond to increased filling of anti-bonding states and weaker binding.

Besides its applicability being restricted to transition metal surfaces, another drawback of the *d*-band centre descriptor is that it yields no information about the spatial distribution of active sites. A descriptor which addresses both of these issues is the Fermi softness[44] of a solid catalyst surface; this measure is analogous to frontier molecular orbital (FMO) theory,[45] which describes the spatial distribution of active sites of a molecule. The local Fermi softness at position r is defined as:

$$S_F(r) = -\int g(E,r) f_T'(E - E_F) dE \qquad 3.1.6$$

where $g(E,r)$ is the DOS projected at position r and $f_T'(E - E_F)$ is the derivative of the Fermi-Dirac distribution function at finite temperature. The negative of the latter provides a weighting factor, which reaches a maximum at E_F, and its inclusion is necessary to reflect the greater degree to which states near the Fermi level contribute to bonding. Huang and colleagues first applied this descriptor to transition metal surfaces to ascertain its reliability (see **Figure 3.1.7**).[44]

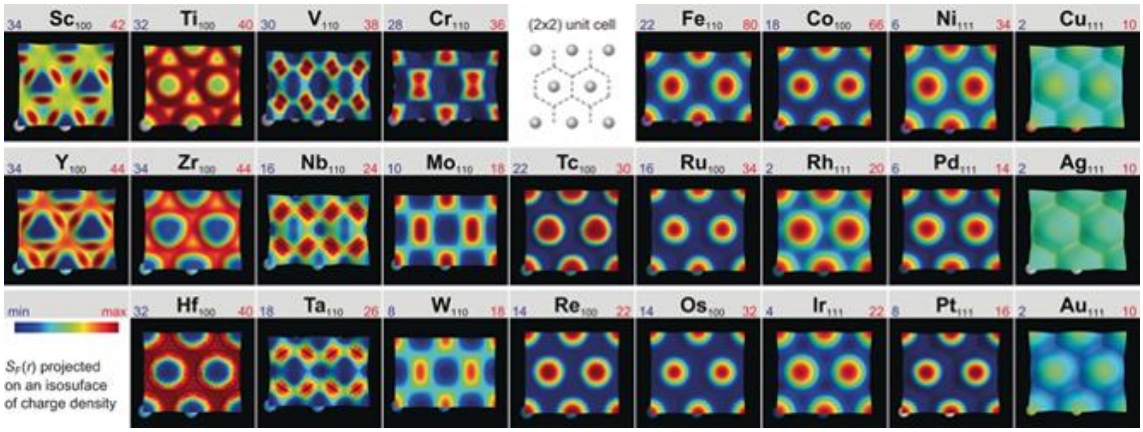

Figure 3.1.7 Local Fermi softness ($\boldsymbol{S_F(r)}$) computed for close-packed surfaces of transition metals. Taken from ref. [44].

Another consideration when approaching the topic of surface reactivity is the presence of defects. For example, oxygen vacancies have been demonstrated as active sites for water

dissociation at the rutile (110) surface[46-47] and ceria surfaces[48] and reduced Ti^{3+} ions have been shown to be active in the chemistry at titania surfaces.[49-50] Results such as these highlight the importance of engineering photocatalytic surfaces for which defects can be produced with moderate energy costs. The energy required to reduce a surface *via* oxygen vacancy (O_V) formation can be computed using:

$$E_{vac} = E_{surf+O_V} + \frac{1}{2}E_{O_2} - E_{surf} \qquad 3.1.7$$

where the first and third terms on the right hand side refer to the total energy of the surface with an O_V and the stoichiometric surface, respectively. The energy is referenced to half the total energy for molecular O_2. In this way, the O_V formation energy can be compared among systems and different vacancy sites to investigate which structures are more reducible and which configurations of O_V are most favourable. In addition, adsorption modes and interaction strengths of species at the catalyst surface can be compared across structures with and without the presence of O_V.

While knowledge of the interaction strength between adsorbates and the catalyst surface is useful, it is not sufficient in predicting the activity of the catalyst towards the desired reaction. For a given reaction involving an adsorbed species there is usually an optimal binding strength for which weaker binding indicates no reaction takes place and stronger binding indicates the adsorbate is too strongly bound for the reaction to proceed. This is further discussed in **Section 3.3** for the example of hydrogen evolution from water, where a descriptor of efficiency is a computed Gibbs free energy of H adsorption close to 0 eV.[51-53]

3.1.3 Conclusions

In this section, we have given an overview of the power of computational quantum chemistry for the understanding and development of photocatalysts. This work should proceed together with experiment, but modelling can give insights that are otherwise not easily obtained from experiment. This facilitates the rational design and screening of candidate materials and sheds light on experimental observations.

To model photocatalysts using DFT, a key aspect is to define a set of descriptors that relate directly to the performance of the candidate catalyst. Commonly, descriptors for the following three key processes in photocatalysis are used:

(1) Aiming to induce light absorption in the visible region of the solar spectrum, then the *energy gap* of the candidate material is important and is a widely used descriptor in modelling. Light absorption produces photoexcited electrons and holes.

(2) The separation of photoexcited electrons and holes and their migration to active surface sites. This prevents recombination of electrons and holes, which reduces the activity of the photocatalyst and a simple DFT model can be used to predict electron/hole localisation and stability, while first principles molecular dynamics can directly probe the migration of electrons and holes.

(3) The adsorption and interaction of feedstock species, such as water or CO_2, at active sites at the catalyst surface. The nature of the active sites, e.g. coordination, electronic structure, charges etc. can be used to predict feedstock adsorption.

Efficient computation of the descriptors for each step can help in assessing the material performance and screening for suitable candidate catalysts. In describing a photocatalyst *via* computational methods, we emphasise that it is vital to consider all key processes in photocatalysis. For example, we may predict a catalyst material to have optimal light

absorption properties, but the nature of the electronic structure means that it will likely suffer from fast charge carrier recombination. This is commonly seen with metal doped TiO_2, where many DFT studies of bulk doping simply predict enhanced visible light absorption but neglect the possibility of charge recombination and do not account for adsorption of feedstock molecules.

In the following sections we consider approaches for the optimisation of OER and HER catalysts through rational design of new materials. With the results from DFT modelling, further consideration must then be given to other important material properties, such as stability, cost, toxicity, abundance and synthesis. However, DFT methods are a powerful tool to screen for candidate photocatalysts.

3.2 Metal Oxides for OER

3.2.1 Introduction

The OER, or water oxidation reaction, proceeds at the anode and the reaction pathway depends on the pH conditions, as mentioned in **Section 1.3**. In alkaline media, the reaction is[54]:

$$4OH^- \rightarrow O_2 + 2H_2O + 4e^- \qquad 3.2.1$$

In acidic media the reaction takes the form[54]:

$$2H_2O \rightarrow O_2 + 4H^+ + 4e^- \qquad 3.2.2$$

In both media, this oxidation reaction involves the transfer of four electrons and can be considered as consisting of four single-electron transfer steps. In alkaline media, a proposed pathway for these steps is as follows[55]:

(A) $$OH^- + (*) \rightarrow {}^*OH + e^-$$

(B) $${}^*OH + OH^- \rightarrow {}^*O + H_2O + e^-$$

(C) $${}^*O + OH^- \rightarrow {}^*OOH + e^-$$

(D) $${}^*OOH + OH^- \rightarrow O_2 + (*) + H_2O + e^-$$

In acidic medium, a widely accepted model for water oxidation describes the steps as follows[33-34, 56-57]:

(A) $$H_2O + (*) \rightarrow {}^*OH + (H^+ + e^-)$$

(B) $${}^*OH \rightarrow {}^*O + (H^+ + e^-)$$

(C) $$H_2O + {}^*O \rightarrow {}^*OOH + (H^+ + e^-)$$

(D) $$^{*}OOH \rightarrow O_2 + (*) + (H^+ + e^-)$$

Each step of these pathways has its associated free energy, ΔG_X, $(X = A, B, C, D)$, the largest of which represents the rate-determining step, G^{OER}:

$$G^{OER} = \max[\Delta G_A, \Delta G_B, \Delta G_C, \Delta G_D] \qquad 3.2.3$$

Based on the free energy of the rate-determining step, one can compute the overpotential required to drive the OER[58]:

$$\eta \rightarrow \frac{G^{OER}}{q} - 1.23\ V \qquad 3.2.4$$

where q is the electron charge. Thus, at an ideal electrode material for the OER, the free energy of each step would be $\Delta G_X = 1.23$ eV, a condition which is never satisfied in reality. The relative stabilities of the reaction intermediates, determined by their binding energies at the surface, governs the rate-limiting step. For example, for surfaces which bind oxygen too strongly or too weakly, the reaction is limited by formation of *OOH (step C) or oxidation of *OH (step B), respectively.[58]

Such observations led to the development of a universal descriptor for the potential of a material to catalyse the OER. The relative binding energies of *OH and *OOH, at both metal and metal oxide surfaces, were found to be related by a constant of ~3.2 eV, (see **Figure 3.2.1**).[58] Thus, the sum of the free energies of steps B and C is 3.2 eV, rather than the ideal 2.46 eV. In practical terms, this defines a lower bound for the overpotential: $(\eta > (3.2 - 2.46)/2\ V)$, and narrows the scope for defining the rate-limiting step:

$$G^{OER} = \max[\Delta G_B, \Delta G_C] = \max[\Delta G_B, 3.2\ eV - \Delta G_B] \qquad 3.2.5$$

This descriptor allows for the screening of materials for OER catalysis based on computations of the free energy of step B, which, in alkaline or acidic media, is the deprotonation of a surface bound hydroxyl.

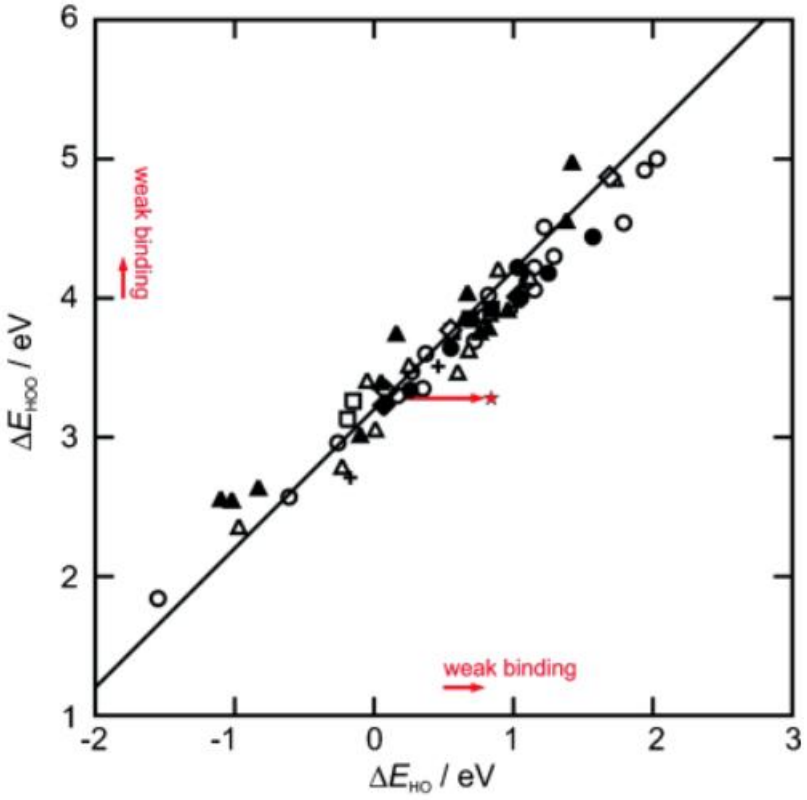

Figure 3.2.1 Linear correlation of binding energies for *OH and *OOH at a wide range of oxide surfaces. The binding energies are computed from DFT and do not account for zero-point energy corrections or entropic contributions. The slope of the linear fit is approximately 1 and the intercept is 3.2 eV ($\Delta E_{OOH} = \Delta E_{OH} + 3.2$ eV). The red star represents the relation between binding energies for the perfect catalyst: $\Delta E_{OOH} = \Delta E_{OH} + 2.46$ eV. Taken from ref. [58]

3.2.2 Metal Oxides

Metal oxides represent a widely studied class of materials for photocatalysis; these are attractive materials due to their earth abundance and low cost. Transition metal oxides

form stable compounds due to the high electronegativity of oxygen, which makes them resistant to photocorrosion.[59-60] Early transition metals, with empty *d*-orbitals (d^0) form oxides with low, O 2*p*-derived valence band (VB) energies so that they are often considered as catalysts for oxidation half reactions. However, their high ionic character results in wide band gaps, limiting their light harvesting capabilities to the UV range. As opposed to the early transition metals, oxides of late transition metals such as Fe and Mn can exhibit smaller band gaps, with *d*-*d* transitions playing a significant role.[59-60] A disadvantage is that low polaron conductivity inhibits the performance of late transition metal oxides in carrier transport and charge separation.[59-60]

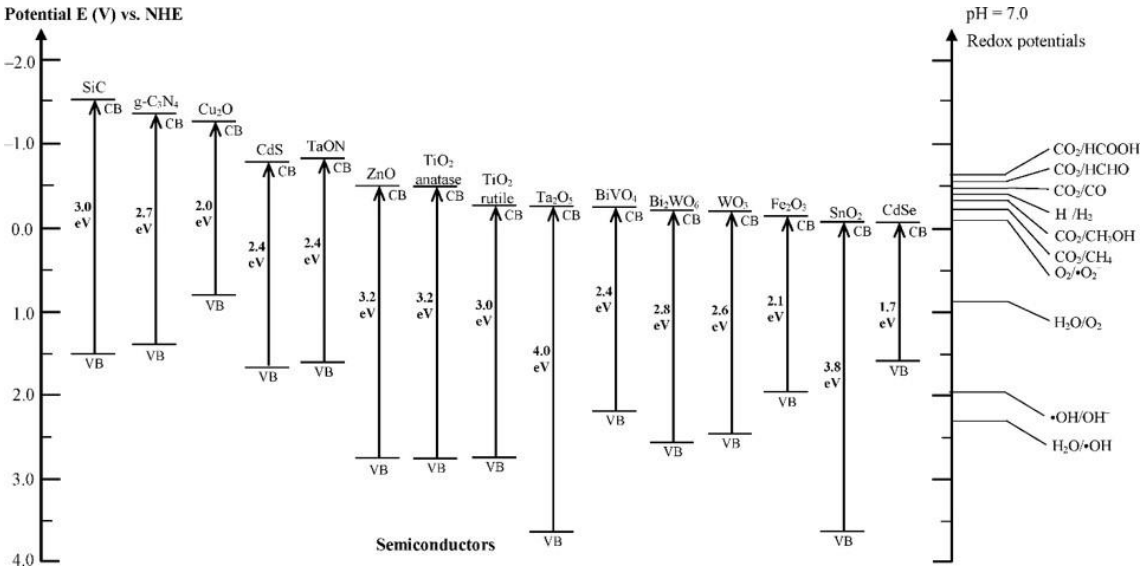

Figure 3.2.2 Illustration of the band gaps and band edges of various semiconductors relative to the reduction and oxidation potentials of some common redox reactions.[61]

3.2.2.1 TiO_2

The most studied of the early transition metal oxides is titanium dioxide (TiO_2),[62-68] which was first reported as a photoanode for water oxidation by Fujishima and Honda in 1972.[69] Titanium dioxide (TiO_2) is present in nature in three main phases: anatase, brookite and

rutile.[70-74] Anatase and brookite are metastable phases and transform irrevocably to the thermodynamically stable rutile phase at high temperatures.[75] Of the three TiO_2 polymorphs, anatase is the most photocatalytically active phase[76] and thus preferred by the ceramics industry for fabrication of light active antimicrobial indoor building materials such as ceramics, glass, tiles and sanitary surfaces.[75, 77]

The photo-activity of anatase arises from its appropriate band edge positions, electron affinity, ionisation potential, and the long lifetime of charge carriers.[78-80] Moreover, transient photo-conductance analysis has revealed that the electron-hole recombination phenomenon in the anatase (101) phase is much slower compared to rutile (110), which is credited, in part, to the indirect band gap of anatase.[81-82]

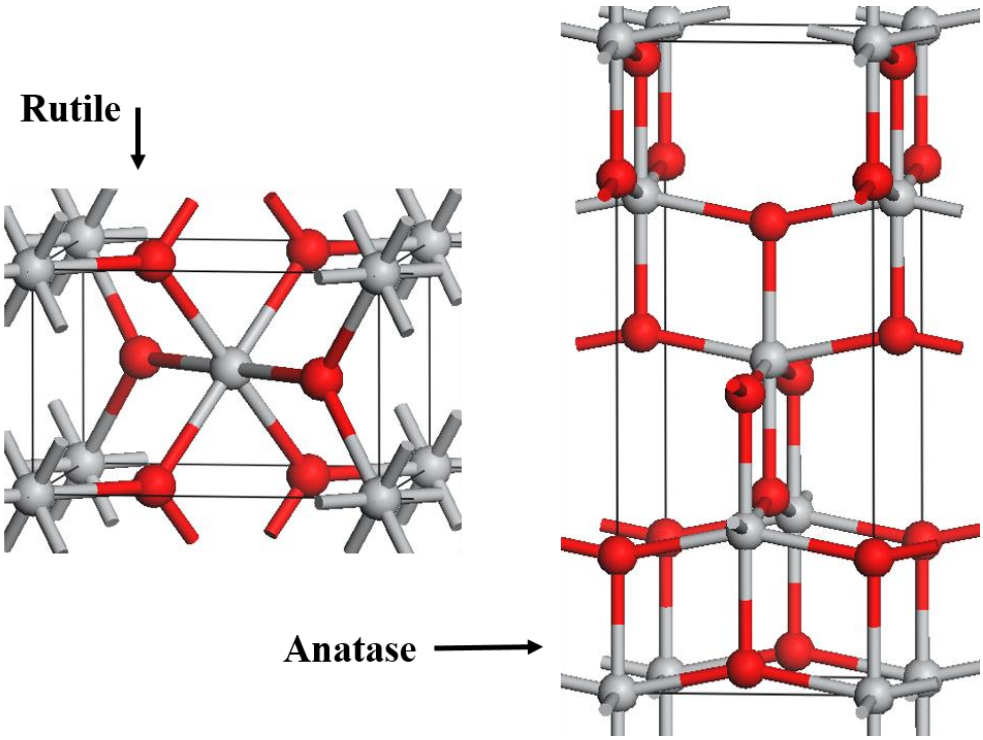

Figure 3.2.3 Unit cells of rutile and anatase TiO_2. Both cells are tetragonal and, as shown, the *c* axis is along the vertical direction.

The anatase to rutile phase transition (ART) generally occurs for temperatures between 600-700 °C and kinetic studies have revealed that the complete ART occurs in the

temperature range of 673-728 °C.[83] The ART temperature depends on various factors, such as the synthesis method, existence of impurities/dopants, and atmosphere.[84] As a consequence, anatase TiO_2 is mainly fabricated at low calcination temperatures (~500 °C) to prevent the ART.[85-87] Anatase TiO_2 is easily prepared at a calcination temperature of ~500 °C, owing to its lower surface free energy, compared to that of rutile.[75, 88] However, typical ceramic processing and manufacturing conditions can involve high temperatures in the range of 600-1000 °C. This necessitates enhancing the thermal stability of the anatase phase and suppressing the ART.

The unit cells of the anatase and rutile phases are composed of TiO_6 octahedra with titanium atoms at the centre and oxygen atoms at the vertices.[88] Both anatase and rutile have tetragonal primitive cells, shown in **Figure 3.2.3** with space groups $I_{41/amd}$ for anatase and $P_{42/mnm}$ for rutile.[88] The lattice parameters of anatase are $a = b = 3.785$ Å and $c = 9.514$ Å, while for rutile they are $a = b = 4.594$ Å and $c = 2.959$ Å. The octahedral structure of the anatase crystal has a distorted, four edge sharing centre (4 corners and 4 edges), whereas rutile has a non-distorted, two edge sharing centre (2 corners and 6 edges).[89] The ART is believed to occur *via* contraction of the anatase c-axis and is characterised by changes in lattice parameters and structural reformation (breaking and making of bonds).[75, 89] The ART is mediated by defects (oxygen vacancies, Ti interstitials), crystal strain, particle size, existence of additives or dopants, and calcination conditions.[88-90]

Despite the difference in activity between anatase and rutile, both polymorphs are widely studied for photocatalytic applications. However, their large band gaps (anatase: 3.2 eV; rutile: 3.05 eV[91]) limit the photoactivity to the UV range. There is considerable scientific literature devoted to enhancing the photocatalytic efficiency of TiO_2 and other metal oxides. Some of these approaches are discussed in the following sections.

3.2.3 Doping Strategies

Strategies to extend the light absorption edge of binary oxides based on early transition metals, such as TiO_2 and WO_3, to longer wavelengths include doping with cations and/or anions.[92-95] Such approaches aim to introduce impurity-derived energy levels in the band gap of the parent oxide, thereby producing a red-shift in light absorption. In addition, doping can result in the formation of oxygen vacancies and reduced cation sites, which play an important role in the catalytic properties of metal oxides.

Cu-doped TiO_2 has garnered attention due to potentially interesting photocatalytic properties.[96-100] Colón *et al* identified oxygen vacancies among the potential causes of an improved photocatalytic activity in Cu-doped anatase TiO_2.[96] Karunakaran *et al* reported an improved efficiency of bacterial disinfection under visible light for Cu-doped mixed phase titania nanoparticles, while photocatalytic activity was diminished by comparison with the un-doped system, under UV irradiation.[97] A number of authors have reported a reduction in the band gap for Cu-doped anatase,[98-99] with a value as low as 2.2 eV obtained in one instance.[100]

Typically, computational studies of doping-schemes emphasise band gap reduction[101-108] and overlook questions of charge localisation and surface reactivity. These are important considerations as the spatial separation of dopants, even at maximum solubility, means that charge transfer to the surface of the catalyst will be slow;[60] moreover, dopant-derived defect states have been shown to act as recombination centres.[67, 109-110] Nevertheless, valuable insight may be gained from such studies, which can inform future directions for optimisation.

There have been some theoretical papers on the topic of Cu-doped titania, and, in a reflection of experimental focus, most of these have dealt with doped anatase.[99, 103, 108, 111]

Zhang and colleagues used DFT+U with a +U correction on Ti 3*d* states of 8 eV,[108] which recovers the bulk TiO_2 energy gap but is not to be recommended for other properties. No +U correction is applied to the O 2*p* or Cu 3*d* states, despite issues with describing these electronic states. Guo *et al* applied no +U correction to Ti, O or Cu.[103] A reduction in the band gap was reported in all studies and this is attributed to a combination of Cu 3*d* and O 2*p* states above the valence band maximum.

Navas *et al* provided a particularly comprehensive study[99] of Cu-doping in anatase, which combined both experiment and theory, including DFT+U calculations, with the +U correction on Ti 3*d* orbitals only. However, a +U correction is necessary for the O 2*p* and Cu 3*d* states, in particular to obtain a localised polaron description[112-114] and correctly describe the Cu^{2+} oxidation state.[115-117] The authors reported a greater band gap reduction with increases in dopant concentration, due to the covalent character of the Cu-O interaction leading to new states at the VBM. Duhalde and colleagues gave a brief theoretical account of Cu-doping in rutile, in the context of the effect of oxygen vacancies on the magnetic moment of Cu-doped TiO_2[118] and the authors reported that vacancies near the Cu impurity are most stable.

Khan and Berk studied Mo-doped TiO_2 and suggested that an impurity level of Mo^{6+}/Mo^{5+} (Mo^{6+} $4d^0 \rightarrow Mo^{5+}$ $4d^1$) could be generated below the conduction band of TiO_2.[119] During photoexcitation, electron transition could occur from the O 2*p* valence band of TiO_2 into the Mo^{6+}/Mo^{5+} impurity level and then to the CB of TiO_2, through *d*(Mo^{5+})-*d*(Ti) transition. The photo-induced electrons could reduce Ti^{4+} ions to Ti^{3+} at the surface.

Kemp and McIntyre investigated the photocatalytic activity of Mo-TiO_2 and found that 34% of TiO_2 anatase content was retained by 1% Mo doping after calcination to 600

°C.[120] Fisher *et al*. studied the antimicrobial activity of Mo-TiO_2 coated films on soiled surfaces in the beer industry under visible light irradiation.[121] Mo-TiO_2 coated films showed 5-log reduction in *Escherichia coli* under dark and light conditions. Recently, Miljević *et al*. examined the photocatalytic and self-cleaning efficiencies of Mo-TiO_2-layer double hydroxide (LDH) nanocomposite coatings under visible light irradiation.[122] The results showed that the photocatalytic and self-cleaning properties of Mo-TiO_2-LDH (Mo/Ti = 0.03 mass ratio) were higher than that of TiO_2-LDH. In another study, Yoon *et al*. reported the photocatalytic activity of transparent Mo-TiO_2 (Mo = 3 at.%) films and showed that the visible light absorption capability of Mo-TiO_2-CNCs was significantly higher than that of bare TiO_2.[123]

A number of theoretical studies have been conducted on N-doped TiO_2 systems.[124-129] Calculations performed by Yang and colleagues indicate that substitutional doping of N at O sites is favoured over interstitial configurations at high dopant concentrations, while the formation energies were comparable at lower concentrations in rutile nanocrystals.[128] Di Valentin *et al* found that N-derived states above the anatase TiO_2 VB result in a red-shift in light absorption, while for rutile TiO_2 an N-induced contraction in the VB produced the opposite effect.[126]

In-doped TiO_2 was studied for the photocatalytic reduction of carbon dioxide (CO_2) under UV light irradiation.[130-131] Dopant concentrations were examined in the range of 0 – 20 wt. % and the calcination temperature was fixed at 500 °C for 5 h. The CO_2 reduction efficiency was increased significantly for the In-doped samples, compared to pure TiO_2. The efficiency of 10 wt. % In-TiO_2 was 7.9 times higher than that of un-doped TiO_2. Wang *et al*. reported on the visible light assisted photocatalytic efficiency of In-TiO_2 for the degradation of 4-chlorophenol.[132] The results suggested that electron-hole recombination was minimised and the photocatalytic activity was enhanced by In doping.

The visible light assisted photocatalytic activity for In-TiO_2 anatase was attributed to the presence of a surface species, O-In-Cl_x (x = 1 or 2).[132] This species introduced a surface state energy level at 0.3 eV below the TiO_2 conduction band (CB).

This work was followed with a study of TiO_2 co-modified with N and In, which included DFT calculations of the electronic band structure and density of states (DOS) for In-TiO_2.[133] While details of the exact computational set-up are lacking, the authors reported that In-derived states emerge at 0.5 eV below the TiO_2 CB, in their generalised gradient approximation (GGA) calculations. Charge compensation *via* oxygen vacancy formation in In-TiO_2 rutile was previously studied using standard DFT, DFT+U and hybrid DFT.[134] A recent GGA study presented an analysis of the band structure and DOS for stoichiometric and charge compensated In-TiO_2 anatase.[135] The details regarding the oxidation states, oxygen vacancy formation, reduction and charge localisation were not provided.

A study of C-cation and C-anion doped TiO_2 reported optical band gap reductions of 0.18 eV and 0.30 eV for C doped at Ti sites in anatase and rutile, respectively.[107] For C doped at O sites, spin-polarised states emerge in the computed band gaps of both polymorphs. An observed red-shift in light absorption for Fe-doped TiO_2 nanorods was attributed to Fe-derived states lowering the CBM, as revealed by DFT calculations of the DOS.[136] Ce-doping of anatase TiO_2 was found to facilitate the formation of oxygen vacancies, leading to the emergence of reduced Ti^{3+}- and Ce^{3+}-derived midgap states.[137] Fe-doping of WO_3 was investigated in a combined experimental and theoretical study.[138] DFT calculations provided deeper insight into experimental observations and attributed the upshift in the VBM and downshift in the CBM to hybridisation among Fe 3*d*, W 5*d* and O 2*p* orbitals. Furthermore, Fe-doping was found to facilitate the formation of oxygen vacancies, thereby increasing the charge carrier density.

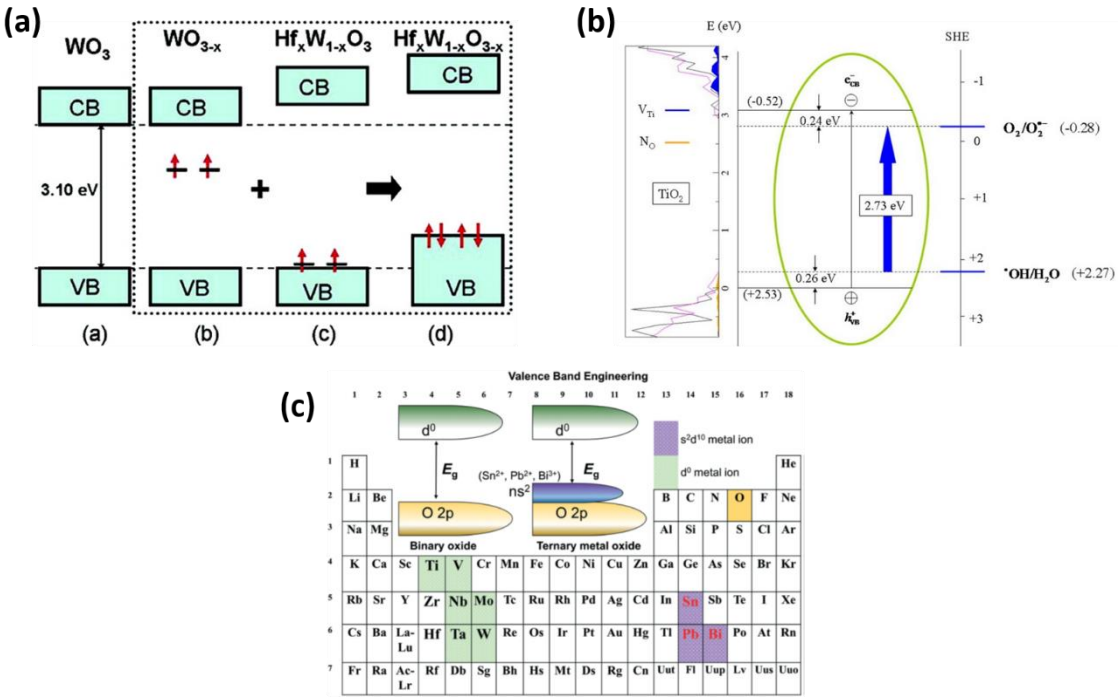

Figure 3.2.4 (a) Schematic representation of the impact of oxygen vacancies and Hf-doping on the band edges of WO_3; dashed horizontal lines indicate the VBM and CBM of pure WO_3.[139] **(b)** Computed DOS plot for (V + N)-doped TiO_2 showing the impact of dopant-derived states on the TiO_2 band edge potentials relative to major species OH and O_2^-.[106] **(c)** Schematic illustrating the concept of band gap reduction for ternary metal oxides.[140]

Passivated anionic and cationic co-doping is proposed as a strategy for inducing red-shifts in light absorption without the creation of recombination centres.[106, 141] Gai *et al* investigated various co-doping pairs computationally, and reported that (Mo + C)-doped TiO_2 yielded the most promising results, producing a significant upward shift in the VBM.[141] Wang and co-workers considered various cation-, anion- and co-doping strategies to shift the band edges of WO_3 to favourable positions relative to the redox potentials of the water splitting reaction.[139] The authors reported that substitution of W with lower-valent Hf lead to the spontaneous formation of oxygen vacancies, with the combined effect of shifting both the VBM and CBM upward while reducing the band gap, as shown in **Figure 3.2.4.a**. Phattalung and colleagues reported a reduced band gap

for (V + N)-doped TiO_2, with computed band edges straddling the redox potentials of OH and O_2^-, as shown in **Figure 3.2.4.b**.[106] A recent study of (Cr + C)-doped rutile TiO_2 indicated that co-doping yielded a reduced band gap and, using computed electron densities, postulated reduced recombination rates due to internal electric fields arising from the stronger Cr-C ionic bonding.[142]

In addition to binary metal oxides, ternary and quaternary metal oxides have been investigated. The vast multitude of such potential systems necessitates efficient and practical screening and in this endeavour, computational studies, equipped with suitable material descriptors, are essential. Ternary oxides, which incorporate metals with s^2d^{10} electron configurations in combination with transition metals, have garnered much attention.[140] The rationale is that the occupied *s* orbitals of the s^2d^{10} metals will extend the VBM to higher energies as shown in **Figure 3.2.4.c**. This effect has been confirmed in computational studies of $BiVO_4$[143] and Sn^{2+}-based ternary oxides, among others.[140]

Doping has also been considered as an approach to modulate the ART at high temperatures.[75] To stabilise the anatase phase at elevated temperatures and to utilise UV and visible light for photocatalysis, chemical modifiers and dopants can be used. These include anion dopants, e.g. carbon,[144-148] nitrogen,[149-152] sulphur[73, 153] and fluorine,[154-155] or metal dopants, e.g. iron,[153, 156]silver,[157-158] chromium[159] and manganese.[160-161] Doping with metal ions has the potential to retard the ART.[77, 89, 162-170] Metal ions could improve the thermal stability of TiO_2 through the reduction of contact points and nucleation sites.[171] However, doping strategies can also have the opposite effect.

Recently, the ART of cobalt-doped TiO_2 (Co-TiO_2) was studied at a single calcination temperature of 600 °C for dopant (Co) concentrations in the range of 0 to 4 mol. %.[172] The results revealed that ART of TiO_2 was promoted by Co doping. Co doping (4%) of

anatase produced a mixture of 78% rutile and 22% anatase at 600 °C. In another study, the impact of silicon (Si) doping on the ART was investigated.[173] The anatase phase of TiO_2 was well maintained up to 800 °C by 0.25% Si doping, with 90% anatase and 10% rutile. Promotion of the ART has been shown for tungsten (W)[174] and vanadium (V)[175] doping. The phase transformation was promoted up to 50 ppm of W^{6+} and was inhibited thereafter (>50 ppm W^{6+}; calcination 500 °C).[174] A calcination temperature of 550 °C yielded 100% rutile after the addition of 6 at. % of V.[175] In a recent study, it was observed that the anatase phase of TiO_2 nanowires was well retained with Ti^{3+} self-doping up to a calcination temperature of 800 °C.[176]

3.2.4 Noble metal loading

Depositing nanoparticles of noble metals at the surface of a catalyst can achieve a number of desirable effects. As mentioned in **Section 3.1.2.2**, the semiconductor-metal interface can promote the separation of photogenerated charge carriers. The Fermi levels of the noble metals are lower than that of TiO_2 and this establishes a Schottky barrier at the interface, which traps electrons in the metal.[67] In this case, the metal modifier acts as a co-catalyst, with reduction proceeding at the metal nanoparticle and oxidation at the oxide support.

Moreover, plasmon resonance in the metal can sensitise the composite structure to wavelengths of light in the visible range.[177] Conduction electrons in the metal nanoparticles oscillate in response to irradiation with light, which is an oscillating electromagnetic field, as shown in **Figure 3.2.5**.[178] These oscillations are greatest at the resonant frequency, which for the noble metals is in the visible range, and produce so-called hot carriers.[179] Excitation in this way enhances the electromagnetic field in the

vicinity of the metal nanoparticle and can result in transfer of hot electrons from the metal to the CB of the oxide support.[180] In this situation, hot electrons in the oxide CB will mediate reduction and, provided they are of sufficient energy, hot holes in the metal will drive oxidation.[181] Further insights into the impact of noble metal loading may be gained from computational studies.[178]

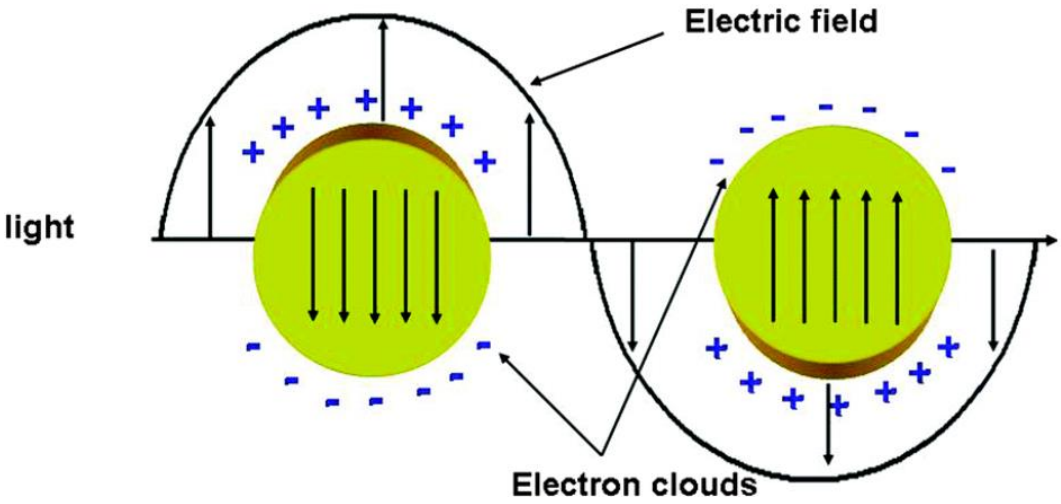

Figure 3.2.5 Schematic showing the collective and cohesive oscillations of electrons in a metal nanoparticle in response to a light-derived electromagnetic wave. Taken from ref. [178].

Hybrid DFT calculations predict decreases in O_V formation energies in the presence of Au and Pt nanoparticles at the TiO_2 rutile (110) surface.[182] Values of 3.62 eV and 2.10 eV were computed for E_{vac} in the presence of Au_2 and Pt_2 nanoparticles, which compare with 4.37 eV for the bare surface. A study of TiO_2 rutile films grown on an Ag (100) substrate predicted an increase of the work function from 4.23 eV for bare Ag to 5 eV for the metal/oxide system, which was attributed to charge transfer from the metal to the empty TiO_2 CB.[183] Wang *et al* used DFT models to study size effects of Pt-nanoparticles at the TiO_2 anatase (101) surface and their results indicate that favourable alignment of Pt states with the CBM of the TiO_2 support promoted photoelectron trapping in the metal, with the effect greater for smaller Pt clusters as shown in **Figure 3.2.6**.[184]

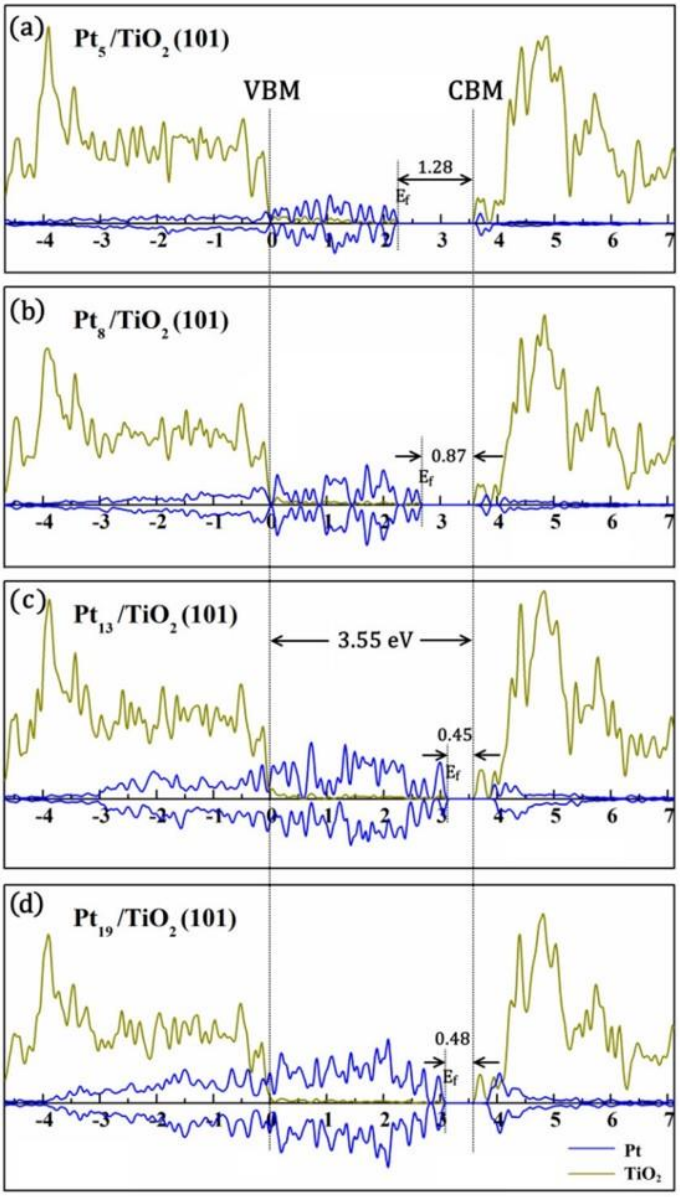

Figure 3.2.6 Computed DOS for Pt nanoparticles of various sizes at the TiO_2 anatase (101) surface; Pt-derived states are shown in blue and anatase states are yellow-green.[184] Dotted vertical lines indicate the VBM and CBM of the anatase surface.

3.2.5 Hetero- and nano-structuring

3.2.5.1 Heterojunctions

As mentioned in **Section 3.1.2.2** semiconductor-semiconductor interfaces can be exploited for photocatalysis. The benchmark material, P25, consists of chemically

interfaced rutile and anatase phases. The enhanced photocatalytic activity of P25 has been attributed to a favourable alignment of the conduction and valence bands at the interface, which facilitates charge transfer between phases and suppresses charge carrier recombination.[185] Recent papers on DFT modelling of explicit models of rutile-anatase interfaces have yielded further insights into the nature of the conduction and valence band edges[186-187] and the role of low-coordinated Ti sites in driving charge localisation.[188]

In addition, the interface can promote the formation of active catalytic sites. This effect can be tuned by considering heterostructures with semiconductors of different compositions. Such composites have been realised experimentally and shown to exhibit enhanced photocatalytic activity.[189-193] A hybrid-DFT study of a monolayer g-C_3N_4/CdS heterostructure found that a van der Waals heterojunction formed at the interface.[194] From calculations of the relative band positions, the authors identified a type II heterostructure with an internal electric field facilitating charge separation at the interface. Similar results were reported for g-C_3N_4/Bi_2MoO_6 (010) and g-C_3N_4/Bi_2WO_6 (010)[195] and g-C_3N_4/TiO_2,[196] which were found to be Z-scheme heterostructures.

Chae *et al*. studied the impact of WO_3 morphology on light absorption and charge carrier separation in heterostructured $BiVO_4$/WO_3.[189] The authors reported higher charge separation efficiency for the heterostructures, relative to bare WO_3, but found that increasing the photocurrent by varying the WO_3 layer thickness was hindered by slow charge transfer across the interface. First principles calculations performed on $BiVO_4$ /WO_3 showed that strong hybridisation of W and V *d*-orbitals with Bi *p*-orbitals results in no staggering of valence bands at the interface, whereas the conduction bands were staggered.[197] This result shed light on experimental observations that electron transfer was more efficient than hole transfer across the interface. Baek and co-workers engineered a triple-layer planar heterojunction (TPH) photoanode of composition

$BiVO_4/WO_3/SnO_2$.[198] The authors reported that the bottom WO_3/SnO_2 interface formed a disordered heterojunction, which lowered interfacial resistance for efficient charge transport and transfer. This combined with enhanced light absorption and charge separation, due to the top $BiVO_4/WO_3$ interface, to increase the water oxidation performance for the $BiVO_4/WO_3/SnO_2$ TPH, with respect to $BiVO_4/WO_3$.

In a study of WO_3/TiO_2 heterostructures, researchers irradiated the titania side of the composite material and reported a colour change on the WO_3 surface.[199] This colour change was attributed to the reduction of W^{6+} to W^{5+} upon electron transfer from TiO_2 to WO_3. The authors reported enhanced photocatalytic performance in the degradation of an organic pollutant, compared to the individual oxides. Sotelo-Vasquez and colleagues combined computation and experiment to study WO_3/TiO_2 heterojunctions.[190] Contrary to previous studies of WO_3/TiO_2 heterostructures, the authors reported electron transfer from WO_3 to TiO_2. Hybrid DFT calculations indicated that the interfacial band alignment would support this direction of charge transfer, as shown in **Figure 3.2.7**. It was postulated by the authors that the inverted charge transfer was due to formation of a WO_3 monoclinic structure, as opposed to the triclinic structure that commonly results from the synthesis methods reported in the literature.

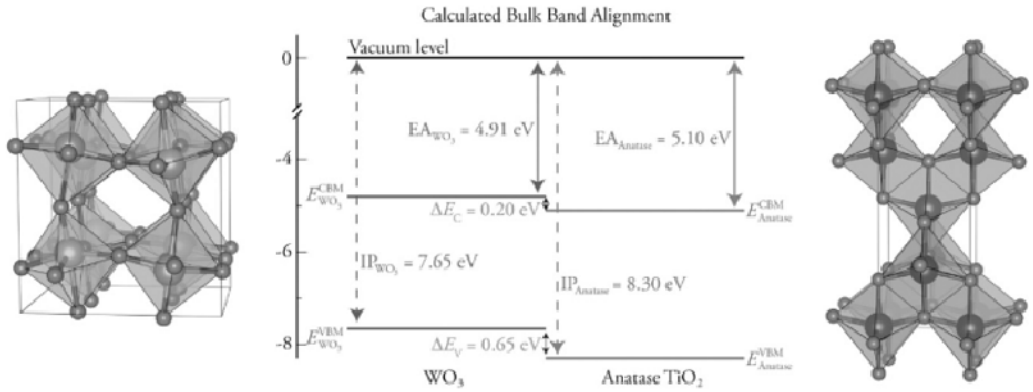

Figure 3.2.7 HSE06 calculated band alignment between monoclinic WO_3 and anatase TiO_2. Taken from ref. [190].

In their work on Cu_2O/TiO_2, Bi_2O_3/TiO_2 and $ZnMn_2O_4/TiO_2$, Bessekhouad and co-workers achieved the heterojunctions by direct mixture of the two semiconductors and assumed that Brownian motion would suffice to permit charge transfer between the two phases.[200] Heterojunctions based on Cu_2O, Bi_2O_3 and $ZnMn_2O_4$ extended the light absorption edge to 650, 460 and 1000 nm, respectively, according to UV-vis spectroscopy. The band alignment of $ZnMn_2O_4$ with TiO_2, shown in **Figure 3.2.8**, did not facilitate transfer of excited charges generated in $ZnMn_2O_4$ under visible (VIS) light irradiation; under UV-vis irradiation, photogenerated charges in TiO_2 transferred to $ZnMn_2O_4$, which effectively deactivated TiO_2. Conversely, Cu_2O/Ti_2O did exhibit VIS-light activity, but the performance was diminished, with respect to pure TiO_2, under UV-vis irradiation. Finally, Bi_2O_3/TiO_2 showed VIS-light activity and an improved performance under UV-vis conditions.

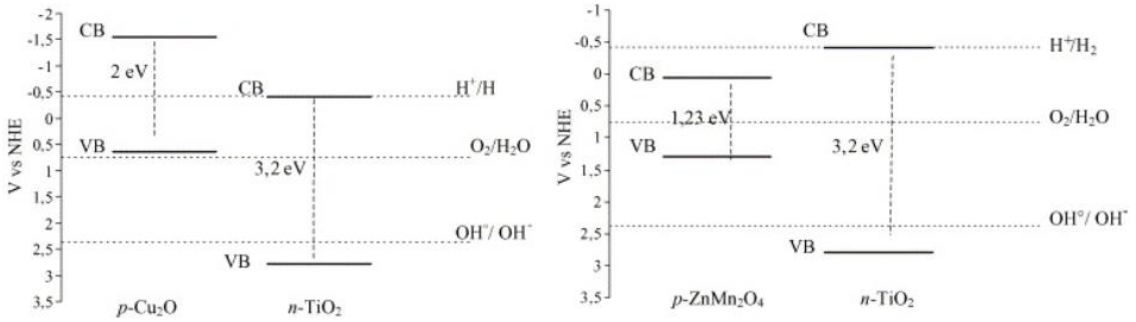

Figure 3.2.8 Band alignments at the Cu_2O/TiO_2 and $ZnMn_2O_4/TiO_2$ heterojunctions. . Electrons and holes generated in $ZnMn_2O_4$ under VIS light irradiation cannot transfer to TiO_2; however, both photogenerated electrons and holes in TiO_2 under UV conditions can transfer to $ZnMn_2O_4$. Taken from ref. [200].

Xie *et al*. studied $BiVO_4/TiO_2$ and found that VIS-light excited electrons in $BiVO_4$ transferred to the TiO_2 CB, prolonging the carrier lifetimes on the scale of milliseconds.[201] The authors also reported excellent performance in photocatalytic water splitting and pollutant degradation. Ho-Kimura and colleagues also studied $BiVO_4/TiO_2$, prepared by

a modified metal-organic decomposition (MOD) method.[202] The authors added the titanium source to the bismuth-vanadium precursor solutions and spin-coated the result onto a substrate to obtain $BiVO_4/TiO_2$ thin films. The resulting catalyst exhibited a four-fold increase in photocurrent, with respect to bare $BiVO_4$.

Niu and colleagues studied anatase TiO_2 interfaced with silicane (SiH) and germanane (GeH), using Hybrid DFT.[203] Silicane and germanane are monolayer materials with a graphene-like hexagonal structure and alternating H atoms on either side of the Si and Ge planes. SiH and GeH have smaller band gaps than the titania support (values of 2.08 and 1.15 eV were computed, respectively, after formation of the heterostructure) and sensitise the composite photocatalyst to longer wavelengths of light. Band structure calculations revealed a type-II heterojunction, such that photogenerated electrons in the SiH and GeH phases will transfer to the titania CB. Wang *et al* interfaced SnO_x (SnO_2 with trace amounts of Sn_2O_3) with Zn_2SnO_4 (ZTO) by a one-pot hydrothermal method.[193] The resulting heterojunction was of type-II and the authors reported photocatalytic performance exceeding that of P25. Moreover, the efficient separation of charge carriers inhibited photocorrosion of the ZTO component, which led to robust and stable activity.

3.2.5.2 Nanostructures

Nanostructuring of metal oxides is another approach to enhance the photocatalytic activity. Nanostructuring can enhance charge transfer kinetics and increase surface area while also providing low-coordinated metal and oxygen sites with which feedstock species can interact.[204-208] Synthesis of nanostructured materials is a developed field and considerable control can be exerted over the morphology and size of metal oxide

structures.[209] Novel materials can be fabricated as nanoparticles, nanowires, nanorods, nanotubes, nanosheets and nanoflakes, as shown in **Figure 3.2.9**.

Garg and colleagues prepared nanostructured $NiCo_2O_4$[210] and Mg_2MnO_4[211] and examined their performance as anodic electrocatalysts for the OER. The resulting materials consisted of nanorods with high surface area and current densities of 140 and 14 mA/cm^2 were recorded for $NiCo_2O_4$ and Mg_2MnO_4, respectively, during electrocatalytic OER. Moreover, the performance of both materials remained stable under alkaline operating conditions.

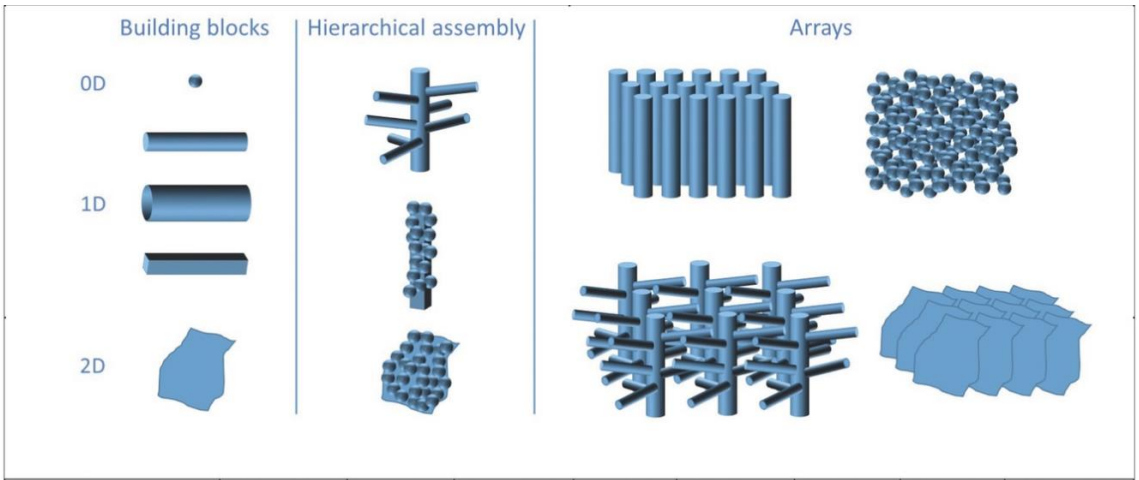

	Enhanced light harvesting	Fast exciton dissociation	Proper band alignment	Fast charge transport	High density catalytic sites	High chem. capacitance	High carrier lifetime	High recomb. resistance
Electrochemical WS				✓	✓	✓	✓	✓
Photoelectrochemical WS	✓	✓	✓	✓	✓	✓	✓	✓

Figure 3.2.9 Schematic representation of some commonly obtained geometries for nanostructured metal oxides. The building blocks, which range from 0D-2D, can be assembled into 3D hierarchical structures. Some of the properties endowed by nanostructuring, and relevant to electrochemical and photoelectrochemical water splitting, are included in the table. Adapted from ref. [209].

Kang *et al.* fabricated TiO_2 nanotube arrays and introduced oxygen vacancies on the surface and interior *via* $NaBH_4$ treatment.[212] The authors found that oxygen vacancies at the surface and in the bulk had beneficial and detrimental impacts, respectively, on the photocatalytic activity. Surface oxygen vacancies acted both as charge carrier traps and

active adsorption sites, where fast transfer of charge to adsorbed species prevented carrier recombination. Conversely, oxygen vacancies in the interior acted as recombination centres. After formation of oxygen vacancies due to $NaBH_4$ treatment, the photocatalyst exhibited a narrowed band gap of 2.46 eV and the photocatalytic activity was extended from the UV range to make use of visible light.

Wang and co-workers reported on the water splitting capabilities of hydrogen-treated TiO_2 (H:TiO_2) nanowire arrays.[213] Hydrogen treatment introduced oxygen vacancies and thereby increased the donor density of TiO_2 by three orders of magnitude. The defect-rich H:TiO_2 nanowires exhibited enhanced photocatalytic performance under simulated solar light, which was mainly attributed to increased activity in the UV range.

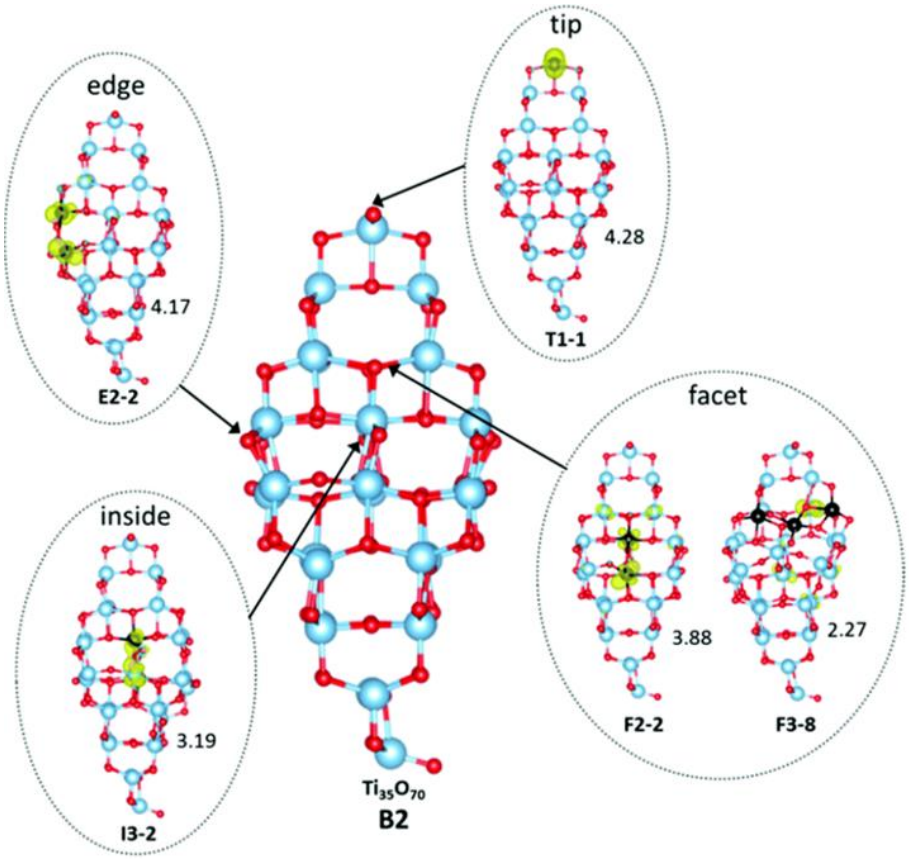

Figure 3.2.10 Atomic structure of a $(TiO_2)_{35}$ nanoparticle, with representative oxygen vacancy structures. Blue and red spheres denote Ti and O, respectively and yellow isosurfaces indicate localisation of excess electrons. Taken from ref. [214].

From a computational perspective, periodic boundary conditions impose constraints on the size of nanoparticles which can be studied using plane-wave based computational methods.[215-216] DFT codes such as FHI-aims,[217] which implement atom centred potentials, and hence remove the necessity for PBCs and large vacuum gaps, are better suited for such studies.[214, 218] Lamiel-Garcia and colleagues presented results which suggested that anatase nanoparticles become bulk-like for sizes of ~20 nm in diameter.[218] A study of anatase nanoparticles of size ~2 nm (see **Figure 3.2.9**) found that oxygen vacancies had low formation energies and that the resulting defect states potentially enhance the photocatalytic efficiency.[214]

3.2.5.3 Surface modification

Modification of catalyst surfaces with dispersed nanoclusters of other materials can combine the favourable properties of hetero- and nano-structuring. Deposition of sub-nm nanoclusters of iron oxide on TiO_2 surfaces was demonstrated experimentally using chemisorption-calcination cycle (CCC)[219] and atomic layer deposition (ALD)[220] and subsequently investigated computationally.[68, 221-222] FeO_x-modified TiO_2 exhibited band gap reduction and enhanced visible light photocatalytic activity and suppressed carrier recombination.[219] DFT simulations attributed the red-shift in light absorption to cluster-derived states above the VBM and identified interfacial surface-to-bulk electron transfer.[68, 219, 221]

Boppana and Lobo modified the surface of zinc gallate ($ZnGa_2O_4$) with SnO_x.[191] This was achieved by adding a suspension of $ZnGa_2O_4$ to a solution of tin chloride precursor and stirring for 2 h at 353 K. The resulting material was tested for its photocatalytic performance in the degradation of cresol, an oxidation reaction. The visible light activity

of the $SnO_x/ZnGa_2O_4$ composite alone was higher than that of unmodified zinc gallate under UV light and the UV activity was also enhanced by modification. The visible light activity was attributed to the presence of Sn^{2+}, which was confirmed by Mössbauer spectroscopy.

Maeda and colleagues investigated rutile TiO_2 thin-films, modified with CoO_x nanoclusters.[223] The modified titania catalyst exhibited visible light absorption, which was attributed to excitation of electrons from the CoO_x modifier to the titania CB, as shown in **Figure 3.2.11.a**. The photocatalytic activity of the composite catalyst for water oxidation depended on the nature of the modifiers at the surface; small, highly dispersed nanoclusters, of composition Co_3O_4, resulted in the highest activity. Heating the composite catalyst to elevated temperatures led to aggregation of the modifiers to form larger clusters, which diminished the activity (see **Figure 3.2.11.b**).

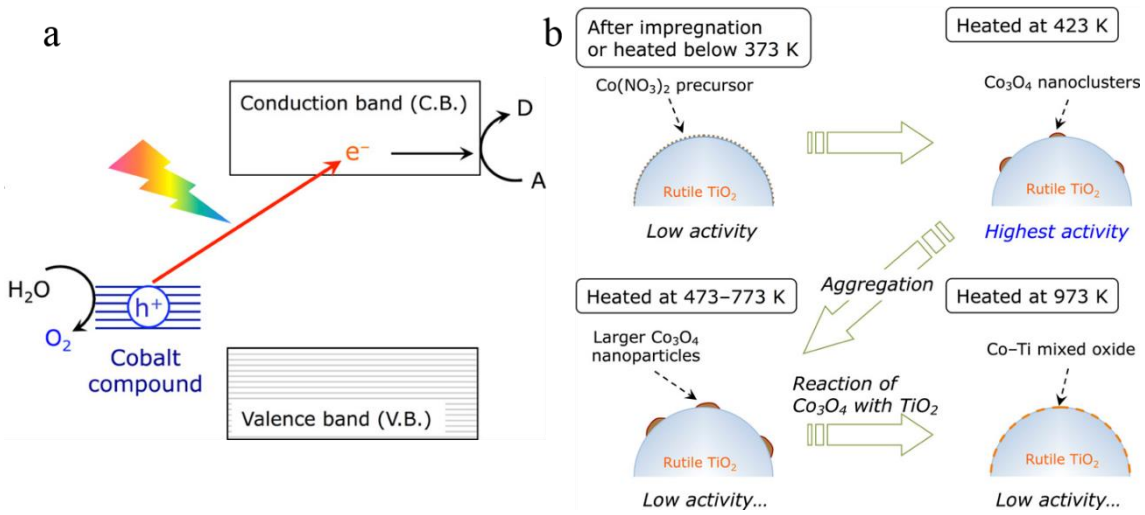

Figure 3.2.11 (a) Representation of visible light induced excitation of electrons from the CoO_x modifier to the titania CB, followed by oxidation at a site of the modifier. **(b)** Schematic showing structural changes of the CoO_x-modifiers at the TiO_2 surface upon heating at different temperatures.

Méndez-Medrano and colleagues studied TiO_2 P25 modified with nanoclusters of CuO for photo-oxidation of organic compounds.[224] Modification with CuO induced visible-light driven photocatalytic activity, owing to the CuO band gap of 1.7 eV. Moreover, time-resolved microwave conductivity (TMRC) analysis indicated that excited electrons transferred from the CB of CuO to that of the P25 component, thereby suppressing charge carrier recombination. However, the authors reported that the holes remaining in CuO would have almost no oxidation power, owing to the high lying VB of CuO.

Jia *et al*. investigated TiO_2 nanowire arrays modified with CuS nanoclusters for photoelectrochemical (PEC) water splitting.[225] The fabrication method for deposition of the clusters on the titania support was successive ionic layer adsorption reaction (SILAR). The resulting photoanode consisted of an array of TiO_2 nanowires, of diameters from 20-150 nm, with dispersed spherical nanoclusters of CuS of size ~5 nm. The modified photoanodes exhibited enhanced PEC activity. The authors reported that the performance depended on the CuS loading, which could be tuned by the number of SILAR cycles; the optimal performance was obtained after five SILAR cycles, and decreased for higher loadings. The proposed mechanism for the enhanced PEC activity involved the transfer of excited electrons from TiO_2 to CuS, which led to partial reduction to Cu_2S, as confirmed experimentally. This increased the lifetime of holes in the titania VB, which mediated the OER.

DFT+U studies show that surface modification of TiO_2 with metal oxide nanoclusters can enhance the reducibility, with moderate energy costs to produce reducing oxygen vacancies.[226-227] This is particularly important for anatase (101), for which vacancies, which are active sites in photocatalysis, form preferentially at subsurface sites rather than at the surface.[228-229] Surface modification can also enhance the interaction of adsorbed species, through provision of low coordinated active sites.

These studies, and the development of similar systems,[192, 230-233] mean that a multitude of nanocluster-surface composites can be investigated for favourable photocatalytic properties. Tuning these systems for optimal performance encompasses composition, surface termination, nanocluster size, and stoichiometry. These considerations govern the light absorption properties, charge carrier mobility and surface reactivity. Computational methods provide insight into experimental observations[221-222, 231-232] and are useful in screening candidate composite materials.[22, 227, 234-242]

3.3 Metal Chalcogenides for HER

3.3.1 Introduction

In this section, we focus on the HER, and for the most part, in acidic conditions as this enhances the HER activity;[243-244] the reverse is true for OER.[245] Moreover, the mechanism for HER in alkaline media is not as well understood.[246] However, progress in the development of HER catalysts that operate in alkaline media has been the subject of a number of recent reviews.[247-248]

The HER proceeds at the cathode in a two-step process and there are two possible pathways: the Volmer-Tafel reaction and the Volmer-Heyrovsky reaction.[249] The Volmer step is common to both pathways and may be described as:

Volmer: $$H^+ + e^- \rightarrow H_{ads}$$ 3.3.1

This is called the "discharge step" as an electron is transferred to a proton at the cathode surface, resulting in a surface bound H species, i.e. H_{ads}. The second step involves desorption, and is described by the Tafel or Heyrovsky reactions:

Tafel: $$H_{ads} + H_{ads} \rightarrow H_2$$ 3.3.2

Heyrovsky: $$H_{ads} + H^+ + e^- \rightarrow H_2$$ 3.3.3

The adsorption (discharge) step competes with the desorption steps and the optimal catalyst will strike a balance between these processes. This balance may be characterised by the Gibbs free energy of adsorption of a H atom (ΔG_H) at the catalyst surface.[250] This quantity is widely accepted as a descriptor for the HER activity of a catalyst and may be computed from first principles *via* DFT using:

$$\Delta G_H = \Delta E_{DFT} + \Delta ZPE - T\Delta S \qquad 3.3.4$$

where ΔE_{DFT}, is the thermodynamic energy difference between the initial and final (H_{ads}) state, computed with DFT; ΔZPE accounts for zero-point energy corrections; and the $T\Delta S$ term contains entropic contributions. Large, positive ΔG_H implies that adsorption is the difficult step whereas large, negative values of ΔG_H indicate strong adsorption of hydrogen and therefore render the desorption step difficult. Thus, consistent with the Sabatier principle, the optimal value for ΔG_H is close to 0 eV, and indeed, this is the case for the benchmark catalyst, Pt, as shown in **Figure 3.3.1** and compared to other metals.

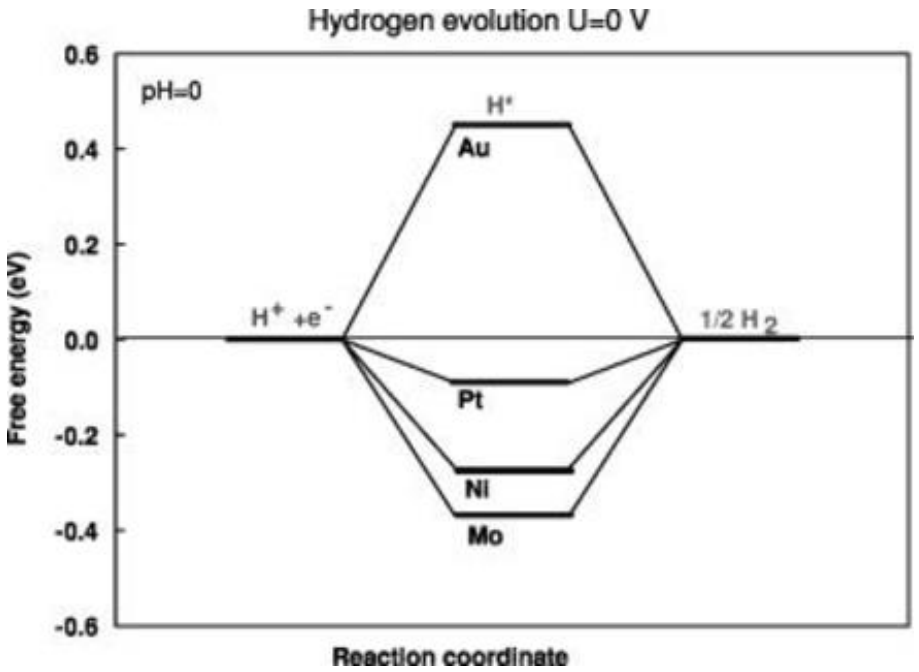

Figure 3.3.1 Free energy diagram for hydrogen evolution at various metal surfaces, with no applied potential, (U=0 V). The modelled conditions correspond to standard temperature and pressure (STP: 300 K, 1 bar) and pH=0. By definition, the free energy of $H^+ + e^-$ is the same as that of $^1/_2$ H_2 at standard conditions. The free energies of adsorption are computed with DFT and corrected for entropy and zero point energies. Coverages of 1/4 are used. From ref. [51].

There are measured quantities that can quantify the intrinsic HER activity of a material. One such parameter is the turnover frequency (TOF) of an active site, which, as the name

suggests, is the number of reactions per unit time. The surface of a given catalyst material will present sites of different types, with variations that depend on factors including ion species, coordination, edge sites and defects. In principle, each site will have an intrinsic activity or TOF, but this is not measurable by experimental means. Instead, practical approaches estimate the average per site TOF, based on measurements of total electrode activity and the number of active sites, or site density, SD.[251-252] Thus, the challenge in evaluating and comparing the intrinsic activities of materials for HER depends on reliable, standardised measurements of the SD.

Strategies for determining the number of catalytic sites include measurements of the specific catalyst surface area *via* electrochemical techniques, such as capacitance measurements, or gaseous adsorption methods, such as BET, among others.[253] These approaches are based on the reasonable assumption that the number of active sites will scale with the surface area. However, they are not applicable to all materials and their accuracy can be hindered by differences in the availability and accessibility of active sites between measurement and HER conditions. This, in turn, makes TOF a challenging parameter to evaluate conclusively, in a way that admits comparison between materials.

Thus, many researchers omit intrinsic activity measurements and opt instead for total electrode activities as the metric to assess the catalyst performance. The quantities used for the measurement of total electrode activity, described below, depend on multiple factors including intrinsic activity, specific surface area, catalyst loading, substrate, and other effects.[251] This means that, for a given material, they can be optimised through electrode preparation and design. Hence, a material with high intrinsic activity may not perform as well as an intrinsically less active material when using total electrode metrics, due to sub-optimal electrode design.

Two quantities commonly used when comparing the total electrode activity of HER catalysts are the Tafel slope and the overpotential.[244, 246] A Tafel plot relates the overpotential (η) to $\log_{10}$ of the measured current density (j), *via*:

$$\eta = m \log_{10} j + c \qquad 3.3.5$$

The rate-limiting step of the HER is elucidated from the slope of the Tafel plot, represented by m in the above formula. Typically, values for the Tafel slope of 120, 30 and 40 mV/dec indicate that the Volmer, Tafel and Heyrovsky steps, respectively, determine the rate of reaction.[254] A small Tafel slope is a desirable quality in a catalyst because this indicates a large change in the current density, in response to small increments in the overpotential.

Another important quantity which emerges from the Tafel plot is the exchange current density, j_0, which is the current density at equilibrium conditions ($\eta \to 0$). This quantifies the ability of a material to catalyze the HER and the best catalysts will exhibit high j_0.

The overpotential, denoted η_j, and measured relative to the standard/reversible/normal hydrogen electrode (SHE/RHE/NHE), is that potential required to produce a current density, j.[251] This value for the current density corresponds to the current per unit area of the electrode and is typically chosen as 10 mA/cm^2, by convention. This convention is used because this current density in a PEC cell corresponds to an STH efficiency of approximately 10%.[244, 255] To avoid the complications of sign, only the magnitudes of η_j will be quoted in this review. The area is simply the geometric area of the electrode and neglects intricacies of the electrode surface. Consequently, considerations such as surface nanostructuring and catalyst loadings are not taken into account.

For comparison purposes, the Tafel slope, the overpotential, η_j, and the exchange current density, j_0, are among the most cited measurements in the literature. A detailed account of these quantities can be found in a review by Anantharaj and colleagues.[256]

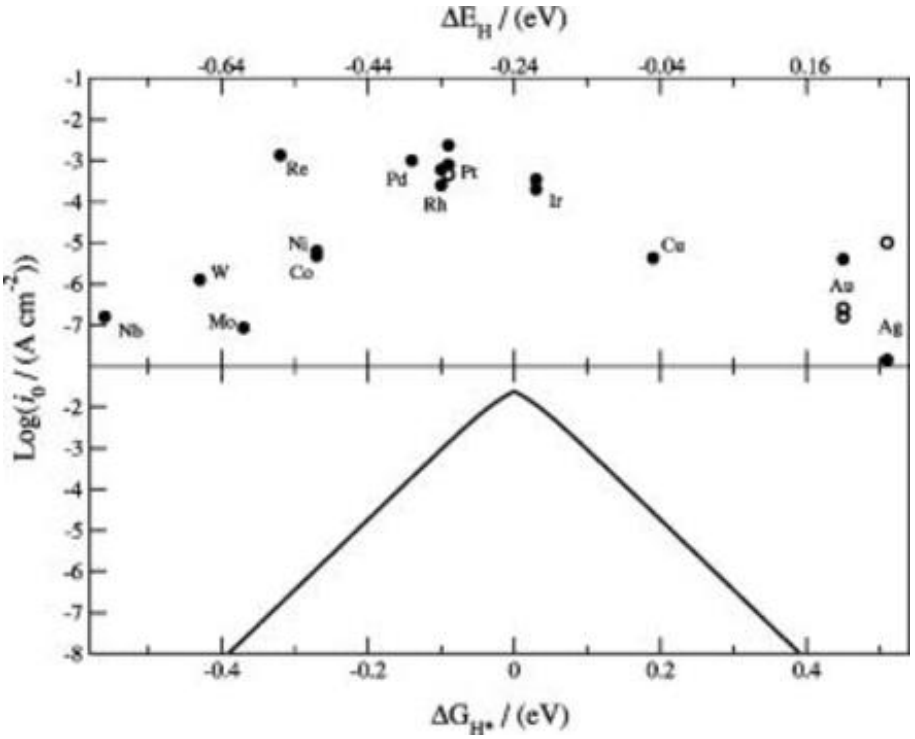

Figure 3.3.2 The top panel shows experimentally measured exchange current, log(i_0), for HER at metal surfaces plotted against the DFT calculated hydrogen chemisorption energy per atom, ΔE_H (top axis). The bottom panel shows a volcano plot which arises from a simple kinetic model of the exchange current plotted against the free energy for hydrogen adsorption, $\Delta G_H* = \Delta E_H + 0.24$ eV. From ref. [51].

For stability tests, some common approaches are to compare the performance of the catalyst after ~1,000-20,000 voltammetry (CV) cycles or to measure variations in the overpotential (current density) required to maintain continuous performance at a fixed current density (overpotential) for N hours.[257] Measurements are referred to as potentiostatic/galvanostatic where the overpotential/current density are maintained constant. Details of these tests are also important performance indicators.

The quantities ΔG_H and j_0 establish a crucial link between computational and experimental results, which can be illustrated using a "volcano plot".[51] The volcano plot in **Figure 3.3.2** shows experimentally measured j_0 for a variety of metals plotted against their computed values for ΔG_H. The Pt-group metals are clustered at the top of the volcano, exhibiting high values for j_0 and computed ΔG_H close to 0 eV. Reactive metals, at which H adsorbs too strongly, appear on the left of the volcano, while the unreactive metals appear on the right hand side.

Equipped with these descriptors, we have criteria against which we can assess the candidacy of a material to catalyse the HER. In particular, computational methods allow for high throughput screening of HER catalysts. However, while ΔG_H is a useful yardstick, other details of the HER should not be neglected. Such details include the catalyst surface area, availability of active sites, coverage effects and the nature of the real catalyst surface. For instance, H coverage can have a strong impact on the computed ΔG_H and must be accounted for when performing simulations of potential HER catalysts.[258-259] As an example of the latter consideration, computing ΔG_H for a pristine metal surface loses relevance should that surface form an oxide layer under operating conditions.

Indeed, the issue of aligning computational models of catalyst surfaces with the physical systems as they present under operating conditions is profound. One consideration is the impact of the solvent, and computational approaches to describing the catalyst-electrolyte interface will be discussed in **Chapter 9**.

While metal oxides are perhaps the most widely studied class of materials for photocatalytic applications, e.g. TiO_2 or Fe_2O_3, they are unsuitable as HER catalysts as hydrogen binds too strongly to oxygen sites in the surface, thereby forming an unreactive

hydroxyl layer. These catalysts therefore need a co-catalyst, such as Pt, or a sacrificial agent to consume electrons. Thus, the focus for HER is on non-noble transition metals and their compounds with elements from groups 13-16 of the periodic table. In this regard, we pay particular attention to the chalcogenides (S, Se and Te), which have recently emerged as interesting candidates for HER catalysts. Metal chalcogenide catalysts show significant promise in the search for cheap, abundant and efficient alternatives to noble metals for the HER. In this section, we focus on a selection of key catalyst materials and results that best highlight advances in this field, particularly from the perspective of how composition and structure can be used to promote the HER.

3.3.2 Identification of Active Sites

Metal chalcogenides, particularly layered transition metal dichalcogenides (TMDs) containing sulphur or selenium, have generated great interest for their catalytic activity towards HER. As they are useful for hydrodesulphurisation (HDS) chemistry,[260-261] they are also of great interest for HER, given that the key reaction steps are similar between both chemistries.

Perhaps the most widely studied of these materials is MoS_2. While bulk MoS_2[246, 262] and the basal planes[263] were found to be inactive, other studies have examined the catalytic performance of MoS_2 supported on substrates.[264-265] MoS_2 dispersed at an NiS_x surface promoted HER and inhibited degradation of the catalyst; the MoS_2 pigmented catalysts operated with overpotentials 50-100 mV below that recorded for bare NiS_x.[264] MoS_2 supported on silica also exhibited good hydrogen evolution properties.[265] Drawing inspiration from these studies and noting similarities with the active site of nitrogenase, an enzyme which efficiently catalyzes the HER, Hinnemann and colleagues presented a

now widely cited computational investigation of MoS_2 as a HER catalyst.[53] This paper can be considered as the beginning of the high level of activity in discovering sulphides for the HER. The authors identified low-coordinated S-sites of the MoS_2 edge as active sites, with ΔG_H comparable to that computed for Pt, as shown in **Figure 3.3.3**.

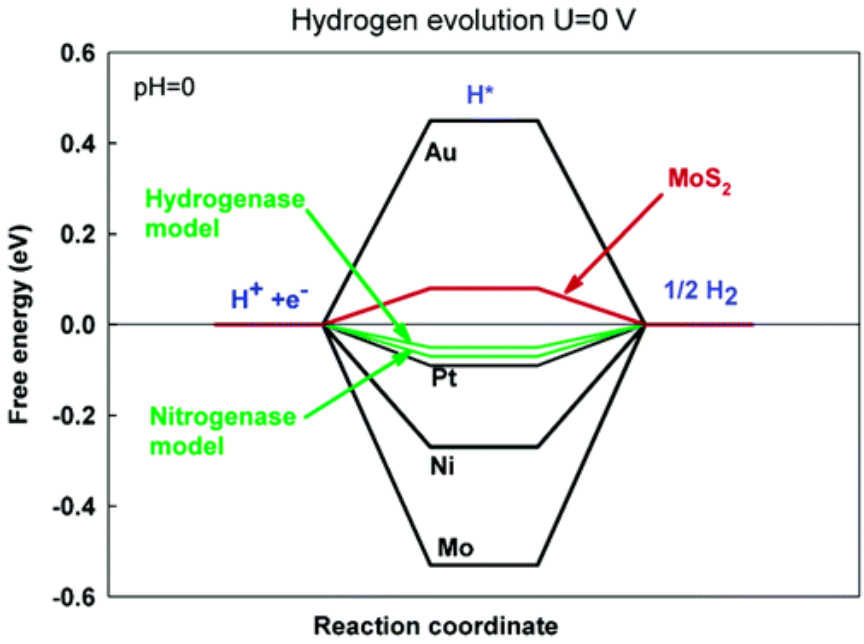

Figure 3.3.3 Computed free energy for HER at STP and a potential of U = 0 vs. SHE, with pH = 0. The result for MoS_2 is the free energy required to increase the hydrogen coverage from 25 to 50%. From ref. [53].

WS_2 has the same layered structure as MoS_2, and has also been studied for its hydrogen evolution properties and corrosion resistance.[266] Silica-supported WS_2 was shown to be an active and stable catalyst for HER; 0.2 mg of the WS_2/SiO_2 catalyst yielded in excess of 0.2 mL/h, with a small drop in performance after 2 h.[266] Conversely, the Pt/SiO_2 catalyst produced 0.1 mL in the first hour, but only 0.04 mL in the second hour. A combined experimental and computational study of MoS_2 and WS_2 nanoparticles found WS_2 to be almost as active as MoS_2.[267] Tafel slopes of 120 mV/dec and 135 mV/dec were recorded for MoS_2 and WS_2 catalysts, respectively. The authors also reported promotion of HER after incorporation of Co into the S-edges of both materials. The Tafel slope

decreased to 101 mV/dec and 132 mV/dec for Co-promoted MoS_2 and WS_2. The computational results of this paper are summarised in **Table 3.3.1**.

Table 3.3.1 Selected data taken from refs [267] and [52]. For details of the precise surfaces and H coverage, the reader should consult the original papers.

Ref.	Material	Site	ΔG_H (eV)
[267]	MoS_2	Mo-edge	0.08
		S-edge	0.18
	Co-Mo-S	S-edge	0.10
	WS_2	W-edge	0.22
		S-edge	0.22
	Co-W-S	S-edge	0.07
[52]	MoS_2	Mo-edge	0.06
		S-edge	-0.45
	WS_2	W-edge	-0.04
		S-edge	-0.06
	$MoSe_2$	Mo-edge	-0.04
		Se-edge	-0.05
	WSe_2	W-edge	0.17
		Se-edge	-0.05

A subsequent study of MoS_2 and WS_2 by the same group adopted a more thorough approach and examined the effects of S- and H-coverage.[52] Consequently, the computational results for ΔG_H were revised and these results are also presented in **Table 3.3.1**. The authors found that H binding was too strong at the S-edge of MoS_2, even at the highest possible coverage. They concluded that active sites for HER were present at the Mo-terminated edge. Conversely, H adsorption at both W- and S-terminated edges of WS_2 was close to thermoneutral.

Selenium is one period below sulphur in the chalcogenides, and consequently has similar chemical properties. A combination of these similarities and some important distinctions have generated significant interest in selenium containing materials for the HER. These distinctions include: (1) more pronounced metallic character with respect to sulphur, suggesting enhanced conductivity; (2) a larger ionic radius for Se and (3) lower ionisation energy relative to S.[246] The high lying *p* state of the anion in these non-oxide materials, where the energy of the n*p* states is in the order O 2*p* < S 3*p* < Se 4*p*, means that materials with S and Se show a more metallic character compared to oxides and this is important for promoting the optimum adsorption free energy of hydrogen.

A DFT study of the active sites of $MoSe_2$ and WSe_2 showed that, similar to their sulphide analogues, the basal planes of these materials are inert, with the active sites being present along the edges.[52] Some results from this work are included in **Table 3.3.1**. A systematic computational study of layered TMDs of the form MX_2 (M = Ti, V, Nb, Ta, Mo, W, Pd, Pt; X = S, Se) identified some key trends with implications for practical implementation of such materials as HER catalysts.[268] The authors assessed the HER activity and stability of these materials based on computed values of ΔG_H and ΔG_{HX}, respectively. The latter quantity is the free energy of HX adsorption and an inverse relationship exists between H and HX binding. This implies that optimizing the HER activity can have detrimental effects on the stability of the catalyst. The authors considered ranges of chalcogen and hydrogen coverages, which can vary in a real system depending on the operating conditions. In general, hydrogen binding weakened with increasing hydrogen coverage. Moreover, through NEB calculations, the authors concluded that the Volmer-Heyrovsky pathway is most likely for these materials as prohibitively high activation barriers impede the Tafel step.

A study comparing the catalytic performance of electrodes consisting of porous arrays of MX_2 nanosheets (M = Mo, W; X = S, Se, Te), found a clear hierarchy in activity following: selenides > sulphides > tellurides. $MoSe_2$ out-performed all other materials, which was attributed, in part, to a low Tafel slope of 77 mV/dec. The authors also postulated that diselenide sites have a higher intrinsic activity relative to equivalent disulphide and ditelluride sites.

Common among these studies that aim to use computational methods and experiment, to determine the origin of the activity of TMDs, is the identification of edges as active sites.[269-271] Computationally, this conclusion is drawn from the comparison of ΔG_H for edge and basal sites. In one experiment, samples of MoS_2 nanoparticles of different sizes on Au(111) were prepared and the electrocatalytic activity correlated linearly with the number of MoS_2 edge sites.[271]

Bentley and colleagues implemented scanning electrochemical cell microscopy (SECCM) to create spatially-resolved measurements of the HER activity at basal and edge sites of bulk MoS_2.[272] Combining SECCM data with topographical information from scanning electron microscopy (SEM) and atomic force microscopy (AFM) showed enhanced activity at defects, steps and crevices. The authors followed up this study with additional measurements of HER at MoS_2, with improved temporal and spatial resolution.[273] The results indicated a uniform activity in the basal plane and that the enhanced activity at the edges scaled with the step height.

These results indicate the necessity to engineer TMD based catalysts that maximise the exposure of edge sites. However, strategies also exist for activating the basal plane. These and other considerations will be discussed in what follows.

3.3.2.1 Engineering Edge Sites

Nanoparticles are characterised by a high specific surface area and an abundance of low-coordinated surface sites and therefore nanostructuring of TMDs is an approach to enhance the HER activity. TMDs consist of 2D layers that interact *via* van der Waals forces and various methods exist for exfoliating these layers to produce nanosheets or nanoflakes.[274-276]

One such method involves applying adhesive tape to bulk TMD to peel off layers before transfer to a substrate material. This mechanical exfoliation technique was first employed by Novoselov and colleagues to isolate 2D single layers of graphene.[277] This method has since been used to deposit single- and few-layer nanosheets of TMDs onto SiO_2 coated Si substrates.[278] Another technique, described as similar to "drawing chalk on a blackboard", was employed by Novoselov *et al* to transfer single layers of BN, graphite, and TMDs to an oxidised silicon wafer.[279] While this approach is low-cost, it does not afford precise control or uniformity of the exfoliated layers and is further hindered by a low yield.

Exfoliation of layers from bulk materials can also be achieved by various methods applied to suspensions of bulk powders in solvents.[274-275, 280] These techniques include sonication, whereby the crystals are suspended in an appropriate solvent and broken apart by exposure to ultrasonic waves. This approach has been used successfully to isolate flakes of layered materials such as TMDs and BN.[281] Sonication can be combined with intercalation, wherein molecules or ionic species are incorporated into the space between layers, weakening interlayer interaction and increasing layer spacing.

The preceding methods are examples of top-down techniques, beginning from bulk materials and deconstructing them by one means or another to obtain nanostructures. Bottom-up strategies involve building layers of materials on a substrate from their constituent parts. Chemical vapour deposition (CVD) is an example of a bottom-up technique. In CVD, a heated substrate is exposed to volatile chemical precursors that react to deposit a layer of desired material. Tuning of operational parameters, such as temperature, the composition of the substrate and precursors, allows for control of the topography of the deposited material.[282] Nanotubes and fullerene-like nanoparticles of MoS_2 were obtained *via* reacting MoO_3 and S in an argon atmosphere.[283]

Dendritic monolayers of MoS_2 were deposited on $SrTiO_3$ and subsequently transferred intact to Au foil.[284] The fractal-like geometry of these samples expose a wealth of active sites for HER and Tafel slopes of 73-85 mV/dec were reported. This compares favourably with values of 140-145 mV/dec, measured for multi-layer MoS_2 grown on glassy carbon electrodes. The authors reported exchange current densities of 5-25 $\mu A/cm^2$, depending on preparation temperature, and durability tests showed a reproducible polarisation plot after 1000 voltammetry cycles. Shi and coworkers deposited hexagonal TaS_2 flakes on Au foil *via* CVD.[285] The authors measured Tafel slopes in the range 33-42 mV/dec for 2H-TaS_2/Au samples, which compare with 31 mV/dec for Pt. The overpotentials, η_{10}, of the 2H-TaS_2 samples were between 65-150 mV and the exchange current densities were 100-179 $\mu A/cm^2$.

Hydrothermal and solvothermal synthesis are other bottom-up techniques, which for TMDs, typically involve the reaction of transition metal salts in aqueous/organic solutions at moderate to high temperatures (80-240 °C).[274, 286-287] These methods allow for considerable control over the product by tuning preparation parameters, and morphologies such as nanorods, nanosheets, and nanoflowers of MoS_2 have been

achieved in this way.[286] Such techniques have been used to grow MoS_2 on TiO_2[288-289] and carbon[290] nanotubes and reduced graphene oxide (rGO).[291]

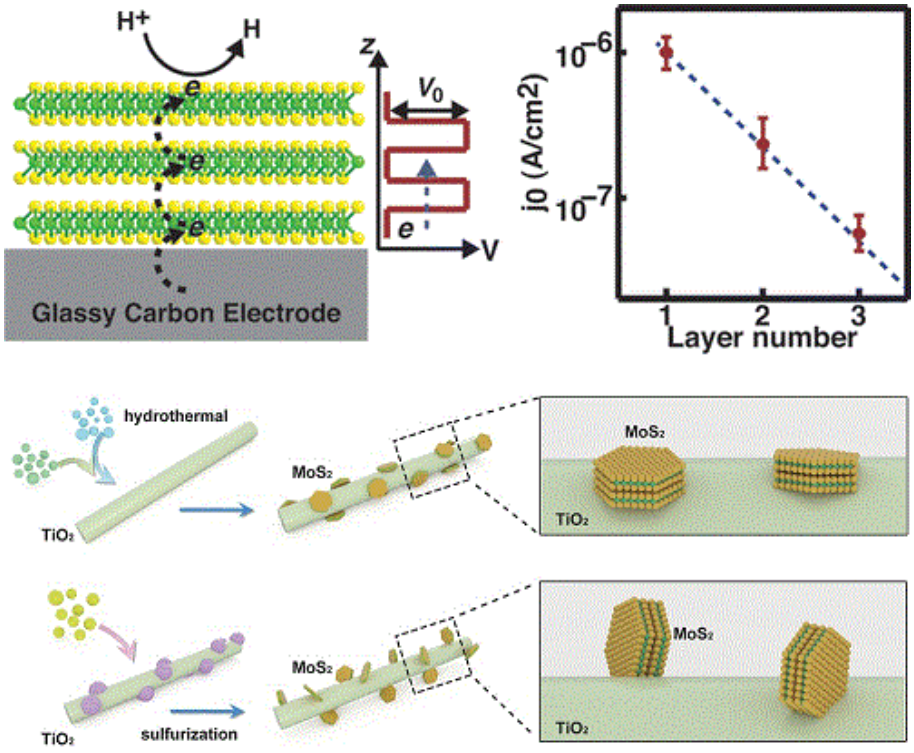

Figure 3.3.4 Top-left: Illustration of electrons hopping across layers of a TMD and the potential barriers in the interlayer gap that must be overcome. Top-right: The exchange current density of the MoS_2 film as a function of the layer number. From ref. [292]. Bottom: Schematic illustration of two methods of preparation of MoS_2/TiO_2 composites. The first is a hydrothermal method where the basal planes of the MoS_2 nanoplates lie flat on the TiO_2 surface. The second method involves CVD followed by sulphurisation to achieve a configuration in which the MoS_2 nanoplates contact with the TiO_2 surface along conductive edge planes. Taken from ref. [293].

These are but a few of the techniques that have been implemented to deposit nanostructured TMDs on substrates and a comprehensive overview of other methods is provided in ref. [274]. A common feature of these techniques is that the nanostructured TMD lies flat on the substrate surface[246, 292-293] which minimises the surface energy.[294] One consequence is that this orientation exposes the inactive basal plane. Secondly, electrons

must transfer from the substrate to the active sites of the outermost layer, and in doing so overcome the interlayer potential barrier (see **Figure 3.3.4**).

He and co-workers addressed this issue by constructing edge-on MoS_2/TiO_2 heterostructures.[293] This was achieved in a two-step process wherein a hydrothermal preparation of MoO_2 on TiO_2 was followed by sulphurisation by CVD. The core idea of this approach is that sulphurisation is faster parallel to the basal plane, owing to the weak inter-layer interaction. A similar effect was achieved for MoS_2 on a carbon fibre paper (CFP) substrate by Hu *et al* using a microwave hydrothermal method.[295] By altering the reaction time, the researchers could control whether the exposed edges of MoS_2 were stepped or flat with respect to each other. The authors measured Tafel slopes of 121, 69, and 59 mV/dec for samples with randomly oriented, flat edged and stepped edge MoS_2, indicating that stepped edges promote HER activity.

CoS_2 was the subject of a combined theoretical and experimental study.[296] CoS_2 microspheres were terminated by vertical arrays of CoS_2 sheets with an abundance of exposed sulphur sites. The authors reported a Tafel slope of 67 mV/dec and a low overpotential of 90 mV at 10 mA/cm^2. DFT analysis of free energies of hydrogen adsorption at different CoS_2 facets, at a coverage of 1/8 ML showed computed values for ΔG_H in the range 0.04-0.06 eV. Wang *et al* reported Tafel slopes of 60 and 77 mV/dec for $MoSe_2$ and WSe_2 films grown vertically on a CFP substrate.[294] The authors concluded that the curvature and roughness of the substrate enhanced the exposure of active sites.

3.3.2.2 Activating the basal plane

Before describing approaches to increasing the activity of basal plane of TMDs we first note that these materials exist predominantly in two polymorphs, denoted 2H and 1T. The

2H phase exhibits tetrahedral coordination while the 1T phase is characterised by octahedral coordination, as shown in **Figure 3.3.5**.

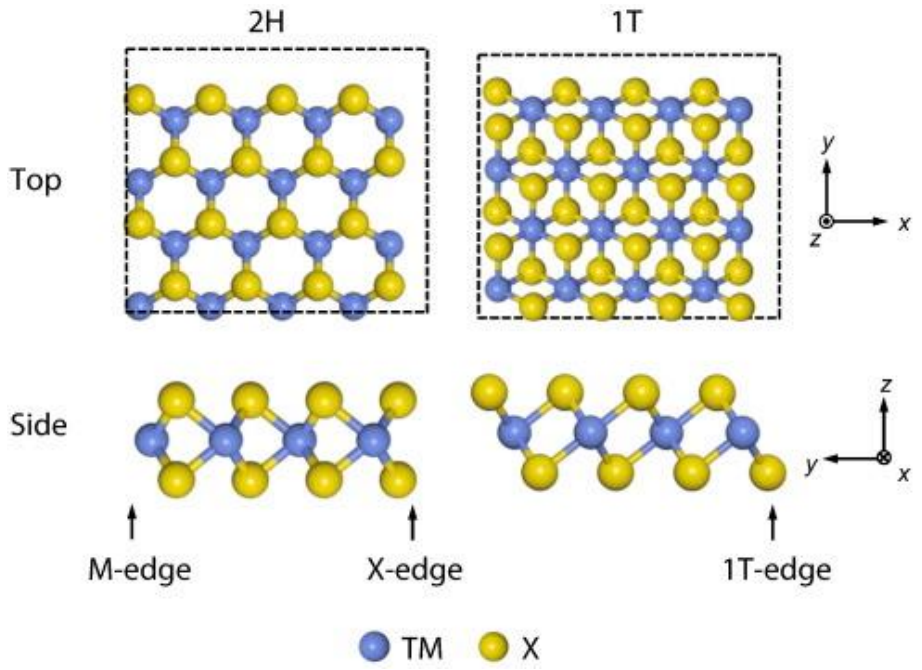

Figure 3.3.5 Unit cells for the basal plane of 2H and 1T TMD structures, showing the top and side views. Three types of edges, the 1T edge, the 2H M-edge, and the 2H X-edge are indicated by the arrows. Image taken from ref. [268].

For bulk group 6 TMDs, such as MoS_2 and WS_2, the 2H phase is thermodynamically favoured over the metastable 1T phase, although this is not true for all TMDs.[268] The electronic properties of these materials depend on the structural geometry. For example, the basal plane of MoS_2 is semiconducting in the 2H phase and becomes metallic in the 1T phase. In addition to enhanced conductivity, the 1T phase has active sites for HER in the basal plane.[246, 268, 297-298] This was deduced from measurements of the activities of 2H- and 1T-MoS_2 samples after oxidation; the activity of 2H-MoS_2 decreased after oxidation of edge sites whereas the activity of 1T-MoS_2 was undiminished, implying the presence of active sites in the basal plane.

This suggests a strategy for promoting the activity of TMDs might be to promote their metallic phase. The 2H-1T phase transition has been shown to occur in samples of MoS_2 upon exfoliation *via* Li intercalation.[251, 297-298] Tafel slopes of 40[297] and 43[298] mV/dec were measured for 1T-MoS_2 samples prepared in this manner. As mentioned above metallic 2H-TaS_2 deposited on Au foil (Tafel slopes: 33-42 mV/dec) showed HER activity comparable to that of Pt (31 mV/dec) [285], and similar results were found for 1T-MoS_2 decorating TiO_2 nanotubes (38-42 mV/dec).[288] Voiry and colleagues measured a Tafel slope of 60 mV/dec for metallic 1T-WS_2, with 110 mV/dec for 2H-WS_2.[299]

Yin and coworkers isolated 1T-$MoSe_2$ nanosheets for which they measured a Tafel slope of 52 mV/dec and η_{10} of 152 mV.[300] The catalyst stability was assessed by cycling the electrodes 1,000 times, which showed negligible losses in current density. Kong and co-workers produced a nanoparticulate $CoSe_2$ film on CFP and the resulting electrode consisted of $CoSe_2$ nanoparticles with dimensions of tens of nanometers.[301] X-ray diffraction (XRD) analysis revealed the presence of predominantly cubic pyrite phase, with some evidence of marcasite and amorphous phases. The metallic property of $CoSe_2$ contributed to the high HER activity, as shown by a Tafel slope of 40 mV/dec and η_{10} of 137 mV.

It is also possible to activate the basal plane of semiconducting 2H-MoS_2. This was first achieved by Li and colleagues through combinations of S-vacancies and strain.[302] The combination of S-vacancies and strain could be tuned such that the optimal condition of $\Delta G_H = 0eV$ was satisfied. The authors identified S-vacancies as active sites and DFT calculations revealed defect gap states that could be shifted towards the Fermi level by application of strain, which would promote the adsorption of hydrogen. Experimentally, this manifested as measured Tafel slopes of 60 mV/dec for the strained sample with S-vacancies; a value of 98 mV/dec was measured for the sample without strain or vacancies.

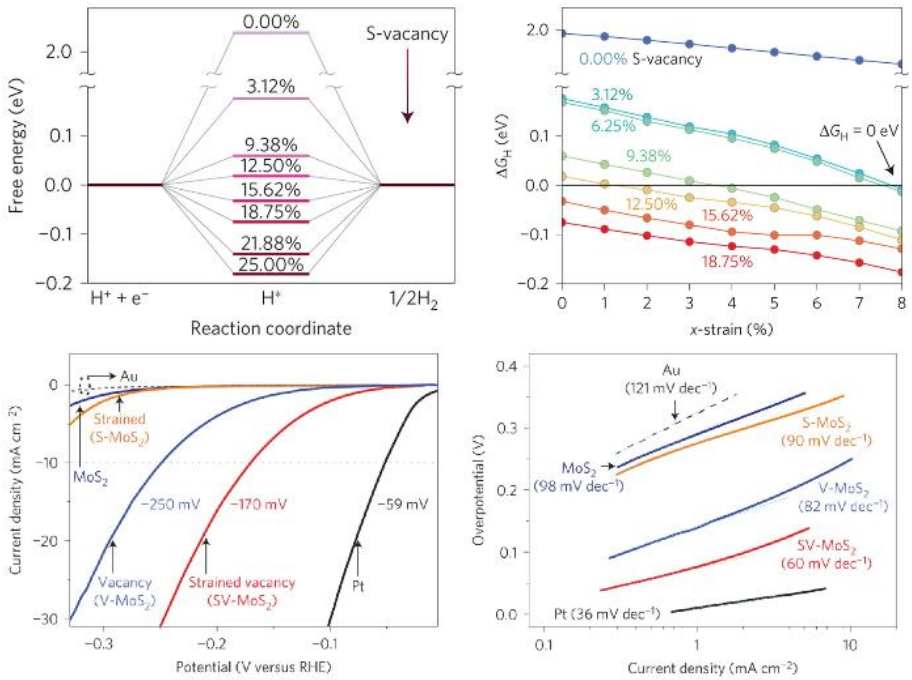

Figure 3.3.6 (a) Free energies of HER at the MoS_2 basal plane, computed for the S-vacancy range of 0–25%. **(b)** ΔG_H vs. %x-strain for the S-vacancy range of 0-18.75%. The black line indicates combinations of S-vacancy and strain that yield the optimal $\Delta G_H = 0$ eV. **(c)** Linear sweep curves for the Au substrate; Pt electrode; unstrained and vacancy-free MoS_2, (MoS_2); strained [~1.35%] MoS_2 without S-vacancies, (S-MoS_2); unstrained MoS_2 with S-vacancies [~12.5%] (V-MoS_2); and strained [~1.35%] MoS_2 with S-vacancies [~12.5%] (SV-MoS_2). **(d)** Tafel plots corresponding to the linear sweep curves in **(c)**. From ref. [302].

The role of gap states in the HER activity was also investigated by Li and coworkers in their study of MoS_2 films grown on a Mo substrate[303]. A combination of S-vacancies and Pt-doping introduced gap states which promote the HER activity. The authors reported a Tafel slope of 38 mV/dec for the Pt/MoS_2/Mo heterostructure, which compared with 68 mV/dec for MoS_2/Mo. Values for η_{10} of 58 and 198 mV were recorded for Pt/MoS_2/Mo and MoS_2/Mo, respectively, further highlighting a crucial role for Pt in the catalytic activity.

A comprehensive study of active sites of MoS_2 reported a maximum in catalytic activity for S-vacancy concentrations in the range of 7-10%.[304] The crystalline quality near the

vacancy also strongly affected the activity of the vacancy. Dong and colleagues described morphological control of MoS_2 flakes prepared *via* CVD, and as a consequence of this method, control of the abundance of S-vacancies.[305] S-vacancies have also been introduced to the basal plane of MoS_2 by electrochemical desulphurisation as a viable alternative to Ar plasma exposure.[306]

Gao *et al* reported a method for heterostructuring defect-rich MoS_2 nanoflakes on exfoliated MoS_2/WS_2 scaffolds, *via* a hydrothermal approach[307] and measured Tafel slopes of 81 and 73 mV/dec for the flakes on MoS_2 and WS_2, respectively. Geng and colleagues approached activating the basal plane by fabricating porous MoS_2,[308] which yielded a Tafel slope of 62 mV/dec. The measured η_{10} was 201 mV and no differences were observed in polarisation curves before and after 3,000 CV cycles. A systematic study of the impact of phase, edge sites and S-vacancies on the HER activity concluded that phase is the major determining factor.[309] The 1T-MoS_2 samples consistently outperformed the 2H phase.

3.3.2.3 Amorphous TMDs

Amorphous MoS_x has also been investigated as a HER catalyst with reports of activities rivalling those of 1T-MoS_2.[310-311] One advantage of amorphous MoS_x is the ease and economy with which it can be synthesised; simple, wet chemical techniques, requiring no high-temperature processing have been reported in the literature.[312-313] Merki *et al* prepared amorphous MoS_2 films using electro-polymerisation procedures and reported high current densities at low overpotentials with a Tafel slope of 40 mV/dec and η_{15} of 200 mV.[310]

A study by Wu and colleagues attributed the high activity of amorphous MoS_2 to similarities with 1T-MoS_2 in terms of bonding character and electronic structure.[311] The authors identified a short Mo-Mo bond, common to 1T-phase and amorphous samples, as a crucial feature for the HER activity. Tafel slopes of 65, 58 and 42 mV/dec were measured for 2H-, 1T- and amorphous MoS_2, respectively. Wang *et al* fabricated copolymer hybrid films consisting of polypyrrole and amorphous MoS_x (x~5).[314] The result exhibited a HER activity comparable to that of commercial Pt/C catalysts with a Tafel slope of 29 mV/dec; however, a clear decrease in current was observed after 5,000 s at a potential of -0.05 V (vs. RHE).

A strategy to further enhance the HER activity of amorphous MoS_x *via* doping with first row transition metals was investigated by Merki *et al*.[315] The Tafel slopes for all samples of M-MoS_3 (M = Mn, Fe, Co, Ni, Cu, Zn) were in the range 39-43 mV/dec. The authors found that Fe-, Co- and Ni-doping promoted growth of the MoS_3 film, resulting in higher surface area and catalyst loading, and consequently, enhanced HER activity. However, the authors also concluded that the improved activity was not attributable solely to morphological effects and that the dopants increased the intrinsic catalytic activity. The impact on activity was pH-dependent, with Fe- and Co-doping performing best under acidic and neutral conditions, respectively.

The use of MoS_x-coated carbon electrodes in microbial electrolysis cells (MECs) under operating conditions was investigated by Kokko and colleagues.[316] MECs can renewably produce H_2 while simultaneously treating wastewater. The best performing MoS_x electrodes exhibited onset potentials only slightly higher than that of a platinum electrode and Tafel slopes were in the range of 40-100 mV/dec. The values for η_{10} were in the range 130-250 mV. Importantly, the catalytic efficiency improved over time whereas the

Pt electrode was slowly deactivated. This latter result is common for amorphous MoS_x electrodes and is attributed to structural changes induced under HER conditions.

Amorphous $MoSe_x$ has also been reported as an efficient catalyst for the HER.[317] While the as-prepared amorphous $MoSe_3$ nanopowder was inactive, exposure to HER conditions rendered the catalyst active. This was attributed to the development of structures with composition close to that of $MoSe_2$. The active catalytic material was more robust than its MoS_x analogue and operated in a wider range of pH solutions. In a pH 0 electrolyte, $MoSe_x$ displayed a Tafel slope of 60 mV/dec and η_{10} of 270 mV.

3.3.2.4 Heterostructuring

Heterostructuring consists of interfacing two or more materials of different composition or phase. In this way it is possible to combine the qualities of each phase and moreover, capitalise on novel properties which emerge at the interface.

Wang and coworkers grew MoS_2 on CoS_2 decorated carbon cloth ($MoS_2/CoS_2/CC$) and investigated the activity of this sandwich-structured electrode for HER.[318] The interplay between the MoS_2 and CoS_2 phases was shown to play a crucial role in both the HER activity and stability of the electrode. This was established by comparing the performance of $MoS_2/CoS_2/CC$, MoS_2/CC and CoS_2/CC, for which Tafel slopes of 37, 50 and 60 mV/dec were measured, respectively. $MoS_2/CoS_2/CC$ exhibited η_{10} of 118 mV and showed no decay in performance after 4,000 CV cycles. The enhanced activity was attributed to optimal adsorption of hydrogen at interfacial S-sites; strong bonding interactions between MoS_2 and CoS_2 were the origin of the superior stability, compared to the individual materials.

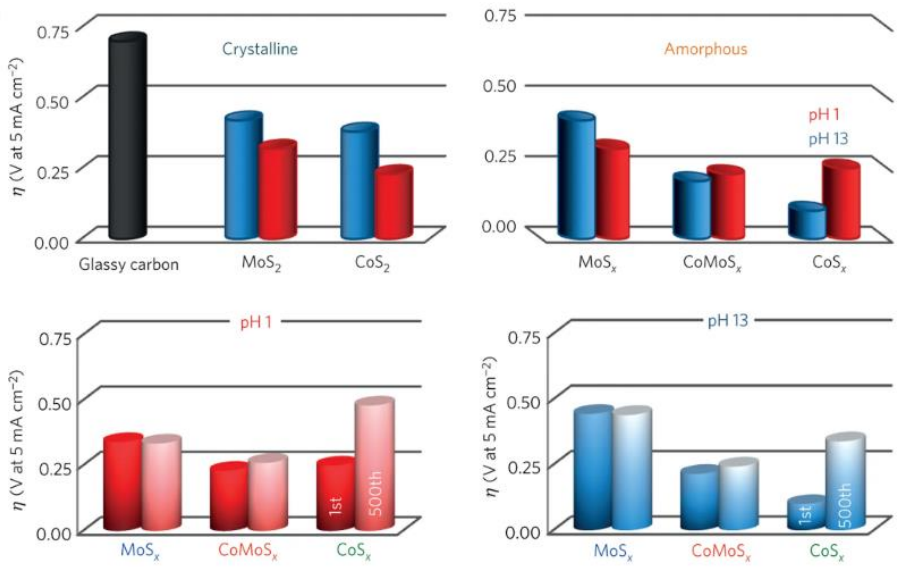

Figure 3.3.7 Top: Overpotentials required for 5 mA/cm^2 current densities, η_5, in pH 1 and pH 13, for both crystalline and amorphous TMS_x. Crystalline CoS_2 is always more active than MoS_2, and both materials are more active in acidic than alkaline solutions. For amorphous samples CoS_x is always more active, particularly in alkaline solution. The activity of $CoMoS_x$ is almost independent of pH. **Bottom:** Overpotentials, η_5, in pH 1 and pH 13, before and after 500 CV cycles. CoS_x is the most active and least stable material. The $CoMoS_x$ chalcogel catalyst is stable and active, and shown as a pH-universal catalyst for the HER. From ref. [319].

In their 2016 paper,[319] Staszak-Jirkovský and colleagues established that while amorphous CoS_x is more active than amorphous MoS_x, as measured by HER activity in acidic and alkaline media, the latter is more stable, and this observation informed the rational design of a low-cost $CoMoS_x$ chalcogel catalyst. The resulting catalyst was highly active and stable, irrespective of pH. In alkaline media there was a large difference in activity, following: $MoS_x \ll CoMoS_x \ll CoS_x$; whereas, in acid solutions the differences were less significant, with $MoS_x < CoS_x \leq CoMoS_x$, as shown in **Figure 3.3.7**. Moreover, the authors noted that less active crystalline MoS_2 and CoS_2 were more stable than their amorphous analogues by a factor of 10, which implies an important role for the density of defects in the relationship between activity and stability.

Zhang and coworkers prepared polymorphic $CoSe_2$ with mixed orthorhombic and cubic phases.[320] The authors described polymorphic $CoSe_2$ (p-CoSe2) as a highly active HER catalyst with activities exceeding those of amorphous CoS_x, cubic $CoSe_2$ and CoSe. The phase and morphology of the samples were tuned *via* the calcination temperature. The measured Tafel slopes were 38, 31, 39 and 55 mV/dec for $CoSe_x$, p-$CoSe_2$, c-$CoSe_2$ and CoSe, respectively. The corresponding values for η_{10} were 180, 150, 200, and 270 mV, indicating that the polymorphic sample had the best activity. The value of η_{10} was found to increase by 8 mV for p-$CoSe_2$ after 40 h of galvanostatic measurement.

3.3.2.5 Ternary TMDs

Ternary TMDs (TTMDs) have also been considered in the pursuit for active and stable HER catalysts.[321] TTMDs have the general formula $M^1_zM^2_{1-z}X_2$ or $MX^1_{2z}X^2_{2(1-z)}$, where M^1, M^2 and M are transition metals ($M^1 \neq M^2$) and X^1, X^2 = S, Se or Te ($X^1 \neq X^2$). The properties of TTMDs can be tuned by altering the composition and the molar ratio, z.

Kiran and co-workers found that $MoS_{2z}Se_{2(1-z)}$ alloys possessed higher HER activity compared to MoS_2 and $MoSe_2$.[322] The authors systematically studied the structure-activity relationship by varying the composition and found that MoS_1Se_1 presented the highest HER activity among the catalysts under study, which they attributed to improved electronic conductivity. Konkena *et al* studied MoSSe interfaced with rGO.[323] The authors reported that the nanocomposite heterostructures were active and stable electrocatalysts for HER. They measured a Tafel slope of 51 mV/dec and η_{10} of 155 mV. Stability tests showed no decrease in performance after 5,000 cycles.

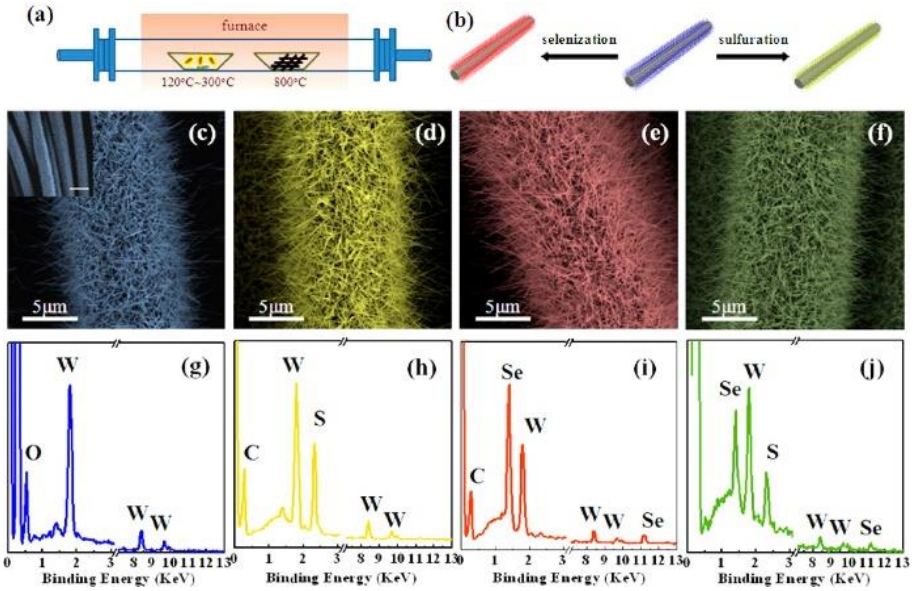

Figure 3.3.8 (a) and **(b)** Schematics of the experimental setup for fabrication of WS_2, WSe_2, and $WS_{2(1-x)}Se_{2x}$ nanotubes. SEM images of (c) WO3 nanowires and (d) WS2, (e) WSe2, and (f) WS2(1–x)Se2x nanotubes. X-ray energy dispersive spectroscopy (EDS) pattern of **(g)** WO_3 NWs and **(h)** WS_2, **(i)** WSe_2, and **(j)** $WS_{2(1-x)}Se_{2x}$ NTs. From ref. [324].

Liu *et al* reported a Tafel slope of 44 mV/dec for $CoS_{2z}Se_{2(1-z)}$ (z = 0.67) nanowires on flexible carbon fiber.[325] This compared with values of 69 and 46 mV/dec for CoS_2 and $CoSe_2$ nanowires, respectively. The authors measured η_{10} of 130 mV, with no decrease in activity after 1,000 cycles. Xu *et al* used CVD to synthesise high-quality WS_2, WSe_2 and $WS_{2z}Se_{2(1-z)}$ nanotubes on carbon fibers (see **Figure 3.3.8**).[324] The WS_2, WSe_2 and $WS_{2z}Se_{2(1-z)}$ (z = 0.48) nanotubes exhibited Tafel slopes of 113, 99, and 105 mV/dec and values for j_0 of 12, 3, and 29 μA/cm^2 . The enhanced activity of these TTMD catalysts is due to improved conductivity, which results from incorporation of Se into the WS_2 lattice, as evidenced by analyses of the electronic structure.

Zhang and colleagues implemented CVD techniques to grow dendritic $WS_{2z}Se_{2(1-z)}$ flakes on a $SrTiO_3$ substrate.[326] The flakes, with a morphology that produces an abundance of active edge sites, were transferred to Au foil to measure their HER capability. The $WS_{2z}Se_{2(1-z)}$ on Au electrode, with an S to Se ratio of 19 to1, presented a Tafel slope and

η_{10} of 67 mV/dec and 156 mV, which were lower than those measured for dendritic WS_2 (87 mV/dec and 310 mV). Other studies of $WS_{2z}Se_{2(1-z)}$ inferred that active sites are present on the basal plane of the TTMD due to lattice strain arising from the different atomic radii of S and Se atoms.[327-328]

Xia *et al* prepared $Ni_zCo_{(1-z)}Se_2$ (z = 0.33) solid solutions by selenisation of a nickel cobalt precursor.[329] The resulting $Ni_zCo_{(1-z)}Se_2$ catalyst consisted of mixed cubic and orthorhombic phases. Through temperature dependent measurements of the conductivity, the authors described the metallic-like electrical conductivity of the TTMD solid solution. The room-temperature conductivity of $Ni_zCo_{(1-z)}Se_2$ was three times that of $CoSe_2$. DFT calculations indicated that incorporation of Ni into the $CoSe_2$ lattice lowered the free energy of hydrogen adsorption at edge sites. $Ni_zCo_{(1-z)}Se_2$ operated under both acidic and alkaline conditions and measurements in an acidic electrolyte yielded a Tafel slope of 35 mV/dec and η_{10} of 65 mV, with no loss of performance after 24h of electrolysis.

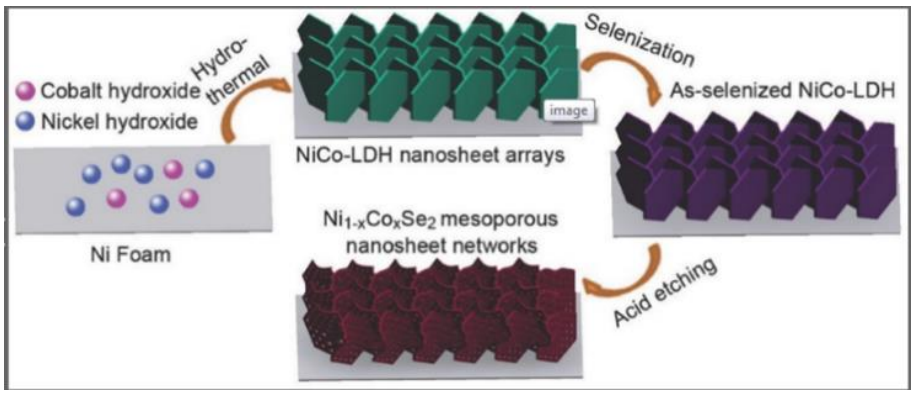

Figure 3.3.9 Schematic showing the process for fabrication of mesoporous $Ni_{(1-z)}Co_zSe_2$ nanosheets. Taken from ref. [330].

Lie *et al* prepared 3D $Ni_{(1-z)}Co_zSe_2$ mesoporous nanosheet networks with tunable stoichiometry (z = 0-0.35), which operated as HER catalysts with excellent stability over a wide pH range.[330] The authors identified $Ni_{(1-z)}Co_zSe_2$ (z = 0.11) as the optimal configuration. DFT calculations revealed that $Ni_{0.89}Co_{0.11}Se_2$ was metallic with high

electrical conductivity. The electronic structure that resulted from substitutional doping of Co into the $NiSe_2$ lattice led to favourable adsorption free energies of H and H_2O at the surface. Tafel slopes of 0.39, 0.78 and 0.52 mV/dec were measured for $Ni_{0.89}Co_{0.11}Se_2$ operating in acidic, neutral and alkaline conditions, respectively.

3.4 Chapter References

1. Mori-Sánchez, P.; Cohen, A. J., The derivative discontinuity of the exchange–correlation functional. *Physical Chemistry Chemical Physics* **2014,** *16* (28), 14378-14387.
2. Mori-Sánchez, P.; Cohen, A. J.; Yang, W., Localization and Delocalization Errors in Density Functional Theory and Implications for Band-Gap Prediction. *Physical Review Letters* **2008,** *100* (14), 146401.
3. Perdew, J. P.; Zunger, A., Self-interaction correction to density-functional approximations for many-electron systems. *Physical Review B* **1981,** *23* (10), 5048-5079.
4. Kohn, W.; Sham, L. J., Self-Consistent Equations Including Exchange and Correlation Effects. *Physical Review* **1965,** *140* (4A), A1133-A1138.
5. Morales-García, Á.; Valero, R.; Illas, F., An Empirical, yet Practical Way To Predict the Band Gap in Solids by Using Density Functional Band Structure Calculations. *The Journal of Physical Chemistry C* **2017,** *121* (34), 18862-18866.
6. Sham, L. J.; Schlüter, M., Density-Functional Theory of the Energy Gap. *Physical Review Letters* **1983,** *51* (20), 1888-1891.
7. Jones, R. O.; Gunnarsson, O., The density functional formalism, its applications and prospects. *Reviews of Modern Physics* **1989,** *61* (3), 689-746.
8. Chan, M.; Ceder, G., Efficient band gap prediction for solids. *Physical review letters* **2010,** *105* (19), 196403.
9. Kulik, H. J., Perspective: Treating electron over-delocalization with the DFT+U method. *The Journal of Chemical Physics* **2015,** *142* (24), 240901.
10. Cramer, C. J.; Truhlar, D. G., Density functional theory for transition metals and transition metal chemistry. *Physical Chemistry Chemical Physics* **2009,** *11* (46), 10757-10816.
11. German, E.; Faccio, R.; Mombrú, A. W., A DFT+U study on structural, electronic, vibrational and thermodynamic properties of TiO2 polymorphs and hydrogen titanate: tuning the Hubbard 'U-term'. *Journal of Physics Communications* **2017,** *1* (5), 055006.
12. Becke, A. D., Density-functional thermochemistry. III. The role of exact exchange. *The Journal of Chemical Physics* **1993,** *98* (7), 5648-5652.
13. Heyd, J.; Scuseria, G. E.; Ernzerhof, M., Hybrid functionals based on a screened Coulomb potential. *The Journal of Chemical Physics* **2003,** *118* (18), 8207-8215.
14. Crowley, J. M.; Tahir-Kheli, J.; Goddard, W. A., Resolution of the Band Gap Prediction Problem for Materials Design. *The Journal of Physical Chemistry Letters* **2016,** *7* (7), 1198-1203.
15. Ko, K. C.; Lamiel-García, O.; Lee, J. Y.; Illas, F., Performance of a modified hybrid functional in the simultaneous description of stoichiometric and reduced TiO_2 polymorphs. *Physical Chemistry Chemical Physics* **2016,** *18* (17), 12357-12367.
16. Viñes, F.; Illas, F., Electronic structure of stoichiometric and reduced ZnO from periodic relativistic all electron hybrid density functional calculations using numeric atom-centered orbitals. *Journal of Computational Chemistry* **2017,** *38* (8), 523-529.
17. de P. R. Moreira, I.; Illas, F.; Martin, R. L., Effect of Fock exchange on the electronic structure and magnetic coupling in NiO. *Physical Review B* **2002,** *65* (15), 155102.
18. Friedrich, C.; Schindlmayr, A., Many-Body Perturbation Theory: The GW Approximation. In *NIC series*, John von Neumann Institute for Computing: Jülich, 2006; Vol. 31, pp 335-355.

19. Di Valentin, C.; Selloni, A., Bulk and surface polarons in photoexcited anatase TiO_2. *The Journal of Physical Chemistry Letters* **2011,** *2* (17), 2223-2228.
20. Henkelman, G.; Arnaldsson, A.; Jónsson, H., A fast and robust algorithm for Bader decomposition of charge density. *Computational Materials Science* **2006,** *36* (3), 354-360.
21. Di Valentin, C.; Fittipaldi, D., Hole Scavenging by Organic Adsorbates on the TiO_2 Surface: A DFT Model Study. *The Journal of Physical Chemistry Letters* **2013,** *4* (11), 1901-1906.
22. Nolan, M., Alkaline earth metal oxide nanocluster modification of rutile TiO_2 (110) promotes water activation and CO_2 chemisorption. *Journal of Materials Chemistry A* **2018,** *6* (20), 9451-9466.
23. Cheng, J.; VandeVondele, J.; Sprik, M., Identifying Trapped Electronic Holes at the Aqueous TiO_2 Interface. *The Journal of Physical Chemistry C* **2014,** *118* (10), 5437-5444.
24. Wallace, S. K.; McKenna, K. P., Facet-Dependent Electron Trapping in TiO_2 Nanocrystals. *The Journal of Physical Chemistry C* **2015,** *119* (4), 1913-1920.
25. Wang, X.; Zhang, G.; Yang, L.; Sharman, E.; Jiang, J., Material descriptors for photocatalyst/catalyst design. *Wiley Interdisciplinary Reviews: Computational Molecular Science* **2018,** *8* (5), e1369.
26. Manz, T. A.; Sholl, D. S., Chemically Meaningful Atomic Charges That Reproduce the Electrostatic Potential in Periodic and Nonperiodic Materials. *Journal of Chemical Theory and Computation* **2010,** *6* (8), 2455-2468.
27. Limas, N. G.; Manz, T. A., Introducing DDEC6 atomic population analysis: part 2. Computed results for a wide range of periodic and nonperiodic materials. *RSC Advances* **2016,** *6* (51), 45727-45747.
28. Manz, T. A.; Limas, N. G., Introducing DDEC6 atomic population analysis: part 1. Charge partitioning theory and methodology. *RSC Advances* **2016,** *6* (53), 47771-47801.
29. Nozik, A. J., Photoelectrochemistry: Applications to Solar Energy Conversion. *Annual Review of Physical Chemistry* **1978,** *29* (1), 189-222.
30. Wang, L.; Ge, J.; Wang, A.; Deng, M.; Wang, X.; Bai, S.; Li, R.; Jiang, J.; Zhang, Q.; Luo, Y.; Xiong, Y., Designing p-Type Semiconductor–Metal Hybrid Structures for Improved Photocatalysis. *Angewandte Chemie* **2014,** *126* (20), 5207-5211.
31. De Waele, S.; Lejaeghere, K.; Sluydts, M.; Cottenier, S., Error estimates for density-functional theory predictions of surface energy and work function. *Physical Review B* **2016,** *94* (23), 235418.
32. Ren, Y.; Zeng, D.; Ong, W.-J., Interfacial engineering of graphitic carbon nitride (g-C3N4)-based metal sulfide heterojunction photocatalysts for energy conversion: A review. *Chinese Journal of Catalysis* **2019,** *40* (3), 289-319.
33. Valdés, Á.; Qu, Z. W.; Kroes, G. J.; Rossmeisl, J.; Nørskov, J. K., Oxidation and Photo-Oxidation of Water on TiO2 Surface. *The Journal of Physical Chemistry C* **2008,** *112* (26), 9872-9879.
34. Liao, P.; Keith, J. A.; Carter, E. A., Water Oxidation on Pure and Doped Hematite (0001) Surfaces: Prediction of Co and Ni as Effective Dopants for Electrocatalysis. *Journal of the American Chemical Society* **2012,** *134* (32), 13296-13309.
35. Nguyen, M.-T.; Piccinin, S.; Seriani, N.; Gebauer, R., Photo-Oxidation of Water on Defective Hematite(0001). *ACS Catalysis* **2015,** *5* (2), 715-721.
36. Rossmeisl, J.; Logadottir, A.; Nørskov, J. K., Electrolysis of water on (oxidized) metal surfaces. *Chemical Physics* **2005,** *319* (1), 178-184.

37. Rossmeisl, J.; Qu, Z. W.; Zhu, H.; Kroes, G. J.; Nørskov, J. K., Electrolysis of water on oxide surfaces. *Journal of Electroanalytical Chemistry* **2007,** *607* (1), 83-89.
38. Henkelman, G.; Uberuaga, B. P.; Jónsson, H., A climbing image nudged elastic band method for finding saddle points and minimum energy paths. *The Journal of Chemical Physics* **2000,** *113* (22), 9901-9904.
39. Jónsson, H.; Mills, G.; Jacobsen, K. W., Nudged elastic band method for finding minimum energy paths of transitions. In *Classical and Quantum Dynamics in Condensed Phase Simulations*, pp 385-404.
40. Hammer, B.; Nørskov, J. K., Theoretical surface science and catalysis—calculations and concepts. In *Advances in Catalysis*, Academic Press: 2000; Vol. 45, pp 71-129.
41. Nørskov, J. K.; Bligaard, T.; Rossmeisl, J.; Christensen, C. H., Towards the computational design of solid catalysts. *Nature Chemistry* **2009,** *1*, 37.
42. Bhattacharjee, S.; Waghmare, U. V.; Lee, S.-C., An improved d-band model of the catalytic activity of magnetic transition metal surfaces. *Scientific Reports* **2016,** *6*, 35916.
43. Lima, F. H. B.; Zhang, J.; Shao, M. H.; Sasaki, K.; Vukmirovic, M. B.; Ticianelli, E. A.; Adzic, R. R., Catalytic Activity−d-Band Center Correlation for the O_2 Reduction Reaction on Platinum in Alkaline Solutions. *The Journal of Physical Chemistry C* **2007,** *111* (1), 404-410.
44. Huang, B.; Xiao, L.; Lu, J.; Zhuang, L., Spatially Resolved Quantification of the Surface Reactivity of Solid Catalysts. *Angewandte Chemie International Edition* **2016,** *55* (21), 6239-6243.
45. Fukui, K., Role of Frontier Orbitals in Chemical Reactions. *Science* **1982,** *218* (4574), 747-754.
46. Henderson, M. A.; Epling, W. S.; Peden, C. H. F.; Perkins, C. L., Insights into Photoexcited Electron Scavenging Processes on TiO_2 Obtained from Studies of the Reaction of O_2 with OH Groups Adsorbed at Electronic Defects on TiO2(110). *The Journal of Physical Chemistry B* **2003,** *107* (2), 534-545.
47. Schaub, R.; Thostrup, P.; Lopez, N.; Lægsgaard, E.; Stensgaard, I.; Nørskov, J. K.; Besenbacher, F., Oxygen Vacancies as Active Sites for Water Dissociation on Rutile TiO_2(110). *Phys. Rev. Lett.* **2001,** *87* (26), 266104.
48. Mullins, D. R.; Albrecht, P. M.; Chen, T.-L.; Calaza, F. C.; Biegalski, M. D.; Christen, H. M.; Overbury, S. H., Water Dissociation on CeO_2(100) and CeO_2(111) Thin Films. *The Journal of Physical Chemistry C* **2012,** *116* (36), 19419-19428.
49. Lira, E.; Wendt, S.; Huo, P.; Hansen, J. Ø.; Streber, R.; Porsgaard, S.; Wei, Y.; Bechstein, R.; Lægsgaard, E.; Besenbacher, F., The Importance of Bulk Ti^{3+} Defects in the Oxygen Chemistry on Titania Surfaces. *Journal of the American Chemical Society* **2011,** *133* (17), 6529-6532.
50. Xiong, L.-B.; Li, J.-L.; Yang, B.; Yu, Y., Ti^{3+} in the Surface of Titanium Dioxide: Generation, Properties and Photocatalytic Application. *Journal of Nanomaterials* **2012,** *2012*, 13.
51. Nørskov, J. K.; Bligaard, T.; Logadottir, A.; Kitchin, J. R.; Chen, J. G.; Pandelov, S.; Stimming, U., Trends in the Exchange Current for Hydrogen Evolution. *Journal of The Electrochemical Society* **2005,** *152* (3), J23-J26.
52. Tsai, C.; Chan, K.; Abild-Pedersen, F.; Nørskov, J. K., Active edge sites in $MoSe_2$ and WSe_2 catalysts for the hydrogen evolution reaction: a density functional study. *Physical Chemistry Chemical Physics* **2014,** *16* (26), 13156-13164.
53. Hinnemann, B.; Moses, P. G.; Bonde, J.; Jørgensen, K. P.; Nielsen, J. H.; Horch, S.; Chorkendorff, I.; Nørskov, J. K., Biomimetic Hydrogen Evolution: MoS_2

Nanoparticles as Catalyst for Hydrogen Evolution. *Journal of the American Chemical Society* **2005,** *127* (15), 5308-5309.
54. Tahir, M.; Pan, L.; Idrees, F.; Zhang, X.; Wang, L.; Zou, J.-J.; Wang, Z. L., Electrocatalytic oxygen evolution reaction for energy conversion and storage: A comprehensive review. *Nano Energy* **2017,** *37*, 136-157.
55. Suen, N.-T.; Hung, S.-F.; Quan, Q.; Zhang, N.; Xu, Y.-J.; Chen, H. M., Electrocatalysis for the oxygen evolution reaction: recent development and future perspectives. *Chemical Society Reviews* **2017,** *46* (2), 337-365.
56. Dahan, M. H.; Caspary Toroker, M., Water Oxidation Catalysis with Fe_2O_3 Constrained at the Nanoscale. *The Journal of Physical Chemistry C* **2017,** *121* (11), 6120-6125.
57. Tymińska, N.; Wu, G.; Dupuis, M., Water Oxidation on Oxygen-Deficient Barium Titanate: A First-Principles Study. *The Journal of Physical Chemistry C* **2017,** *121* (15), 8378-8389.
58. Man, I. C.; Su, H.-Y.; Calle-Vallejo, F.; Hansen, H. A.; Martínez, J. I.; Inoglu, N. G.; Kitchin, J.; Jaramillo, T. F.; Nørskov, J. K.; Rossmeisl, J., Universality in Oxygen Evolution Electrocatalysis on Oxide Surfaces. *ChemCatChem* **2011,** *3* (7), 1159-1165.
59. Jafari, T.; Moharreri, E.; Amin, A. S.; Miao, R.; Song, W.; Suib, S. L., Photocatalytic Water Splitting—The Untamed Dream: A Review of Recent Advances. *Molecules* **2016,** *21* (7), 900.
60. Sivula, K.; van de Krol, R., Semiconducting materials for photoelectrochemical energy conversion. *Nature Reviews Materials* **2016,** *1*, 15010.
61. Ong, W.-J.; Tan, L.-L.; Ng, Y. H.; Yong, S.-T.; Chai, S.-P., Graphitic Carbon Nitride (g-C_3N_4)-Based Photocatalysts for Artificial Photosynthesis and Environmental Remediation: Are We a Step Closer To Achieving Sustainability? *Chemical Reviews* **2016,** *116* (12), 7159-7329.
62. Fujishima, A.; Zhang, X.; Tryk, D. A., TiO_2 photocatalysis and related surface phenomena. *Surface Science Reports* **2008,** *63* (12), 515-582.
63. Ni, M.; Leung, M. K. H.; Leung, D. Y. C.; Sumathy, K., A review and recent developments in photocatalytic water-splitting using TiO_2 for hydrogen production. *Renewable and Sustainable Energy Reviews* **2007,** *11* (3), 401-425.
64. Dimitrijevic, N. M.; Vijayan, B. K.; Poluektov, O. G.; Rajh, T.; Gray, K. A.; He, H.; Zapol, P., Role of Water and Carbonates in Photocatalytic Transformation of CO_2 to CH_4 on Titania. *Journal of the American Chemical Society* **2011,** *133* (11), 3964-3971.
65. Habisreutinger, S. N.; Schmidt-Mende, L.; Stolarczyk, J. K., Photocatalytic Reduction of CO_2 on TiO_2 and Other Semiconductors. *Angewandte Chemie International Edition* **2013,** *52* (29), 7372-7408.
66. Pelaez, M.; Nolan, N. T.; Pillai, S. C.; Seery, M. K.; Falaras, P.; Kontos, A. G.; Dunlop, P. S. M.; Hamilton, J. W. J.; Byrne, J. A.; O'Shea, K.; Entezari, M. H.; Dionysiou, D. D., A review on the visible light active titanium dioxide photocatalysts for environmental applications. *Applied Catalysis B: Environmental* **2012,** *125*, 331-349.
67. Etacheri, V.; Di Valentin, C.; Schneider, J.; Bahnemann, D.; Pillai, S. C., Visible-light activation of TiO_2 photocatalysts: Advances in theory and experiments. *Journal of Photochemistry and Photobiology C: Photochemistry Reviews* **2015,** *25*, 1-29.
68. Tada, H.; Jin, Q.; Iwaszuk, A.; Nolan, M., Molecular-scale transition metal oxide nanocluster surface-modified titanium dioxide as solar-activated environmental catalysts. *The Journal of Physical Chemistry C* **2014,** *118* (23), 12077-12086.
69. Fujishima, A.; Honda, K., Electrochemical photolysis of water at a semiconductor electrode. *Nature* **1972,** *238* (5358), 37-8.

70. Hu, Y.; Tsai, H. L.; Huang, C. L., Effect of brookite phase on the anatase–rutile transition in titania nanoparticles. *Journal of the European Ceramic Society* **2003,** *23* (5), 691-696.
71. Carp, O.; Huisman, C. L.; Reller, A., Photoinduced reactivity of titanium dioxide. *Progress in Solid State Chemistry* **2004,** *32* (1), 33-177.
72. de Farias, R. F.; Silva, C. C.; Restivo, T. A., Thermal study of the anatase-rutile structural transitions in sol-gel synthesized titanium dioxide powders. *Journal of the Serbian Chemical Society* **2005,** *70* (4), 675-679.
73. Periyat, P.; Pillai, S. C.; McCormack, D. E.; Colreavy, J.; Hinder, S. J., Improved high-temperature stability and sun-light-driven photocatalytic activity of sulfur-doped anatase TiO_2. *The Journal of Physical Chemistry C* **2008,** *112* (20), 7644-7652.
74. Etacheri, V.; Seery, M. K.; Hinder, S. J.; Pillai, S. C., Oxygen Rich Titania: A Dopant Free, High Temperature Stable, and Visible-Light Active Anatase Photocatalyst. *Advanced Functional Materials* **2011,** *21* (19), 3744-3752.
75. Hanaor, D. A.; Sorrell, C. C., Review of the anatase to rutile phase transformation. *Journal of Materials science* **2011,** *46* (4), 855-874.
76. Luttrell, T.; Halpegamage, S.; Tao, J.; Kramer, A.; Sutter, E.; Batzill, M., Why is anatase a better photocatalyst than rutile? - Model studies on epitaxial TiO_2 films. *Scientific Reports* **2014,** *4* (1), 4043.
77. Fagan, R.; Synnott, D. W.; McCormack, D. E.; Pillai, S. C., An effective method for the preparation of high temperature stable anatase TiO_2 photocatalysts. *Applied Surface Science* **2016,** *371*, 447-452.
78. Dubey, R., Temperature-dependent phase transformation of TiO_2 nanoparticles synthesized by sol-gel method. *Materials Letters* **2018,** *215*, 312-317.
79. Xia, X.; Peng, S.; Bao, Y.; Wang, Y.; Lei, B.; Wang, Z.; Huang, Z.; Gao, Y., Control of interface between anatase TiO_2 nanoparticles and rutile TiO_2 nanorods for efficient photocatalytic H_2 generation. *Journal of Power Sources* **2018,** *376*, 11-17.
80. Kernazhitsky, L.; Shymanovska, V.; Gavrilko, T.; Naumov, V.; Fedorenko, L.; Baran, J., Dark-blue titanium dioxide: Effect of phenothiazine on structural and optical properties of nanocrystalline anatase TiO_2. *Journal of Physics and Chemistry of Solids* **2019,** *126*, 234-241.
81. Maity, P.; Mohammed, O. F.; Katsiev, K.; Idriss, H., Study of the bulk charge carrier dynamics in anatase and rutile TiO_2 single crystals by femtosecond time-resolved spectroscopy. *The Journal of Physical Chemistry C* **2018,** *122* (16), 8925-8932.
82. Xu, M.; Gao, Y.; Moreno, E. M.; Kunst, M.; Muhler, M.; Wang, Y.; Idriss, H.; Wöll, C., Photocatalytic activity of bulk TiO_2 anatase and rutile single crystals using infrared absorption spectroscopy. *Physical Review Letters* **2011,** *106* (13), 138302.
83. Wang, C.-L.; Hwang, W.-S.; Chu, H.-L.; Lin, H.-J.; Ko, H.-H.; Wang, M.-C. J. C. I., Kinetics of anatase transition to rutile TiO_2 from titanium dioxide precursor powders synthesized by a sol-gel process. **2016,** *42* (11), 13136-13143.
84. Hanaor, D. A.; Sorrell, C. C. J. J. o. M. s., Review of the anatase to rutile phase transformation. **2011,** *46* (4), 855-874.
85. Shirai, K.; Fazio, G.; Sugimoto, T.; Selli, D.; Ferraro, L.; Watanabe, K.; Haruta, M.; Ohtani, B.; Kurata, H.; Di Valentin, C., Water-assisted hole trapping at the highly curved surface of nano-TiO_2 photocatalyst. *Journal of the American Chemical Society* **2018,** *140* (4), 1415-1422.
86. Xu, F.; Zhang, J.; Zhu, B.; Yu, J.; Xu, J., $CuInS_2$ sensitized TiO_2 hybrid nanofibers for improved photocatalytic CO_2 reduction. *Applied Catalysis B: Environmental* **2018,** *230*, 194-202.

87. Jia, T.; Fu, F.; Yu, D.; Cao, J.; Sun, G., Facile synthesis and characterization of N-doped TiO_2/C nanocomposites with enhanced visible-light photocatalytic performance. *Applied Surface Science* **2018,** *430*, 438-447.
88. Yin, W.-J.; Wen, B.; Zhou, C.; Selloni, A.; Liu, L.-M., Excess electrons in reduced rutile and anatase TiO_2. *Surface Science Reports* **2018,** *73* (2), 58-82.
89. Khatun, N.; Tiwari, S.; Vinod, C.; Tseng, C.-M.; Wei Liu, S.; Biring, S.; Sen, S., Role of oxygen vacancies and interstitials on structural phase transition, grain growth, and optical properties of Ga doped TiO_2. *Journal of Applied Physics* **2018,** *123* (24), 245702.
90. Gaur, L. K.; Kumar, P.; Kushavah, D.; Khiangte, K. R.; Mathpal, M. C.; Agrahari, V.; Gairola, S.; Soler, M. A.; Swart, H.; Agarwal, A., Laser induced phase transformation influenced by Co doping in TiO_2 nanoparticles. *Journal of Alloys and Compounds* **2019,** *780*, 25-34.
91. Kavan, L.; Grätzel, M.; Gilbert, S. E.; Klemenz, C.; Scheel, H. J., Electrochemical and Photoelectrochemical Investigation of Single-Crystal Anatase. *Journal of the American Chemical Society* **1996,** *118* (28), 6716-6723.
92. Banerjee, S.; Pillai, S. C.; Falaras, P.; O'Shea, K. E.; Byrne, J. A.; Dionysiou, D. D., New Insights into the Mechanism of Visible Light Photocatalysis. *The Journal of Physical Chemistry Letters* **2014,** *5* (15), 2543-2554.
93. Kumar, S. G.; Devi, L. G., Review on Modified TiO_2 Photocatalysis under UV/Visible Light: Selected Results and Related Mechanisms on Interfacial Charge Carrier Transfer Dynamics. *The Journal of Physical Chemistry A* **2011,** *115* (46), 13211-13241.
94. Serpone, N., Is the Band Gap of Pristine TiO_2 Narrowed by Anion- and Cation-Doping of Titanium Dioxide in Second-Generation Photocatalysts? *The Journal of Physical Chemistry B* **2006,** *110* (48), 24287-24293.
95. Nie, X.; Zhuo, S.; Maeng, G.; Sohlberg, K., Doping of polymorphs for altered optical and photocatalytic properties. *International Journal of Photoenergy* **2009,** *2009*, 22.
96. Colón, G.; Maicu, M.; Hidalgo, M. C.; Navío, J. A., Cu-doped TiO_2 systems with improved photocatalytic activity. *Applied Catalysis B: Environmental* **2006,** *67* (1–2), 41-51.
97. Karunakaran, C.; Abiramasundari, G.; Gomathisankar, P.; Manikandan, G.; Anandi, V., Cu-doped TiO_2 nanoparticles for photocatalytic disinfection of bacteria under visible light. *Journal of colloid and interface science* **2010,** *352* (1), 68-74.
98. Choudhury, B.; Dey, M.; Choudhury, A., Defect generation, dd transition, and band gap reduction in Cu-doped TiO_2 nanoparticles. *International Nano Letters* **2013,** *3* (1), 1-8.
99. Navas, J.; Sánchez-Coronilla, A.; Aguilar, T.; Hernández, N. C.; Desireé, M.; Sánchez-Márquez, J.; Zorrilla, D.; Fernández-Lorenzo, C.; Alcántara, R.; Martín-Calleja, J., Experimental and theoretical study of the electronic properties of Cu-doped anatase TiO_2. *Physical Chemistry Chemical Physics* **2014,** *16* (8), 3835-3845.
100. Wang, D.-Y.; Lin, H.-C.; Yen, C.-C., Influence of metal plasma ion implantation on photo-sensitivity of anatase TiO_2 thin films. *Thin Solid Films* **2006,** *515* (3), 1047-1052.
101. Chand, R.; Obuchi, E.; Katoh, K.; Luitel, H. N.; Nakano, K., Enhanced photocatalytic activity of TiO_2/SiO_2 by the influence of Cu-doping under reducing calcination atmosphere. *Catal. Commun.* **2011,** *13* (1), 49-53.
102. Cui, Y.; Du, H.; Wen, L., Doped-TiO_2 photocatalysts and synthesis methods to prepare TiO2 films. *J. Mater. Sci. Technol.* **2008,** *24* (05), 675-689.

103. Guo, M.; Du, J., First-principles study of electronic structures and optical properties of Cu, Ag, and Au-doped anatase TiO_2. *Physica B: Condensed Matter* **2012,** *407* (6), 1003-1007.
104. Long, R.; English, N. J., First-principles calculation of synergistic (N, P)-codoping effects on the visible-light photocatalytic activity of anatase TiO_2. *J. Phys. Chem. C* **2010,** *114* (27), 11984-11990.
105. Long, R.; English, N. J., Synergistic effects on band gap-narrowing in titania by codoping from first-principles calculations. *Chem. Mater.* **2010,** *22* (5), 1616-1623.
106. Na Phattalung, S.; Limpijumnong, S.; Yu, J., Passivated co-doping approach to bandgap narrowing of titanium dioxide with enhanced photocatalytic activity. *Applied Catalysis B: Environmental* **2017,** *200*, 1-9.
107. Yang, K.; Dai, Y.; Huang, B.; Whangbo, M.-H., Density functional characterization of the visible-light absorption in substitutional C-anion- and C-cation-doped TiO_2. *The Journal of Physical Chemistry C* **2009,** *113* (6), 2624-2629.
108. Zhang, H.; Yu, X.; McLeod, J. A.; Sun, X., First-principles study of Cu-doping and oxygen vacancy effects on TiO_2 for water splitting. *Chemical Physics Letters* **2014,** *612*, 106-110.
109. Herrmann, J.-M., Detrimental cationic doping of titania in photocatalysis: why chromium Cr^{3+}-doping is a catastrophe for photocatalysis, both under UV- and visible irradiations. *New Journal of Chemistry* **2012,** *36* (4), 883-890.
110. Li, W., Influence of electronic structures of doped TiO_2 on their photocatalysis. *physica status solidi (RRL) – Rapid Research Letters* **2015,** *9* (1), 10-27.
111. Wang, Y.; Zhang, R.; Li, J.; Li, L.; Lin, S., First-principles study on transition metal-doped anatase TiO_2. *Nanoscale research letters* **2014,** *9* (1), 1.
112. Nolan, M.; Watson, G. W., Hole localization in Al doped silica: a DFT+U description. *The Journal of chemical physics* **2006,** *125* (14), 144701.
113. Nolan, M.; Watson, G. W., The electronic structure of alkali doped alkaline earth metal oxides: Li doping of MgO studied with DFT-GGA and GGA+U. *Surface science* **2005,** *586* (1), 25-37.
114. Scanlon, D. O.; Walsh, A.; Morgan, B. J.; Nolan, M.; Fearon, J.; Watson, G. W., Surface sensitivity in lithium-doping of MgO: a density functional theory study with correction for on-site Coulomb interactions. *The Journal of Physical Chemistry C* **2007,** *111* (22), 7971-7979.
115. Carey, J. J.; Nolan, M., Dissociative adsorption of methane on the Cu and Zn doped (111) surface of CeO_2. *Applied Catalysis B: Environmental* **2016,** *197*, 324-336.
116. Nolan, M.; Elliott, S. D., The p-type conduction mechanism in Cu_2O: a first principles study. *Physical Chemistry Chemical Physics* **2006,** *8* (45), 5350-5358.
117. Maimaiti, Y.; Nolan, M.; Elliott, S. D., Reduction mechanisms of the CuO(111) surface through surface oxygen vacancy formation and hydrogen adsorption. *Physical Chemistry Chemical Physics* **2014,** *16* (7), 3036-3046.
118. Duhalde, S.; Vignolo, M. F.; Golmar, F.; Chiliotte, C.; Torres, C. E. R.; Errico, L. A.; Cabrera, A. F.; Rentería, M.; Sánchez, F. H.; Weissmann, M., Appearance of room-temperature ferromagnetism in Cu-doped $TiO_{2-\delta}$ films. *Physical Review B* **2005,** *72* (16), 161313.
119. Khan, H.; Berk, D., Characterization and mechanistic study of Mo^{+6} and V^{+5} codoped TiO_2 as a photocatalyst. *Journal of Photochemistry and Photobiology A: Chemistry* **2014,** *294*, 96-109.
120. Kemp, T. J.; McIntyre, R. A., Transition metal-doped titanium (IV) dioxide: Characterisation and influence on photodegradation of poly (vinyl chloride). *Polymer Degradation and Stability* **2006,** *91* (1), 165-194.

121. Fisher, L.; Ostovapour, S.; Kelly, P.; Whitehead, K.; Cooke, K.; Storgårds, E.; Verran, J., Molybdenum doped titanium dioxide photocatalytic coatings for use as hygienic surfaces: the effect of soiling on antimicrobial activity. *Biofouling* **2014,** *30* (8), 911-919.
122. Miljević, B.; van der Bergh, J.; Vučetić, S.; Lazar, D.; Ranogajec, J., Molybdenum doped TiO_2 nanocomposite coatings: Visible light driven photocatalytic self-cleaning of mineral substrates. *Ceramics International* **2017,** *43* (11), 8214-8221.
123. Yoon, Y.; Lee, S.; Gwon, J.; Cho, H.; Wu, Q.; Kim, Y.; Lee, W., Photocatalytic performance of highly transparent and mesoporous molybdenum-doped titania films fabricated by templating cellulose nanocrystals. *Ceramics International* **2018,** *44* (14), 16647-16653.
124. Batalović, K.; Bundaleski, N.; Radaković, J.; Abazović, N.; Mitrić, M.; Silva, R. A.; Savić, M.; Belošević-Čavor, J.; Rakočević, Z.; Rangel, C. M., Modification of N-doped TiO_2 photocatalysts using noble metals (Pt, Pd) – a combined XPS and DFT study. *Physical Chemistry Chemical Physics* **2017,** *19* (10), 7062-7071.
125. Di Valentin, C.; Finazzi, E.; Pacchioni, G.; Selloni, A.; Livraghi, S.; Paganini, M. C.; Giamello, E., N-doped TiO_2: Theory and experiment. *Chemical Physics* **2007,** *339* (1), 44-56.
126. Di Valentin, C.; Pacchioni, G.; Selloni, A., Origin of the different photoactivity of N-doped anatase and rutile TiO_2. *Physical Review B* **2004,** *70* (8), 085116.
127. Wu, H.-C.; Lin, Y.-S.; Lin, S.-W., Mechanisms of Visible Light Photocatalysis in N-Doped Anatase TiO_2 with Oxygen Vacancies from GGA+U Calculations. *International Journal of Photoenergy* **2013,** *2013*, 7.
128. Yang, K.; Dai, Y.; Huang, B.; Han, S., Theoretical Study of N-Doped TiO_2 Rutile Crystals. *The Journal of Physical Chemistry B* **2006,** *110* (47), 24011-24014.
129. Cao Khang, N.; Van Khanh, N.; Hoai Anh, N.; Thi Nga, D.; Van Minh, N., The origin of visible light photocatalytic activity of N-doped and weak ferromagnetism of Fe-doped TiO_2 anatase. *Advances in Natural Sciences: Nanoscience and Nanotechnology* **2011,** *2* (1), 015008.
130. Tahir, M.; Amin, N. S. J. A. C. B. E., Indium-doped TiO_2 nanoparticles for photocatalytic CO_2 reduction with H2O vapors to CH4. **2015,** *162*, 98-109.
131. Tahir, M.; Amin, N. S. J. A. C. A. G., Photocatalytic CO2 reduction and kinetic study over In/TiO_2 nanoparticles supported microchannel monolith photoreactor. **2013,** *467*, 483-496.
132. Wang, E.; Yang, W.; Cao, Y., Unique Surface Chemical Species on Indium Doped TiO_2 and Their Effect on the Visible Light Photocatalytic Activity. *J. Phys. Chem. C* **2009,** *113* (49), 20912-20917.
133. Wang, E.; Zhang, P.; Chen, Y.; Liu, Z.; He, T.; Cao, Y. J. J. o. M. C., Improved visible-light photocatalytic activity of titania activated by nitrogen and indium modification. **2012,** *22* (29), 14443-14449.
134. Iwaszuk, A.; Nolan, M., Charge compensation in trivalent cation doped bulk rutile TiO_2. *J. Phys.: Condens. Matter* **2011,** *23* (33), 334207.
135. Khan, M.; Lan, Z.; Zeng, Y., Analysis of Indium Oxidation State on the Electronic Structure and Optical Properties of TiO_2. *Materials* **2018,** *11* (6), 952.
136. Yu, J.; Xiang, Q.; Zhou, M., Preparation, characterization and visible-light-driven photocatalytic activity of Fe-doped titania nanorods and first-principles study for electronic structures. *Applied Catalysis B: Environmental* **2009,** *90* (3), 595-602.
137. Albuquerque, A. R.; Bruix, A.; dos Santos, I. M. G.; Sambrano, J. R.; Illas, F., DFT Study on Ce-Doped Anatase TiO_2: Nature of Ce^{3+} and Ti^{3+} Centers Triggered by

Oxygen Vacancy Formation. *The Journal of Physical Chemistry C* **2014,** *118* (18), 9677-9689.
138. Zhang, T.; Zhu, Z.; Chen, H.; Bai, Y.; Xiao, S.; Zheng, X.; Xue, Q.; Yang, S., Iron-doping-enhanced photoelectrochemical water splitting performance of nanostructured WO_3: a combined experimental and theoretical study. *Nanoscale* **2015,** *7* (7), 2933-2940.
139. Wang, F.; Di Valentin, C.; Pacchioni, G., Doping of WO_3 for Photocatalytic Water Splitting: Hints from Density Functional Theory. *The Journal of Physical Chemistry C* **2012,** *116* (16), 8901-8909.
140. Noureldine, D.; Takanabe, K., State-of-the-art Sn^{2+}-based ternary oxides as photocatalysts for water splitting: electronic structures and optoelectronic properties. *Catalysis Science & Technology* **2016,** *6* (21), 7656-7670.
141. Gai, Y.; Li, J.; Li, S. S.; Xia, J. B.; Wei, S. H., Design of narrow-gap TiO_2: a passivated codoping approach for enhanced photoelectrochemical activity. *Phys Rev Lett* **2009,** *102* (3), 036402.
142. Chen, H.; Li, X.; Wan, R.; Kao-Walter, S.; Lei, Y., A DFT study of the electronic structures and optical properties of (Cr, C) co-doped rutile TiO_2. *Chemical Physics* **2018,** *501*, 60-67.
143. Walsh, A.; Yan, Y.; Huda, M. N.; Al-Jassim, M. M.; Wei, S.-H., Band Edge Electronic Structure of $BiVO_4$: Elucidating the Role of the Bi s and V d Orbitals. *Chemistry of Materials* **2009,** *21* (3), 547-551.
144. Fagan, R.; McCormack, D. E.; Dionysiou, D. D.; Pillai, S. C., A review of solar and visible light active TiO_2 photocatalysis for treating bacteria, cyanotoxins and contaminants of emerging concern. *Materials Science in Semiconductor Processing* **2015**.
145. Irie, H.; Watanabe, Y.; Hashimoto, K., Carbon-doped anatase TiO_2 powders as a visible-light sensitive photocatalyst. *Chemistry Letters* **2003,** *32* (8), 772-773.
146. Sakthivel, S.; Kisch, H., Daylight photocatalysis by carbon-modified titanium dioxide. *Angewandte Chemie International Edition* **2003,** *42* (40), 4908-4911.
147. Etacheri, V.; Michlits, G.; Seery, M. K.; Hinder, S. J.; Pillai, S. C., A Highly Efficient $TiO_{2-x}C_x$ Nano-heterojunction Photocatalyst for Visible Light Induced Antibacterial Applications. *ACS applied materials & interfaces* **2013,** *5* (5), 1663-1672.
148. Byrne, C.; Fagan, R.; Hinder, S.; McCormack, D. E.; Pillai, S. C., New approach of modifying the anatase to rutile transition temperature in TiO_2 photocatalysts. *RSC Advances* **2016,** *6* (97), 95232-95238.
149. Fujishima, A.; Zhang, X., Titanium dioxide photocatalysis: present situation and future approaches. *Comptes Rendus Chimie* **2006,** *9* (5), 750-760.
150. Oropeza, F. E.; Harmer, J.; Egdell, R.; Palgrave, R. G., A critical evaluation of the mode of incorporation of nitrogen in doped anatase photocatalysts. *Physical Chemistry Chemical Physics* **2010,** *12* (4), 960-969.
151. Choi, H.; Antoniou, M. G.; Pelaez, M.; De la Cruz, A. A.; Shoemaker, J. A.; Dionysiou, D. D., Mesoporous nitrogen-doped TiO_2 for the photocatalytic destruction of the cyanobacterial toxin microcystin-LR under visible light irradiation. *Environmental science & technology* **2007,** *41* (21), 7530-7535.
152. Fang, X.; Zhang, Z.; Chen, Q.; Ji, H.; Gao, X., Dependence of nitrogen doping on TiO_2 precursor annealed under NH 3 flow. *Journal of Solid State Chemistry* **2007,** *180* (4), 1325-1332.
153. Yadav, H. M.; Otari, S. V.; Koli, V. B.; Mali, S. S.; Hong, C. K.; Pawar, S. H.; Delekar, S. D., Preparation and characterization of copper-doped anatase TiO_2

nanoparticles with visible light photocatalytic antibacterial activity. *Journal of Photochemistry and Photobiology A: Chemistry* **2014,** *280*, 32-38.
154. Padmanabhan, S. C.; Pillai, S. C.; Colreavy, J.; Balakrishnan, S.; McCormack, D. E.; Perova, T. S.; Gun'ko, Y.; Hinder, S. J.; Kelly, J. M., A simple sol-gel processing for the development of high-temperature stable photoactive anatase titania. *Chemistry of Materials* **2007,** *19* (18), 4474-4481.
155. Czoska, A.; Livraghi, S.; Chiesa, M.; Giamello, E.; Agnoli, S.; Granozzi, G.; Finazzi, E.; Valentin, C. D.; Pacchioni, G., The nature of defects in fluorine-doped TiO_2. *The Journal of Physical Chemistry C* **2008,** *112* (24), 8951-8956.
156. Janes, R.; Knightley, L.; Harding, C., Structural and spectroscopic studies of iron (III) doped titania powders prepared by sol-gel synthesis and hydrothermal processing. *Dyes and pigments* **2004,** *62* (3), 199-212.
157. Kőrösi, L.; Papp, S.; Ménesi, J.; Illés, E.; Zöllmer, V.; Richardt, A.; Dékány, I., Photocatalytic activity of silver-modified titanium dioxide at solid–liquid and solid–gas interfaces. *Colloids and Surfaces A: Physicochemical and Engineering Aspects* **2008,** *319* (1), 136-142.
158. Nolan, N. T.; Seery, M. K.; Hinder, S. J.; Healy, L. F.; Pillai, S. C., A systematic study of the effect of silver on the chelation of formic acid to a titanium precursor and the resulting effect on the anatase to rutile transformation of TiO_2. *The Journal of Physical Chemistry C* **2010,** *114* (30), 13026-13034.
159. Karvinen, S., The effects of trace elements on the crystal properties of TiO_2. *solid state sciences* **2003,** *5* (5), 811-819.
160. HEO, K. C.; OK, C. I.; KIM, J. W.; MOON, B. K., The effects of manganese ions and their magnetic properties on the anatase-rutile phase transition of nanocrystalline TiO_2: Mn prepared by using the solvothermal method. *Journal of the Korean Physical Society* **2005,** *47* (5), 861-865.
161. Arroyo, R.; Cordoba, G.; Padilla, J.; Lara, V., Influence of manganese ions on the anatase–rutile phase transition of TiO_2 prepared by the sol–gel process. *Materials Letters* **2002,** *54* (5), 397-402.
162. Byrne, C.; Moran, L.; Hermosilla, D.; Merayo, N.; Blanco, Á.; Rhatigan, S.; Hinder, S.; Ganguly, P.; Nolan, M.; Pillai, S. C., Effect of Cu Doping on the Anatase-to-Rutile Phase Transition in TiO_2 Photocatalysts: Theory and Experiments. *Applied Catalysis B: Environmental* **2019**.
163. Nolan, N. T.; Seery, M. K.; Pillai, S. C., Spectroscopic investigation of the anatase-to-rutile transformation of sol− gel-synthesized TiO_2 photocatalysts. *The Journal of Physical Chemistry C* **2009,** *113* (36), 16151-16157.
164. da Silva, L. F.; Avansi Jr, W.; Catto, A. C.; Rodrigues, J. E.; Bernardi, M. I.; Mastelaro, V. R., The Role of Nb Addition in TiO_2 Nanoparticles: Phase Transition and Photocatalytic Properties. *physica status solidi (a)* **2018,** *215* (21), 1800321.
165. Zanatta, A.; Scoca, D.; Alvarez, F., Influence of the Anatase and Rutile phases on the luminescent properties of rare-earth-doped TiO2 films. *Journal of Alloys and Compounds* **2019,** *780*, 491-497.
166. Loan, T. T.; Long, N. N., Effect of Co^{2+} doping on Raman spectra and the phase transformation of TiO_2:Co^{2+} nanowires. *Journal of Physics and Chemistry of Solids* **2019,** *124*, 336-342.
167. Zou, K.; Dong, G.; Liu, J.; Xu, B.; Wang, D., Effects of calcination temperature and Li+ ions doping on structure and upconversion luminescence properties of TiO_2: Ho^{3+}-Yb^{3+} nanocrystals. *Journal of materials science & technology* **2019,** *35* (4), 483-490.

168. Arantes, D. C.; de Mayrinck, C.; Santos, J. D.; Maia, L. F.; Oliveira, L. F.; Schiavon, M. A.; Pasquini, D.; de Lima, R. C.; de Morais, L. C.; Esbenshade, J., Effect of structural and Eu^{3+} amount in TiO_2 semiconductor material on downconversion photoluminescence properties. *Optical Materials* **2019,** *88*, 522-533.
169. Suwannaruang, T.; Kidkhunthod, P.; Chanlek, N.; Soontaranon, S.; Wantala, K., High anatase purity of nitrogen-doped TiO_2 nanorice particles for the photocatalytic treatment activity of pharmaceutical wastewater. *Applied Surface Science* **2019**.
170. Zikriya, M.; Nadaf, Y.; Bharathy, P. V.; Renuka, C., Luminescent characterization of rare earth Dy^{3+} ion doped TiO_2 prepared by simple chemical co-precipitation method. *Journal of Rare Earths* **2019,** *37* (1), 24-31.
171. Feltrin, J.; De Noni Jr, A.; Hotza, D.; Frade, J., Design guidelines for titania-silica-alumina ceramics with tuned anatase to rutile transformation. *Ceramics International* **2018**.
172. Giraldi, T. R.; Dias, J. A.; Baggio, C. M.; Maestrelli, S. C.; Oliveira, J. A. J. J. o. S.-G. S.; Technology, Anatase-to-rutile transition in co-doped TiO_2 pigments. **2017,** *83* (1), 115-123.
173. Yadav, A. K.; Khatun, N.; Kumar, S.; Tseng, C.-M.; Biring, S.; Sen, S. J. J. o. M. S. M. i. E., Size and strain dependent anatase to rutile phase transition in TiO_2 due to Si incorporation. **2017,** *28* (24), 19017-19024.
174. Kondamareddy, K. K.; Neena, D.; Lu, D.; Peng, T.; Lopez, M. A. M.; Wang, C.; Yu, Z.; Cheng, N.; Fu, D.; Zhao, X.-Z. J. A. S. S., Ultra-trace (parts per million-ppm) W 6+ dopant ions induced anatase to rutile transition (ART) of phase pure anatase TiO_2 nanoparticles for highly efficient visible light-active photocatalytic degradation of organic pollutants. **2018**.
175. Khatun, N.; Rajput, P.; Bhattacharya, D.; Jha, S.; Biring, S.; Sen, S. J. C. I., Anatase to rutile phase transition promoted by vanadium substitution in TiO_2: A structural, vibrational and optoelectronic study. **2017,** *43* (16), 14128-14134.
176. Makal, P.; Das, D. J. A. S. S., Self-doped TiO_2 nanowires in TiO_2-B single phase, TiO_2-B/anatase and TiO_2-anatase/rutile heterojunctions demonstrating individual superiority in photocatalytic activity under visible and UV light. **2018,** *455*, 1106-1115.
177. Hou, W.; Cronin, S. B., A review of surface plasmon resonance-enhanced photocatalysis. *Advanced Functional Materials* **2013,** *23* (13), 1612-1619.
178. Bumajdad, A.; Madkour, M., Understanding the superior photocatalytic activity of noble metals modified titania under UV and visible light irradiation. *Physical Chemistry Chemical Physics* **2014,** *16* (16), 7146-7158.
179. Román Castellanos, L.; Hess, O.; Lischner, J., Single plasmon hot carrier generation in metallic nanoparticles. *Communications Physics* **2019,** *2* (1), 47.
180. Zhang, X.; Ke, X.; Yao, J., Recent development of plasmon-mediated photocatalysts and their potential in selectivity regulation. *Journal of Materials Chemistry A* **2018,** *6* (5), 1941-1966.
181. Ranno, L.; Forno, S. D.; Lischner, J., Computational design of bimetallic core-shell nanoparticles for hot-carrier photocatalysis. *npj Computational Materials* **2018,** *4* (1), 31.
182. Ammal, S. C.; Heyden, A., Modeling the noble metal/TiO_2 (110) interface with hybrid DFT functionals: A periodic electrostatic embedded cluster model study. *The Journal of Chemical Physics* **2010,** *133* (16), 164703.
183. Atrei, A.; Cortigiani, B.; Ferrari, A. M., Epitaxial growth of TiO_2 films with the rutile (110) structure on Ag(100). *Journal of Physics: Condensed Matter* **2012,** *24* (44), 445005.

184. Wang, D.; Liu, Z.-P.; Yang, W.-M., Revealing the Size Effect of Platinum Cocatalyst for Photocatalytic Hydrogen Evolution on TiO_2 Support: A DFT Study. *ACS Catalysis* **2018,** *8* (8), 7270-7278.
185. Scanlon, D. O.; Dunnill, C. W.; Buckeridge, J.; Shevlin, S. A.; Logsdail, A. J.; Woodley, S. M.; Catlow, C. R. A.; Powell, M. J.; Palgrave, R. G.; Parkin, I. P.; Watson, G. W.; Keal, T. W.; Sherwood, P.; Walsh, A.; Sokol, A. A., Band alignment of rutile and anatase TiO_2. *Nature Materials* **2013,** *12*, 798.
186. Deskins, N. A.; Kerisit, S.; Rosso, K. M.; Dupuis, M., Molecular Dynamics Characterization of Rutile-Anatase Interfaces. *The Journal of Physical Chemistry C* **2007,** *111* (26), 9290-9298.
187. Garcia, J. C.; Nolan, M.; Deskins, N. A., The nature of interfaces and charge trapping sites in photocatalytic mixed-phase TiO_2 from first principles modeling. *The Journal of Chemical Physics* **2015,** *142* (2), 024708.
188. Nolan, M.; Deskins, N. A.; Schwartzenberg, K. C.; Gray, K. A., Local Interfacial Structure Influences Charge Localization in Titania Composites: Beyond the Band Alignment Paradigm. *The Journal of Physical Chemistry C* **2016,** *120* (3), 1808-1815.
189. Chae, S. Y.; Lee, C. S.; Jung, H.; Joo, O.-S.; Min, B. K.; Kim, J. H.; Hwang, Y. J., Insight into Charge Separation in $WO_3/BiVO_4$ Heterojunction for Solar Water Splitting. *ACS Applied Materials & Interfaces* **2017,** *9* (23), 19780-19790.
190. Sotelo-Vazquez, C.; Quesada-Cabrera, R.; Ling, M.; Scanlon, D. O.; Kafizas, A.; Thakur, P. K.; Lee, T.-L.; Taylor, A.; Watson, G. W.; Palgrave, R. G.; Durrant, J. R.; Blackman, C. S.; Parkin, I. P., Evidence and Effect of Photogenerated Charge Transfer for Enhanced Photocatalysis in WO_3/TiO_2 Heterojunction Films: A Computational and Experimental Study. *Advanced Functional Materials* **2017,** *27* (18), 1605413.
191. Boppana, V. B. R.; Lobo, R. F., SnO_x–$ZnGa_2O_4$ Photocatalysts with Enhanced Visible Light Activity. *ACS Catalysis* **2011,** *1* (8), 923-928.
192. Boppana, V. B. R.; Jiao, F.; Newby, D.; Laverock, J.; Smith, K. E.; Jumas, J. C.; Hutchings, G.; Lobo, R. F., Analysis of visible-light-active Sn(ii)–TiO_2 photocatalysts. *Physical Chemistry Chemical Physics* **2013,** *15* (17), 6185-6189.
193. Wang, J.; Li, H.; Meng, S.; Zhang, L.; Fu, X.; Chen, S., One-pot hydrothermal synthesis of highly efficient SnO_x/Zn_2SnO_4 composite photocatalyst for the degradation of methyl orange and gaseous benzene. *Applied Catalysis B: Environmental* **2017,** *200*, 19-30.
194. Liu, J., Origin of High Photocatalytic Efficiency in Monolayer g-C_3N_4/CdS Heterostructure: A Hybrid DFT Study. *The Journal of Physical Chemistry C* **2015,** *119* (51), 28417-28423.
195. Opoku, F.; Govender, K. K.; Sittert, C. G. C. E. v.; Govender, P. P., Insights into the photocatalytic mechanism of mediator-free direct Z-scheme g-C_3N_4/Bi_2MoO_6(010) and g-C_3N_4/Bi_2WO_6 (010) heterostructures: A hybrid density functional theory study. *Applied Surface Science* **2018,** *427*, 487-498.
196. Liu, J.; Cheng, B.; Yu, J., A new understanding of the photocatalytic mechanism of the direct Z-scheme g-C_3N_4/TiO_2 heterostructure. *Physical Chemistry Chemical Physics* **2016,** *18* (45), 31175-31183.
197. Ràfols i Bellés, C.; Selim, S.; Harrison, N. M.; Ahmad, E. A.; Kafizas, A., Beyond band bending in the $WO_3/BiVO_4$ heterojunction: insight from DFT and experiment. *Sustainable Energy & Fuels* **2019,** *3* (1), 264-271.
198. Baek, J. H.; Kim, B. J.; Han, G. S.; Hwang, S. W.; Kim, D. R.; Cho, I. S.; Jung, H. S., $BiVO_4/WO_3/SnO_2$ Double-Heterojunction Photoanode with Enhanced Charge Separation and Visible-Transparency for Bias-Free Solar Water-Splitting with a Perovskite Solar Cell. *ACS Applied Materials & Interfaces* **2017,** *9* (2), 1479-1487.

199. Makwana, N. M.; Quesada-Cabrera, R.; Parkin, I. P.; McMillan, P. F.; Mills, A.; Darr, J. A., A simple and low-cost method for the preparation of self-supported TiO_2–WO_3 ceramic heterojunction wafers. *Journal of Materials Chemistry A* **2014,** *2* (41), 17602-17608.
200. Bessekhouad, Y.; Robert, D.; Weber, J. V., Photocatalytic activity of Cu_2O/TiO_2, Bi_2O_3/TiO_2 and $ZnMn_2O4/TiO_2$ heterojunctions. *Catalysis Today* **2005,** *101* (3), 315-321.
201. Xie, M.; Fu, X.; Jing, L.; Luan, P.; Feng, Y.; Fu, H., Long-Lived, Visible-Light-Excited Charge Carriers of $TiO_2/BiVO_4$ Nanocomposites and their Unexpected Photoactivity for Water Splitting. *Advanced Energy Materials* **2014,** *4* (5), 1300995.
202. Ho-Kimura, S.; Moniz, S. J. A.; Handoko, A. D.; Tang, J., Enhanced photoelectrochemical water splitting by nanostructured $BiVO_4$–TiO_2 composite electrodes. *Journal of Materials Chemistry A* **2014,** *2* (11), 3948-3953.
203. Niu, M.; Cheng, D.; Cao, D., SiH/TiO_2 and GeH/TiO_2 Heterojunctions: Promising TiO_2-based Photocatalysts under Visible Light. *Scientific Reports* **2014,** *4* (1), 4810.
204. Bhatia, S.; Verma, N., Photocatalytic activity of ZnO nanoparticles with optimization of defects. *Materials Research Bulletin* **2017,** *95*, 468-476.
205. Gordon, T. R.; Cargnello, M.; Paik, T.; Mangolini, F.; Weber, R. T.; Fornasiero, P.; Murray, C. B., Nonaqueous Synthesis of TiO2 Nanocrystals Using TiF4 to Engineer Morphology, Oxygen Vacancy Concentration, and Photocatalytic Activity. *Journal of the American Chemical Society* **2012,** *134* (15), 6751-6761.
206. Zhang, J.; Salles, I.; Pering, S.; Cameron, P. J.; Mattia, D.; Eslava, S., Nanostructured WO_3 photoanodes for efficient water splitting via anodisation in citric acid. *RSC Advances* **2017,** *7* (56), 35221-35227.
207. Ong, C. B.; Ng, L. Y.; Mohammad, A. W., A review of ZnO nanoparticles as solar photocatalysts: Synthesis, mechanisms and applications. *Renewable and Sustainable Energy Reviews* **2018,** *81*, 536-551.
208. Wang, G.; Ling, Y.; Li, Y., Oxygen-deficient metal oxide nanostructures for photoelectrochemical water oxidation and other applications. *Nanoscale* **2012,** *4* (21), 6682-6691.
209. Concina, I.; Ibupoto, Z. H.; Vomiero, A., Semiconducting Metal Oxide Nanostructures for Water Splitting and Photovoltaics. *Advanced Energy Materials* **2017,** *7* (23), 1700706.
210. Garg, N.; Basu, M.; Upadhyaya, K.; Shivaprasad, S. M.; Ganguli, A. K., Controlling the aspect ratio and electrocatalytic properties of nickel cobaltite nanorods. *RSC Advances* **2013,** *3* (46), 24328-24336.
211. Garg, N.; Menaka; Ramanujachary, K. V.; Lofland, S. E.; Ganguli, A. K., Nanostructured dimagnesium manganese oxide (Spinel): Control of size, shape and their magnetic and electro catalytic properties. *Journal of Solid State Chemistry* **2013,** *197*, 392-397.
212. Kang, Q.; Cao, J.; Zhang, Y.; Liu, L.; Xu, H.; Ye, J., Reduced TiO_2 nanotube arrays for photoelectrochemical water splitting. *Journal of Materials Chemistry A* **2013,** *1* (18), 5766-5774.
213. Wang, G.; Wang, H.; Ling, Y.; Tang, Y.; Yang, X.; Fitzmorris, R. C.; Wang, C.; Zhang, J. Z.; Li, Y., Hydrogen-Treated TiO_2 Nanowire Arrays for Photoelectrochemical Water Splitting. *Nano Letters* **2011,** *11* (7), 3026-3033.
214. Kim, S.; Ko, K. C.; Lee, J. Y.; Illas, F., Single oxygen vacancies of $(TiO_2)_{35}$ as a prototype reduced nanoparticle: implication for photocatalytic activity. *Physical Chemistry Chemical Physics* **2016,** *18* (34), 23755-23762.
215. Barnard, A. S.; Erdin, S.; Lin, Y.; Zapol, P.; Halley, J. W., Modeling the structure and electronic properties of TiO_2 nanoparticles. *Physical Review B* **2006,** *73* (20), 205405.

216. Yinkai, L.; Huijun, L.; Wei, X., First principles study of the size effect of TiO_2 anatase nanoparticles in dye-sensitized solar cell. *Modelling and Simulation in Materials Science and Engineering* **2010,** *18* (2), 025004.
217. Blum, V.; Gehrke, R.; Hanke, F.; Havu, P.; Havu, V.; Ren, X.; Reuter, K.; Scheffler, M., Ab initio molecular simulations with numeric atom-centered orbitals. *Computer Physics Communications* **2009,** *180* (11), 2175-2196.
218. Lamiel-Garcia, O.; Ko, K. C.; Lee, J. Y.; Bromley, S. T.; Illas, F., When Anatase Nanoparticles Become Bulklike: Properties of Realistic TiO_2 Nanoparticles in the 1–6 nm Size Range from All Electron Relativistic Density Functional Theory Based Calculations. *Journal of Chemical Theory and Computation* **2017,** *13* (4), 1785-1793.
219. Jin, Q.; Fujishima, M.; Tada, H., Visible-light-active iron oxide-modified anatase titanium(iv) dioxide. *The Journal of Physical Chemistry C* **2011,** *115* (14), 6478-6483.
220. Libera, J. A.; Elam, J. W.; Sather, N. F.; Rajh, T.; Dimitrijevic, N. M., Iron(iii)-oxo centers on TiO_2 for visible-light photocatalysis. *Chemistry of Materials* **2010,** *22* (2), 409-413.
221. Nolan, M., Electronic coupling in iron oxide-modified TiO_2 leads to a reduced band gap and charge separation for visible light active photocatalysis. *Physical Chemistry Chemical Physics* **2011,** *13* (40), 18194-18199.
222. Nolan, M.; Iwaszuk, A.; Tada, H., Molecular metal oxide cluster-surface modified titanium dioxide photocatalysts. *Australian Journal of Chemistry* **2012,** *65* (6), 624-632.
223. Maeda, K.; Ishimaki, K.; Okazaki, M.; Kanazawa, T.; Lu, D.; Nozawa, S.; Kato, H.; Kakihana, M., Cobalt Oxide Nanoclusters on Rutile Titania as Bifunctional Units for Water Oxidation Catalysis and Visible Light Absorption: Understanding the Structure–Activity Relationship. *ACS Applied Materials & Interfaces* **2017,** *9* (7), 6114-6122.
224. Méndez-Medrano, M. G.; Kowalska, E.; Ohtani, B.; Uribe, D. B.; Colbeau-Justin, C.; Rau, S.; Rodríguez-López, J. L.; Remita, H., Heterojunction of CuO nanoclusters with TiO_2 for photo-oxidation of organic compounds and for hydrogen production. *The Journal of Chemical Physics* **2020,** *153* (3), 034705.
225. Jia, S.; Li, X.; Zhang, B.; Yang, J.; Zhang, S.; Li, S.; Zhang, Z., TiO_2/CuS heterostructure nanowire array photoanodes toward water oxidation: The role of CuS. *Applied Surface Science* **2019,** *463*, 829-837.
226. Rhatigan, S.; Nolan, M., Impact of surface hydroxylation in MgO-/SnO-nanocluster modified TiO_2 anatase (101) composites on visible light absorption, charge separation and reducibility. *Chinese Chemical Letters* **2018,** *29* (6), 757-764.
227. Fronzi, M.; Daly, W.; Nolan, M., Reactivity of metal oxide nanocluster modified rutile and anatase TiO_2: Oxygen vacancy formation and CO_2 interaction. *Applied Catalysis A:* **2016,** *521*, 240-249.
228. He, Y.; Dulub, O.; Cheng, H.; Selloni, A.; Diebold, U., Evidence for the Predominance of Subsurface Defects on Reduced Anatase TiO_2 (101). *Physical Review Letters* **2009,** *102* (10), 106105.
229. Scheiber, P.; Fidler, M.; Dulub, O.; Schmid, M.; Diebold, U.; Hou, W.; Aschauer, U.; Selloni, A., (Sub)Surface Mobility of Oxygen Vacancies at the TiO_2 Anatase (101) Surface. *Physical Review Letters* **2012,** *109* (13), 136103.
230. Fronzi, M.; Iwaszuk, A.; Lucid, A.; Nolan, M., Metal oxide nanocluster-modified TiO_2 as solar activated photocatalyst materials. *Journal of Physics: Condensed Matter* **2016,** *28* (7), 074006.
231. Iwaszuk, A.; Nolan, M.; Jin, Q.; Fujishima, M.; Tada, H., Origin of the visible-light response of nickel(ii) oxide cluster surface modified titanium(iv) dioxide. *The Journal of Physical Chemistry C* **2013,** *117* (6), 2709-2718.

232. Jin, Q.; Fujishima, M.; Nolan, M.; Iwaszuk, A.; Tada, H., Photocatalytic activities of tin(iv) oxide surface-modified titanium(iv) dioxide show a strong sensitivity to the TiO_2 crystal form. *The Journal of Physical Chemistry C* **2012,** *116* (23), 12621-12626.
233. Bhachu, D. S.; Sathasivam, S.; Carmalt, C. J.; Parkin, I. P., PbO-Modified TiO_2 Thin Films: A Route to Visible Light Photocatalysts. *Langmuir* **2014,** *30* (2), 624-630.
234. Park, J. B.; Graciani, J.; Evans, J.; Stacchiola, D.; Ma, S.; Liu, P.; Nambu, A.; Sanz, J. F.; Hrbek, J.; Rodriguez, J. A., High catalytic activity of $Au/CeO_x/TiO_2(110)$ controlled by the nature of the mixed-metal oxide at the nanometer level. *Proceedings of the National Academy of Sciences* **2009,** *106* (13), 4975-4980.
235. Graciani, J.; Plata, J. J.; Sanz, J. F.; Liu, P.; Rodriguez, J. A., A theoretical insight into the catalytic effect of a mixed-metal oxide at the nanometer level: The case of the highly active $metal/CeO_x/TiO_2(110)$ catalysts. *The Journal of Chemical Physics* **2010,** *132* (10), 104703.
236. Rhatigan, S.; Nolan, M., Impact of surface hydroxylation in MgO-/SnO-nanocluster modified TiO_2 anatase (101) composites on visible light absorption, charge separation and reducibility. *Chinese Chemical Letters* **2017**.
237. Rhatigan, S.; Nolan, M., CO_2 and water activation on ceria nanocluster modified TiO2 rutile (110). *Journal of Materials Chemistry A* **2018,** *6* (19), 9139-9152.
238. Nolan, M., Surface modification of TiO_2 with metal oxide nanoclusters: a route to composite photocatalytic materials. *Chemical Communications* **2011,** *47* (30), 8617-8619.
239. Nolan, M., First-principles prediction of new photocatalyst materials with visible-light absorption and improved charge separation: surface modification of rutile TiO_2 with nanoclusters of MgO and Ga_2O_3. *ACS Applied Materials & Interfaces* **2012,** *4* (11), 5863-5871.
240. Iwaszuk, A.; Nolan, M., Lead oxide-modified TiO_2 photocatalyst: tuning light absorption and charge carrier separation by lead oxidation state. *Catalysis Science & Technology* **2013,** *3* (8), 2000-2008.
241. Nolan, M.; Iwaszuk, A.; Gray, K. A., Localization of photoexcited electrons and holes on low coordinated Ti and O sites in free and supported TiO_2 Nanoclusters. *The Journal of Physical Chemistry C* **2014,** *118* (48), 27890-27900.
242. Lucid, A.; Iwaszuk, A.; Nolan, M., A first principles investigation of Bi_2O_3-modified TiO2 for visible light Activated photocatalysis: The role of TiO_2 crystal form and the Bi^{3+} stereochemical lone pair. *Materials Science in Semiconductor Processing* **2014,** *25*, 59-67.
243. Hu, C.; Zhang, L.; Gong, J., Recent progress made in the mechanism comprehension and design of electrocatalysts for alkaline water splitting. *Energy & Environmental Science* **2019,** *12* (9), 2620-2645.
244. Vesborg, P. C. K.; Seger, B.; Chorkendorff, I., Recent Development in Hydrogen Evolution Reaction Catalysts and Their Practical Implementation. *The Journal of Physical Chemistry Letters* **2015,** *6* (6), 951-957.
245. Browne, M. P.; Stafford, S.; O'Brien, M.; Nolan, H.; Berner, N. C.; Duesberg, G. S.; Colavita, P. E.; Lyons, M. E. G., The goldilocks electrolyte: examining the performance of iron/nickel oxide thin films as catalysts for electrochemical water splitting in various aqueous NaOH solutions. *Journal of Materials Chemistry A* **2016,** *4* (29), 11397-11407.
246. Zou, X.; Zhang, Y., Noble metal-free hydrogen evolution catalysts for water splitting. *Chemical Society Reviews* **2015,** *44* (15), 5148-5180.

247. Mohammed-Ibrahim, J.; Sun, X., Recent progress on earth abundant electrocatalysts for hydrogen evolution reaction (HER) in alkaline medium to achieve efficient water splitting – A review. *Journal of Energy Chemistry* **2019,** *34*, 111-160.
248. Wei, J.; Zhou, M.; Long, A.; Xue, Y.; Liao, H.; Wei, C.; Xu, Z. J., Heterostructured Electrocatalysts for Hydrogen Evolution Reaction Under Alkaline Conditions. *Nano-Micro Letters* **2018,** *10* (4), 75.
249. Xiao, P.; Chen, W.; Wang, X., A Review of Phosphide-Based Materials for Electrocatalytic Hydrogen Evolution. *Advanced Energy Materials* **2015,** *5* (24), 1500985.
250. Dubouis, N.; Grimaud, A., The hydrogen evolution reaction: from material to interfacial descriptors. *Chemical Science* **2019,** *10* (40), 9165-9181.
251. Benck, J. D.; Hellstern, T. R.; Kibsgaard, J.; Chakthranont, P.; Jaramillo, T. F., Catalyzing the Hydrogen Evolution Reaction (HER) with Molybdenum Sulfide Nanomaterials. *ACS Catalysis* **2014,** *4* (11), 3957-3971.
252. Luo, F.; Choi, C. H.; Primbs, M. J. M.; Ju, W.; Li, S.; Leonard, N. D.; Thomas, A.; Jaouen, F.; Strasser, P., Accurate Evaluation of Active-Site Density (SD) and Turnover Frequency (TOF) of PGM-Free Metal–Nitrogen-Doped Carbon (MNC) Electrocatalysts using CO Cryo Adsorption. *ACS Catalysis* **2019,** *9* (6), 4841-4852.
253. Trasatti, S.; Petrii, O. A., Real surface area measurements in electrochemistry. **1991,** *63* (5), 711.
254. Shinagawa, T.; Garcia-Esparza, A. T.; Takanabe, K., Insight on Tafel slopes from a microkinetic analysis of aqueous electrocatalysis for energy conversion. *Scientific Reports* **2015,** *5* (1), 13801.
255. Gorlin, Y.; Jaramillo, T. F., A Bifunctional Nonprecious Metal Catalyst for Oxygen Reduction and Water Oxidation. *Journal of the American Chemical Society* **2010,** *132* (39), 13612-13614.
256. Anantharaj, S.; Ede, S. R.; Karthick, K.; Sam Sankar, S.; Sangeetha, K.; Karthik, P. E.; Kundu, S., Precision and correctness in the evaluation of electrocatalytic water splitting: revisiting activity parameters with a critical assessment. *Energy & Environmental Science* **2018,** *11* (4), 744-771.
257. Chen, Z.; Duan, X.; Wei, W.; Wang, S.; Ni, B.-J., Recent advances in transition metal-based electrocatalysts for alkaline hydrogen evolution. *Journal of Materials Chemistry A* **2019,** *7* (25), 14971-15005.
258. Gao, Y.; Li, H.; Wang, J.; Ma, J.; Ren, H., New Insight on Hydrogen Evolution Reaction Activity of MoP_2 from Theoretical Perspective. *Nanomaterials* **2019,** *9* (9), 1270.
259. Yang, L.; Liu, P.; Li, J.; Xiang, B., Two-Dimensional Material Molybdenum Disulfides as Electrocatalysts for Hydrogen Evolution. . *Catalysts* **2017,** *7* (10), 285.
260. Tanimu, A.; Alhooshani, K., Advanced Hydrodesulfurization Catalysts: A Review of Design and Synthesis. *Energy & Fuels* **2019,** *33* (4), 2810-2838.
261. Vasudevan, P. T.; Fierro, J. L. G., A Review of Deep Hydrodesulfurization Catalysis. *Catalysis Reviews* **1996,** *38* (2), 161-188.
262. Yan, Y.; Xia, B.; Xu, Z.; Wang, X., Recent Development of Molybdenum Sulfides as Advanced Electrocatalysts for Hydrogen Evolution Reaction. *ACS Catalysis* **2014,** *4* (6), 1693-1705.
263. Raybaud, P.; Hafner, J.; Kresse, G.; Kasztelan, S.; Toulhoat, H., Ab Initio Study of the H_2–H_2S/MoS_2 Gas–Solid Interface: The Nature of the Catalytically Active Sites. *Journal of Catalysis* **2000,** *189* (1), 129-146.
264. Nidola, A.; Schira, R., New sulphide coatings for hydrogen evolution in KOH electrolysis. *International Journal of Hydrogen Energy* **1986,** *11* (7), 449-454.

265. Sobczynski, A., Molybdenum disulfide as a hydrogen evolution catalyst for water photodecomposition on semiconductors. *Journal of Catalysis* **1991,** *131* (1), 156-166.
266. Sobczynski, A.; Yildiz, A.; Bard, A. J.; Campion, A.; Fox, M. A.; Mallouk, T.; Webber, S. E.; White, J. M., Tungsten disulfide: a novel hydrogen evolution catalyst for water decomposition. *The Journal of Physical Chemistry* **1988,** *92* (8), 2311-2315.
267. Bonde, J.; Moses, P. G.; Jaramillo, T. F.; Nørskov, J. K.; Chorkendorff, I., Hydrogen evolution on nano-particulate transition metal sulfides. *Faraday Discussions* **2009,** *140* (0), 219-231.
268. Tsai, C.; Chan, K.; Nørskov, J. K.; Abild-Pedersen, F., Theoretical insights into the hydrogen evolution activity of layered transition metal dichalcogenides. *Surface Science* **2015,** *640*, 133-140.
269. Bollinger, M. V.; Jacobsen, K. W.; Nørskov, J. K., Atomic and electronic structure of MoS_2 nanoparticles. *Phys. Rev. B.* **2003,** *67* (8), 085410.
270. Lauritsen, J. V.; Bollinger, M. V.; Lægsgaard, E.; Jacobsen, K. W.; Nørskov, J. K.; Clausen, B. S.; Topsøe, H.; Besenbacher, F., Atomic-scale insight into structure and morphology changes of MoS_2 nanoclusters in hydrotreating catalysts. *Journal of Catalysis* **2004,** *221* (2), 510-522.
271. Jaramillo, T. F.; Jørgensen, K. P.; Bonde, J.; Nielsen, J. H.; Horch, S.; Chorkendorff, I., Identification of Active Edge Sites for Electrochemical H_2 Evolution from MoS_2 Nanocatalysts. *Science* **2007,** *317* (5834), 100-102.
272. Bentley, C. L.; Kang, M.; Maddar, F. M.; Li, F.; Walker, M.; Zhang, J.; Unwin, P. R., Electrochemical maps and movies of the hydrogen evolution reaction on natural crystals of molybdenite (MoS_2): basal vs. edge plane activity. *Chemical Science* **2017,** *8* (9), 6583-6593.
273. Bentley, C. L.; Kang, M.; Unwin, P. R., Nanoscale Structure Dynamics within Electrocatalytic Materials. *Journal of the American Chemical Society* **2017,** *139* (46), 16813-16821.
274. Chandrasekaran, S.; Yao, L.; Deng, L.; Bowen, C.; Zhang, Y.; Chen, S.; Lin, Z.; Peng, F.; Zhang, P., Recent advances in metal sulfides: from controlled fabrication to electrocatalytic, photocatalytic and photoelectrochemical water splitting and beyond. *Chemical Society Reviews* **2019,** *48* (15), 4178-4280.
275. Ganguly, P.; Harb, M.; Cao, Z.; Cavallo, L.; Breen, A.; Dervin, S.; Dionysiou, D. D.; Pillai, S. C., 2D Nanomaterials for Photocatalytic Hydrogen Production. *ACS Energy Letters* **2019,** *4* (7), 1687-1709.
276. Gao, E.; Lin, S.-Z.; Qin, Z.; Buehler, M. J.; Feng, X.-Q.; Xu, Z., Mechanical exfoliation of two-dimensional materials. *Journal of the Mechanics and Physics of Solids* **2018,** *115*, 248-262.
277. Novoselov, K. S.; Geim, A. K.; Morozov, S. V.; Jiang, D.; Zhang, Y.; Dubonos, S. V.; Grigorieva, I. V.; Firsov, A. A., Electric Field Effect in Atomically Thin Carbon Films. *Science* **2004,** *306* (5696), 666-669.
278. Li, H.; Lu, G.; Wang, Y.; Yin, Z.; Cong, C.; He, Q.; Wang, L.; Ding, F.; Yu, T.; Zhang, H., Mechanical Exfoliation and Characterization of Single- and Few-Layer Nanosheets of WSe2, TaS2, and TaSe2. *Small* **2013,** *9* (11), 1974-1981.
279. Novoselov, K. S.; Jiang, D.; Schedin, F.; Booth, T. J.; Khotkevich, V. V.; Morozov, S. V.; Geim, A. K., Two-dimensional atomic crystals. *Proceedings of the National Academy of Sciences of the United States of America* **2005,** *102* (30), 10451.
280. Nicolosi, V.; Chhowalla, M.; Kanatzidis, M. G.; Strano, M. S.; Coleman, J. N., Liquid Exfoliation of Layered Materials. *Science* **2013,** *340* (6139), 1226419.
281. Coleman, J. N.; Lotya, M.; O'Neill, A.; Bergin, S. D.; King, P. J.; Khan, U.; Young, K.; Gaucher, A.; De, S.; Smith, R. J.; Shvets, I. V.; Arora, S. K.; Stanton, G.;

Kim, H.-Y.; Lee, K.; Kim, G. T.; Duesberg, G. S.; Hallam, T.; Boland, J. J.; Wang, J. J.; Donegan, J. F.; Grunlan, J. C.; Moriarty, G.; Shmeliov, A.; Nicholls, R. J.; Perkins, J. M.; Grieveson, E. M.; Theuwissen, K.; McComb, D. W.; Nellist, P. D.; Nicolosi, V., Two-Dimensional Nanosheets Produced by Liquid Exfoliation of Layered Materials. *Science* **2011,** *331* (6017), 568-571.
282. Zhang, Y.; Yao, Y.; Sendeku, M. G.; Yin, L.; Zhan, X.; Wang, F.; Wang, Z.; He, J., Recent Progress in CVD Growth of 2D Transition Metal Dichalcogenides and Related Heterostructures. *Advanced Materials* **2019,** *31* (41), 1901694.
283. Li, X. L.; Li, Y. D., Formation of MoS2 Inorganic Fullerenes (IFs) by the Reaction of MoO_3 Nanobelts and S. *Chemistry – A European Journal* **2003,** *9* (12), 2726-2731.
284. Zhang, Y.; Ji, Q.; Han, G.-F.; Ju, J.; Shi, J.; Ma, D.; Sun, J.; Zhang, Y.; Li, M.; Lang, X.-Y.; Zhang, Y.; Liu, Z., Dendritic, Transferable, Strictly Monolayer MoS_2 Flakes Synthesized on $SrTiO_3$ Single Crystals for Efficient Electrocatalytic Applications. *ACS Nano* **2014,** *8* (8), 8617-8624.
285. Shi, J.; Wang, X.; Zhang, S.; Xiao, L.; Huan, Y.; Gong, Y.; Zhang, Z.; Li, Y.; Zhou, X.; Hong, M.; Fang, Q.; Zhang, Q.; Liu, X.; Gu, L.; Liu, Z.; Zhang, Y., Two-dimensional metallic tantalum disulfide as a hydrogen evolution catalyst. *Nature Communications* **2017,** *8* (1), 958.
286. Zhang, X.; Ma, G.; Wang, J., Hydrothermal synthesis of two-dimensional MoS_2 and its applications. *Tungsten* **2019,** *1* (1), 59-79.
287. Chen; Fan, R., Low-Temperature Hydrothermal Synthesis of Transition Metal Dichalcogenides. *Chemistry of Materials* **2001,** *13* (3), 802-805.
288. He, H. Y., Efficient hydrogen evolution activity of 1T-MoS_2/Si-doped TiO_2 nanotube hybrids. *International Journal of Hydrogen Energy* **2017,** *42* (32), 20739-20748.
289. Xu, X.; Fan, Z.; Ding, S.; Yu, D.; Du, Y., Fabrication of MoS2 nanosheet@TiO_2 nanotube hybrid nanostructures for lithium storage. *Nanoscale* **2014,** *6* (10), 5245-5250.
290. Zhang, X.; Selkirk, A.; Zhang, S.; Huang, J.; Li, Y.; Xie, Y.; Dong, N.; Cui, Y.; Zhang, L.; Blau, W. J.; Wang, J., MoS_2/Carbon Nanotube Core–Shell Nanocomposites for Enhanced Nonlinear Optical Performance. *Chemistry – A European Journal* **2017,** *23* (14), 3321-3327.
291. Li, Y.; Wang, H.; Xie, L.; Liang, Y.; Hong, G.; Dai, H., MoS_2 Nanoparticles Grown on Graphene: An Advanced Catalyst for the Hydrogen Evolution Reaction. *Journal of the American Chemical Society* **2011,** *133* (19), 7296-7299.
292. Yu, Y.; Huang, S.-Y.; Li, Y.; Steinmann, S. N.; Yang, W.; Cao, L., Layer-Dependent Electrocatalysis of MoS_2 for Hydrogen Evolution. *Nano Letters* **2014,** *14* (2), 553-558.
293. He, H.; Lin, J.; Fu, W.; Wang, X.; Wang, H.; Zeng, Q.; Gu, Q.; Li, Y.; Yan, C.; Tay, B. K.; Xue, C.; Hu, X.; Pantelides, S. T.; Zhou, W.; Liu, Z., MoS2/TiO2 Edge-On Heterostructure for Efficient Photocatalytic Hydrogen Evolution. *Advanced Energy Materials* **2016,** *6* (14), 1600464.
294. Wang, H.; Kong, D.; Johanes, P.; Cha, J. J.; Zheng, G.; Yan, K.; Liu, N.; Cui, Y., $MoSe_2$ and WSe_2 Nanofilms with Vertically Aligned Molecular Layers on Curved and Rough Surfaces. *Nano Letters* **2013,** *13* (7), 3426-3433.
295. Hu, J.; Huang, B.; Zhang, C.; Wang, Z.; An, Y.; Zhou, D.; Lin, H.; Leung, M. K. H.; Yang, S., Engineering stepped edge surface structures of MoS_2 sheet stacks to accelerate the hydrogen evolution reaction. *Energy & Environmental Science* **2017,** *10* (2), 593-603.
296. Wang, A.; Zhang, M.; Li, H.; Wu, F.; Yan, K.; Xiao, J., Combination of Theory and Experiment Achieving a Rational Design of Electrocatalysts for Hydrogen Evolution

on the Hierarchically Mesoporous CoS_2 Microsphere. *The Journal of Physical Chemistry C* **2019,** *123* (22), 13428-13433.
297. Voiry, D.; Salehi, M.; Silva, R.; Fujita, T.; Chen, M.; Asefa, T.; Shenoy, V. B.; Eda, G.; Chhowalla, M., Conducting MoS_2 Nanosheets as Catalysts for Hydrogen Evolution Reaction. *Nano Letters* **2013,** *13* (12), 6222-6227.
298. Lukowski, M. A.; Daniel, A. S.; Meng, F.; Forticaux, A.; Li, L.; Jin, S., Enhanced Hydrogen Evolution Catalysis from Chemically Exfoliated Metallic MoS_2 Nanosheets. *Journal of the American Chemical Society* **2013,** *135* (28), 10274-10277.
299. Voiry, D.; Yamaguchi, H.; Li, J.; Silva, R.; Alves, D. C. B.; Fujita, T.; Chen, M.; Asefa, T.; Shenoy, V. B.; Eda, G.; Chhowalla, M., Enhanced catalytic activity in strained chemically exfoliated WS_2 nanosheets for hydrogen evolution. *Nature Materials* **2013,** *12* (9), 850-855.
300. Yin, Y.; Zhang, Y.; Gao, T.; Yao, T.; Zhang, X.; Han, J.; Wang, X.; Zhang, Z.; Xu, P.; Zhang, P.; Cao, X.; Song, B.; Jin, S., Synergistic Phase and Disorder Engineering in 1T-$MoSe_2$ Nanosheets for Enhanced Hydrogen-Evolution Reaction. *Advanced Materials* **2017,** *29* (28), 1700311.
301. Kong, D.; Wang, H.; Lu, Z.; Cui, Y., CoSe2 Nanoparticles Grown on Carbon Fiber Paper: An Efficient and Stable Electrocatalyst for Hydrogen Evolution Reaction. *Journal of the American Chemical Society* **2014,** *136* (13), 4897-4900.
302. Li, H.; Tsai, C.; Koh, A. L.; Cai, L.; Contryman, A. W.; Fragapane, A. H.; Zhao, J.; Han, H. S.; Manoharan, H. C.; Abild-Pedersen, F.; Nørskov, J. K.; Zheng, X., Activating and optimizing MoS_2 basal planes for hydrogen evolution through the formation of strained sulphur vacancies. *Nature Materials* **2016,** *15* (1), 48-53.
303. Li, J.; Kang, J.; Cai, Q.; Hong, W.; Jian, C.; Liu, W.; Banerjee, K., Boosting Hydrogen Evolution Performance of MoS_2 by Band Structure Engineering. *Advanced Materials Interfaces* **2017,** *4* (16), 1700303.
304. Li, G.; Zhang, D.; Qiao, Q.; Yu, Y.; Peterson, D.; Zafar, A.; Kumar, R.; Curtarolo, S.; Hunte, F.; Shannon, S.; Zhu, Y.; Yang, W.; Cao, L., All The Catalytic Active Sites of MoS2 for Hydrogen Evolution. *Journal of the American Chemical Society* **2016,** *138* (51), 16632-16638.
305. Dong, L.; Guo, S.; Wang, Y.; Zhang, Q.; Gu, L.; Pan, C.; Zhang, J., Activating MoS_2 basal planes for hydrogen evolution through direct CVD morphology control. *Journal of Materials Chemistry A* **2019,** *7* (48), 27603-27611.
306. Tsai, C.; Li, H.; Park, S.; Park, J.; Han, H. S.; Nørskov, J. K.; Zheng, X.; Abild-Pedersen, F., Electrochemical generation of sulfur vacancies in the basal plane of MoS_2 for hydrogen evolution. *Nature Communications* **2017,** *8* (1), 15113.
307. Gao, G.; Xie, X.; Kang, S.; Lei, Y.; Trampert, A.; Cai, L., Toward heterostructured transition metal hybrids with highly promoted electrochemical hydrogen evolution. *RSC Advances* **2019,** *9* (35), 19924-19929.
308. Geng, S.; Liu, H.; Yang, W.; Yu, Y. S., Activating the MoS_2 Basal Plane by Controllable Fabrication of Pores for an Enhanced Hydrogen Evolution Reaction. *Chemistry – A European Journal* **2018,** *24* (71), 19075-19080.
309. Yin, Y.; Han, J.; Zhang, Y.; Zhang, X.; Xu, P.; Yuan, Q.; Samad, L.; Wang, X.; Wang, Y.; Zhang, Z.; Zhang, P.; Cao, X.; Song, B.; Jin, S., Contributions of Phase, Sulfur Vacancies, and Edges to the Hydrogen Evolution Reaction Catalytic Activity of Porous Molybdenum Disulfide Nanosheets. *Journal of the American Chemical Society* **2016,** *138* (25), 7965-7972.
310. Merki, D.; Fierro, S.; Vrubel, H.; Hu, X., Amorphous molybdenum sulfide films as catalysts for electrochemical hydrogen production in water. *Chemical Science* **2011,** *2* (7), 1262-1267.

311. Wu, L.; Longo, A.; Dzade, N. Y.; Sharma, A.; Hendrix, M. M. R. M.; Bol, A. A.; de Leeuw, N. H.; Hensen, E. J. M.; Hofmann, J. P., The Origin of High Activity of Amorphous MoS_2 in the Hydrogen Evolution Reaction. *ChemSusChem* **2019,** *12* (19), 4383-4389.
312. Morales-Guio, C. G.; Hu, X., Amorphous Molybdenum Sulfides as Hydrogen Evolution Catalysts. *Accounts of Chemical Research* **2014,** *47* (8), 2671-2681.
313. Benck, J. D.; Chen, Z.; Kuritzky, L. Y.; Forman, A. J.; Jaramillo, T. F., Amorphous Molybdenum Sulfide Catalysts for Electrochemical Hydrogen Production: Insights into the Origin of their Catalytic Activity. *ACS Catalysis* **2012,** *2* (9), 1916-1923.
314. Wang, T.; Zhuo, J.; Du, K.; Chen, B.; Zhu, Z.; Shao, Y.; Li, M., Electrochemically Fabricated Polypyrrole and MoS_x Copolymer Films as a Highly Active Hydrogen Evolution Electrocatalyst. *Advanced Materials* **2014,** *26* (22), 3761-3766.
315. Merki, D.; Vrubel, H.; Rovelli, L.; Fierro, S.; Hu, X., Fe, Co, and Ni ions promote the catalytic activity of amorphous molybdenum sulfide films for hydrogen evolution. *Chemical Science* **2012,** *3* (8), 2515-2525.
316. Kokko, M.; Bayerköhler, F.; Erben, J.; Zengerle, R.; Kurz, P.; Kerzenmacher, S., Molybdenum sulphides on carbon supports as electrocatalysts for hydrogen evolution in acidic industrial wastewater. *Applied Energy* **2017,** *190*, 1221-1233.
317. Nguyen, Q. T.; Nguyen, P. D.; N. Nguyen, D.; Truong, Q. D.; Kim Chi, T. T.; Ung, T. T. D.; Honma, I.; Liem, N. Q.; Tran, P. D., Novel Amorphous Molybdenum Selenide as an Efficient Catalyst for Hydrogen Evolution Reaction. *ACS Applied Materials & Interfaces* **2018,** *10* (10), 8659-8665.
318. Wang, P.; Wan, L.; Lin, Y.; Wang, B., MoS_2 supported CoS_2 on carbon cloth as a high-performance electrode for hydrogen evolution reaction. *International Journal of Hydrogen Energy* **2019,** *44* (31), 16566-16574.
319. Staszak-Jirkovský, J.; Malliakas, Christos D.; Lopes, Pietro P.; Danilovic, N.; Kota, Subrahmanyam S.; Chang, K.-C.; Genorio, B.; Strmcnik, D.; Stamenkovic, Vojislav R.; Kanatzidis, M. G.; Markovic, N. M., Design of active and stable Co–Mo–S_x chalcogels as pH-universal catalysts for the hydrogen evolution reaction. *Nature Materials* **2016,** *15* (2), 197-203.
320. Zhang, H.; Yang, B.; Wu, X.; Li, Z.; Lei, L.; Zhang, X., Polymorphic $CoSe_2$ with Mixed Orthorhombic and Cubic Phases for Highly Efficient Hydrogen Evolution Reaction. *ACS Applied Materials & Interfaces* **2015,** *7* (3), 1772-1779.
321. Wang, L.; Hu, P.; Long, Y.; Liu, Z.; He, X., Recent advances in ternary two-dimensional materials: synthesis, properties and applications. *Journal of Materials Chemistry A* **2017,** *5* (44), 22855-22876.
322. Kiran, V.; Mukherjee, D.; Jenjeti, R. N.; Sampath, S., Active guests in the MoS_2/$MoSe_2$ host lattice: efficient hydrogen evolution using few-layer alloys of MoS2(1−x)Se2x. *Nanoscale* **2014,** *6* (21), 12856-12863.
323. Konkena, B.; Masa, J.; Xia, W.; Muhler, M.; Schuhmann, W., MoSSe@reduced graphene oxide nanocomposite heterostructures as efficient and stable electrocatalysts for the hydrogen evolution reaction. *Nano Energy* **2016,** *29*, 46-53.
324. Xu, K.; Wang, F.; Wang, Z.; Zhan, X.; Wang, Q.; Cheng, Z.; Safdar, M.; He, J., Component-Controllable $WS_{2(1-x)}Se_{2x}$ Nanotubes for Efficient Hydrogen Evolution Reaction. *ACS Nano* **2014,** *8* (8), 8468-8476.
325. Liu, K.; Wang, F.; Xu, K.; Shifa, T. A.; Cheng, Z.; Zhan, X.; He, J., $CoS_{2x}Se_{2(1-x)}$ nanowire array: an efficient ternary electrocatalyst for the hydrogen evolution reaction. *Nanoscale* **2016,** *8* (8), 4699-4704.

326. Zhang, Y.; Liu, K.; Wang, F.; Shifa, T. A.; Wen, Y.; Wang, F.; Xu, K.; Wang, Z.; Jiang, C.; He, J., Dendritic growth of monolayer ternary $WS_{2(1-x)}Se_{2x}$ flakes for enhanced hydrogen evolution reaction. *Nanoscale* **2017,** *9* (17), 5641-5647.
327. Fu, Q.; Yang, L.; Wang, W.; Han, A.; Huang, J.; Du, P.; Fan, Z.; Zhang, J.; Xiang, B., Synthesis and Enhanced Electrochemical Catalytic Performance of Monolayer $WS_{2(1-x)}Se_{2x}$ with a Tunable Band Gap. *Advanced Materials* **2015,** *27* (32), 4732-4738.
328. Wang, F.; Li, J.; Wang, F.; Shifa, T. A.; Cheng, Z.; Wang, Z.; Xu, K.; Zhan, X.; Wang, Q.; Huang, Y.; Jiang, C.; He, J., Enhanced Electrochemical H2 Evolution by Few-Layered Metallic $WS_{2(1-x)}Se_{2x}$ Nanoribbons. *Advanced Functional Materials* **2015,** *25* (38), 6077-6083.
329. Xia, C.; Liang, H.; Zhu, J.; Schwingenschlögl, U.; Alshareef, H. N., Active Edge Sites Engineering in Nickel Cobalt Selenide Solid Solutions for Highly Efficient Hydrogen Evolution. *Advanced Energy Materials* **2017,** *7* (9), 1602089.
330. Liu, B.; Zhao, Y.-F.; Peng, H.-Q.; Zhang, Z.-Y.; Sit, C.-K.; Yuen, M.-F.; Zhang, T.-R.; Lee, C.-S.; Zhang, W.-J., Nickel–Cobalt Diselenide 3D Mesoporous Nanosheet Networks Supported on Ni Foam: An All-pH Highly Efficient Integrated Electrocatalyst for Hydrogen Evolution. *Advanced Materials* **2017,** *29* (19), 1606521.

4 Doped TiO_2

4.1 Introduction

This chapter presents the results of three combined experimental and computational studies examining the impact of substitutional doping of TiO_2 on the anatase-to-rutile transition (ART) temperature and photocatalytic activity. The dopants are copper (Cu);[1] molybdenum (Mo);[2] and indium (In).[3] Each study description begins with the presentation of selected experimental results before an in-depth discussion of the computational results.

The computational analysis includes an assessment of the local atomic structure in the vicinity of the dopant and the formation energies of charge compensating and reducing oxygen vacancies, which are implicated in the ART. It is hypothesised that making this process more difficult may be achieved by doping, which will impede the transition. Thus, should the presence of the dopant increase the energy required to produce oxygen vacancies then this might correspond to a suppression of the ART. We analyse the impact of the dopant on the light absorption properties of the titania host through projected electronic density of states (PEDOS) plots. We examine charge localisation and oxidation states by analysing Bader charges and excess spin density plots. For In-doped anatase TiO_2 we also examine the formation of In_2O_3 at the anatase surface and the reduction of this composite surface *via* oxygen vacancy formation.

A description of the computational set-up for these studies is provided in **Chapter 2** and a complete Materials and Methods are provided in **Appendix A**.

4.2 *Cu-doped TiO_2*

What follows is adapted from an article entitled: "***Effect of Cu Doping on the Anatase-to-Rutile Phase Transition in TiO_2 Photocatalysts: Theory and Experiments***", published in Applied Catalysis B: Environmental.[1]

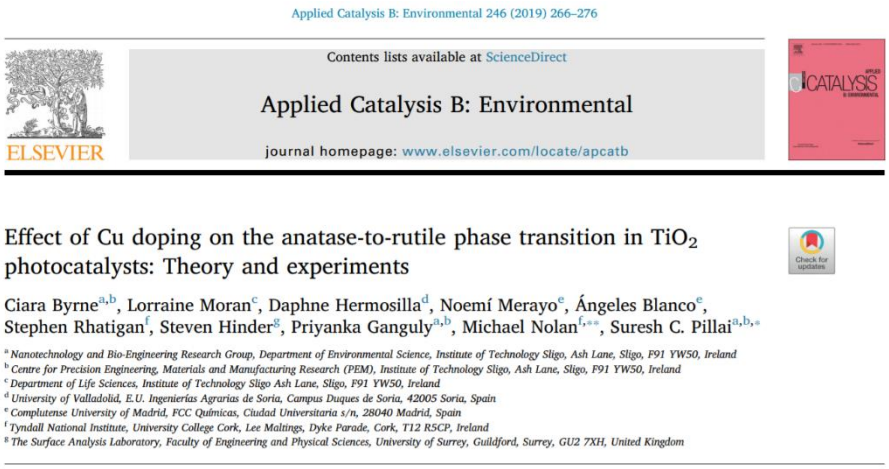
Applied Catalysis B: Environmental 246 (2019) 266–276

Contents lists available at ScienceDirect

Applied Catalysis B: Environmental

journal homepage: www.elsevier.com/locate/apcatb

Effect of Cu doping on the anatase-to-rutile phase transition in TiO_2 photocatalysts: Theory and experiments

Ciara Byrne[a,b], Lorraine Moran[c], Daphne Hermosilla[d], Noemí Merayo[e], Ángeles Blanco[e], Stephen Rhatigan[f], Steven Hinder[g], Priyanka Ganguly[a,b], Michael Nolan[f,**], Suresh C. Pillai[a,b,*]

[a] Nanotechnology and Bio-Engineering Research Group, Department of Environmental Science, Institute of Technology Sligo, Ash Lane, Sligo, F91 YW50, Ireland
[b] Centre for Precision Engineering, Materials and Manufacturing Research (PEM), Institute of Technology Sligo, Ash Lane, Sligo, F91 YW50, Ireland
[c] Department of Life Sciences, Institute of Technology Sligo Ash Lane, Sligo, F91 YW50, Ireland
[d] University of Valladolid, E.U. Ingenierías Agrarias de Soria, Campus Duques de Soria, 42005 Soria, Spain
[e] Complutense University of Madrid, FCC Químicas, Ciudad Universitaria s/n, 28040 Madrid, Spain
[f] Tyndall National Institute, University College Cork, Lee Maltings, Dyke Parade, Cork, T12 R5CP, Ireland
[g] The Surface Analysis Laboratory, Faculty of Engineering and Physical Sciences, University of Surrey, Guildford, Surrey, GU2 7XH, United Kingdom

DOI: https://doi.org/10.1016/j.apcatb.2019.01.058

https://cora.ucc.ie/handle/10468/7354

4.2.1 Introduction

Copper has previously been investigated as a dopant in TiO_2, but to date a detailed systematic analysis of the effect of Cu doping on the phase stability of TiO_2 is lacking.[4] In an important contribution, Yoong *et al*. examined Cu-doped Degussa P25 TiO_2 for different weight % of Cu (0, 2, 5, 10, 15 %) at three temperatures (300, 400, 500 °C).[4] However, the highest temperature in this work is below the anatase-rutile phase transition. Hence, there is no comprehensive understanding of the effect of copper doping on the anatase-rutile phase transition in TiO_2. Unravelling the role of Cu-doping in this phase

transition will inform endeavours to stabilise the more photoactive anatase phase of TiO_2 at higher temperatures.

Therefore, the aim of this investigation was to carry out a systematic and detailed study of the impact of copper doping of titanium dioxide on the anatase content, having calcined the samples to temperatures in the range 400-700 °C. Having determined the crystalline composition of the samples, we examined the resulting photocatalytic activity. Cu-doped titania was prepared with four different Cu concentrations, namely 0, 2, 4 and 8 mol. % Cu. Density functional theory (DFT) studies of Cu doping of bulk rutile and anatase were carried out to explore the effect of doping on the cation oxidation states, oxygen vacancy formation and any changes to the electronic structure of rutile and anatase after doping. X-ray diffraction (XRD) analysis and Raman spectroscopy were used for determining the phase composition of each sample. X-ray photoelectron spectroscopy (XPS) was used for identifying the bonding that was present in samples.

The photocatalytic performance of Cu-doped TiO_2 is assessed through measurements of 1, 4 dioxane removal. As 1, 4 dioxane is removed *via* an oxidation process, improvement of a modified catalyst in this regards may also have implications for the water oxidation activity, which is one of the main focuses of this thesis.

4.2.2 Results

4.2.2.1 Selected Experimental Results

X-ray Diffraction (XRD) Characterisation

X-ray Diffraction (XRD) was used to determine the effect of copper on the anatase to rutile transition temperature in TiO_2. The intensities of the main anatase and rutile peaks ((101) and (110), respectively) were used to determine the ratios of anatase and rutile

present in each sample. There were no peaks present relating to copper metal (which would appear at approx. 2θ = 43, 50 and 74°).[5] The only peaks that were present were those for titanium dioxide. All samples were 100% anatase phase at 400 °C and 500 °C. At 600 °C, the control (0% Cu) was 34.3% anatase and 65.7% rutile, while the Cu-doped samples remained 100% anatase. After calcination to 650 °C, the 0% and 2% Cu-TiO_2 samples contained 100% rutile. However, at the same temperature, the 4% and 8% Cu-TiO_2 samples had 27.3% and 74.3% of anatase respectively (**Figure 4.2.1.a**). All samples were 100% rutile phase after calcination to 700 °C. **Figure 4.2.1.b** shows the temperature-dependent anatase-rutile composition profile of the Cu-doped samples.

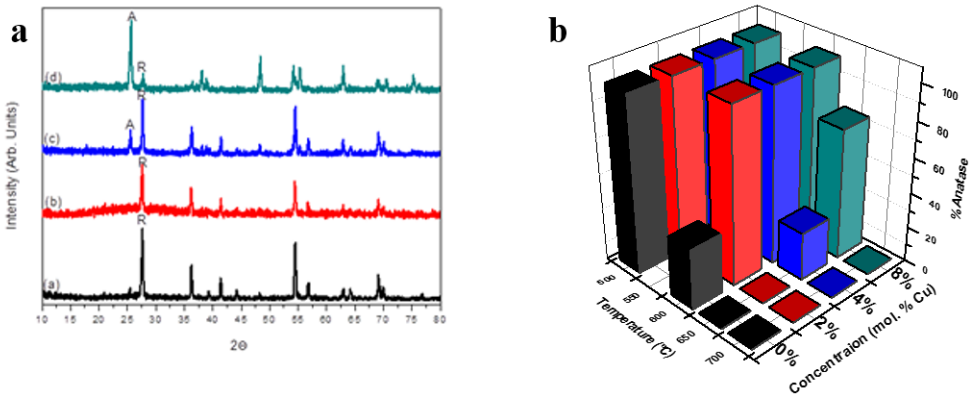

Figure 4.2.1 (a) XRD of (black) 0% Cu-TiO_2, (red) 2% Cu-TiO_2, (blue) 4% Cu-TiO_2 and (green) 8% Cu-TiO_2 after calcination to 650°C. A = anatase and R = Rutile. **(b)** Percentage of the anatase phase in Cu-doped TiO_2 samples.

X-ray Photoelectron Spectroscopy (XPS)

The X-ray Photoelectron spectroscopy (XPS) measurements were performed to analyse the elemental composition and metal oxidation states of each sample. **Figure 4.2.2** displays the survey spectrum for the 8% Cu-doped samples, which were calcined at 600, 650 and 700 °C. The survey spectrum indicates the presence of Ti, O, Cu and S. Carbon (C) 1*s* peaks (at binding energies (BE) of 284.9-285.0 eV) are present in all samples and

are attributed to adventitious carbon (C-C, C=C and/or C-H bonds), which arise due to contamination during synthesis and calcination.[6-8] Sulphur is present at *ca.* 4 at. % in the 8% Cu-doped material calcined at 600 °C. The presence of sulphur in Cu-doped TiO_2 at this concentration is mostly likely due to the release of sulphur dioxide from the Cu precursor ($CuSO_4$) during the calcination process.[9] However, the sulphur content reduces to below 1 at. % in the composites calcined at 700°C, which is also evident from the S 2*p* spectrum in **Figure 4.2.2.e**.

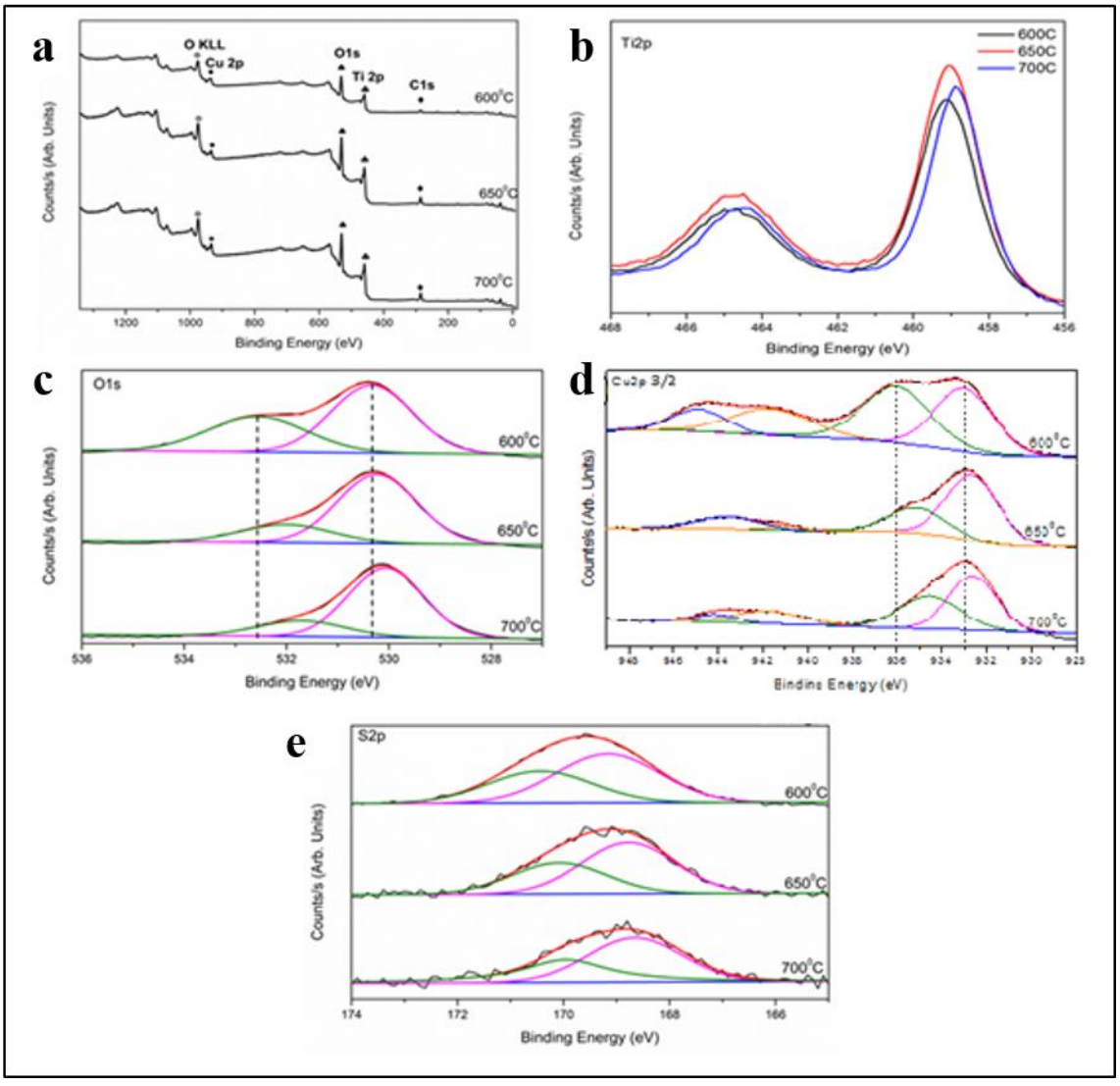

Figure 4.2.2 XPS spectra for the example of 8% Cu-TiO_2 that was calcined at 600 °C, 650 °C and 700 °C. Panel **(a)** shows the survey spectrum and the BE regions are shown for **(b)** Ti 2*p*, **(c)** O 1*s*, **(d)** Cu $2p_{3/2}$ and **(e)** S 2*p*.

The peaks for the Ti $2p_{3/2}$ spectrum show the presence of Ti-O binding. The slight decrease in the binding energy (464.6-464.4 eV) as the temperature increases indicates that samples are becoming oxygen deficient, see **Figure 4.2.2.b**.[7, 10-11] This also indicates reduction of Ti^{4+} to Ti^{3+} at higher temperatures.[7, 10-11] There is a similar decrease in the binding energy of the O 1*s* peak (BE = 530.4-530.1 eV), shown in **Figure 4.2.2.c**, which further indicates the formation of oxygen vacancies.[7, 10-11] Oxygen vacancy formation signifies that the anatase phase is beginning the transformation to the rutile phase.[7, 10-13] The second dominant peak in the O 1*s* spectra is at 532.6 eV in Cu-TiO_2 calcined at 600 °C and shifts to 531.7 eV, when calcined at 700 °C. These peaks are assigned to oxygen in the sulphate and oxygen bound to Cu (as Cu^{2+}), respectively.[14]

XPS is significantly more sensitive than XRD and Raman to minute compositional changes. Such changes can be detected from XPS analysis, i.e. any copper oxides that may form can be detected in XPS but not in XRD and Raman spectra.[15-16] **Figure 4.2.2.d** shows the Cu $2p_{3/2}$ spectra. The sample calcined at 600 °C exhibits a broad asymmetric curve from 930 to 937 eV. The deconvolution of this curve gave two prominent peaks at 933.1 eV and 936 eV, corresponding to Cu^{2+} in CuO and $CuSO_4$, respectively. Calcining at higher temperatures of 650 °C and 700 °C resulted in a slight shift in these peaks. At 700 °C, the peaks were observed at 932.6 eV and 934.1 eV, corresponding to Cu^{1+} and Cu^{2+} oxidation states, respectively. Hence, XPS results reveal the presence of copper in two oxidation states. Moreover, two satellite peaks of Cu $2p_{3/2}$, which correspond to Cu^{2+}, are observed at 941 eV and 944 eV; the peak intensities gradually decrease as the calcination temperature increases.[17-20] The S 2*p* (**Figure 4.2.2.e**) XPS spectrum shows two sub-component peaks at 170.1 eV and 168.8 eV; these are attributed to S $2p_{1/2}$ and S $2p_{3/2}$, respectively and these binding energies suggest the presence of sulphur in the S^{6+} state.[21]

Photocatalytic Analysis

The degradation of 1, 4-dioxane was used to assess the photocatalytic performance of the Cu-doped TiO_2 catalysts. All Cu concentrations were considered and measurements were performed after calcination to 600 and 650 °C, and the results are presented in **Figure 4.2.3**. The highest degradation of 1, 4-dioxane was achieved for un-doped TiO_2 prepared at 500 °C. With this sample, the majority of the 1, 4-dioxane was degraded within 240 minutes. Increasing the temperature to 600 or 650 °C limited the extent of 1, 4-dioxane degradation.

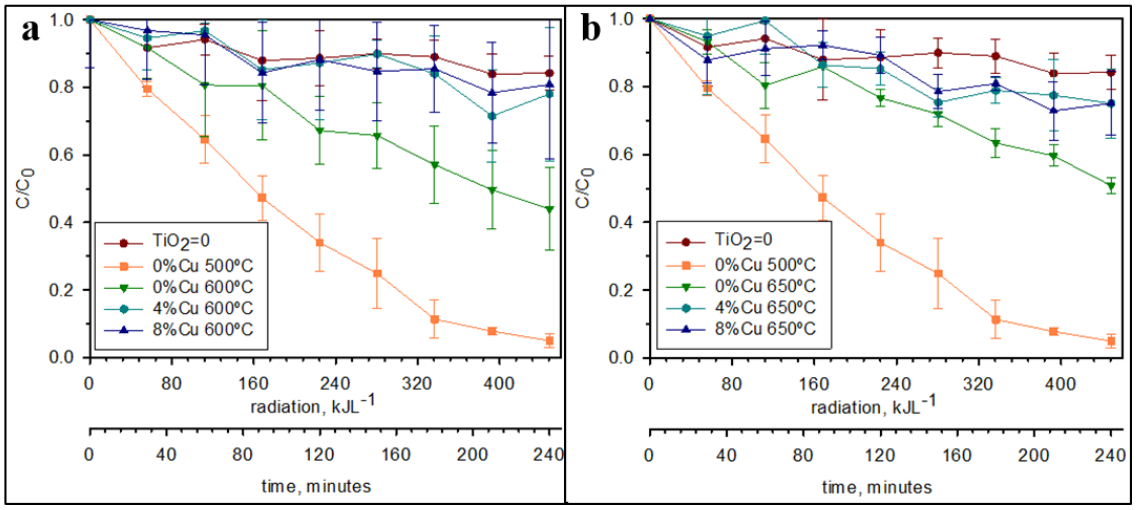

Figure 4.2.3 Degradation of 1, 4-dioxane by Cu-doped TiO_2 photocatalysis at **(a)** 600 °C and **(b)** 650 °C compared with TiO_2 prepared at 500 °C and irradiation without catalyst.

The inclusion of Cu does not result in any improvement in the photocatalytic activity of TiO_2. This is also irrespective of the polymorph of TiO_2 present as a result of Cu-doping and calcination temperature. Thus, while Cu doping can be used to enhance the stability of anatase TiO_2 to higher temperatures, and give a higher anatase content, the incorporation of Cu has the effect of reducing photocatalytic activity towards dioxane removal.

This behaviour agrees with previous studies, in which Cu-doping did not always yield an improvement of the photocatalytic efficiency of Cu-TiO_2 even in the anatase phase.[22-24] This is usually attributed to the recombination of electron-hole pairs at defect centres, as well as to the prevention of photon absorption by TiO_2 due to the presence of Cu.[23]

4.2.2.2 Computational Results

Atomic and Electronic Structure of Cu-Doped TiO_2

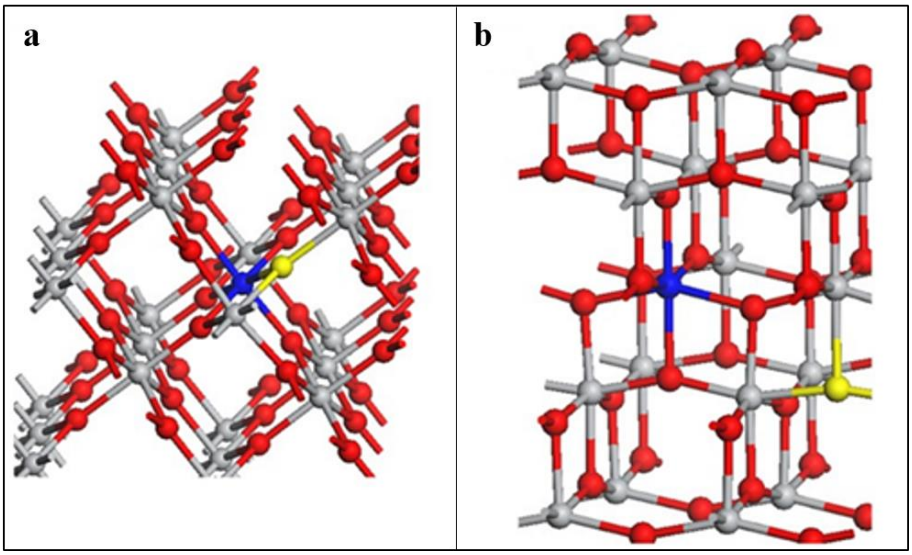

Figure 4.2.4 Local atomic structure in the vicinity of the Cu-dopant for **(a)** rutile and **(b)** anatase. Cu is represented by a blue sphere, Ti is grey and O is red. The yellow sphere marks the location of the oxygen hole polaron.

The local atomic structure that results from substituting Cu on a Ti site in Cu-doped bulk rutile and anatase TiO_2 (see **Figure 4.2.4**), is distorted about the dopant site. Replacing a Ti^{4+} cation with a Cu^{2+} cation results in a deficiency of two electrons and formation of two oxygen holes ($Ti_{Ti}^{X} + 2O_{O}^{X} \rightarrow Cu_{Ti}'' + 2O_{O}^{\bullet}$). Two computational set-ups were implemented: standard DFT and DFT+U. For standard DFT, the local atomic structure is distorted symmetrically about the dopant, with the distortion arising from differences in

ionic radii between copper and titanium. For the DFT+U calculations, two energy minima are found. In the first, the geometry is distorted symmetrically, similar to the standard DFT solution. The second solution is an asymmetric distortion to the geometry.

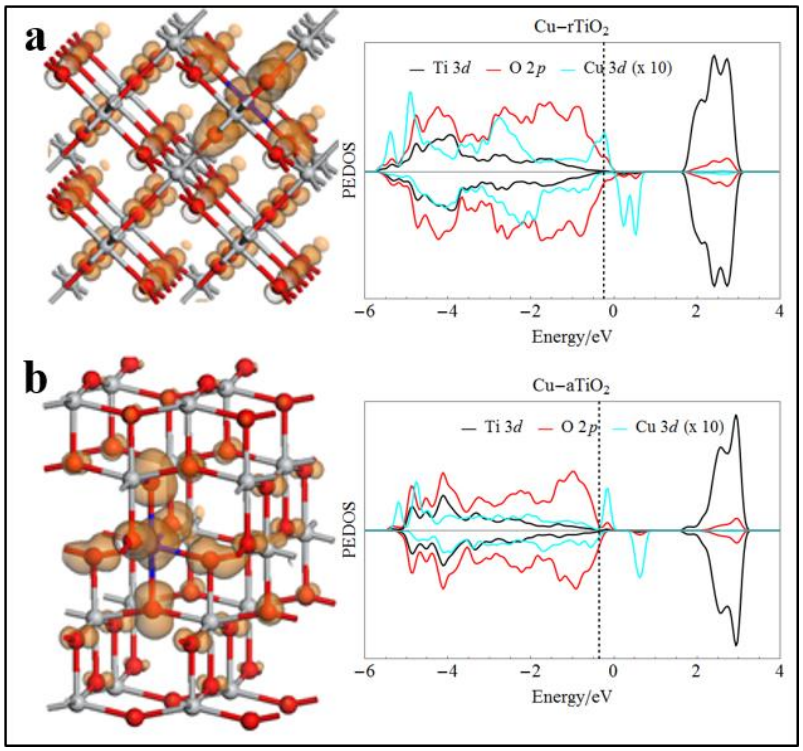

Figure 4.2.5 Spin density and PEDOS plots for **(a)** Cu-doped rutile TiO_2 and **(b)** Cu-doped anatase TiO_2, computed with standard DFT. The Cu dopant is represented in blue and the spin isosurfaces are set to 0.02 electrons $Å^{-3}$.

In the first solution, the four-equatorial dopant-O distances are equal (1.96 Å (1.91 Å) for rutile (anatase)), as are the two apical dopant-O distances (1.97 Å (1.97 Å) for rutile (anatase)). In un-doped rutile (anatase), the equatorial/apical Ti-O distances are 1.96/1.98 Å (1.93/2.01 Å). Upon doping, the equatorial and apical Cu-O distances are shorter than the equivalent Ti-O distances in un-doped TiO_2. The symmetric structure is consistent with delocalisation of the oxygen holes and the results for rutile are similar to those previously reported.[25] **Figure**s **4.2.5.a** and **4.2.5.b** show that with standard DFT, the

oxygen holes that form upon Cu doping are delocalised over all oxygen ions in rutile and more localised in anatase, but still notably delocalised.

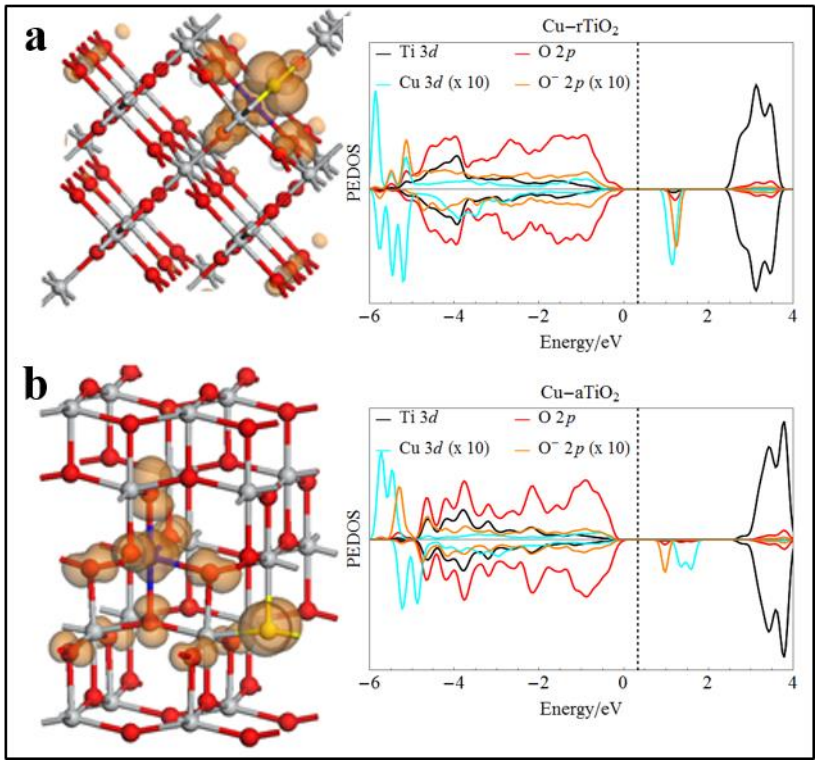

Figure 4.2.6 Spin density and PEDOS plots for **(a)** Cu-doped rutile TiO_2 and **(b)** Cu-doped anatase TiO_2, computed with DFT+U. Cu is represented in blue with yellow marking the position of the oxygen polarons. The spin isosurfaces are set to 0.02 electrons $Å^{-3}$.

The asymmetric solution, with a geometry distortion about the dopant, shows non-uniform dopant-O distances. For rutile, there is one elongated Cu-O distance, consistent with a longer bond between Cu and an oxygen hole polaron. This has also been observed in In-doped rutile TiO_2[26] and Li-doped MgO[27] and ZnO,[28] among other materials.[29-32] That the effect is less strong in Cu-doped TiO_2 can be attributed to the presence of a second hole which is less localised, being distributed over oxygen ions neighbouring the dopant, as shown by the spin density plot in **Figure 4.2.6.a**. This diminishes the

Coulombic attraction and lengthens the cation-O bonds.[28] We find that a solution starting with two fully localised holes relaxes to this partially localised hole distribution.

In the case of anatase, the polaron is not bound directly to the dopant and sits at an equatorial site of a neighbouring Ti (yellow sphere in **Figure 4.2.6.b**). The polaron induces a significant extension of the Ti-O distances of 0.07-0.1 Å, when compared to un-doped TiO_2. The second polaron is also partially localised over oxygen ions near the dopant.

The asymmetric polaronic solution is more stable by 0.2 eV in rutile and anatase, within the present DFT+U computational set-up. The asymmetric solution is not stable with standard DFT, consistent with previous work showing that only symmetric solutions are stable with standard DFT.[26]

The location of the polaron is further confirmed through the calculated Bader atomic charges and spin magnetisations. For a polaronic oxygen, the computed Bader charge is reduced from 7.4 electrons (lattice O^{2-}) to 6.7 (6.9) electrons for Cu-doped rutile (anatase). The spin magnetisations for these O ions are 0.85 (0.71) μ_B in rutile (anatase). In rutile, the other five oxygen ions neighbouring the dopant have spin magnetisations in the range of 0.16-0.22 μ_B. Similarly, in anatase, five of the six oxygen ions neighbouring the dopant have spin magnetisations in the range of 0.12-0.17 μ_B, with a value of 0.33 μ_B on a sixth oxygen, namely, the lower apical oxygen bonded to the dopant in **Figure 4.2.6.d**. The Bader charges of the Cu dopant are 9.6 electrons for rutile and 9.7 electrons for anatase, consistent with the Cu^{2+} oxidation state.[33]

Figures **4.2.5** and **4.2.6** display the projected electronic density of states (PEDOS), projected onto the Ti and Cu 3*d* states and the O 2*p* states. The PEDOS plots show qualitatively similar behaviour for both doped phases. The PEDOS for the standard DFT

calculations, with the delocalised symmetric solution, have states associated with the oxygen holes positioned just above the VB, crossing the Fermi level, as shown in **Figure 4.2.5**. For anatase, in which the polaron is partially localised over oxygen ions near the dopant, even without the +U correction, an O 2*p* state appears in the gap, just above the VB. These results concur with previous *ab initio* studies of rutile[25] and anatase.[34]

Applying the +U correction to the O 2*p*, Ti 3*d* and Cu 3*d* states, proved necessary to obtain a properly localised polaron description[27, 29-30] and the PEDOS plots consequently display the typical empty oxygen hole polaron state in the middle of the VB-CB energy gap, as shown in **Figure 4.2.6**. The onsite Coulomb interaction pushes the defect state into the middle of the gap, as opposed to an unoccupied continuum state at the top of the valence band. With standard DFT, the empty Cu 3*d* states lie just above the valence band edge, while with the +U correction on the Cu 3*d* states there is clear shift of these states into the energy gap. Examining the position of the empty Cu 3*d* states, one may conclude that the TiO_2 energy gap could be reduced by up to 0.5 eV upon Cu doping.

The charge compensation mechanism for doping of TiO_2 with lower valence cation dopants is the formation of oxygen vacancies ($Cu''_{Ti} + 2O^{\bullet}_{O} \rightarrow Cu''_{Ti} + O^{X}_{O} + V''_{O}$). Therefore, given the +2 oxidation state of Cu, one neutral oxygen species per Cu is removed from different sites in Cu-doped rutile and anatase. Apical and equatorial oxygen sites neighbouring the dopant were determined to be most stable for compensating oxygen vacancy formation, with vacancy formation energies of 0.46 (0.16) eV and 0.02 (-0.40) eV in rutile (anatase). This trend corroborates that found in a previous study of the effect of oxygen vacancies on the magnetic moment of Cu-doped rutile TiO_2.[25] These oxygen sites show either negative or small, positive formation energies, confirming that oxygen vacancy formation is the charge compensation mechanism in Cu-doped TiO_2.

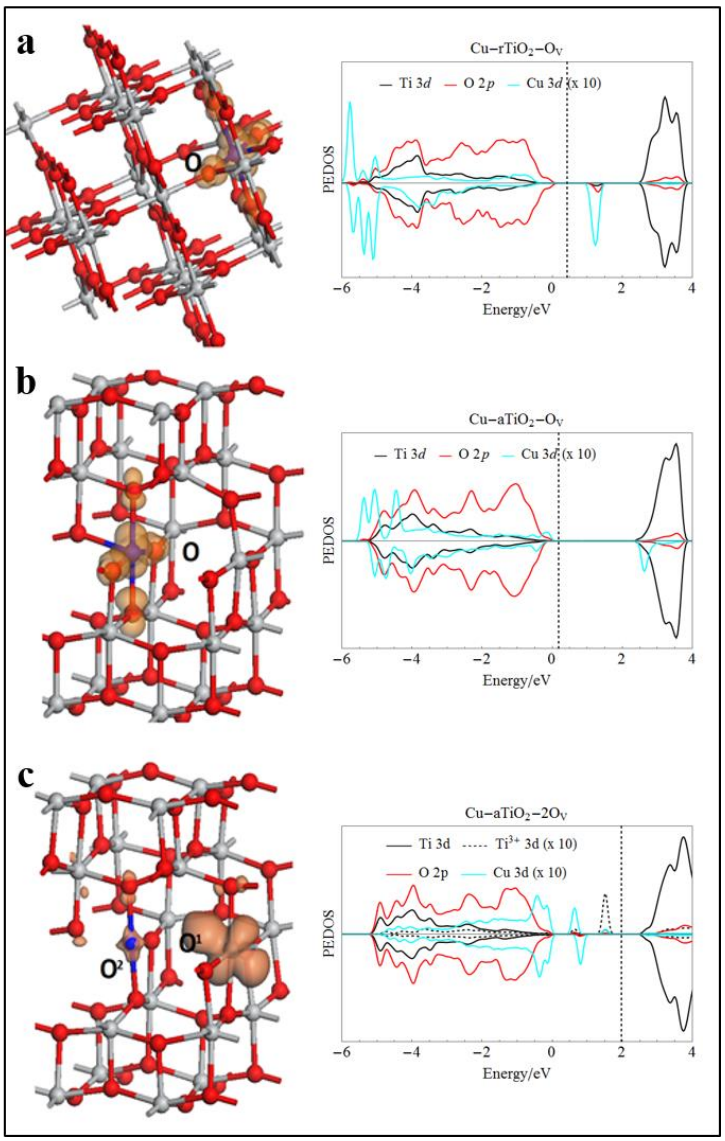

Figure 4.2.7 Excess spin density and PEDOS plots of charge compensated Cu-doped **(a)** rutile and **(b)** anatase TiO_2. Cu is represented by a blue sphere and the black circle marks the location of the charge compensating oxygen vacancy. **(c)** Cu-doped anatase with a second, reducing oxygen vacancy, where O^1 and O^2 indicate the site of the compensating and reducing oxygen vacancies. The spin density isosurface is set to 0.02 electrons $Å^{-3}$.

Figure 4.2.7 shows the geometry of the charge compensated structures of Cu-doped TiO_2. For rutile and anatase the copper dopant and two neighbouring titanium ions each coordinate to five oxygen ions. This under-coordination leads to a distortion, with the titanium ions moving off their lattice sites and outwards from the vacancy site along the direction of the missing bond. This distortion is accompanied by a shortened Ti-O bond

to the oxygen ion positioned opposite the vacancy. For rutile, this shortened bond is 1.84 Å, compared to 2.02 Å for equivalent bonds away from the vacancy site. In anatase, the Ti-O distances are shortened by up to 0.15 Å. The oxygen vacancy has little effect on the remaining Cu-O bonds.

Figure 4.2.7 also shows the excess spin density plots and the associated PEDOS for the compensating oxygen vacancy. The same trend is exhibited in the excess spin density plots of both rutile (**Figure 4.2.7.a**) and anatase (**Figure 4.2.7.b**), in that the excess spin is localised on the Cu dopant. The small spin on four neighbouring oxygen ions arises from covalency in the Cu-O bonds. The fifth oxygen, in both cases, is that positioned at an equatorial site opposite the vacancy. The computed Bader charges for Cu are 9.7 and 9.8 electrons for rutile and anatase, consistent with a Cu^{2+} oxidation state, which is unaffected by the charge compensation process.

For both TiO_2 polymorphs, the PEDOS plots are significantly altered upon forming the compensating vacancy. The PEDOS displays a peak attributed to the empty 3*d* orbital of the Cu^{2+} oxidation state. For rutile, this peak lies in the gap just below the CB minimum, whereas for anatase, this peak coincides with the bottom of the CB. For both polymorphs, the charge compensating vacancy thus shifts the Cu 3*d* states closer to the CB edge of TiO_2. Around the valence band region, Cu-doped anatase shows a filled Cu 3*d* state above the TiO_2 valence band edge, while for rutile, this state lies below the valence band edge. The empty oxygen hole states disappear after charge compensation, as expected.

Thus, a small reduction in the band gap at this Cu doping concentration is proposed for rutile and anatase. For rutile, the shift is 0.3 eV and for anatase the proposed band gap decrease is 0.2 eV. Since these results should be regarded with caution, given that this DFT+U set-up is not quantitatively describing the band gap of TiO_2, we ran single point

hybrid DFT calculations of Cu-doped TiO_2. These use the HSE06 functional, with 25% Fock exchange and a screening parameter of 0.2 $Å^{-1}$. The PEDOS in **Figure 4.2.8** for doped anatase shows similar trends as the DFT+U result, despite the differences in the DFT+U and hybrid DFT energy gaps. With no charge compensating oxygen vacancy, the position of Cu 3*d* and O 2*p* polaron states are similar to those from DFT+U. With the charge compensating vacancy, the occupied Cu 3*d* states are similar to those found with DFT+U, but the empty Cu 3*d* states lie above the TiO_2 conduction band edge. This gives a band gap reduction of 0.2 eV, similar to DFT+U. Thus, both DFT approaches appear to suggest that doping with Cu induces only a small, if any, red shift in light absorption.

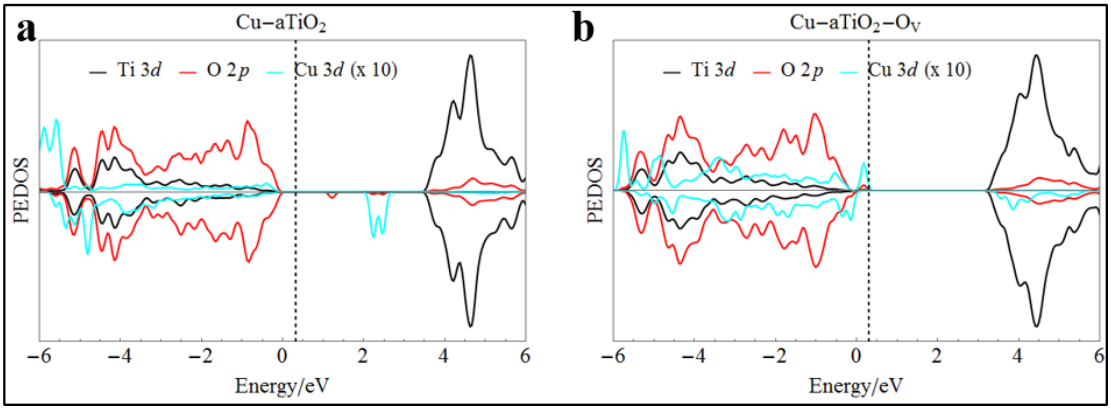

Figure 4.2.8 Hybrid DFT-computed PEDOS for Cu-doped TiO_2. **(a)** Cu-doped anatase with no compensating oxygen vacancy, **(b)** Cu-doped anatase with the compensating oxygen vacancy.

Finally, the formation of a neutral oxygen vacancy in charge compensated Cu-doped anatase has been studied. This is motivated by the experiments described previously, in which TiO_2 is calcined to over 500 °C, at which temperatures the formation of oxygen vacancy defects is likely. We compute a formation energy of 3.3 eV for the most stable oxygen vacancy site in charge compensated 3% Cu-doped anatase, with the atomic structure, spin density and PEDOS shown in **Figure 4.2.7.c**. Given the elevated temperatures in the experiments, such reducing oxygen vacancies will be present and we

can examine the effect of these vacancies on the electronic properties of Cu-doped anatase. We note that the computed oxygen vacancy formation energy of Cu-doped anatase is lower than that of un-doped anatase, which is 4.92 eV in our DFT+U set-up, suggesting that Cu-doping promotes the formation of oxygen vacancies, which would then lower the temperature at which the phase transition takes place. However, we find that as the concentration of oxygen vacancies increases, the computed formation energy in Cu-doped anatase increases from 3.3 eV to 3.6 eV for a third vacancy. We can conclude that the mechanism that underpins the experimental observation that the anatase phase persists to higher temperatures with Cu doping cannot be fully accounted for by the thermodynamics of simple oxygen vacancy formation. It is possible the sulphate in the copper precursor also contributes to inhibiting the phase transformation.[35]

After formation of the second oxygen vacancy, the computed Bader charge on Cu is 10.4 electrons, with a spin of 0.1 μ_B, which is consistent with reduction to Cu^{1+}. One Ti cation has a Bader charge of 10.5 electrons and a spin of 0.95 μ_B, which is consistent with a Ti^{3+} cation (all other Ti cations are Ti^{4+} with computed Bader charges of 9.6 electrons). The formation of a neutral oxygen vacancy thus reduces one Ti cation to Ti^{3+} and the Cu dopant to Cu^{1+}. Comparing with the XPS data, this is consistent with the assignment of reduced Cu^{1+} at elevated temperatures. The decrease in peak intensities of the Cu^{2+} satellites with increasing temperature is also consistent with Cu^{2+} reduction by oxygen vacancy formation. Finally, the PEDOS in **Figure 4.2.7.c** shows the introduction of occupied Cu^{1+} states in the TiO_2 valence-conduction band energy gap. These states can enhance charge recombination after excitation, which could result in reduced photocatalytic activity, as was observed in the photocatalytic measurements.

4.3 *Mo-doped TiO_2*

What follows is adapted from an article entitled: "***Mo doped TiO_2: impact on oxygen vacancies, anatase phase stability and photocatalytic activity***", published in the Journal of Physics: Materials.[2]

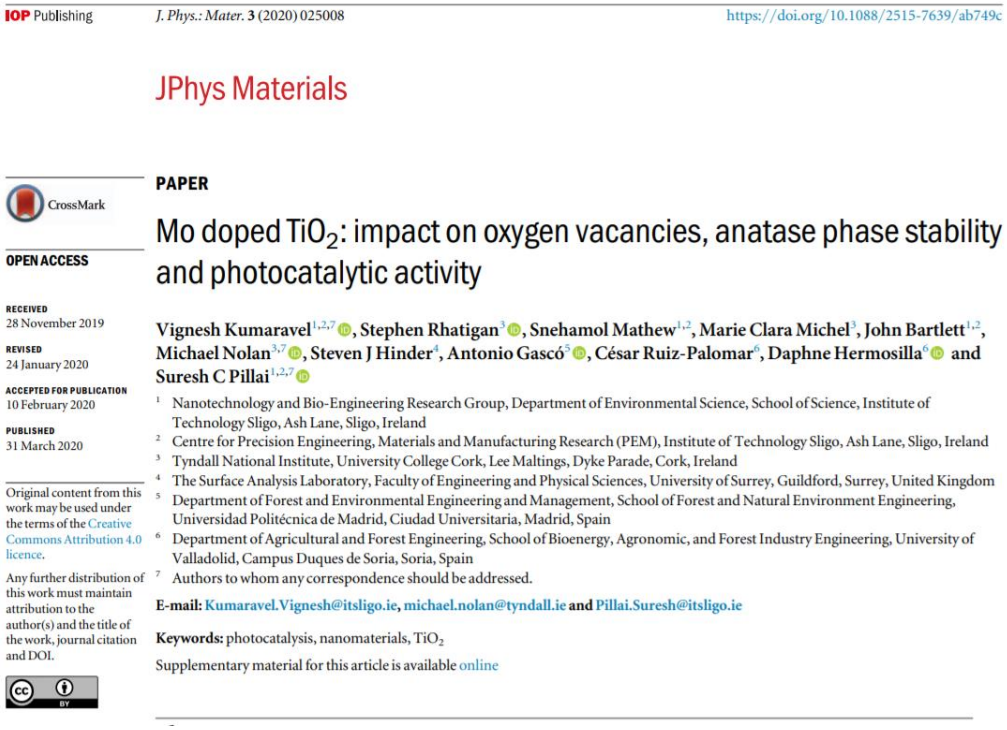

IOP Publishing J. Phys.: Mater. 3 (2020) 025008 https://doi.org/10.1088/2515-7639/ab749c

JPhys Materials

CrossMark

OPEN ACCESS

RECEIVED
28 November 2019

REVISED
24 January 2020

ACCEPTED FOR PUBLICATION
10 February 2020

PUBLISHED
31 March 2020

PAPER

Mo doped TiO_2: impact on oxygen vacancies, anatase phase stability and photocatalytic activity

Vignesh Kumaravel[1,2,7], Stephen Rhatigan[3], Snehamol Mathew[1,2], Marie Clara Michel[5], John Bartlett[1,2], Michael Nolan[3,7], Steven J Hinder[4], Antonio Gascó[5], César Ruiz-Palomar[6], Daphne Hermosilla[6] and Suresh C Pillai[1,2,7]

[1] Nanotechnology and Bio-Engineering Research Group, Department of Environmental Science, School of Science, Institute of Technology Sligo, Ash Lane, Sligo, Ireland
[2] Centre for Precision Engineering, Materials and Manufacturing Research (PEM), Institute of Technology Sligo, Ash Lane, Sligo, Ireland
[3] Tyndall National Institute, University College Cork, Lee Maltings, Dyke Parade, Cork, Ireland
[4] The Surface Analysis Laboratory, Faculty of Engineering and Physical Sciences, University of Surrey, Guildford, Surrey, United Kingdom
[5] Department of Forest and Environmental Engineering and Management, School of Forest and Natural Environment Engineering, Universidad Politécnica de Madrid, Ciudad Universitaria, Madrid, Spain
[6] Department of Agricultural and Forest Engineering, School of Bioenergy, Agronomic, and Forest Industry Engineering, University of Valladolid, Campus Duques de Soria, Soria, Spain
[7] Authors to whom any correspondence should be addressed.

E-mail: Kumaravel.Vignesh@itsligo.ie, michael.nolan@tyndall.ie and Pillai.Suresh@itsligo.ie

Keywords: photocatalysis, nanomaterials, TiO_2

Supplementary material for this article is available online

DOI: https://doi.org/10.1088/2515-7639/ab749c

https://cora.ucc.ie/handle/10468/9708

4.3.1 Introduction

Doping TiO_2 with an element of higher oxidation state compared to Ti^{4+} can improve charge carrier separation on the photocatalyst surface.[36] Molybdenum (Mo; with a highest oxidation state of Mo^{6+}) as a dopant is inexpensive, non-toxic and has high solubility in the TiO_2 anatase lattice.[36] The ionic radius of Mo^{6+} is almost identical to that of Ti^{4+},

being 0.062 nm and 0.068 nm, respectively, facilitating the substitution of Mo^{6+} ions at Ti^{4+} sites in the anatase crystal lattice.[37-38] This kind of doping would minimise lattice distortions.[38-39] Mo doping could also generate energy states within the band gap of TiO_2 to enhance light absorption and minimise electron-hole recombination.[38-40]

Various studies[36, 41-43] (discussed in more detail in **Chapter 3**) show that Mo-doping has the potential to improve the photocatalytic performance of TiO_2. Mo doping could influence the surface characteristics, oxygen vacancies, crystallinity, and formation of Ti^{3+} centres. However, there are still no comprehensive studies on the antimicrobial activity of high-temperature stable anatase Mo–TiO_2. Thus, the focus of this study was to investigate, systematically, the influence of Mo doping on the phase stability of anatase, formation of oxygen vacancies, and the photocatalytic activity of anatase. The results show that Mo doping can preserve the anatase content at high calcination temperatures and thus enhance the activity of TiO_2.

A comprehensive analysis on the relationship between the dopant concentration and the surface characteristics of TiO_2 is discussed. Electron–hole recombination was studied through photoluminescence (PL) spectra. DFT calculations were performed to examine the Mo oxidation state and the formation energy of oxygen vacancies and their role in the oxidation states of the cations and the resulting electronic structure, which is vital for the photocatalytic activity. The photocatalytic activity of Mo-doped anatase was studied using the disinfection of total bacteria in wastewater under UVA-LED light irradiation.

4.3.2 Results

4.3.2.1 Selected Experimental Results

X-ray Diffraction (XRD) Characterisation

Table 4.3.1 Phase percentages of Mo-TiO2 samples calcined at various temperatures. (A = anatase; R = rutile).

	500 °C		600 °C		700 °C		750 °C		800 °C	
Samples	**A**	**R**	**A**	**R**	**A**	**R**	**A**	**R**	**A**	**R**
0.0 % Mo-TiO_2	100	-	7	93	-	100	-	100	-	100
0.5 % Mo-TiO_2	100	-	30	71	7	93	4	96	-	100
1.0 % Mo-TiO_2	100	-	84	16	52	48	15	85	-	100
1.5 % Mo-TiO_2	100	-	100	-	87	13	14	86	-	100
2.0 % Mo-TiO_2	100	-	100	-	87	13	67	33	-	100

The phase percentages, determined from XRD analysis, of Mo-TiO_2 samples calcined at 600, 700, 750 and 800 °C are shown in **Table 4.3.1**. The anatase phase of TiO_2 is significantly preserved up to 750 °C by Mo doping.[41] A small red shift was observed for the anatase peak when the Mo content is increased from 0 to 2 mol. %, suggesting dopant-induced lattice distortion.[44] Doping sites of TiO_2 are mainly decided through the ionic radii, coordination numbers and valence electrons of the dopant.[45] The ionic radius of Mo^{6+} (0.062 nm) is close to that of Ti^{4+} (0.068 nm), suggesting substitutional doping of Mo^{6+} at Ti^{4+} sites in the anatase lattice.

X-ray Photoelectron Spectroscopy (XPS)

Binding interactions and oxidation states of elements in Mo-TiO_2 were analysed by XPS. Scans of Ti 2*p*, O 1*s*, and Mo 3*d* for un-doped TiO_2, calcined at 500 °C, and 2 mol. % Mo-TiO_2, calcined at 750 °C, are displayed in **Figure 4.3.1**. The representative spin-orbit

coupling peaks of Ti 2*p* (Ti $2p_{3/2}$, Ti $2p_{1/2}$) are observed at 458.86 eV and 464.53 eV, as shown in **Figure 4.3.1.a**, which are ascribed to Ti^{4+}.[46-47] The O 1*s* spectrum of TiO_2 is composed of two peaks, shown in **Figure 4.3.1.b**. The peak located at 530.03 eV is attributed to lattice O^{2-} in TiO_2[47] and the surface O-H group of TiO_2 is detected around 531.94 eV.[46-47]

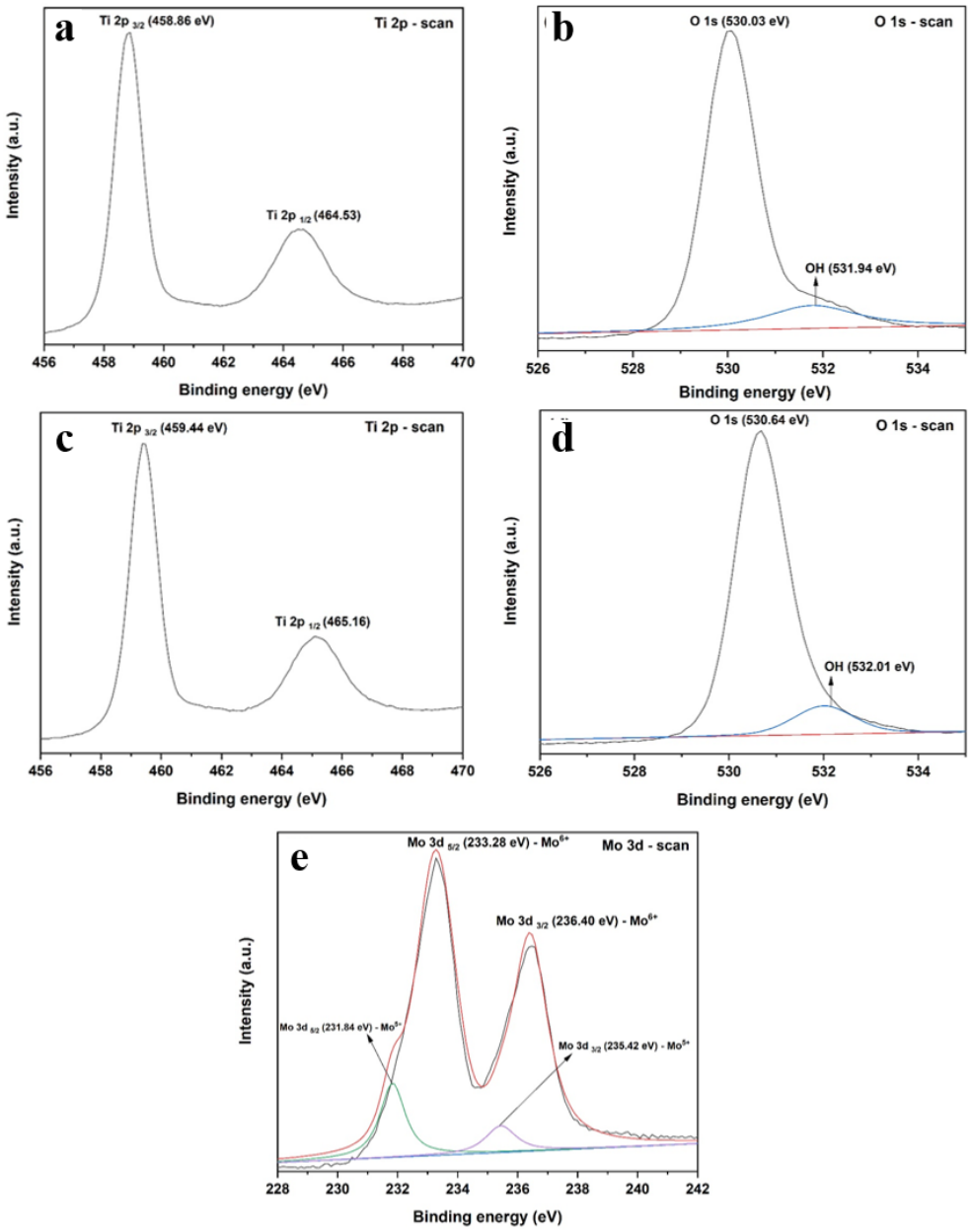

Figure 4.3.1 XPS scans for un-doped TiO_2, calcined at 500 °C (**(a)** Ti 2*p* and **(b)** O 1*s*), and for 2 mol. % Mo-TiO_2, calcined at 750 °C (**(c)** Ti 2*p* **(d)** O 1*s* **(e)** Mo 3*d*).

The peak positions of Ti 2*p* and O 1*s* are shifted for 2 mol. % Mo-TiO_2, compared to pure TiO_2, as shown in **Figure**s **4.3.1.c** and **4.3.1.d**. This is attributed to the high electronegativity of Mo compared to Ti, and suggests a lattice shift due to substitution of Mo^{6+} for Ti^{4+}. [37]

The peaks observed at 233.28 eV and 236.40 eV, in **Figure 4.3.1.e**, are attributed to Mo $3d_{5/2}$ and Mo $3d_{3/2}$ of Mo^{6+}. The sub components, detected by peak fitting, at 231.84 eV and 235.42 eV, are ascribed to Mo $3d_{5/2}$ and Mo $3d_{3/2}$ of Mo^{5+}. XPS results showed that the percentage of Mo^{6+} is higher than that of Mo^{5+}. The existence of Mo^{5+} denotes that the oxygen atoms in the anatase lattice are inadequate to reinforce Mo^{6+} ions[38] and based on DFT calculations this is consistent with reduction to Mo^{5+} after oxygen vacancy formation (see below).

Photoluminescence (PL)

PL spectra of Mo-TiO_2 samples calcined at 700 °C are shown in **Figure 4.3.2**. The PL emission peaks of pure TiO_2 are quenched by introduction of the Mo dopant. The intensity of the PL peaks are in the order: anatase (500 °C) > rutile (700 °C) > 0.5 Mo-TiO_2 > 2 Mo-TiO_2 > 1.5 Mo-TiO_2 > 1 Mo-TiO_2. As will be shown in the computed PEDOS plots, Mo doping introduces states in the TiO_2 band gap, just below the TiO_2 CBM and this could suppress radiative electron-hole recombination processes.[48] Photo-generated electrons may become trapped and localised at the Mo dopant ($Mo^{6+} \rightarrow Mo^{5+}$), reducing the probability of photo-generated electron-hole recombination.[49] In addition, the PL intensity could be influenced through the mobility of carriers.[50]

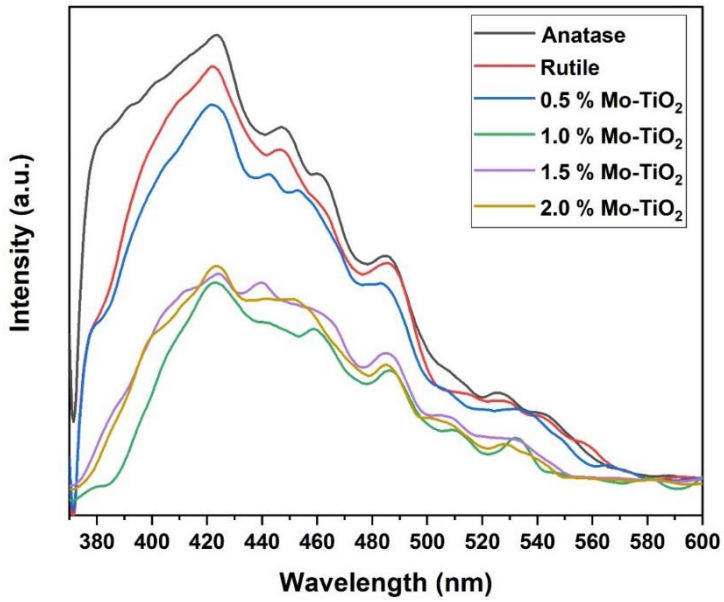

Figure 4.3.2 . PL spectra of anatase, calcined at 500 °C, rutile and Mo-TiO_2, calcined at 700 °C.

Photocatalytic Wastewater Disinfection

The photocatalytic activity of un-doped anatase (calcined at 500 °C) and 2 mol. % Mo-TiO_2 (calcined at 750 °C) for the removal of total bacteria in WW under 385 nm and 395 nm UVA LED light irradiation is displayed in **Figure 4.3.3**. N/N_0 percentages were plotted against the irradiation time. N and N_0 are the number of bacteria (CFU/mL) at irradiation times 't' and 0, respectively. The efficiency is denoted by a rate coefficient, 'b', from the exponential decay curves.

For 385 nm LED light irradiation, total bacteria removal for 2 mol. % Mo-TiO_2 is ~1.5 times higher than that of TiO_2. However, total bacteria removal for 2 mol. % Mo-TiO_2 is ~2.8 times higher than pure TiO_2 under 395 nm LED light irradiation. Total disinfection was achieved in almost 30 min of 395 nm LED light irradiation. The high activity of Mo-TiO_2 under 395 nm LED light is attributed to the maximum light absorption with respect

to its band gap and electronic properties, suggesting the generation of more charge carriers responsible for microbial disinfection.[51]

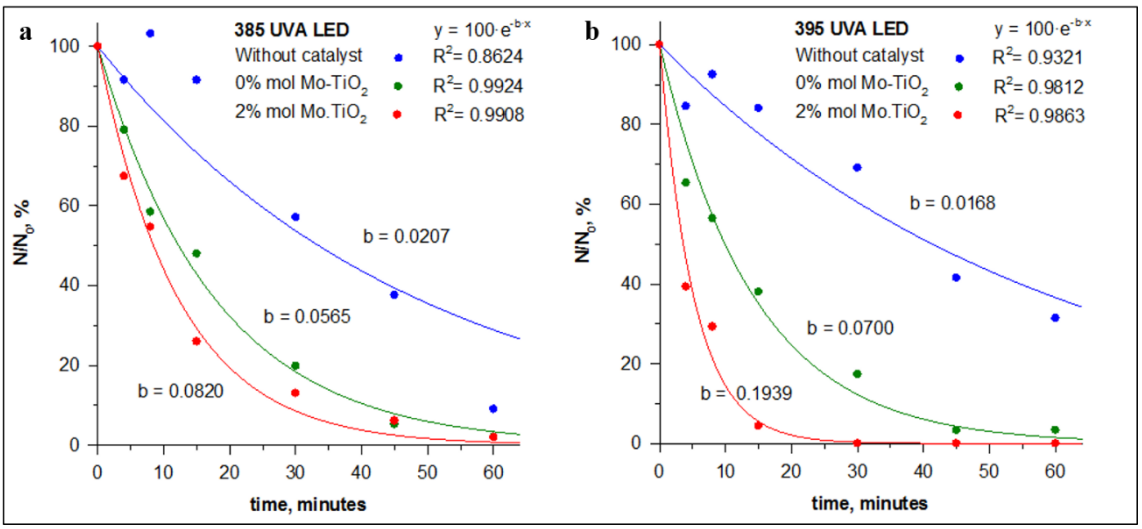

Figure 4.3.3 Photocatalytic disinfection efficiency of TiO_2 and Mo-TiO_2 under UVA LED light irradiation (**(a)** 385 nm and **(b)** 395 nm).

The photocatalytic activity could be influenced by the competitive reaction between the microbes and other organic matter in the WW.[52] Mo doping could enhance the surface active sites and interfacial charge transfer.[51, 53] The Mo dopant could influence the crystallite size and surface active sites of TiO_2 to promote the adsorption of microbes on the photocatalyst surface,[54] with Mo-derived gap states extending the lifetime of photo-induced charge carriers.

4.3.2.2 Computational Results

Local Atomic Structure and Oxygen Vacancy Formation

Formation of lattice oxygen vacancies and the emergence of energy levels in Mo-TiO_2 were studied *via* DFT calculations. The relaxed structure of Mo-doped anatase TiO_2 is shown in **Figure 4.3.4.a**. The computed Bader charge for Mo is 9.13 electrons,

corresponding to Mo^{6+}, based on comparisons with the Bader charge computed for Mo in bulk MoO_3. Mo-O distances are 1.94 Å and 2.01 Å for oxygen ions in equatorial and apical positions, respectively. These values are almost identical to those computed for Ti-O distances in the un-doped supercell (1.94 Å and 2.00 Å), owing to the similar ionic radii of Mo^{6+} and Ti^{4+}. These bond lengths compare with experimentally determined Ti-O distances of 1.94 Å and 1.96 Å,[55] for apical and equatorial oxygen sites.

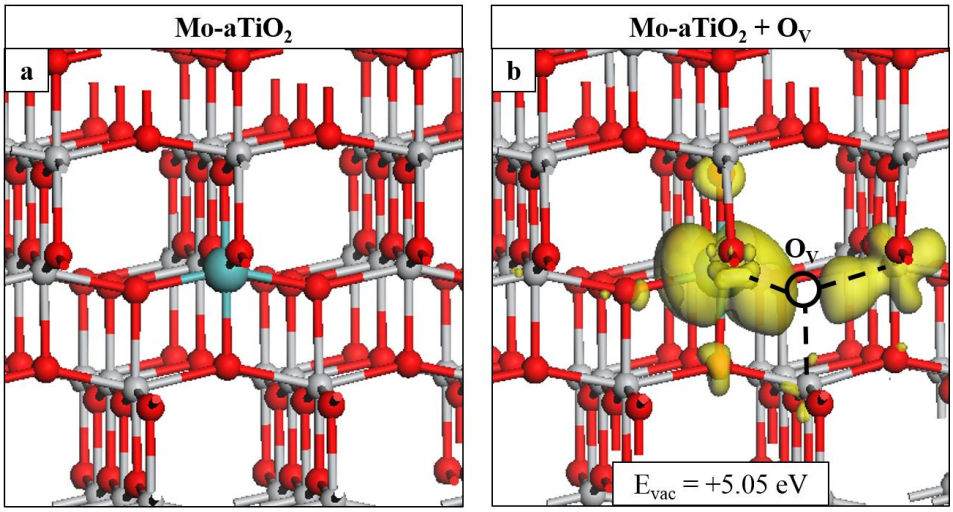

Figure 4.3.4 Relaxed geometry of Mo-doped anatase TiO_2 for **(a)** stoichiometric Mo-TiO_2 and **(b)** after formation of a single, reducing oxygen vacancy. The vacancy site sits at an equatorial position relative to the Mo-dopant and the formation energy is included in the inset of panel **(b)**. The yellow iso-surface encloses spin densities of up to 0.02 eV/Å^3. The site of the removed O ion is indicated by the black circle and dashed black lines show the ions to which the removed oxygen was bound. In this and subsequent figures, Ti is represented by grey spheres, O by red and Mo by blue

---

We consider reduction of the system *via* oxygen vacancy formation, as such defects are implicated in the ART.[1, 3, 56-57] The most stable site for the formation of an oxygen vacancy is an equatorial site of the Mo-dopant and the relaxed geometry and excess spin density are shown in **Figure 4.3.4.b**. The formation energy is 5.05 eV and this is more stable than the next most stable vacancy by 0.1 eV. By comparison, the vacancy formation

energy in the un-doped anatase supercell is 5.26 eV and so Mo-doping, at this concentration, will not promote vacancy formation to a significant degree.

After formation of a neutral oxygen vacancy, two electrons are released and these localise in the vicinity of the vacancy site, as shown in the excess spin density plot of **Figure 4.3.4.b**. The computed Bader charge for Mo increases from 9.13 electrons, in the stoichiometric system, to 9.91 electrons in the reduced system, indicating reduction to Mo^{5+}. The spin magnetisation in the *d*-orbital of Mo is 1.1 μ_B. For one of the Ti ions to which the removed oxygen was bound, the Bader charge increases from 9.61 to 9.91 electrons. This Ti ion has a computed spin magnetisation of 0.2 μ_B. These results suggest that the excess charge occupies the vacancy site rather than localising at only the Mo and Ti ions (**Figure 4.3.4.b**). Typically, Ti^{3+} ions exhibit computed Bader charges of 10.0-10.5 electrons and spin magnetisations of 0.8-1.0 μ_B.[1, 58] The values computed for the partially reduced Ti ion in the current work are consistent with our work on In-doped TiO_2, which will be discussed in the next section.[3] This study showed excess charge distributed over the vacancy site in the reduced system, rather than localised at cation sites; the computed Bader charge and spin magnetisation for Ti sites neighbouring the vacancy were 9.7/9.8 electrons and 0.1/0.2 μ_B, respectively. The excess spin density plot in **Figure 4.3.4.b** shows that the charges are distributed over Mo and Ti and the electron density extends towards the vacancy site.

Electronic Properties

The projected electronic density of states (PEDOS) were computed for the stoichiometric and reduced system, with one oxygen vacancy, and these are shown in **Figure 4.3.5**. For the stoichiometric system (**Figure 4.3.5.a**), Mo *s*-states emerge at the CBM of the TiO_2 host and the Mo *d*-states overlap with the titania CB. GGA studies of Mo-doped TiO_2

also report the emergence of Mo-derived defect states below the CBM.[39, 59] These studies identify Mo *d*-states below the CBM, but there is no discussion of the Mo *s*-states. In the current work, we find that Mo *d*-states lie above the CBM and this may be due to the implementation of a Hubbard U on Mo *d*-states, which shifts these states with respect to the TiO_2 CBM. After vacancy formation and reduction of Ti and Mo, occupied Ti and Mo *d*-states emerge in the band gap at 1.65 eV above the valence band maximum (VBM), as shown in **Figure**s **4.3.5.b** and **4.3.5.c**.

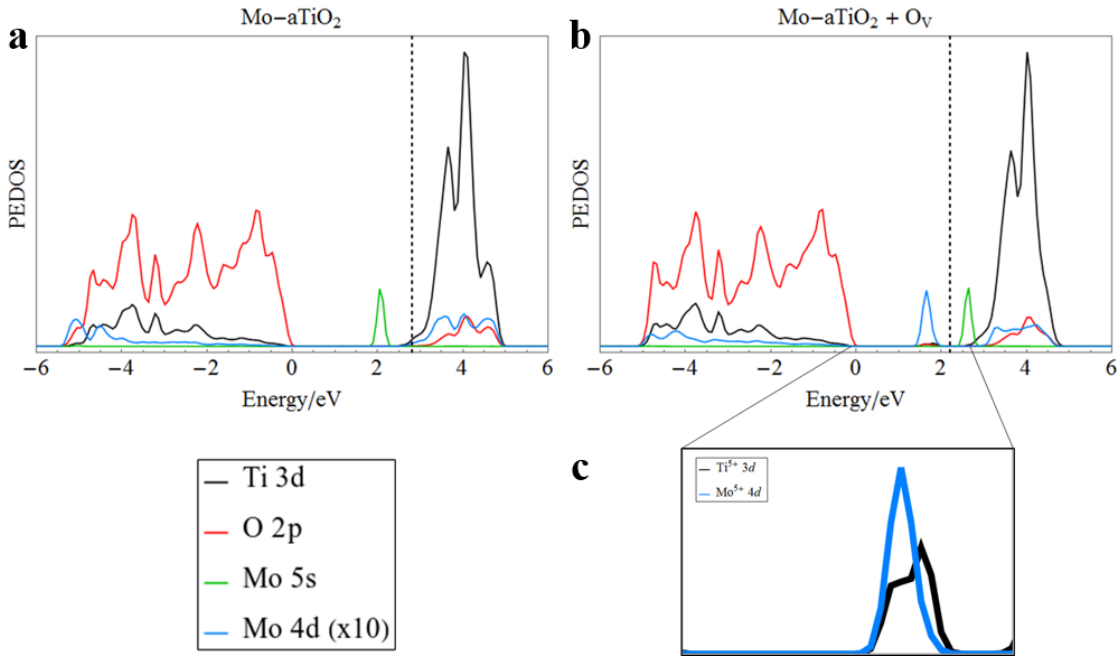

Figure 4.3.5 Computed PEDOS for **(a)** stoichiometric Mo-doped anatase TiO_2 and **(b)** reduced Mo-doped anatase TiO_2, with one oxygen vacancy. Panel **(c)** shows the occupied Ti^{3+} and Mo^{5+} states which emerge in the band gap after vacancy formation.

4.4 *In-doped TiO_2*

What follows is adapted from an article entitled: "***In-doped TiO_2 photocatalysts with high temperature anatase stability***", published in the Journal of Physical Chemistry C.[3]

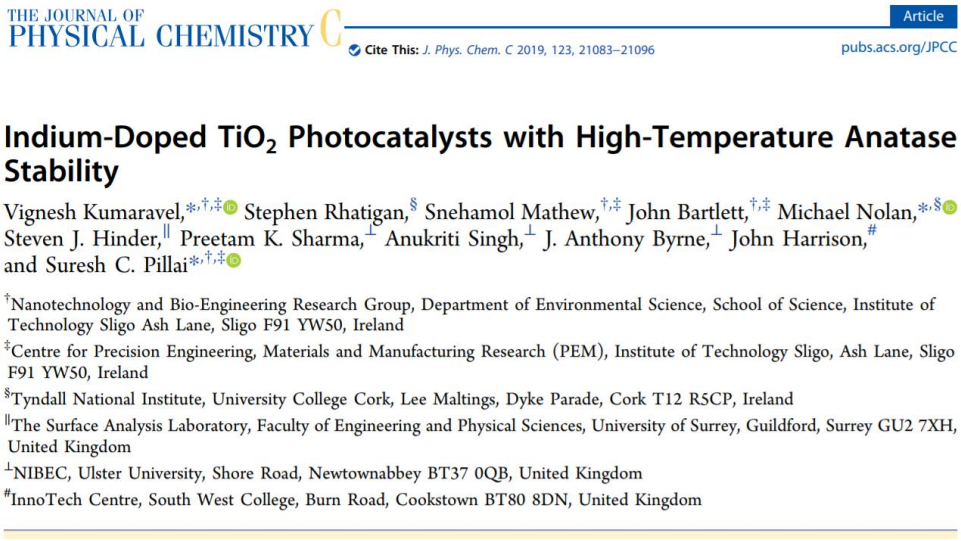

THE JOURNAL OF PHYSICAL CHEMISTRY C
Article
Cite This: J. Phys. Chem. C 2019, 123, 21083−21096
pubs.acs.org/JPCC

Indium-Doped TiO_2 Photocatalysts with High-Temperature Anatase Stability

Vignesh Kumaravel,[*,†,‡] Stephen Rhatigan,[§] Snehamol Mathew,[†,‡] John Bartlett,[†,‡] Michael Nolan,[*,§] Steven J. Hinder,[∥] Preetam K. Sharma,[⊥] Anukriti Singh,[⊥] J. Anthony Byrne,[⊥] John Harrison,[#] and Suresh C. Pillai[*,†,‡]

[†]Nanotechnology and Bio-Engineering Research Group, Department of Environmental Science, School of Science, Institute of Technology Sligo Ash Lane, Sligo F91 YW50, Ireland
[‡]Centre for Precision Engineering, Materials and Manufacturing Research (PEM), Institute of Technology Sligo, Ash Lane, Sligo F91 YW50, Ireland
[§]Tyndall National Institute, University College Cork, Lee Maltings, Dyke Parade, Cork T12 R5CP, Ireland
[∥]The Surface Analysis Laboratory, Faculty of Engineering and Physical Sciences, University of Surrey, Guildford, Surrey GU2 7XH, United Kingdom
[⊥]NIBEC, Ulster University, Shore Road, Newtownabbey BT37 0QB, United Kingdom
[#]InnoTech Centre, South West College, Burn Road, Cookstown BT80 8DN, United Kingdom

DOI: https://doi.org/10.1021/acs.jpcc.9b06811

4.4.1 Introduction

Indium (In) is a transition metal with 5*s*2 5*p*1 electronic configuration and it generally takes a +3 oxidation state. It has the tendency to create oxygen vacancies in TiO_2.[60-61] Indium is considered an effective dopant for TiO_2, owing to its electronic properties and low toxicity.[61-62] Doping of such metal ions into TiO_2 would be beneficial to enrich the photocatalytic activity[63] by inhibiting photo-generated charge carrier recombination and promoting the adsorption of microbes/pollutants at active sites of the photocatalyst.[61]

There are no comprehensive or systematic studies available in the literature on the ART of In-TiO_2. In this paper, we studied the ART of In-doped TiO_2 (In-TiO_2) nanoparticles,

calcined for 2 h at temperatures in the range of 500-900 °C; this range includes the temperature at which un-doped anatase transforms to rutile. In-TiO_2 was synthesised using a sol-gel technique with different mol. percentages of In (0, 2, 4, 8 and 16%). The energetics involved in the formation of charge compensating and subsequent oxygen vacancies, the DOS of the ground state and reduced system, and charge localisation after reducing oxygen vacancy formation were investigated through DFT. The anatase phase of TiO_2 is well maintained by the In dopant up to 800 °C. Charge carrier recombination is highly minimised *via* the emergence of In 5*s* states in the TiO_2 band gap.

The formation energies of charge compensating and reducing oxygen vacancies in In-TiO_2 were computed through the DFT model. There is no impact on the band gap due to In-doping in the charge compensated system, however, after localisation of charge in the vicinity of the In-dopant after the formation of a reducing oxygen vacancy, occupied states emerge in the band gap of TiO_2. A model of a nanocluster of composition In_4O_6 at the anatase (101) surface (denoted In_4O_6-a101) was considered to examine the impact of In_2O_3 formation at high calcination temperatures.

4.4.2 Results

4.4.2.1 Selected Experimental Results

X-ray Diffraction (XRD) Characterisation

The phase percentages, determined from XRD analysis, of In-TiO_2 samples calcined at 600, 700, 750, 800 and 850 °C are shown in **Table 4.4.1**. At 500 °C, the diffraction peaks of all samples corresponded to the anatase phase TiO_2. At 600 °C, un-doped TiO_2 is composed of 90% rutile and 10% anatase. The anatase phase is well retained for In-TiO_2

samples up to 700 °C. A mixture of anatase and rutile phases is formed for In-TiO_2 samples at 800 °C and all samples are 100% rutile for calcination at 850 °C and above.

Table 4.4.1 Phase percentages of In-TiO_2 samples calcined at various temperatures. (A = anatase; R = rutile).

	600 °C		700 °C		750 °C		800 °C		850 °C	
Samples	**A**	**R**	**A**	**R**	**A**	**R**	**A**	**R**	**A**	**R**
0 % In-TiO_2	9.3	90.7	-	100	-	100	-	100	-	100
2 % In-TiO_2	100	-	100	-	81.9	18.0	4.9	95.1	-	100
4 % In-TiO_2	100	-	100	-	92.6	7.4	34.3	65.7	-	100
8 % In-TiO_2	100	-	100	-	100	-	52.4	47.6	-	100
16 % In-TiO_2	100	-	100	-	100	-	63.7	36.3	-	100

XRD patterns of pristine TiO_2 and In-TiO_2 calcined at 800 and 900 °C are shown in **Figure 4.4.1** and display additional peaks due to the formation of indium oxide (In_2O_3). The peak intensities for In_2O_3 increase with the In dopant concentration.

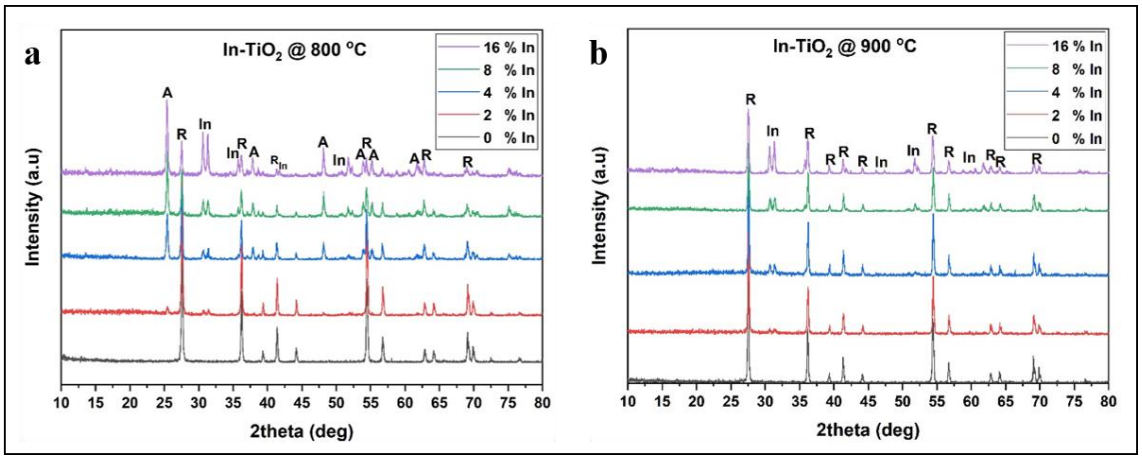

Figure 4.4.1 XRD patterns of In-TiO2 calcined at **(a)** 800 °C and **(b)** 900 °C. (A = anatase; R = rutile; In = In_2O_3).

X-ray Photoelectron Spectroscopy (XPS)

The oxidation states of the elements in In-TiO_2 were examined by XPS and the results are displayed in **Figure 4.4.2** for 16% In-TiO_2. The electron binding energies of Ti $2p_{3/2}$

and Ti $2p_{1/2}$ are observed at 458.78 eV and 464.45 eV, respectively, corresponding to Ti^{4+} (**Figure 4.4.2.a**).[1, 64] There are no peaks observed for Ti^{3+} and Ti^{2+} states. The electronegativity of In^{3+} (1.78) is higher than that of Ti^{4+} (1.54), which may cause electron transfer from Ti^{4+} and O^{2-} to In^{3+},[65] thereby increasing the binding energies of Ti 2*p* and O 1*s*.

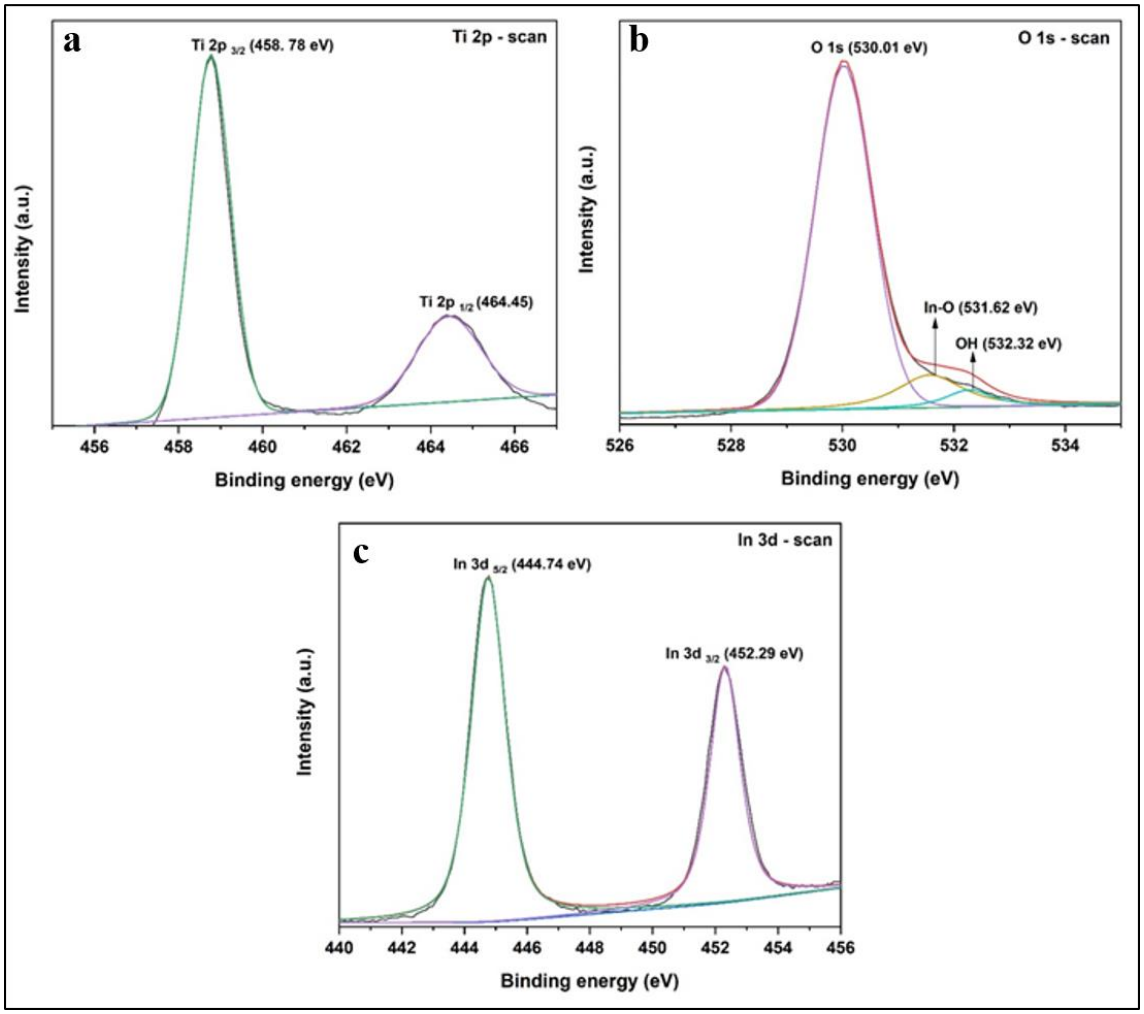

Figure 4.4.2 XPS spectra of 16% In-TiO_2, calcined at 800 °C: **(a)** Ti 2*p*, **(b)** O 1*s*, and **(c)** In 3*d*.

The O 1*s* spectrum of In-TiO_2 is comprised of three peaks, shown in **Figure 4.4.2.b**; the main peak at 530.01 eV is ascribed to lattice oxygen (O^{2-}) in TiO_2. The additional peaks at 531.62 eV and 532.32 eV are attributed to In-O and surface hydroxyl groups, respectively.[65-66] The presence of more surface hydroxyl groups is beneficial to the

photocatalytic activity,[64] through the formation of hydroxyl radicals. **Figure 4.4.2.c** shows peaks for In $3d_{5/2}$ and In $3d_{3/2}$ at 444.74 eV and 452.29 eV, respectively, indicating In^{3+} in In_2O_3.[67]

Photoluminescence (PL)

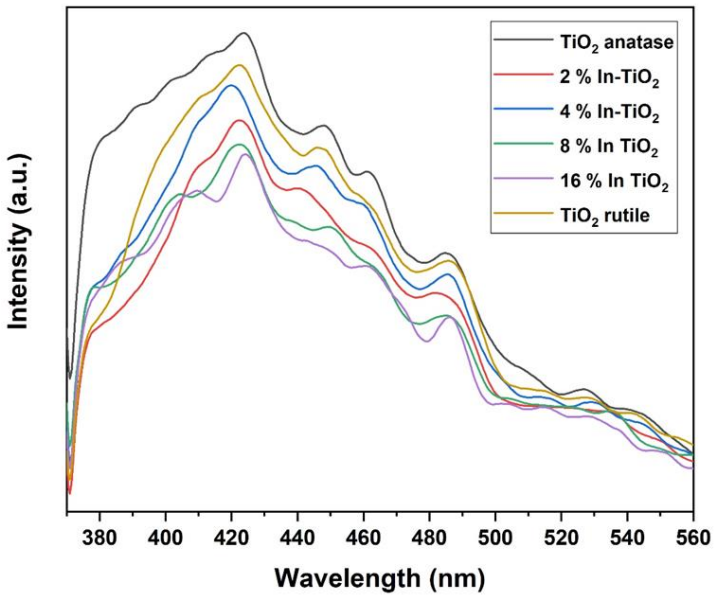

Figure 4.4.3 PL spectra of TiO_2 anatase, TiO_2 rutile and In-TiO_2 samples.

PL spectra of pure TiO_2 anatase, calcined at 500 °C, pure TiO_2 rutile and In-TiO_2, calcined at 800 °C, are shown in **Figure 4.4.3**. Besides CB to VB radiative recombination, PL emission spectra also show recombination of electrons and holes wherein the electron reaches a defect state *via* a non-radiative processes before radiative recombination with a VB hole;[68] the latter signals are mainly attributed to the existence of surface states and defects.[67] The peaks at 461 nm are associated with TiO_2 anatase.[64, 69] The peak at 423 nm is related to the formation of oxygen vacancies in TiO_2 due to In doping. The peaks at 485 nm and 527 nm are ascribed to the transition of electrons (two trapped and one trapped) from the oxygen vacancies to the VB of TiO_2.[68]

For electron-hole recombination, photo-generated electrons can transfer first from the CB to the oxygen vacancies (non-radiative process) and then to the TiO_2 VB (fluorescence emission). **Figure 4.4.3** shows that the intensity of PL peaks decreases with increases in In dopant concentration. This indicates that the transition of electrons from the CB of TiO_2 to the oxygen vacancies is suppressed by the creation of new In-derived energy levels. As we will see in the next section, the formation of In-derived states in the band gap is confirmed by DFT+U calculations, which show In 5*s* states in the TiO_2 energy gap. PL results show that the photo-generated electron-hole recombination in TiO_2 is suppressed by In doping, which may lead to a higher photocatalytic activity.[69-71]

Photocatalytic H_2 Production

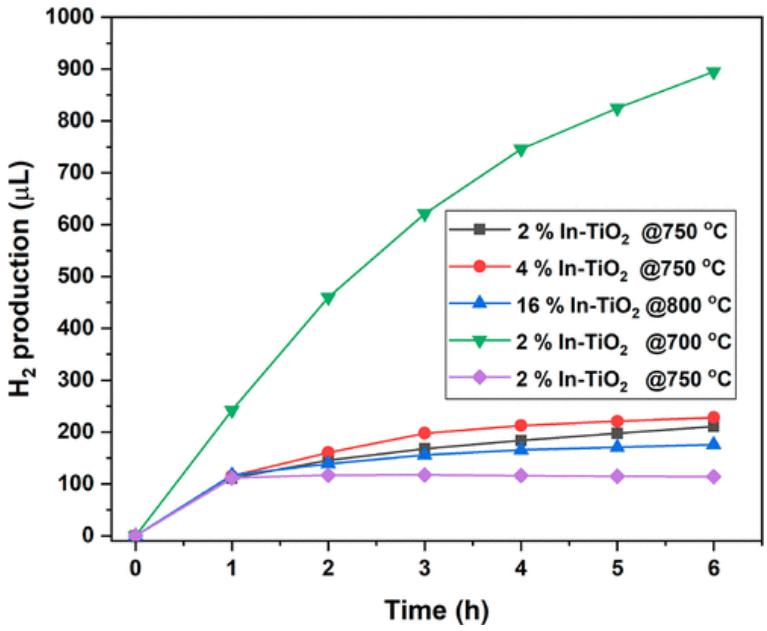

Figure 4.4.4 H_2 production efficiency of In-TiO_2 (0.5 g/L) under simulated solar light irradiation.

The samples were tested for photocatalytic H_2 production efficiency *via* water splitting under simulated solar light irradiation. The H_2 production efficiencies of 2% In-TiO_2

(calcined at 700, 750 and 850 °C), 4% In-TiO_2 (750 °C) and 16 % In-TiO_2 (800 °C) are shown in **Figure 4.4.4.** The H_2 production rates (μL/h) are presented, in order of activity, in **Table 4.4.2**. The photocatalytic activity of 2% In-TiO_2 (700 °C) is comparable with that of pure anatase (0% In-TiO_2 (500 °C)). The efficiency of In-TiO_2 is strongly influenced by the anatase percentage, calcination temperature and In concentration. The water splitting efficiency decreases with increasing In content, which is attributed to poor dispersion, agglomeration, and a decrease of active surface area at high In content.[72-78]

Table 4.4.2 H_2 production rates for In-doped samples with different In concentrations and calcination temperatures. The production rates (μL/h) are listed in order (highest-lowest).

Sample	**H_2 production rate (μL/h)**
0% In-TiO_2 (500 °C; anatase)	145.6
2% In-TiO_2 (700 °C)	105.2
0% In-TiO_2 (800 °C; rutile)	65.4
4% In-TiO_2 (750 °C)	31.5
2% In-TiO_2 (750 °C)	28.2
16% In-TiO_2 (800 °C)	25.6
2% In-TiO_2 (850 °C)	19.2

The colour of nanoparticles changed from white to black during 6 h of light irradiation. This is attributed to the photo-reduction of In(III) to In(I) or In(0), and indicates poisoning of catalyst surface under prolonged light irradiation. Excesses of In dopant may act as electron-hole recombination centres.[72] This could be rectified with the help of a suitable co-catalyst.[79] There are no detailed studies for the water splitting efficiency of In-TiO_2 samples. In a recent study, a similar trend was observed for In-doped barium titanate (In-$BaTiO_3$).[72] The efficiency of In-$BaTiO_3$ was improved with the help of a cadmium selenide co-catalyst. However, the efficiency decreased for In concentrations of more than 2%.

4.4.2.2 Computational Results

4.4.2.2.1 In-doped Anatase TiO_2

Local Atomic Structure

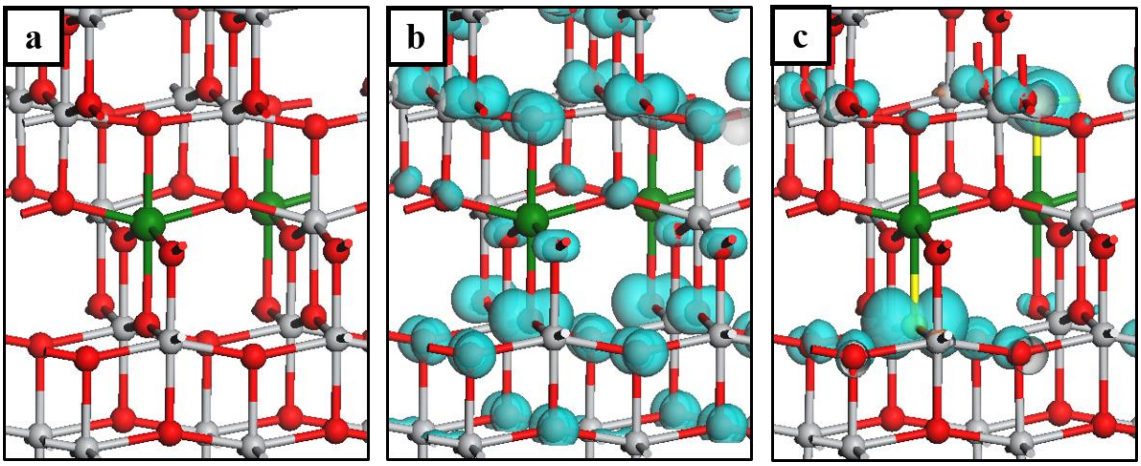

Figure 4.4.5 Panel **(a)** shows the positions of In-dopant in the anatase lattice. Panel **(b)** shows the excess spin density plot for the computational set up with no +U correction on the O 2*p* states. Panel **(c)** shows the excess spin density plot for the computational set up with an additional +U correction on the O 2*p* states and for which the geometry was distorted from symmetry prior to relaxation. Ti is represented by grey spheres, O by red spheres, In by green spheres and the oxygen hole polarons (O^-) are highlighted in yellow. The blue iso-surface encloses spin densities up to 0.02 electrons/$Å^3$.

Figure 4.4.5.a shows the $(2 \times 2 \times 1)$ anatase supercell and the local atomic structure in the vicinity of In dopants. The most favourable dopant configuration is that in which both In ions are incorporated at Ti sites in the same Ti (001) sub-lattice plane, as shown in **Figure 4.4.5**. However, a number of other configurations were very close in energy (within 0.2-6.0 meV per TiO_2 unit). The geometry about the dopant sites is symmetric. In-O distances are 2.22 Å for apical (O_{ap}) and 2.03 Å for equatorial (O_{eq}) oxygen sites. These values compare with values of 2.00 Å and 1.94 Å for equivalent Ti-O distances in un-doped anatase. Replacing two Ti^{4+} with two In^{3+} ions means a deficit of two valence electrons and, in this computational set up, the excess charge is distributed over all O ions in the supercell as shown in **Figure 4.4.5.b**.

Applying +U correction to the O 2*p* states, with U = 5.5 eV, yields a solution in which the excess charge is distributed only over the O ions found at apical positions relative to the In-dopants. Bader charges for these sites decrease from 7.2 to 7.1 electrons and computed spin magnetisations are 0.3 μ_B. After this localisation of charge, each In-O_{ap} distance increases to 2.24 Å. If we now distort the initial structure about the dopant sites to break the symmetry, the geometry relaxes to an asymmetric solution, which is more favourable than the symmetric solution by 0.34 eV (**Figure 4.4.5.c**). In this configuration, the excess charge localises predominantly on a single apical oxygen site neighbouring each In-dopant ($2Ti_{Ti}^{X} + 2O_{O}^{X} \rightarrow 2In_{Ti}' + 2O_{O}^{\bullet}$). The computed Bader charges decrease from 7.2 to 6.8 electrons and the computed spin magnetisations are 0.7 μ_B for these oxygen sites, indicating the formation of oxygen polarons (O^-).[73-74] It is this localisation of charge that produces the asymmetric geometry distortion. In-O^- distances are 2.31 Å, In-O_{ap} distances are 2.19 Å and In-O_{eq} distances are 2.02-2.05 Å.

Oxygen Vacancy Formation

Oxygen vacancy formation is the mechanism by which the charge mismatch that results from substitution of Ti ions with lower valent In-dopants is compensated ($2In_{Ti}' + 2O_{O}^{\bullet} \rightarrow 2In_{Ti}' + O_{O}^{X} + V_{O}^{\bullet\bullet}$).[1] The computed formation energies for a single compensating oxygen vacancy were in the range -0.24 eV to +0.84 eV, depending on the O site considered. The negative oxygen vacancy formation energy confirms that the charge compensated structure is favourable. Formation of the most stable vacancy was more favourable than the next most stable by 0.12 eV and the resulting geometry is shown in the top panels of **Figure 4.4.6**. The most stable oxygen vacancy in the fully relaxed structure has a formation energy of -0.11 eV, which shows that oxygen vacancy formation takes place to charge balance the In dopant.

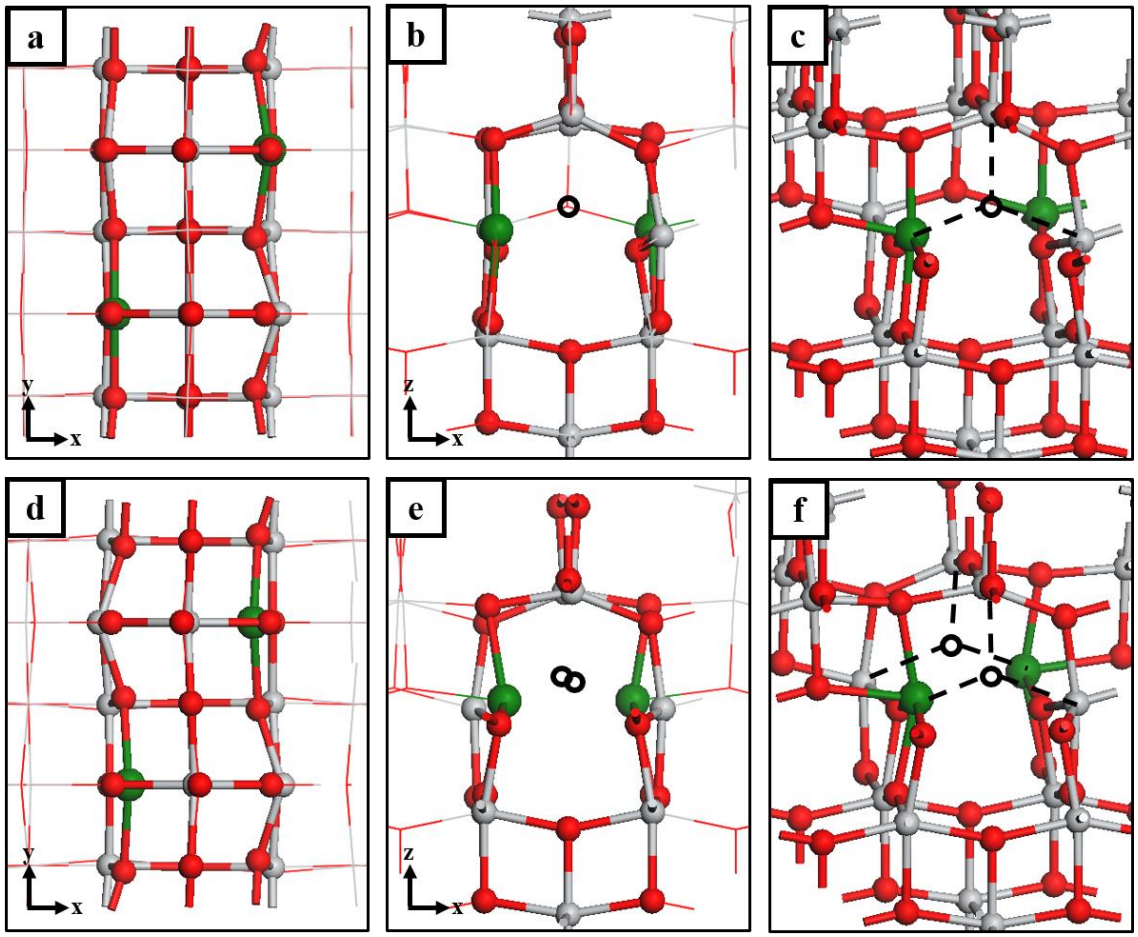

Figure 4.4.6 The top panels display distortions to the lattice of In-doped anatase TiO_2 in response to the charge compensating oxygen vacancy. Bottom panels show the atomic structure after formation of a second, reducing oxygen vacancy. The xy-plane geometry, shown in **(a)** and **(d)**, and the xz-plane geometry, shown in **(b)** and **(e)**, highlight the movement of the In-dopants towards the vacancy sites and the movement of Ti ions away from the vacancies, represented by black circles. Panel **(c)** and **(f)** indicate the cations to which the removed oxygen ions were bound.

The removed O ion was in an equatorial position relative to the In-dopant and, after formation of a vacancy at this site, the neighbouring Ti and In sites are five-fold coordinated. The Ti ions move off their lattice sites by 0.2 Å, away from the vacancy, and the Ti-O distances opposite the vacancy are shortened by 0.10-0.14 Å, relative to the bond lengths prior to vacancy formation. The In-dopant moves 0.2 Å closer to the vacancy and, since there are no oxygen polarons after charge compensation, the In-O_{ap} distances are shortened to 2.09 and 2.15 Å. The remaining In-O_{eq} distances are 2.00-2.08 Å. For the

second In-dopant, away from the vacancy site, the In-O_{ap} distances are 2.14 and 2.19 Å and the In-O_{eq} distances are 2.02-2.12 Å.

Formation of a second, reducing oxygen vacancy, which is implicated in the ART, was considered, and the computed formation energies lie in the range of 3.80-5.84 eV. Energies at the lower end of this range mean that the In-doped system is reducible with moderate energy costs, and given the elevated preparation temperatures, such reducing oxygen vacancies will be expected to form. In the fully relaxed super cell, the most stable reducing oxygen vacancy forms with an energy cost of 4.41 eV. While this cost is larger than that in the fixed supercell, it is still moderate when compared with an energy cost of 5.2 eV to produce a single, reducing oxygen vacancy in the $(2 \times 2 \times 1)$ un-doped anatase supercell, computed with the same input parameters. The most stable site for the formation of a reducing vacancy is an equatorial site of the second In-dopant, as shown in the bottom panels of **Figure 4.4.6**. In this instance, the In-dopants move 0.4 Å off the lattice site and towards the vacancy sites, while the Ti ions move 0.1-0.3 Å outwards from the vacancy sites. The geometry in the vicinity of both In dopants is similar; the In-O_{ap} distances are 2.18 Å, two In-O_{eq} distances are 2.10 Å and the third, opposite the vacancy, is longer, at 2.22 Å.

With two oxygen vacancies in In-doped anatase, there is an excess of two electrons and the computed Bader charges reveal that some of this charge is distributed over the cations to which the removed oxygen ions were bound. For the In-dopants the Bader charges increase from 11.0 to 11.5 electrons and these sites have spin magnetisations of 0.2 μ_B. For the Ti sites, the Bader charges increase from 9.6 to 9.7/9.8 electrons, where the vacancy sits in an equatorial/apical position relative to the Ti ion. Similarly, these Ti sites have computed spin magnetisations of 0.1/0.2 μ_B. These values, in particular those for the spin magnetisation, indicate that the excess electrons are not fully localised. The excess

spin density plots in **Figure 4.4.7** show that the charge is distributed over site of the removed oxygen atom, similar to an F-centre, and with some localisation onto neighbouring Ti and In sites.

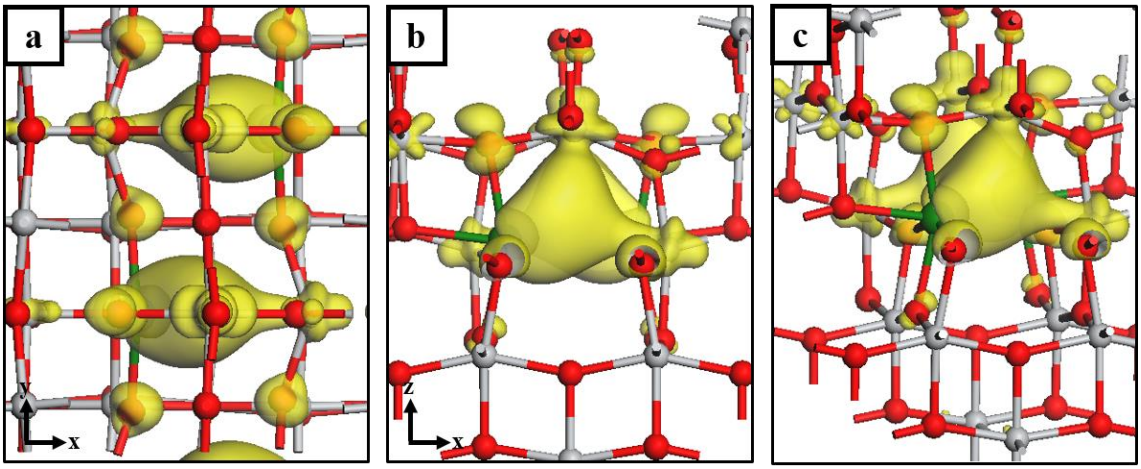

Figure 4.4.7 Excess spin density plots showing the localisation of electrons after formation of a second, reducing oxygen vacancy in In-doped anatase TiO_2. Panels **(a)**, **(b)** and **(c)** display the geometry in the xy-plane, xz-plane and from an angled view. The yellow isosurface encloses spin densities up to 0.02 electrons/$Å^3$.

The energy cost to produce a third oxygen vacancy is in the range of 5.1-5.9 eV, depending on the vacancy site. This can be compared with an energy cost of 5.2 eV to produce a single, reducing oxygen vacancy in the $(2 \times 2 \times 1)$ un-doped anatase supercell, computed with the same input parameters. Thus, In doping can lead to less favourable vacancy formation, although the precise details of the ART mechanism may be more complicated than simple oxygen vacancy formation.

Electronic Properties

The projected electronic density of states (PEDOS) plots are shown in **Figure 4.4.8** for **(a)** un-doped anatase, **(c)** the ground state In-doped system, with a single, compensating oxygen vacancy, and **(d)** the reduced In-doped system, with two oxygen vacancies. For reference, the computed PEDOS for In-doped anatase prior to charge compensation is

shown in **Figure 4.4.4.b**. However, as this does not represent a physical system, due to oxygen vacancies forming spontaneously at 0 K, it is included only for completeness.

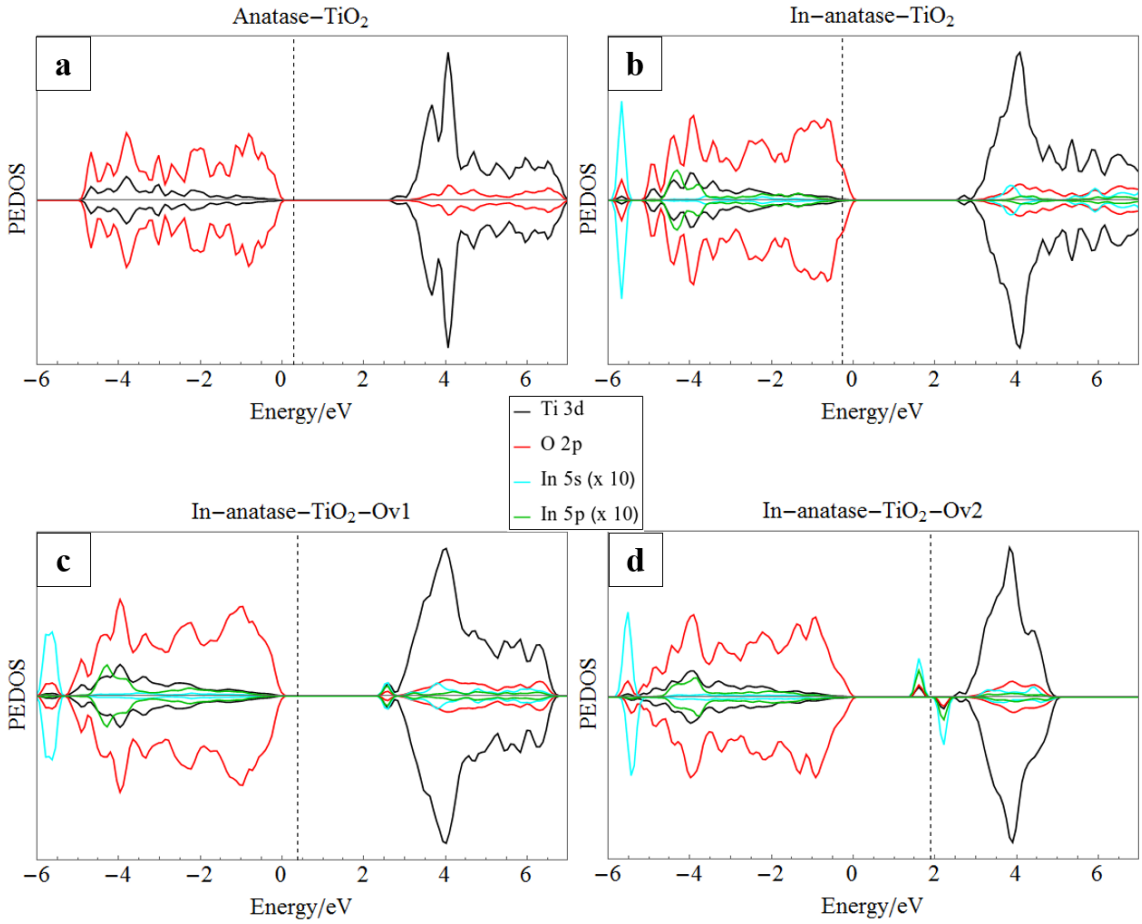

Figure 4.4.8 The projected electronic density of states (PEDOS) computed for **(a)** un-doped anatase and **(b)** In-doped anatase with no oxygen vacancies are included for reference. The PEDOS of the ground state structure, with a single, charge compensating oxygen vacancy and the reduced system with two oxygen vacancies are shown in panels **(c)** and **(d)**.

For the ground state In-doped system, the PEDOS plot in **Figure 4.4.8.c** yields a band gap of 2.44 eV, which compares with a value of 2.70 eV for the un-doped system. For the PEDOS plot in **Figure 4.4.8.d**, the titania-derived band gap is 2.49 eV and states emerge in this gap due to cation reduction in response to formation of a second, reducing oxygen vacancy and are associated with the spin density as shown in **Figure 4.4.7**. The first peak emerges at 1.59 eV above the valence band maximum (VBM) of the TiO_2 host and is

associated with the singly-occupied, 5*s* orbitals of the In-dopants. The next states lie higher in energy, at 2.17 eV above the TiO_2 VBM, and are derived from the empty 5*s* orbitals of the In-dopants.

4.4.2.2.2 In_4O_6-modified Anatase (101)

Atomic Structure and Oxygen Vacancy Formation

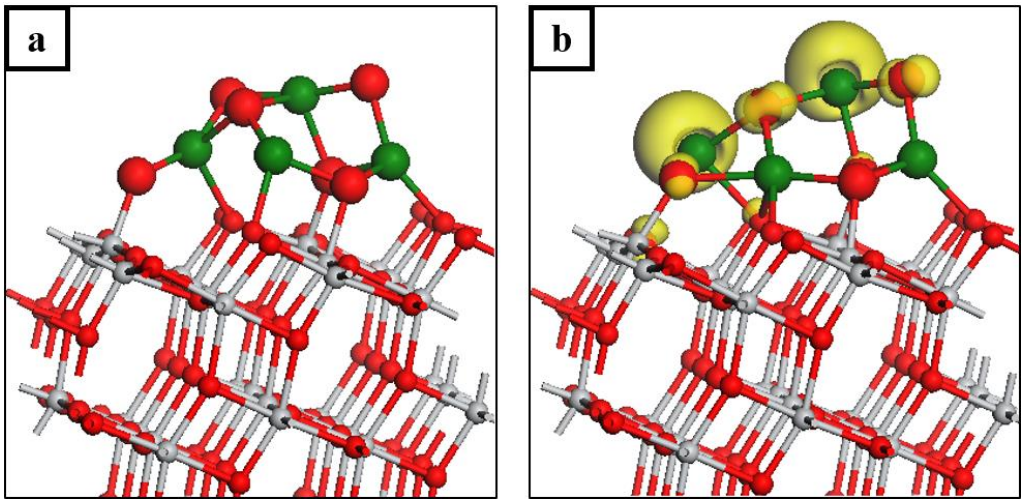

Figure 4.4.9 The relaxed atomic structure of **(a)** stoichiometric In_4O_6-a101 and **(b)** reduced In_4O_5-a101. The yellow iso-surface encloses spin densities up to 0.02 electrons/Å^3.

To examine the influence of In_2O_3 on the properties of In-doped anatase, a model of an In_4O_6 nanocluster modifying the anatase (101) surface (In_4O_6-a101) was implemented. The computed adsorption energy is -3.42 eV, showing that the cluster-surface interaction is favourable. However, at high calcination temperatures, it is possible that the nanoclusters will desorb or migrate and aggregate at the surface to form larger nanoclusters. The latter eventuality would lead to enhanced In_2O_3 signals in the XRD spectrum.

The relaxed structure of stoichiometric In_4O_6-a101 is shown in **Figure 4.4.9.a**. In_4O_6 binds to the surface *via* the formation of three In-O and three Ti-O bonds. Three In ions are four-fold coordinated and the fourth In ion is three-fold coordinated; In-O bond lengths are in the range 1.96-2.19 Å. Three cluster O ions are three-fold coordinated and the remaining three O ions are doubly coordinated. The interfacial Ti-O distances are 1.86-2.08 Å. The computed Bader charges for In ions in the stoichiometric cluster are 11.2-11.3 electrons, to which we ascribe an oxidation state of In^{3+}.

The formation energy for the most stable oxygen vacancy in the supported In_4O_6 nanocluster is computed as 2.19 eV. The relaxed structure of In_4O_5-a101 is shown in **Figure 4.4.9.b**. In this configuration, there are seven interfacial bonds (four In-O and three Ti-O bonds); In-O distances are in the range 2.06-2.36 Å and interfacial Ti-O distances are 1.88-1.96 Å. Two electrons are released after the formation of a neutral oxygen vacancy and these localise at In ions, as shown in the excess spin density plot (**Figure 4.4.9.b**); the Bader charges for these sites increase from 11.2 and 11.3 electrons to 11.8 electrons. Electron localisation is further confirmed by computed spin magnetisations of 0.3 and 0.4 μ_B. Based on these results, and given the moderate oxygen vacancy formation energy, should In_2O_3 form at the anatase surface, In ions will be present in a mixture of oxidation states. In particular, localisation of charge at In ions at the surface may contribute to the photocatalytic activity.

Electronic Properties

The PEDOS of In_4O_6-a101 and In_4O_5-a101 are shown in **Figure 4.4.10.a** and **4.4.10.b**, respectively. For In_4O_6-a101, states derived from cluster O ions extend to 0.2 eV above the VBM of titania. In addition, In-derived states emerge in the bandgap at 0.5 eV below the CBM. For the reduced system (In_4O_5-a101), cluster O 2*p*-derived states persist to 0.4

eV above the VBM and additional In-derived occupied states emerge in the titania bandgap at 1.3 eV above the VBM. For both stoichiometric In_4O_6-a101 and reduced In_4O_5-a101 systems, these features suggest a red-shift in the light absorption edge and could enhance the lifetime of charge carriers on the photocatalyst surface as compared to bare anatase (101).

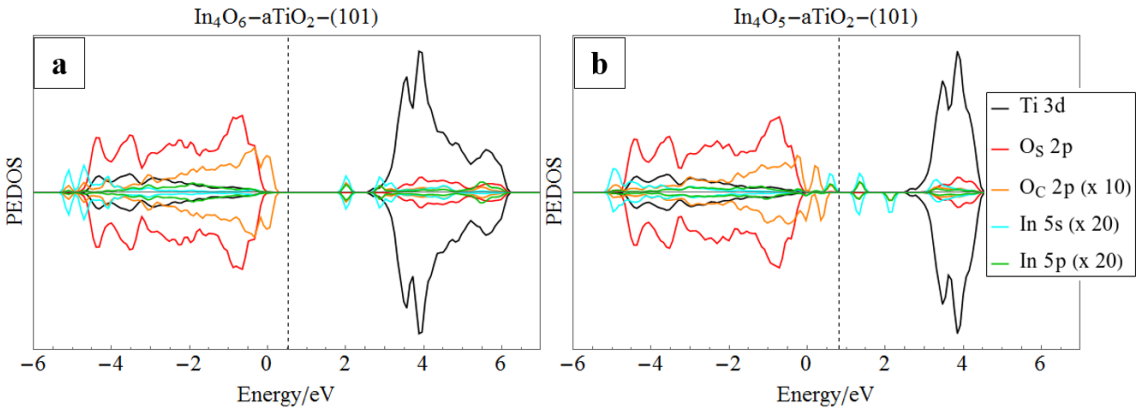

Figure 4.4.10 Projected electronic density of states (PEDOS) computed for **(a)** stoichiometric In_4O_6-a101 and **(b)** reduced In_4O_5-a101.

4.5 Conclusions

Anatase to Rutile Transition

In this chapter, we have examined the impact of Cu-, Mo- and In-doping of anatase TiO_2 on the anatase to rutile phase transition at elevated temperatures. Cu-doped samples retain more of the anatase phase at elevated temperatures, than un-doped TiO_2. At 600 °C, un-doped TiO_2 contained 34.3% anatase, while all doped samples were 100% anatase. At 650 °C, 4% and 8% Cu-TiO_2 had anatase contents of 27.3% and 74.3% respectively. All samples heated to 700 °C were 100% rutile.

Mo doping also strongly influences the ART; 67% of the anatase phase was retained at 750 °C for the 2% Mo-doped sample. Similarly, the results show that In is an effective dopant to preserve the anatase content of TiO_2; up to 64% at a temperature as high as 800 °C (16% In-doping). The impact of doping on the ART varies with dopant concentration. XRD results revealed that In^{3+} retards the crystallisation of TiO_2 through the substitution of Ti^{4+} ions.

Oxygen vacancies

For Cu-TiO_2, DFT results show that charge compensating oxygen vacancies form to balance the lower +2 oxidation state of Cu and computed formation energies for the formation of reducing oxygen vacancies are lower compared to un-doped anatase, although the energy cost increases with vacancy concentration. Thus, the increases in the ART transition temperature are most likely not solely due to oxygen vacancy formation, with sulphate from the copper precursor potentially playing a role. Formation of reducing oxygen vacancies reduces Cu^{2+} to Cu^{1+} and Ti^{4+} to Ti^{3+}, with a localised Cu-derived gap state that can act as a recombination centre and degrade the photocatalytic activity of

anatase. XPS also showed that increases in temperature resulted in copper being reduced from Cu^{2+} to Cu^{1+}.

The computed energy required for oxygen vacancy formation in Mo-TiO_2 is comparable to that of un-doped anatase and, hence, vacancies should be present in the doped system in similar concentrations to pure anatase, under equivalent preparation conditions. After vacancy formation, the dopant is reduced to Mo^{5+} and Ti^{3+} is also present. XPS results show the existence of Mo^{5+} in addition to Mo^{6+} in Mo-TiO_2 samples.

Charge compensating oxygen vacancies form spontaneously in In-doped TiO_2 and the formation of further, reducing oxygen vacancies has moderate energy costs. Considerations of oxygen vacancy formation as the primary mechanism in the ART is therefore insufficient in accounting for the inhibition of the transition reported in the experimental findings.

Electronic Properties

For Cu-TiO_2, the density of states shows localised peaks near the valence and conduction band edges, arising from the empty Cu 3*d* state of Cu^{2+}. These result in a predicted small red shift in the adsorption edge. After formation of reducing oxygen vacancies, additional energy levels emerge in the gap due to localised Cu^{1+} and Ti^{3+} states.

For Mo-TiO_2, analysis of the computed PEDOS plot for the stoichiometric system indicates that Mo 5*s* states emerge below the CBM of TiO_2. Vacancy formation leads to the emergence of occupied Mo 4*d* and Ti 3*d* states in the energy gap. PL analysis showed that electron-hole recombination is minimised *via* the appearance of Mo electronic states below the CB of TiO_2. The lifetime of photo-induced charge carriers is extended by Mo-doping.

The computed DOS plots for In-doped bulk anatase TiO_2 reveal that, upon formation of reducing oxygen vacancies, states emerge in the bandgap due to localisation of charge in the vicinity of the In-dopants. Our model for In_2O_3 formation at the anatase (101) surface indicates that the In_4O_6 nanocluster is bound at the surface with a moderate adsorption energy. We predict that for higher calcination temperatures the In_2O_3 at the surface will desorb or migrate and aggregate at the surface. The latter outcome would explain the enhanced In_2O_3 signals in the XRD spectrum for those samples calcined at higher temperatures. Formation of a reducing oxygen vacancy in the surface-bound In_2O_3 has moderate formation energies, with the resulting excess charge localizing at In sites at the surface. The presence of In_2O_3 at the surface extends the VBM of the titania support to higher energies and, in combination with In-derived states in the bandgap for both stoichiometric and reduced In_2O_3, a red shift in the light absorption edge is predicted. The lifetime of photo-generated charge carriers in TiO_2 was also extended by In doping.

Photocatalytic activity

Photocatalysis studies indicated that inclusion of copper induced a significant reduction in the rate of photodegradation of 1, 4-dioxane. The sample with the highest photocatalytic activity was the 0% Cu-TiO_2 (100% anatase), which showed a 1, 4-dioxane removal of approx. 90% after 450kJL^{-1} (240 minutes). All copper doped samples showed 1, 4-dioxane removal of between 20-40% over the same time and radiation. When we compare these findings to the DFT results, we suggest that the reduction in activity over un-doped TiO_2 most likely arises from the presence of the Cu^{1+}/Cu^{2+}-induced defect states, which act as bulk traps for charges and thus promote recombination.

The photocatalytic activity of Mo-TiO_2 was tested for the removal of microbes from wastewater. The findings suggest that Mo-TiO_2 is an excellent candidate for the

fabrication of indoor building materials with light active antimicrobial characteristics. The photocatalytic activity of 2% In-TiO_2, calcined at 700 °C, is comparable to that of pure anatase, but the activity decreases with increasing In-content. For low levels of In-doping, the activity could be further improved with the help of an appropriate co-catalyst. The photocatalytic activity is strongly affected by the calcination temperature and anatase percentage. Overall, the results demonstrate that In is an effective dopant for the fabrication of thermally stable anatase TiO_2 with photocatalytic activity.

.

4.6 Chapter References

1. Byrne, C.; Moran, L.; Hermosilla, D.; Merayo, N.; Blanco, Á.; Rhatigan, S.; Hinder, S.; Ganguly, P.; Nolan, M.; Pillai, S. C., Effect of Cu Doping on the Anatase-to-Rutile Phase Transition in TiO_2 Photocatalysts: Theory and Experiments. *Applied Catalysis B: Environmental* **2019**.
2. Kumaravel, V.; Rhatigan, S.; Mathew, S.; Michel, M. C.; Bartlett, J.; Nolan, M.; Hinder, S. J.; Gascó, A.; Ruiz-Palomar, C.; Hermosilla, D.; Pillai, S. C., Mo doped TiO_2: impact on oxygen vacancies, anatase phase stability and photocatalytic activity. *Journal of Physics: Materials* **2020,** *3* (2), 025008.
3. Kumaravel, V.; Rhatigan, S.; Mathew, S.; Bartlett, J.; Nolan, M.; Hinder, S. J.; Sharma, P. K.; Singh, A.; Byrne, J. A.; Harrison, J., Indium Doped TiO_2 Photocatalysts with High Temperature Anatase Stability. *The Journal of Physical Chemistry C* **2019**.
4. Yoong, L.; Chong, F. K.; Dutta, B. K., Development of copper-doped TiO_2 photocatalyst for hydrogen production under visible light. *Energy* **2009,** *34* (10), 1652-1661.
5. Theivasanthi, T.; Alagar, M., X-ray diffraction studies of copper nanopowder. *arXiv preprint arXiv:1003.6068* **2010**.
6. Etacheri, V.; Seery, M. K.; Hinder, S. J.; Pillai, S. C., Highly Visible Light Active $TiO_{2-x}N_x$ Heterojunction Photocatalysts†. *Chemistry of Materials* **2010,** *22* (13), 3843-3853.
7. Etacheri, V.; Seery, M. K.; Hinder, S. J.; Pillai, S. C., Oxygen Rich Titania: A Dopant Free, High Temperature Stable, and Visible-Light Active Anatase Photocatalyst. *Advanced Functional Materials* **2011,** *21* (19), 3744-3752.
8. Etacheri, V.; Michlits, G.; Seery, M. K.; Hinder, S. J.; Pillai, S. C., A Highly Efficient $TiO_{2-x}C_x$ Nano-heterojunction Photocatalyst for Visible Light Induced Antibacterial Applications. *ACS applied materials & interfaces* **2013,** *5* (5), 1663-1672.
9. Siriwardane, R. V.; Poston Jr, J. A.; Fisher, E. P.; Shen, M.-S.; Miltz, A. L., Decomposition of the sulfates of copper, iron (II), iron (III), nickel, and zinc: XPS, SEM, DRIFTS, XRD, and TGA study. *Applied Surface Science* **1999,** *152* (3), 219-236.
10. Berger, H.; Tang, H.; Lévy, F., Growth and Raman spectroscopic characterisation of TiO_2 anatase single crystals. *Journal of crystal growth* **1993,** *130* (1), 108-112.
11. Dvoranová, D.; Brezová, V.; Mazúr, M.; Malati, M. A., Investigations of metal-doped titanium dioxide photocatalysts. *Applied Catalysis B, Environmental* **2002,** *37* (2), 91-105.
12. Yang, J.; Bai, H.; Tan, X.; Lian, J., IR and XPS investigation of visible-light photocatalysis—Nitrogen–carbon-doped TiO_2 film. *Applied Surface Science* **2006,** *253* (4), 1988-1994.
13. Byrne, C.; Fagan, R.; Hinder, S.; McCormack, D. E.; Pillai, S. C., New approach of modifying the anatase to rutile transition temperature in TiO_2 photocatalysts. *RSC Advances* **2016,** *6* (97), 95232-95238.
14. Gao, H.; Wang, G.; Luan, Y.; Chaikittikul, K.; Zhang, X.; Yang, M.; Dong, W.; Shi, Z., A fast synthesis of hierarchical yolk–shell copper hydroxysulfates at room temperature with adjustable sizes. *CrystEngComm* **2014,** *16* (12), 2520-2526.
15. Periyat, P.; Pillai, S. C.; McCormack, D. E.; Colreavy, J.; Hinder, S. J., Improved high-temperature stability and sun-light-driven photocatalytic activity of sulfur-doped anatase TiO_2. *The Journal of Physical Chemistry C* **2008,** *112* (20), 7644-7652.

16. Zhou, S.; Potzger, K.; Talut, G.; von Borany, J.; Skorupa, W.; Helm, M.; Fassbender, J., Using x-ray diffraction to identify precipitates in transition metal doped semiconductors. *Journal of Applied Physics* **2008,** *103* (7), 07D530.
17. Strohmeier, B. R.; Levden, D. E.; Field, R. S.; Hercules, D. M., Surface spectroscopic characterisation of CuAl2O3 catalysts. *Journal of Catalysis* **1985,** *94* (2), 514-530.
18. Schön, G., ESCA studies of Cu, Cu_2O and CuO. *Surface Science* **1973,** *35*, 96-108.
19. Liu, Y.; Bailey, P.; Noakes, T. C.; Thompson, G. E.; Skeldon, P.; Alexander, M. R., Chemical environment of copper at the surface of a $CuAl_2$ model alloy: XPS, MEIS and TEM analyses. *Surface and interface analysis* **2004,** *36* (4), 339-346.
20. McIntyre, N.; Sunder, S.; Shoesmith, D.; Stanchell, F., Chemical information from XPS—applications to the analysis of electrode surfaces. *Journal of Vacuum Science and Technology* **1981,** *18* (3), 714-721.
21. Kelemen, S.; George, G.; Gorbaty, M., Direct determination and quantification of sulphur forms in heavy petroleum and coals: 1. The X-ray photoelectron spectroscopy (XPS) approach. *Fuel* **1990,** *69* (8), 939-944.
22. López, R.; Gómez, R.; Llanos, M. E., Photophysical and photocatalytic properties of nanosized copper-doped titania sol–gel catalysts. *Catalysis Today* **2009,** *148* (1), 103-108.
23. Wong, R. S.; Feng, J.; Hu, X.; Yue, P. L., Discoloration and mineralisation of non-biodegradable azo dye orange II by copper-doped TiO_2 nanocatalysts. *Journal of Environmental Science and Health, Part A* **2004,** *39* (10), 2583-2595.
24. Colón, G.; Maicu, M.; Hidalgo, M. C.; Navío, J. A., Cu-doped TiO_2 systems with improved photocatalytic activity. *Applied Catalysis B: Environmental* **2006,** *67* (1–2), 41-51.
25. Duhalde, S.; Vignolo, M. F.; Golmar, F.; Chiliotte, C.; Torres, C. E. R.; Errico, L. A.; Cabrera, A. F.; Rentería, M.; Sánchez, F. H.; Weissmann, M., Appearance of room-temperature ferromagnetism in Cu-doped $TiO_{2-\delta}$ films. *Phys. Rev. B.* **2005,** *72* (16), 161313.
26. Iwaszuk, A.; Nolan, M., Charge compensation in trivalent cation doped bulk rutile TiO_2. *J. Phys.: Condens. Matter* **2011,** *23* (33), 334207.
27. Nolan, M.; Watson, G. W., The electronic structure of alkali doped alkaline earth metal oxides: Li doping of MgO studied with DFT-GGA and GGA+U. *Surface science* **2005,** *586* (1), 25-37.
28. Du, M.-H.; Zhang, S. B., Impurity-bound small polarons in ZnO: Hybrid density functional calculations. *Physical Review B* **2009,** *80* (11), 115217.
29. Nolan, M.; Watson, G. W., Hole localisation in Al doped silica: a DFT+U description. *The Journal of chemical physics* **2006,** *125* (14), 144701.
30. Scanlon, D. O.; Walsh, A.; Morgan, B. J.; Nolan, M.; Fearon, J.; Watson, G. W., Surface sensitivity in lithium-doping of MgO: a density functional theory study with correction for on-site Coulomb interactions. *The Journal of Physical Chemistry C* **2007,** *111* (22), 7971-7979.
31. Schirmer, O. F., O − bound small polarons in oxide materials. *J. Phys.: Condens. Matter* **2006,** *18* (43), R667.
32. Stoneham, A. M.; Gavartin, J.; Shluger, A. L.; Kimmel, A. V.; Ramo, D. M.; Rønnow, H. M.; Aeppli, G.; Renner, C., Trapping, self-trapping and the polaron family. *J. Phys.: Condens. Matter* **2007,** *19* (25), 255208.

33. Maimaiti, Y.; Nolan, M.; Elliott, S. D., Reduction mechanisms of the CuO(111) surface through surface oxygen vacancy formation and hydrogen adsorption. *Physical Chemistry Chemical Physics* **2014,** *16* (7), 3036-3046.
34. Zhang, H.; Yu, X.; McLeod, J. A.; Sun, X., First-principles study of Cu-doping and oxygen vacancy effects on TiO_2 for water splitting. *Chemical Physics Letters* **2014,** *612*, 106-110.
35. Yoganarasimhan, S. R.; Rao, C. N. R., Mechanism of crystal structure transformations. Part 3.—Factors affecting the anatase-rutile transformation. *Trans. Faraday Society* **1962,** *58* (0), 1579-1589.
36. Miljević, B.; van der Bergh, J.; Vučetić, S.; Lazar, D.; Ranogajec, J., Molybdenum doped TiO_2 nanocomposite coatings: Visible light driven photocatalytic self-cleaning of mineral substrates. *Ceramics International* **2017,** *43* (11), 8214-8221.
37. Zhang, T.; Yu, B.; Wang, D.; Zhou, F., Molybdenum-doped and anatase/rutile mixed-phase TiO_2 nanotube photoelectrode for high photoelectrochemical performance. *Journal of Power Sources* **2015,** *281*, 411-416.
38. Erdogan, N.; Park, J.; Ozturk, A., Synthesis and enhanced photocatalytic activity of molybdenum, iron, and nitrogen triple-doped titania nanopowders. *Ceramics International* **2016,** *42* (15), 16766-16774.
39. Khan, M.; Xu, J.; Cao, W.; Liu, Z.-K., Mo-Doped TiO_2 with Enhanced Visible Light Photocatalytic Activity: A Combined Experimental and Theoretical Study. *Journal of Nanoscience and Nanotechnology* **2014,** *14* (9), 6865-6871.
40. Zhou, J.; Feng, B.; Lu, X.; Duan, K., Novel one-step fabrication of highly ordered Mo-doped TiO_2 nanotubes arrays with enhanced visible light catalytic activity. *Journal of Materials Science: Materials in Electronics* **2018,** *29* (21), 18388-18396.
41. Kemp, T. J.; McIntyre, R. A., Transition metal-doped titanium (IV) dioxide: Characterisation and influence on photodegradation of poly (vinyl chloride). *Polymer Degradation and Stability* **2006,** *91* (1), 165-194.
42. Fisher, L.; Ostovapour, S.; Kelly, P.; Whitehead, K.; Cooke, K.; Storgårds, E.; Verran, J., Molybdenum doped titanium dioxide photocatalytic coatings for use as hygienic surfaces: the effect of soiling on antimicrobial activity. *Biofouling* **2014,** *30* (8), 911-919.
43. Yoon, Y.; Lee, S.; Gwon, J.; Cho, H.; Wu, Q.; Kim, Y.; Lee, W., Photocatalytic performance of highly transparent and mesoporous molybdenum-doped titania films fabricated by templating cellulose nanocrystals. *Ceramics International* **2018,** *44* (14), 16647-16653.
44. Khan, H.; Berk, D., Characterisation and mechanistic study of Mo^{+6} and V^{+5} codoped TiO_2 as a photocatalyst. *Journal of Photochemistry and Photobiology A: Chemistry* **2014,** *294*, 96-109.
45. Thi, T. V.; Rai, A. K.; Gim, J.; Kim, S.; Kim, J., Effect of Mo^{6+} doping on electrochemical performance of anatase TiO_2 as a high performance anode material for secondary lithium-ion batteries. *Journal of Alloys and Compounds* **2014,** *598*, 16-22.
46. Avilés-García, O.; Espino-Valencia, J.; Romero, R.; Rico-Cerda, J. L.; Arroyo-Albiter, M.; Natividad, R., W and Mo doped TiO_2: Synthesis, characterisation and photocatalytic activity. *Fuel* **2017,** *198*, 31-41.
47. Dorraj, M.; Goh, B. T.; Sairi, N. A.; Woi, P. M.; Basirun, W. J., Improved visible-light photocatalytic activity of TiO_2 co-doped with copper and iodine. *Applied Surface Science* **2018,** *439*, 999-1009.
48. Gomathi Devi, L.; Narasimha Murthy, B., Characterisation of Mo Doped TiO_2 and its Enhanced Photo Catalytic Activity Under Visible Light. *Catalysis Letters* **2008,** *125* (3), 320-330.

49. Wang, S.; Bai, L. N.; Sun, H. M.; Jiang, Q.; Lian, J. S., Structure and photocatalytic property of Mo-doped TiO_2 nanoparticles. *Powder Technology* **2013,** *244*, 9-15.
50. Choudhury, B.; Choudhury, A., Oxygen vacancy and dopant concentration dependent magnetic properties of Mn doped TiO_2 nanoparticle. *Current Applied Physics* **2013,** *13* (6), 1025-1031.
51. Yan, Y.; Zhou, X.; Lan, J.; Li, Z.; Zheng, T.; Cao, W.; Zhu, N.; Liu, W., Efficient photocatalytic disinfection of Escherichia coli by N-doped TiO_2 coated on coal fly ash cenospheres. *Journal of Photochemistry and Photobiology A: Chemistry* **2018,** *367*, 355-364.
52. Mecha, A.; Onyango, M.; Ochieng, A.; Momba, M., UV and solar photocatalytic disinfection of municipal wastewater: Inactivation, reactivation and regrowth of bacterial pathogens. *International Journal of Environmental Science and Technology* **2019,** *16* (7), 3687-3696.
53. Venieri, D.; Fraggedaki, A.; Kostadima, M.; Chatzisymeon, E.; Binas, V.; Zachopoulos, A.; Kiriakidis, G.; Mantzavinos, D., Solar light and metal-doped TiO_2 to eliminate water-transmitted bacterial pathogens: Photocatalyst characterisation and disinfection performance. *Applied Catalysis B: Environmental* **2014,** *154*, 93-101.
54. You, J.; Guo, Y.; Guo, R.; Liu, X., A review of visible light-active photocatalysts for water disinfection: Features and prospects. *Chemical Engineering Journal* **2019**.
55. Rao, K. V. K.; Naidu, S. V. N.; Iyengar, L., Thermal Expansion of Rutile and Anatase. *Journal of the American Ceramic Society* **1970,** *53* (3), 124-126.
56. Pillai, S. C.; Periyat, P.; George, R.; McCormack, D. E.; Seery, M. K.; Hayden, H.; Colreavy, J.; Corr, D.; Hinder, S. J., Synthesis of high-temperature stable anatase TiO_2 photocatalyst. *The Journal of Physical Chemistry C* **2007,** *111* (4), 1605-1611.
57. Fagan, R.; McCormack, D. E.; Hinder, S.; Pillai, S. C., Improved high temperature stability of anatase TiO_2 photocatalysts by N, F, P co-doping. *Materials & Design* **2016,** *96*, 44-53.
58. Byrne, C.; Rhatigan, S.; Hermosilla, D.; Merayo, N.; Blanco, Á.; Michel, M. C.; Hinder, S.; Nolan, M.; Pillai, S., Modification of TiO_2 with *h*BN: High temperature anatase phase stabilisation and photocatalytic degradation of 1,4-dioxane. *Journal of Physics: Materials* **2019**.
59. Yu, X.; Hou, T.; Sun, X.; Li, Y., The Influence of Defects on Mo-Doped TiO_2 by First-Principles Studies. *ChemPhysChem* **2012,** *13* (6), 1514-1521.
60. Reddy, B. M.; Sreekanth, P. M.; Reddy, E. P.; Yamada, Y.; Xu, Q.; Sakurai, H.; Kobayashi, T. J. T. J. o. P. C. B., Surface Characterization of La_2O_3–TiO_2 and V_2O_5/La_2O_3–TiO_2 Catalysts. **2002,** *106* (22), 5695-5700.
61. Tahir, M.; Amin, N. S. J. A. C. A. G., Photocatalytic CO_2 reduction and kinetic study over In/TiO_2 nanoparticles supported microchannel monolith photoreactor. **2013,** *467*, 483-496.
62. Yu, Y.; Wang, E.; Yuan, J.; Cao, Y. J. A. S. S., Enhanced photocatalytic activity of titania with unique surface indium and boron species. **2013,** *273*, 638-644.
63. Zhang, Y.; Xu, H.; Xu, Y.; Zhang, H.; Wang, Y. J. J. o. P.; Chemistry, P. A., The effect of lanthanide on the degradation of RB in nanocrystalline Ln/TiO_2 aqueous solution. **2005,** *170* (3), 279-285.
64. Tahir, M.; Amin, N. S. J. A. C. B. E., Indium-doped TiO_2 nanoparticles for photocatalytic CO_2 reduction with H_2O vapors to CH_4. **2015,** *162*, 98-109.
65. Zhang, W.; Pei, X.; Chen, J.; He, H. J. M. S. i. S. P., Effects of Al doping on properties of xAl–3% In–TiO_2 photocatalyst prepared by a sol–gel method. **2015,** *38*, 24-30.

66. Tahir, B.; Tahir, M.; Amin, N. S. J. A. S. S., Gold–indium modified TiO_2 nanocatalysts for photocatalytic CO_2 reduction with H_2 as reductant in a monolith photoreactor. **2015,** *338*, 1-14.
67. Sasikala, R.; Shirole, A.; Sudarsan, V.; Sudakar, C.; Naik, R.; Rao, R.; Bharadwaj, S. J. A. C. A. G., Enhanced photocatalytic activity of indium and nitrogen co-doped TiO_2–Pd nanocomposites for hydrogen generation. **2010,** *377* (1-2), 47-54.
68. Wang, E.; Yang, W.; Cao, Y., Unique Surface Chemical Species on Indium Doped TiO_2 and Their Effect on the Visible Light Photocatalytic Activity. *J. Phys. Chem. C* **2009,** *113* (49), 20912-20917.
69. Wang, E.; Yang, W.; Cao, Y. J. T. J. o. P. C. C., Unique surface chemical species on indium doped TiO_2 and their effect on the visible light photocatalytic activity. **2009,** *113* (49), 20912-20917.
70. Beula, R. J.; Devadason, S.; Vidhya, B. J. A. N., Incorporation of indium in TiO_2-based photoanodes for enhancing the photovoltaic conversion efficiency of dye-sensitized solar cells. **2018**, 1-9.
71. de Castro, S.; da Silva, A. F.; Felix, J. F.; Piton, M. R.; Galeti, H. V. A.; Rodrigues, A. D. G.; Gobato, Y. G.; Al Saqri, N.; Henini, M.; Albadri, A. M. J. J. o. A.; Compounds, Effect of growth techniques on the structural, optical and electrical properties of indium doped TiO_2 thin films. **2018,** *766*, 194-203.
72. Zhong, D.; Liu, W.; Tan, P.; Zhu, A.; Qiao, L.; Bian, Y.; Pan, J., Efficient hydrogen generation of indium doped $BaTiO_3$ decorated with CdSe quantum dots: Novel understanding of the effect of doping strategy. *International Journal of Hydrogen Energy* **2019,** *44* (3), 1627-1639.
73. Mathew, S.; Ganguly, P.; Rhatigan, S.; Kumaravel, V.; Byrne, C.; Hinder, S.; Bartlett, J.; Nolan, M.; Pillai, S., Cu-Doped TiO_2: Visible Light Assisted Photocatalytic Antimicrobial Activity. *Applied Sciences* **2018,** *8* (11), 2067.
74. Iwaszuk, A.; Nolan, M., Charge compensation in trivalent cation doped bulk rutile TiO_2. *J. Phys.: Condens. Matter* **2011,** *23* (33), 334207.

5 Surface-modified TiO_2

5.1 Introduction

This chapter presents the results of four computational studies of surface-modified titania. The modifiers are MgO and SnO;[1] *h*BN;[2] CeO_2;[3] and MnO_x.[4] In each study, we analyse the stability of the composite surfaces; their interfacial atomic structure; the impact of modification on the valence and conduction band edges of the titania supports; and charge localisation after excitation.

For the metal oxide modifiers, further analysis includes an assessment of the ground state stoichiometry and reduction *via* oxygen vacancy formation. Point defects, such as oxygen vacancies, are active sites at metal oxide surfaces. A more reducible surface will lose oxygen more readily and be more active in solar thermal[5] or Mars van Krevelen processes.[6-7] The importance of oxygen vacancies as active sites for water dissociation at the rutile (110) surface[8-9] and ceria surfaces[10] has been widely discussed and reduced Ti^{3+} ions are active in the chemistry at titania surfaces.[11-12] For anatase TiO_2, oxygen vacancies are more stable at subsurface sites than on the surface.[13-14] However, the surface can be reduced by electron bombardment[14-15] and the reaction of these vacancy sites with water and O_2 results in water dissociation. These studies highlight the necessity of engineering photocatalytic surfaces for which vacancies can be produced with moderate energy costs.

Water adsorption at CeO_2-TiO_2 and MnO_x-TiO_2 will be discussed in **Chapter 6**. Computational methodology and Supporting Information for each study in this chapter are provided in **Chapter 2** and **Appendix B**.

5.2 *MgO- and SnO-modified TiO_2*

What follows is adapted from an article entitled: "***Impact of surface hydroxylation in MgO-/SnO-nanocluster modified TiO_2 anatase (101) composites on visible light absorption, charge separation and reducibility*",** published, by invitation, in Chinese Chemical Letters.[1]


Chinese Chemical Letters 29 (2018) 757–764

Contents lists available at ScienceDirect

Chinese Chemical Letters

journal homepage: www.elsevier.com/locate/cclet

Communication

Impact of surface hydroxylation in MgO-/SnO-nanocluster modified TiO_2 anatase (101) composites on visible light absorption, charge separation and reducibility

Stephen Rhatigan, Michael Nolan*

Tyndall National Institute, University College Cork, Lee Maltings, Cork T12 R5CP, Ireland

DOI: https://doi.org/10.1016/j.cclet.2017.11.036

5.2.1 Introduction

In this paper, we present a DFT study of TiO_2 anatase (101) modified with sub-nm nanoclusters of compositions Sn_4O_4 and Mg_4O_4. Importantly, we go beyond the perfect, clean surface models of TiO_2 and investigate the impact of surface hydroxylation, through adsorption of dissociated water, on the nanocluster adsorption and stability. This builds on previous work,[16-17] which showed that surface hydroxylation has a significant impact on the properties of the nanocluster-TiO_2 composite system.

We predict that modification of anatase (101) will induce a red shift in light absorption due to the emergence of nanocluster derived electronic states that shift the valence band

to higher energy, irrespective of the state of the anatase surface. Surface modification promotes charge separation, with electrons and holes localising on surface cation and nanocluster anion sites, respectively. Finally, we show that the reducibility of the composite systems is enhanced over bare anatase (101) and we predict that the composite surfaces will be more reactive. Combined with a red shift in light absorption, these results yield an insight into the design of new photocatalytic materials.

5.2.2 Results

Local Atomic Structure

To examine the impact of surface hydroxyl species on the interfacial chemistry, calculations were performed on a model where four water molecules are adsorbed dissociatively at the anatase (101) surface. This corresponds to a partial water coverage of 50%. Note that we are not trying to determine the most favourable water adsorption coverage and structure on anatase (101), but instead use this model to examine the effect of the presence of surface hydroxyl groups on the nanocluster-TiO_2 composite system.

The bare and hydroxylated anatase (101) surfaces are henceforth denoted as **oxidised (o-anatase)** and **hydroxylated (oh-anatase)**. **Figure 5.2.1.a** shows the atomic structure of the ideal, extended anatase (101) surface, free from point defects and surface hydroxyls. The surface is terminated by alternating rows of two- (O_{2f}) and three-fold (O_{3f}) coordinated oxygen atoms. Of the two sublayers of Ti atoms, the outermost consists of rows of five-fold coordinated Ti_{5f} atoms and the next sublayer has rows of six-fold coordinated Ti_{6f} atoms. With 16 Ti atoms accessible on our (2×4) surface supercell, the eight outermost Ti_{5f} atoms act as sites for water adsorption. In our model hydroxylated surface, we adsorb four dissociated water molecules, as shown in **Figure 5.2.1.b**, at 50%

coverage. This is not aiming for the most stable water adsorption structure at the anatase (101) surface, but is a reasonable model to explore the influence of surface hydroxylation.

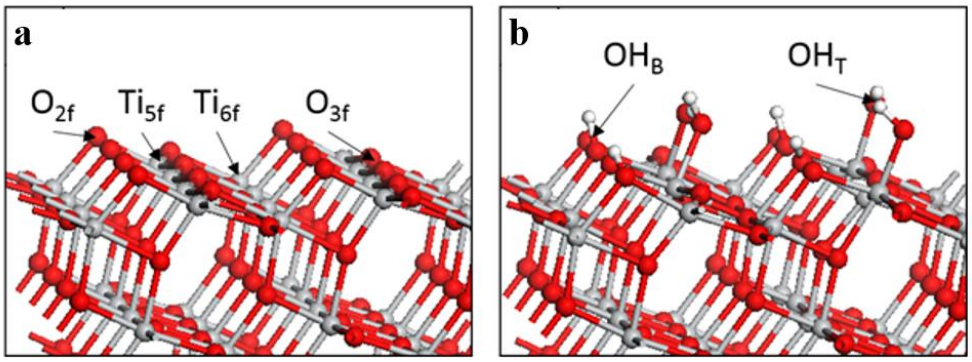

Figure 5.2.1 Atomic structure of **(a)** the bare and **(b)** hydroxylated anatase (101) surface. In this and subsequent figures, Ti is indicated by a grey sphere, O by a red sphere and H by a white sphere.

We adopt the following notation for the different atoms present in the composites: surface oxygen atoms are denoted O_S and further differentiated by coordination number (O_{2f} and O_{3f}), as are surface Ti atoms (Ti_{5f} and Ti_{6f}). Cluster oxygen atoms are denoted O_C and oxygen atoms present in hydroxyls are labelled O_W.

The relaxed atomic structures of the MgO- and SnO-modified surfaces are presented in **Figures 5.2.2** and **5.2.3**. The adsorption energies of the nanoclusters at the o-anatase and oh-anatase (101) surfaces are -5.73 eV and -7.49 eV for Mg_4O_4 and -1.89 eV and -2.16 eV for Sn_4O_4. The negative values indicate a favourable nanocluster-surface interaction while the magnitudes suggest that the nanoclusters will be stable against desorption and surface migration, particularly for MgO modification. The most stable gas phase geometries for the Mg_4O_4 and Sn_4O_4 nanoclusters are cubes and adsorption on the anatase (101) surface changes these structures substantially. This allows for the formation of more metal-oxygen interfacial bonds, which strengthens the interaction between the cluster and the surface.

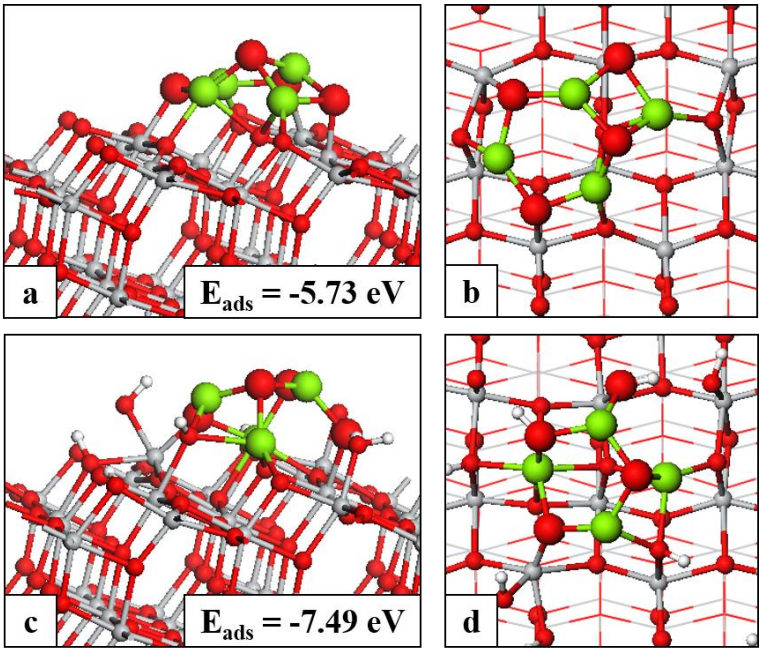

Figure 5.2.2 Atomic structures of **(a)** and **(b)** Mg_4O_4-o-anatase, **(c)** and **(d)** Mg_4O_4-oh-anatase (101). Insets of panels on the left show adsorption energies. Atoms of the clusters are enlarged for clarity. Ti is light grey, O is red, H is white and Mg is green.

For Mg_4O_4, the interaction between the nanocluster and both surfaces is strong with more favourable adsorption at the hydroxylated surface. The atomic structure of Mg_4O_4 adsorbed at the o-anatase (101) surface is shown in **Figures 5.2.2.a** and **5.2.2.b**. Three of the four cluster oxygen atoms form a bond with surface Ti_{5f} atoms. Two Mg atoms in the cluster make two bonds with surface O_{2f} and O_{3f} ions and are four-fold coordinated. The other Mg atoms are three-fold coordinated with one sharing a bond with a single surface O_{2f} and the other bonded only to O_C atoms. Adsorption involves the formation of eight bonds between the nanocluster and the bare surface; of these, three are Ti-O_C bonds with lengths in the range of 1.9-2.1 Å. These Ti atoms migrate out from the Ti_{5f} plane by up to 0.4 Å. Four of the five interfacial Mg-O_S bonds have distances in the range of 2.1-2.2 Å; the fifth Mg-O_S distance, which involves a three-fold coordinated Mg cation, is 1.9 Å. The single O_{3f} site involved migrates out from the surface layer by 0.3 Å; this distortion breaks the bond between the O_{3f} site and the Ti_{6f} sub-surface atom.

Comparing with adsorption at the oh-anatase (101) surface (**Figure 5.2.2.c** and **5.2.2.d**), we see that only two of the O_C atoms form bonds with surface Ti_{5f} atoms, with Ti-O distances of 1.9 and 2.0 Å. This is to be expected as the presence of the OH_T groups results in fewer Ti_{5f} atoms being accessible. However, one Mg atom forms bonds with four surface oxygen ions (two O_{2f} and two O_{3f}) to make it six-fold coordinated, with Mg-O_S distances of 2.1-2.2 Å. Another Mg atom is four-fold coordinated and binds with two surface O_{2f} and an O_W atom from an adsorbed terminal hydroxyl (OH_T) group. The two remaining cluster cations are three-fold coordinated with one sharing a bond with an O_W and the other bonded only to cluster oxygen ions. The MgO-anatase interaction at the oh-anatase surface results in surface Ti atoms, which form bonds to the nanocluster, migrating out of the Ti_{5f} plane to a more significant degree than observed in adsorption at the o-anatase surface. In one instance, in which a surface Ti atom shares bonds with both the supported nanocluster and an adsorbed OH_T group, the Ti migrates out from the Ti_{5f} plane by 1.0 Å and this distortion leads to the breaking of two Ti-O_S bonds. The two O_{3f} atoms that form bonds to the nanocluster migrate out from the surface layer by 0.4 Å.

For the Sn_4O_4 nanocluster, the interaction of Sn_4O_4 with the o-anatase and oh-anatase (101) surfaces is weaker than that of the Mg_4O_4 nanocluster. Nanocluster adsorption is more favourable at the hydroxylated surface by 0.27 eV. We can attribute the weak adsorption to the formation of fewer interfacial bonds between SnO and anatase, compared to MgO and anatase, with only five and four interfacial bonds formed for adsorption at the bare and hydroxylated surfaces, respectively. **Figures 5.2.3.a** and **5.2.3.b** show the atomic structure of the Sn_4O_4 nanocluster adsorbed at the o-anatase (101) surface. Two oxygen atoms in the nanocluster do not bind with the anatase surface. The third oxygen forms a bond with a single surface Ti_{5f} cation and the fourth O_C atom is two-fold coordinated, sharing one interfacial bond with a surface Ti_{5f} cation. This contrasts

with the Mg_4O_4 case in which each of the O_C ions are three-fold coordinated with three forming bonds with the surface. Each of the four Sn atoms in the nanocluster are three-fold coordinated and three have interfacial bonds with a single row of bridging surface O_{2f} ions. The two Ti-O_C distances are 1.8 and 1.9 Å, with the shorter distance corresponding to the lower-coordinated O_C site. The Sn-O_S distances are in the range of 2.1 to 2.3 Å. For adsorption of the Sn_4O_4 nanocluster at the oh-anatase (101) surface (**Figures 5.2.3.c** and **5.2.3.d**), none of the cluster oxygen ions bind to the surface and all four interfacial bonds involve three-fold coordinated cluster Sn ions. Two of these bind to O_W atoms, with Sn-O_W distances of 2.1 and 2.3 Å, and two to bridging surface O_{2f} ions with bond lengths of 2.1 and 2.2 Å.

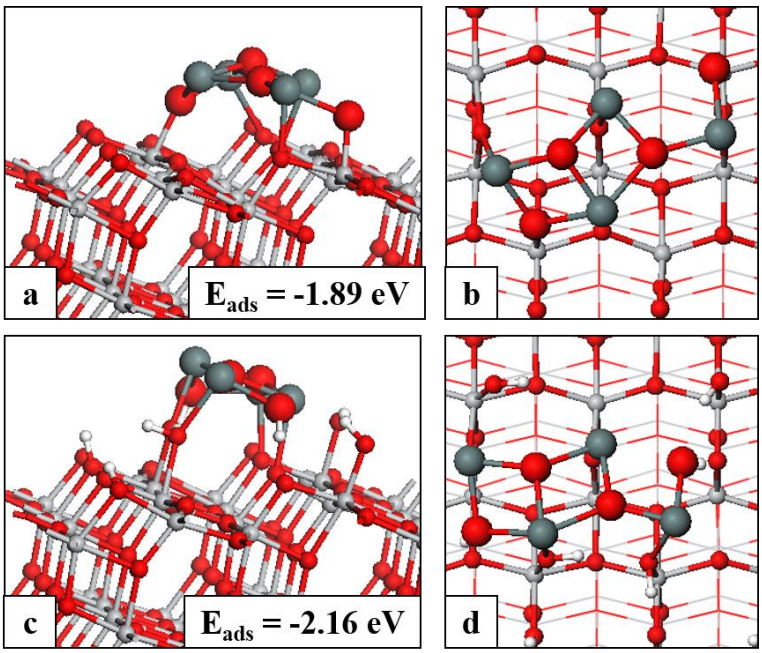

Figure 5.2.3 Atomic structures of **(a)** and **(b)** Sn_4O_4-o-anatase, **(c)** and **(d)** Sn_4O_4-oh-anatase (101). Insets of panels on the left show adsorption energies. Atoms of the clusters are enlarged for clarity. Ti is light grey, O is red, H is white and Sn is dark grey.

Upon adsorption and relaxation of both nanoclusters at the oh-anatase (101) surface we observe migration of H atoms from surface hydroxyls to bind with O_C atoms. In the Mg_4O_4 case, one H atom migrates from a surface O_{2f} bridging hydroxyl (OH_B) to a two-

fold coordinated O_C atom. This facilitates the formation of new bonds between a Mg site and the surface O_{2f} site. Another H atom migrates from an adsorbed OH_T group to bind with a nanocluster oxygen leaving a terminal, singly coordinated O_W bound to a surface Ti_{5f}. This is accompanied by a distortion in which the surface Ti is drawn out from the Ti_{5f} plane by 0.6 Å, breaking a bond with a subsurface O_S and leaving the oxygen atom two-fold coordinated. Migration of H atoms from the hydroxylated surface to oxygen sites of the adsorbed Mg_4O_4 nanocluster makes each O_C site three-fold coordinated, as in the Mg_4O_4-o-anatase (101) case.

When the Sn_4O_4 nanocluster adsorbs at the oh-anatase surface two H atoms migrate from surface O_{2f} to O_C ions. Again this facilitates the formation of interfacial Sn-O bonds through the provision of more low-coordinated O_S sites to which the Sn cations can bind. However, in this instance not all O_C sites are rendered three-fold coordinated through this migration; one O_C site is two-fold coordinated such that the coordination configuration of the Sn_4O_4 nanocluster at the hydroxylated surface is the same as that at the bare surface.

Electronic Properties

Figures 5.2.4.a and **5.2.4.b** display the calculated spin polarised projected electronic density of states (PEDOS) of the Mg_4O_4 nanocluster modifying the o-anatase and oh-anatase (101) surfaces, respectively. In each instance, the top panels show the contribution to the DOS due to surface Ti 3*d* and cluster Mg 3*s* and 3*p* states. The bottom panels show the contribution due to O 2*p* states, separated according to whether the oxygen ion is found in the surface (O_S), the supported nanocluster (O_C) or adsorbed water/hydroxyl (O_W). The PEDOS plots for the unmodified bare and hydroxylated anatase (101) surfaces are presented in **Figure B.1.1** in **Appendix B**.

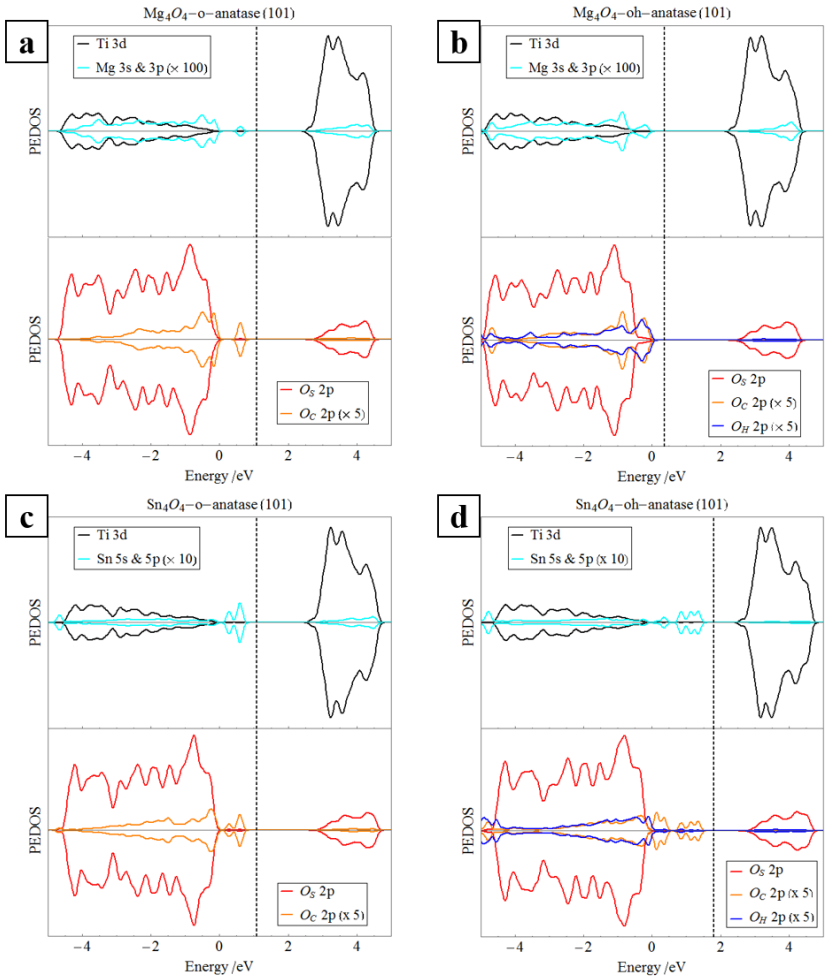

Figure 5.2.4 Spin polarised projected electron density of states plots for **(a)** Mg_4O_4-o-anatase (101), **(b)** Mg_4O_4-oh-anatase (101), **(c)** Sn_4O_4-o-anatase (101) and **(d)** Sn4O4-oh-anatase (101). Top panels display metal PEDOS and bottom panels display oxygen 2*p* PEDOS.

Examination of the PEDOS shows that modification of o-anatase and oh-anatase (101) with Mg_4O_4 introduces new states into the gap just above the VB edge. Focusing on Mg_4O_4 at the o-anatase (101) surface (**Figure 5.2.4.a**), we see that modification results in an enhanced DOS at the VB edge and the emergence of O_C 2*p* derived states around 0.5 eV above the VBM. From this qualitative description of the DOS we predict a red shift in the band gap due to the Mg_4O_4 modification, which could lead to improved photoactivity in the visible range. Enhanced UV activity is also postulated due to the

increased DOS at the VB edge and the presence of empty Mg-derived states above the CB edge.[18]

Similar features are observed in the PEDOS of Mg_4O_4 modifying the oh-anatase (101) surface (**Figure 5.2.4.b**). However, the presence of hydroxyl species on the surface, in combination with the Mg_4O_4 modification, appears to extend the valence band to higher energy, into the anatase band gap, pushing the VB edge to 0.5 eV above that of bare TiO_2, as shown in the inset of **Figure 5.2.4.b**. The overall effect on the band gap is comparable to that observed in the bare surface and the same conclusions may be drawn regarding improvements in activity, in both the visible and UV range.

The top panels of **Figures 5.2.4.c** and **5.2.4.d** present the Ti 3*d* and Sn 5*s* and 5*p* PEDOS for Sn_4O_4 modifying the o-anatase (101) and oh-anatase (101) surfaces, respectively; bottom panels show DOS contributions from O_S, O_C and O_W 2*p*. In both instances features emerge in the anatase energy gap, which are attributable to the surface modification. For Sn_4O_4 modifying the o-anatase (101) surface (**Figure 5.2.4.c**), the impact on the electronic band structure is similar to that of the Mg_4O_4 modification (**Figure 5.2.4.a**). O_C 2*p*-derived states are present at the top of the TiO_2-derived VB and contribute to a new state that lies 0.5 eV above the TiO_2 VBM. Sn-derived states also appear in the TiO_2 band gap, at around 0.5 eV above the VBM, with empty Sn-derived states lying above the TiO_2 CB edge. This arises from the Sn^{2+} oxidation state and the highest lying occupied states show contributions from both Sn 5*s*/5*p* and O 2*p* states.[19-21]

The effect of modification on the electronic structure is more dramatic for Sn_4O_4 at the oh-anatase (101) surface (**Figure 5.2.4.d**). O_W and O_C 2*p* states enhance the DOS at the TiO_2 VB edge with some O_C 2*p*-derived states appearing as much as 1 eV above the VBM. Sn 5*s*/5*p*-derived states lie at similar positions at the top of the VB.

For each of the four heterostructures presented, we propose that modification will result in a reduction of the energy gap of anatase TiO_2, thus inducing a red shift in light absorption. We also predict improved UV photocatalytic activity, with the alignments of the surface and nanocluster energy bands facilitating charge separation.

Photoexcitation Model

Table 5.2.1 Vertical singlet-triplet energy difference ($E^{vertical}$), the relaxed singlet-triplet energy difference (E^{excite}) and the relaxation energy (E^{relax}) for nanocluster modified o-anatase and oh-anatase (101). Values for unmodified o-anatase and oh-anatase (101) have been included for reference.

Composite structure	**$E^{vertical}$ (eV)**	**E^{excite} (eV)**	**E^{relax} (eV)**
Bare-anatase (101)	2.70	1.76	0.94
Mg_4O_4-**o-anatase** (101)	2.50	0.96	1.53
Sn_4O_4-**o-anatase** (101)	2.38	1.09	1.29
Hydroxylated-anatase (101)	2.69	1.39	1.30
Mg_4O_4-**oh-anatase** (101)	2.63	0.59	2.05
Sn_4O_4-**oh-anatase** (101)	1.69	0.40	1.29

Table 5.2.1 presents the energies computed from the model of the photoexcited state, introduced in **Chapter 2**. The underestimation of the band gap inherent in approximate DFT is present in the current DFT+U computational set-up. The +U corrections are chosen to localise electrons and holes rather than to reproduce the band gap of bulk TiO_2. This underestimation is clear in the computed values for $E^{vertical}$ and E^{excite} which are clearly smaller than the experimental values. However, what is important is the change in these quantities with modification of the anatase surfaces.

We note that E^{excite} is always smaller than the simple VB-CB energy gap and $E^{vertical}$, as the former energy includes ionic relaxations and polaron formation in response to "exciting" the electron, which then lowers the energy of the triplet electronic state. However, comparison of these computed energies across different structures yields valid qualitative information.[19, 22-26] In particular, a reduction in $E^{vertical}$ for a composite structure, relative to the unmodified metal oxide, will correspond to light absorption at lower energies for the surface modified system.

Table 5.2.1 shows that the modification of anatase, whether bare or hydroxylated, with MgO and SnO nanoclusters always results in a red shift, with both the vertical and excitation energies being reduced upon modification. The reduction in the excitation energy arises from the greater degree of structural relaxation in the nanocluster, as evidenced by the values for E^{relax}. The relaxation, or trapping energy, is an indication of the stability of the electron-hole pair and the larger relaxation energy for hydroxylated anatase indicates a higher stability of the localised electron-hole pair compared to the o-anatase (101) surface.

Looking at differences between the nanoclusters, we see that MgO modification has a more significant effect than SnO modification of the o-anatase (101) surface; modification with Mg_4O_4 and Sn_4O_4 gives reductions in E^{excite} of 1.80 and 0.67 eV relative to the bare surface. The opposite is true for the oh-anatase (101) surface; E^{excite} is calculated to be lower by 0.80 (0.99) eV upon modification with Mg_4O_4 (Sn_4O_4). These results, in combination with analysis of the ground state PEDOS, indicate a red shift in light absorption for the modified surfaces. In terms of the stability of the localised electrons and holes, Mg_4O_4 modification shows significantly enhanced electron and hole trapping at both the bare and hydroxylated surfaces. The presence of hydroxyls at the surface facilitates the trapping of the electron-hole pair for both the bare surface and that

modified with Mg_4O_4, but has no impact on the trapping energy of the Sn_4O_4-modified surface.

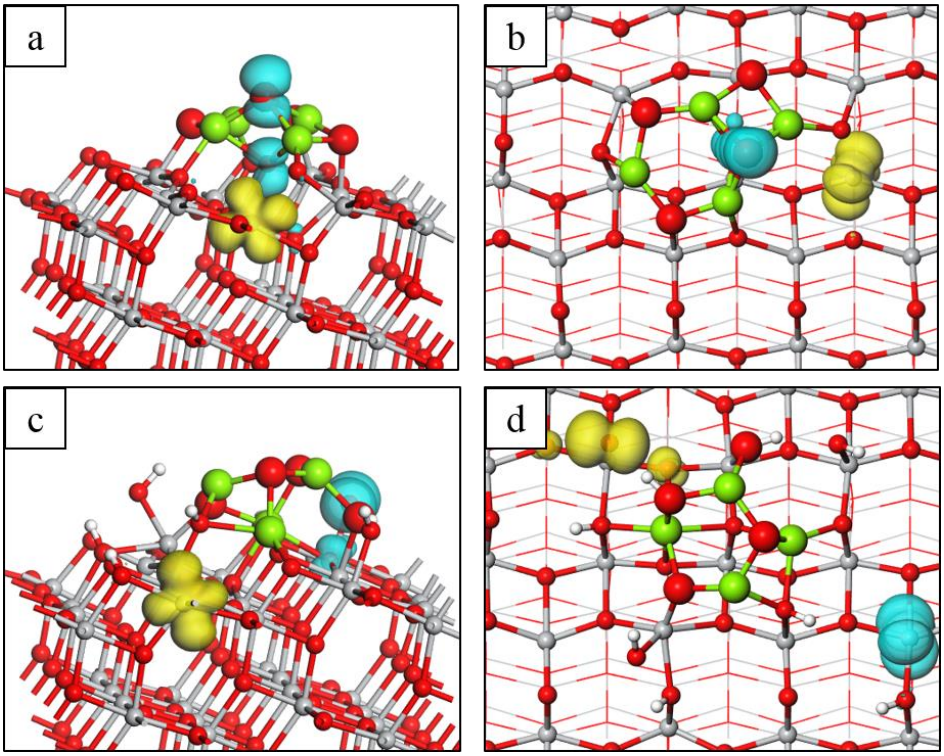

Figure 5.2.5 Spin density plots for the photoexcited electron and hole in **(a)** and **(b)** Mg_4O_4-o-anatase, **(c)** and **(d)** Mg_4O_4-oh-anatase (101). The spin density isosurfaces enclose spin densities up to 0.2 electrons/Å^3. Yellow isosurfaces represent electrons and blue isosurfaces represent holes.

In addition to energy gap considerations, another factor affecting the efficiency of photocatalytic materials is the fate of photoexcited charge carriers. Charge recombination must be suppressed and charge separation promoted. In addition, a higher relaxation energy indicates higher stability of the photoinduced charges. We have examined the localisation of photoexcited charges through analysis of computed Bader charges, spin magnetisations and excess spin density plots.

Figure 5.2.5 shows the spin density plots for the Mg_4O_4-modified o-anatase and oh-anatase (101) surfaces after relaxation of the triplet state. For both modified surfaces we

see that the electron localises on a single surface Ti_{5f} atom. The computed Bader charge for Ti^{4+} cations is 1.27 electrons. The Bader charge increases to 1.70 electrons at the site on which the electron is localised. These Bader charges are consistent with formation of a localised Ti^{3+} electronic state. The computed spin magnetisation for the Ti^{3+} site is 0.99 μ_B and compares with values of less than 0.03 μ_B for all other Ti sites. Finally, the Ti-O distances around this site are elongated by 0.1 Å relative to the singlet ground state, which is typical of the formation of a localised, reduced Ti^{3+} state.

For Mg_4O_4 supported on the bare surface (**Figures 5.2.5.a** and **5.2.5.b**), the hole state predominantly localises at a three-fold coordinated oxygen site in the nanocluster. The computed Bader charge for the O_C atom is reduced from 7.93 electrons to 7.23 electrons upon localisation of the hole state. The computed spin magnetisation is 0.67 μ_B, which is usual for a localised oxygen hole in the DFT+U formalism.[27] These values indicate the formation of a localised oxygen hole state. There is some spreading of the hole state to a neighbouring surface O_{2f} site, which shares multiple bonds with the nanocluster. This spreading is reflected in a computed spin magnetisation of 0.21 μ_B at the O_{2f} site, an elongation of the Ti_{6f}-O_{2f} bond by 0.1 Å and the breaking of the Ti_{5f}-O_{2f} bond.

For Mg_4O_4 supported on the oh-anatase (101) surface (**Figures 5.2.5.c** and **5.2.5.d**) we can see that the hole state localises at a singly coordinated, originally hydroxyl, oxygen site, O_W. Hole localisation is accompanied by a reduction in the Bader charge for the terminal oxygen from 7.16 electrons in the singlet state to 6.73 electrons in the triplet state. The computed spin magnetisation is 0.81 μ_B. Again these values are typical of a localised oxygen hole species. The Ti-O distance is elongated by 0.2 Å relative to that in the singlet ground state, consistent with the formation of a localised oxygen hole polaron.

The spin density plots for the Sn_4O_4-modified o-anatase (**Figures 5.2.6.a** and **5.2.6.b**) and oh-anatase (101) (**Figures 5.2.6.c** and **5.2.6.d**) surfaces show an electron localised on a single Ti lattice site. In both instances, these are surface Ti_{5f} and the computed Bader charges (spin magnetisations) are 1.72 electrons (0.97 μ_B) and 1.67 electrons (0.99 μ_B) on the o-anatase and oh-anatase (101) surfaces, respectively. These results indicate the formation of a reduced, localised Ti^{3+} species and further confirmation is provided by the distortions of the atomic structure in the vicinity of the localisation. The Ti^{3+}-O bond lengths increased by as much as 0.13 Å in the excited state, relative to the equivalent distances in the ground state.

For Sn_4O_4 modifying the o-anatase (101) surface (**Figures 5.2.6.a** and **5.2.6.b**) the hole state is distributed over two doubly-coordinated O_C atoms and a cluster Sn atom to which they are each bonded. This localisation arises because the top of the valence band is composed of Sn 5*s* + 5*p* and O 2*p* states from the SnO nanocluster. The computed Bader charges decrease from 7.3-7.4 and 12.64 electrons for oxygen and tin in the singlet ground state, to 7.15-7.18 and 12.36 electrons for the same atoms in the relaxed triplet state. Considering that a Bader charge of 12.75 electrons is computed for Sn^{2+} ions in the gas phase Sn_4O_4 nanocluster, we assign a +3 oxidation state to the Sn atom at which hole localisation occurs. Correspondingly, a -1 oxidation state (oxygen hole) is assigned to the two O_C sites over which the hole is distributed. The charge is uniformly spread over the three sites with spin magnetisations of 0.19, 0.22 and 0.24 μ_B computed for the two oxygen sites and the tin site, respectively. These values compare with computed spin magnetisations of less than 0.01 μ_B on the other Sn and O sites; there is a small distribution of charge to a neighbouring O_S site, as shown in **Figure 5.2.6.a**, and this is reflected in a computed spin magnetisation of 0.06 μ_B.

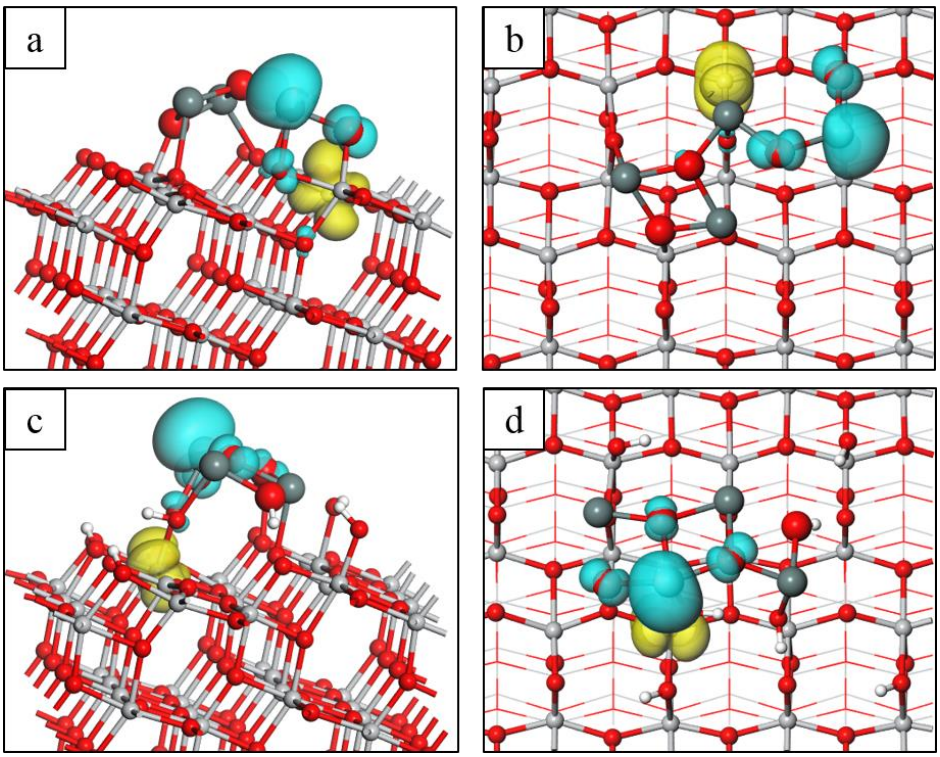

Figure 5.2.6 Spin density plots for the photoexcited electron and hole in **(a)** and **(b)** Sn_4O_4-o-anatase, **(c)** and **(d)** Sn_4O_4-oh-anatase (101). The spin density isosurfaces enclose spin densities up to 0.2 electrons/Å^3. Yellow isosurfaces represent electrons and blue isosurfaces represent holes.

Electron localisation is accompanied by an extension of the Ti-O_C bond by 0.1 Å, but the distances between the various sites over which the hole is distributed are contracted relative to the ground state. The two Sn^{3+}-O_C and the Sn^{3+}-O_S bond lengths are reduced by 0.09-0.15 Å and this distortion contributes to the breaking of a Sn-O_C bond involving one of the oxygen polaron sites; the O_C in question was three-fold coordinated in the ground state (**Figure 5.2.3.b**) and is two-fold coordinated in the excited state (**Figure 5.2.6.b**), so that both O_C sites at which hole localisation occurs are two-fold coordinated.

For the Sn_4O_4-modified oh-anatase (101) surface (**Figures 5.2.6.c** and **5.2.6.d**), we see that the hole state is distributed over a tin site and three oxygen sites in the supported Sn_4O_4 cluster. The computed Bader charge and spin magnetisations are 12.26 electrons and 0.28 μ_B for the Sn site, to which we assign a +3 oxidation state. The computed spin

magnetisations for the three O_C sites are 0.08, 0.15 and 0.15 μ_B; the computed Bader charges are 7.25, 7.62 and 7.65 electrons. The distances between the cluster sites over which the hole state is distributed are contracted, with a reduction of 0.09-0.17 Å in the Sn^{3+}-O_C bond lengths.

For all systems studied, the model photoexcited state results in the localisation of an electron at a surface Ti_{5f} site to form a reduced Ti^{3+} polaron species. This is consistent with the nature of the lowest lying conduction band states, which are dominated by Ti 3*d* states. The nature of the hole states depends on the identity of the nanocluster modifier and the state of the anatase (101) surface. For modification with the Mg_4O_4 nanocluster, the hole can localise at a single O_C site (bare surface) or O_W site (hydroxylated surface). For the Sn_4O_4 nanocluster modifier, the hole is distributed over metal and oxygen sites in the nanocluster.

The proximity of the charge carriers to each other contrasts with previous work on surface modified rutile (110) where electron localisation occurred at subsurface Ti sites.[22-24] Still, the stability of the electron and hole and their spatial separation are improved relative to the bare anatase (101) surface (**Figure B.1.2** in **Appendix B**). Modification with larger nanoclusters may improve charge separation, as the general trend observed in previous work is that hole localisation occurs at the lower-coordinated sites in the cluster.[19, 22-23, 25] However, the impact of an increase in cluster size on the light absorption properties of the heterostructures would need to be reassessed, due to well-known size effects.

Surface modification promotes separation of photoexcited charge, with holes, localised on or distributed over sites of the nanocluster, available for participation in oxidation reactions. However, for this separation and localisation to result in enhanced

photocatalytic activity, reductant species must preferentially adsorb at the nanocluster modifier rather than the TiO_2 support.

Oxygen Vacancy Formation

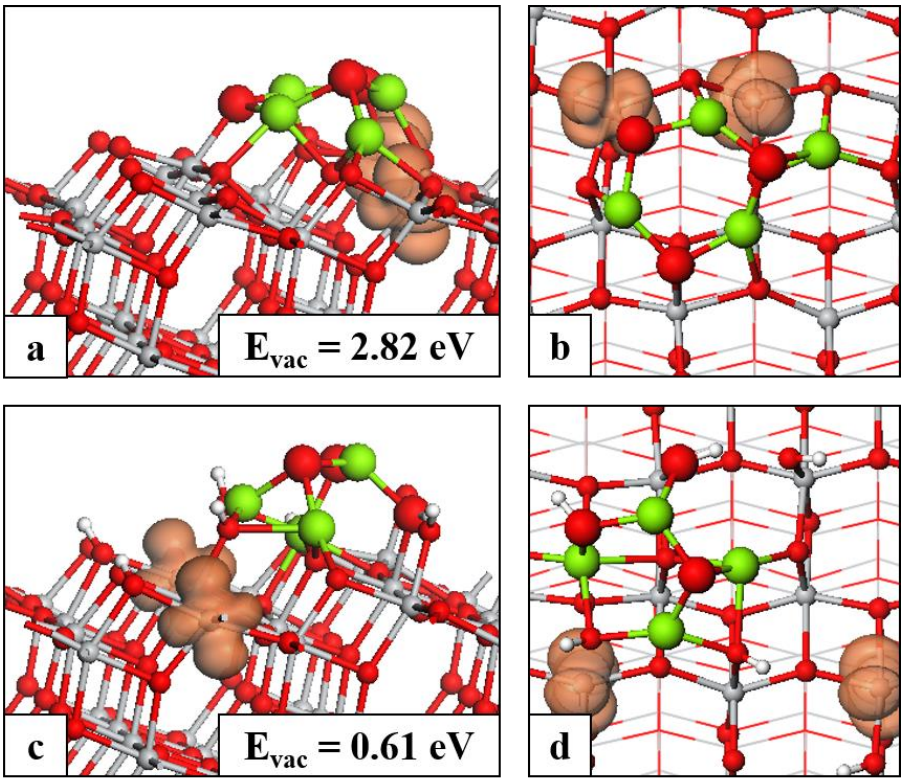

Figure 5.2.7 Relaxed atomic structure of the nanocluster modified TiO_2 surfaces after formation of the most stable oxygen vacancies. **(a)** and **(b)** Mg_4O_4-o-anatase (101), **(c)** and **(d)** Mg_4O_4-oh-anatase (101). Insets of panels on the left show vacancy formation energies. The orange spin density isosurfaces enclose spin densities up to 0.2 electrons/**Å^3.**

Labelling the cluster oxygen atoms I-IV (**Figure B.1.3** in **Appendix B**), we examine oxygen vacancy formation by removing each nanocluster oxygen and relaxing. The results of these calculations, presented in **Table B.1.1** of **Appendix B**, allow us to examine the reducibility of modified anatase and any impact of surface hydroxylation.

The relaxed geometries of the composite surfaces upon formation of the most stable oxygen vacancy are presented in **Figures 5.2.7** and **5.2.8**.

For MgO-o-anatase (101), the most stable oxygen vacancy has a formation energy of 2.82 eV, while for SnO-o-anatase (101), the cost is 1.82 eV. Hence, the energy required to produce the most stable oxygen vacancy in the nanocluster-modified surface is notably reduced over the unmodified anatase surface, for which the formation energy of an oxygen vacancy is 3.6-3.8 eV, from a study with similar computational parameters.[28]

For the MgO-o-anatase (101) system, the most favourable configuration with one O vacancy site is shown in **Figures 5.2.7.a** and **5.2.7.b**. The relatively high energy cost is probably due to the resulting under-coordination of the cluster metal ions in the non-stoichiometric structure, as a result of a lack of oxygen sites with which the Mg atoms can form bonds. After oxygen vacancy formation, new interfacial Mg-O_{3f} bonds were established and all cluster metal ions were at least three-fold coordinated upon relaxation. This draws the O_{3f} atoms out from the surface, breaking Ti_{6f}-O_{3f} bonds and leaving Ti_{6f} ions under-coordinated at the surface. Thus, the surface distortions that accompany oxygen vacancy formation act against the gain in energy when the structure relaxes in response to oxygen vacancy formation.

For the Sn_4O_4 modifier at the o-anatase (101) surface (**Figures 5.2.8.a** and **5.2.8.b**), the most stable oxygen vacancy site in the nanocluster has a cost of 1.82 eV. For the most stable oxygen vacancy, the removed oxygen atom was originally two-fold coordinated. The single Sn site that was bound to the removed oxygen atom maintains its three-fold coordination by forming a new bond with a surface O_{3f} site; this means that the atoms of the nanocluster maintain the same coordination configuration as in the stoichiometric case. The O_{3f} site migrates out from the surface by 0.3 Å to accommodate this bond and

this breaks a bond with a subsurface Ti site. The Ti_{5f} site to which the removed oxygen was bound relaxes back into the surface and rebinds to an O_S site in the substrate to remain five-fold coordinated.

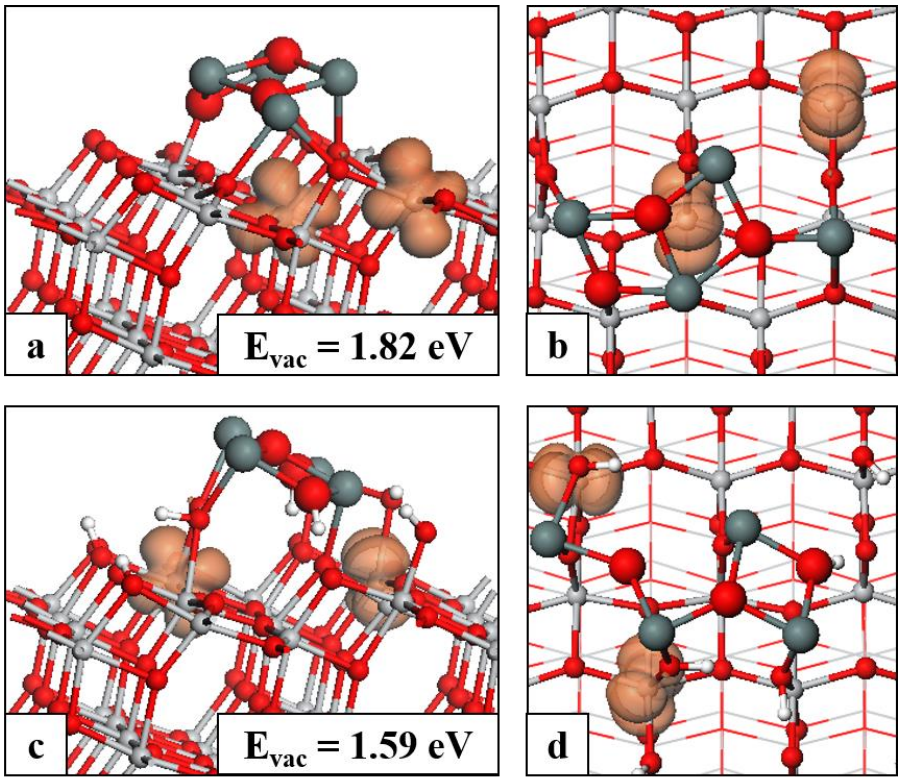

Figure 5.2.8 Relaxed atomic structure of the nanocluster modified TiO_2 surfaces after formation of the most stable oxygen vacancies. **(a)** and **(b)** Sn_4O_4-o-anatase (101), **(c)** and **(d)** Sn_4O_4-oh-anatase (101). Insets of panels on the left show vacancy formation energies. The orange spin density isosurfaces enclose spin densities up to 0.2 electrons/**Å^3.**

Turning now to the hydroxylated, modified surfaces, the problem of cation under-coordination that results in a large vacancy formation energy for Mg_4O_4-anatase is alleviated when the nanocluster is supported on the hydroxylated surface. This is because the surface terminating OH groups provide additional sites, close to the nanocluster, for the formation of new interfacial metal-oxygen bonds that maintain the Mg coordination. Two of the four Mg cations are four-fold coordinated, strengthening the interaction with the surface (**Figures 5.2.7.c** and **5.2.7.d).** This is reflected in the quite favourable oxygen

vacancy formation energy of 0.61 eV. The Mg-O interaction is strong enough that a surface Ti_{5f} site is rendered four-fold coordinated upon reduction, with an OH_T group migrating from the Ti site to a Mg site in the nanocluster.

For SnO-modified oh-anatase, (**Figures 5.2.8.c** and **5.2.8.d**) each of the O_C and Sn atoms are three-fold coordinated. The reduced Sn_4O_3 nanocluster interacts too weakly to form the interfacial bonds necessary to stabilise it at the surface; however, in the presence of hydroxyls at the surface, the energy required to produce the most stable oxygen vacancy, at 1.59 eV, is reduced by 0.2 eV relative to the Sn_4O_4-modified o-anatase (101) surface. The formation of a neutral oxygen vacancy releases two electrons. Through an analysis of the excess spin density plots, shown in **Figures 5.2.7** and **5.2.8**, and computed Bader charges and spin magnetisations we find that, for all systems, the electrons localise at two surface Ti sites. Electrons localise at low-coordinated Ti sites, whether these are Ti_{5f} sites or Ti_{6f} sites which have lower coordination due to surface restructuring in response to nanocluster adsorption and reduction.

For Mg_4O_3 at the hydroxylated surface, one electron localises at a four-fold coordinated Ti site. The exception is Sn_4O_3 at the hydroxylated surface where electron localisation occurs at two Ti_{5f} sites which are six-fold coordinated due to the presence of OH_T species; these OH_T species form Sn-O_W bonds with the reduced nanocluster. In all instances, electron localisation is accompanied by an increase in the computed Bader charges of 0.4 electrons; spin magnetisations are in the range of 0.97 – 1.00 μ_B. These values indicate the formation of reduced Ti^{3+} species.

It is difficult to predict *a priori* the impact of surface hydroxylation on oxygen vacancy formation. For the Mg_4O_4 modifier, the formation energy decreased in the presence of surface hydroxylation; while this was true of the Sn_4O_4 modifier, the effect was much less

pronounced. We expect that these results depend on the geometry of the nanoclusters and the degree of surface coverage with hydroxyl groups. The strength of interaction at the nanocluster-surface interface may also play a role, particularly the metal-surface interaction.

5.3 *hBN-modified TiO_2*

What follows is adapted from an article entitled: "***Modification of TiO_2 with hBN: High Temperature Anatase Phase Stabilisation and Photocatalytic Degradation of 1, 4-Dioxane***", published in the Journal of Physics: Materials.[2]

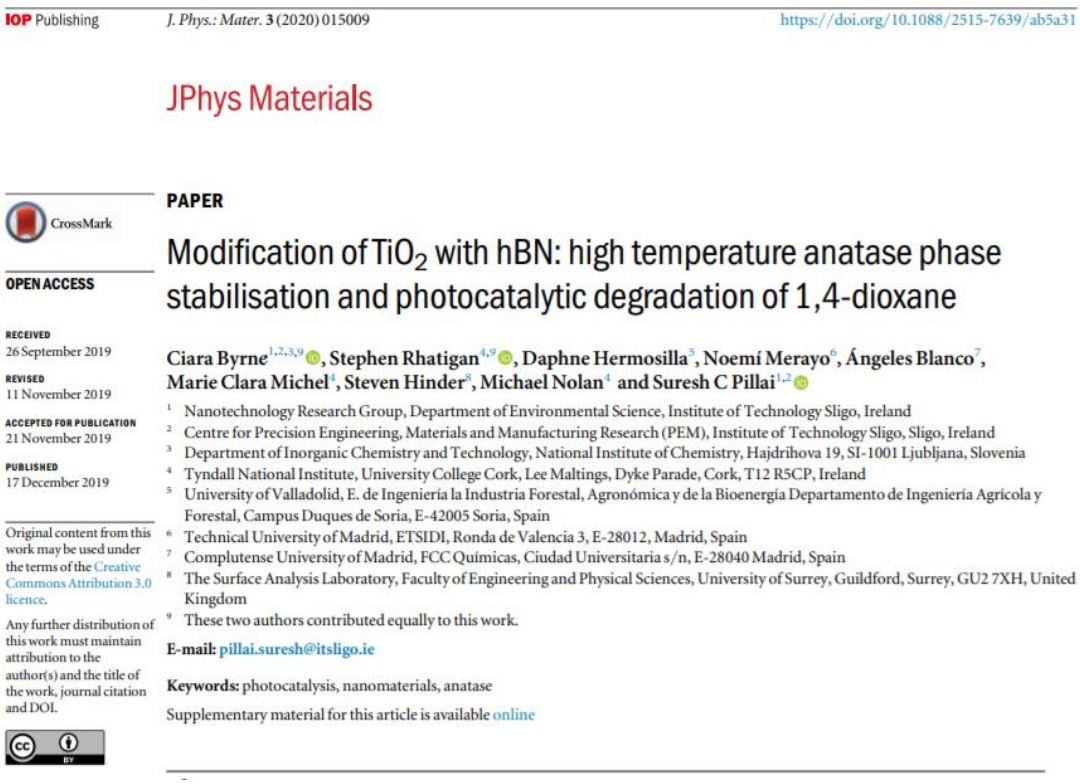

IOP Publishing J. Phys.: Mater. 3 (2020) 015009 https://doi.org/10.1088/2515-7639/ab5a31

JPhys Materials

PAPER

Modification of TiO_2 with hBN: high temperature anatase phase stabilisation and photocatalytic degradation of 1,4-dioxane

Ciara Byrne[1,2,3,9], Stephen Rhatigan[4,9], Daphne Hermosilla[5], Noemí Merayo[6], Ángeles Blanco[7], Marie Clara Michel[1], Steven Hinder[8], Michael Nolan[4] and Suresh C Pillai[1,2]

[1] Nanotechnology Research Group, Department of Environmental Science, Institute of Technology Sligo, Ireland
[2] Centre for Precision Engineering, Materials and Manufacturing Research (PEM), Institute of Technology Sligo, Sligo, Ireland
[3] Department of Inorganic Chemistry and Technology, National Institute of Chemistry, Hajdrihova 19, SI-1001 Ljubljana, Slovenia
[4] Tyndall National Institute, University College Cork, Lee Maltings, Dyke Parade, Cork, T12 R5CP, Ireland
[5] University of Valladolid, E. de Ingeniería la Industria Forestal, Agronómica y de la Bioenergía Departamento de Ingeniería Agrícola y Forestal, Campus Duques de Soria, E-42005 Soria, Spain
[6] Technical University of Madrid, ETSIDI, Ronda de Valencia 3, E-28012, Madrid, Spain
[7] Complutense University of Madrid, FCC Químicas, Ciudad Universitaria s/n, E-28040 Madrid, Spain
[8] The Surface Analysis Laboratory, Faculty of Engineering and Physical Sciences, University of Surrey, Guildford, Surrey, GU2 7XH, United Kingdom
[9] These two authors contributed equally to this work.

E-mail: pillai.suresh@itsligo.ie

Keywords: photocatalysis, nanomaterials, anatase

Supplementary material for this article is available online

CrossMark

OPEN ACCESS

RECEIVED
26 September 2019

REVISED
11 November 2019

ACCEPTED FOR PUBLICATION
21 November 2019

PUBLISHED
17 December 2019

DOI: https://doi.org/10.1088/2515-7639/ab5a31

https://research.thea.ie/handle/20.500.12065/3043

5.3.1 *Introduction*

Boron nitride (BN) modification of titania has been investigated in recent years as a means to modify the properties of TiO_2.[29-34] Various of these studies have found that BN-modification enhances the photodegradation activity of titania, including under visible

light.[30, 32, 35] However, to date there have been no comprehensive, systematic studies on the effect of the concentrations of BN and calcination temperatures on the anatase to rutile phase transition (ART) and the resulting photocatalytic activity of BN-modified TiO_2. For the latter, we chose removal of 1, 4-dioxane as a model system.

The primary materials advance in this work is the comprehensive examination of the impact that BN-modification has on the ART and on the photocatalytic activity of TiO_2 for 1,4-dioxane removal. TiO_2 was interfaced with BN at five different concentrations (0-16% BN-TiO_2) and samples were calcined at four temperatures (500-700 °C). These interfacial materials were characterised using X-ray diffraction (XRD), Raman Spectroscopy and X-ray photoelectron spectroscopy (XPS). DFT studies were performed to provide detailed insights into the bonding of BN with the anatase surface and the origin of the enhanced photocatalytic activity. Details for the materials and methods are provided in **Appendix A** and for the model constructions in **Chapter 2** and **Appendix B**.

5.3.2 Results

5.3.2.1 Selected Experimental Results

X-ray Diffraction (XRD) Characterisation

XRD was used to determine the phase of each sample and from this analysis the impact on the transition temperature can also be concluded. The intensities of the main anatase (25°) and rutile (27°) peaks were used to determine the ratios of anatase and rutile present in each sample. The XRD patterns for the unmodified TiO_2 and BN-modified samples, calcined at 600 °C, are shown in **Figure 5.3.1.a**. Additionally, **Figure 5.3.1.a** shows the presence of bulk boron nitride peaks, with the peak at 26° indicating the graphite-like *h*BN structure.[36-39] All samples were 100% anatase when calcined up to 500 °C. At 600 °C, 0% BN-TiO_2 had converted to 100% rutile, while the BN-modified samples with 2%,

4%, 8% and 16% BN show anatase contents of 13.2%, 25.9%, 64.4% and 65.5%, respectively. All samples converted to the rutile phase when calcined at 650 and 700 °C, irrespective of BN concentration. The peak at 26° is only present for 16% BN-TiO_2 when calcined at 600 °C and above.

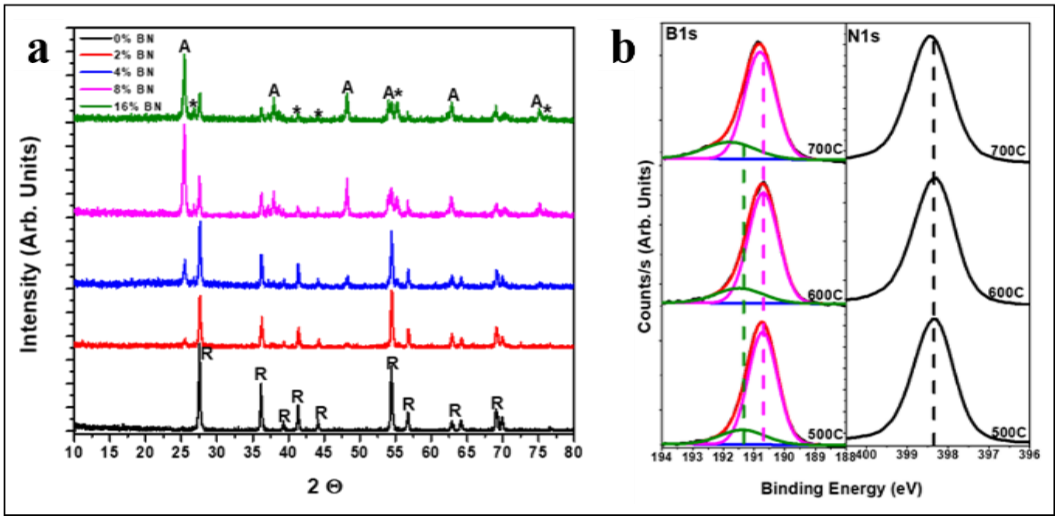

Figure 5.3.1 (a) XRD of all BN-TiO2 samples calcined at 600°C. (A = anatase; R = rutile and * = BN). **(b)** XPS spectra of B 1*s* and N 1*s* for 16% BN-TiO_2, calcined at 500, 600 and 700 °C.

X-ray Photoelectron Spectroscopy (XPS)

XPS analysis was used to determine the elemental composition and oxidation states of elements that were found on or close to the surface of pure and BN-modified TiO_2, calcined at 500, 600 and 700 °C. The elements found in the samples were carbon, boron, nitrogen, oxygen and titanium; the atomic (at.) % varied depending on the samples.

The composite samples (2%-16% BN-TiO_2) contained B 1*s* and N 1*s* peaks; the spectra for 16% BN-TiO_2 can be seen in **Figure 5.3.1.b**. The B 1*s* spectra show the presence of two peaks, the first at 190.68-190.78 eV and the second at 191.36-191.83 eV. The fitted peaks at ~190 eV (pink) show the presence of elemental boron when examining boron doped TiO_2.[40] The second fitted peak at ~191 eV (green) has a significantly lower

intensity and indicates the presence of doping with B^{3+} ions in interstitial modes.[40] Liu *et al*. suggested that this peak could also be a result of "*edge/interfacial boron dangling bonds*" which are linked with -OH.[30] It is important to note that the XPS analysis does not show the presence of Ti-B bonds (187 eV) or boron being incorporated into TiO_2 and its environment (Ti-B-O at 192 eV).[41] Finally, the N 1*s* peaks that are present in the 16% BN-TiO_2 range from 398.28-398.48 eV, which relate to B-N bonding and refer to the trigonal units of BN layers (BN_3 and NB_3).[30] The peak which indicates Ti-N interactions (~396 eV) is not present in the N 1*s* spectra.[42-43]

Photocatalytic Degradation of 1, 4-dioxane

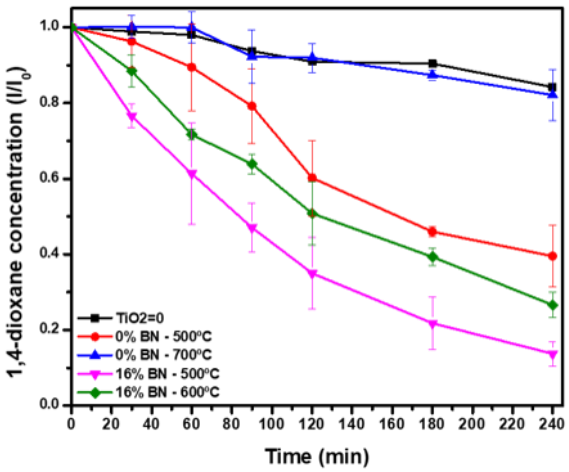

Figure 5.3.2 Photocatalytic removal of 1,4-dioxane for pure anatase, pure rutile and 16% BN-modified titania.

The photocatalytic activity of 16% BN-TiO_2 materials was determined by examining the photodegradation of 1, 4-dioxane and compared to pure TiO_2. The reduction of 1, 4-dioxane under solar light with no photocatalyst present (TiO_2 = 0) was also examined and this showed the removal of 15.8% of 1, 4-dioxane after 4 hours, shown in **Figure 5.3.2**.

At 500 and 700 °C, the 16% BN-TiO_2 photocatalyts showed a removal rate of 86.3% and 73.4%, respectively, after 4 hours (**Figure 5.3.2**). For un-doped anatase TiO_2, calcined at

500 °C, the removal rate was 60.5% (**Figure 5.3.2**), while after calcination to 700 °C (pure rutile), only 17.9% of 1, 4-dioxane was removed after 4 hours, which is not significantly different from the activity with no catalyst. Therefore, the 16% BN-TiO_2 at given temperatures showed a significant improvement in the photocatalytic activity compared to pure anatase and rutile.

5.3.2.2 Computational Results

Local Atomic Structure

The relaxed geometries of the anatase TiO_2 surface modified with one, two and three *h*BN rings are shown in **Figure 5.3.3** and the adsorption energies are included in the insets. The large, negative adsorption energies indicate that the interaction between the *h*BN rings and the surface is favourable and the magnitudes of the energies increase approximately linearly with the number of adsorbed rings. For the anatase surface modified with one and two *h*BN rings, multiple starting geometries were considered. Those presented in **Figure 5.3.3** correspond to the most stable structures of those sampled. Additional interfacial structures are described in **Section B.2** of **Appendix B**. However, it was found that key properties of the interfacial system are not dependent on the precise orientation of the *h*BN rings at the anatase (101) surface.

The geometries presented herein were computed with the DFT-D2 approach to account for vdW interactions (see **Appendix B**). The geometries computed within vdW-DF are qualitatively equivalent with the exception that interfacial bonds are slightly elongated (< 0.01 Å) in the latter scheme. The adsorption energies are moderated in the vdW-DF calculations; the difference between the computed adsorption energies is at most 0.3 eV per *h*BN ring.

For 1-$(BN)_3$-a101, shown in **Figure 5.3.3.a**, five interfacial bonds are established between the *h*BN ring and the titania surface. There are two Ti-N bonds, each of length 2.00 Å, and the interaction draws the Ti ions out from the surface by 0.1 Å. There are three B-O bonds; of these, two involve bridging O ions (O_{br}), with B-O distances of 1.44 Å, and the third involves an in-plane O ion (O_{ip}), with a B-O distance of 1.48 Å. B-N distances elongate from 1.36 Å in the gas-phase and are in the range 1.42-1.47 Å.

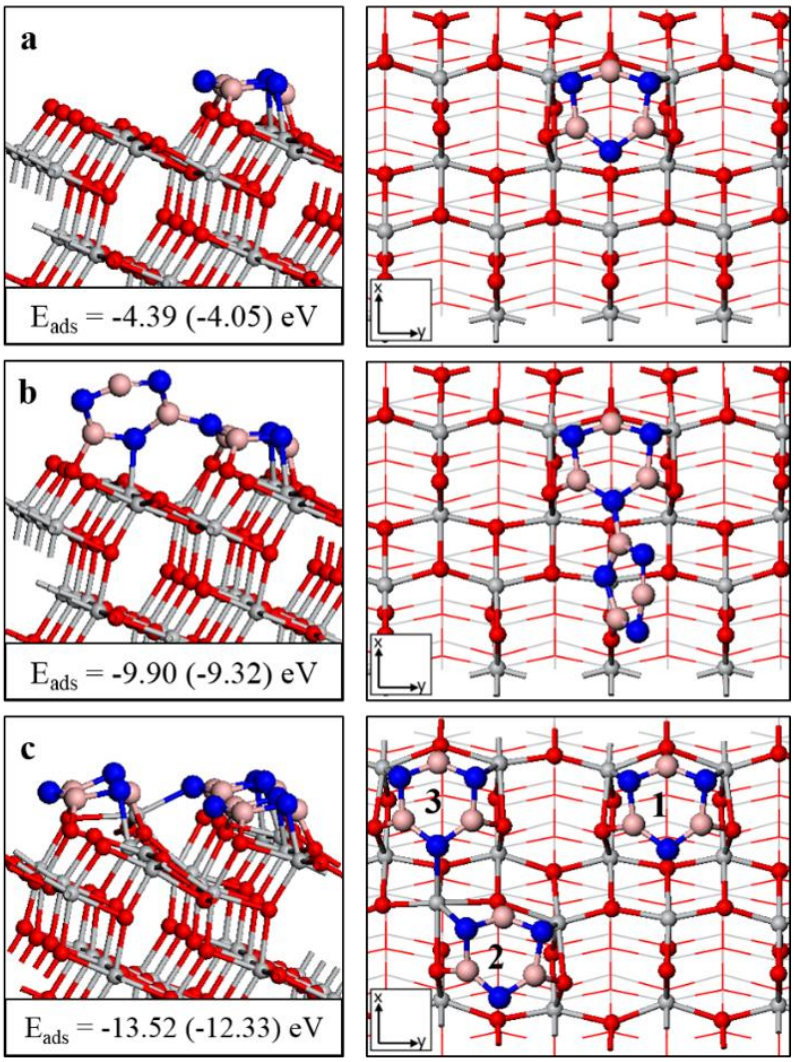

Figure 5.2.3 Relaxed structures of **(a)** 1-$(BN)_3$-a101, **(b)** 2-$(BN)_3$-a101 and **(c)** 3-$(BN)_3$-a101. The adsorption energies, computed within the DFT-D2 (vdW-DF) approach, are included in the insets of the panels on the left. The panels on the right show the top view of the modified surface. In this and subsequent figures, Ti are represented by grey spheres, O by red, B by pink and N by blue.

In the gas phase $(BN)_3$ rings, the N ions exhibit computed Bader charges of 8.0 electrons, correspondig to N^{3-}. The computed Bader charges for the two N ions that bind to Ti decrease from 8.0 electrons, in the gas-phase, to 7.5 electrons. The computed Bader charge for the third N ion decreases from 8.0 to 7.8 electrons. This charge is distributed over the TiO_2 surface. In particular, the computed Bader charge for the O_{ip} bonded to B increases from 7.2 to 7.5 electrons.

In the 2-$(BN)_3$-a101 system, shown in **Figure 5.3.3.b**, a second *h*BN ring is adsorbed at the surface, neighbouring the first. The geometry of the first ring at the surface is consistent with that described for 1-$(BN)_3$-a101, while the second *h*BN ring is adsorbed edgewise, forming two bonds with the surface, B-O_{br} and Ti-N, of lengths 1.46 Å and 1.87 Å. A third bond is established between the *h*BN rings with a B-N distance of 1.51 Å. The Bader charges for the three N ions that bind to Ti of the surface decrease by 0.5-0.6 electrons and an O_{ip} ion and O_{br} ion gain 0.3 and 0.6 electrons, respectively.

Figure 5.3.3.c shows the relaxed structure of 3-$(BN)_3$-a101, in which the three *h*BN rings adsorbed at the surface are not in direct interaction. The geometry of the rings at the surface is similar to that described for 1-$(BN)_3$-a101, above. However, N ions of the rings labelled 2 and 3 in **Figure 5.3.3.c** bind to the same Ti ion; this Ti ion moves out from the surface by 0.9 Å. This distortion shortens the bond length to the N ion of ring 2 to 1.97 Å and the Ti ion binds to the third N ion of ring 3 with a bond length of 2.14 Å. The Bader charges for the N ions decrease by 0.2-0.5 electrons, and correspondingly, 10 O ions of the surface gain between 0.1-0.6 electrons.

The relaxed structure of $(BN)_{24}$-a101 is shown in **Figure 5.3.4** and adsorption energies of -13.71 and -13.60 eV are computed within the DFT-D2 and vdW-DF frameworks; in each case this corresponds to adsorption energies of -0.57 eV per BN unit. The relaxed

geometries are qualitatively consistent, but computed bond lengths are elongated by 0.01-0.02 Å in the vdW-DF set-up, relative to those computed in DFT-D2.

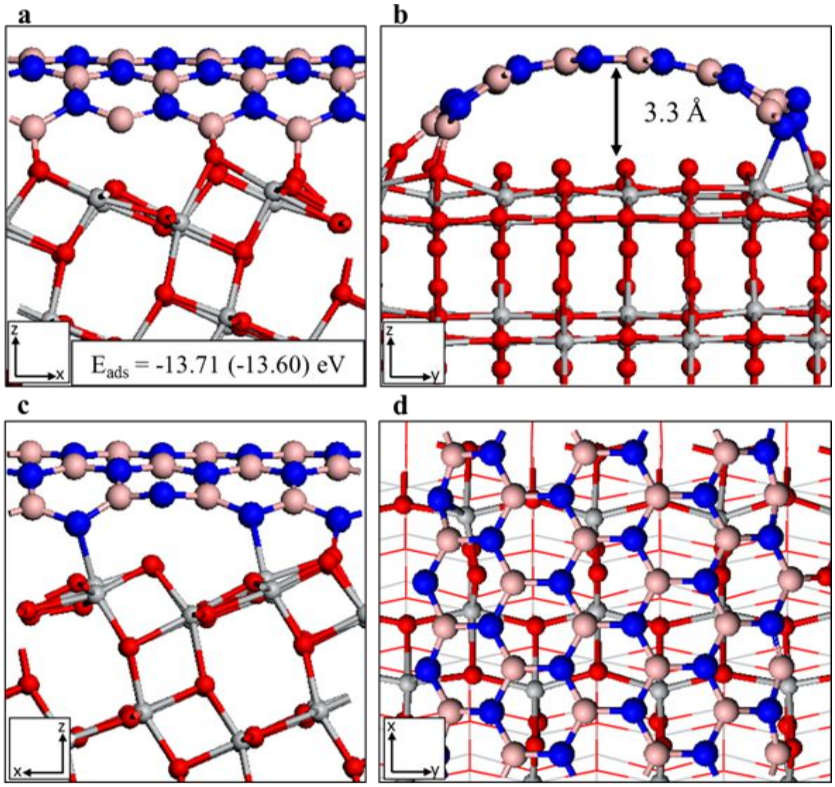

Figure 5.3.4 Relaxed atomic structure of $(BN)_{24}$-a101. Panels **(a)** and **(c)** show the interfacial bonds formed along the B-terminated and N-terminated edges of the *h*BN ribbon, respectively. Panel **(b)** shows the interfacial distance between the centre of *h*BN ribbon and anatase (101) surface and panel **(d)** shows a top view of the modified surface. The adsorption energies are included in the inset of the panel **(a)**, as computed *via* DFT-D2 (vdW-DF).

One side of the *h*BN strip has B ions at the outermost edge (**Figure 5.3.4.a**), while the other consists of N ions (**Figure 5.3.4.c**). At the B-terminated edge, three B-O bonds are formed of lengths in the range 1.35-1.42 Å. Two bonds involve O_{br} and the third involves O_{ip}; these ions migrate out from the surface by 0.3-0.5 Å. At the N-terminated edge there are three interfacial bonds, two Ti-N bonds of length 2.04 Å and the distance of edge N to the nearest surface O is 1.43 Å. The Ti ions move out from the surface by 0.2-0.3 Å. The *h*BN-layer is anchored at the surface by the interfacial bonds at the B- and N-

terminated edges and bows towards the centre of the strip to a maximum distance of 3.3 Å.

Bader charges for Ti^{4+} and O^{2-} ions are in the range 9.6-9.7 and 7.1-7.2 electrons, respectively. The Bader charges for two surface Ti ions along the B-terminated edge increase to 10.0 electrons and the computed spin magnetisations are 0.9 μ_B; these values are typical of reduction to Ti^{3+}. A third Ti ion in the vicinity of the B-terminated edge has a computed Bader charge of 9.8 electrons and a spin magnetisation of 0.3 μ_B, indicating partial reduction. The reduction of these cations along the B-terminated edge results from charge transfer along the B-O-Ti bond, which is established to maintain the oxidation state of the B ions. This is further confirmed by increased Bader charges of 7.7 electrons for those surface O ions that bind to the B sites of the *h*BN ribbon. Along the N-terminated edge, the N ion which does not bind to the surface has a computed Bader charge of 7.1 electrons and a spin magnetisation of 0.6 μ_B, indicating a localised hole state, due to under-coordination. The N and O ions which share a bond each have a Bader charge of 6.8 electrons. These results indicate a considerable reorganisation of charge at the interface; in total, two electrons are transferred from the *h*BN ribbon to the TiO_2 surface.

The relaxed geometry of the second ribbon model, $(BN)_{42}$-a101, is shown **Figure 5.3.5**. Adsorption energies of -15.04 and -14.74 eV are computed within DFT-D2 and vdW-DF, respectively, corresponding to adsorption energies of -0.36 and -0.35 eV per BN unit. Six interfacial bonds are established along each edge of the ribbon (**Figure 5.3.5.a** and **5.3.5.b**). Of these interfacial bonds, six are B-O_{br} bonds with lengths in the range 1.40-1.45 Å. The six Ti-N bonds have lengths of 2.02-2.17 Å. Once again, these bond lengths are elongated by 0.01-0.02 Å, in the vdW-DF set-up.

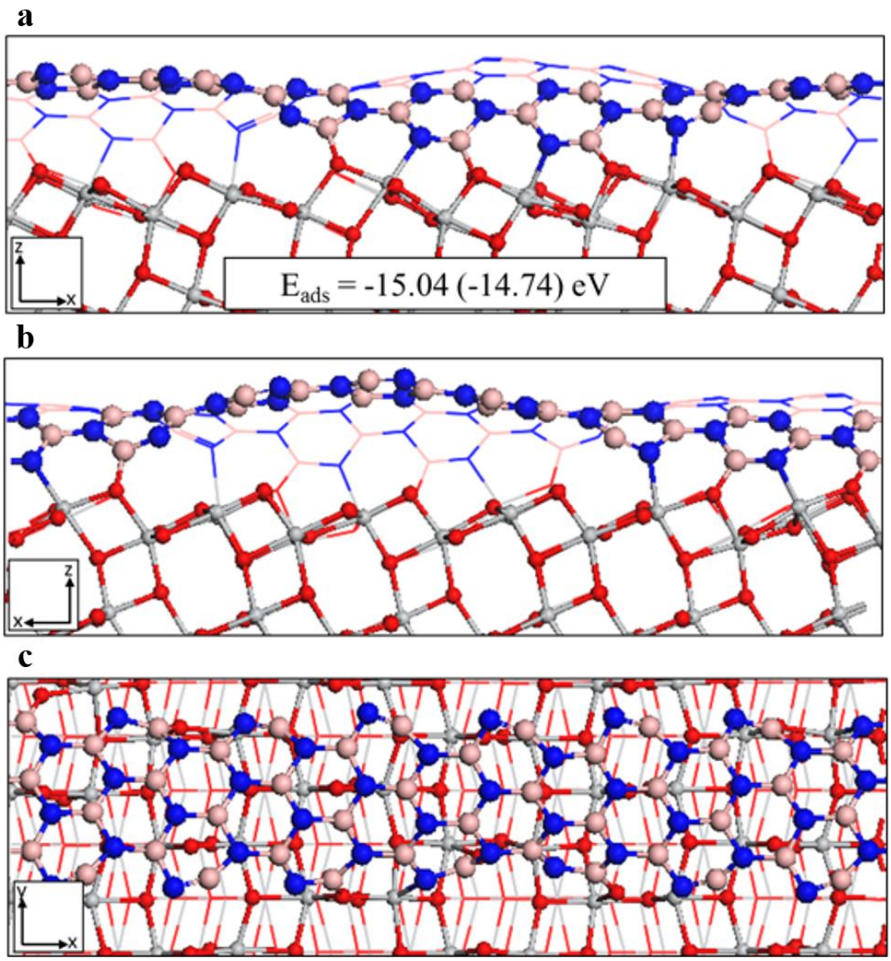

Figure 5.3.5 Relaxed atomic structure of $(BN)_{42}$-a101. Panels **(a)** and **(b)** show the interfacial bonds formed along the edges of the ribbon and panel **(c)** shows a top view of the modified surface. The adsorption energies are included in the inset of the panel **(a)**, as computed *via* DFT-D2 (vdW-DF).

Those ions of the ribbon that bind to the surface neighbour each other along their shared edge, as shown in **Figure 5.3.5.a**, and the ions of the edge opposite this binding site are not bound to the surface. Hence, the ribbon is twisted at the surface in this binding configuration.

For $(BN)_{42}$-a101, there is no interfacial charge transfer, although there is some redistribution of charge. The computed Bader charges for those O_{br} ions which bind to B increase from 7.1 to 7.6 electrons, while the Bader charges for N sites which bind to the surface decrease from 8.0 to 7.5-7.8 electrons. For $(BN)_{42}$-a101, 12 of the 28 edge sites

bind to the surface; this compares with six of eight edge sites binding to the surface in $(BN)_{24}$-a101. This is reflected in the adsorption energies per BN-unit, which are -0.35 and -0.57 eV for $(BN)_{24}$-a101 and $(BN)_{42}$-a101, respectively.

Electronic Properties

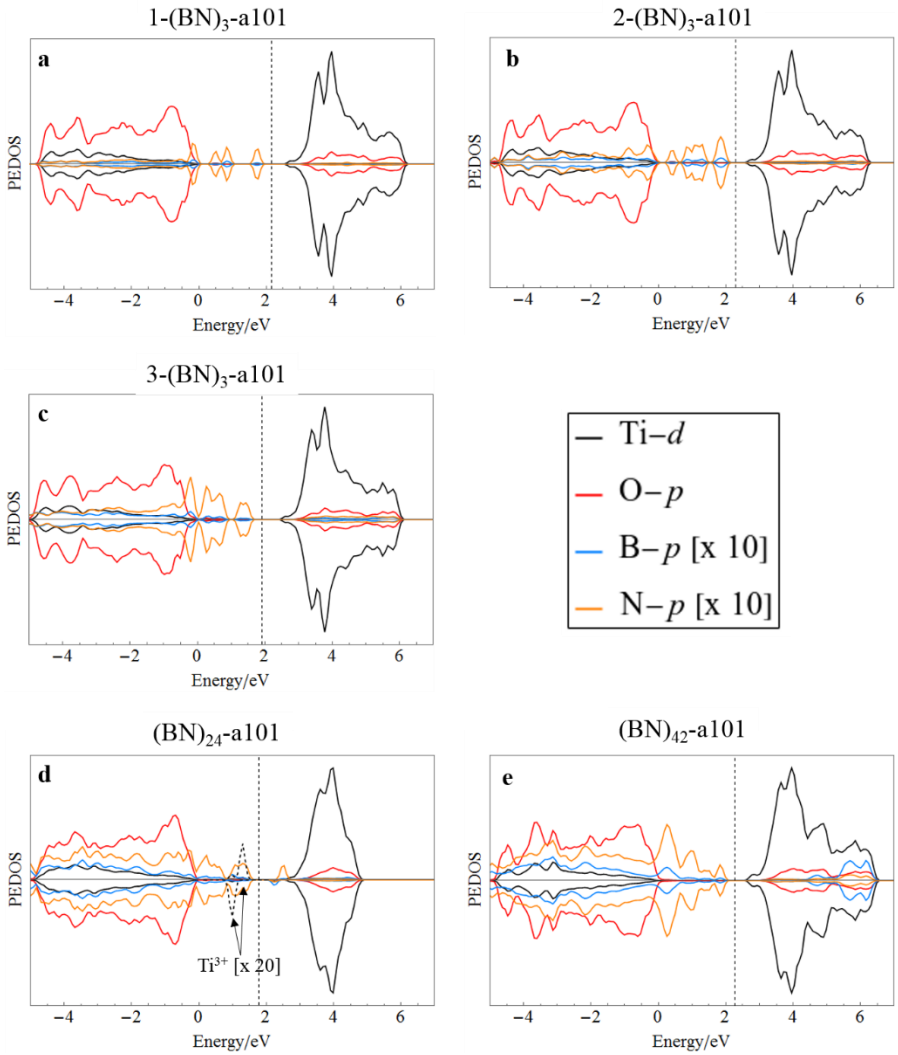

Figure 5.3.6 Computed PEDOS plots for **(a)** 1-$(BN)_3$-a101, **(b)** 2-$(BN)_3$-a101, **(c)** 3-$(BN)_3$-a101, **(d)** $(BN)_{24}$-a101 and **(e)** $(BN)_{42}$-a101. The VBM of the titania support is set to 0 eV.

The computed projected electronic density of states (PEDOS) plots for BN-modified TiO_2 are shown in **Figure 5.3.6**. For 1-$(BN)_3$-a101 (**Figure 5.3.6.a**), N-*p* derived peaks emerge at 0.5, 0.8 and 1.7 eV above the VBM of the titania support. For 2-$(BN)_3$-a101 (**Figure**

5.3.6.b), N-*p* derived peaks emerge at 0.4 and 1.8 eV, with additional peaks extending from 0.8 to 1.3 eV, above the VBM. For 3-$(BN)_3$-a101, shown in **Figure 5.3.6.c**, N-*p* states extend to 1.4 eV above the O-*p* derived VBM.

Figure 5.3.6.d shows the PEDOS for $(BN)_{24}$-a101 and we see that N-*p* states extend to 1.5 eV above the titania VBM. Reduced Ti^{3+} states emerge in the titania energy gap at 1.0 and 1.3 eV above the VBM, as indicated by the dashed peaks in **Figure 5.3.6.d**. In addition, the N ion at which the hole localises, as described previously, contributes an empty state just below the CBM. For $(BN)_{42}$-a101 (**Figure 5.3.6.e**), N-*p* states extend to 1.8 eV above the VBM.

The PEDOS plots computed for *h*BN-modified anatase TiO_2 show that modification has a significant impact on the energy gap. In particular, for the *h*BN ring models, modification enhances the DOS at the VBM while having little or no effect on the titania CBM. For the *h*BN ribbon model, the features of the DOS depend on the nature of the bonds formed at the interface. Under-coordinated B ions will bind to O sites of the surface and transfer charge across the interface, reducing surface Ti ions to Ti^{3+} and these occupied states will emerge in the band gap. Holes localise at low-coordinated N ions and this results in empty states below the titania CBM. Consistent across all models are N-*p* states that extend into the energy gap and we predict that modification of TiO_2 with *h*BN will yield a red-shift in the light absorption edge.

The extent of the impact on the DOS is coverage dependent. At low coverages, N-*p* peaks emerge in the energy gap, as shown in **Figures 5.3.6.a** and **5.3.6.b**, while at higher coverages a continuum of states extend the VBM to higher energies. These features suggest facile charge transfer from the *h*BN modifiers to the TiO_2 support, with consequences for the photocatalytic activity.

Table 5.3.1 Energies computed in the photoexcitation model. Vertical singlet-triplet energy difference ($E^{vertical}$), the relaxed singlet-triplet energy difference (E^{excite}) and the relaxation energy (E^{relax}) for *h*BN-modified anatase (101). Values computed for the unmodified TiO_2 anatase (101) surface have been included for reference.

Composite structure	$E^{vertical}$ (eV)	E^{excite} (eV)	E^{relax} (eV)
Anatase (101)	2.72	2.19	0.53
1-$(BN)_3$-a101	1.63	0.31	1.32
2-$(BN)_3$-a101	1.64	0.51	1.13
3-$(BN)_3$-a101	1.47	0.31	1.17
$(BN)_{42}$-a101	0.98	0.20	0.79

The photoexcitation model is applied only to the *h*BN ring modified surfaces and $(BN)_{42}$-a101, as the accumulation of charge at the interface of $(BN)_{24}$-a101 complicates implementation of the model with this system. Within this model, three energies are computed: the vertical single-triplet energy ($E^{vertical}$); the singlet-triplet energy (E^{excite}); and the relaxation, or trapping energy (E^{relax}). These computed energies are presented in **Table 5.3.1**.

From the values for $E^{vertical}$ in **Table 5.3.1**, it is clear that the underestimation of the band gap, which is inherent in approximate DFT, persists in the current computational setup. Despite these shortcomings, inferences regarding the impact of the modification may be drawn by comparing the energies computed in the photoexcitation model across the different systems and, in particular, with reference to the unmodified anatase (101) surface.[1, 3-4]

The values for $E^{vertical}$ indicate that modification with *h*BN results in a reduction of the optical band gap. This is expected from analysis of the DOS plots, which show N-*p* states

lying higher in energy than O-*p* states of the anatase support, so that the modified energy gap involves transitions from the occupied N-*p* states to the Ti-*d* dominated CBM. Values for $E^{vertical}$ of 1.63 eV, 1.64 eV, 1.47 eV, and 0.98 eV are computed for 1-$(BN)_3$-a101, 2-$(BN)_3$-a101, 3-$(BN)_3$-a101 and $(BN)_{42}$-a101, which can be compared with a computed value of 2.72 eV for the unmodified surface.

In addition to decreases in the values for $E^{vertical}$, the modification also enhances the stability of the photoexcited electrons and holes. The values for E^{excite} between 0.2-0.5 eV indicate that the stability of the triplet electronic state is significantly enhanced with respect to the unmodified surface and suggest a facile transfer of charge across the *h*BN-TiO_2 interface. Further evidence for the stability of the charges is given by the values for E^{relax} which are larger for the ring-modified surfaces by 0.6-0.8 eV and for $(BN)_{42}$-a101 by 0.2 eV, relative to bare anatase (101).

Localisation of electrons and holes is shown in the excess spin density plots in **Figure 5.3.7** for the *h*BN-modified anatase surfaces. For each of the surfaces the electron localises at a surface Ti site; the computed Bader charge increases from 9.6 to 9.9 electrons for Ti in 1-$(BN)_3$-a101, 2-$(BN)_3$-a101 and $(BN)_{42}$-a101, and from 9.7 to 10.0 electrons for 3-$(BN)_3$-a101.

For each system, the spin magnetisation computed for the Ti ion at which the electron localises is 0.9 μ_B. These results correspond to reduction of Ti to Ti^{3+}. The hole predominantly localises at a two-fold coordinated N site for 1-$(BN)_3$-a101 (**Figure 5.3.7.a**), 3-$(BN)_3$-a101 (**Figure 5.3.7.c**) and $(BN)_{42}$-a101 (**Figure 5.3.7.d**). For these sites the Bader charges decrease from 7.8 to 7.1 electrons and the computed spin magnetisations are 0.6 μ_B. For 2-$(BN)_3$-a101 (**Figure 5.3.7.b**), the hole is distributed over

two doubly-coordinated N ions; for these sites the Bader charges decrease from 7.9 to 7.5 electrons and the spin magnetisations are 0.3 μ_B.

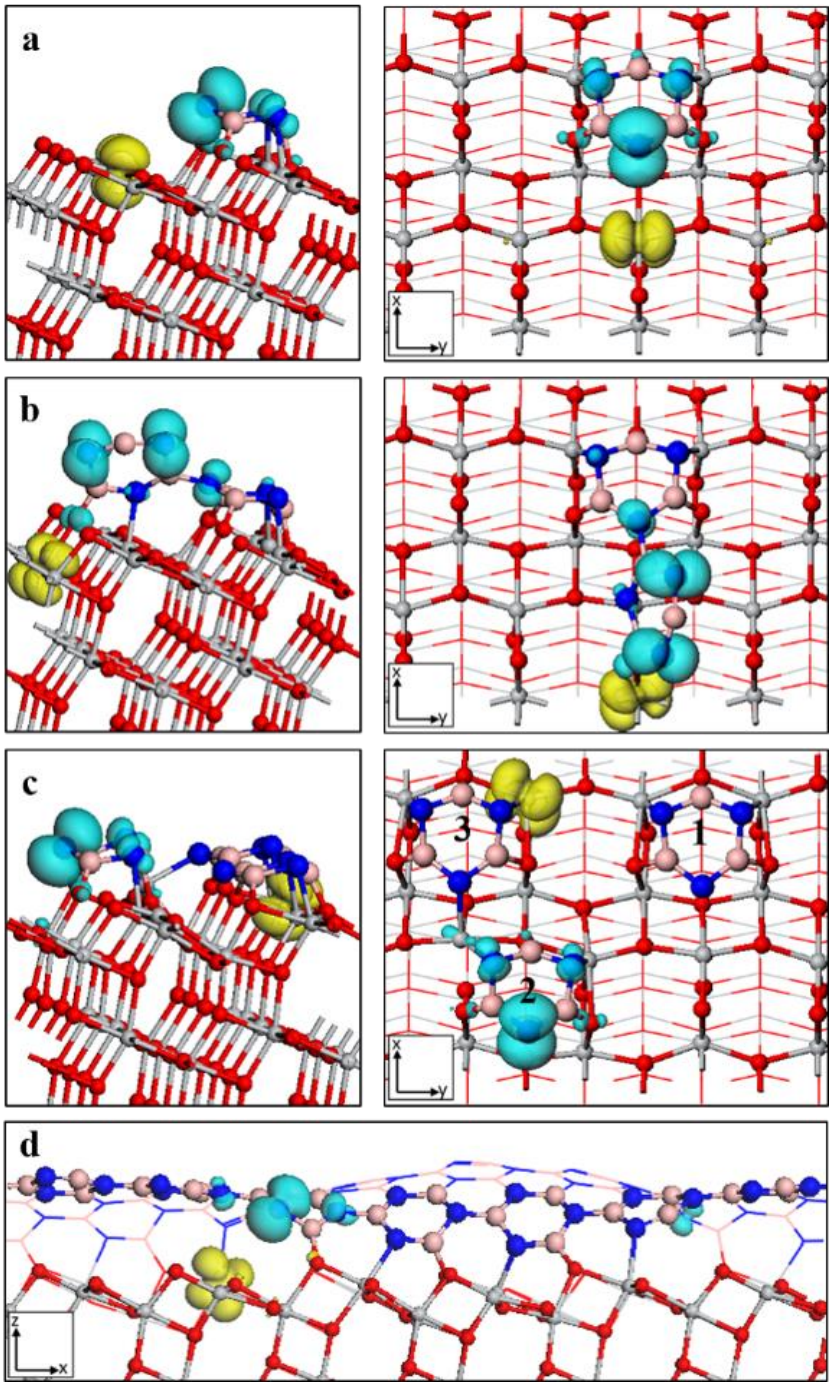

Figure 5.3.7 Excess spin density plots showing the localisation of photoexcited electrons and holes in **(a)** 1-$(BN)_3$-a101, **(b)** 2-$(BN)_3$-a101, **(c)** 3-$(BN)_3$-a101 and **(d)** $(BN)_{42}$-a101. The spin density isosurfaces are yellow for electrons and blue for holes and enclose spin densities of up to 0.02 electrons/$Å^3$.

5.3.3 Discussion

The anatase to rutile transition occurs between 600-700 °C. The BN-TiO_2 samples showed an increased transition temperature when compared with the control (0% BN-TiO_2). The control is 100% rutile from 600 °C, while the modified samples were mixed phased at this temperature and only converted to 100% rutile at 650 °C. In addition to TiO_2 peaks, XRD also showed the presence of hexagonal BN, based on its characteristic peak at 26°. Due to Ti-B or Ti-B-O not being present in the XPS analysis, we conclude that the BN is present on the TiO_2 surface and is not doped within the TiO_2 crystal lattice structure. While DFT calculations suggest the prescence of Ti-N bonds at the interface, XPS analysis did not show the presence of Ti-N peaks.[43]

The photocatalytic activity of the 0% and 16% BN-TiO_2 were evaluated by examining the photocatalytic oxidation of 1, 4-dioxane. The absence of the more photocatalytically active anatase phase after calcination at 700 ºC reduces the catalytic efficiency and the removal rate was not significantly different to that obtained without a catalyst. Unmodified anatase TiO_2, calcined at 500 ºC, removes part of the 1, 4 dioxane after 240 minutes (~60%).

The 16% BN-TiO_2 samples calcined at 500 and 600 °C both showed a significant improvement compared to the unmodified anatase catalyst. The 16% BN-TiO_2 (500 °C) yielded the best removal efficiency, probably due to the higher proportion of the anatase phase (100% versus 65.5% for 16% BN-TiO_2 (600 °C)) and the presence of BN. Although 16% BN-TiO_2 (500 °C) and unmodified TiO_2 (500 °C) consist of 100% anatase phase, with similar particle sizes, the presence of BN clearly enhances the removal efficiency and kinetics. This could be due to the better visible light response of BN-TiO_2 in comparison to unmodified TiO_2.[30, 35] Different authors report that the formation of B-O-

Ti bonding extends the absorption edge from UV to the visible range, which has implications for photocatalytic treatment under solar conditions.[30, 35]

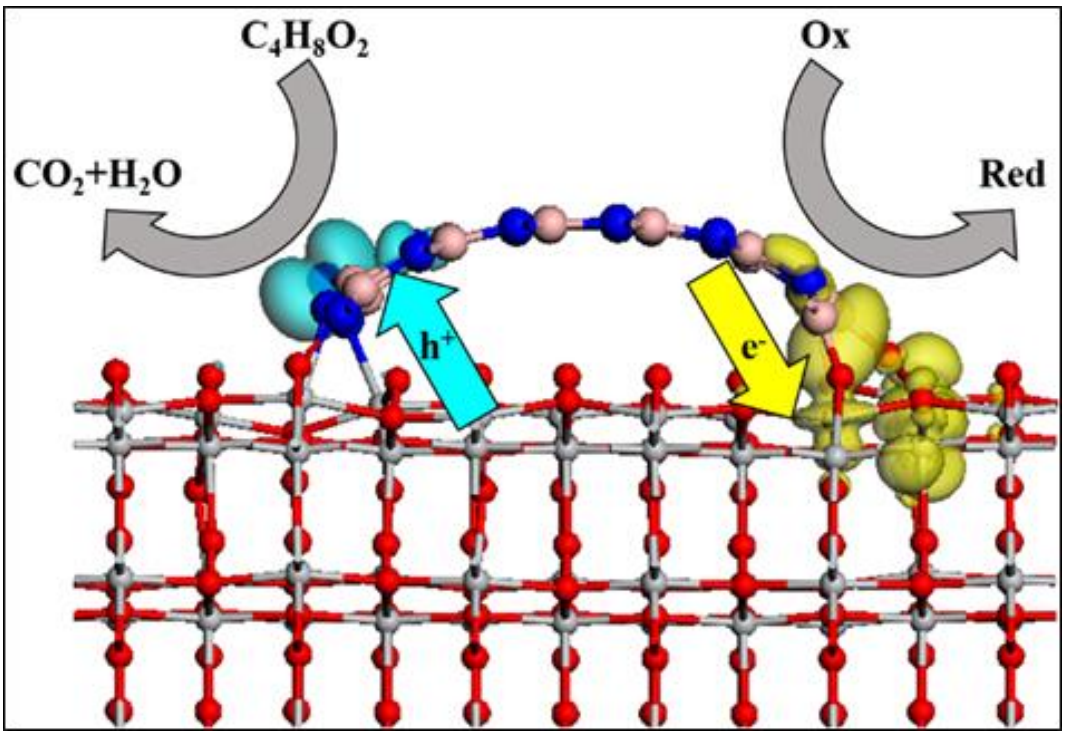

Figure 5.3.8 Proposed photocatalytic mechanism of BN-TiO_2 nanocomposites.

Lui *et al*. and Singh *et al*. propose that the TiO_2 nanoparticles are bonded onto the *h*BN sheets and suggest that this is done *via* a B-O-Ti bond.[30, 35] Sheng e*t al*. further confirmed this during their examination of the BN-TiO_2 nanocomposites for the photocatalytic degradation of Rhodamine B and methylene blue.[34] **Figure 5.3.8** shows the proposed photocatalytic mechanism that occurs between *h*BN and TiO_2. The photogenerated electrons transfer across the B-O-Ti bond from the TiO_2 CB to BN, seen in **Figure 5.3.8**.[30, 35] The electrons are not in a fixed position within the π-π conjugate system of BN.[35] As a result of this, there is a slower rate of recombination of the electron-hole pair. This results in an increased rate of photocatalysis for TiO_2.[35]

5.4 CeO_x-modified TiO_2

What follows is adapted from an article entitled: "***CO_2 and Water Activation on Ceria Nanocluster Modified TiO_2 Rutile (110)***", published in the Journal of Materials Chemistry A.[3]

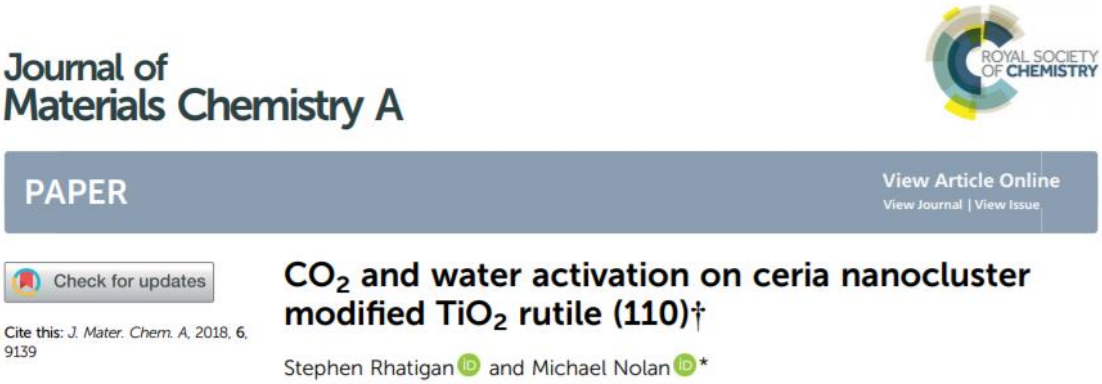

DOI: https://doi.org/10.1039/C8TA01270A

https://cora.ucc.ie/handle/10468/6042

Note: Despite the title of this article, and in the interests of brevity and remaining on topic with the rest of this thesis, results pertaining to CO_2 activation are omitted from this section.

5.4.1 Introduction

In this paper, we present a DFT study of heterostructures of TiO_2 rutile (110) modified with sub-nm nanoclusters of CeO_2. The clusters have compositions Ce_5O_{10} and Ce_6O_{12} and complement earlier work on Ce_2O_3 reduced nanoclusters supported on rutile (110).[44-46] Ceria is an interesting modifier as Ce 4*f* states are crucial in optical properties, reducibility and reactivity.[47-48] The facile conversion between Ce^{4+} and Ce^{3+} oxidation

states has important implications for catalytic performance and metal/CeO_x/TiO_2 composites with Ce^{3+} cations display enhanced activity for the water gas shift (WGS) reaction.[44-46, 49]

5.4.2 Results

Stoichiometric CeO_2-modified TiO_2 structures

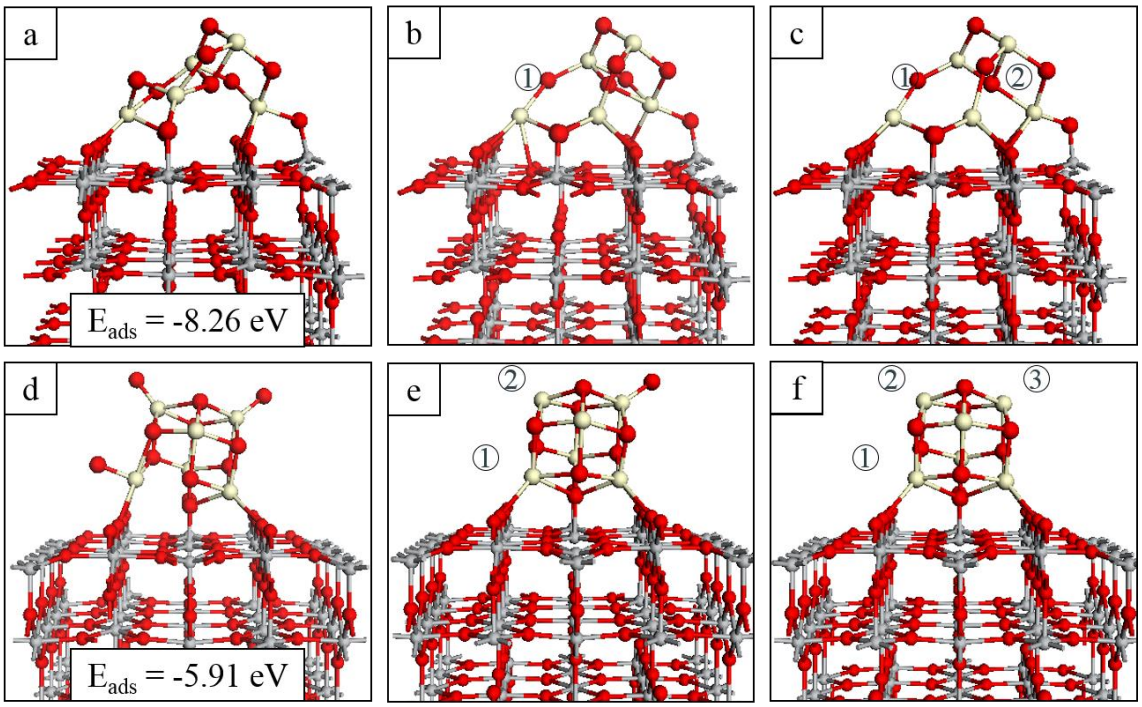

Figure 5.4.1 Top panels show the relaxed atomic structure of the Ce_5O_{10}-rutile-(110) composite in **(a)** stoichiometric form and after the formation of **(b)** one (ground state) and **(c)** two (reduced state) oxygen vacancies. Bottom panels show the atomic structure of the Ce_6O_{12}-rutile-(110) composite in **(d)** stoichiometric form and after the formation of **(e)** two (ground state) and **(f)** three (reduced state) oxygen vacancies. Insets of the left panels show the adsorption energies of the stoichiometric nanoclusters. The numbers in the black circles indicate the order in which oxygen atoms are removed from the nanocluster and are consistent with **Table 5.3.1**. In this and subsequent figures, Ti is indicated by a grey sphere, O by a red sphere and Ce by a cream sphere.

We focus on ceria nanoclusters of two compositions, Ce_5O_{10} and Ce_6O_{12}, and we first examine the stoichiometric nanocluster adsorption energies and structures shown in **Figures 5.4.1.a** and **5.4.1.d**. The adsorption energies are -8.26 eV for Ce_5O_{10} and -5.91 eV for Ce_6O_{12} adsorption on rutile (110). The negative adsorption energies show that adsorption is favourable, with the magnitude of the energy indicating the strength of the interaction. From the adsorption energies we expect the nanoclusters to be stable at the surface without desorbing or migrating over the surface to form aggregates. Henceforth, the composites will be denoted as Ce_5O_x-rutile-(110) and Ce_6O_x-rutile-(110), where the subscript x will vary according to the stoichiometry. Oxygen atoms of the surface and nanocluster are denoted O_S and O_C, respectively.

In the Ce_5O_{10}-rutile-(110) composite (**Figure 5.4.1.a**), two Ce ions are coordinated to four O_C atoms; three Ce cations are five-fold coordinated and form interfacial bonds with bridging O_S ions with Ce-O distances of 2.3-2.4 Å. Each O_C ion is two-fold coordinated with the exception of one at the centre of the cluster which coordinates to three cluster cations. Three O_C ions bind to surface Ti ions with Ti-O_C distances of 1.8-2.0 Å.

For Ce_6O_{12}-rutile-(110) (**Figure 5.4.1.d**), five Ce are five-fold coordinated with one four-fold coordinated Ce cation. Two cluster Ce each bind to two bridging O_S with Ce-O distances of 2.4-2.6 Å. The O_C ions bind to three metal cations with the exception of three terminal O_C, which are singly coordinated to Ce ions. Ce-O distances involving singly coordinated O_C ions are 1.9 Å and compare with typical Ce-O distances in the range of 2.1-2.6 Å for the other O_C atoms. Two O_C each form a single interfacial bond with surface titanium ions, with Ti-O_C distances of 1.8 Å and 1.9 Å.

The interfacial bonding between the nanocluster and the surface results in an appreciable distortion of the local atomic structure at the surface. Where a bridging O_S is bound to a

nanocluster cation, the Ti-O_S bond is elongated by up to 10% compared with a typical unmodified bond length of 1.88 Å. Ti atoms that bind with O_C migrate out of the surface plane towards the cluster by as much as 0.92 Å, increasing the subsurface Ti-O distance.

Reduction of CeO_2-rutile by oxygen vacancy formation.

Table 5.4.1 Computed oxygen vacancy formation energies in CeO_2-rutile composites. The listed values correspond to the most favourable configuration after removal of one, two or three oxygen atoms in the cluster and correspond to the numbering in **Figure 5.4.1**.

Reaction	**Oxygen vacancy**	**Formation energy (eV)**
$Ce_5O_{10} \rightarrow Ce_5O_9$	$E_{vac,1}$	+0.02
$Ce_5O_9 \rightarrow Ce_5O_8$	$E_{vac,2}$	+1.33
$Ce_6O_{12} \rightarrow Ce_6O_{11}$	$E_{vac,1}$	-0.26
$Ce_6O_{11} \rightarrow Ce_6O_{10}$	$E_{vac,2}$	-0.62
$Ce_6O_{10} \rightarrow Ce_6O_9$	$E_{vac,3}$	+0.31

From the relaxed, stoichiometric nanocluster-surface composites, we remove O_C ions and compute the corresponding vacancy formation energies. Previous work on small CeO_2 structures on rutile (110) has shown that these prefer to be reduced, with loss of oxygen in the ground state, giving composition Ce_2O_3.[46-47] It is not known if a similar composition would be found for larger but still sub-nm ceria clusters. The oxygen vacancy formation energies are important as their stability determines the stoichiometry of the composite. If the composite is then reduced, the formation energy can be a further important factor in determining if feedstock species will interact with the CeO_x-rutile composites. If the energy cost to form a reducing vacancy is low, the system favours non-stoichiometry and fixation and activation of molecular species, *via* a redox or Mars van Krevelen process,

may not occur and no reactions can take place. Conversely, while large vacancy formation energies can promote reoxidation *via* feedstock reduction, these require a large initial energy input and may also result in too strong interaction with molecular species, leading to poisoning of the surface.

Table 5.4.1 presents the most favourable computed oxygen vacancy formation energies in each supported ceria nanocluster; a full set of vacancy formation energies is presented in **Table B.3.1** in **Appendix B**. The most stable oxygen vacancy in Ce_5O_{10}-rutile-(110), which forms Ce_5O_9-rutile-(110), has a small cost of +0.02 eV so that the ground state is off-stoichiometric. For a second oxygen vacancy, to give Ce_5O_8-rutile-(110), the most stable vacancy site has an energy cost of +1.33 eV, relative to Ce_5O_9-rutile-(110). Thus the second oxygen vacancy is the reducing oxygen vacancy and this has a moderate cost.

For Ce_6O_{12}-rutile-(110), the first two oxygen vacancies have negative formation energies, of -0.26 eV and -0.62 eV, and will form spontaneously at T = 0 K; the ground state is highly off-stoichiometric, with composition Ce_6O_{10}-rutile-(110). This instability of the stoichiometric composite sheds light on the small adsorption energy of Ce_6O_{12} relative to Ce_5O_{10}. The energy cost required to produce the most stable third oxygen vacancy, giving Ce_6O_9-rutile-(110), is +0.31 eV. This cost is moderate and we consider the Ce_6O_9-rutile-(110) composite as being in a reduced state. Thus, for rutile modified by a sub-nm ceria nanocluster, we expect a highly non-stoichiometric system with multiple potential activation sites at moderate temperatures, consistent with the work of Graciani *et al.*[47]

Figure 5.4.1 shows the atomic structures of the non-stoichiometric ground state (**5.4.1.b** and **5.4.1.e**) and reduced (**5.4.1.c** and **5.4.1.f**) nanocluster-surface composites; black circles in the images indicate the site number of the removed oxygen, corresponding to **Table 5.4.1**.

After formation of the first oxygen vacancy in Ce_5O_{10}-rutile-(110), the two Ce ions which were bound to this oxygen maintain their coordination by binding to O_S atoms (**Figure 5.4.1.b**). In total, three new nanocluster-surface bonds are formed, two involving bridging O_S and the third involving an in-plane O_S, which migrates out from the surface by 0.1 Å. One Ce-O_S bond is broken during the relaxation; the coordination of the Ce is maintained by binding to the central O_C atom with the latter now four-fold coordinated. After formation of the second vacancy, yielding Ce_5O_8-rutile-(110) (**Figure 5.4.1.c**), one Ce ion is three-fold coordinated, while the remaining Ce are four- and five-fold coordinated. In both the ground state, with one O vacancy, and the reduced composite, with two O vacancies, there are nine interfacial bonds, up from seven in the stoichiometric Ce_5O_{10}-rutile-(110) composite.

For Ce_6O_{12}-rutile-(110), the formation of oxygen vacancies to produce the ground state, Ce_6O_{10}-rutile-(110) (**Figure 5.4.1.e**), and reduced, Ce_6O_9-rutile-(110) (**Figure 5.4.1.f**), composites has no impact on the number of interfacial bonds. However, the Ce ions to which the removed terminal O atoms were bound relax towards the nanocluster, increasing their coordination by binding to other O_C atoms.

In these non-stoichiometric nanocluster-surface composites we expect to find two electrons released for each neutral oxygen vacancy and spin density plots are used to determine the location of the electrons after relaxation. Spin density plots for the ground and reduced states of CeO_x-rutile are presented in **Figure 5.4.2**. Electron localisation occurs at Ce atoms in each nanocluster, which results in the formation of reduced Ce^{3+} cations. Ce^{3+} form in preference to Ti^{3+} cations, as also reported in DFT+U studies of Ce-doped TiO_2[50-52] and some surfaces.[44-45]

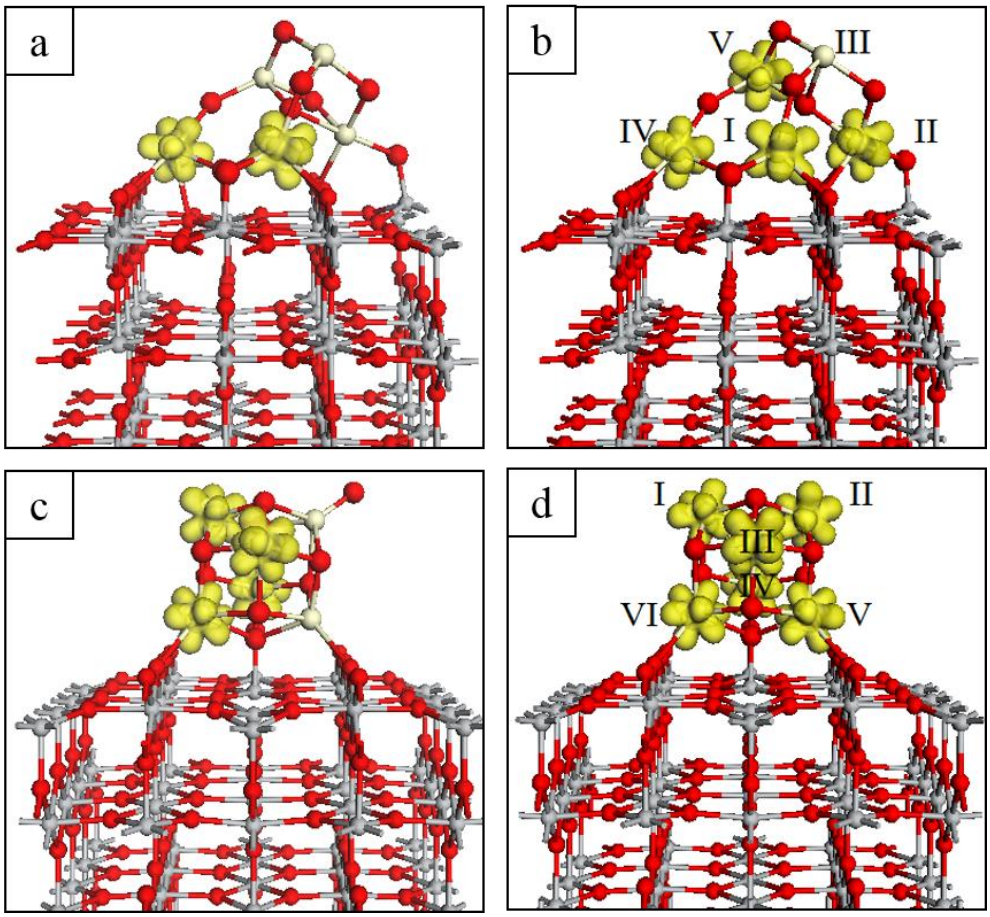

Figure 5.4.2 Excess spin density plots for Ce_5O_{10}-modified rutile (110) with **(a)** one (ground state) and **(b)** two (reduced) oxygen vacancies and Ce_6O_{12}-modified rutile (110) with **(c)** two (ground state) and **(d)** three (reduced) oxygen vacancies. The spin density isosurfaces are yellow and enclose spin densities of up to 0.2 electrons/$Å^3$. The roman numerals in the panels on the right hand side correspond with the labelling in **Table** 5**.4.2**.

For the non-stoichiometric ground states, with compositions Ce_5O_9-rutile-(110) and Ce_6O_{10}-rutile-(110), two and four Ce atoms are reduced as shown in **Figures 5.4.2.a** and **5.4.2.c**. When the composites are reduced, giving compositions Ce_5O_8-rutile-(110) (**Figure 5.4.2.b**) and Ce_6O_9-rutile-(110) (**Figure 5.4.2.d**), four and six Ce atoms are reduced respectively.

Table 5.4.2 Computed Bader charges for the cerium ions in the supported nanoclusters before and after formation of one or more oxygen vacancies. Superscripts [a], [b], and [c] denote the stoichiometric, off-stoichiometric ground state, and reduced nanocluster-surface composites respectively. Reduced Ce^{3+} are highlighted in bold.

	$^{a}Ce_5O_{10}$	$^{b}Ce_5O_9$	$^{c}Ce_5O_8$		$^{a}Ce_6O_{12}$	$^{b}Ce_6O_{10}$	$^{c}Ce_6O_9$
Ce_I	9.6	**9.9**	**9.9**	Ce_I	9.7	**10.0**	**10.0**
Ce_{II}	9.6	9.6	**9.9**	Ce_{II}	9.7	9.8	**10.0**
Ce_{III}	9.8	9.8	9.8	Ce_{III}	9.8	**10.0**	**10.0**
Ce_{IV}	9.7	**9.9**	**9.9**	Ce_{IV}	9.7	**9.9**	**9.9**
Ce_V	9.7	9.7	**10.0**	Ce_V	9.7	9.7	**9.9**
				Ce_{VI}	9.7	**9.9**	**9.9**

These results are confirmed through Bader charge analysis, shown in **Table 5.4.2**. Typical net atomic charge values for Ce^{4+} ions are in the range of 9.6 to 9.8 electrons for the stoichiometric nanoclusters. Upon oxygen vacancy formation and the subsequent localisation of excess spin on Ce atoms, the net atomic charges increase by 0.2 electrons for reduced cations; this is typical for $Ce^{4+} \rightarrow Ce^{3+}$ reduction.[50] The computed spin magnetisations for reduced Ce^{3+} cations are 0.97-0.98 μ_B.

In general, Ce-O distances involving Ce^{3+} species are elongated by 0.1-0.2 Å due to the larger ionic radius of Ce^{3+} compared to Ce^{4+}; this effect is less strong in cases where the reduced Ce ions have a lower coordination or where the Ce ion was previously bound to a singly coordinated O atom. See **Table B.3.2** in **Appendix B** for details of the Ce-O distances in each case.

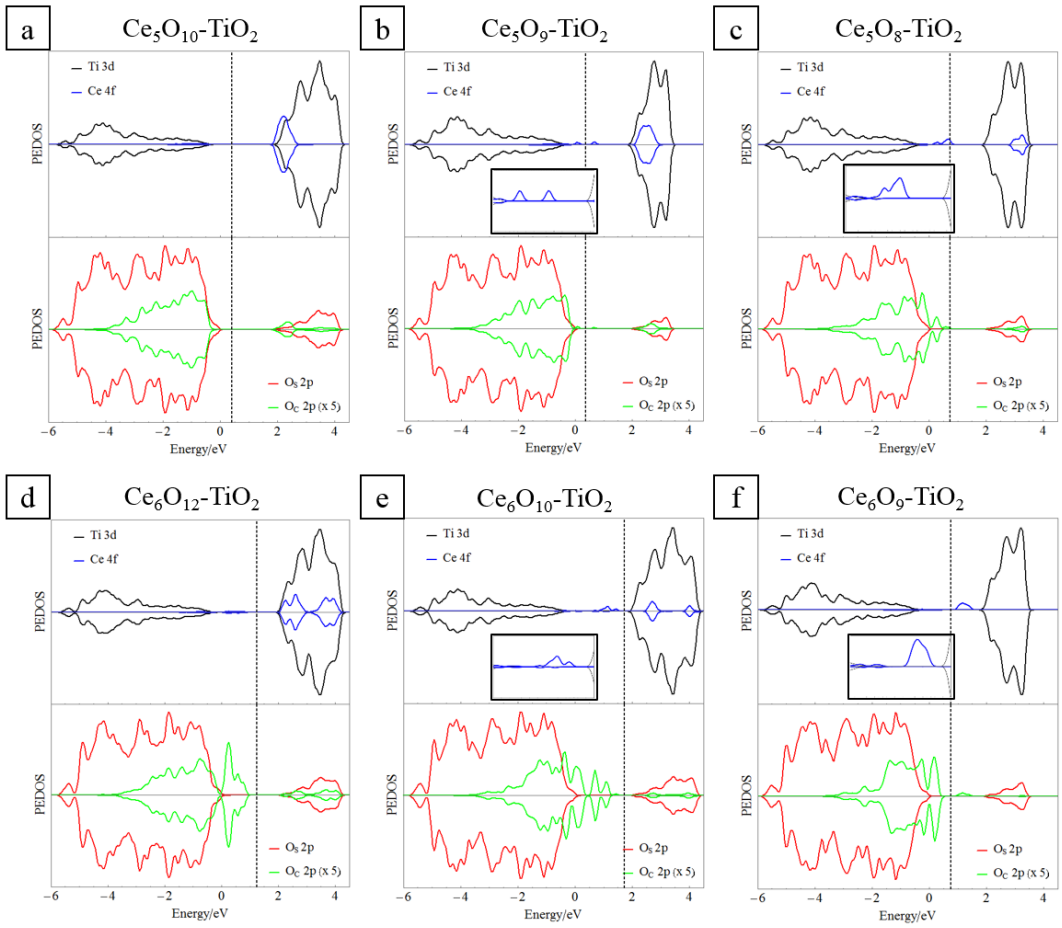

Figure 5.4.3 Spin polarised projected electron density of states (PEDOS) for **(a)** Ce_5O_{10}-, **(b)** Ce_5O_9-, **(c)** Ce_5O_8-, **(d)** Ce_6O_{12}-, **(e)** Ce_6O_{10}- and **(f)** Ce_6O_9-rutile-(110). The top half of each panel displays Ti 3*d*- and Ce 4*f*-derived states. Bottom halves of the panels display contributions to the DOS from surface (O_S) and nanocluster (O_C) oxygen 2*p*-derived states. Insets in the top panels show the mid-gap Ce-derived states in the range [-0.25 eV, + 2.25 eV].

The spin polarised projected electronic density of states (PEDOS) for the stoichiometric, off-stoichiometric ground state and reduced nanocluster-surface composites are presented in **Figure 5.4.3**. **Figures 5.4.3.a** and **5.4.3.d** show the stoichiometric configurations, where the most obvious feature is the presence of states at the top of the VB for the Ce_6O_{12} nanocluster. These states are due to singly coordinated O_C ions (see **Figure 5.4.1.d**). However, nanocluster-derived oxygen 2*p* states above the TiO_2 VB persist even after

removing these oxygen ions. In **Figures 5.4.3.b**, **5.4.3.c**, **5.4.3.e** and **5.4.3.f**, which correspond to the off-stoichiometric CeO_x-rutile composites, new states emerge in the TiO_2-derived band gap, due to the singly occupied $4f^1$ orbital configuration of reduced Ce^{3+} cations in the oxygen deficient nanoclusters. Modification of rutile with CeO_x nanoclusters will result in a red shift of the TiO_2 adsorption edge; this is due to a combination of 2*p* states of low coordinated O_C sites pushing the VBM to higher energy and the emergence of mid-gap states associated with reduced Ce^{3+} ions in the off-stoichiometric composites. Absorption spectra were computed for unmodified rutile (110) and for the ground state composites, Ce_5O_9- and Ce_6O_{10}-rutile-(110) and are shown in **Figure B.3.2** of **Appendix B**. The results show a red shift in the adsorption edge due to modification and corroborate the analysis of the DOS plots.

Photoexcitation Model

We apply the photoexcited model to the ground state systems, Ce_5O_9-rutile-(110) and Ce_6O_{10}-rutile-(110). **Table 5.4.3** presents the computed vertical, singlet-triplet and the electron-hole localisation (relaxation) energies, as discussed in **Chapter 2**. Comparison of these computed energies across different structures yields useful qualitative information about the effect of surface modification. In particular, a reduction in $E^{vertical}$ for a composite structure relative to the unmodified metal oxide will correspond to a red shift in light absorption for the surface modified system.

We note that E^{excite} is always smaller than $E^{vertical}$ and the simple VB-CB energy difference, as the former includes ionic relaxations and polaron formation in response to "exciting" the electron, which stabilise the triplet electronic state. The energies presented in **Table 5.4.3** show that modification of rutile (110) with CeO_2 nanoclusters leads to a

red shift in light absorption, whether we consider the vertical or excitation energies. This effect is stronger for the larger nanocluster, consistent with the PEDOS. Relaxation energies of 0.8 eV upon charge localisation in each heterostructure indicate high stability of the photogenerated electron-hole pairs.

Table 5.4.3 Vertical singlet-triplet energy difference ($E^{vertical}$), the relaxed singlet-triplet energy difference (E^{excite}) and the relaxation energy (E^{relax}) for nanocluster rutile (110). Values for unmodified rutile (110) have been included for reference.

Composite structure	**$E^{vertical}$ (eV)**	**E^{excite} (eV)**	**E^{relax} (eV)**
Bare-rutile (110)	2.02	1.97	0.05
Ce_5O_9-rutile (110)	1.76	0.96	0.80
Ce_6O_{10}-rutile (110)	1.30	0.51	0.80

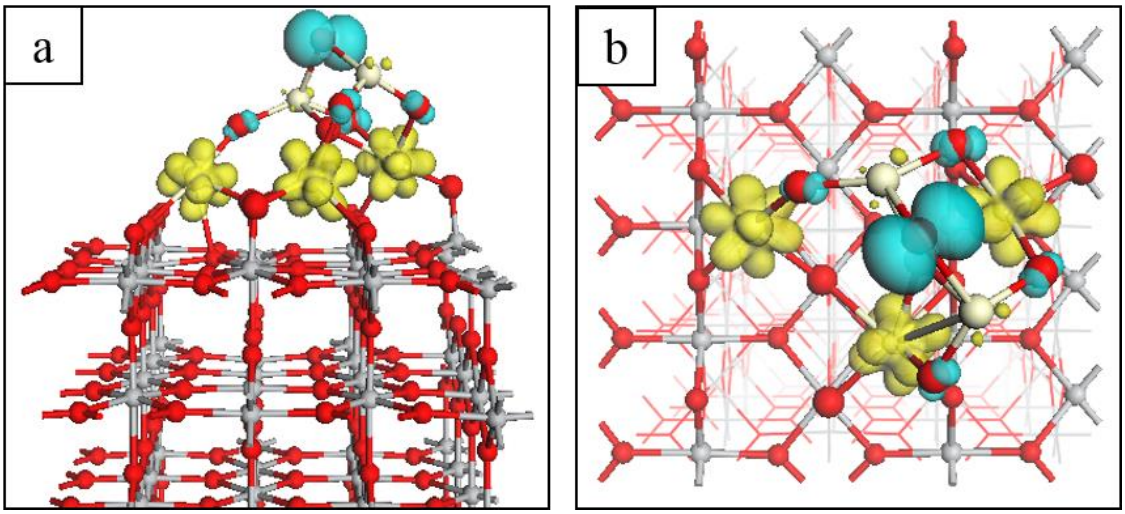

Figure 5.4.4 Spin density plots for the photoexcited electron and hole in Ce_5O_9-rutile-(110) for **(a)** side and **(b)** top view. The spin density isosurfaces are yellow for electrons and blue for holes and enclose spin densities of up to 0.02 electrons/$Å^3$.

We can also examine the localisation of the electron-hole pair through analysis of computed Bader charges, spin magnetisations and excess spin density plots. **Figure 5.4.4** shows the spin density plots for Ce_5O_9-rutile-(110) after relaxation of the triplet state; electrons are shown in yellow and holes in blue. Spin density plots and analysis for the excited state model applied to Ce_6O_{10}-rutile-(110) can be found in **Section B.3** of **Appendix B**.

Since the modifier is off-stoichiometric in the ground state, reduced Ce^{3+} ions are present prior to imposing the excited state. For Ce_5O_9-rutile-(110), shown in **Figure 5.4.4**, there are three unpaired electrons; two are due to the neutral oxygen vacancy and are localised at Ce_I and Ce_{IV} (compare with **Figure 5.4.2.a**). The third electron is the photoexcited electron and is localised on Ce_{II}; this Ce ion, which was five-fold coordinated in the ground state, is four-fold coordinated after localisation of the photoexcited electron and the Ce-O bonds are elongated by as much as 10%. Electron localisation at the Ce ion increases the computed Bader charge by 0.2 electrons, similar to the trend presented in **Table 5.4.2**, and the computed spin magnetisations are 0.97 μ_B.

The hole predominantly localises on a single, low-coordinated O_C site, shown in blue in **Figure 5.4.4**. For Ce_5O_9-rutile-(110), the oxygen site at which the hole predominantly localises is two-fold coordinated both before and after photoexcitation; the Ce-O distances increase from 2.1 Å in the ground state to 2.4 Å in the excited state. Hole localisation is accompanied by a change in the computed Bader charge of the oxygen ion from 7.1 to 6.7 electrons. There is some spreading of the hole to neighbouring two-fold coordinated O_C sites. This is accompanied by changes of <0.1 electrons in the computed Bader charges; we can conclude the hole predominantly localises on one O_C site. This is confirmed by a computed spin magnetisation of 0.73 μ_B for the oxygen hole on Ce_5O_9-rutile-(110).

For the CeO_x-rutile-(110) composites, both the electron and hole localise on the nanocluster modifiers, which may have consequences for recombination. However, the spatial separation of the charges is maximal (see **Figures 5.4.4** and **B.3.3**), given that both electrons and holes localise at nanocluster sites. In addition, the large relaxation or trapping energies act to impede migration of the charges and thus the impact on recombination should be minor. We note that this photoexcited model, which imposes a triplet state to induce a transition from the VB to the CB, precludes transitions from the highest occupied, Ce 4*f*-derived states of the off-stoichiometric ground states (see **Figures 5.4.3.b** and **5.4.3.e**). Such transitions amount to electron hopping between Ce sites of the nanocluster with no change in electronic configuration after "excitation". Rather, our model with a triplet electronic state (in addition to the unpaired electrons on reduced Ce^{3+}) will induce transitions from O_C 2*p*-derived states, which sit at the top of the titania-derived VB, to the unoccupied Ce 4*f* states.

5.5 *MnO_x-modified TiO_2*

What follows is adapted from an article entitled: "***Activation of water on MnO_x-nanocluster-modified rutile (110) and anatase (101) TiO_2 and the role of cation reduction***", published in Frontiers in Chemistry.[4]

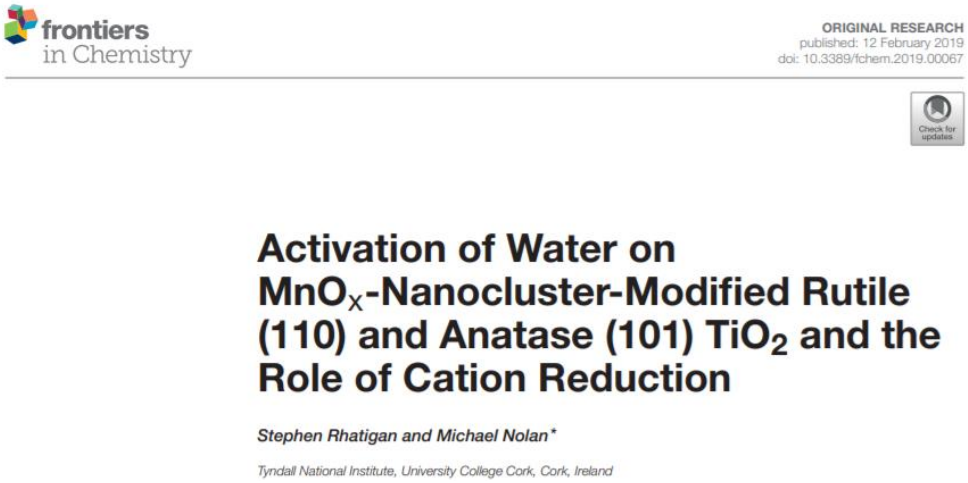

DOI: https://doi.org/10.3389/fchem.2019.00067

https://cora.ucc.ie/handle/10468/8827

5.5.1 Introduction

In this study, we examine the photocatalytic properties of manganese oxide modified TiO_2, using model systems of Mn_4O_6-nanoclusters modifying the rutile (110) and anatase (101) surfaces and consider the role of partial surface hydroxylation in the interfacial chemistry.

MnO_x is an interesting modifier as manganese is a multi-valent, reducible element, which crystallises in oxides with a variety of oxidation states;[53] this will have implications for the light absorption properties and reducibility of sub-nm nanoclusters of MnO_x dispersed

at the titania surfaces. We have previously studied similar systems of MnO_x-modified TiO_2, in collaboration with experiment, to interrogate their activity for CO_2 capture and reduction.[17]

We investigate the impact of surface hydroxylation on the reduction of the heterostructures *via* oxygen vacancy formation and apply a model for photoexcitation to examine the associated energetics and charge localisation. In ref. [17], the Mn_4O_6-TiO_2 composites were found to be stoichiometric in the ground state for both modified rutile and anatase, albeit with moderate costs to produce reducing oxygen vacancies (+0.59 eV for rutile and +1.1 eV for anatase). However, the impact of surface hydroxyls on the formation of oxygen vacancies was not investigated; in this paper we show that vacancy formation is promoted with hydroxyls already present at the TiO_2 surfaces. The photoexcited state model, which examines localisation of electrons and holes at nanocluster metal and oxygen sites, sheds light on experimental observations, which suggest that the MnO_x-modifiers may facilitate recombination.[17] In addition, active oxygen vacancy sites play a crucial role in the subsequent interaction of water molecules and their adsorption modes, which will be discussed in **Chapter 6**. In particular, dissociation is favoured for the reduced systems; this is an important step in the water oxidation reaction.

5.5.2 Results

Stoichiometric Mn_4O_6-modified TiO_2 OH-rutile (110) and OH-anatase (101).

To model surface hydroxylation (before the nanoclusters are adsorbed) and the impact on the heterostructure chemistry, four water molecules are dissociatively adsorbed at the clean rutile (110) and anatase (101) surfaces, which gives a partial coverage of 50%. The

computed energy gain when the TiO_2 surfaces are hydroxylated at half coverage is -1.03 eV per water molecule for rutile (110) and -0.80 eV for anatase (101), referenced to the total energy of four gas phase water molecules. These indicate favourable water adsorption and surface hydroxylation and these models have been used in our previous studies.[16-17, 54-55] The nature of water molecules adsorbed at metal oxide surfaces, and in particular TiO_2 surfaces, is widely investigated both experimentally and computationally [54-56] and readers are referred to ref.[57] for a review of the state of the art.

These models are representative of hydroxylated rutile and anatase surfaces and we are not attempting to describe the most stable solutions for water or dissociative water adsorption at these titania surfaces.[16, 54-55] The hydroxylated surfaces are denoted by OH-r110 and OH-a101. Oxygen atoms of the surface, cluster and surface bound hydroxyls are denoted O_S, O_C and O_{OH}, respectively, and similar notation is adopted for OH groups. For the interaction of water with the modified surfaces, water-derived oxygen and hydroxyls are denoted O_W and OH_W.

Figures 5.5.1.a and **5.5.1.b** show the adsorption energies and relaxed atomic structures of the stoichiometric Mn_4O_6-nanocluster modifying the OH-r110 and OH-a101 surfaces. The large, negative adsorption energies indicate that the nanocluster-surface interaction is favourable and that the nanoclusters will be stable against desorption and aggregation.[3, 54-55, 58-60] For Mn_4O_6-OH-r110 (**Figure 5.5.1.a**), three Mn ions are four-fold coordinated and to each of these is bound a terminal OH. Of these OH groups, one has migrated from a Ti site in the rutile surface to an Mn ion of the cluster (OH_{OH}) and two OH groups result from the migration of hydrogen from surface hydroxyls to O_C atoms (OH_C). The fourth Mn ion is five-fold coordinated and is bound to three O_C and two O_S ions (one bridging O_S and one in-plane O_S). Five O ions of the OH-r110 surface bind with Mn of the nanocluster (three O_S and two O_{OH}) and two O_C ions bind to Ti of the surface. Mn-O

distances are in the range 1.8-2.1 Å; the shorter distances involve two-fold coordinated O ions and for Mn bound to the in-plane O_S ion the Mn-O distance is 2.2 Å. Ti ions which bind to the nanocluster migrate out from the surface by 0.1 Å, however, distortions to the geometry of the rutile (110) surface are minimal.

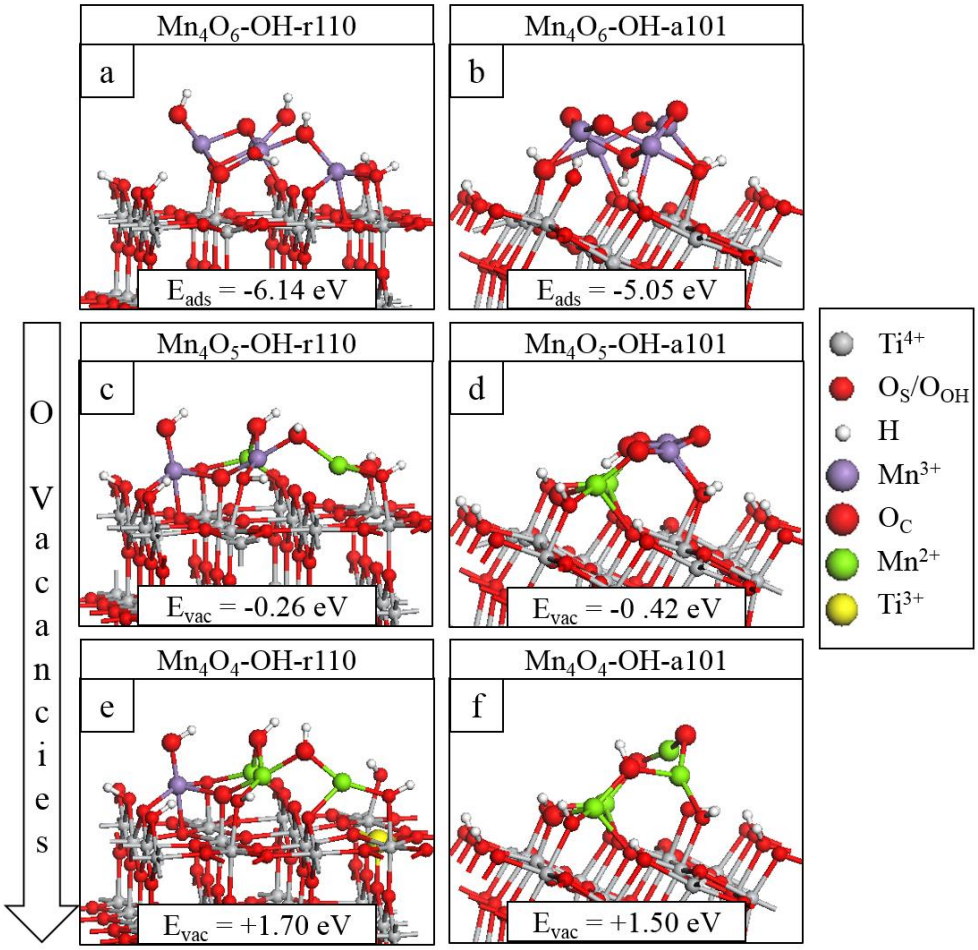

Figure 5.5.1 Relaxed atomic structures of Mn_4O_x modifying the hydroxylated titania surfaces. The stoichiometric composites are shown in **(a)** for Mn_4O_6-OH-r110 and **(b)** for Mn_4O_6-OH-a101; the nanocluster adsorption energies are included in the inset. The atomic structures after formation of the most stable single O_V are shown in panels **(c)** for Mn_4O_5-OH-r110 and **(d)** for Mn_4O_5-OH-a101. The atomic structures of the most stable composites with two O_V are shown in panels **(e)** for Mn_4O_4-OH-r110 and **(f)** for Mn_4O_4-OH-a101. The energy costs to produce O_V are included and computed relative to the structure with one less O_V. Atomic species and oxidation states are indicated by the colours in the legend on the right hand side.

For Mn_4O_6-OH-a101 (**Figure 5.5.1b**), three Mn ions are four-fold coordinated and one Mn is five-fold coordinated. Five O_C sites are two-fold coordinated with one O_C ion binding to three Mn ions and a H atom which has migrated from a bridging O_S site. Of the six interfacial bonds between the Mn_4O_6 nanocluster and OH-a101, three involve Mn and OH_{OH} groups; two involve Mn and bridging O_S sites and the sixth is a Ti-O_C bond. Mn-O distances are in the range 1.7-2.1 Å.

For Mn_4O_6 adsorbed at OH-r110 and OH-a101, the computed Bader charge for each of the Mn ions is 11.3 electrons, which is typical of Mn^{3+} ions (see **Table 5.5.1**).[17] The spin magnetisations for these sites are each 3.9 μ_B, which reflects the $3d^4$ configuration of the Mn^{3+} ion.

Table 5.5.1 Computed Bader charges for the manganese ions in the supported nanoclusters, before and after formation of one or more O_V. Also included are Bader charges for titanium ions of the support which are reduced after vacancy formation. Reduced Mn^{2+} and Ti^{3+} are highlighted in bold.

Surface	OH-r110				OH-a101		
Modifier	Mn_4O_6	Mn_4O_5	Mn_4O_4		Mn_4O_6	Mn_4O_5	Mn_4O_4
Mn_I	11.3	**11.5**	**11.5**	Mn_I	11.3	**11.5**	**11.5**
Mn_{II}	11.3	11.2	11.2	Mn_{II}	11.3	11.3	**11.6**
Mn_{III}	11.3	11.2	**11.5**	Mn_{III}	11.3	11.3	**11.6**
Mn_{IV}	11.3	**11.5**	**11.5**	Mn_{IV}	11.3	**11.5**	**11.5**
Ti_I	1.3	1.3	**1.7**				

For the Mn_4O_6 nanocluster adsorbed at OH-a101, there is an accumulation of positive charge at those O_C sites that are doubly-coordinated to Mn ions of the nanocluster. Computed Bader charges of 7.0 electrons for these O_C sites compare with 7.3-7.7 electrons computed for O^{2-} anions of the OH-a101 surface. The nanocluster-surface interaction is not as strong at the OH-a101 surface, as indicated by the smaller adsorption

energy. As a consequence, the supported nanocluster retains characteristics of the gas phase, for which the O_C ions have computed Bader charges in the range 7.0-7.1 electrons.

Oxygen Vacancy Formation

The most stable modified surfaces with a single O_V are shown in **Figure 5.5.1.c** for Mn_4O_5-OH-r110 and **Figure 5.5.1.d** for Mn_4O_5-OH-a101. For the modified OH-r110 surface the formation energy of a single O_V is -0.26 eV and this formation energy indicates that O_V will form spontaneously. The next three most stable vacancy sites have formation energies in the range 0.60-0.82 eV. After formation of the most stable vacancy, two Mn ions are three-fold coordinated and the third and fourth Mn cations are four- and five-fold coordinated. Two bridging and one in-plane surface oxygen are bound to Mn ions of the nanocluster. Two O_C ions bind to surface Ti sites, while three O_C ions are bound only to Mn and H ions.

The formation of the neutral oxygen vacancy releases two electrons. Bader charge analysis reveals that the electrons localise at the three-fold coordinated Mn sites of the nanocluster. The computed Bader charges on these sites increase from 11.3 to 11.5 electrons; see **Table 5.5.1** for computed Bader charges of reduced Ti and all Mn sites. The computed spin magnetisations are 4.6 μ_B for these Mn sites; this is typical of the formation of reduced Mn^{2+} ions, which has an electronic configuration of $3d^5$.

The most favourable structure with one O_V is more stable than the second most favourable by 0.9 eV. However, the relaxed atomic structures of these configurations are very similar (compare **Figure 5.5.1.c** with **Figure B.4.2.a** in **Appendix B**). The difference in energy arises from the distribution of excess charge. For the O_V structure shown in **Figure B.4.2.a**, one excess charge localises at a five-fold coordinated surface Ti site, for which

the Bader charge increases from 1.3 to 1.7 electrons. A computed spin magnetisation of 1.0 μ_B reflects the $3d^1$ configuration of reduced Ti^{3+}.

For the modified OH-a101 surface, the most stable O_V has a formation energy of -0.42 eV, which indicates that it will form spontaneously, so that the ground state is off-stoichiometric (vacancy formation energies for other sites of the nanocluster were in the range 0.5-1.3 eV). This compares with Mn_4O_6 modifying bare anatase (101) which was found to be stoichiometric in the ground state.[17] After the formation of this O_V, two Mn ions relax towards the titania surface and bind with bridging O_S sites so that, in this configuration, each Mn ion is four-fold coordinated. Bader charge analysis and computed spin densities indicate that two Mn ions are reduced to Mn^{2+}, having computed Bader charges of 11.5 electrons and computed spin magnetisations of 4.6 μ_B. The next most stable structure with one O_V is shown in **Figure B.4.2.b**; in this configuration three Mn ions are reduced to Mn^{2+} and this is accompanied by an accumulation of postive charge on two-fold coordinated O_C ions, for which the Bader charges were computed as 7.0 electrons.

The formation of the second O_V has a moderate energy cost for both MnO_x-modified TiO_2 surfaces, however the modified anatase surface is reducible at a lower energy cost. Given that the anatase surface is more easily hydroxylated,[57] which these results indicate promotes vacancy formation, one would expect more O_V present on modified anatase. That O_V formation is more facile for modified anatase corroborates previous experimental work on MnO_x-TiO_2.[17] The most stable configurations of the heterostructures with two O_V are shown in **Figures 5.5.1.e** and **5.5.1.f** for Mn_4O_4-OH-r110 and Mn_4O_4-OH-a101, respectively. For Mn_4O_4-OH-r110, the two most stable O_C sites for formation of a second O_V had similar formation energies. One such configuration is described here and the other is included in **Section B.4** of **Appenxix B**. For the structure shown in **Figure 5.5.1.e**, the

removed O_C ion was two-fold coordinated to a cluster Mn and surface Ti ion. After vacancy formation the Mn ion binds to a bridging O_S ion and remains three-fold coordinated. In this configuration three Mn ions are reduced; the Bader charges and spin magnetisations for these sites are 11.5 electrons and 4.6 μ_B, respectively. Similarly, for the Ti site to which the removed O_C was bound, the Bader charge and spin magnetisation are 1.7 electrons and 1.0 μ_B. Hence, the Mn_4O_4-OH-r110 heterostructure with two oxygen vacancies has one Ti^{3+} and three Mn^{2+} ions.

For the modified OH-a101 surface, a three-fold coordinated O_C site, which forms a hydroxyl group bridging two Mn ions, has the lowest cost to produce a second O_V. One Mn ion that was bound to the removed O_C atom is two-fold coordinated, having been originally coordinated to three O_C ions and one O_{OH} ion. The second Mn ion is three-fold coordinated, having been four-fold coordinated prior to vacancy formation. The H ion which was bound to the removed O_C migrates to another O_C ion. In this Mn_4O_4-OH-a101 configuration, there are four Mn^{2+} ions, with computed Bader charges of 11.5-11.6 electrons and spin magnetisations of 4.6 μ_B.

Additional structures with two O_V are presented in **Figures B.4.2.c**, for Mn_4O_4-OH-r110, and **B.4.2.d**, for Mn_4O_4-OH-a101; these are close in energy to the configurations described above, and differ in the distribution of excess charge over Mn and Ti sites. Hence, Mn and Ti sites should be present at the surface in a variety of oxidation states.

The localisation of electrons at Ti and Mn sites is also accompanied by localised geometry distortions. The cation-O distances increase by ~0.1 Å after reduction, reflecting the larger ionic radii of Mn^{2+} and Ti^{3+}, compared to $Mn^{3+}$and Ti^{4+}.[61]

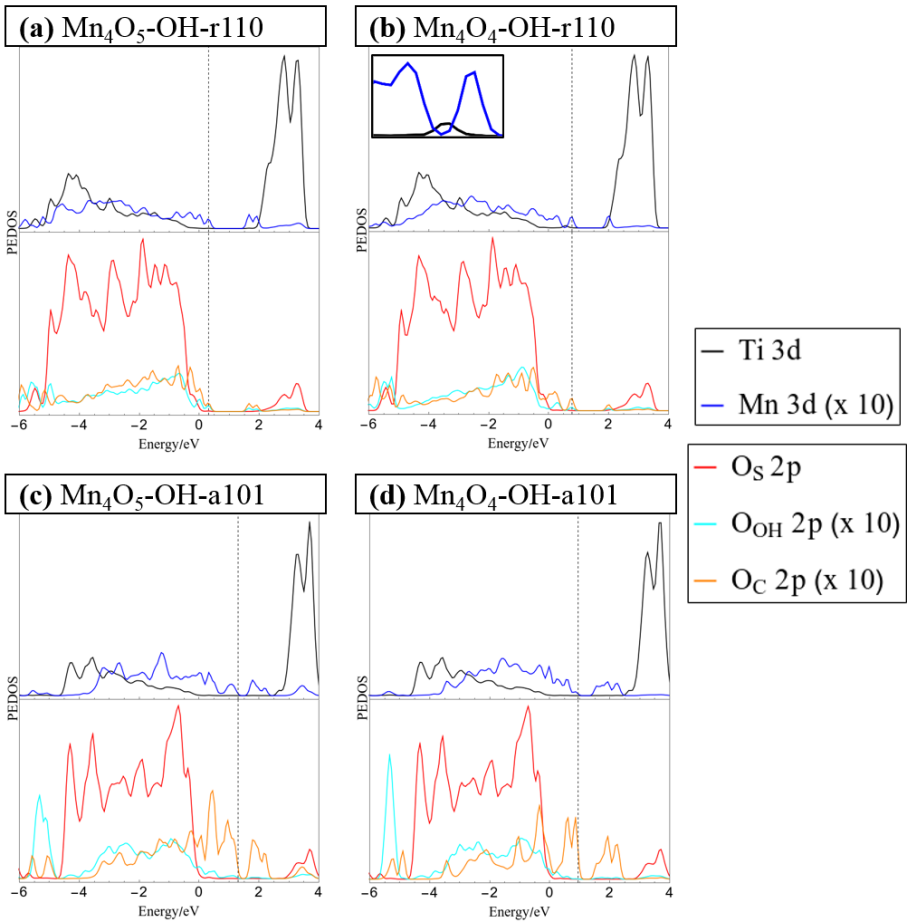

Figure 5.5.2 Projected electronic density of states (PEDOS) plots for **(a)** Mn_4O_5-, and **(b)** Mn_4O_4-OH-r110 and **(c)** Mn_4O_5-, and **(d)** Mn_4O_4-OH-a101. The titania VBM is set to 0 eV and the Fermi energy is indicated with a dashed line. The top half of each panel displays Ti and Mn 3*d* states. The bottom halves of the panels show contributions from O 2*p* states of the surface (O_S), surface bound hydroxyls (O_{OH}) and nanocluster (O_C). The inset in panel **(b)** shows the mid-gap occupied Ti 3*d* states in the range [0 eV, 1 eV].

The projected electronic density of states (PEDOS) for the heterostructures are presented in **Figure 5.5.2**. Since the heterostructures are off-stoichiometric in the ground state, the PEDOS plot for Mn_4O_6-OH-r110 and Mn_4O_6-OH-a101 have been omitted from **Figure 5.5.2**, and are included in **Figure B.4.3** in **Appendix B**, for completeness. The top panels of **Figure 5.5.2** show the PEDOS of modified OH-r110 for (**5.5.2.a**) the ground state with one O_V and (**5.5.2.b**) the reduced state with two O_V. Occupied nanocluster-derived states

(Mn 3*d* and O_C 2*p*) extend to 0.3 and 0.8 eV above the valence band maximum (VBM) of the rutile support for Mn_4O_5- and Mn_4O_4-OH-r110, respectively. Unoccupied Mn 3*d*-derived states also emerge in the titania band gap at 0.1 and 0.3 eV below the conduction band minimum (CBM) for the ground state with one O_V and the reduced state with two O_V. Additional states emerge in the band gap due to occupied Ti^{3+} states (see inset of **Figure 5.5.2.b**), for the heterostructure with two O_V.

The bottom panels of **Figure 5.5.2** display the PEDOS of the modified OH-a101 surface for (**5.5.2.c**) the ground state, with one O_V, and (**5.5.2.d**) reduced state with two O_V. The PEDOS plot for the ground state, with one O_V, shows that occupied Mn 3*d*- and O_C 2*p*-derived states extend to 1.3 eV above the titania derived VBM, while unoccupied Mn 3*d* states emerge at 1 eV below the CBM, leading to a significant reduction in the computed energy gap relative to TiO_2. For the reduced structure, with two O_V, each of the Mn ions is reduced to Mn^{2+}, and the highest occupied of these states is 1 eV above the VBM. The lowest energy, unoccupied state is Mn-derived and is 1 eV below the CBM. For Mn_4O_4-OH-a101 the energy gap is 0.6 eV, with our DFT+U set-up showing a reduction over unmodified anatase.

These features of the PEDOS for Mn_4O_x-TiO_2 can be attributed to formation of interfacial bonds, the presence of low-coordinated Mn and O_C sites, and the facile formation of O_V in the supported metal oxide nanocluster. Modification pushes the VBM to higher energy and results in the emergence of empty states below the CBM; these effects, and the consequent red shift, are greater for modified anatase, consistent with previous reports.[17] These metal oxide nanocluster-modified surfaces are of interest for the oxygen evolution half reaction (OER) of the water splitting process and in this context raising the VBM from that of TiO_2 and towards the water oxidation potential is a desirable effect. Lowering of the titania CBM from its favourable position straddling the water reduction potential

is detrimental to the hydrogen evolution reaction (HER) activity. However, as H adsorbs too strongly at metal oxide surfaces, such heterostructures will in any case not be suitable photocathodes for water splitting.

Photoexcitation Model

Table 5.5.2 Vertical singlet-triplet energy difference ($E^{vertical}$), the relaxed singlet-triplet energy difference (E^{excite}) and the relaxation energy (E^{relax}) for Mn_4O_5-OH-r110 and Mn_4O_5-OH-a101. Values for hydroxylated rutile (110) and anatase (101) surfaces have been included for reference.

Composite structure	**$E^{vertical}$ (eV)**	**E^{excite} (eV)**	**E^{relax} (eV)**
OH-rutile (110)	2.08	1.61	0.46
Mn_4O_5-OH-rutile (110)	2.00	0.68	1.31
OH-anatase (101)	2.71	1.52	1.19
Mn_4O_5-OH-anatase (101)	2.37	0.95	1.43

We apply the model for the photoexcited state to the ground state systems, Mn_4O_5-OH-r110 and Mn_4O_5-OH-a101. **Table 5.5.2** presents the computed vertical, singlet-triplet and electron-hole trapping energies, as discussed in **Chapter 2**. Comparison of these computed energies across different structures nonetheless yields useful qualitative information about the effect of surface modification and results for the unmodified OH-r110 and OH-a101 surfaces are included for reference. In particular, $E^{vertical}$ is analogous to the optical band gap, and a reduction in this value for a heterostructure relative to unmodified titania implies that modification leads to a red shift in light absorption.

When comparing Mn_4O_5-OH-r110 with unmodified OH-r110, we can see that the values for $E^{vertical}$ are similar, however E^{excite} is reduced by 0.93 eV for the modified surface.

Comparing Mn_4O_5-OH-a101 with unmodified OH-a101, decreases in $E^{vertical}$ and E^{excite} by 0.34 and 0.57 eV, respectively, indicate that modification leads to a significant red shift in light absorption. These results corroborate the analysis of the PEDOS. E^{relax} is the energy gained by the system after structural relaxation in response to the triplet electronic state and is related to the stability of the trapped electron and hole. The relaxation energy is larger for Mn_4O_5-OH-r110 than that computed for unmodified OH-r110 (1.31 eV vs 0.46 eV) and reflects the greater flexibility of the modified system in accommodating the triplet electronic state. The relaxation energies for Mn_4O_5-OH-a101 and unmodified OH-a101 are comparable. The mixture of Mn oxidation states and the proximity of the Mn ions to each other at the anatase surface (neighbouring Mn-Mn distances are in the range 2.9-3.2 Å for Mn_4O_5-OH-a101 and 3.0-3.9 Å for Mn_4O_5-OH-r110) restricts the degree to which the nanocluster can respond structurally to the localisation of photoexcited charges.

Through analysis of Bader charges and spin magnetisations we can determine the electron and hole localisation sites and the results of this analysis are represented graphically in **Figure 5.5.3**. For Mn_4O_5-OH-r110, in **Figure 5.5.3.a** and **5.5.3.b**, the electron localises at an Mn site; the Bader charge and spin magnetisation for this site are 11.5 electrons and 4.6 μ_B after electron localisation, which are typical of Mn^{2+} formation. The hole localises at an O_C site, which is two-fold coordinated to the Mn^{2+} ion and a surface Ti. In this instance the Bader charge is 6.8 electrons and the spin magnetisation is 0.8 μ_B, which are consistent with formation of O^-. The Mn^{2+}-O^- distance increases by 0.2 Å, relative to the ground state. The Ti-O^- distance decreases by 0.1 Å.

For Mn_4O_5-OH-a101 (**Figures 5.5.3.c** and **5.5.3.d**), the photoexcited electron localises at an Mn site of the nanocluster, as confirmed by a computed Bader charge of 11.5 electrons and spin magnetisation of 4.5 μ_B. The hole state localises predominantly at an O_C site that bridges Mn^{2+} and Mn^{3+} ions. After hole localisation the Bader charge for the O^- ion is 6.7

electrons and the spin magnetisation is 0.8 μ_B. The Mn^{2+}-O distances increase by 0.2-0.3 Å.

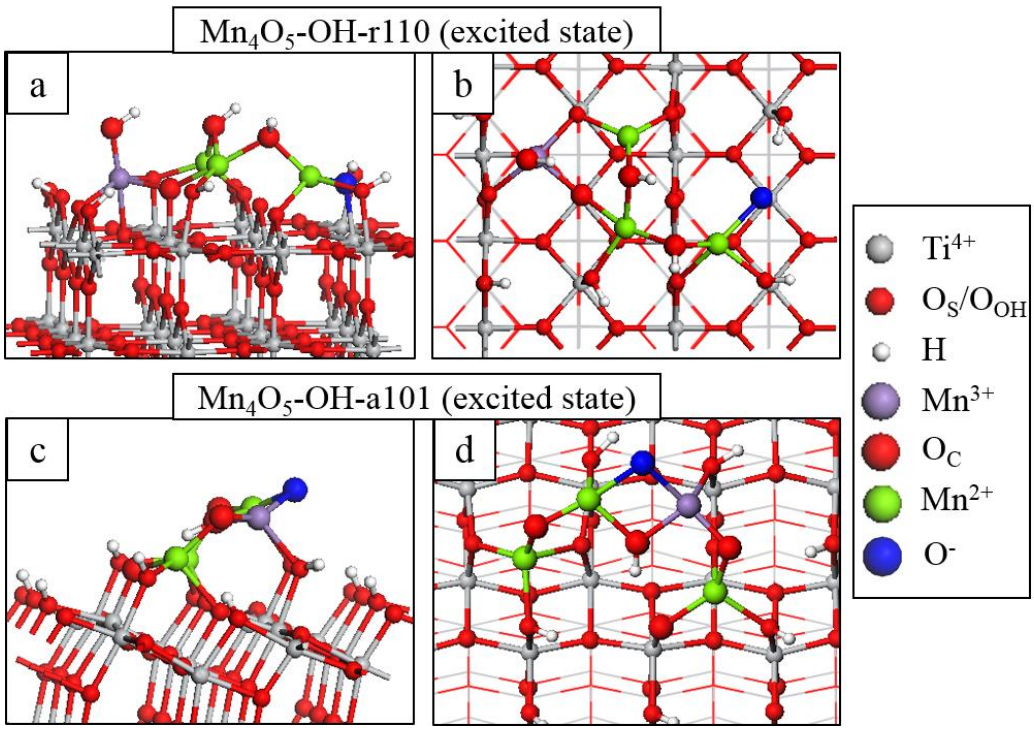

Figure 5.5.3 Atomic structure of the fully relaxed triplet electronic state imposed on Mn_4O_6-OH-r110 for **(a)** side and **(b)** top view and Mn_4O_5-OH-a101 for **(c)** side and **(d)** top view. Charge localisation and changes in oxidation state are distinguished by colour according to the legend on the right hand side.

These results show that the electron localises at an Mn site of the supported nanocluster and the hole state localises at a neighbouring O_C site. Based on this model for the photoexcited state, we can conclude that modification does not necessarily promote the spatial separation of photoexcited charges. However, both electrons and holes will be available at the modified surface for transfer to adsorbed species.

5.6 Conclusions

Nanocluster Adsorption

In each of the composite surfaces studied in this chapter, the nanocluster surface interaction was favourable – the nanoclusters adsorbed strongly at the titania surfaces. This indicates that the heterostructures are robust and that the nanocluster modifiers are stable against desorption.

For the MgO and SnO modifiers, presented in **Section 5.2**, the presence of surface hydroxyls improves nanocluster adsorption by facilitating formation of interfacial bonds. The results of **Section 5.3** show that, at low coverages, *h*BN rings adsorb strongly at the surface with the formation of B-O and Ti-N bonds at the interface. For higher coverages, *h*BN layers are anchored at the surface by bonds between B- and N-terminated edge sites and the TiO_2 surface. For the *h*BN ribbon model, adsorption at the anatase surface led to electron transfer from the *h*BN modifier to the TiO_2 support.

For the Mn_2O_3 modifiers adsorbed at hydroxylated titania surfaces, as described in **Section 5.5**, the properties depend on the phase of the TiO_2 substrate. For Mn_4O_6 adsorbed at the hydroxylated anatase (101) surface, one interfacial bond is established between a cluster oxygen ion and the surface and Mn ions bind mostly to oxygen ions of the surface bound hydroxyls. Conversely, for Mn_4O_6 at hydroxylated rutile (110), the nanocluster-surface interaction is more intimate, with Mn ions binding to bridging and in-plane oxygen ions of the rutile surface.

Stoichiometry

In considering oxygen vacancy formation, we found that both CeO_2- and Mn_2O_3-modified TiO_2 exhibit off-stoichiometric ground states. In CeO_2-TiO_2, described in **Section 5.4**,

one or more oxygen vacancies form spontaneously or at very low energy cost, so that under typical experimental conditions, there will be oxygen vacancies present. As a consequence, Ce^{3+} ions will be present in the nanoclusters in their ground state. The CeO_2-rutile composites are more reducible compared to unmodified rutile (110) and moderate energy inputs are required to produce multiple oxygen vacancies. Electrons released after oxygen vacancy formation localise on Ce sites in the supported nanoclusters.

Both Mn_4O_x-OH-r110 and Mn_4O_x-OH-a101 favour non-stoichiometry, in contrast to unhydroxylated modified TiO_2 surfaces, as oxygen vacancies form spontaneously and both composites can be considered highly reducible with moderate energy costs for subsequent oxygen vacancy formation. Bader charge analysis shows that Mn ions are present in a mixture of oxidation states at the hydroxylated surfaces. Both Mn and Ti ions are reduced in response to vacancy formation.

The reduction of the MgO- and SnO-modified composites is significantly enhanced compared to bare anatase (101), so that this modification will result in a more reactive surface. The role played by surface hydroxyls in the reducibility of the modified surfaces depends on nanocluster composition. For Mg_4O_4-anatase surface hydroxyls lead to a significant decrease in the energy cost to reduce the composite.

Electronic Properties

The impact of surface-modification on the electronic properties depends on the composition of the modifiers. MgO- and SnO-modification of the oxidised and hydroxylated anatase (101) surfaces enhances the DOS at the VBM, to give rise to a red shift in light absorption. Moreover, for the hydroxylated surfaces, hydroxyl O 2*p* states contribute to the DOS at the VBM. For each *h*BN-modified system, modification has a

significant effect on the energy gap. Occupied N-*p* states extend the VBM to higher energies, which should produce a red shift in light absorption.

For CeO_2-modified rutile TiO_2, which has an off-stoichiometric ground state, occupied Ce 4*f*-derived states emerge in the TiO_2-derived band gap and O 2*p* states are present above the TiO_2 VB, due to low-coordinated oxygen atoms in the supported nanoclusters. Modification with Mn_4O_x has a significant impact on the light absorption properties. Occupied Mn 3*d* states extend the VBM of the composites to higher energies relative to that of the titania support and empty states emerge below the CBM. These features may induce a red shift in light absorption, making these systems visible light active.

Photoexcitation Model

In all cases, surface modification can enhance the stability and spatial separation of photoexcited charges. For MgO- and SnO-modified TiO_2, electrons localise at surface Ti atoms and holes localise at low-coordinated nanocluster or hydroxyl sites and the presence of surface hydroxyls increases the stability of the photogenerated electron-hole pair. For *h*BN-modified anatase, the photoexcitation model corroborated analysis of the computed PEDOS plots and showed electron excitation from high-lying N-*p* states to the TiO_2 conduction band, with a hole localised on the *h*BN modifier.

For CeO_2-modified rutile TiO_2, both electron and hole localisation occur at Ce and low-coordinated O_C sites, respectively. However, this proximity may not be detrimental as the electron-hole pair has a large trapping energy of 0.8 eV, so this can reduce the migration of charges over the nanocluster. For MnO_x-TiO_2, the red shift in the light absorption edge, predicted by analysis of the DOS, is confirmed by our model for the photoexcited state. In particular, the vertical energy, decreases significantly for Mn_4O_5-OH-a101 relative to that computed for the unmodified, hydroxylated anatase (101) surface. Analysis of this

model shows that electrons and holes localise at Mn and neighbouring O_C sites, respectively, so that modification may not promote separation of photoexcited charges, but the trapping energies of the electron and hole are quite high, suggesting high stability.

In conclusion, surface modification can impart properties important for photocatalytic applications. These properties include enhanced reducibility, leading to a higher prevalence of active oxygen vacancy sites at the surface, a red shift in light absorption, and enhanced stability of excited charges. Experimental corroboration was provided in our study of *h*BN-modified anatase TiO_2. The photocatalytic activity of TiO_2 was successfully increased by interfacing titania with BN. Along with higher anatase contents, the red shift in light absorption and promotion of charge carrier separation, which arise due to *h*BN modification, contribute to the observed enhancements in photocatalytic performance. The DFT analysis presented in this chapter can be implemented to inform the design and aid in the screening of new photocatalytic materials.

5.7 Chapter References

1. Rhatigan, S.; Nolan, M., Impact of surface hydroxylation in MgO-/SnO-nanocluster modified TiO_2 anatase (101) composites on visible light absorption, charge separation and reducibility. *Chinese Chemical Letters* **2018,** *29* (6), 757-764.
2. Byrne, C.; Rhatigan, S.; Hermosilla, D.; Merayo, N.; Blanco, Á.; Michel, M. C.; Hinder, S.; Nolan, M.; Pillai, S., Modification of TiO_2 with $_h$BN: High temperature anatase phase stabilisation and photocatalytic degradation of 1,4-dioxane. *Journal of Physics: Materials* **2019**.
3. Rhatigan, S.; Nolan, M., CO_2 and water activation on ceria nanocluster modified TiO_2 rutile (110). *Journal of Materials Chemistry A* **2018,** *6* (19), 9139-9152.
4. Rhatigan, S.; Nolan, M., Activation of Water on MnO_x-Nanocluster-Modified Rutile (110) and Anatase (101) TiO_2 and the Role of Cation Reduction. *Frontiers in Chemistry* **2019,** *7* (67).
5. Muhich, C. L.; Ehrhart, B. D.; Al-Shankiti, I.; Ward, B. J.; Musgrave, C. B.; Weimer, A. W., A review and perspective of efficient hydrogen generation via solar thermal water splitting. *Wiley Interdisciplinary Reviews: Energy and Environment* **2016,** *5* (3), 261-287.
6. Ganduglia-Pirovano, M. V.; Hofmann, A.; Sauer, J., Oxygen vacancies in transition metal and rare earth oxides: Current state of understanding and remaining challenges. *Surface Science Reports* **2007,** *62* (6), 219-270.
7. Mars, P.; van Krevelen, D. W., *Oxidation Carried Out by Means of Vandium Oxide Catalysts*. 1954; Vol. 3, p 41-59.
8. Henderson, M. A.; Epling, W. S.; Peden, C. H. F.; Perkins, C. L., Insights into Photoexcited Electron Scavenging Processes on TiO2 Obtained from Studies of the Reaction of O_2 with OH Groups Adsorbed at Electronic Defects on TiO_2(110). *The Journal of Physical Chemistry B* **2003,** *107* (2), 534-545.
9. Schaub, R.; Thostrup, P.; Lopez, N.; Lægsgaard, E.; Stensgaard, I.; Nørskov, J. K.; Besenbacher, F., Oxygen Vacancies as Active Sites for Water Dissociation on Rutile TiO_2. *Phys. Rev. Lett.* **2001,** *87* (26), 266104.
10. Mullins, D. R.; Albrecht, P. M.; Chen, T.-L.; Calaza, F. C.; Biegalski, M. D.; Christen, H. M.; Overbury, S. H., Water Dissociation on CeO_2(100) and CeO_2(111) Thin Films. *The Journal of Physical Chemistry C* **2012,** *116* (36), 19419-19428.
11. Lira, E.; Wendt, S.; Huo, P.; Hansen, J. Ø.; Streber, R.; Porsgaard, S.; Wei, Y.; Bechstein, R.; Lægsgaard, E.; Besenbacher, F., The Importance of Bulk Ti^{3+} Defects in the Oxygen Chemistry on Titania Surfaces. *Journal of the American Chemical Society* **2011,** *133* (17), 6529-6532.
12. Xiong, L.-B.; Li, J.-L.; Yang, B.; Yu, Y., Ti^{3+} in the Surface of Titanium Dioxide: Generation, Properties and Photocatalytic Application. *Journal of Nanomaterials* **2012,** *2012*, 13.
13. He, Y.; Dulub, O.; Cheng, H.; Selloni, A.; Diebold, U., Evidence for the Predominance of Subsurface Defects on Reduced Anatase TiO_2 (101). *Phys. Rev. Lett.* **2009,** *102* (10), 106105.
14. Scheiber, P.; Fidler, M.; Dulub, O.; Schmid, M.; Diebold, U.; Hou, W.; Aschauer, U.; Selloni, A., (Sub)Surface Mobility of Oxygen Vacancies at the TiO_2 Anatase (101) Surface. *Phys. Rev. Lett.* **2012,** *109* (13), 136103.

15. Setvin, M.; Aschauer, U.; Hulva, J.; Simschitz, T.; Daniel, B.; Schmid, M.; Selloni, A.; Diebold, U., Following the Reduction of Oxygen on TiO_2 Anatase (101) Step by Step. *Journal of the American Chemical Society* **2016,** *138* (30), 9565-9571.
16. Fronzi, M.; Iwaszuk, A.; Lucid, A.; Nolan, M., Metal oxide nanocluster-modified TiO_2 as solar activated photocatalyst materials. *Journal of Physics: Condensed Matter* **2016,** *28* (7), 074006.
17. Schwartzenberg, K. C.; Hamilton, J. W. J.; Lucid, A. K.; Weitz, E.; Notestein, J.; Nolan, M.; Byrne, J. A.; Gray, K. A., Multifunctional photo/thermal catalysts for the reduction of carbon dioxide. *Catalysis Today* **2017,** *280*, 65-73.
18. Nolan, M.; Iwaszuk, A.; Tada, H., Molecular metal oxide cluster-surface modified titanium dioxide photocatalysts. *Australian Journal of Chemistry* **2012,** *65* (6), 624-632.
19. Iwaszuk, A.; Nolan, M., SnO-nanocluster modified anatase TiO_2 photocatalyst: exploiting the Sn(ii) lone pair for a new photocatalyst material with visible light absorption and charge carrier separation. *Journal of Materials Chemistry A* **2013,** *1* (22), 6670-6677.
20. Walsh, A.; Watson, G. W., Influence of the Anion on Lone Pair Formation in Sn(II) Monochalcogenides: A DFT Study. *The Journal of Physical Chemistry B* **2005,** *109* (40), 18868-18875.
21. Walsh, A.; Watson, G. W., Electronic structures of rocksalt, litharge, and herzenbergite SnO by density functional theory. *Physical Review B* **2004,** *70* (23), 235114.
22. Nolan, M.; Iwaszuk, A.; Gray, K. A., Localization of photoexcited electrons and holes on low coordinated Ti and O sites in free and supported TiO_2 Nanoclusters. *The Journal of Physical Chemistry C* **2014,** *118* (48), 27890-27900.
23. Lucid, A.; Iwaszuk, A.; Nolan, M., A first principles investigation of Bi_2O_3-modified TiO_2 for visible light Activated photocatalysis: The role of TiO_2 crystal form and the Bi^{3+} stereochemical lone pair. *Materials Science in Semiconductor Processing* **2014,** *25*, 59-67.
24. Nolan, M., First-principles prediction of new photocatalyst materials with visible-light absorption and improved charge separation: surface modification of rutile TiO_2 with nanoclusters of MgO and Ga_2O_3. *ACS Applied Materials & Interfaces* **2012,** *4* (11), 5863-5871.
25. Iwaszuk, A.; Nolan, M., Lead oxide-modified TiO_2 photocatalyst: tuning light absorption and charge carrier separation by lead oxidation state. *Catalysis Science & Technology* **2013,** *3* (8), 2000-2008.
26. Jin, Q.; Fujishima, M.; Nolan, M.; Iwaszuk, A.; Tada, H., Photocatalytic activities of tin(iv) oxide surface-modified titanium(iv) dioxide show a strong sensitivity to the TiO_2 crystal form. *The Journal of Physical Chemistry C* **2012,** *116* (23), 12621-12626.
27. Nolan, M., Charge Compensation and Ce^{3+} Formation in Trivalent Doping of the CeO_2(110) Surface: The Key Role of Dopant Ionic Radius. *The Journal of Physical Chemistry C* **2011,** *115* (14), 6671-6681.
28. Haa, M.-A.; Alexandrova, A. N., Oxygen vacancies of anatase(101): extreme sensitivity to the density functional theory method. *Journal of Chemical Theory and Computation* **2016,** *12* (6), 2889-2895.
29. Raddaha, N. S.; Cordero-Arias, L.; Cabanas-Polo, S.; Virtanen, S.; Roether, J. A.; Boccaccini, A. R., Electrophoretic deposition of chitosan/h-BN and chitosan/h-BN/TiO_2 composite coatings on stainless steel (316L) substrates. *Materials* **2014,** *7* (3), 1814-1829.
30. Liu, D.; Zhang, M.; Xie, W.; Sun, L.; Chen, Y.; Lei, W., Porous BN/TiO_2 hybrid nanosheets as highly efficient visible-light-driven photocatalysts. *Applied Catalysis B: Environmental* **2017,** *207*, 72-78.

31. Su, C.-Y.; Tang, H.-Z.; Zhu, G.-D.; Li, C.-C.; Lin, C.-K., The optical properties and sunscreen application of spherical h-BN–TiO_2/mica composite powder. *Ceramics International* **2014,** *40* (3), 4691-4696.
32. Fu, X.; Hu, Y.; Yang, Y.; Liu, W.; Chen, S., Ball milled h-BN: an efficient holes transfer promoter to enhance the photocatalytic performance of TiO_2. *Journal of hazardous materials* **2013,** *244*, 102-110.
33. Xie, W.; Zhang, M.; Liu, D.; Lei, W.; Sun, L.; Wang, X., Reactive Yellow 161 Decolorization by TiO_2/Porous Boron Nitride Nanosheet Composites in Cotton Dyeing Effluent. *ACS Sustainable Chemistry & Engineering* **2016,** *5* (2), 1392-1399.
34. Sheng, Y.; Yang, J.; Wang, F.; Liu, L.; Liu, H.; Yan, C.; Guo, Z., Sol-gel synthesized hexagonal boron nitride/titania nanocomposites with enhanced photocatalytic activity. *Applied Surface Science* **2019,** *465*, 154-163.
35. Singh, B.; Singh, P.; Singh, K.; Sharma, J.; Kumar, M.; Bala, R.; Meena, R.; Sharma, S. K.; Kumar, A., Nanostructured BN–TiO_2 composite with ultra-high photocatalytic activity. *New Journal of Chemistry* **2017,** *41* (20), 11640-11646.
36. Matović, B.; Luković, J.; Nikolić, M.; Babić, B.; Stanković, N.; Jokić, B.; Jelenković, B., Synthesis and characterization of nanocrystaline hexagonal boron nitride powders: XRD and luminescence properties. *Ceramics International* **2016,** *42* (15), 16655-16658.
37. Chen, T.; Xiao, J.; Yang, G., Cubic boron nitride with an intrinsic peroxidase-like activity. *RSC Advances* **2016,** *6* (74), 70124-70132.
38. Deura, M.; Kutsukake, K.; Ohno, Y.; Yonenaga, I.; Taniguchi, T., Nanoindentation measurements of a highly oriented wurtzite-type boron nitride bulk crystal. *Japanese Journal of Applied Physics* **2017,** *56* (3), 030301.
39. Yuan, C.; Duan, B.; Li, L.; Xie, B.; Huang, M.; Luo, X., Thermal conductivity of polymer-based composites with magnetic aligned hexagonal boron nitride platelets. *ACS applied materials & interfaces* **2015,** *7* (23), 13000-13006.
40. Wang, X.; Wang, W.; Wang, X.; Zhang, J.; Zhao, J.; Gu, Z.; Zhou, L., Synthesis, structural characterization and evaluation of floating BN codoped TiO_2/expanded perlite composites with enhanced visible light photoactivity. *Applied Surface Science* **2015,** *349*, 264-271.
41. Lu, N.; Quan, X.; Li, J.; Chen, S.; Yu, H.; Chen, G., Fabrication of boron-doped TiO2 nanotube array electrode and investigation of its photoelectrochemical capability. *The Journal of Physical Chemistry C* **2007,** *111* (32), 11836-11842.
42. Fagan, R.; McCormack, D. E.; Hinder, S.; Pillai, S. C., Improved high temperature stability of anatase TiO_2 photocatalysts by N, F, P co-doping. *Materials & Design* **2016,** *96*, 44-53.
43. Saitow, K.-i.; Wang, Y.; Takahashi, S., Mechano-synthesized orange TiO_2 shows significant photocatalysis under visible light. *Scientific reports* **2018,** *8* (1), 15549.
44. Park, J. B.; Graciani, J.; Evans, J.; Stacchiola, D.; Senanayake, S. D.; Barrio, L.; Liu, P.; Sanz, J. F.; Hrbek, J.; Rodriguez, J. A., Gold, Copper, and Platinum Nanoparticles Dispersed on CeO_x/TiO_2(110) Surfaces: High Water-Gas Shift Activity and the Nature of the Mixed-Metal Oxide at the Nanometer Level. *Journal of the American Chemical Society* **2010,** *132* (1), 356-363.
45. Johnston-Peck, A. C.; Senanayake, S. D.; Plata, J. J.; Kundu, S.; Xu, W.; Barrio, L.; Graciani, J.; Sanz, J. F.; Navarro, R. M.; Fierro, J. L. G.; Stach, E. A.; Rodriguez, J. A., Nature of the Mixed-Oxide Interface in Ceria–Titania Catalysts: Clusters, Chains, and Nanoparticles. *The Journal of Physical Chemistry C* **2013,** *117* (28), 14463-14471.
46. Graciani, J.; Plata, J. J.; Sanz, J. F.; Liu, P.; Rodriguez, J. A., A theoretical insight into the catalytic effect of a mixed-metal oxide at the nanometer level: The case of the

highly active metal/CeO_x/TiO_2(110) catalysts. *The Journal of Chemical Physics* **2010,** *132* (10), 104703.
47. Graciani, J.; Mudiyanselage, K.; Xu, F.; Baber, A. E.; Evans, J.; Senanayake, S. D.; Stacchiola, D. J.; Liu, P.; Hrbek, J.; Sanz, J. F.; Rodriguez, J. A., Highly active copper-ceria and copper-ceria-titania catalysts for methanol synthesis from CO_2. *Science* **2014,** *345* (6196), 546-550.
48. Wang, Y.; Zhao, J.; Wang, T.; Li, Y.; Li, X.; Yin, J.; Wang, C., CO_2 photoreduction with H_2O vapor on highly dispersed CeO_2/TiO_2 catalysts: Surface species and their reactivity. *Journal of Catalysis* **2016,** *337* (Supplement C), 293-302.
49. Park, J. B.; Graciani, J.; Evans, J.; Stacchiola, D.; Ma, S.; Liu, P.; Nambu, A.; Sanz, J. F.; Hrbek, J.; Rodriguez, J. A., High catalytic activity of Au/CeO_x/TiO_2(110) controlled by the nature of the mixed-metal oxide at the nanometer level. *Proceedings of the National Academy of Sciences* **2009,** *106* (13), 4975-4980.
50. Iwaszuk, A.; Nolan, M., Electronic structure and reactivity of Ce- and Zr-doped TiO_2: assessing the reliability of density functional theory approaches. *The Journal of Physical Chemistry C* **2011,** *115* (26), 12995-13007.
51. Albuquerque, A. R.; Bruix, A.; dos Santos, I. M. G.; Sambrano, J. R.; Illas, F., DFT Study on Ce-Doped Anatase TiO2: Nature of Ce^{3+} and Ti^{3+} Centers Triggered by Oxygen Vacancy Formation. *The Journal of Physical Chemistry C* **2014,** *118* (18), 9677-9689.
52. Albuquerque, A. R.; Bruix, A.; Sambrano, J. R.; Illas, F., Theoretical Study of the Stoichiometric and Reduced Ce-Doped TiO_2 Anatase (001) Surfaces. *The Journal of Physical Chemistry C* **2015,** *119* (9), 4805-4816.
53. Franchini, C.; Podloucky, R.; Paier, J.; Marsman, M.; Kresse, G., Ground-state properties of multivalent manganese oxides: Density functional and hybrid density functional calculations. *Physical Review B* **2007,** *75* (19), 195128.
54. Rhatigan, S.; Nolan, M., Impact of surface hydroxylation in MgO-/SnO-nanocluster modified TiO2 anatase (101) composites on visible light absorption, charge separation and reducibility. *Chinese Chemical Letters* **2017**.
55. Fronzi, M.; Nolan, M., Surface Modification of Perfect and Hydroxylated TiO_2 Rutile (110) and Anatase (101) with Chromium Oxide Nanoclusters. *ACS Omega* **2017,** *2* (10), 6795-6808.
56. Valdés, Á.; Qu, Z. W.; Kroes, G. J.; Rossmeisl, J.; Nørskov, J. K., Oxidation and Photo-Oxidation of Water on TiO_2 Surface. *The Journal of Physical Chemistry C* **2008,** *112* (26), 9872-9879.
57. Mu, R.; Zhao, Z.-j.; Dohnálek, Z.; Gong, J., Structural motifs of water on metal oxide surfaces. *Chemical Society Reviews* **2017,** *46* (7), 1785-1806.
58. Nolan, M., Alkaline earth metal oxide nanocluster modification of rutile TiO_2 (110) promotes water activation and CO_2 chemisorption. *Journal of Materials Chemistry A* **2018,** *6* (20), 9451-9466.
59. Fronzi, M.; Daly, W.; Nolan, M., Reactivity of metal oxide nanocluster modified rutile and anatase TiO_2: Oxygen vacancy formation and CO_2 interaction. *Applied Catalysis A:* **2016,** *521*, 240-249.
60. Nolan, M.; Iwaszuk, A.; Lucid, A. K.; Carey, J. J.; Fronzi, M., Design of novel visible light active photocatalyst materials: surface modified TiO_2. *Advanced Materials* **2016,** *28* (27), 5425-5446.
61. Shannon, R. D.; Prewitt, C. T., Effective ionic radii in oxides and fluorides. *Acta Crystallographica Section B* **1969,** *25* (5), 925-946.

6 Water Adsorption and Oxidation

6.1 Introduction

This chapter presents the results of studies of the interaction of H_2O with TiO_2 surfaces modified with metal oxide nanoclusters. This is important for a number of reactions, such as water gas shift or water oxidation and one of the limiting steps in these reactions is water dissociation, which usually has an energy cost and an activation barrier. **Section 6.2** describes the interaction of water with CeO_2- and MnO_x-modified TiO_2, which were characterised in detail in **Chapter 5.** We focus particularly on oxygen vacancies and reduced cations as active sites and identify the characteristics of activation, such as dissociation, geometry distortions and charge transfer to the adsorbed species. Given that oxygen vacancies have exothermic or moderate formation energies for the modified systems, such defects will be present in these composite materials under operating conditions or can be induced to form by pre-catalytic treatments.

Section 6.3 presents the results of a combined experimental and computational study of the oxygen evolution reaction (OER) activity of rutile (110) modified with alkaline earth oxide (AEO) modifiers, MgO and CaO. The OER is accepted as the bottleneck in overall water splitting. A combination of experimental characterisation and DFT elucidates the role of AEO-modification in improving the photocatalytic performance. The modified surfaces are characterised in terms of photocatalytic material descriptors, similar to the analysis of **Chapter 5**. This study goes beyond the initial water adsorption to investigate pathways to water oxidation at various sites of the AEO-modified rutile TiO_2 surfaces.

6.2 Water adsorption at CeO_x- and MnO_x-modified TiO_2

6.2.1 Water adsorption at CeO_x-modified TiO_2

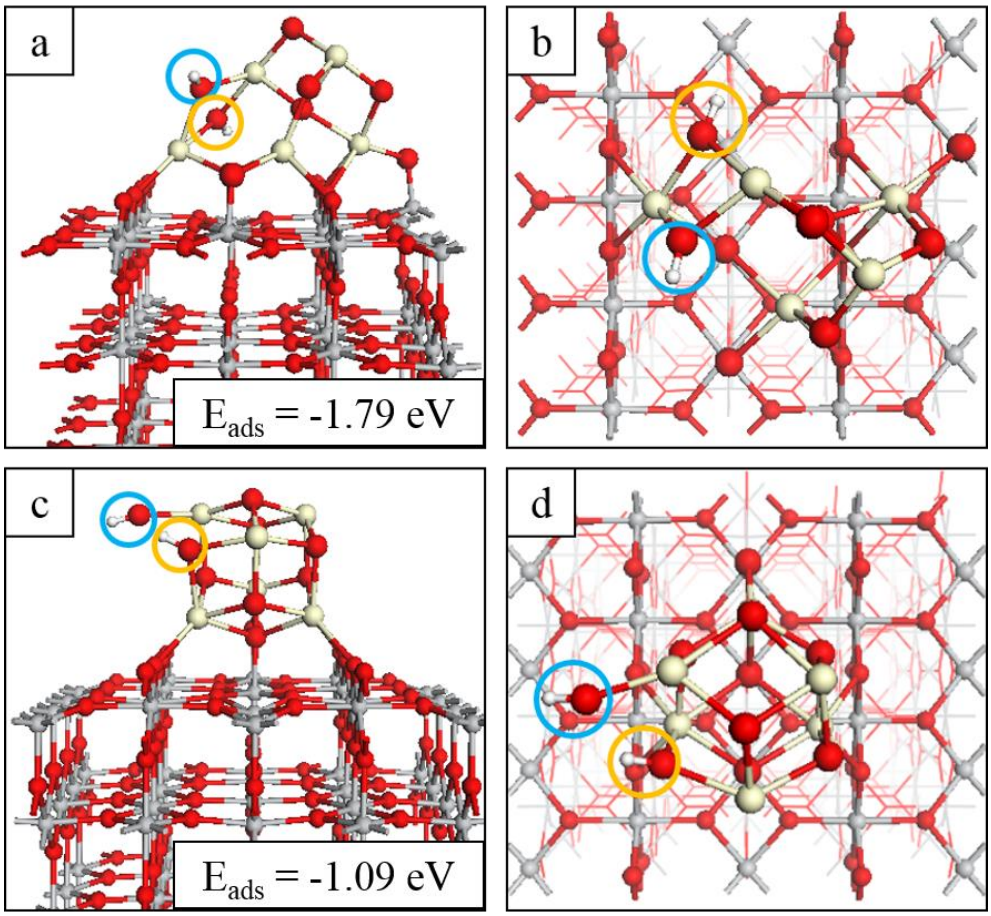

Figure 6.2.1 Relaxed atomic structures of the most stable configurations of H_2O adsorbed at **(a)** and **(b)** Ce_5O_8-rutile-(110) and **(c)** and **(d)** Ce_6O_9-rutile-(110). Hydroxyl groups arising from the spontaneous dissociation at the surface are circled in blue for the water-derived OH and in orange for the OH involving O_C sites. H atoms are represented by small white spheres.

We examined how water interacts at vacancy sites in the reduced CeO_x-rutile-(110) composites, described in **Chapter 5**, and computed the adsorption energies. Water adsorption is favourable at multiple sites on the supported CeO_x nanoclusters. Adsorption energies for the most stable adsorption configurations of water are -1.79 eV on Ce_5O_8-rutile-(110) and -1.09 eV on Ce_6O_9-rutile-(110); the corresponding geometries are

displayed in **Figure 6.2.1**. **Figure B.3.4** in **Appendix B** shows additional adsorption sites and energies for the H_2O-CeO_x-TiO_2 interaction.

Starting from water adsorption in molecular form, the most stable adsorption mode is that in which the water molecule dissociates spontaneously upon relaxation. This dissociation involves the transfer of a H atom to an O_C site and the hydroxyl from the water molecule bridges two cluster Ce sites. For Ce_6O_9-rutile-(110), the moderate adsorption energy means that hydroxyls should not be over-stabilized and could be active in catalysis. Thus, water dissociation and activation can be promoted on these ceria-rutile composites.

For adsorption of water at Ce_5O_8-rutile-(110) (**Figures 6.2.1.a** and **6.2.1.b**), the water molecule interacts with low-coordinated cluster sites. The OH group fills a vacancy site (O_1 from **Figure 5.4.1.b**), and binds to two Ce^{3+} sites that were four- and three-fold coordinated; the latter being the lowest coordinated cluster cation. The second H atom transfers to a two-fold coordinated O_C site which neighbours the Ce sites bound to the hydroxyl and is among the lowest-coordinated O_C sites. Ce-O bond lengths involving both cluster- and water-derived OH groups are elongated by up to 0.3 Å, relative to equivalent Ce-O distances prior to water adsorption. Bader charge analysis reveals that there is no charge transfer between the nanocluster and water and no Ce^{3+} cations are re-oxidised. There is a charge redistribution, with an increase in charge of 0.3 electrons in the nanocluster as a result of formation of hydroxyls, which is predominantly transferred to the O_C that binds with hydrogen.

The dissociative adsorption of water at Ce_6O_9-rutile-(110) is qualitatively similar to adsorption at Ce_5O_8-rutile-(110). For the reduced Ce_6O_9 nanocluster, the O sites (Ce sites) show three-fold (four-fold) or higher coordination. The water molecule dissociates upon adsorption with transfer of an H atom to an O_C site and the OH group binding to a single

neighbouring Ce ion (**Figures 6.2.1.c** and **6.2.1.d**). The O_C and Ce adsorption sites remain three- and four-fold coordinated after the interaction due to the breaking of their mutual bond. Ce-O bond lengths involving the cluster-derived OH group are elongated by 0.15 Å, relative to their values before water adsorption. The distances between the Ce atom at which the water-derived OH group is adsorbed and the O_C atoms with which it still shares bonds are similarly elongated. Despite this distortion of the larger nanocluster upon H_2O adsorption, the interaction is strong and favourable, as shown by an adsorption energy of -1.09 eV. After water adsorption, there is a redistribution of charge, with water oxygen transferring 0.3 electrons to the nanocluster and this charge is donated to the nanocluster oxygen that binds with hydrogen from water.

These results compare with studies of water dissociation at Ce_2O_3-TiO_2.[1-2] In these studies the authors followed the energy pathway from water adsorbed in molecular form to dissociation, finding that the dissociation process was exothermic (-0.70 eV) with a small energy barrier of 0.04 eV. We found that dissociation of molecular water occurred spontaneously, suggesting that the size of the supported CeO_x nanocluster and the number of Ce^{3+} sites play a role in the ability of the composite to dissociate water.

While the ability of metal oxides to dissociate H_2O is well established, the mechanism which promotes dissociation remains of interest. A number of studies have looked at CeO_2 surfaces as model systems to study water dissociation, in which the presence of reduced Ce^{3+} species plays an important role.[3-6] Defects, step edges and terraces in surfaces play a role as such features provide low-coordinated adsorption sites. CeO_2 (100) and (111) surfaces with O vacancies and Ce^{3+} ions show a preference for dissociative water adsorption, relative to the pristine surfaces, where there is little energetic difference between adsorption in molecular and dissociated form.[7] Similar results were reported in another study of CeO_2 (111);[8] the presence of O vacancies made dissociative adsorption

more favourable, by 1.1 eV relative to molecular water, with no energy barrier. The authors also found that Ni and Ni_4 at the surface introduced Ce^{3+} ions and had a moderating effect on the water adsorption energies; for $Ni/CeO_2(111)$, dissociation was favoured by 0.3 eV with a small energy barrier of 0.13 eV. High lying 2*p* states, derived from low coordinated O_C sites, with the presence of Ce^{3+} states in the gap, facilitates interactions with water to break O-H bonds.

A recent study showed that increased lattice strain in the CeO_2 (111) surface promotes dissociation of H_2O over molecular adsorption.[9] For the reduced Ce_6O_9-rutile-(110) composite, the Ce-O distances at the sites of H_2O adsorption (see **Figures 6.2.1.c** and **6.2.1.d**), are longer by ~1% relative to typical distances (~2.37 Å) in the pristine CeO_2 (111) surface. This suggests that tensile strain may indeed contribute to promoting the dissociation of water. In Ce_5O_8-rutile-(110), Ce-O distances are shorter (~2.2 Å), due to the lower coordination of the O_C sites, and elongate after the dissociative adsorption of H_2O. However, the Ce-Ce distance prior to water adsorption is 4.2 Å, which is considerably longer than neighbouring Ce-Ce distances (~3.9 Å) in CeO_2 (111). After dissociative adsorption of water, this Ce-Ce distance decreases to 3.6 Å, further indicating that tensile strain may play a role in driving dissociation.

Figure 6.2.2 shows the PEDOS of the H_2O molecule and reduced Ce_5O_8-rutile-(110) composite in the non-interacting case (H_2O + surface) and after dissociative adsorption (H_2O-surface). Similar analysis is provided for Ce_6O_9-rutile-(110) in **Figure B.3.5** of **Appendix B**. For the non-interacting system the molecule and surface are relaxed in the same unit cell with sufficient spatial separation such that they do not interact. In the non-interacting case (**Figure 6.2.2.a**), the water-derived O_W 2*p* states show well defined peaks at energies of -2.9 eV and -0.8 eV relative to the VBM (0 eV) of the TiO_2 support. For the interacting case (**Figure 6.2.2.b**) the O_W 2*p*-derived states overlap the O_C 2*p*-derived

states near the VBM of the titania host. For water adsorbed at Ce_5O_8-rutile-(110), the O_W 2*p* states broaden and lie below the VBM, overlapping with O_C derived states, as the OH groups each bridge two Ce sites of the nanocluster. Comparing **Figures 6.2.2.a** and **6.2.2.b**, the O_W-derived states are shifted to lower energies upon dissociative adsorption.

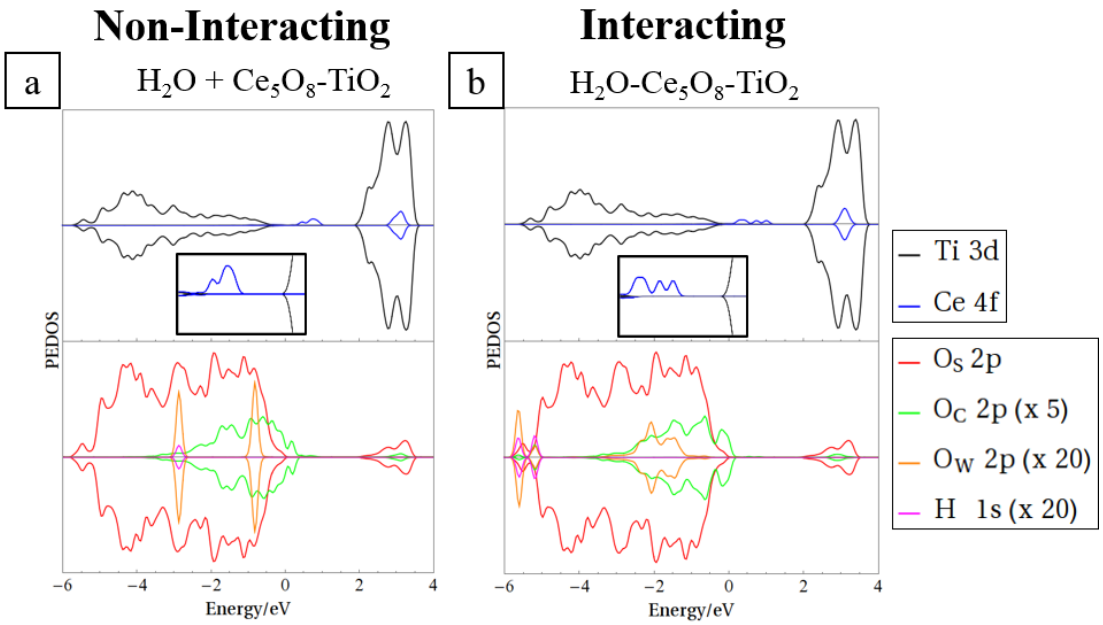

Figure 6.2.2 Spin polarized projected electron density of states (PEDOS) for **(a)** H_2O + Ce_5O_8-rutile-(110) (non-interacting) and **(b)** H_2O-Ce_5O_8-rutile-(110) (interacting). The top half of each panel displays Ti 3*d*- and Ce 4*f*-derived states. Bottom halves of the panels display contributions to the DOS from surface (O_S), nanocluster (O_C) and water (O_W) oxygen 2*p*-derived states and H *1s* states. Insets in the top panels show the mid-gap Ce-derived states in the range [-0.25 eV, +2.25 eV].

The interaction increases the gap between the occupied Ce 4*f*-derived states and the CBM of the TiO_2 host (see insets of panels in **Figure 5.4.6**); i.e. the occupied Ce^{3+} states are pushed to lower energy after interaction. In addition, integrating the O_C and O_W-derived DOS lying above the TiO_2 VBM in both the non-interacting and interacting cases shows that after interaction the occupied states are driven to lower energies. The number of states lying above the TiO_2 VBM is reduced by 2 in the interacting case relative to the non-

interacting system; this suggests that passivation of high lying O 2*p* states is a factor driving the interaction of water with the reduced CeO_x-rutile-(110) composite surfaces.

6.2.2 Water adsorption at MnO_x-OH-TiO_2

For the interaction of water at the MnO_x-modified rutile and anatase surfaces, only those composites with O_V present were considered, as such vacancies are known to be active sites at metal oxide surfaces.[10-13] Water adsorption is favourable at multiple sites of both modified surfaces and the geometries of the most stable adsorption configurations are displayed in **Figure 6.2.3**, while other, less stable, water adsorption structures are shown in **Appendix B**.

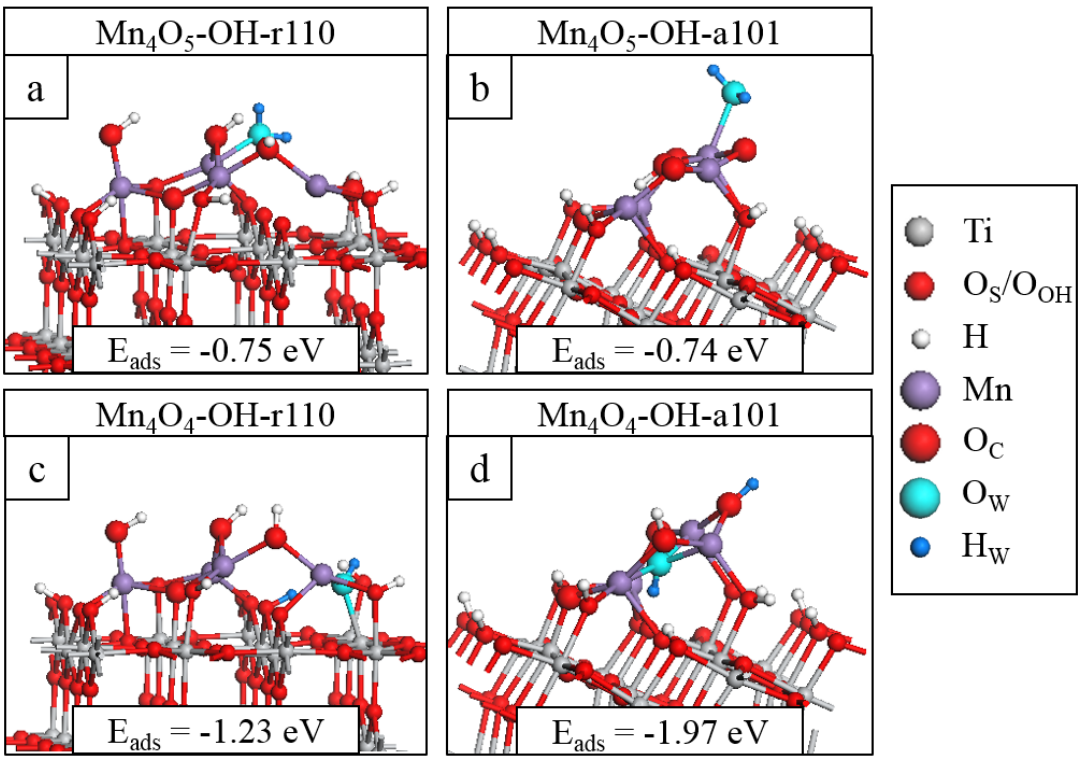

Figure 6.2.3 Relaxed atomic structures of the most stable configurations of H_2O adsorbed at **(a)** Mn_4O_5-OH-r110, **(b)** Mn_4O_5-OH-a101, **(c)** Mn_4O_4-OH-r110 and **(d)** Mn_4O_4-OH-a101. Atomic species are distinguished by colour according to the legend on the right hand side.

We adsorb water in molecular form at the heterostructures and relax the geometry. For Mn_4O_5-OH-r110, shown in **Figure 6.2.3.a**, water is adsorbed exothermically in molecular form with a computed adsorption energy of -0.75 eV. In this instance, the water molecule binds to a three-fold coordinated Mn^{2+} site with a Mn-O_W distance of 2.3 Å. **Figure B.4.4.a** shows dissociative water adsorption at the Mn_4O_5-OH-r110 surface, which has an adsorption energy of -0.31 eV. Upon dissociation, an H atom migrates to a bridging O_S site and the water-derived hydroxyl (OH_W) is singly coordinated to a Mn site with an Mn-O_W distance of 1.9 Å. The dissociation is accompanied by a transfer of charge from O_W to the nanocluster modifier, indicated by a decrease of 0.4 electrons in the computed Bader charge for the O_W ion. The Bader charges and spin magnetisations of cation sites are unchanged by the adsorption and dissociation.

Water adsorbs molecularly at Mn_4O_5-OH-a101, as shown in **Figure 6.2.3.b**, with an adsorption energy of -0.74 eV. The H_2O binds to a four-fold coordinated Mn^{3+} ion with a Mn-O_W distance of 2.2 Å. Since Mn_4O_5-OH-r110 and Mn_4O_5-OH-a101 are the ground states of the systems, the single O_V having formed spontaneously, these composites favour non-stoichiometry so that the strength of interaction with the water molecule is not sufficient to promote spontaneous dissociation and adsorption in molecular form is favoured.

The surfaces with two O_V show higher reactivity to water, as indicated by the larger adsorption energies in **Figures 6.2.3.c** and **6.2.3.d**. Water adsorbs and spontaneously dissociates at both Mn_4O_4-OH-r110 (**Figure 6.2.3.c**) and Mn_4O_4-OH-a101 (**Figure 6.2.3.d**). For Mn_4O_4-OH-r110, the water molecule adsorbs at an O_V site. An H atom migrates to a bridging O_S site and the OH_W group is doubly coordinated to a Mn and a surface Ti site. The Mn-O_W and Ti-O_W distances are 2.2 Å. Bader charge analysis reveals that 0.3 electrons are transferred from the O_W to the surface. Despite this charge transfer,

the Ti ion which binds to OH_W and which was reduced to Ti^{3+} due to O_V formation prior to water adsorption, remains in the Ti^{3+} state. This agrees with work by Henderson *et al* in which no charge transfer was observed between Ti^{3+} and bridging hydroxyls bound at oxygen vacancy sites at the TiO_2 rutile (110) surface.[14] The authors found that the reduced Ti site was only oxidised after interaction of O_2 with the Ti^{3+}-OH group. After water adsorption and dissociation, the distribution of cation oxidation states is unchanged so that there are three Mn^{2+} ions and one Ti^{3+}. The Bader charge for the bridging O_S site to which the H ion binds increases from 7.3 to 7.7 electrons which, as discussed in **Chapter 2**, is typical of hydroxyl formation.

For Mn_4O_4-OH-a101, the water molecule adsorbs at an O_V site and after dissociation a H atom migrates to an O_C ion, which shows an increase in Bader charge, from 7.1 to 7.6 electrons. The OH_W group binds to three Mn^{2+} ions; the Bader charges and spin magnetisations for cation sites are unchanged so that these ions are not involved in the charge transfer. However, for the water adsorption configuration shown in **Figure B.4.4.d**, a Mn^{2+} ion is re-oxidized to Mn^{3+} after dissociation of the water molecule. In this instance the adsorption energy is -1.89 eV and the OH_W group is singly-coordinated to the re-oxidized Mn ion.

6.2.3 Conclusions

On both reduced ceria-modified TiO_2 systems, water adsorption is exothermic and favourable and, importantly, this leads to spontaneous dissociation of water to form surface bound hydroxyls. For MnO_x-TiO_2, oxygen vacancies have an impact on the strength of interaction and the most favourable adsorption mode of H_2O at the modified surfaces. For Mn_4O_5-OH-a101, with a spontaneously formed O_V, water adsorbs only in

molecular form. With formation of reducing oxygen vacancies, water adsorption becomes more exothermic and leads to spontaneous dissociation to surface bound hydroxyls, similar to observations for water interacting at reduced TiO_2[13-14] and CeO_2[7] surfaces.

6.3 *Water oxidation steps at AEO-modified TiO_2*

What follows is adapted from an article entitled: "***Surface modification of Rutile TiO_2 with Alkaline-Earth Oxide Nanoclusters for Enhanced Oxygen Evolution***", published in ACS Applied Nano Materials.[15]

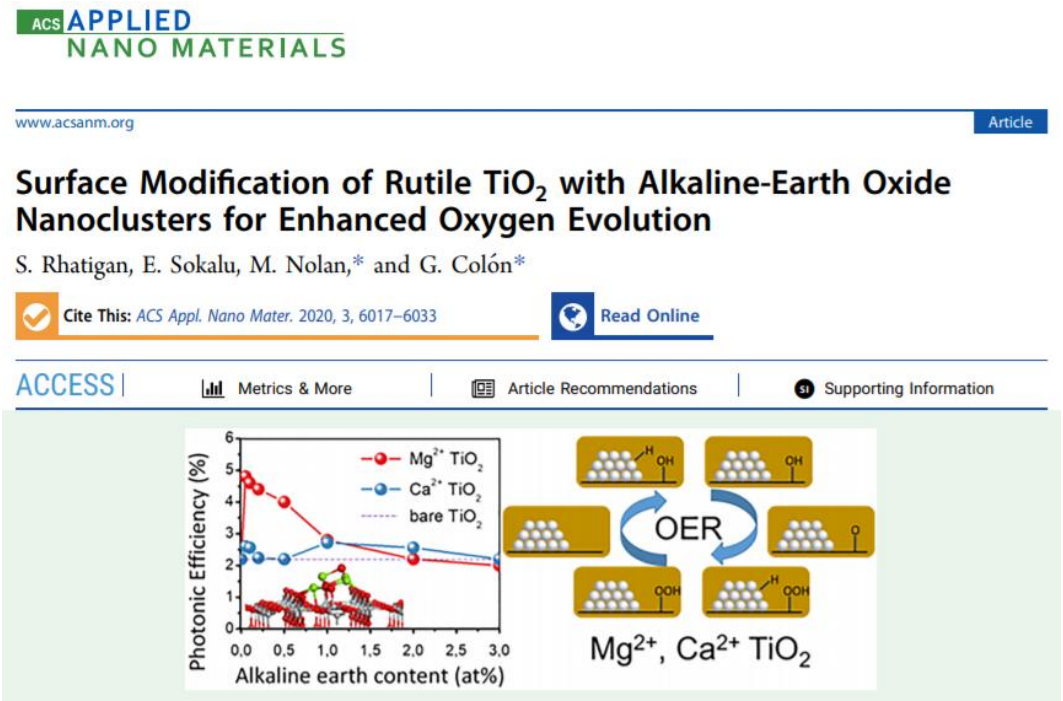

DOI: https://doi.org/10.1021/acsanm.0c01237

https://cora.ucc.ie/handle/10468/10315

6.3.1 Introduction

In this work, we present an experimental and theoretical study of rutile TiO_2 modified with nanoclusters of the alkaline-earth oxides (AEO), CaO and MgO. The combination of experiment and computation yields a comprehensive and cohesive analysis of the activity of AEO-modified rutile TiO_2 as a catalyst for the OER.

The synthesis method in this work is incipient impregnation, which is a well-established technique for the deposition of modifiers at semiconductor surfaces.[16-18] A similar synthesis approach has been used to deposit nanoclusters of PtO_x,[16, 19] SnO_x,[19] ZnO,[20] and MoO_3,[21] on TiO_2. Thus, based on this synthesis procedure, the rutile TiO_2 surface will be modified with dispersed AEO nanoclusters, rather than being doped with the alkaline-earths incorporated onto lattice sites. Samples were prepared with different loadings of the AEO nanocluster modifiers and the performance of nanocluster modified TiO_2 as a catalyst for the OER was determined.

In our DFT calculations, we implement models whose use has been widely reported in the literature and whose outputs are accepted as material descriptors for the photocatalytic performance. We apply this model approach to provide a comprehensive analysis of the OER activity of AEO-modified TiO_2 and this is complemented by direct comparisons with experiment.

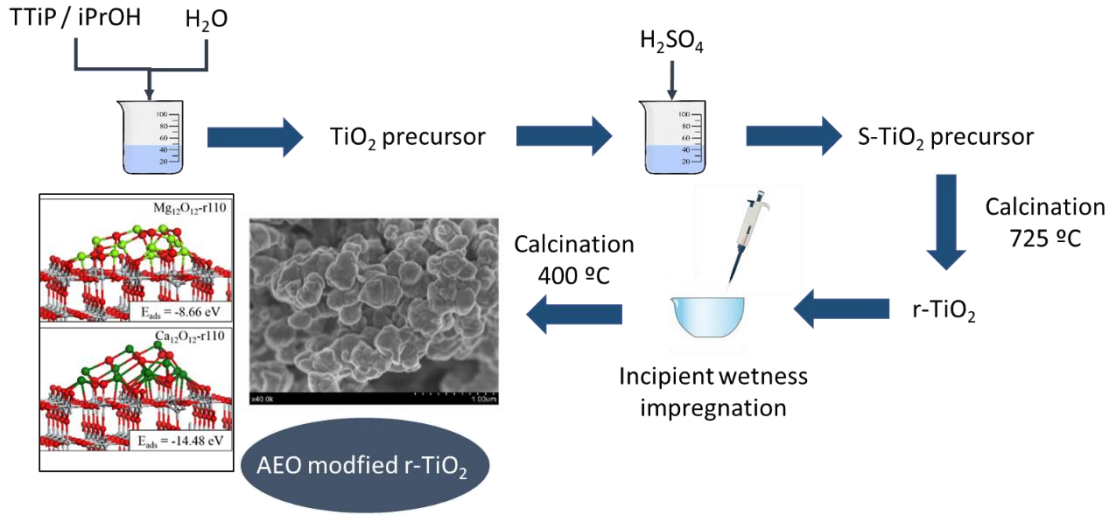

Scheme 6.3.1 Multistep preparation synthetic route for alkaline earth oxide supported on rutile TiO_2. Rational design and photocatalytic studies for OER.

AEO modification has been previously reported to enhance the photoactivity of anatase TiO_2 for dye degradation or H_2 production using Pt as a co-catalyst.[22-23] However, as far

as we know, this is the first time that the use of alkaline earth oxide nanocluster modification of rutile for OER is reported. **Scheme 6.3.1** summarises the experimental and modelling approach in developing AEO nanocluster modified rutile for OER.

We observe clear differences in the activities of CaO- and MgO-modified TiO_2 for OER, depending on the loading of the AEO nanocluster. In particular, low coverages of highly-dispersed MgO-nanoclusters yield a significant enhancement, doubling the photonic efficiency relative to unmodified rutile.

We characterise the modified surfaces experimentally and computationally. The structure of the heterostructured surfaces was investigated *via* X-ray diffraction (XRD) and X-ray photoelectron spectroscopy (XPS). Further insight into this characterisation is provided through DFT calculations. We examine the aggregation of the nanoclusters at the rutile surface and, by comparison with metal-oxygen binding energies and formation energies, explain trends in the dispersion of the nanoclusters at the rutile surface. In addition, we assess the reducibility, *via* oxygen vacancy formation, of the composite systems.

UV-vis diffuse reflectance spectroscopy and photoluminescence (PL) spectroscopy show the impact of modification on the light absorption properties and charge carrier dynamics, respectively. The analysis is supported by DFT computations of the density of states (DOS) and a model for photoexcitation, through which we assess the stability of the excited state and the localisation of photogenerated electrons and holes.

To investigate active sites of AEO-modified TiO_2 for the OER, we use DFT calculations to examine water adsorption at various sites of the stoichiometric and reduced nanocluster modified surfaces. This includes water adsorption at nanocluster sites, adsorption at the interface between the nanocluster modifier and the titania surface, and water adsorption at an already hydroxylated heterostructure. Here, we note that many DFT studies of water

oxidation at surfaces ignore the role of surface hydroxylation. We find that reduction of the system, and the presence of reduced Ti^{3+} cations, play a crucial role in the photocatalytic performance by stabilising OER intermediates at the surface. Moreover, we identify interfacial sites as active sites and this, importantly, indicates that small, dispersed nanoclusters will yield the highest OER activity.

The following sections present selected experimental results, performed by our collaborators, and the results of complementary computational studies, performed by the author.

6.3.2 Results

6.3.2.1 Photocatalytic Performance for Water Oxidation

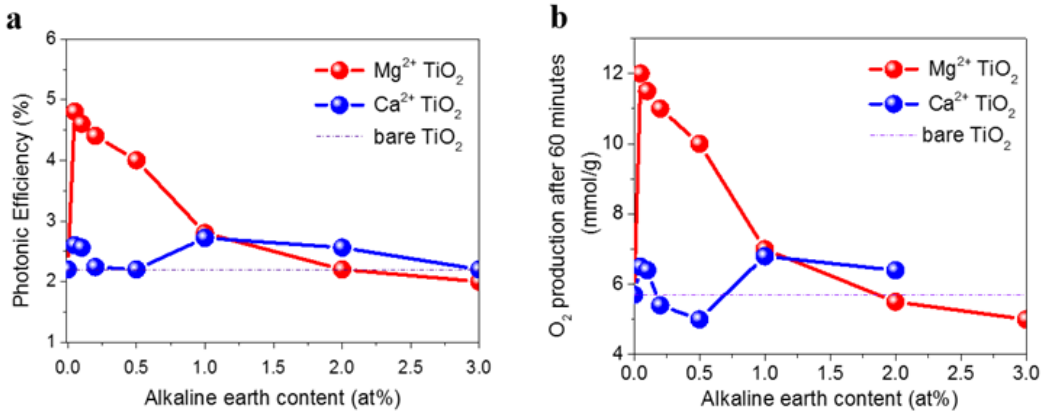

Figure 6.3.1 (a) Photonic efficiencies for MgO- and CaO-modified TiO_2 for the OER. **(b)** Photocatalytic O_2 evolution (mmol/g) after 60 min for MgO- and CaO-modified TiO_2 (0.5 g/L catalyst, 0.02 M $AgNO_3$, Hg lamp 125 W).

A series of MgO- and CaO-modified rutile samples were prepared with alkaline earth loadings ranging from 0.05-3 at. %, (see **Section B.5** of **Appendix B**). In **Figure 6.3.1** we show the photoactivity of the AEO-modified rutile materials for the OER, with a silver nitrate electron scavenger. Depending on the loading of the modifier, surface

modification of rutile with both MgO and CaO can lead to improvements in the OER activity and the photonic efficiency.

This improvement is most pronounced for MgO-modified TiO_2 (**Figure 6.3.1**). In particular, for an MgO loading of 0.05 at. %, the photonic efficiency and O_2 production after 60 minutes are double that measured for bare TiO_2 rutile. This is a remarkable result considering the extremely low levels of surface modification. The efficiency decays as the Mg^{2+} content increases, eventually reaching photoactivities similar to those of bare TiO_2 for loadings of 2-3 at. %. Such an effect has been observed in other studies of surface-modification schemes, where increased loadings of the modifier have a detrimental effect on the activity.[24-26] This suggests a bi-functionality, where sites of both the surface and the modifier play a role in the catalytic activity and indicates a key role for nanostructured MgO supported on TiO_2.

For CaO modification, the highest efficiency is attained at a higher Ca^{2+} ion content, compared to Mg^{2+}, but the improvement is less significant compared to MgO modification. It is clear that the presence of these modifiers affects the photocatalytic activity of rutile TiO_2 in different ways. To understand the influence of AEO-modification we have performed a wide surface, structural and electronic characterisation of the catalysts. This analysis is complemented by first principles calculations, with particular focus on identifying active sites of water oxidation at the AEO-modified TiO_2 surface.

6.3.2.2 Structural and Surface Characterisation

Experimental Results

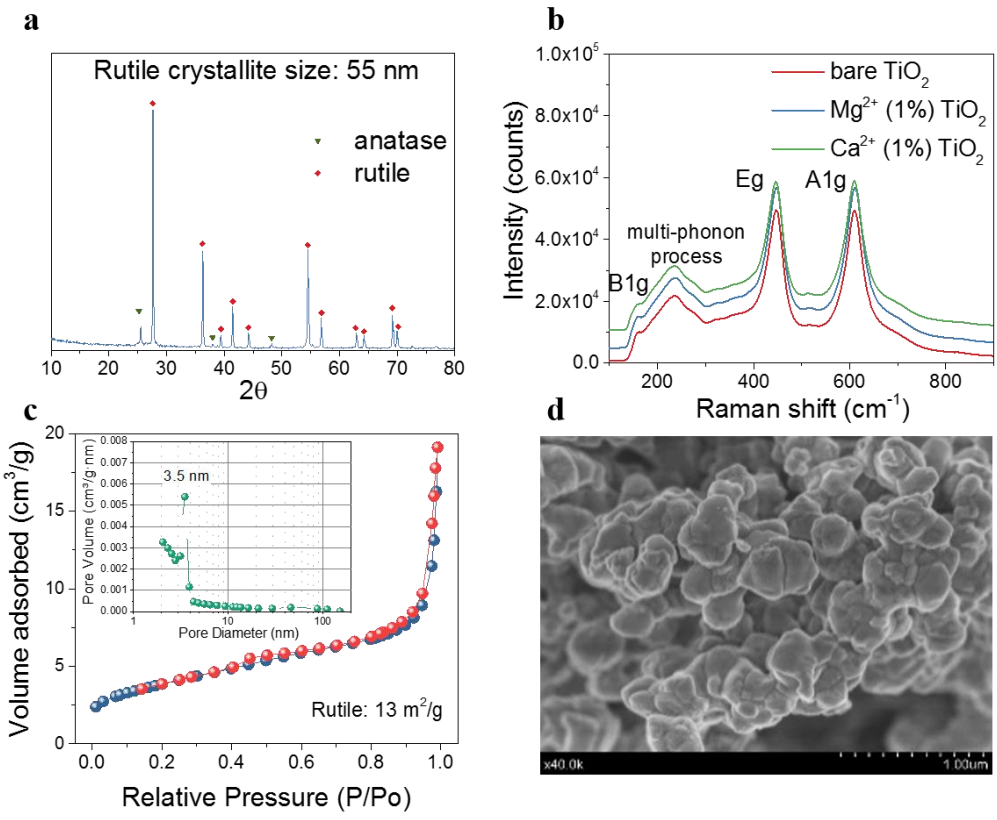

Figure 6.3.2 Structural and textural properties of TiO_2 rutile photocatalysts: **(a)** XRD pattern of r-TiO_2 support; **(b)** Raman spectra of bare r-TiO_2 and alkaline modified r-TiO_2; **(c)** N_2 adsorption-desorption isotherm (inset: pore size distribution plot) of r-TiO_2 support; **(d)** SEM image of r-TiO_2 support.

TiO_2 rutile was prepared by precipitation and further sulphuric acid pre-treatment. Sulphuric acid pre-treatment, prior to the calcination step, can delay the anatase to rutile transformation and favours the formation of well-crystallised anatase structures with relatively high surface areas.[27] Thus, the presence of surface anchored sulphate groups stabilises the anatase structure at high temperatures, such as 650 °C. The transition to rutile phase takes place once surface sulphates evolve during calcination. By calcination

at 725 ºC, the TiO_2 samples show a dominant rutile phase, with a crystallite size of 55 nm, which denotes a high degree of crystallisation (**Figure 6.3.2.a**).

Raman spectra in **Figure 6.3.2.b** provide further evidence of the predominance of the rutile phase. Characteristic rutile Raman modes at 157 cm^{-1} (B1g), 235 cm^{-1} (multi-phonon process), 447 cm^{-1} (Eg) and 610 cm^{-1} (A1g) are present. Since Raman spectroscopy is very sensitive to different crystalline structures, in accordance with the XRD data, tiny bands corresponding to the anatase phase can be seen. There are no strong distortions or shifts of the Raman modes after modification with the alkaline earths, indicating that there is no doping of the metals onto Ti sites in the rutile lattice. Doping would result in formation of oxygen vacancies to compensate the lower oxidation state of Mg and Ca, which would distort the local atomic structure and hence the Raman peaks. Due to the high calcination temperature to assure the rutile phase, the TiO_2 support shows a notably low specific surface area of 13 m^2/g, with a negligible porosity (**Figure 6.3.2.c**). As expected, the impregnation with the alkaline-earth oxide nanoclusters does not induce any notable change in the structure of modified rutile. The morphology of the sample in **Figure 6.3.2.d** for TiO_2 rutile from SEM also confirms the sample sintering due to the high calcination temperature (**Figure 6.3.2.d**).

The presence and dispersion of alkaline-earth ions at the rutile surface have been studied by XPS analysis. In **Figure 6.3.3**, we show the Mg 1*s* and Ca 1*p* XPS spectra for samples with different coverages of the alkaline earth oxides. The core electron binding energy is 1304 eV for Mg 1*s* and 347 eV for Ca 2*p*, which correspond to Mg^{2+} and Ca^{2+}.[28-29] For Ti 2*p*, the observed binding energies all lie around 458.5 eV, which is the typical value for Ti^{4+} in TiO_2. With the introduction of the alkaline earth modifiers, there is a small shift in the Ti 2*p* position towards lower binding energies. This shift has also been observed for Mg modified systems and indicates the formation of Ti-O-Mg bonds,[30]

which would be present with alkaline earth oxide nanoclusters supported on the rutile TiO_2 surface coordinating to surface oxygen atoms.

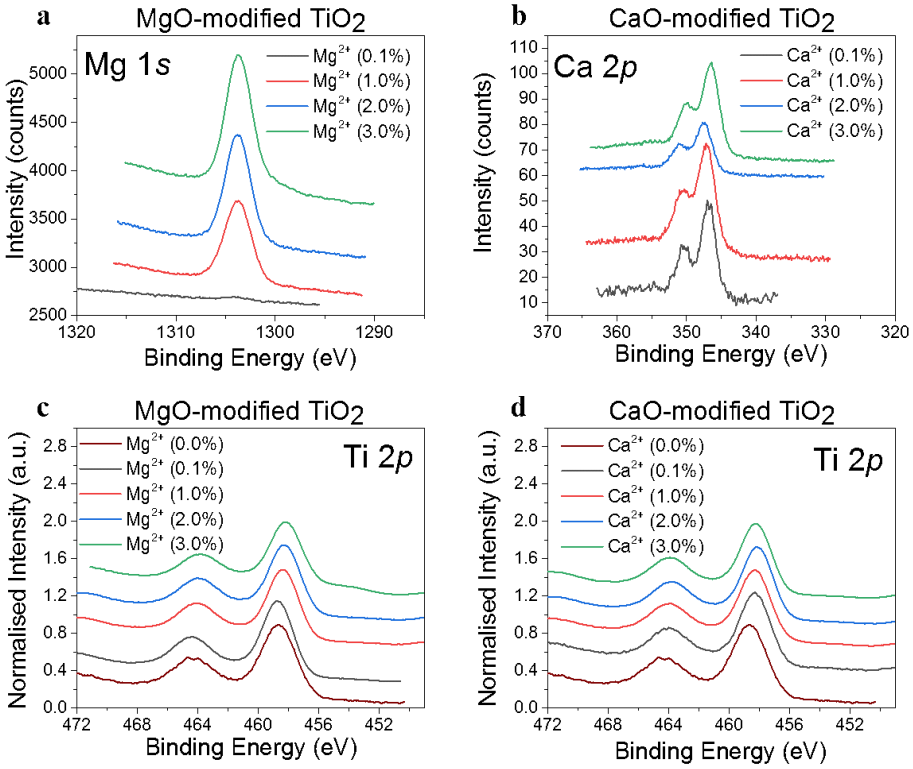

Figure 6.3.3 XPS spectra for alkaline earth modified TiO_2 rutile photocatalysts.

Differences between Mg and Ca modification can be seen by comparing the chemical features of the surface, represented by the data in **Table 6.3.1**. The Mg/Ti ratio for MgO-modified TiO_2 at the lowest loadings is significantly lower when compared to Ca-modification at the same nominal loading and compared to higher Mg-loadings. This suggests a higher dispersion of Mg^{2+} at the rutile surface, but this dispersion is not observed for Ca^{2+}, even at the lowest loadings. Moreover, as the alkaline-earth content increases, the AE/Ti ratio progressively increases for both modifiers, which denotes a lower degree of dispersion. This can be due to aggregation to form larger nanoclusters at the surface. For higher content samples, Ca/Ti atomic ratios are significantly lower than for Mg.

Table 6.3.1 Surface features of AEO-modified rutile TiO_2 from XPS.

AE-modified TiO_2		AE/Ti ratio	O/Ti	OH (%)
Bare TiO_2		---	2.21	11.0
Mg^{2+}	0.10	0.015	2.54	36.1
	1.00	0.587	2.88	27.0
	2.00	0.796	2.90	19.5
	3.00	0.867	2.64	18.0
Ca^{2+}	0.10	0.107	2.32	9.2
	1.00	0.147	2.87	16.9
	2.00	0.260	2.79	14.0
	3.00	0.479	3.08	21.9

MgO-modified TiO_2 samples with the lowest loadings show the highest level of surface hydroxylation, 36.1% for 0.1% Mg, and the trends in hydroxylation coverage with AE loading behave differently for MgO and CaO. For MgO modified rutile, the higher dispersion of Mg^{2+} ions at low coverages appears to favour hydroxylation. For example, the sample with Mg 0.1 at. % shows both high dispersion (lower Mg/Ti value of 0.015) and a high degree of surface hydroxylation (36.1%). This effect is not observed for the CaO-modified series, for which hydroxylation coverage increases with Ca^{2+} content.

This result is consistent with previous work which showed that water dissociation is favourable for MgO nanoclusters supported on TiO_2[31] and on ultra-thin MgO films supported on metals (Ag and Mo), but is not favourable on bulk MgO or beyond 3 monolayer (ML) thick films.[32-34] Therefore, as the loading of Mg increases, hydroxylation will become less favourable. By contrast, previous work clearly shows that water dissociation is favourable on CaO films and on the (100) bulk cleaved surface,[35-36] so that

the degree of hydroxylation, as a result of water dissociation at the oxide, increases with an increase in the loading of CaO on rutile.

Computational Results

Further insight into the dispersion of AEO nanoclusters at the titania surface is provided by DFT calculations. To model AEO-modified rutile TiO_2, the most stable rutile surface, the (110) facet, is modified with MgO and CaO nanoclusters of three compositions, 4, 8, and 12 MgO/CaO units, shown in **Figure 6.3.4**. The starting geometries for these clusters were published in the work of Haertelt *et al*.[37] In this way, we investigate the effects of dispersion/aggregation and coverage, for comparison with experimental results.

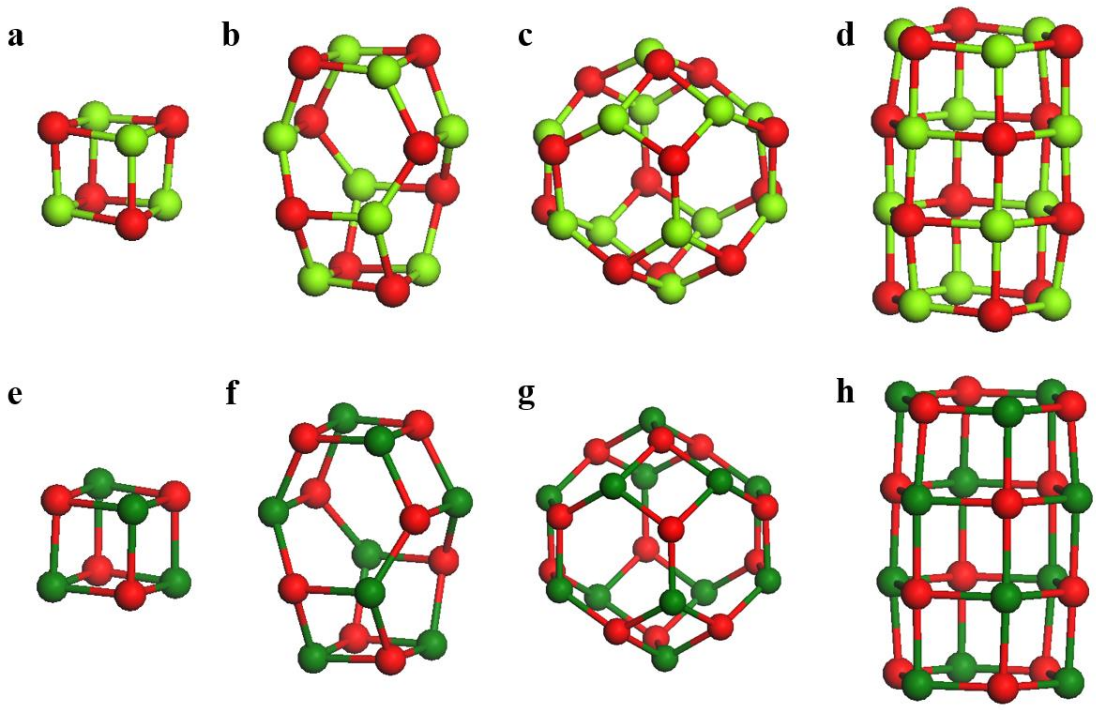

Figure 6.3.4 Relaxed geometries of the gas phase nanoclusters of MgO and CaO. Structures shown are **(a)** Mg_4O_4, **(b)** Mg_8O_8, **(c)** and **(d)** $Mg_{12}O_{12}$, **(e)** Ca_4O_4, **(f)** Ca_8O_8, **(g)** and **(h)** $Ca_{12}O_{12}$. In this and subsequent Figures Mg is represented by light green spheres, Ca by dark green and O by red.

For both MgO and CaO, the 4- and 8-unit clusters have similar geometries in the gas phase **Figure 6.3.4**. For the 12-unit clusters, two geometries are considered: a spherical cage structure and a cylindrical tube structure. For $Mg_{12}O_{12}$, the spherical geometry (**Figure 6.3.4.c**) is more stable by 0.26 eV, whereas for $Ca_{12}O_{12}$ the spherical geometry (**Figure 6.3.4.h**) is more stable by 1.74 eV.

In addition, two and three 4-unit nanoclusters (NCs) were adsorbed at the surface in various configurations for comparison with adsorption of the 8 and 12-unit NCs. The most stable configurations, henceforth denoted M_4O_4-, M_8O_8- and $M_{12}O_{12}$-r110 (M = Mg, Ca), were used in subsequent calculations and these are shown in **Figure 6.3.5**. Additional geometries and discussion are presented in **Appendix B** (**Figures B.5.2** and **B.5.3**). The systems shown in **Figure 6.3.5** correspond to coverages of 25-50% for modification with NCs of sizes 4-12 MO units (M = Mg, Ca).

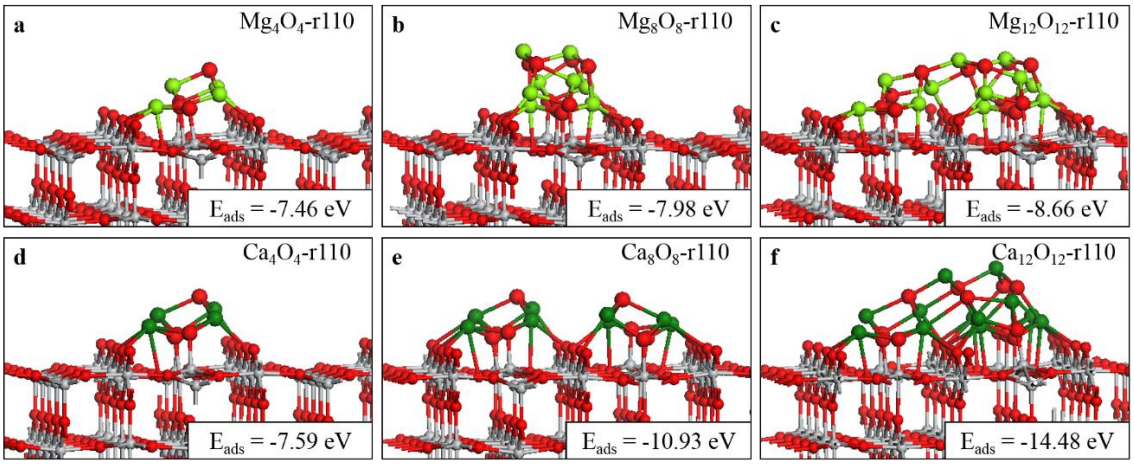

Figure 6.3.5 The top panels show the relaxed atomic structure of rutile (110) modified with nanoclusters of composition **(a)** Mg_4O_4, **(b)** Mg_8O_8 and **(c)** $Mg_{12}O_{12}$. The bottom panels show the relaxed atomic structure of rutile (110) modified with nanoclusters of composition **(d)** Ca_4O_4, **(e)** Ca_8O_8 and **(f)** $Ca_{12}O_{12}$. The adsorption energies are included in the insets. In this and subsequent figures Ti is represented by grey spheres, O by red, Mg by light green and Ca by dark green. Atoms of the nanoclusters have been enlarged.

The modified surfaces shown in **Figure 6.3.5** do not necessarily represent global minima, as the space of possible adsorption configurations is too large to easily investigate. Rather, these geometries are representative structures for which we may compute material descriptors relevant to the photocatalytic activity. They are the most favourable structures we have found in our search of different configurations. Previous work on modified metal oxide surfaces shows that key properties determining the chemistry of these structures are not sensitive to the precise adsorption structure of the modifiers at the surface. The properties of the modified surface are consistent, so long as the nanocluster modifier binds with the surface through new interfacial bonds; that is, new bonds that form between cations and anions in the surface and the nanocluster.[38] To explore this, we analysed in detail a less stable $Mg_{12}O_{12}$-r110 geometry, **Figure B.5.2.a**, for which the results are discussed in the **Appendix B**. This analysis shows that there are small quantitative, but not qualitative, differences in the computed properties, so that the sensitivity to the precise structure is not significant.

In each structure shown in **Figure 6.3.5**, the adsorbed geometry of the nanocluster differs considerably from the most stable gas-phase structures, which are shown in **Figure 6.3.4**. Upon relaxation, it is more energetically favourable for the MgO and CaO nanoclusters to wet over the rutile surface. This is driven by the formation of interfacial bonds between surface Ti and nanocluster oxygen as well as surface oxygen and nanocluster cations. Ti-O or Mg/Ca-O distances shorter than 2.47 Å[39] and 2.58/3.11 Å[40] are considered as metal-oxygen bonds. These bonds anchor the nanoclusters at the rutile surface.

For the example of Mg_4O_4-r110, (**Figure 6.3.5.a**), 8 interfacial bonds are established between the cluster and the surface. Of these, 3 are Ti to nanocluster oxygen (O_C) bonds, 4 are Mg to bridging surface oxygen (O_{br}) bonds and there is a single Mg to surface in-plane oxygen (O_{ip}) bond.

For the Mg_8O_8 and $Mg_{12}O_{12}$ nanocluster, we can adsorb a single nanocluster or two/three Mg_4O_4 nanoclusters. The most stable relaxed geometries result from an initial structure whereby the nanoclusters are adsorbed as two and three Mg_4O_4 units, shown in **Figures 6.3.5.b** and **6.3.5.c**. In the relaxed heterostructures the surface Ti to O_C distances are 1.76-2.12 Å. Distances for Mg to surface oxygen sites are 1.92-2.45 Å for O_{br} and 2.10-2.38 Å for O_{ip}.

The CaO-TiO_2 surface modification shows similar changes in the nanocluster structures upon adsorption and relaxation. The relaxed Ca_4O_4-r110 structure (**Figure 6.3.5.d**) is qualitatively similar to that of Mg_4O_4-r110 (**Figure 6.3.5.a**), with the formation of 8 interfacial bonds, consisting of 3 Ti-O_C bonds, 4 Ca-O_{br} bonds and 1 Ca-O_{ip} bond. For Ca_8O_8-r110 (**Figure 6.3.5.e**), the most stable adsorption configuration is that in which two Ca_4O_4 nanoclusters are adsorbed in proximity but without interacting *via* shared bonds. The most stable $Ca_{12}O_{12}$-r110 structure (**Figure 6.3.5.f**) corresponds to three Ca_4O_4 nanoclusters in a contiguous cluster at the surface. The Ti-O_C bond lengths from the surface to the nanocluster are 1.80-1.94 Å, the Ca-O_{br} and Ca-O_{ip} bond lengths between the nanocluster and the surface are 2.14-2.93 Å and 2.43-3.05 Å, respectively.

The effect of the modification with MgO and CaO on the rutile (110) surface is most notable for those Ti ions that bind to oxygen atoms of the adsorbed nanoclusters. These Ti ions migrate out from the surface, towards the nanoclusters, by up to 0.8 Å, breaking bonds to subsurface oxygen ions. However, modification of the rutile surface with AEO-modifiers does not lead to a substantial reconstruction of the surface; this confirms the results of the experimental characterisation of the AEO-modified TiO_2 systems.

The magnitudes of the computed adsorption energies, shown in **Figure 6.3.5**, indicate that the nanoclusters adsorb strongly at rutile (110) and require significant temperatures

to desorb. Mg_4O_4 and Ca_4O_4 have similar computed adsorption energies, -7.46 eV and -7.59 eV, while differences emerge in the computed adsorption energies of the larger nanoclusters. The adsorption energies for Mg_8O_8 and $Mg_{12}O_{12}$ are -7.98 eV and -8.66 eV, respectively, which are comparable to that of Mg_4O_4, indicating that there is little energy gained in the aggregation of MgO to form larger nanoclusters at the surface. Conversely, Ca_8O_8 and $Ca_{12}O_{12}$ have computed adsorption energies of -10.93 eV and -14.48 eV, which, although not so large as to prohibit the dispersion of smaller clusters at the surface, indicate that aggregation to larger clusters is preferred for CaO. These results are consistent with the experimental analysis that for low Mg contents, the MgO modifier is highly dispersed at the rutile surface, whereas CaO will be less dispersed and present as larger structures.

As the loading increases, the configurations in which the modifiers form contiguous clusters, as shown in **Figures 6.3.5.c** and **6.3.5.f**, are more stable by similar amounts, 2.25 eV for $Mg_{12}O_{12}$ and 2.11 eV for $Ca_{12}O_{12}$, than the next most stable configurations, which consist of three isolated Mg_4O_4 and Ca_4O_4 nanoclusters, shown in **Figures B.5.2** and **B.5.3** of **Appendix B**.

To investigate these trends in aggregation, we compare the per-unit binding energies of the AEO nanoclusters in the gas phase. The per-unit binding energy is defined as:

$$E_b = \frac{E(\mathrm{M_n O_n}) - n[E(\mathrm{M}) + 1/2\mathrm{E}(\mathrm{O_2})]}{\mathrm{n}} \qquad 6.3.1$$

The binding energies of the 4-, 8-, and 12-unit MgO nanoclusters are -2.93, -3.76 and -4.14 eV, respectively; for CaO, the binding energies are -4.16, -4.56, and -4.86 eV. Thus, in comparing nanoclusters of similar sizes, CaO nanoclusters are more stable than their MgO analogues, in absolute terms. Based on this analysis, aggregation to form larger CaO nanoclusters is more favourable compared to aggregation of MgO. A similar trend was

reported by Malliavin *et al* in their study of $(MgO)_n$ and $(CaO)_n$ clusters with $n \leq 6$.[41] Similarly, bulk calculations for the formation energies of Mg-O and Ca-O showed that CaO has a larger formation energy (-6.55 eV) compared to MgO (-6.12 eV).[42] Moreover, Chen and colleagues reported greater stability of MgO nanoclusters relative to bulk MgO, as compared with the stability of CaO nanoclusters relative to CaO bulk.[43-44] These results suggest that CaO favours aggregation to larger structures compared to MgO. Moreover, for the 12-unit nanoclusters at the rutile surface, there are 23 interfacial Ca-O bonds formed, compared with 13 interfacial Mg-O bonds; this is likely the result of the larger ionic radius of Ca^{2+} (1.06 Å) compared to Mg^{2+} (0.78 Å)[44] and indicates a stronger interaction of CaO at the rutile surface.

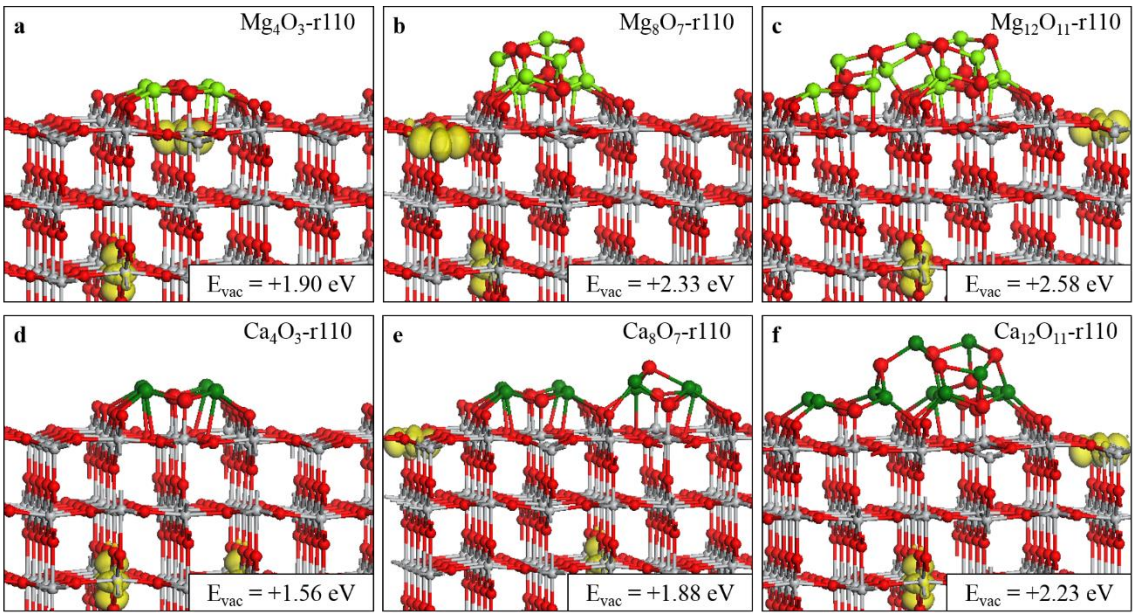

Figure 6.3.6 Relaxed atomic structures of AEO-modified rutile (110) with a single, reducing oxygen vacancy. Top panels show **(a)** Mg_4O_3-, **(b)** Mg_8O_7- and **(c)** $Mg_{12}O_{11}$-r110. Bottom panels show **(d)** Ca_4O_3-, **(e)** Ca_8O_7- and **(f)** $Ca_{12}O_{11}$-r110. The yellow isosurfaces enclose spin densities of up to 0.02 electrons/$Å^3$.

To examine reducibility, the formation of a neutral oxygen vacancy was investigated at each oxygen site in the supported nanoclusters. The most stable structures with one oxygen vacancy are shown in **Figure 6.3.6**, along with the computed formation energies.

The full set of oxygen vacancy formation energies is included in **Table B.5.2** in **Appendix B**. On all MgO-modified and CaO-modified TiO_2 structures the energy cost to produce an oxygen vacancy increases with the size of the nanocluster. This is in agreement with an increase in the M-O binding energy with increasing nanocluster size.[41] Despite this, the modified surfaces are clearly more reducible than bare rutile (110), for which the computed energy cost to produce a single oxygen vacancy from a bridging oxygen site is +4.50 eV.

On MgO-modified rutile TiO_2, the formation energies in **Figures 6.3.6.a**, **6.3.6.b** and **6.3.6.c** suggest that reducibility is enhanced at the lowest loadings, in which small MgO clusters are widely dispersed over the surface. As the coverage increases, and the modifiers aggregate to form larger nanoclusters, the energy cost to produce an oxygen vacancy increases. Similarly, for CaO modifiers, oxygen vacancy formation is computed to have lower energy costs for smaller clusters. However, for CaO-modified TiO_2, aggregation to form larger clusters is favourable, even at lower coverages and this, combined with larger binding energies for CaO nanoclusters, means that the formation energies for oxygen vacancies are larger than on MgO-TiO_2.

After formation of a neutral oxygen vacancy, two electrons are released and their localisation is visualised with the excess spin density plots in **Figure 6.3.6**. These charge distributions emerge after relaxation of the systems with one O ion removed. In all cases, the two electrons localise on Ti sites on the rutile (110) surface, since Mg is not reducible. One electron localises at a subsurface Ti site, typical for reduced rutile (110).[45-46] While there are studies in the literature showing that there are different energetics of different Ti^{3+} localisation patterns in unmodified rutile (110),[45-46] we stress that in our nanocluster-modified rutile structures, structural distortions are already present in the surface layer of the rutile substrate, which will promote the localisation of the second electron.

While the impact of electron localisation on different Ti sites could be examined, this will not change the key finding that the cost to remove an oxygen is significantly lower in surface modified rutile compared to the bare surface. The location of the second electron depends on the size of the modifier. On all reduced MgO-r110 structures, the second electron localises at a surface Ti. For Ca_4O_3-r110, both electrons localise at sub-surface Ti sites, while Ca_8O_7-r110 and $Ca_{12}O_{11}$-r110 show electron localisation similar to the corresponding MgO-TiO_2 structures. The electron localisation at Ti sites is further confirmed by an increase in the computed Bader charge of Ti from 9.6-9.7 electrons, for Ti^{4+}, to 9.9-10.0 electrons, for Ti^{3+},[31, 47-48] while the computed spin magnetisations for Ti^{3+} sites are in the range 0.8-0.9 μ_B. Finally, the Ti^{3+}-O distances increase by up to 0.2 Å.

6.3.2.3 Effect of AEO-modification on Light Absorption

Experimental Results

An absorption spectrum, produced *via* UV-vis diffuse reflectance spectroscopy is presented in **Figure 6.3.7**. Unmodified rutile and MgO- and CaO-modified rutile show similar band gaps around 3.1 eV, typical for the TiO_2 rutile phase.[49] However, examination of the absorption edge shows that, for the MgO and CaO modified samples, some light absorption is apparent in the visible range. This absorption should correspond to the emergence of states in the TiO_2 valence to conduction band energy gap, due to the presence of the modifier or vacancies at the rutile surface. This red-shift in absorption is more pronounced for Ca^{2+} modified TiO_2.

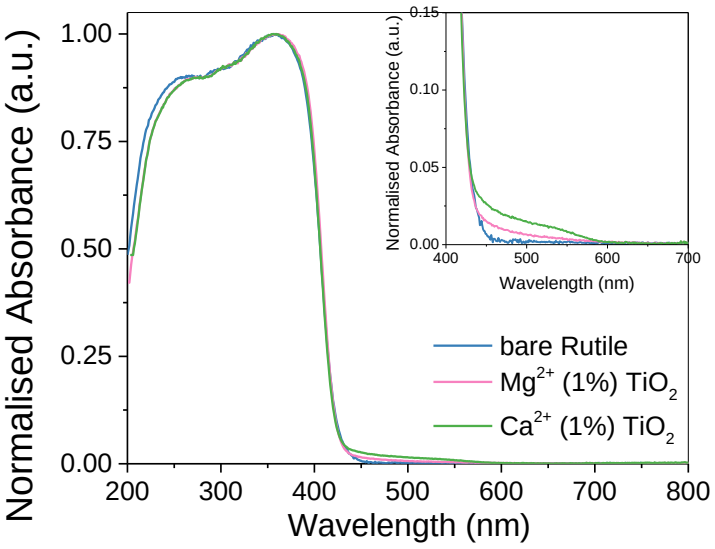

Figure 6.3.7 Absorption spectra for MgO- and CaO-modified rutile TiO_2 (1 at. %).

Computational Results

DFT insights into the optical properties of AEO-modified TiO_2 rutile are provided through analysis of the computed projected electronic density of states (PEDOS), focused on the 4- and 12-unit nanoclusters modifying the TiO_2 surface. **Figure 6.3.8** displays the PEDOS plots for the stoichiometric ground states (**Figure 6.3.8.a**, **6.3.8.b**) and the reduced states, in which one oxygen vacancy is present, as described above, (**Figure 6.3.8.c**, **6.3.8.d)**. The top half of each panel shows the contribution to the PEDOS from Ti-3*d* and Mg/Ca-(*s* + *p*) states while the bottom half shows the 2*p* states of surface oxygen (O_S) and nanocluster oxygen (O_C).

The PEDOS for the bare rutile (110) surface is given in **Figure B.5.5** in **Appendix B** for comparison and within our computational set-up the valence to conduction band energy gap is 2.2 eV. This underestimation of the energy gap is of course typical of approximate DFT methods and while it is possible to tune the +U correction to reproduce the experimental band-gap, this results in a poorer description of other material properties

and so is not advised. Rather, the Coulomb correction is implemented to overcome the self-interaction error (SIE) of standard DFT and to describe localised electronic states. However, comparison of the PEDOS across the different modified TiO_2 structures yields qualitative information about the impact of AEO-modification.

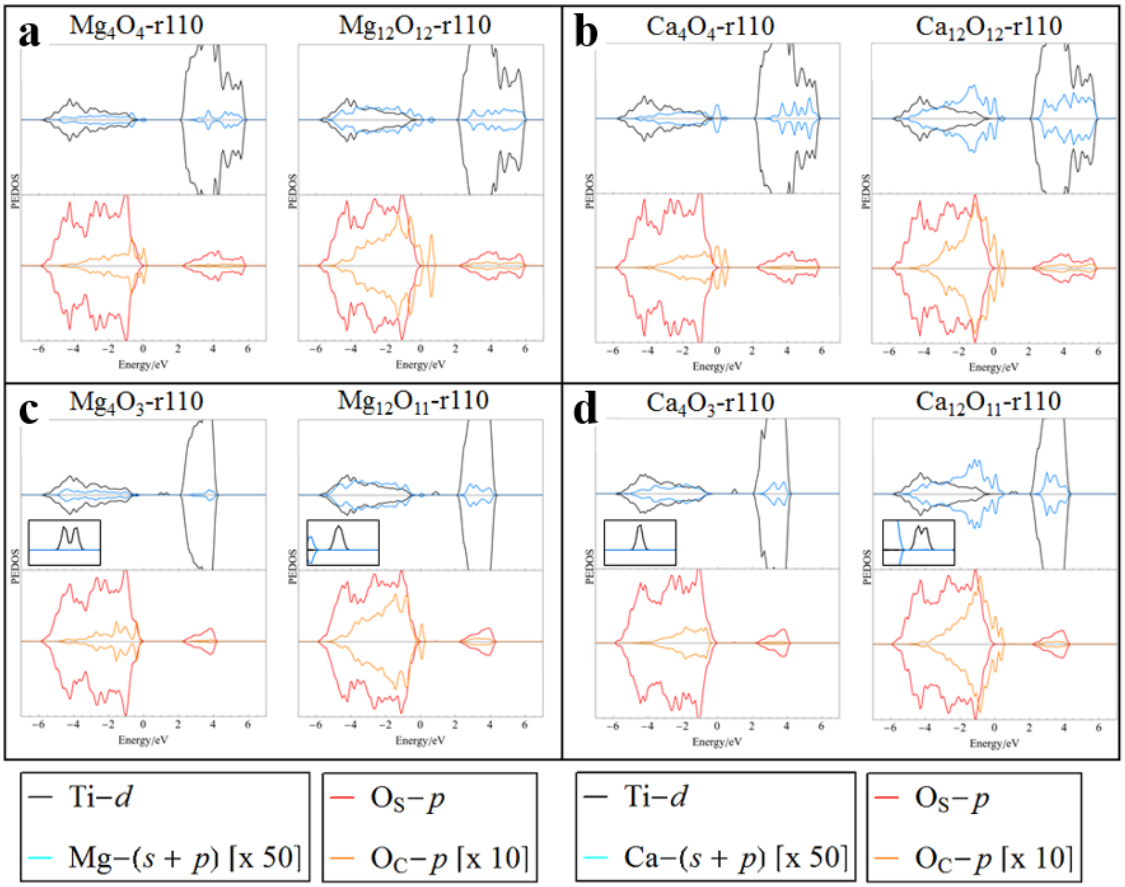

Figure 6.3.8 Computed projected electronic density of states (PEDOS) plots for AEO-modified rutile (110). Top panels display the PEDOS for the stoichiometric ground states **(a)** Mg_4O_4-r110 and $Mg_{12}O_{12}$-r110 and **(b)** Ca_4O_4-r110 and $Ca_{12}O_{12}$-r110. The PEDOS in the bottom panels were computed after formation of a single oxygen vacancy and represent **(c)** Mg_4O_3-r110 and $Mg_{12}O_{11}$-r110 and **(d)** Ca_4O_3-r110 and $Ca_{12}O_{11}$-r110. The top half of each plot shows the contributions due to Ti-*d* (black) and M-(s + p) (M = Mg, Ca; blue). The bottom half of each plot displays O_S-*p* (red) and O_C-*p* (orange) contributions. The rutile (110) VBM is set to 0 eV and the insets in the bottom panels show occupied Ti^{3+} states in the band-gap in the range [0 eV, 2 eV].

For stoichiometric structures, the computed PEDOS predicts a small red-shift in the band gap due to modifier-derived O 2*p*-states extending the valence band maximum (VBM) to higher energy and this effect is greater for the larger modifiers, and for CaO when compared to MgO. After modification, Ti 3*d*-states continue to dominate the conduction band minimum (CBM) with unoccupied Mg- and Ca-derived states lying higher in energy. For the reduced structures, the smaller nanoclusters show no O_C-derived states above the VBM of the TiO_2 support. Mid-gap states, due to reduced Ti^{3+}, emerge at 1.0 eV and 1.3 eV above the VBM for Mg_4O_3-r110 (the two peaks result from an asymmetric distribution of the two electrons) and at 1.0 eV above the VBM for Ca_4O_3-r110. Similarly, for $Mg_{12}O_{11}$-r110, high lying O_C states are removed so that fewer nanocluster-derived states are present above the titania VBM and Ti^{3+} states emerge in the band gap at 0.9 eV. For $Ca_{12}O_{11}$-r110, cluster-derived states persist above the VBM after oxygen vacancy formation and Ti^{3+} states emerge at 1.0 eV and 1.2 eV above the VBM.

In the context of measurements of the absorption edge of MgO-modified rutile TiO_2, at 1 at.% loading, analysis of the computed PEDOS for such a system, namely Mg_4O_3-r110 (**Figure 6.3.8.c**), suggests that any impact on the light absorption properties will be minimal and due only to transitions from occupied Ti^{3+} states, which emerge in the band-gap after reduction. For CaO-modification, the computed PEDOS plots indicate a potential red-shift in the absorption edge due to cluster-derived states above the titania VBM. While oxygen vacancy formation is promoted in CaO-r110 relative to unmodified rutile, the effect on the valence band edge persists after reduction in the case of larger CaO nanoclusters.

6.3.3 Photoluminescence and Charge Separation

Experimental Results

The influence of alkaline-earth modification on the charge carrier dynamics can be assessed using photoluminescence (PL) spectroscopy (**Figure 6.3.9**). The presence of both MgO and CaO induces a reduction in the magnitude of the PL signal compared to unmodified rutile TiO_2, upon excitation at 320 nm. Therefore, it can be inferred that surface modification with these alkaline-earth ions enhances the separation of photogenerated charges and suppresses electron-hole recombination. Similar behaviour was reported by other authors for alkaline-earth doped ZnO systems.[28] In that case, the difference in PL signal observed for doped systems was associated to the different ionic radii. In our case, small interesting differences can be noticed between Mg^{2+} and Ca^{2+}. While for Mg^{2+} the PL signal is not strongly affected by the loading, for Ca^{2+} the modification with 0.05 at.% shows somewhat higher PL when compared to higher Ca^{2+} content.

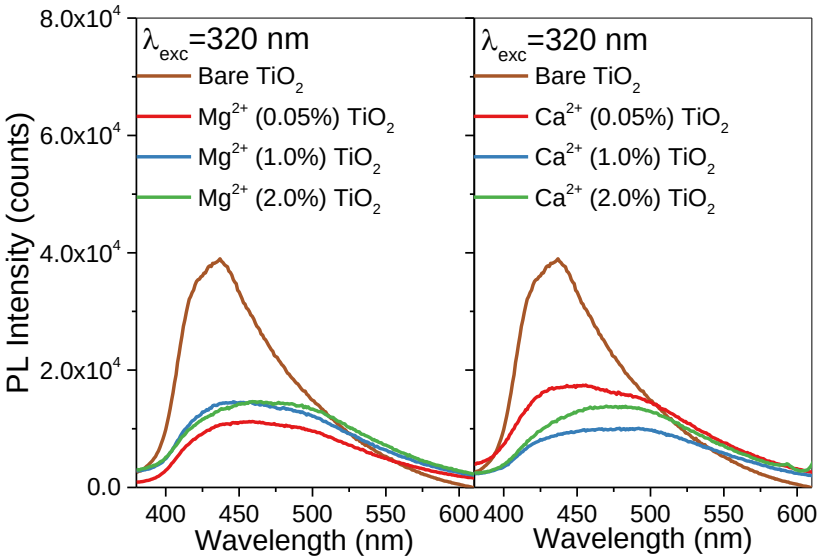

Figure 6.3.9 Photoluminescence spectra for Mg^{2+} and Ca^{2+} modified TiO_2 upon excitation at 320 nm.

Thus, both MgO and CaO positively influence the charge separation upon excitation. In addition, for CaO modified systems we have observed a slight absorption in the visible range, probably due to intermediate states in the bandgap. However, the better photocatalytic behaviour shown by MgO-modified TiO_2 is likely correlated with the surface features of the heterostructure, as already discussed, i.e. MgO modified TiO_2 at low loadings exhibits a high degree of surface hydroxylation, as well as a notable Mg^{2+} ion dispersion, compared to the CaO modified systems. In addition, given that the MgO modifiers are present at the surface as small, dispersed nanoclusters, whereas the CaO modifiers tend to form larger aggregations, the MgO-modified systems are more reducible than the CaO-modified systems.

Computational Results

Table 6.3.2 Energies computed in the photoexcitation model. Vertical singlet-triplet energy difference ($E^{vertical}$), the relaxed singlet-triplet energy difference (E^{excite}) and the relaxation energy (E^{relax}) for the stoichiometric ground states of AEO-modified rutile (110). Values computed for the unmodified TiO_2 rutile (110) surface have been included for reference.

Composite structure	$E^{vertical}$ **(eV)**	E^{excite} **(eV)**	E^{relax} **(eV)**
Rutile (110)	2.35	1.85	0.50
Mg_4O_4-r110	2.28	1.21	1.06
$Mg_{12}O_{12}$-r110	1.98	0.62	1.36
Ca_4O_4-r110	2.39	0.19	2.20
$Ca_{12}O_{12}$-r110	2.06	0.99	1.07

To explore the impact of AEO-modification on charge carrier separation and localisation within DFT, we impose a triplet electronic state and compute the vertical, singlet-triplet, and the electron-hole relaxation (trapping) energies (see **Chapter 2** for full details). These energies are presented in **Table 6.3.2** and values computed for the bare rutile (110) surface are included for reference. The values for $E^{vertical}$ represent the simple VB-CB energy difference and are analogous to the optical band gap. Hence, the energy gap for bare rutile (110) is 2.35 eV, and again, the underestimation of the bandgap, which is inherent in approximate DFT, persists with our computational set-up.

The results in **Table 6.3.2** show that modification of rutile (110) with the smaller nanoclusters, Mg_4O_4 and Ca_4O_4, has little effect on the optical band-gap; values for $E^{vertical}$ of 2.28 eV and 2.39 eV are computed for the surfaces modified with these nanoclusters. Surface modification with the larger nanoclusters, $Mg_{12}O_{12}$ and $Ca_{12}O_{12}$, yields values for $E^{vertical}$ of 1.98 eV and 2.06 eV, corresponding to decreases of 0.4 eV and 0.3 eV, respectively, so that at higher coverages, a small red shift in light absorption is predicted.

The values for E^{excite}, which is the energy difference between the fully relaxed triplet state and singlet ground state, accounts for structural relaxations and polaron formation in response to electron and hole localisation in the triplet electronic state. The energy gain in relaxation in the excited state is given by the values for E^{relax}, which represent the stability of the photogenerated electron-hole pairs and their trapping. The values for E^{relax} are considerably larger for the modified surfaces (1.06-2.20 eV) relative to that computed for the bare rutile (110) surface (0.50 eV). This reflects the greater degree of structural relaxation that is possible in nanocluster-modified TiO_2 to accommodate the polarons formed in the triplet electronic state and suggests the photoexcited electron and hole will be more stable in the modified rutile structures.

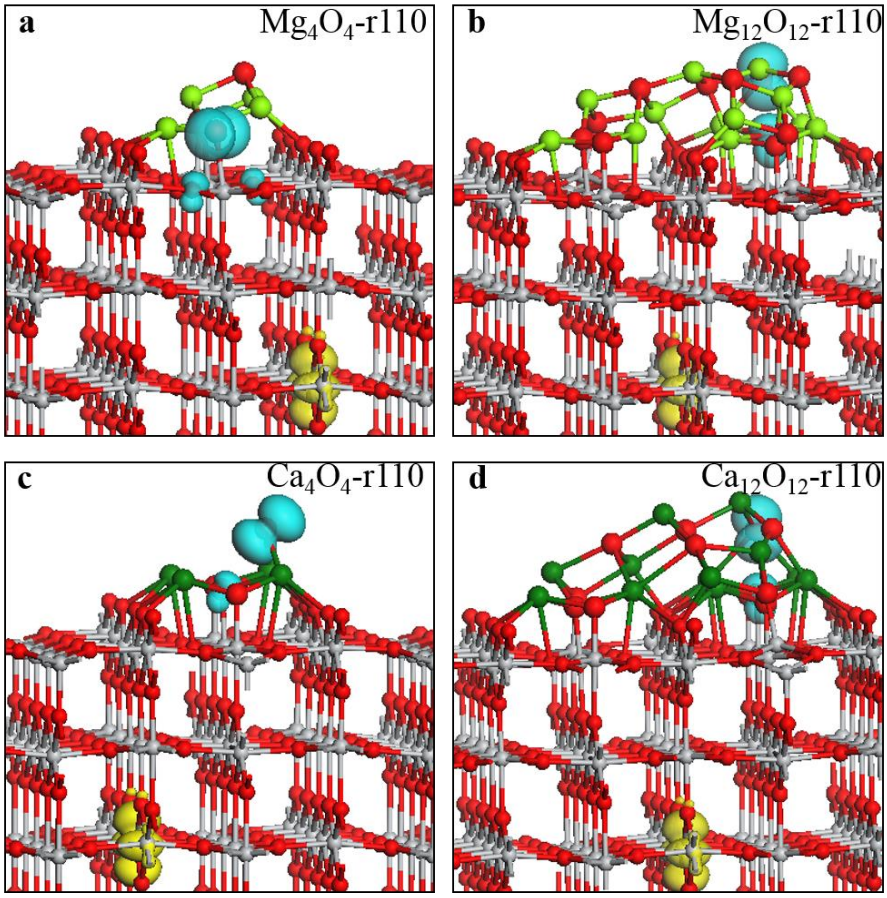

Figure 6.3.10 Spin density plots for the photoexcited model applied to **(a)** Mg_4O_4-r110, **(b)** $Mg_{12}O_{12}$-r110, **(c)** Ca_4O_4-r110 and **(d)** $Ca_{12}O_{12}$-110. Localisation of electron and holes is indicated by yellow and blue isosurfaces, respectively, which enclose spin densities up to 0.02 electrons/$Å^3$.

Another important factor in the stability of photoexcited charges is their spatial separation, which we assess through excess spin density plots and the computed Bader charges. The excess spin density plots are shown in **Figure 6.3.10**. The charge localisation scheme is similar for each AEO-modified TiO_2 structure. The photoexcited holes localise at oxygen sites on the nanocluster and the electrons localise at subsurface Ti sites in rutile (110). For Mg_4O_4-r110, an originally three-fold coordinated O_C ion is now two-fold coordinated after hole localisation. For $Mg_{12}O_{12}$-r110, the O_C ion at which the hole state localises is three-fold coordinated to Mg ions both before and after photoexcitation; however, the Mg-O_C bond lengths increase by as much as 0.3 Å in the excited state.

For Ca_4O_4-r110, the O_C ion at which the hole localises is two-fold coordinated to Ca ions and was originally three-fold coordinated in the ground state. For $Ca_{12}O_{12}$-r110, after hole localisation at O_C, the ion remains three-fold coordinated, however, the Ca-O_C bond lengths increase by 0.2 Å.

Hole localisation at O_C ions is confirmed by a change in the computed Bader charge from 7.2 to 6.8 electrons and a computed spin magnetisation of 0.7 μ_B. These values are typical of oxygen hole polaron formation. For those Ti sites at which the photoexcited electrons localise, the Bader charges increase from 9.6 to 9.9 electrons and the computed spin magnetisations are 0.8 μ_B, indicating reduction to Ti^{3+}. The results of this model suggest that modification of rutile (110) with AEO nanoclusters can promote the separation of photoexcited electrons and holes and thereby suppress charge carrier recombination, corroborating analysis of the PL spectra.

6.3.3.1 Origin of Enhanced OER on AEO-modified Rutile (110)

6.3.3.1.1 Water Adsorption at AEO-modified Rutile (110)

To better understand the improved OER activity on MgO-modified TiO_2, we studied water adsorption at MgO- and CaO-modified rutile (110) and the subsequent water oxidation pathways with the standard computational approach for OER,[50-53] introduced in **Chapter 2**. We investigated multiple adsorption configurations of water at each stoichiometric and reduced AEO-modified rutile surface. Three adsorption schemes were considered: **(1)** adsorption of water at sites on the nanocluster, **(2)** adsorption of water at an interfacial site between the modifier and the rutile surface, and **(3)** adsorption of a second water at the interface site with dissociatively adsorbed water already present on the nanocluster. The 3rd model aims to elucidate the impact of hydroxylation, which has

been shown to be important on AEO-modified TiO_2 structures, on the relative stabilities of the water oxidation intermediates and the free energies of each step in the OER model.

Table 6.3.3 Adsorption energies computed for water adsorbed at cluster sites ($(H_2O)_C$), interfacial sites ($(H2O)_I$), and interfacial sites after cluster hydroxylation ($(H_2O)_C$-$(H_2O)_I$). The top and bottom data sets correspond to the stoichiometric and reduced surfaces, respectively.

Adsorption site	**Adsorption energy (eV)**			
	Mg_4O_4-r110	**Ca_4O_4-r110**	**$Mg_{12}O_{12}$-r110**	**$Ca_{12}O_{12}$-r110**
$(H_2O)_C$	-3.32	-3.50	-2.68	-2.34
$(H_2O)_I$	-0.98	-0.95	-1.15	-1.63
$(H_2O)_C$-$(H_2O)_I$	-1.10	-1.00	-1.11	-0.97
Adsorption site	**Adsorption energy (eV)**			
	Mg_4O_3-r110	**Ca_4O_3-r110**	**$Mg_{12}O_{11}$-r110**	**$Ca_{12}O_{11}$-r110**
$(H_2O)_C$	-1.97	-1.48	-2.39	-1.96
$(H_2O)_I$	-1.21	-1.02	-1.18	-1.00
$(H_2O)_C$-$(H_2O)_I$	-1.11	-0.91	-1.55	-1.01

Table 6.3.3 presents the computed adsorption energies of water at different sites at AEO-modified TiO_2. The adsorption geometries are shown in **Figures 6.3.11-6.3.16**, and the computed adsorption energies are shown in the insets. For all adsorption sites, the adsorption of one water molecule is exothermic and leads to spontaneous dissociation to surface-bound hydroxyls. In the stoichiometric systems, the computed adsorption energies of water at sites of the nanoclusters are between -2.3 and -3.5 eV, which provides an origin for the previously discussed hydroxylation of the AEO-modified materials.

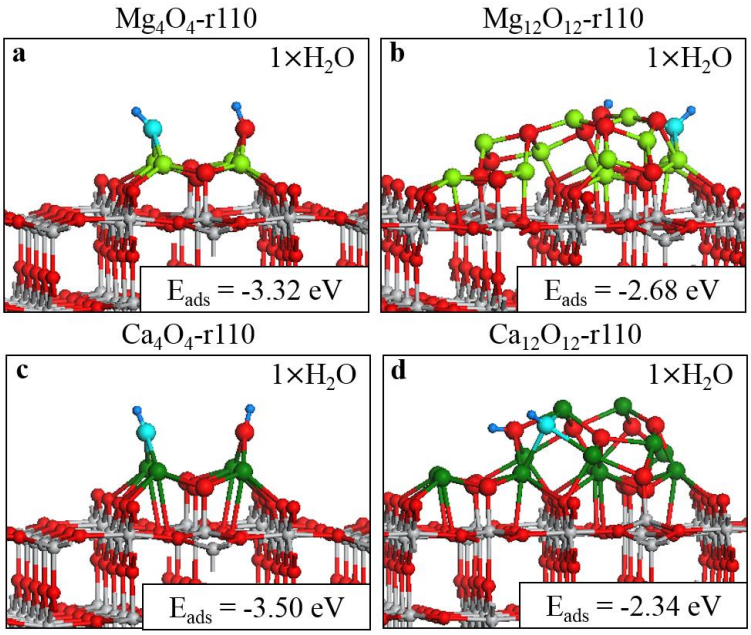

Figure 6.3.11 The relaxed geometry of a **single water molecule adsorbed at cluster sites of stoichiometric AEO-modified rutile (110)**. The panels show water adsorbed at **(a)** Mg_4O_4-, **(b)** $Mg_{12}O_{12}$-, **(c)** Ca_4O_4-, and **(d)** $Ca_{12}O_{12}$-r110. In this and subsequent figures, water-derived O and ions are represented with light blue and dark blue spheres.

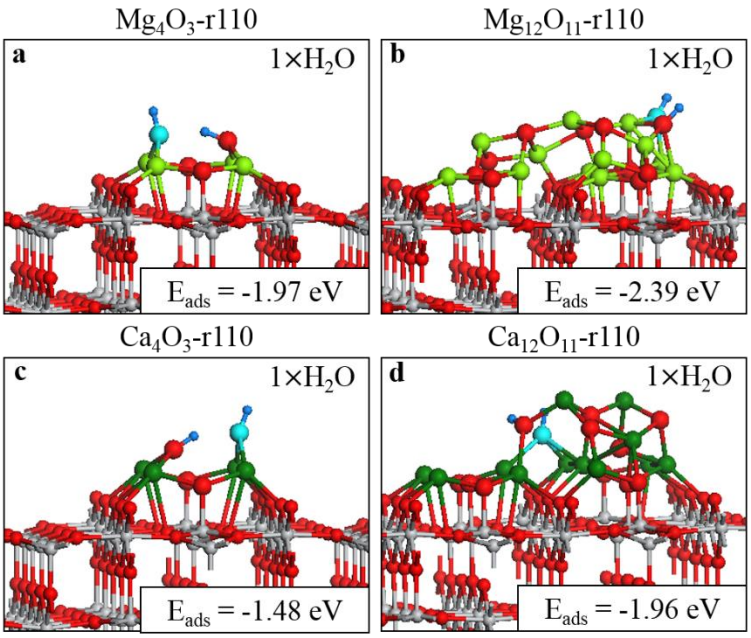

Figure 6.3.12 The relaxed geometry of a **single water molecule adsorbed at cluster sites of reduced AEO-modified rutile (110)**. The panels show water adsorbed at **(a)** Mg_4O_3-, **(b)** $Mg_{12}O_{11}$-, **(c)** Ca_4O_3-, and **(d)** $Ca_{12}O_{11}$-r110.

The computed adsorption energies for water at the same cluster sites on reduced AEO-TiO_2 are in the range of -2.4 eV to -1.5 eV, somewhat moderated from the stoichiometric cluster, but still highly exothermic. Thus, the nanocluster modifiers will promote hydroxyl formation through water dissociation. The atomic structure of these adsorption sites is shown in **Figures 6.3.11** and **6.3.12**.

For the interfacial adsorption sites, shown in **Figures 6.3.13** and **6.3.14** for the stoichiometric and reduced surfaces, respectively, the computed adsorption energies are less obviously dependent on whether the surface is stoichiometric or reduced. In addition, these are clearly less exothermic than adsorption on the nanocluster, with computed adsorption energies in the range of -1.2 eV to -1.0 eV. The exception is for water adsorbed at the interfacial site of $Ca_{12}O_{12}$-r110, for which the computed adsorption energy is -1.6 eV (**Figure 6.3.13.d**).

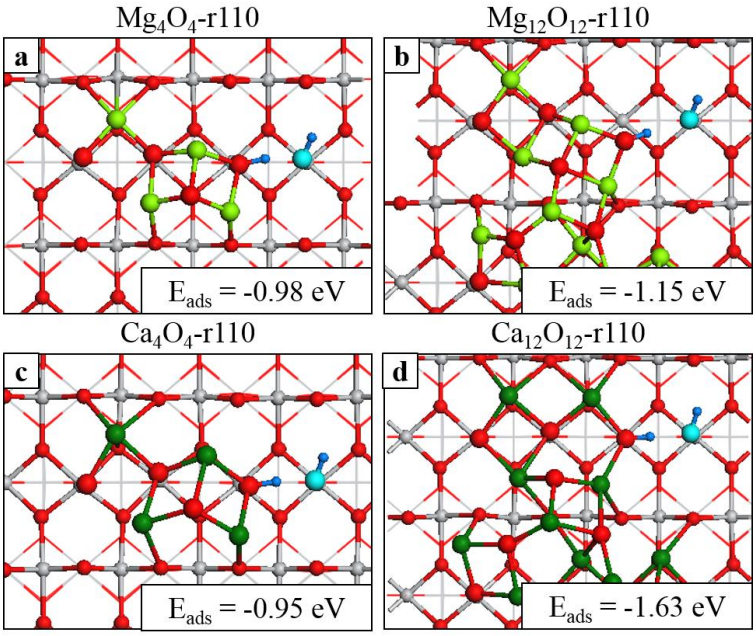

Figure 6.3.13 The relaxed geometry of a **single water molecule adsorbed at interfacial sites of stoichiometric AEO-modified rutile (110)**. The panels show water adsorbed at **(a)** Mg_4O_4-, **(b)** $Mg_{12}O_{12}$-, **(c)** Ca_4O_4-, and **(d)** $Ca_{12}O_{12}$-r110.

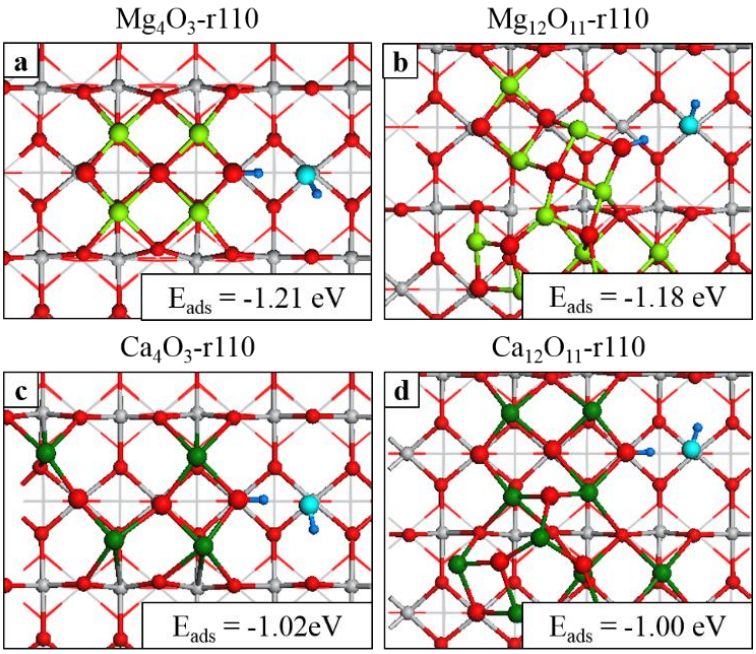

Figure 6.3.14 The relaxed geometry of a **single water molecule adsorbed at interfacial sites of reduced AEO-modified rutile (110)**. The panels show water adsorbed at **(a)** Mg_4O_3-, **(b)** $Mg_{12}O_{11}$-, **(c)** Ca_4O_3-, and **(d)** $Ca_{12}O_{11}$-r110.

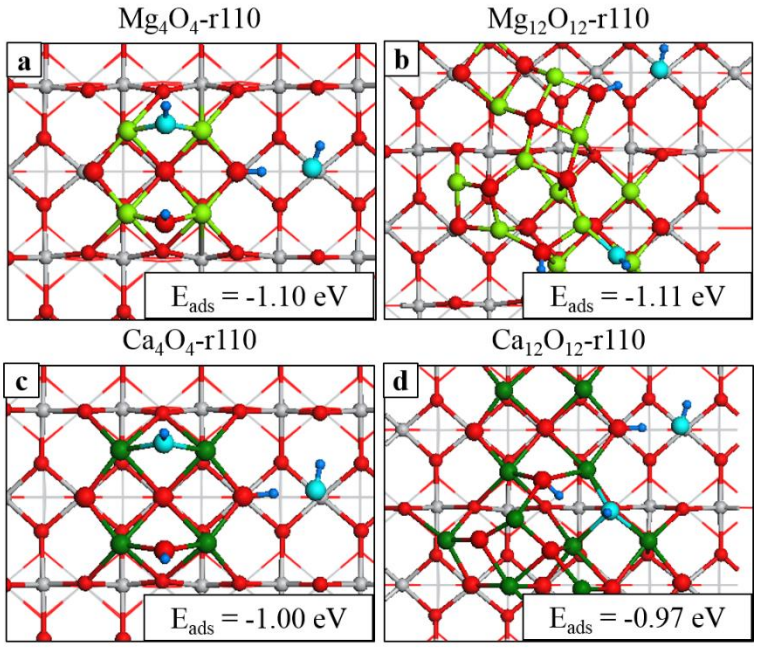

Figure 6.3.15 The relaxed geometry of a **water molecule adsorbed at interfacial sites of stoichiometric AEO-modified rutile (110), after dissociative water adsorption at cluster sites**. The panels show water adsorbed at **(a)** Mg_4O_4-, **(b)** $Mg_{12}O_{12}$-, **(c)** Ca_4O_4-, and **(d)** $Ca_{12}O_{12}$-r110.

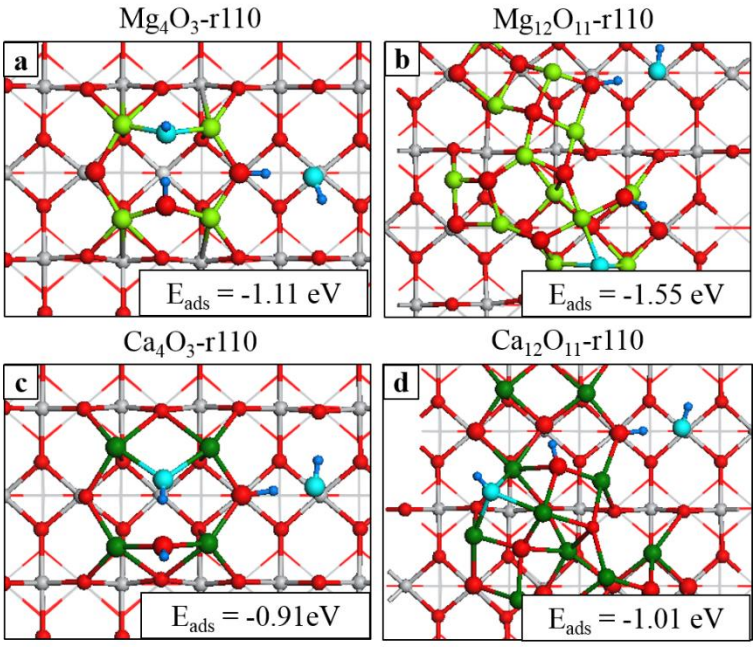

Figure 6.3.16 The relaxed geometry of a **water molecule adsorbed at interfacial sites of reduced AEO-modified rutile (110), after initial dissociation of water at cluster sites**. The panels show water adsorbed at **(a)** Mg_4O_3-, **(b)** $Mg_{12}O_{11}$-, **(c)** Ca_4O_3-, and **(d)** $Ca_{12}O_{11}$-r110.

After the dissociative adsorption of the first water molecule at cluster sites, the computed adsorption energies for the subsequent adsorption of a second water at interfacial sites of the modified surfaces are in the range of -1.6 eV to -0.9 eV. These results indicate that, for the coverages investigated, hydroxylation of the modifiers has little impact on water adsorption at interfacial sites. The adsorption geometries for water adsorbed at interfacial sites of AEO-modified surfaces, in which the modifiers are hydroxylated, are shown in **Figure 6.3.15** and **6.3.16** for the stoichiometric and reduced systems, respectively.

6.3.3.2 Water Oxidation at AEO-modified Rutile (110)

In what follows, we examine the water oxidation pathway using the four PCET step model described in **Chapter 2**. In this model, the water adsorption configurations just described

represent the end of sub-step A1, in which water adsorbs and dissociates to surface bound hydroxyls.

In general, we find that for water adsorbed at stoichiometric AEO-TiO_2, the surface-bound intermediates of the water oxidation pathway have high free energy costs for the subsequent OER steps. This is due to localisation of hole states at surface-bound *O species after dehydrogenation (sub-step A2 and step B) of the hydroxyls produced from dissociative water adsorption.

This effect is mitigated for the reduced systems because electrons can transfer from a reduced Ti^{3+} site to stabilise under-coordinated *O species. Spin magnetisations of 0.4-1.0 μ_B were computed for *O species after dehydrogenation at the stoichiometric systems. At reduced AEO-TiO_2, the same *O species have spin magnetisations of 0 μ_B indicating a charge transfer from TiO_2 to *O. At the same time, Ti ions of the surface cycle between Ti^{3+} and Ti^{4+}, indicated by computed spin magnetisations of 0.8-0.9 μ_B and 0 μ_B, before and after formation of *O, respectively. After each dehydrogenation, one Ti^{3+} is oxidised to Ti^{4+}, with the electron transferring to the resulting *O species. Moreover, for water oxidation at cluster sites of the reduced systems, we find that the final step, evolution of a molecule of O_2, is excessively endothermic as the surface bound O_2 species is over-stabilised at cluster sites. For these reasons, we focus in particular on the OER proceeding at interfacial sites of the reduced AEO-modified surfaces.

Water oxidation at interfacial sites of reduced AEO-TiO_2, without prior nanocluster hydroxylation

We consider the water oxidation pathway, using the model for water oxidation described in **Chapter 2**. This model was applied to the bare rutile (110) surface[51] (see **Table B.5.3**

in **Appendix B**), for which the highest Gibbs free energy (ΔG) of a single step (*viz* the dehydrogenation of a surface OH group) was computed as +2.20 eV (step A). In identifying favourable reaction pathways at the modified surfaces, we consider that should the free energy cost of any PCET step (indicated previously as A, B, C or D in **Chapter 2**) exceed 2.20 eV there will be no enhancement in the OER over bare rutile (110).

Table 6.3.4 Computed free energies for water oxidation PCET steps starting from a single water molecule adsorbed at interfacial sites of AEO-modified rutile (110) in the reduced state with one oxygen vacancy.

1 x H_2O	**Mg_4O_3-r110**	**$Mg_{12}O_{11}$-r110**	**Ca_4O_3-r110**	**$Ca_{12}O_{11}$-r110**
	ΔG (eV)	**ΔG (eV)**	**ΔG (eV)**	**ΔG (eV)**
Step A1	-0.53	-0.50	-0.34	-0.32
Step A2	0.81	0.52	0.62	0.64
Step A	**0.28**	**0.02**	**0.29**	**0.32**
Step B	**0.82**	**1.84**	**0.99**	**1.03**
Step C1	1.49	0.01	-0.96	2.61
Step C2	0.31	1.95	2.25	0.38
Step C	**1.79**	**1.96**	**1.29**	**2.99**
Step D	**2.03**	**1.09**	**2.35**	**0.58**
Sum	**4.92**	**4.92**	**4.92**	**4.92**

We use reduced AEO-modified rutile as a model system because the ease of reduction means that oxygen vacancies will be present and, as discussed, the OER at the stoichiometric surface is not favoured. We summarise the results of the calculations of steps A-D in the OER, without and with hydroxylation of the AEO nanocluster, in **Tables 6.3.4** and **6.3.5**.

The adsorption geometries in **Figures 6.3.14** and **6.3.16** show water molecules dissociatively adsorbed at interfacial sites of the reduced AEO-modified systems, both without and with hydroxylation of the nanocluster. At the interfacial site, the water-derived hydroxyl group is bound to a Ti site of the surface and a second hydroxyl forms after migration of the other hydrogen from water to bind with an O_C site. Adsorption of OH at a Ti site results in the Ti ions migrating out from the surface and breaking a bond with subsurface oxygen.

The adsorption geometries that are shown in **Figure 6.3.14** represent the end of sub-step A1, *viz* dissociative water adsorption at the interface of the reduced AEO nanocluster and the rutile support. The computed free energies of this and subsequent steps are presented in **Table 6.3.4**. Only two of the reaction pathways shown in **Table 6.3.4** meet the criterion that each PCET step has a computed ΔG of less than +2.20 eV. These are both for water oxidation on the reduced MgO-TiO_2 structures.

On all reduced AEO-modified TiO_2 structures, sub-step A1 is exothermic, with computed ΔG_{A1} in the range -0.53 eV to -0.32 eV. The first dehydrogenation step (sub-step A2) is moderately uphill, with ΔG_{A2} in the range +0.52 eV to +0.81 eV. Thus, the PCET step A proceeds with overall free energies in the range +0.02 eV to +0.32 eV.

The second dehydrogenation (step B) requires a larger free energy cost, with computed ΔG_B in the range +0.82 eV to +1.84 eV. These free energies are however, well below the value of +2.20 eV, computed for bare rutile. After step B, a terminal oxygen ion is singly coordinated to a Ti ion of the surface and acts as a site for the adsorption of a second water molecule for step C.

The computed free energies of step C are in the range +1.29 to +1.96 eV, with the exception of $Ca_{12}O_{11}$-r110 for which ΔG_C is +2.99 eV, which is significantly larger than

the same energy step for bare rutile. Step D involves the evolution of O_2 accompanied by the release of the fourth proton and an electron. For Mg_4O_3-r110 and $Mg_{12}O_{11}$-r110 the computed free energies are +2.03 eV and +1.09 eV, respectively. For Ca_4O_3-r110, the computed free energy, ΔG_D, is +2.35 eV and so this pathway requires a larger energy input than that computed for bare rutile (110).

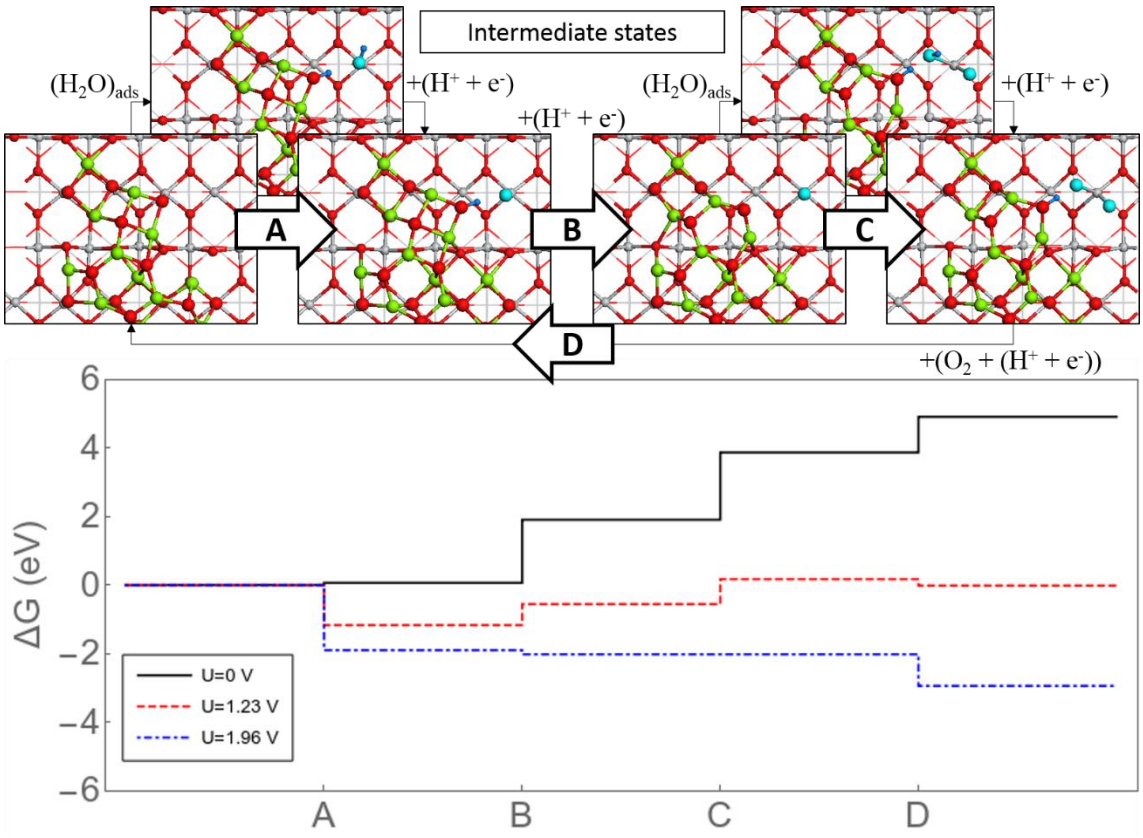

Figure 6.3.17 Reaction pathway for water oxidation starting from dissociative water adsorption at **an interfacial site of the reduced $Mg_{12}O_{11}$-r110 composite surface**. The free energy profile of the pathway is shown for overpotentials U = 0, 1.23 and 1.96 V. At the equilibrium potential, U = 1.23 V, steps C and D are uphill and at U = 1.96 eV all reaction steps are downhill in free energy. The intermediate states in the upper panels represent the end-points of reaction sub-steps A1 and C1. In this figure, water-derived O ions are light blue and H ions are dark blue.

The intermediate states of the water oxidation pathway proceeding at the interfacial site of reduced $Mg_{12}O_{11}$-r110 (with no nanocluster hydroxylation) are shown in **Figure**

6.3.17, and for Mg_4O_3-r110 in **Figure B.5.6** in **Appendix B**. The first dehydrogenation, step A, is most favourable from the surface-bound hydroxyl group and leaves a terminal *O species and a hydroxyl group on the cluster. Step B involves dehydrogenation of the cluster-bound hydroxyl so that the reduced $Mg_{12}O_{11}$ nanocluster and the terminal *O species remain at the rutile (110) surface.

After the second water adsorption (sub-step C1), *O and *OH species are bound to the surface Ti site and a second hydroxyl forms due to migration of the H atom to oxygen on the nanocluster. In sub-step C2, dehydrogenation occurs from the *OH species bound at the Ti site so that after relaxation, two *O species are bound to the same Ti site of the surface. In step D, these *O species desorb, as does the cluster-bound H atom.

The energy profiles in **Figures 6.3.17** and **B.5.6** are based on the free energies presented in **Table 6.3.4** with the inclusion of a potential bias term, ΔG_U, which shifts the free energy of each PCET step by an amount $-eU$, where U is the electrode potential relative to the standard hydrogen electrode. For each profile we consider three applied biases: $U = 0$ V; the equilibrium potential: $U = 1.23$ V; and the potential at which each PCET step becomes downhill in free energy. The difference between this potential and 1.23 V is the overpotential required for the oxygen evolution reaction to proceed at the modified TiO_2 surface.

From the free energy profile, we see that at the equilibrium potential, 1.23 V, steps B and C are uphill and an applied bias of 1.96 V is required to render all steps downhill, corresponding to an overpotential of 0.73 V. Similarly, for the Mg_4O_3-r110 surface, as discussed in **Appendix B**, the computed overpotential is 0.80 V. For Ca_4O_3-r110 and $Ca_{12}O_{11}$-r110, the computed overpotentials are 1.07 V and 1.76 V respectively. This means that water oxidation is inhibited compared to the bare rutile surface. This result is

reflected in the experimental findings of decreased oxygen evolution activity for CaO-modified rutile at low loadings.

These results compare with an overpotential of 0.97 V, computed for water oxidation at the bare rutile surface by Valdés *et al*[51] and indicates a favourable effect of the MgO-modifier. On hematite, the highest free energy cost is 1.82 eV, which corresponds to an overpotential of 0.71 V, given that the authors computed a free energy of 1.11 eV per PCET step.[52] A more recent study of OER at hematite surfaces demonstrated a considerable reduction in the overpotential (0.47 V) after formation of oxygen vacancies in the (110) surface.[54] Similarly, oxygen vacancies reduced the overpotential by 0.3 V for water oxidation at the hematite (0001) surface.[55] A first principles study of water oxidation on pristine and oxygen-deficient barium titanate found that, contrary to our results and experiment, the overpotential increased from 0.45 V for the pristine surface to 1.47 V in the presence of oxygen vacancies.[53] This was attributed to the strong stabilisation of *OH and *O species for the latter system, which is not observed in the current study.

Water oxidation at interfacial sites of reduced AEO-TiO_2, with prior nanocluster hydroxylation

The role of prior hydroxylation of the catalyst surface is often overlooked in first principles OER studies. In the following, we examine the impact of hydroxylation of the AEO modifiers on the water oxidation pathways. In **Table 6.3.5**, we present the computed free energies for water oxidation proceeding at interfacial sites of the reduced AEO-modified systems, in which the nanocluster is hydroxylated by dissociative water adsorption (see **Figure 6.3.16**).

Table 6.3.5 Computed free energies for water oxidation PCET steps starting from a water molecule adsorbed at interfacial sites of AEO-modified rutile (110) in the reduced state with one oxygen vacancy, after dissociative water adsorption at a cluster site.

2 x H_2O	**Mg_4O_3-r110**	**$Mg_{12}O_{11}$-r110**	**Ca_4O_3-r110**	**$Ca_{12}O_{11}$-r110**
	ΔG (eV)	**ΔG (eV)**	**ΔG (eV)**	**ΔG (eV)**
Step A1	-0.43	-0.87	-0.23	-0.33
Step A2	0.40	1.05	0.52	0.66
Step A	**-0.03**	**0.18**	**0.29**	**0.33**
Step B	**1.02**	**0.98**	**1.03**	**1.01**
Step C1	1.88	2.06	2.38	2.08
Step C2	0.09	-0.21	0.08	0.00
Step C	**1.97**	**1.85**	**2.46**	**2.08**
Step D	**1.96**	**1.91**	**1.14**	**1.50**
Sum	**4.92**	**4.92**	**4.92**	**4.92**

For each surface, sub-step A1 is exothermic with free energies in the range -0.87 eV to -0.23 eV and the dehydrogenation step, sub-step A2, proceeds with ΔG_{A2} in the range +0.40 eV to +1.05 eV. Thus, the overall step A, has free energies between -0.03 and 0.33 eV. The dehydrogenation in step B has ΔG_B in the range +0.98 eV to +1.03 eV. These energies are comparable to those computed for the water oxidation pathway with no hydroxyls at the cluster sites; one exception is step B at $Mg_{12}O_{11}$-r110, which decreases by 0.86 eV in the presence of cluster-bound hydroxyls.

Steps C and D have the highest free energy costs, with the free energies for step C in the range +1.85 eV to +2.08 eV and free energies of +1.50 eV to +1.96 eV for step D. For Ca_4O_3-r110, step C has the highest energy cost, with $\Delta G_C = +2.46$ eV, indicating no enhancement relative to the bare surface. This is consistent with the low OER activity measured for low Ca loadings.

However, water oxidation at the interface of $Ca_{12}O_{11}$-r110 is more favourable after hydroxylation of the cluster; the highest energy step decreases from +2.99 eV to +2.08 eV, corresponding to an overpotential of 0.85 V. Conversely, hydroxylation of the cluster in Ca_4O_3-r110 renders water oxidation less favourable and increases the required overpotential by 0.1 V.

The water oxidation pathway proceeding at the interfacial site of reduced, hydroxylated $Mg_{12}O_{11}$-r110 (Mg_4O_3-r110) is shown in **Figure 6.3.18** (**Figure B.5.7**). The reaction site is highlighted with a black circle in the panel on the left. After water adsorption at the interfacial site, the water-derived hydroxyl is singly coordinated to a 5-fold coordinated Ti site, as previously described. The second H ion migrates to a neighbouring O_C ion.

Here we describe the reaction intermediates for $Mg_{12}O_{11}$-r110 and the details for Mg_4O_3-r110 are provided in **Appendix B**. The first dehydrogenation is most favourable from the cluster-bound hydroxyl group and leaves a *OH species bound at the rutile (110) surface. After step B the terminal *O species remains at the surface. After the water adsorption described by sub-step C1, an *OOH species is bound to the surface Ti site and a second hydroxyl forms due to migration of the H atom to an O_C site. In sub-step C2, dehydrogenation occurs from the *OOH species bound at the Ti site so that after relaxation, an $*O_2$ species is bound to the surface. In step D, the O_2 molecule evolves with the release of the cluster-bound H atom.

The energy profiles in **Figures 6.3.18** and **B.5.7** are based on the free energies presented in **Table 6.3.7**. An applied bias of 1.91 V is required to render all steps downhill, corresponding to an overpotential of 0.68 V. Similarly, for the Mg_4O_3-r110 surface, as discussed in **Appendix B**, the computed overpotential is 0.74 V.

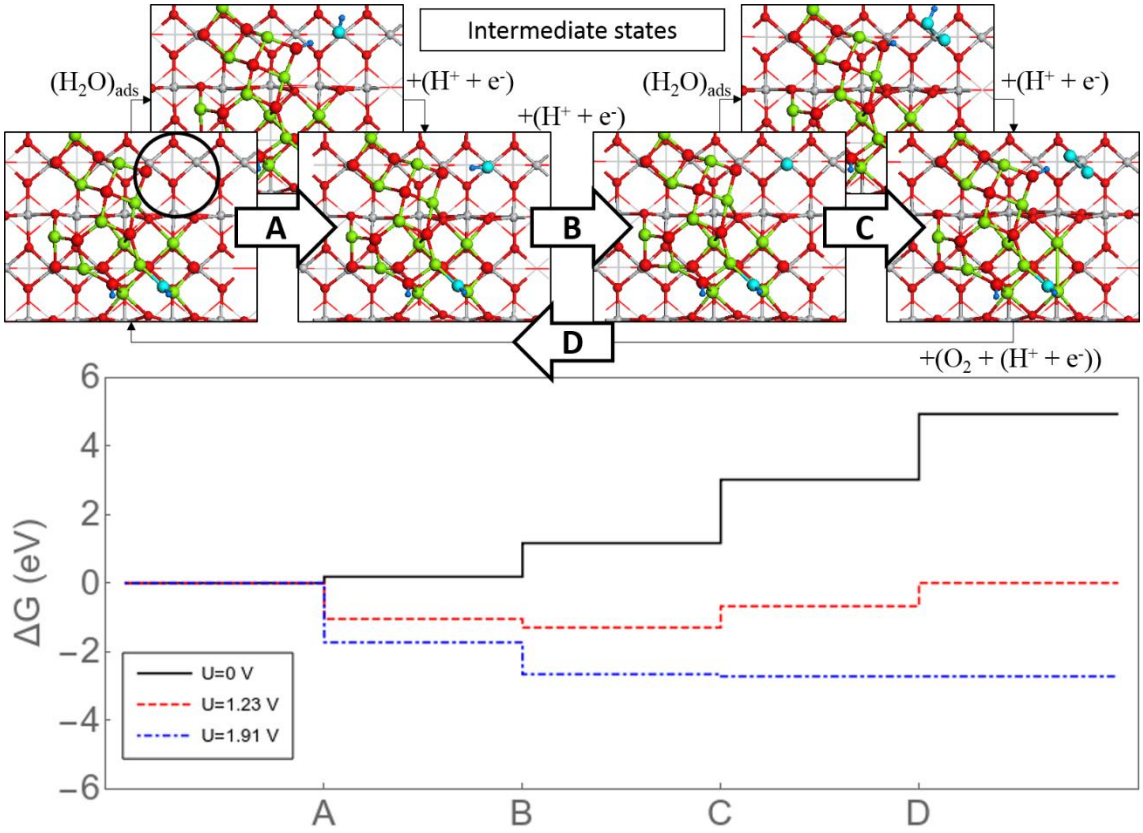

Figure 6.3.18 Reaction pathway for water oxidation starting from dissociative water adsorption at **an interfacial site of the reduced $Mg_{12}O_{11}$-r110 composite surface, after hydroxylation of the cluster**. The free energy profile of the pathway is shown for overpotentials U = 0, 1.23 and 1.91 V. At the equilibrium potential, U = 1.23 V, steps C and D are uphill and at U = 1.91 eV all reaction steps are downhill in free energy. The intermediate states in the upper panels represent the end-points of reaction sub-steps A1 and C1. The reaction site is highlighted with the black circle in the panel on the left.

In summary, we identify water oxidation proceeding favourably at *interfacial sites* of reduced MgO-modified rutile (110), with lower free energy costs for the PCET steps compared to water oxidation at rutile (110). These results highlight the role played by oxygen vacancies and the presence of reduced cations (Ti^{3+}), which are produced by enhanced reduction of the MgO-TiO_2 system, in promoting the oxygen evolution reaction. Furthermore, there is an important role for the water adsorption site, where water adsorption at the interface of the nanocluster modifier and the support is the most active site for OER. We also see that, after an initial dissociative water adsorption at cluster

sites, water oxidation proceeds with similar energy costs at interfacial sites of Mg_4O_3-r110 and $Mg_{12}O_{11}$-r110; the values for ΔG are within 0.1 eV for these surfaces, with and without cluster-bound hydroxyls.

While quantifying these results in the context of measured oxygen evolution activities is beyond the scope of the current models, our results corroborate those of experiment. We confirm an enhancement for water oxidation at MgO-modified rutile at low loadings and a negative impact due to CaO-modification, relative to unmodified TiO_2.

6.3.4 Conclusions

By simple surface modification of TiO_2 rutile with nanoscale MgO and CaO, the photoactivity for O_2 evolution can be improved. The enhancement in OER activity is considerable for MgO at very low loadings and high dispersion, and decreases at higher loadings. From this we infer that both the surface and modifier are involved in the water oxidation reaction and this is confirmed by a first principles investigation of active sites of the nanocluster-modified surfaces. From the range of AEO modifier contents examined, it is expected that the modifier is present as a nanocluster on the rutile surface. This feature permits a close correlation with our theoretical models, and indeed, we achieved good agreement between experimental and computational results. In addition, the results show that the modifier must be in the nanocluster regime to modify the chemistry of the TiO_2 support effectively.

From the structural and textural properties, the surface modification does not induce any major changes to rutile. However, the charge carrier dynamics are improved by the presence of alkaline ions at low loadings, which leads to lower recombination. DFT simulations show that the spatial separation of electrons and holes is promoted for the

modified systems. It has also been stated that alkaline ion dispersion on TiO_2 surface was better for Mg^{2+} than for Ca^{2+}. This high dispersion on Mg^{2+} at very low content is also accompanied by a higher hydroxylation degree. The greater dispersion of MgO at the surface was confirmed by first principles calculations, which indicate that aggregation of CaO to larger clusters is favoured.

Oxygen vacancies form with moderate energy costs for the modified systems, leading to the reduction of Ti^{4+} to Ti^{3+}. This has consequences for the DOS, however, the impact of modification on the light absorption properties was found to be small, both experimentally and based on computational results.

Using a model for the water oxidation pathway we have computed the applied overpotential required for the OER to proceed. In general, for water adsorbed at cluster sites, the water oxidation intermediates are over-stabilised, impeding the reaction. We have identified a reaction pathway that proceeds at interfacial sites of the reduced MgO-modified systems, which drives an enhancement of the O_2 evolution activity relative to bare rutile TiO_2.

These results highlight the importance of nanocluster modifiers, oxygen vacancies and Ti reduction in promoting the OER and identify interfacial sites, present at low coverages of nanocluster MgO, as active sites for water oxidation. Moreover, this model confirms the enhanced performance for MgO-modification, relative to CaO-modification. Thus, by rational design, we have interpreted and explained the better photocatalytic performance that arises from alkaline earth modification of rutile TiO_2, particularly due to Mg^{2+} modification at low loading.

6.4 Chapter References

1. Graciani, J.; Plata, J. J.; Sanz, J. F.; Liu, P.; Rodriguez, J. A., A theoretical insight into the catalytic effect of a mixed-metal oxide at the nanometer level: The case of the highly active metal/CeO/TiO_2(110) catalysts. *The Journal of Chemical Physics* **2010,** *132* (10), 104703.
2. Park, J. B.; Graciani, J.; Evans, J.; Stacchiola, D.; Senanayake, S. D.; Barrio, L.; Liu, P.; Sanz, J. F.; Hrbek, J.; Rodriguez, J. A., Gold, copper, and platinum nanoparticles dispersed on CeO_x/TiO_2 (110) surfaces: high water-gas shift activity and the nature of the mixed-metal oxide at the nanometer level. *Journal of the American Chemical Society* **2009,** *132* (1), 356-363.
3. Yang, Z.; Xie, L.; Ma, D.; Wang, G., Origin of the High Activity of the Ceria-Supported Copper Catalyst for H_2O Dissociation. *The Journal of Physical Chemistry C* **2011,** *115* (14), 6730-6740.
4. Fuente, S.; Branda, M. M.; Illas, F., Role of step sites on water dissociation on stoichiometric ceria surfaces. *Theoretical Chemistry Accounts* **2012,** *131* (3), 1190.
5. Molinari, M.; Parker, S. C.; Sayle, D. C.; Islam, M. S., Water Adsorption and Its Effect on the Stability of Low Index Stoichiometric and Reduced Surfaces of Ceria. *The Journal of Physical Chemistry C* **2012,** *116* (12), 7073-7082.
6. Marrocchelli, D.; Yildiz, B., First-Principles Assessment of H_2S and H_2O Reaction Mechanisms and the Subsequent Hydrogen Absorption on the CeO_2(111) Surface. *The Journal of Physical Chemistry C* **2012,** *116* (3), 2411-2424.
7. Mullins, D. R.; Albrecht, P. M.; Chen, T.-L.; Calaza, F. C.; Biegalski, M. D.; Christen, H. M.; Overbury, S. H., Water Dissociation on CeO_2(100) and CeO_2(111) Thin Films. *The Journal of Physical Chemistry C* **2012,** *116* (36), 19419-19428.
8. Carrasco, J.; López-Durán, D.; Liu, Z.; Duchoň, T.; Evans, J.; Senanayake, S. D.; Crumlin, E. J.; Matolín, V.; Rodríguez, J. A.; Ganduglia-Pirovano, M. V., In Situ and Theoretical Studies for the Dissociation of Water on an Active Ni/CeO_2 Catalyst: Importance of Strong Metal–Support Interactions for the Cleavage of O–H Bonds. *Angewandte Chemie International Edition* **2015,** *54* (13), 3917-3921.
9. Fan, J.; Xu, B.; Zhao, J. Z.; Xu, H., Controllable dissociation of H_2O on a CeO_2(111) surface. *Physical Chemistry Chemical Physics* **2018**.
10. Ruiz Puigdollers, A.; Schlexer, P.; Tosoni, S.; Pacchioni, G., Increasing Oxide Reducibility: The Role of Metal/Oxide Interfaces in the Formation of Oxygen Vacancies. *ACS Catalysis* **2017,** *7* (10), 6493-6513.
11. Wang, F.; Wei, S.; Zhang, Z.; Patzke, G. R.; Zhou, Y., Oxygen vacancies as active sites for H_2S dissociation on the rutile TiO_2(110) surface: a first-principles study. *Physical Chemistry Chemical Physics* **2016,** *18* (9), 6706-6712.
12. Zhang, Y.; Dai, R.; Hu, S., Study of the role of oxygen vacancies as active sites in reduced graphene oxide-modified TiO_2. *Physical Chemistry Chemical Physics* **2017,** *19* (10), 7307-7315.
13. Schaub, R.; Thostrup, P.; Lopez, N.; Lægsgaard, E.; Stensgaard, I.; Nørskov, J. K.; Besenbacher, F., Oxygen Vacancies as Active Sites for Water Dissociation on Rutile TiO_2. *Phys. Rev. Lett.* **2001,** *87* (26), 266104.
14. Henderson, M. A.; Epling, W. S.; Peden, C. H. F.; Perkins, C. L., Insights into Photoexcited Electron Scavenging Processes on TiO2 Obtained from Studies of the Reaction of O_2 with OH Groups Adsorbed at Electronic Defects on TiO_2(110). *The Journal of Physical Chemistry B* **2003,** *107* (2), 534-545.

15. Rhatigan, S.; Sokalu, E.; Nolan, M.; Colón, G., Surface Modification of Rutile TiO_2 with Alkaline-Earth Oxide Nanoclusters for Enhanced Oxygen Evolution. *ACS Applied Nano Materials* **2020,** *3* (6), 6017-6033.
16. Majrik, K.; Pászti, Z.; Korecz, L.; Trif, L.; Domján, A.; Bonura, G.; Cannilla, C.; Frusteri, F.; Tompos, A.; Tálas, E., Study of PtO_x/TiO_2 Photocatalysts in the Photocatalytic Reforming of Glycerol: The Role of Co-Catalyst Formation. *Materials* **2018,** *11* (1927).
17. Munnik, P.; de Jongh, P. E.; de Jong, K. P., Recent Developments in the Synthesis of Supported Catalysts. *Chemical Reviews* **2015,** *115* (14), 6687-6718.
18. Lamai, W.; Bunphung, A.; Junumpun, I.; Wongkaew, A., Synthesis and Characterization of Ni@Pt core-shell catalyst over TiO_2 support prepared by incipient wetness impregnation and electroless deposition. *Materials Today: Proceedings* **2019,** *17*, 1396-1402.
19. Tálas, E.; Pászti, Z.; Korecz, L.; Domján, A.; Németh, P.; Szíjjártó, G. P.; Mihály, J.; Tompos, A., PtO_x-SnO_x-TiO_2 catalyst system for methanol photocatalytic reforming: Influence of cocatalysts on the hydrogen production. *Catalysis Today* **2018,** *306*, 71-80.
20. Ahmad, W.; Mehmood, U.; Al-Ahmed, A.; Al-Sulaiman, F. A.; Aslam, M. Z.; Kamal, M. S.; Shawabkeh, R. A., Synthesis of zinc oxide/titanium dioxide (ZnO/TiO_2) nanocomposites by wet incipient wetness impregnation method and preparation of ZnO/TiO_2 paste using poly(vinylpyrrolidone) for efficient dye-sensitized solar cells. *Electrochimica Acta* **2016,** *222*, 473-480.
21. Yang, H.; Li, X.; Wang, A.; Wang, Y.; Chen, Y., Photocatalytic degradation of methylene blue by MoO_3 modified TiO_2 under visible light. *Chinese Journal of Catalysis* **2014,** *35* (1), 140-147.
22. Castro, Y.; Durán, A., Ca doping of mesoporous TiO_2 films for enhanced photocatalytic efficiency under solar irradiation. *Journal of Sol-Gel Science and Technology* **2016,** *78* (3), 482-491.
23. Lv, C.; Lan, X.; Wang, L.; Yu, Q.; Zhang, M.; Sun, H.; Shi, J., Alkaline-earth-metal-doped TiO_2 for enhanced photodegradation and H2 evolution: insights into the mechanisms. *Catalysis Science & Technology* **2019,** *9* (21), 6124-6135.
24. Subbaraman, R.; Tripkovic, D.; Strmcnik, D.; Chang, K.-C.; Uchimura, M.; Paulikas, A. P.; Stamenkovic, V.; Markovic, N. M., Enhancing Hydrogen Evolution Activity in Water Splitting by Tailoring Li^+-$Ni(OH)_2$-Pt Interfaces. *Science* **2011,** *334* (6060), 1256-1260.
25. Christoforidis, K. C.; Fornasiero, P., Photocatalytic Hydrogen Production: A Rift into the Future Energy Supply. *ChemCatChem* **2017,** *9* (9), 1523-1544.
26. Xiang, Z.; Zhong, J.; Huang, S.; Li, J.; Chen, J.; Wang, T.; Li, M.; Wang, P., Efficient charge separation of Ag_2CO_3/ZnO composites prepared by a facile precipitation approach and its dependence on loading content of Ag_2CO_3. *Materials Science in Semiconductor Processing* **2016,** *52*, 62-67.
27. Colón, G. H., M. C.; Munuera, G.; Ferino, I.; Cutrufello, M. G.; Navío, J. A., Structural and surface approach to the enhanced photocatalytic activity of sulfated TiO_2 photocatalyst. *Appl. Catal. B: Environ.* **2006,** *63* (1), 45-59.
28. Haja Hameed, A. S.; Karthikeyan, C.; Sasikumar, S.; Senthil Kumar, V.; Kumaresan, S.; Ravi, G., Impact of alkaline metal ions Mg^{2+}, Ca^{2+}, Sr^{2+} and Ba^{2+} on the structural, optical, thermal and antibacterial properties of ZnO nanoparticles prepared by the co-precipitation method. *Journal of Materials Chemistry B* **2013,** *1* (43), 5950-5962.

29. Zaki, M. I.; Ramadan, W.; Katrib, A.; Rabee, A. I. M., Surface chemical and photocatalytic consequences of Ca-doping of $BiFeO_3$ as probed by XPS and H_2O_2 decomposition studies. *Applied Surface Science* **2014,** *317*, 929-934.
30. Olowoyo, J. O.; Kumar, M.; Singhal, N.; Jain, S. L.; Babalola, J. O.; Vorontsov, A. V.; Kumar, U., Engineering and modeling the effect of Mg doping in TiO_2 for enhanced photocatalytic reduction of CO_2 to fuels. *Catalysis Science & Technology* **2018,** *8* (14), 3686-3694.
31. Nolan, M., Alkaline earth metal oxide nanocluster modification of rutile TiO_2 (110) promotes water activation and CO_2 chemisorption. *Journal of Materials Chemistry A* **2018,** *6* (20), 9451-9466.
32. Song, Z.; Fan, J.; Xu, H., Strain-induced water dissociation on supported ultrathin oxide films. *Scientific Reports* **2016,** *6*, 22853.
33. Jung, J.; Shin, H.-J.; Kim, Y.; Kawai, M., Controlling water dissociation on an ultrathin MgO film by tuning film thickness. *Physical Review B* **2010,** *82* (8), 085413.
34. Mu, R.; Zhao, Z.-j.; Dohnálek, Z.; Gong, J., Structural motifs of water on metal oxide surfaces. *Chemical Society Reviews* **2017,** *46* (7), 1785-1806.
35. Hu, X. L.; Carrasco, J.; Klimeš, J.; Michaelides, A., Trends in water monomer adsorption and dissociation on flat insulating surfaces. *Physical Chemistry Chemical Physics* **2011,** *13* (27), 12447-12453.
36. Fujimori, Y.; Zhao, X.; Shao, X.; Levchenko, S. V.; Nilius, N.; Sterrer, M.; Freund, H.-J., Interaction of Water with the CaO(001) Surface. *The Journal of Physical Chemistry C* **2016,** *120* (10), 5565-5576.
37. Haertelt, M.; Fielicke, A.; Meijer, G.; Kwapien, K.; Sierka, M.; Sauer, J., Structure determination of neutral MgO clusters—hexagonal nanotubes and cages. *Physical Chemistry Chemical Physics* **2012,** *14* (8), 2849-2856.
38. Byrne, C.; Rhatigan, S.; Hermosilla, D.; Merayo, N.; Blanco, Á.; Michel, M. C.; Hinder, S.; Nolan, M.; Pillai, S. C., Modification of TiO2 with hBN: high temperature anatase phase stabilisation and photocatalytic degradation of 1,4-dioxane. *Journal of Physics: Materials* **2019,** *3* (1), 015009.
39. Gagné, O. C.; Hawthorne, F. C., Bond-Length Distributions for Ions Bonded to Oxygen: Results for the Transition Metals and Quantification of the Factors Underlying Bond-Length Variation in Inorganic Solids. *ChemRxiv. Preprint* **2020**.
40. Gagne, O. C.; Hawthorne, F. C., Bond-length distributions for ions bonded to oxygen: alkali and alkaline-earth metals. *Acta Crystallographica Section B* **2016,** *72* (4), 602-625.
41. Malliavin, M. J.; Coudray, C., Ab initio calculations on $(MgO)_n$, $(CaO)_n$, and $(NaCl)_n$ clusters (n=1–6). *The Journal of Chemical Physics* **1997,** *106* (6), 2323-2330.
42. Yan, J.; Hummelshøj, J. S.; Nørskov, J. K., Formation energies of group I and II metal oxides using random phase approximation. *Physical Review B* **2013,** *87* (7), 075207.
43. Chen, M.; Felmy, A. R.; Dixon, D. A., Structures and Stabilities of $(MgO)_n$ Nanoclusters. *The Journal of Physical Chemistry A* **2014,** *118* (17), 3136-3146.
44. Chen, M.; Thanthiriwatte, K. S.; Dixon, D. A., Structures and Stabilities of (CaO)n Nanoclusters. *The Journal of Physical Chemistry C* **2017,** *121* (41), 23025-23038.
45. Chrétien, S.; Metiu, H., Electronic Structure of Partially Reduced Rutile TiO2(110) Surface: Where Are the Unpaired Electrons Located? *The Journal of Physical Chemistry C* **2011,** *115* (11), 4696-4705.
46. Deskins, N. A.; Rousseau, R.; Dupuis, M., Distribution of Ti^{3+} Surface Sites in Reduced TiO_2. *The Journal of Physical Chemistry C* **2011,** *115* (15), 7562-7572.

47. Rhatigan, S.; Nolan, M., Activation of Water on MnO_x-Nanocluster-Modified Rutile (110) and Anatase (101) TiO_2 and the Role of Cation Reduction. *Frontiers in Chemistry* **2019,** *7* (67).
48. Rhatigan, S.; Nolan, M., Impact of surface hydroxylation in MgO-/SnO-nanocluster modified TiO_2 anatase (101) composites on visible light absorption, charge separation and reducibility. *Chinese Chemical Letters* **2018,** *29* (6), 757-764.
49. Miyoshi, A.; Nishioka, S.; Maeda, K., Water Splitting on Rutile TiO_2-Based Photocatalysts. *Chemistry – A European Journal* **2018,** *24* (69), 18204-18219.
50. Dahan, M. H.; Caspary Toroker, M., Water Oxidation Catalysis with Fe_2O_3 Constrained at the Nanoscale. *The Journal of Physical Chemistry C* **2017,** *121* (11), 6120-6125.
51. Valdés, Á.; Qu, Z. W.; Kroes, G. J.; Rossmeisl, J.; Nørskov, J. K., Oxidation and Photo-Oxidation of Water on TiO_2 Surface. *The Journal of Physical Chemistry C* **2008,** *112* (26), 9872-9879.
52. Liao, P.; Keith, J. A.; Carter, E. A., Water Oxidation on Pure and Doped Hematite (0001) Surfaces: Prediction of Co and Ni as Effective Dopants for Electrocatalysis. *Journal of the American Chemical Society* **2012,** *134* (32), 13296-13309.
53. Tymińska, N.; Wu, G.; Dupuis, M., Water Oxidation on Oxygen-Deficient Barium Titanate: A First-Principles Study. *The Journal of Physical Chemistry C* **2017,** *121* (15), 8378-8389.
54. Zhang, X.; Klaver, P.; van Santen, R.; van de Sanden, M. C. M.; Bieberle-Hütter, A., Oxygen Evolution at Hematite Surfaces: The Impact of Structure and Oxygen Vacancies on Lowering the Overpotential. *The Journal of Physical Chemistry C* **2016,** *120* (32), 18201-18208.
55. Nguyen, M.-T.; Piccinin, S.; Seriani, N.; Gebauer, R., Photo-Oxidation of Water on Defective Hematite(0001). *ACS Catalysis* **2015,** *5* (2), 715-721.

7 HER at metal chalcogenide-modified TiO_2

What follows is adapted from an article entitled "**Modification of TiO_2 with Metal Chalcogenide Nanoclusters for Hydrogen Evolution**", published in Journal of Physics: Energy.[1]

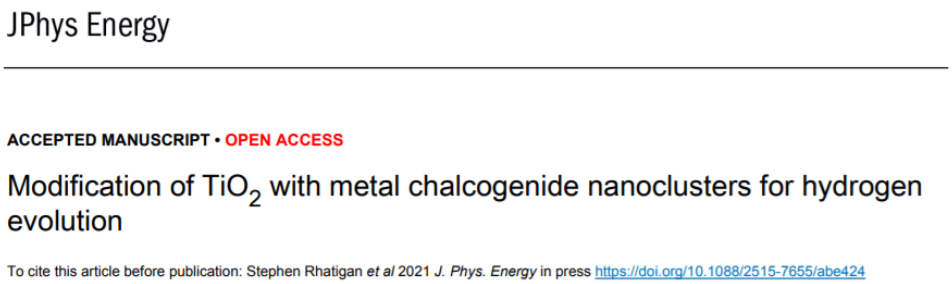
JPhys Energy

ACCEPTED MANUSCRIPT • OPEN ACCESS

Modification of TiO_2 with metal chalcogenide nanoclusters for hydrogen evolution

To cite this article before publication: Stephen Rhatigan *et al* 2021 *J. Phys. Energy* in press https://doi.org/10.1088/2515-7655/abe424

DOI: https://doi.org/10.1088/2515-7655/abe424

7.1 Introduction

In this work, we examine modification of the TiO_2 rutile (110) surface with nanoclusters of composition M_4X_4 (M = Sn, Zn; X = S, Se). Surface modification in this way can be performed using atomic layer deposition,[2] incipient wetness impregnation,[3-5] or chemisorption-calcination cycles[6-7] and permits modulation of the light absorption properties of the titania substrate, promotes separation and stability of photoexcited electrons and holes, and provides low coordinated active sites for catalytic reactions. In the context of hydrogen evolution, this strategy enables us to combine the desirable

properties of TiO_2 through modification with nanoclusters that display low-coordinated, active chalcogen sites, which promote the HER.

By computing the projected electronic density of states (PEDOS), we analyse the impact of modification on the energy gap and light absorption. The modification with the chalcogen nanoclusters extends the valence band maximum (VBM) to higher energies, thereby inducing a redshift in light absorption compared to unmodified TiO_2. Modification promotes the separation of electrons and holes and enhances their stability in the excited state.

Finally, we investigate the HER activity of the modified surface *via* computations of ΔG_H. To be consistent with the literature and allow for errors in computed energies within the DFT set-up, we consider the range of $\Delta G_H = (-0.15\ \text{eV}, +0.15\ \text{eV})$ to be relevant for assessment of the potential for HER. As metal oxide surfaces easily form surface bound hydroxyls,[8] we first compute ΔG_H for H adsorbed at sites of the titania support and consider coverages that range from 1 H to enough hydrogen to saturate the available surface sites. For H adsorption at surface sites, we consider only the bridging oxygen sites (O_{br}) that have no interfacial bonds with the nanocluster modifier. For each surface H coverage, we then compute ΔG_H for H adsorption at cluster sites. In these calculations, all chalcogen sites of the modifiers are considered and the most stable configurations that we find are discussed. We find that the sulphide modifiers exhibit free energies close to thermoneutral and within our desired range at most coverages. By contrast, for the selenide modifiers, the cluster sites are active only for low surface coverages of H. We rationalise these findings on the basis of the electronic structure of the chalcogen modifiers and propose metal sulphide-modified TiO_2 as a material for hydrogen evolution.

7.2 Methodology

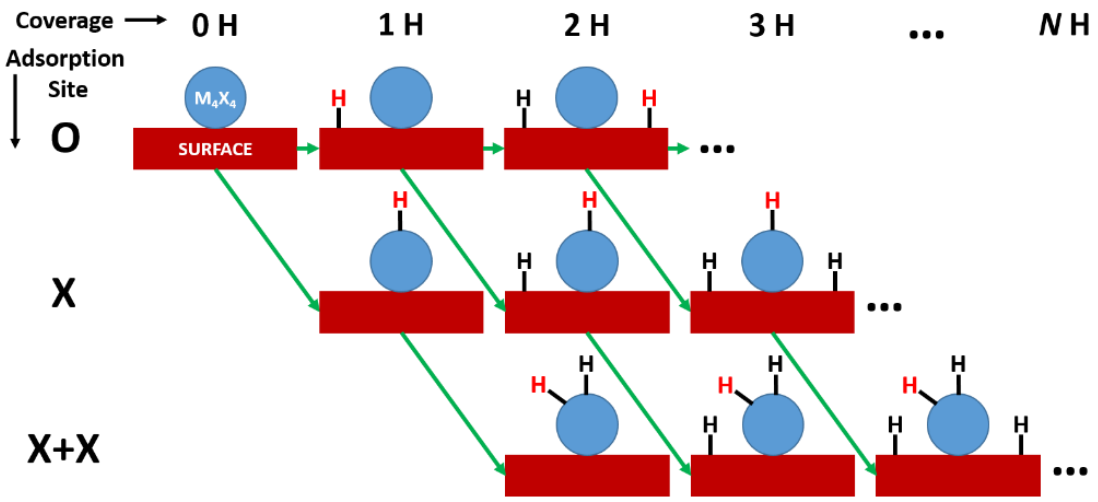

Figure 7.1 Schematic of the workflow for the study of hydrogen adsorption at the M_4X_4-modified rutile (110) surface. In the first set of calculations, shown in the top row, H atoms are adsorbed at the titania surface, up to saturation of the surface (O_{br}) sites. In the second set of calculations, shown in the second row, for each coverage of H at the TiO_2 surface, one H is adsorbed at a site on the chalcogenide nanocluster. For those configurations for which the hydrogen adsorption free energy at a cluster site is in the active range, we proceed with the third set of calculations in which a second H is adsorbed at a chalcogen nanocluster site, as shown in the third row. In each image, the red "H" represents the current calculation.

Hydrogen adsorption is examined at both the surface and the nanocluster. We explore adsorption of H at twofold coordinated bridging O ions (O_{br}) of the rutile (110) surface and at chalcogen sites of the modifiers. We follow the workflow shown in the schematic in **Figure 7.1** and begin with H adsorption at O_{br} surface sites. These calculations, represented by the top row of **Figure 7.1**, are performed first and we identify the most stable configuration for each hydrogen coverage ranging from 0 H to saturation of the surface sites. The adsorption energy of the n^{th} H atom at the most stable surface with an existing coverage of $(n-1)$ H atoms is computed *via*:

$$\Delta E_H = E_{nH@surf} - E_{(n-1)H@surf} - \frac{1}{2}(E_{H_2}) \quad 7.1$$

Where $E_{nH@surf}$, $E_{(n-1)surf}$, and E_{H_2} are the computed energies of the surface with n H atoms adsorbed, the surface with $(n-1)$ H atoms, and an isolated, gas phase H_2 molecule.

In the second set of calculations, represented by the second row of **Figure 7.1**, for each surface coverage of hydrogen, we examine hydrogen adsorption at chalcogen sites. For a surface coverage of $(n-1)$ H, the adsorption energy of the n^{th} H atom at a cluster site is computed *via*:

$$\Delta E_H = E_{H@cluster} - E_{(n-1)H@surf} - \frac{1}{2}(E_{H_2}) \quad 7.2$$

where $E_{H@cluster}$ is the energy of the system with 1 H at a cluster site and $(n-1)$ H adsorbed at surface sites. These calculations elucidate the impact of surface hydrogen coverage on the strength of interaction between H and the cluster site. For those configurations with adsorption free energies within our range, we proceed with the third set of calculations, represented by the third row in **Figure 7.1**, and examine adsorption of a second H atom at a cluster site to assess any trends in H coverage on the nanocluster modifier.

From the chemisorption energies (ΔE_H), we compute the free energy of adsorption using:

$$\Delta G_H = \Delta E_H + \Delta E_{ZPE} - T\Delta S_H \quad 7.3$$

Where ΔE_{ZPE} is the difference in zero point energy (ZPE) between the H atom adsorbed at the surface and in the gas phase; and $T\Delta S_H$ accounts for the difference in entropy between the final and initial state. These quantities are calculated according to the description in **Chapter 2**. In this way, we compute $\Delta E_{ZPE} - T\Delta S_H$ values of 0.35, 0.29,

and 0.26 eV for H adsorbed at O, S, and Se sites, respectively and these are consistent with other values used in the literature.[9-12]

7.3 Results

7.3.1 Atomic structure

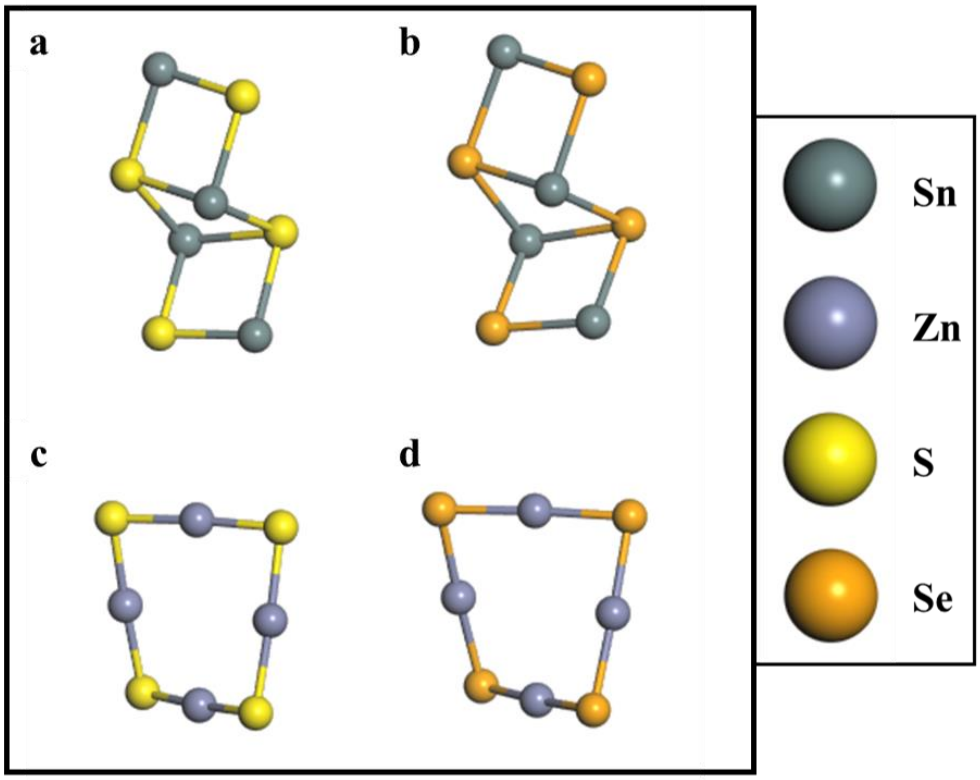

Figure 7.2 Relaxed atomic structures of **(a)** Sn_4S_4, **(b)** Sn_4Se_4, **(c)** Zn_4S_4 and **(d)** Zn_4Se_4.

The relaxed structures of the M_4X_4 nanoclusters in the gas phase are shown in **Figure 7.2** and the composite M_4X_4-r110 surfaces are shown in **Figure 7.3**; the computed adsorption energies are included in the insets. The negative adsorption energies indicate that the modifier-surface interaction is favourable and the magnitudes of these energies suggest that the nanoclusters are strongly bound at the surface.[13-17]

For Sn_4S_4-r110, shown in **Figure 7.3.a**, there are two Ti-S bonds of length 2.5 Å and three Sn-O bonds of lengths 2.2-2.4 Å. For Sn_4Se_4-r110, in **Figure 7.3.b**, there are two Ti-Se bonds of lengths 2.7 and 2.8 Å and two Sn-O bonds of length 2.2 Å. For both Sn_4S_4-r110 and Sn_4Se_4-r110, an additional bond forms between one Sn ion and a surface Ti with a bond length of 2.9 Å.

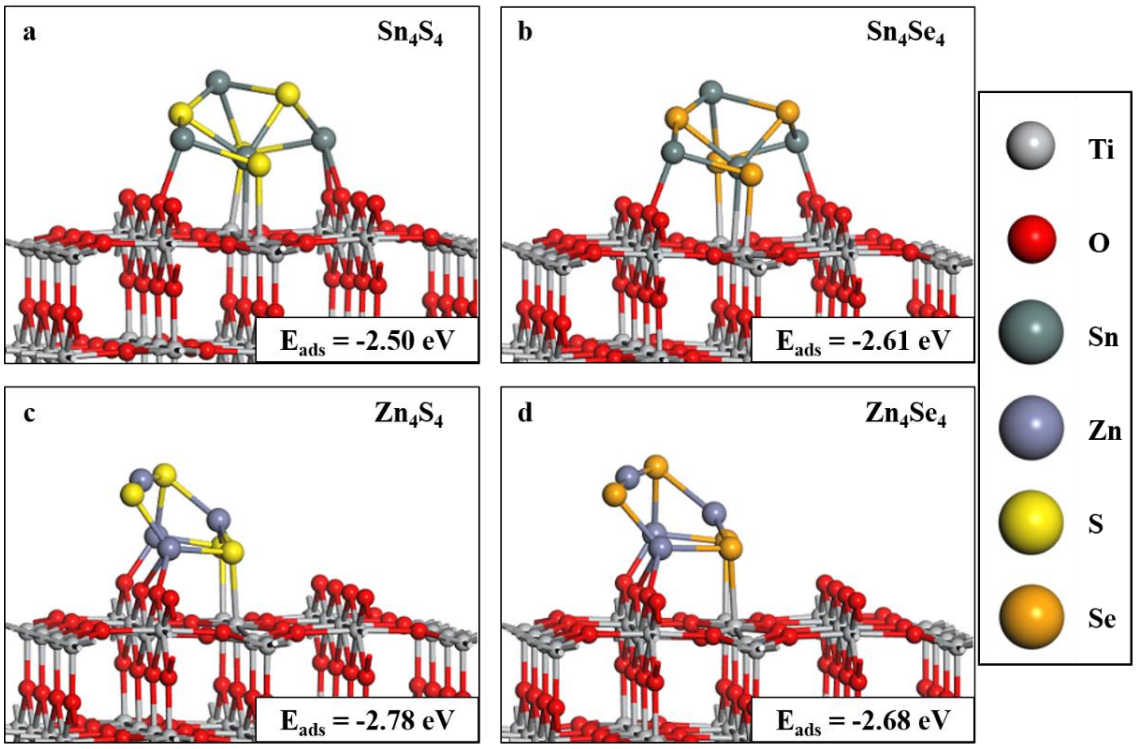

Figure 7.3 Relaxed geometries of **(a)** Sn_4S_4-, **(b)** Sn_4Se_4-, **(c)** Zn_sS_4-, and **(d)** Zn_4Se_4-r110. The adsorption energies of the nanoclusters at the rutile (110) surface are included in the insets. The colour scheme in the legend on the right applies to this and subsequent figures.

For Zn_4S_4-r110, shown in **Figure 2.c**, there are two Ti-S bonds, both of length 2.5 Å and three Zn-O bonds; one Zn-O bond is 1.9 Å and two have length 2.1 Å. For Zn_4Se_4-r110, in **Figure 2.d**, there are two Ti-Se bonds of lengths 2.6 and 2.7 Å and three Zn-O bonds of lengths 1.9, 2.1 and 2.1 Å.

From these data, we can see that the Ti-S bonds are shorter than the Ti-Se bonds. This is expected as Se has a larger ionic radius than S.[18-19] Nanocluster metal-S bonds are also shorter than metal-Se bonds, both in the gas-phase and after adsorption at the rutile TiO_2 surface. Metal-S bonds are consistently shorter by 0.12-0.16 Å, than equivalent bonds in the selenide structures. These values are in agreement with the ionic radii of S^{2-} and Se^{2-}, which are 1.84 and 1.98 Å, respectively.[20] However, despite differences in the composition of the nanocluster modifiers, the adsorption energies are similar in all cases.

7.3.2 Density of states

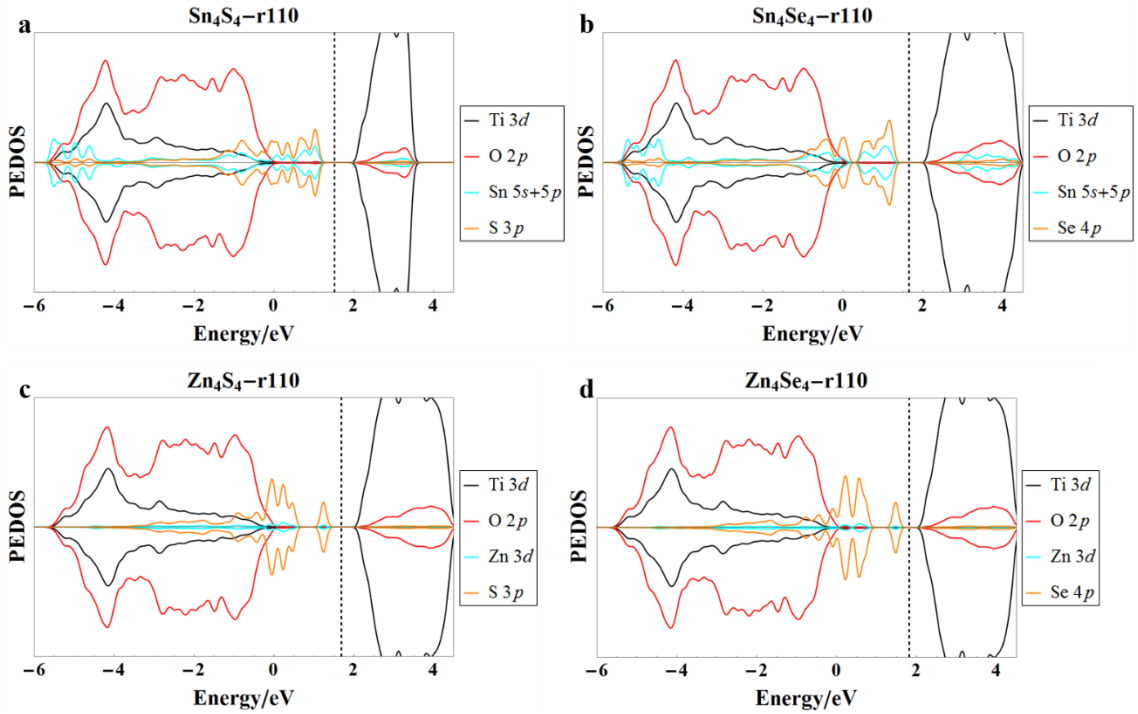

Figure 7.4 Density of states (DOS) plots for **(a)** Sn_4S_4-, **(b)** Sn_4Se_4-, **(c)** Zn_4S_4-, and **(d)** Zn_4Se_4-r110. The VBM of the titania support is set to 0 eV and the dashed vertical lines indicate the Fermi level. Nanocluster contributions, (M = Sn, Zn and X = S, Se), are shown (× 10) for clarity.

The projected electronic density of states (PEDOS) plots, computed for the M_4X_4-r110 heterostructures, are shown in **Figure 7.4**. The VBM of the titania support has been set

to 0 eV and the band gap of the rutile (110) surface, from this computational set-up, is 2.20 eV. After modification, occupied cluster-derived electronic states, which are predominantly chalcogen *p* states, extend into the energy gap. Occupied states emerge at 1.18, 1.30, 1.33 and 1.57 eV above the titania VBM for modification with Sn_4S_4, Sn_4Se_4, Zn_4S_4 and Zn_4Se_4, respectively. This is combined with an enhancement of the DOS near the VBM of the titania support due to modification. Moreover, for Sn_4X_4 modification, Sn-derived states emerge in the energy gap. These states are due to the lone pair, as has been discussed in previous work on Sn chalcogenides.[21-22]

Thus, the modified surfaces exhibit a redshift in the energy gap, with respect to the unmodified rutile (110) surface. Moreover, modifier-derived states near the Fermi level will have important consequences for the HER activity.

7.3.3 Photoexcitation model

Table 7.1 Energies computed from the photoexcitation model. Vertical singlet-triplet energy difference (E^{vert}), the relaxed singlet-triplet energy difference (E^{exc}) and the relaxation energy (E^{relax}) for M_4X_4-modified rutile (110). Values computed for the unmodified TiO_2 rutile (110) surface have been included for reference.

System	E^{vert} (eV)	E^{exc} (eV)	E^{relax} (eV)
Bare r110	2.03	1.60	0.43
Sn_4S_4-r110	1.17	0.16	1.01
Sn_4Se_4-r110	1.11	0.14	0.97
Zn_4S_4-r110	1.58	0.46	1.12
Zn_4Se_4-r110	1.30	0.13	1.17

The energies computed from the photoexcitation model are presented in **Table 7.1**. First, the model applied to the bare rutile (110) surface yields a vertical energy, E^{vert}, of 2.03

eV. The values for E^{vert} indicate that modification induces a redshift in the energy gap, as was also shown in analysis of the PEDOS plots. Optical gaps of 1.17, 1.11, 1.58 and 1.30 eV are computed for the rutile (110) surface modified with Sn_4S_4, Sn_4Se_4, Zn_4S_4 and Zn_4Se_4, respectively. The excitation energy, E^{exc}, is the energy difference between the singlet ground state and the fully relaxed triplet excited state. Each of the modified surfaces exhibit a reduction in this value, with respect to that computed for the bare rutile (110) surface. The computed relaxation energies, E^{rel}, are larger for the modified systems. E^{rel} represents the energy gained by the system after structural changes and relaxation in the excited state and is a measure of the stability of electron and hole localisation.

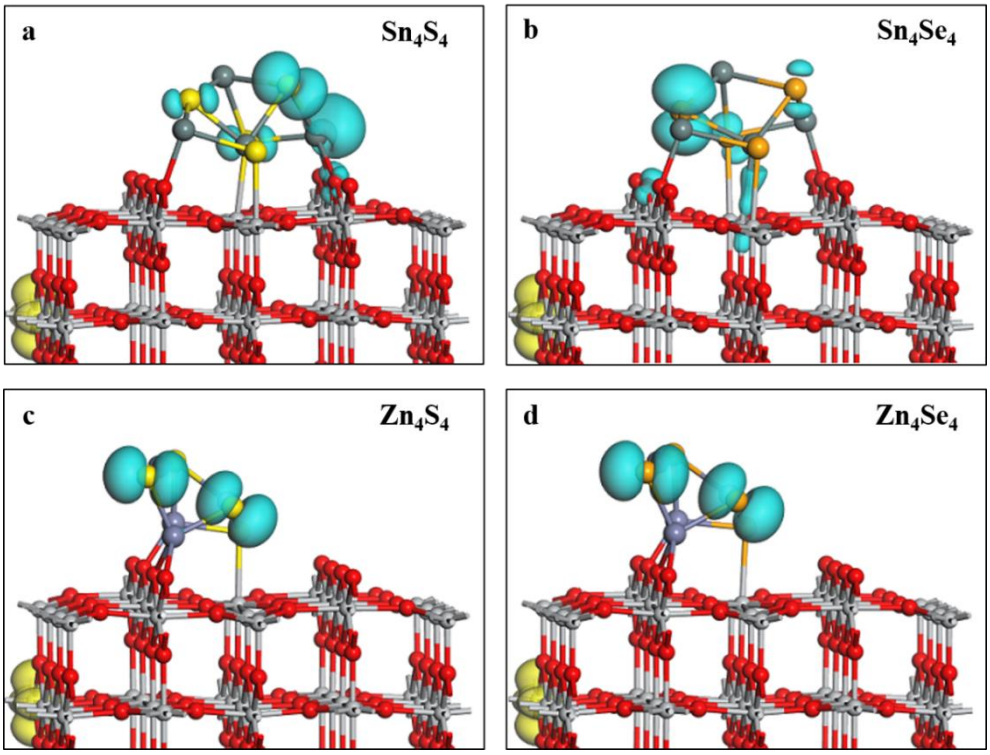

Figure 7.5 Excess spin density plots computed for the excited state of **(a)** Sn_4S_4-, **(b)** Sn_4Se_4-, **(c)** Zn_4S_4-, and **(d)** Zn_4Se_4-r110, after structural relaxation. The isosurfaces enclose spin densities of up to 0.02 eV/Å^3. Electrons are indicated by yellow and holes by blue.

To take part in photocatalytic reactions, photoexcited charges must separate and migrate to active surface sites and this entails overcoming the electron-hole binding energy, which

is not accounted for in this simple model for photoexcitation. However, low-coordinated surface sites can act as charge traps and suppress carrier recombination, and this is captured in our model. Moreover, the computed values E^{rel} are useful as a measure of the stability of charge trapping and indicate that this is enhanced upon modification with the metal chalcogenide nanoclusters. Taken together, the values shown in **Table 7.1** indicate that modification of rutile (110) with nanoclusters of composition M_4X_4 induces a redshift in light absorption and enhances the stability of photoexcited charges.

By examining the excess spin density plots, shown in **Figure 7.5**, in combination with analysis of computed Bader charges and spin magnetisations, we identify at which ions the photoexcited charges localise. For each system, the electrons and holes localise at the surface and modifier, respectively, which promotes charge separation. The yellow isosurfaces show that the electrons localise at sub-surface Ti ions, resulting in a reduction from Ti^{4+} to Ti^{3+}. This is corroborated by an increase in Bader charge from 1.3 electrons for Ti^{4+} to 1.6/1.7 electrons for Ti^{3+} and a computed spin magnetisation of 0.94 μ_B for the reduced Ti^{3+} ion.

For Sn_4S_4-r110, the hole state localises predominantly on an S ion and a neighbouring Sn ion. For the S ion, the Bader charge decreases from 6.9 to 6.7 electrons and this ion has a spin magnetisation of 0.29 μ_B. For the Sn ion, the Bader charge decreases from 12.8 to 12.6 electrons, indicating some hole localisation on Sn, consistent with the DOS analysis; the spin magnetisation for this Sn ion is 0.19 μ_B. For Sn_4Se_4-r110, the hole localises on an Se ion, for which the Bader charge decreases from 6.8 to 6.4 electrons; the spin magnetisation for this ion is 0.41 μ_B.

For both Zn_4S_4-r110 and Zn_4Se_4-r110, the hole state is distributed over two chalcogen ions; the S ions have computed spin magnetisations of 0.27 and 0.39 μ_B, while for the Se

ions the spin magnetisations are 0.32 and 0.35 μ_B. For Zn_4S_4-r110, the Bader charges for these S ions decrease from 6.9 and 6.8 electrons to 6.7 and 6.5 electrons, respectively. Similarly, the Bader charges for the Se ions at which the hole localises in Zn_4Se_4-r110 decrease from 6.8 to 6.5 electrons and from 6.6 to 6.4 electrons. In summary, each of the modified surfaces exhibit a reduction in the optical gap and an enhanced stability of excited charges, with respect to bare rutile (110). Moreover, after modification, the photoexcited electrons and holes are spatially separated; the electrons localise at subsurface Ti sites and the holes localise at chalcogen ions of the supported modifiers.

7.3.4 Hydrogen adsorption

Next, we examine the free energy of H adsorption at the modified surfaces and, as mentioned in the introduction, we consider that these modified materials will promote HER should they exhibit H adsorption free energies close to thermoneutral, i.e. 0 eV. For practical purposes, values of ΔG_H between -0.15 eV and 0.15 eV are in the active range. For H adsorption at the rutile (110) surface, only the two-fold coordinated O_{br} ions are investigated. After modification, there are five such sites for Sn_4S_4-, Zn_4S_4- and Zn_4Se_4-r110, and six for Sn_4Se_4-r110; full coverage of the surface sites corresponds to five or six H atoms ($N = 5$ or 6). For each surface coverage of $n = (1 \rightarrow N)$ H, we identify the most stable configuration for the n^{th} H atom adsorbed at a surface site by computing ΔG_H relative to a surface coverage of $(n - 1)$ H atoms for each available site, using equation 7.1. The results of these computations are shown in the rows labelled '**O**' for each surface in **Table 7.2**.

For surface coverages between 0 and *N* hydrogens, we then examine hydrogen adsorption at all chalcogen sites and the computed ΔG_H for the most stable chalcogen sites are

presented in **Table 7.2**, in the rows labelled '**X**', (**X**=S, Se). The adsorption free energy of the n^{th} H atom at a cluster site is calculated relative to the surface with $(n-1)$ H at surface sites, according to equation 7.2. Henceforth, we distinguish between "coverage" and "surface coverage"; the former refers to the total H coverage, including adsorption sites at the nanoclusters, whereas the latter refers only to H adsorbed on O sites of the rutile (110) support.

Table 7.2 Free energies (in eV) for H adsorption at surface sites (O) and cluster sites (S, Se) of Sn_4S_4-, Sn_4Se_4-, Zn_4S_4-, and Zn_4Se_4-r110. The data presented herein follows from the procedure described in the methodology section and summarized in **Figure 7.2**. For cluster sites, adsorption free energies in the active range are highlighted in bold.

Modifier	Site	0H	1H	2H	3H	4H	5H	6H
Sn_4S_4	**O**	0.00	-0.85	-0.36	-0.18	-0.44	-0.16	
	S		-0.34	-0.25	**-0.08**	0.29	**-0.00**	**0.04**
	S+S			**-0.09**	0.35	**0.15**	**-0.13**	0.25
Sn_4Se_4	**O**	0.00	-0.65	-0.59	-0.30	-0.18	-0.12	-0.15
	Se		**-0.12**	0.28	0.28	0.50	0.52	0.51
	Se+Se			0.47				
Zn_4S_4	**O**	0.00	-0.81	-0.32	-0.21	-0.22	-0.06	
	S		-0.35	-0.19	**-0.10**	**-0.08**	**0.02**	**0.12**
	S+S			**0.07**	0.67	**0.12**	0.52	0.74
Zn_4Se_4	**O**	0.00	-0.56	-0.59	-0.25	-0.13	-0.08	
	Se		**0.15**	**0.08**	0.20	0.33	0.40	0.29
	Se+Se			0.45				

For each modified surface, H adsorption at TiO_2 bridging oxygen sites is exothermic for all surface coverages. As the surface coverage increases, approaching full occupation of O_{br} sites, ΔG_H decreases. However, for all coverages, H adsorption at surface sites is more favourable than adsorption at chalcogen sites. Thus, for the n^{th} H atom, ΔG_H for

adsorption at a cluster site is computed relative to the system with a surface coverage of $(n-1)$ H.

For configurations with a H atom adsorbed at a cluster site with a free energy in the active range, we also investigate ΔG_H for adsorption at a second cluster site. The results of these computations are included in the rows labelled '**X+X**' (**X**=S, Se). All adsorption configurations for the data in **Table 7.2** are shown in **Figures 7.6**, for the example of Sn_4S_4-r110, and for this and the remaining heterostructures, the adsorption configurations at cluster sites with energies in the active range are summarised in **Figure 7.7**. All adsorption configurations for the other heterostructures are shown in **Figures 7.8-7.10** at the end of this chapter.

At all coverages, the bonds formed upon H adsorption at anion sites are consistent; O-H, S-H and Se-H bonds measure in the ranges (0.97-1.00), (1.35-1.40) and (1.47-1.49) Å, respectively. For Sn_4S_4-r110 and Zn_4S_4-r110, the first H atoms adsorb strongly at both surface and cluster sites; ΔG_H of -0.85 and -0.81 eV are computed for surface O_{br} sites and the computed ΔG_H is -0.34 and -0.35 eV for S sites. These values are quite exothermic and suggest that, at this coverage, the surface will be hydroxylated and the S-H bond is too stable for HER. However, starting from coverages of 2H, the computed ΔG_H for cluster sites are generally in the active range (-0.15 eV, 0.15 eV).

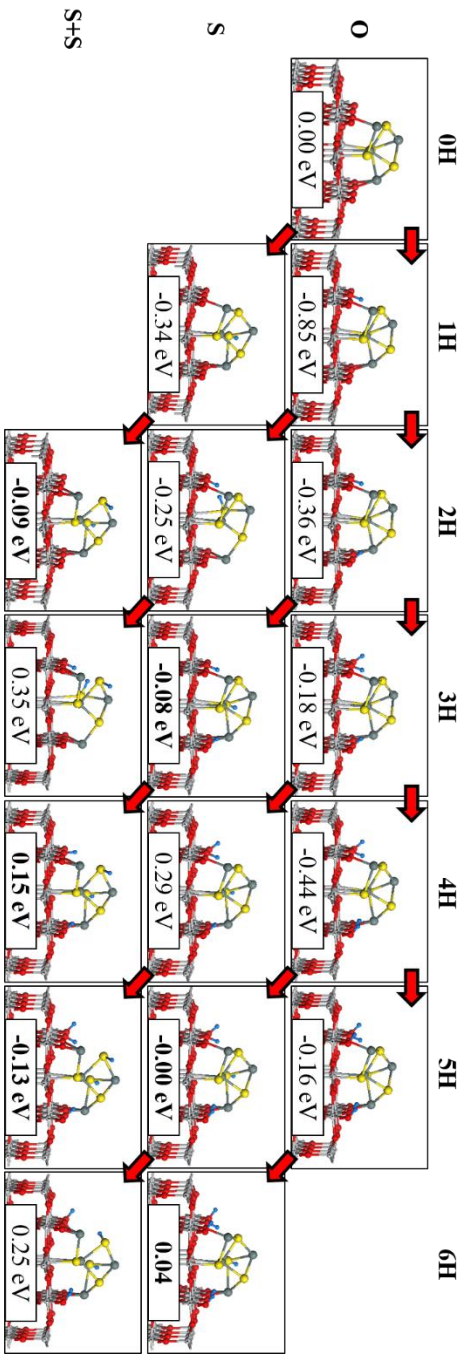

Figure 7.6 Adsorption configurations of H adsorbed at Sn_4S_4-r110 for coverages between one and six H atoms. The top row shows H adsorbed only at surface (O_{br}) sites, the second row shows configurations in which 1 H is adsorbed at a cluster (S) site, at each coverage. The configurations in the third row have 2 H adsorbed at S sites, for each coverage. The adsorption free energies, ΔG_H, are included in the insets and the red arrows indicate the configurations relative to which ΔG_H is computed. At all coverages, H adsorption at O_{br} sites is more favourable than adsorption at cluster sites. In this and subsequent figures, values for ΔG_H in the active range are highlighted in bold, for cluster sites.

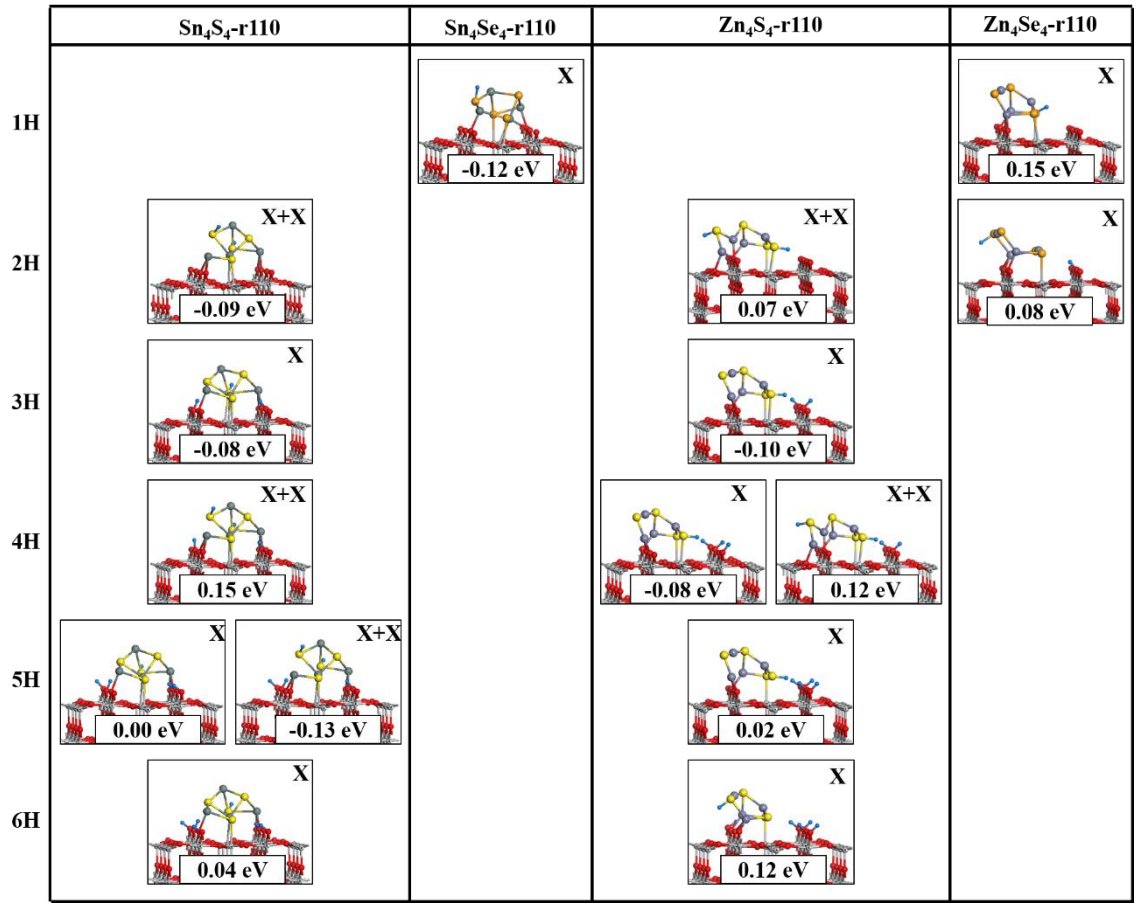

Figure 7.7 H adsorption configurations with free energies in the range (-0.15 eV, +0.15 eV), for adsorption at cluster sites of Sn_4S_4-, Sn_4Se_4-, Zn_4S_4-, and Zn_4Se_4-r110. The total H coverages are shown on the left hand side. "X" = adsorption of a single H at a chalcogen site of the cluster; "X+X" = adsorption of two H at chalcogen sites of the cluster.

By contrast, for Sn_4Se_4-r110, only the first H adsorption free energy at a cluster site is within the active range, irrespective of the surface H coverage. Similarly, for Zn_4Se_4-r110, only two adsorption configurations are in the active range, at coverages of 1H and 2H. For higher coverages, while adsorption at O sites is favourable, adsorption at Se sites is endothermic and the free energies are outside the active range.

In summary, the data presented in **Table 7.2** indicate that the sulphide-modified surfaces will be more active in HER, with respect to the selenide-modified surfaces. In general, H adsorption at S sites is more favourable than adsorption at Se sites; adsorption at Se sites is mostly too endothermic for HER activity. This result is in agreement with a recent study

on the stabilisation of hydrogen adsorption on Chevrel-Phase Mo_6X_8 (X=S, Se, Te) electrocatalysts.[23] Through a combination of experiment and computation, the authors reported that H adsorption strength increased with the electronegativity of the chalcogen (S = 2.58; Se = 2.55).[24] This result manifests in the electronic structure as a lower *p*-band centre. The *p*-band centre is defined as:

$$\text{X } p\text{-band centre} = \frac{\int_{-\infty}^{\infty} E \cdot D_{X_P}(E) dE}{\int_{-\infty}^{\infty} D_{X_P}(E) dE} - E_F \qquad 7.4$$

This quantity can be extrapolated from the computed PEDOS and values of -2.08, -1.69, -2.23 and -1.97 eV were computed for the chalcogen species of Sn_4S_4-, Sn_4Se_4-, Zn_4S_4- and Zn_4Se_4-r110, respectively. The lower *p*-band centres for the sulphide-modified systems reflect the stronger hydrogen adsorption at cluster sites of these composite surfaces. The computed values for the *p*-band centres are lower for the ZnX modifiers, with respect to the SnX modifiers. However, this does not manifest in appreciable differences in the H adsorption free energies between ZnX and SnX modification, as shown in **Table 2**. Thus, the role of the metal in the M_4X_4 modifiers, whether Sn or Zn, does not appear to affect the HER activity and the nature of the chalcogen, whether S or Se, plays a greater role. Finally, hydroxylation of the rutile support, beyond a surface coverage of 1 H, does not qualitatively affect the strength of adsorption of H at cluster sites.

For each of the H adsorption configurations at cluster sites with ΔG_H in the range (-0.15 eV, 0.15 eV), highlighted in bold in **Table 7.2**, we examine the subsequent Heyrovsky step in which a H atom interacts with H bound at S or Se of the nanocluster. This results in the formation and desorption of a H_2 molecule in a process which amounts to the reverse of H adsorption; thus, the free energy corrections, $\Delta E_{ZPE} - T\Delta S_H$, are the negative of those computed for H adsorption, i.e. -0.29 eV and -0.26 eV for desorption from S and

Se, respectively. For Sn_4S_4-r110, of the six adsorption configurations with ΔG_H in the active range, the desorption free energies are in the range (-0.19 eV, +0.20 eV). For the four active configurations on Zn_4S_4-r110, the desorption energies are in the range (-0.34 eV, 0.14 eV). The free energies are 0.40 eV for desorption from Sn_4Se_4- and -0.19 and 0.53 eV for desorption from Zn_4Se_4-r110. This suggests that formation of H_2 through the Heyrovsky step should be favourable on metal sulphide modified TiO_2.

7.4 Conclusions

Metal chalcogenides have emerged as promising candidates for HER catalysis. Extensive experimental and computational studies of TMDs have revealed that low-coordinated chalcogen sites are active sites for HER. This is attributed to the near optimal adsorption free energy of H at chalcogen sites.

In this work, we have examined, *via* DFT+U computations, the surface modification of TiO_2 rutile (110) with nanoclusters of composition M_4X_4 (M = Sn, Zn; X = S, Se). Surface modification strategies aim to combine the desirable properties of the substrate (TiO_2) with those of the nanocluster modifiers. In this instance, the M_4X_4 modifiers provide low-coordinated chalcogen sites, which we have investigated for their HER activity *via* computations of the free energy of H adsorption.

Our results indicate that the M_4X_4 modifiers bind to the rutile surface with the formation of interfacial M-O and Ti-X bonds. The modification induces a red shift in light absorption due to the emergence of occupied, nanocluster-derived (predominantly chalcogen 2*p*) states in the titania energy gap. In addition, modification with M_4X_4

nanoclusters promotes the spatial separation of photoexcited charges and enhances their stability in the excited state.

Analysis of the free energies of H adsorption, ΔG_H, reveals that the sulphide modifiers exhibit values close to thermoneutral, (-0.15 eV, +0.15 eV), for most H coverages, whereas this is only true for the selenide modifiers at low coverages. This is a widely accepted descriptor for HER activity and suggests that sulphide-modification will promote the HER to a greater extent than selenide modification. In general, H binding at sulphur sites is more favourable than at selenium sites; we attribute this to the higher electronegativity of S, with respect to Se. This effect is manifested in the computed *p*-band centres of the modified systems – the sulphide-modified systems exhibit lower *p*-band centres than the selenide-modified systems.

In conclusion, modification of titania with dispersed metal chalcogenide nanoclusters has the potential to enhance the HER activity of the titania support. However, despite their desirable photocatalytic properties, chalcogenides can suffer from poor chemical stability[25] and this must be accounted for in the design of practical photocatalysts. While metal chalcogenides can oxidise in aqueous environments, many of the catalysts presented in the review in **Chapter 3** exhibit stable performances under HER conditions. Thus, one strategy for preserving the integrity of metal chalcogenide catalysts for water splitting applications will entail the design of a suitable photoelectrochemical cell, in which the OER and HER proceed in separate compartments. Another approach to promote the stability is to deposit very thin, protective layers *via* ALD or similar techniques.[26-28]

Careful analysis is required to elucidate the impact of modification on the properties which govern the photocatalytic HER activity. However, rational selection of the

composition of the modifiers, in combination with first principles computations of appropriate material descriptors can facilitate high-throughput screening of candidate materials.

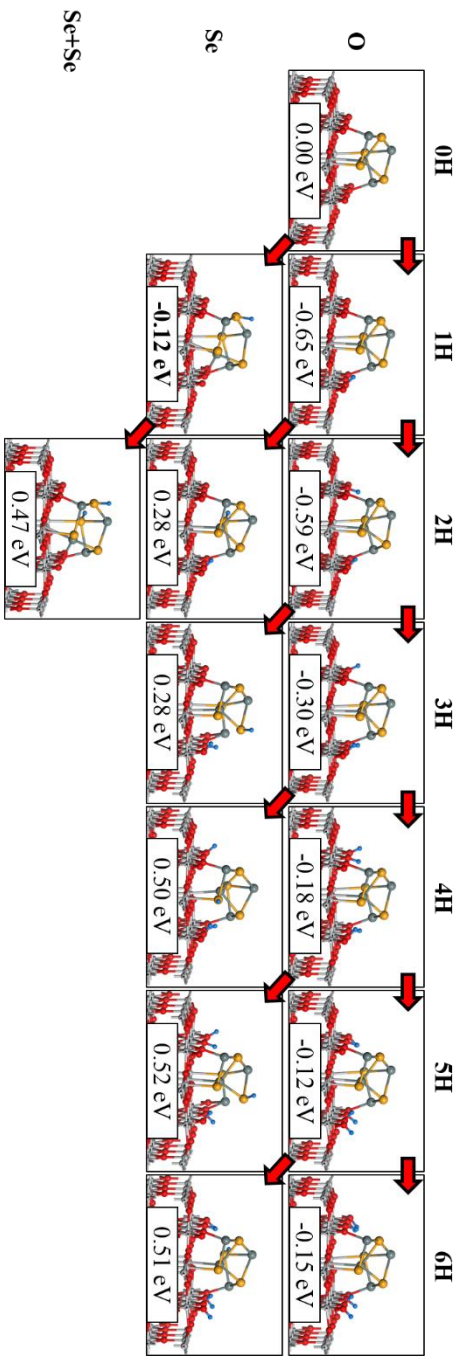

Figure 7.8 Adsorption configurations of H adsorbed at Sn_4Se_4-r110 for coverages between one and six H atoms. The top row shows H adsorbed only at surface (O_{br}) sites, the second row shows configurations in which 1 H is adsorbed at a cluster (Se) site, at each coverage. The configuration in the third row has 2 H adsorbed at Se sites. The adsorption free energies, ΔG_H, are included in the insets and the red arrows indicate the configurations relative to which ΔG_H is computed. At all coverages, H adsorption at O_{br} sites is more favourable than adsorption at cluster sites.

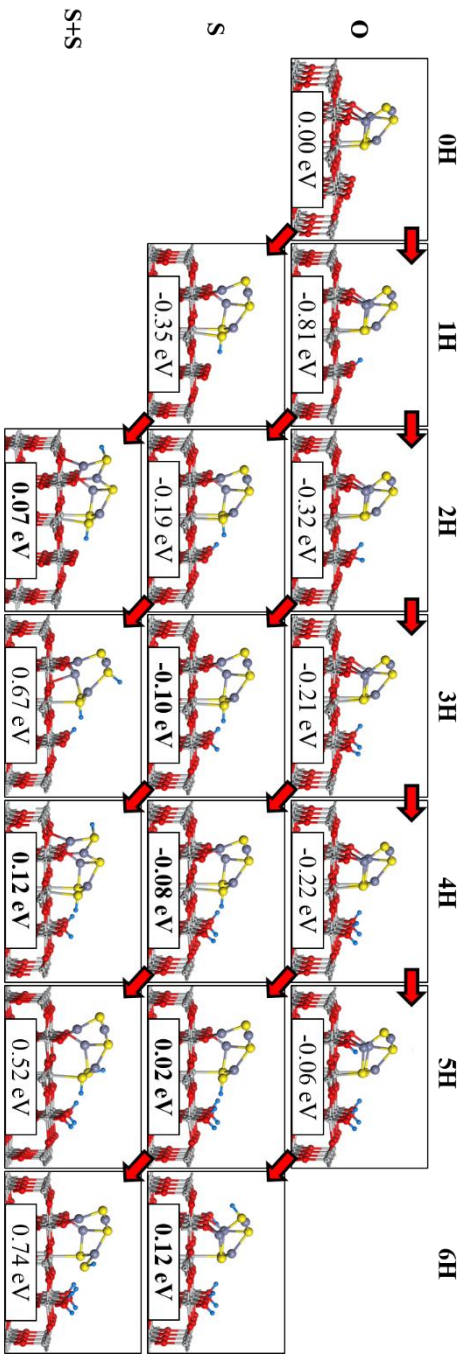

Figure 7.9 Adsorption configurations of H adsorbed at Zn_4S_4-r110 for coverages between one and six H atoms. The top row shows H adsorbed only at surface (O_{br}) sites, the second row shows configurations in which 1 H is adsorbed at a cluster (S) site, at each coverage. The configurations in the third row have 2 H adsorbed at S sites, for each coverage. The adsorption free energies, ΔG_H, are included in the insets and the red arrows indicate the configurations relative to which ΔG_H is computed. At all coverages, H adsorption at O_{br} sites is more favourable than adsorption at cluster sites.

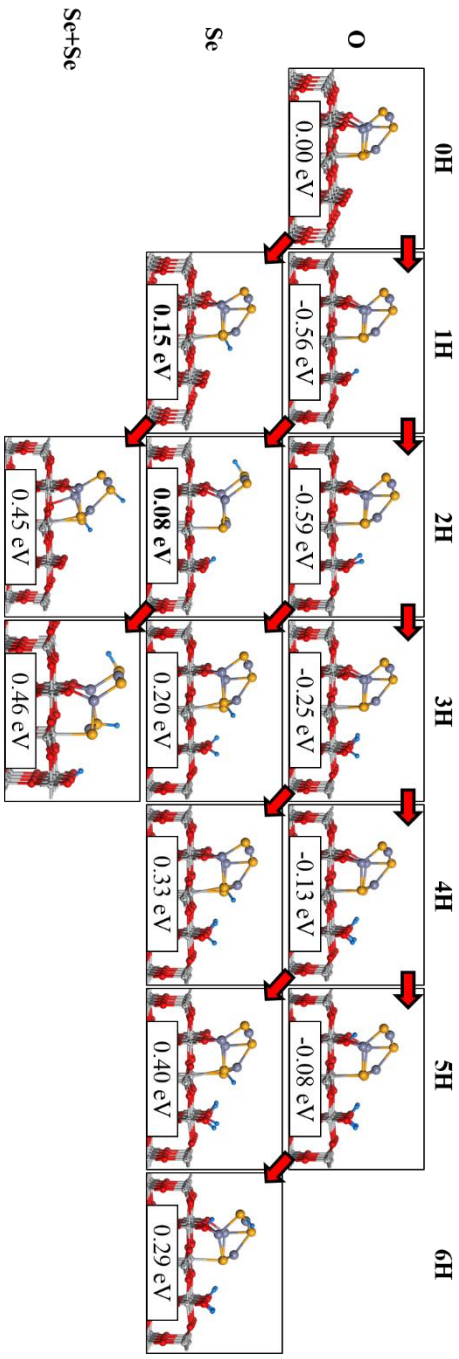

Figure 7.10 Adsorption configurations of H adsorbed at Zn_4Se_4-r110 for coverages between one and six H atoms. The top row shows H adsorbed only at surface (O_{br}) sites, the second row shows configurations in which 1 H is adsorbed at a cluster (Se) site, at each coverage. The configuration in the third row has 2 H adsorbed at Se sites. The adsorption free energies, ΔG_H, are included in the insets and the red arrows indicate the configurations relative to which ΔG_H is computed. At all coverages, H adsorption at O_{br} sites is more favourable than adsorption at cluster sites.

7.5 Chapter References

1. Rhatigan, S.; Niemitz, L.; Nolan, M., Modification of TiO_2 with Metal Chalcogenide Nanoclusters for Hydrogen Evolution. *Journal of Physics: Energy* **2021**.
2. Libera, J. A.; Elam, J. W.; Sather, N. F.; Rajh, T.; Dimitrijevic, N. M., Iron(iii)-oxo centers on TiO_2 for visible-light photocatalysis. *Chemistry of Materials* **2010,** *22* (2), 409-413.
3. Majrik, K.; Pászti, Z.; Korecz, L.; Trif, L.; Domján, A.; Bonura, G.; Cannilla, C.; Frusteri, F.; Tompos, A.; Tálas, E., Study of PtO_x/TiO_2 Photocatalysts in the Photocatalytic Reforming of Glycerol: The Role of Co-Catalyst Formation. *Materials* **2018,** *11* (1927).
4. Munnik, P.; de Jongh, P. E.; de Jong, K. P., Recent Developments in the Synthesis of Supported Catalysts. *Chemical Reviews* **2015,** *115* (14), 6687-6718.
5. Lamai, W.; Bunphung, A.; Junumpun, I.; Wongkaew, A., Synthesis and Characterization of Ni@Pt core-shell catalyst over TiO_2 support prepared by incipient wetness impregnation and electroless deposition. *Materials Today: Proceedings* **2019,** *17*, 1396-1402.
6. Jin, Q.; Fujishima, M.; Tada, H., Visible-light-active iron oxide-modified anatase titanium(iv) dioxide. *The Journal of Physical Chemistry C* **2011,** *115* (14), 6478-6483.
7. Tada, H.; Jin, Q.; Iwaszuk, A.; Nolan, M., Molecular-scale transition metal oxide nanocluster surface-modified titanium dioxide as solar-activated environmental catalysts. *The Journal of Physical Chemistry C* **2014,** *118* (23), 12077-12086.
8. Tamura, H.; Mita, K.; Tanaka, A.; Ito, M., Mechanism of Hydroxylation of Metal Oxide Surfaces. *Journal of Colloid and Interface Science* **2001,** *243* (1), 202-207.
9. Gajaria, T. K.; Roondhe, B.; Dabhi, S. D.; Śpiewak, P.; Kurzydłowski, K. J.; Jha, P. K., Hydrogen evolution reaction electrocatalysis trends of confined gallium phosphide with substitutional defects. *International Journal of Hydrogen Energy* **2020,** *45* (44), 23928-23936.
10. Baraiya, B. A.; Mankad, V.; Jha, P. K., Adsorption Energetics of Atoms and Diatomic Gases with Electrocatalysis Approach towards Hydrogen and Oxygen Evolution Reaction on Pt Surfaces. *ChemistrySelect* **2018,** *3* (37), 10515-10525.
11. Nørskov, J. K.; Bligaard, T.; Logadottir, A.; Kitchin, J. R.; Chen, J. G.; Pandelov, S.; Stimming, U., Trends in the Exchange Current for Hydrogen Evolution. *Journal of The Electrochemical Society* **2005,** *152* (3), J23-J26.
12. Liao, P.; Keith, J. A.; Carter, E. A., Water Oxidation on Pure and Doped Hematite (0001) Surfaces: Prediction of Co and Ni as Effective Dopants for Electrocatalysis. *Journal of the American Chemical Society* **2012,** *134* (32), 13296-13309.
13. Byrne, C.; Rhatigan, S.; Hermosilla, D.; Merayo, N.; Blanco, Á.; Michel, M. C.; Hinder, S.; Nolan, M.; Pillai, S., Modification of TiO_2 with hBN: High temperature anatase phase stabilisation and photocatalytic degradation of 1,4-dioxane. *Journal of Physics: Materials* **2019**.
14. Rhatigan, S.; Nolan, M., Activation of Water on MnO_x-Nanocluster-Modified Rutile (110) and Anatase (101) TiO2 and the Role of Cation Reduction. *Frontiers in Chemistry* **2019,** *7* (67).
15. Rhatigan, S.; Nolan, M., CO_2 and water activation on ceria nanocluster modified TiO_2 rutile (110). *Journal of Materials Chemistry A* **2018,** *6* (19), 9139-9152.

16. Rhatigan, S.; Nolan, M., Impact of surface hydroxylation in MgO-/SnO-nanocluster modified TiO_2 anatase (101) composites on visible light absorption, charge separation and reducibility. *Chinese Chemical Letters* **2018,** *29* (6), 757-764.
17. Rhatigan, S.; Sokalu, E.; Nolan, M.; Colón, G., Surface Modification of Rutile TiO_2 with Alkaline-Earth Oxide Nanoclusters for Enhanced Oxygen Evolution. *ACS Applied Nano Materials* **2020,** *3* (6), 6017-6033.
18. Rhatigan, S.; Michel, M. C.; Nolan, M., Hydrogen evolution on non-metal oxide catalysts. *Journal of Physics: Energy* **2020**.
19. Zou, X.; Zhang, Y., Noble metal-free hydrogen evolution catalysts for water splitting. *Chemical Society Reviews* **2015,** *44* (15), 5148-5180.
20. Shannon, R., Revised effective ionic radii and systematic studies of interatomic distances in halides and chalcogenides. *Acta Crystallographica Section A* **1976,** *32* (5), 751-767.
21. Walsh, A.; Watson, G. W., Influence of the Anion on Lone Pair Formation in Sn(II) Monochalcogenides: A DFT Study. *The Journal of Physical Chemistry B* **2005,** *109* (40), 18868-18875.
22. Iwaszuk, A.; Nolan, M., SnO-nanocluster modified anatase TiO_2 photocatalyst: exploiting the Sn(ii) lone pair for a new photocatalyst material with visible light absorption and charge carrier separation. *Journal of Materials Chemistry A* **2013,** *1* (22), 6670-6677.
23. Ortiz-Rodríguez, J. C.; Singstock, N. R.; Perryman, J. T.; Hyler, F. P.; Jones, S. J.; Holder, A. M.; Musgrave, C. B.; Velázquez, J. M., Stabilizing Hydrogen Adsorption through Theory-Guided Chalcogen Substitution in Chevrel-Phase Mo6X8 (X=S, Se, Te) Electrocatalysts. *ACS Applied Materials & Interfaces* **2020,** *12* (32), 35995-36003.
24. Allred, A. L., Electronegativity values from thermochemical data. *Journal of Inorganic and Nuclear Chemistry* **1961,** *17* (3), 215-221.
25. Nie, L.; Zhang, Q., Recent progress in crystalline metal chalcogenides as efficient photocatalysts for organic pollutant degradation. *Inorganic Chemistry Frontiers* **2017,** *4* (12), 1953-1962.
26. Dasgupta, N. P.; Lee, H.-B.-R.; Bent, S. F.; Weiss, P. S., Recent Advances in Atomic Layer Deposition. *Chemistry of Materials* **2016,** *28* (7), 1943-1947.
27. Noh, J. H.; Lee, S.; Kim, J. Y.; Lee, J.-K.; Han, H. S.; Cho, C. M.; Cho, I. S.; Jung, H. S.; Hong, K. S., Functional Multilayered Transparent Conducting Oxide Thin Films for Photovoltaic Devices. *The Journal of Physical Chemistry C* **2009,** *113* (3), 1083-1087.
28. Yang, W.; Prabhakar, R. R.; Tan, J.; Tilley, S. D.; Moon, J., Strategies for enhancing the photocurrent, photovoltage, and stability of photoelectrodes for photoelectrochemical water splitting. *Chemical Society Reviews* **2019,** *48* (19), 4979-5015.

8 TiO_2 nanoparticle

What follows is adapted from an article entitled "**On the use of DFT+U to describe the electronic structure of TiO_2 nanoparticles: $(TiO_2)_{35}$ as a case study**", published in the Journal of Chemical Physics.[1]

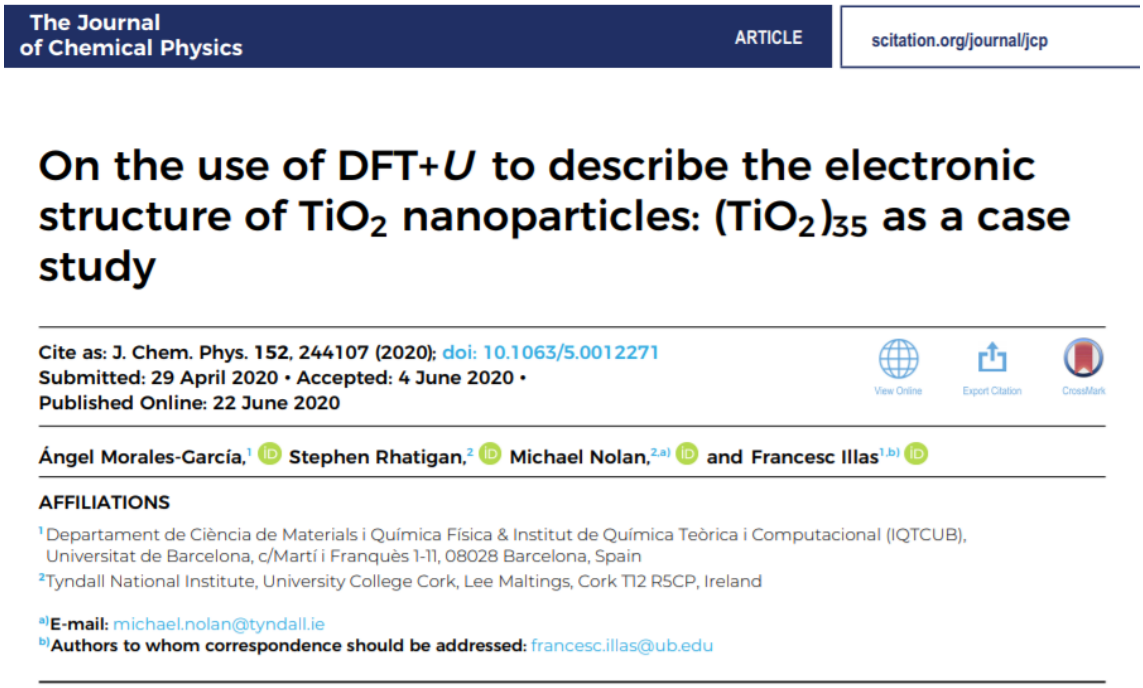

The Journal of Chemical Physics ARTICLE scitation.org/journal/jcp

On the use of DFT+*U* to describe the electronic structure of TiO_2 nanoparticles: $(TiO_2)_{35}$ as a case study

Cite as: J. Chem. Phys. 152, 244107 (2020); doi: 10.1063/5.0012271
Submitted: 29 April 2020 • Accepted: 4 June 2020 •
Published Online: 22 June 2020

View Online Export Citation CrossMark

Ángel Morales-García,[1] Stephen Rhatigan,[2] Michael Nolan,[2,a)] and Francesc Illas[1,b)]

AFFILIATIONS

[1]Departament de Ciència de Materials i Química Física & Institut de Química Teòrica i Computacional (IQTCUB), Universitat de Barcelona, c/Martí i Franquès 1-11, 08028 Barcelona, Spain
[2]Tyndall National Institute, University College Cork, Lee Maltings, Cork T12 R5CP, Ireland

[a)]E-mail: michael.nolan@tyndall.ie
[b)]Authors to whom correspondence should be addressed: francesc.illas@ub.edu

DOI: https://doi.org/10.1063/5.0012271

8.1 Introduction

Titanium dioxide, TiO_2, nanoparticles involving a mixture of anatase and rutile polymorphs, in particular, in the commercialised Degussa P25 form, constitute the most studied photocatalytic material and a model system for the mechanisms involved in photocatalysis.[2-5] The performance of TiO_2 depends largely on its optical, electronic, structural, morphological and surface properties,[6-8] and one of the key properties of TiO_2,

especially in the anatase polymorph, is the formation of photogenerated charge carriers (holes and electrons), activated by the absorption of ultraviolet (UV) light. Indeed, the need for UV radiation constitutes one of the major bottlenecks towards developing efficient TiO_2 photocatalysts that can work under sunlight, as only ~5% of the incident solar spectrum corresponds to UV light. Hence, a major challenge in the development of competitive TiO_2-based photocatalysts is reducing the energy gap to the visible (VIS) region.[9]

In principle, the properties of TiO_2 can be modulated by designing nanoparticles (NPs) with different sizes, shapes, crystallinities, and surface facets.[10-13] However, to determine the relationship between structural and electronic properties of TiO_2 nanoparticles, experimentally, is not a simple task. Alternatively, computational techniques provide a feasible, accurate, and unbiased approach to study such correlations and, consequently, can contribute to build connections between experiment and theory.[14]

Density functional theory (DFT)[15-16] has been widely used to study the properties of different types of materials with high accuracy in the prediction of crystal structures and reasonable description of electronic structure features at a moderate computational cost[17] and with a well-established reproducibility.[18] Unfortunately, energy gaps computed using the popular local density approximation (LDA) and the generalised gradient approximation (GGA) are consistently underestimated by 30–100%.[19-20] The error arises from the inherent lack of derivative discontinuity and the delocalisation error.[21-23] To overcome the drawbacks of LDA and GGA for estimating this electronic property, hybrid functionals, which include a part of the nonlocal Fock exchange, have been proposed and widely employed.[24-25] Depending on the type of basis set, the use of hybrid functionals can represent a significant increase in the cost of the calculations. Inspired by the Hubbard Hamiltonian,[26] Anisimov et *al.*[27] proposed to avoid the computational load inherent to

hybrid functionals by implementing an empirical on-site Hubbard (U) correction to a selected atomic energy level, within standard DFT. The resulting method is often referred to as DFT+U, an unfortunate term as DFT is an exact theory. DFT+U has been broadly used, especially after the contribution of Dudarev *et al.*[28] and is particularly useful in the description of the partially filled *d*-states of the transition metals – in the case of TiO_2, the U-correction is applied to the Ti 3*d* orbital.[29-30]

The DFT+U method combines the high efficiency of standard DFT with an explicit, albeit approximate and empirical, treatment of electron on-site correlation, and constitutes one of the simplest approaches to describe the ground state of strongly correlated systems.[31] However, the choice of appropriate U parameter value for each compound is a challenge. This obstacle can be solved through (*i*) a linear response, fully consistent method,[32] or (*ii*) alternative routes based on comparison with experimental results for some physical property of interest, such as magnetic moment, energy gap, redox potentials or reaction enthalpies.[33-35] For instance, the latter strategy has been employed in the study of the electron transport in the rutile phase,[36-37] reduced forms of TiO_2,[38-39] and ultrathin films of the rutile phase.[40]

Nevertheless, the selection of the U parameter is not straightforward. Moreover, the choice of the appropriate form of the projector functions inherent to the method is also a concern,[41] especially after the work of Kick *et al.*[42] who recently implemented DFT+U with a numerical atomic orbital basis set. The authors showed that the value for U depends on the choice of projector function, which in turn depends on the type of basis set (atomic orbitals or plane waves) used. The aim of the current study is to evaluate the effect of the basis sets in the selection of the U value necessary to describe the electronic structure of semiconducting nanoparticles, taking a previously investigated, well-defined $(TiO_2)_{35}$ bipyramidal NP as a case study.[43]

Nanoparticles exhibit features that are not present in bulk or extended surface models; these include large surface areas, low-coordinated surface sites and quantum confinement effects. Such features endow NPs with unique properties, which make them of interest, in particular, for photocatalytic applications.[44] TiO_2 NPs have been the subject of a number of DFT studies at different levels of the theory.[45-53] An understanding of the performance of different implementations of DFT in the description of the structural and electronic properties of isolated nanoparticle systems is crucial for the effective application of computational methods.

8.2 Methodology

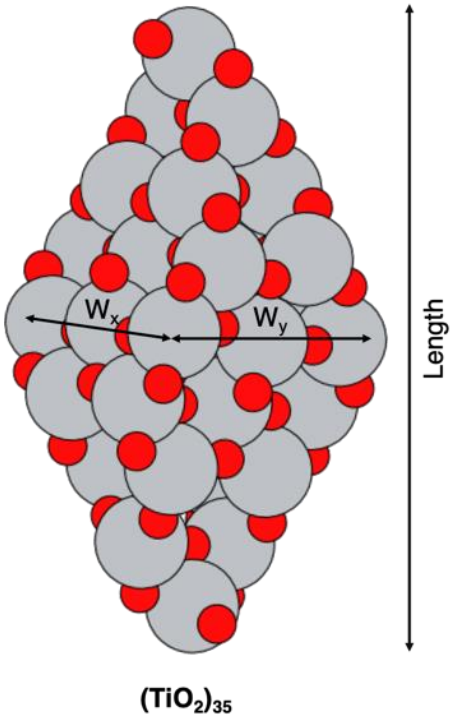

Figure 8.1 Stoichiometric $(TiO_2)_{35}$ anatase NP with bipyramidal morphology. All the exposed facets correspond to the (101) surface. The dimensions of the NP are indicated with double arrows. Wx and W_y denote the nanoparticle width in the *x* and *y* direction, respectively. Gray and red spheres represent Ti and O atoms, respectively.

The well-defined bipyramidal stoichiometric $(TiO_2)_{35}$ anatase NP, which fulfills the requirement of a Wulff construction,[54] and was used in previous studies,[42] is selected for the present study (**Figure 8.1**). This nanoparticle exposes the most favorable (101) facets only, as found in experiments.[7] Furthermore, its ~2 nm size is also appropriate to rationalise experimental results reported for TiO_2 anatase NPs.[55]

The calculations reported here have been carried out using two widely used codes, namely the Vienna *Ab Initio* Simulation Package (VASP)[56-57] and the Fritz Haber Institute *ab initio* molecular simulations (FHI-aims).[58] VASP calculations were carried out in Tyndall, by the author, and use the computational set-up described in **Chapter 2**. However, the details are provided again here, to facilitate comparison with the FHI-aims set-up. The FHI-aims calculations were performed in the University of Barcelona. In both cases, the Perdew-Wang (PW91) exchange-correlation functional[59] is used and spin-polarisation is accounted for explicitly, although the final results do not exhibit any spin-polarisation. The partially filled Ti_{3d} states are consistently described by applying the Hubbard U correction[26] under the simplified rotationally invariant approach introduced by Dudarev *et al*.[27] In the following, we will refer to the resulting approach as PW91+U, which is more appropriate.

The calculations carried out with VASP employ a plane waves (PWs) basis set with a kinetic energy cut-off of 396 eV. To account for the effect of inner electrons on the valence density, we implement the projector augmented wave (PAW) method of Bloch,[60] as implemented by Kresse and Joubert,[61] with 12 and 6 valence electrons for Ti and O atoms, respectively. The $(TiO_2)_{35}$ NP is included in a $20 \times 20 \times 40$ Å supercell to give a vacuum gap of 11 Å in the *x*- and *y*-directions and 20 Å in the *z*-direction. Γ-point sampling is used and the convergence criteria for the energy and forces are 10^{-4} eV and 0.02 eV/ $Å^{-2}$, respectively.

On the other hand, the calculations carried out by the FHI-aims code include all electrons (AEs) and account for relativistic effects through the so-called zero-order regular approximation (ZORA)[62-63] proposed earlier by Chang *et al.*.[64] A tier-1 light grid numerical atom-centered orbital (NAO) basis set has been used, with a quality comparable to that of a triple-zeta valence polarised (TZVP) Gaussian Type Orbital basis set for TiO_2.[Error! Bookmark not defined.] Here, for the implementation of the Hubbard U correction, the projection functions for Ti_{3d} states are introduced as an explicit linear combination of the NAO basis functions with the double-counting correction in the fully localised limit (FLL); see details in ref. **Error! Bookmark not defined.**. The convergence threshold for the energy is 10^{-4} eV. Note that, hereinafter, the notation of PW and NAO is used to refer to the calculations performed with VASP and FHI-aims, respectively.

8.3 Results

To provide a sound reference for the study, we first discuss the energy gap of fully relaxed anatase and rutile bulk phases as predicted from spin polarised DFT calculations with the PW91 GGA type density functional and using either PW or NAO basis sets. To avoid problems arising from a difference in the quality of the basis sets we increase the kinetic energy cutoff for the PW to 550 eV and used a more extended NAO basis set of tier-2 tight quality. For rutile, the PW/NAO calculated band gap is 1.94/1.91 eV whereas for anatase the PW/NAO calculated band gap amounts to 2.25/2.10 eV. The difference in the anatase phase must be attributed to small differences in the optimised structure arising from the different treatment of the core electrons. In any case, the PW and NAO calculations for bulk rutile and anatase lead essentially to the same results with a deviation

of at most 0.15 eV in the band gap. Clearly, these calculated energy gaps are underestimated with respect to the experimental values, which are 3.0 and 3.2 eV, for rutile and anatase phases, respectively.[65-67] Hybrid functionals with an *ad-hoc* amount of non-local Fock exchange are known to provide a better estimate, as discussed for instance by Ko *et al.*.[68] In this paper, based on calculations performed with FHI-aims, the authors tuned the percentage of Fock exchange in the PBE0 hybrid functional to reproduce the experimental band gap of bulk rutile and anatase TiO_2. With 12.5% of Fock exchange, denoted PBEx, the bandgap of anatase was computed as 3.22 eV. A similar computational setup in VASP yields a value of 3.21 eV for the bulk anatase energy gap. While DFT+U can also be tuned to recover the experimental band gap, this is usually at the cost of a poorer description of other materials properties.

Next we focus on the representative $(TiO_2)_{35}$ anatase NP, depicted in **Figure 8.1**. The atomic structure of this NP has been obtained from a geometry optimisation using both VASP and FHI-aims computational packages and PW91+U. However, to perform a rigorous comparison of the effect of U when using PW or NAO basis sets, we consider four different situations, which are as follows:

(i) The structure is optimised in FHI-aims with PW91 (U=0) and single-point calculations are run with both FHI-aims and VASP at each U value, *U*=0-10 eV;

(ii) The structure is optimised in VASP with PW91 (U=0) and single-point calculations are run with both FHI-aims and VASP at each U value, *U*=0-10 eV;

(iii) The structure is fully optimised in both FHI-aims and VASP at each *U*=0-10 eV.

(iv) Each structure obtained by FHI-aims (VASP) in *(iii)* is submitted to a single point calculation in VASP (FHI-aims) at the same *U*-value.

The first and second sets of calculations allow one to investigate differences in the description of the electronic structure that are not due to a difference in the atomic structure, but to the different type of basis set and the implementation of the +U term.[Error! Bookmark not defined.] The third set of calculations provides information about differences in the final optimised structure, and the effect of this optimisation on the energy gap. Finally, the fourth set of calculations shows to what extent the fully relaxed atomic structure impacts on the electronic structure. In each of these data sets we can compare the results of the different set-ups by a linear fit of the data.

8.3.1 Structural analysis

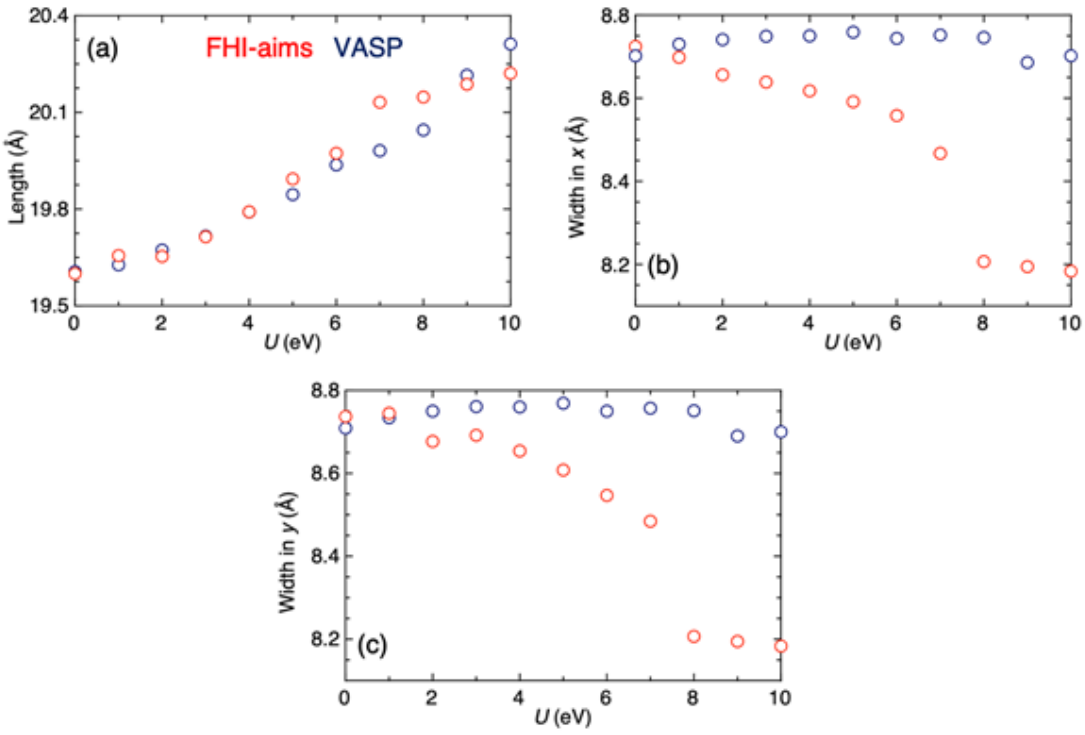

Figure 8.2 Evolution of the dimensionality of the stoichiometric $(TiO_2)_{35}$ anatase NP based on **(a)** length, **(b)** width in x and **(c)** width in y as a function of the U parameter for fully optimised structures by using VASP (blue dots) and FHI-aims (red dots) codes.

We start the discussion by analysing the structural properties of the $(TiO_2)_{35}$ NP, focusing mainly on its length and width (**Figure 8.2**). The PW91 (U=0) fully optimised structures of the $(TiO_2)_{35}$ NP predicted by VASP and FHI-aims are almost the same. In both cases, the nanoparticle length, which is taken from the terminal atoms located in the apical region (see **Figure 8.1**), is 19.61 Å. For the width of the NP, FHI-aims predicts a width that is 0.02 Å larger than VASP. Hence, in the absence of U, both types of basis set lead to the same structure, as expected.[17]

Therefore, any difference in the PW91+U structure predicted by the two types of basis sets (codes) has to be attributed to differences in the implementation of U. Regarding the atomic structure, the main effect of U is to slightly increase the nanoparticle length (**Figure 8.2.a**). The tendency is consistent, regardless of the basis set, up to U = 5 eV. When U is larger than 5 eV, the lengths predicted by VASP and FHI-aims follow different trends.

The analysis of the nanoparticle width presents some interesting features (**Figures 8.2.b** and **8.2.c**). Here, the effect of U is different depending on whether the calculation is carried out with a PW or NAO basis set. When using NAO, the optimised NP width decreases almost linearly with increasing U up to U = 7 eV, whereas when using PW, the dependence with U is very small, almost negligible. We note that, when using PW, the trends are very stable along the interval of U. However, this is not the case when the NAO basis set is employed, and the regular trend is broken at U = 7 eV. Note also that the breaking of the trend at U > 7 eV for the NAO calculations indicates that this value is too large to correctly describe correlation effects, as it has an exceedingly large influence on the properties of the nanoparticle and induces structural discontinuities. Similar observations on the effect of U on the phase stability of TiO_2 have been reported.[33] It is assumed that the large effect of U on the atomic structure predicted by the calculations

using the NAO basis set arise from the more localised character of the atomic NAO Hubbard projectors as implemented in FHI-aims.[41]

8.3.2 Energy Gap Analysis

The analysis of the energy gap of the $(TiO_2)_{35}$ anatase NP provides further interesting comparisons. The Kohn-Sham energy gaps, computed in the set-ups described in scenarios *(i)* and *(ii)*, above, are shown in **Figure 8.3** and **Table 8.1**. This data corresponds to two structures, each optimised with the respective codes, FHI-aims and VASP, at the PW91 (U=0) level. We begin by comparing the results of the single-point PW calculations performed on the FHI-aims (green) and VASP (blue) relaxed structures. At each *U*-value, the difference in computed energy gap between the two structures is negligible; in this case, the PW basis set implementation of +U is not sensitive to the geometry at which the electronic structure is computed.

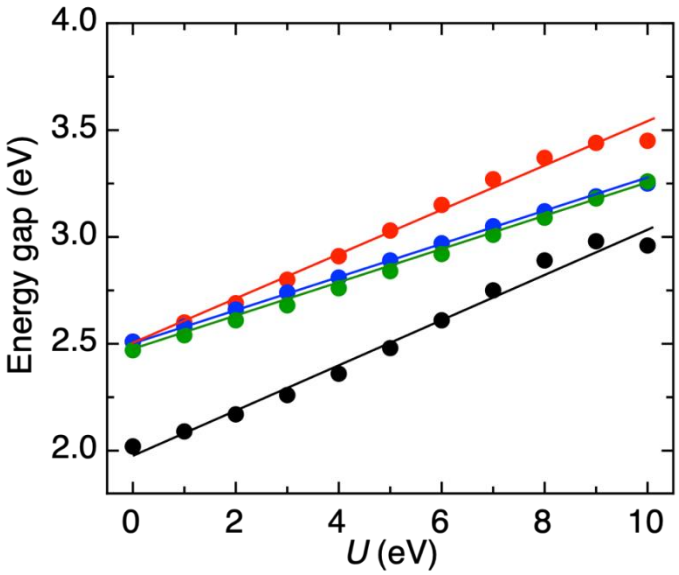

Figure 8.3 Variation of the energy gap with the parameter of U. The energy gap trends of *(i)* optimised $(TiO_2)_{35}$ anatase NP with FHI-aims code at U = 0 eV are calculated by performing single point calculations with FHI-aims code (red) and VASP (green) and *(ii)* optimised structure with VASP code at U = 0 eV by using single point calculations with

FHI-aims (black) and VASP (blue). Details of the linear fit ($E_{gap} = aU + b$) data for each trendline are listed in **Table 8.1**.

This result contrasts with the NAO data: for each *U*-value, NAO calculations predict a larger energy gap for the FHI-aims structure, relative to the VASP structure. The energy gaps computed from single point NAO calculations over the FHI-aims relaxed structure (red) are positively offset by ~0.5 eV with respect to those values computed over the VASP relaxed structure (black).

Table 8.1 Linear fit ($E_{gap} = aU + b$) data for *(i)* optimised $(TiO_2)_{35}$ anatase NP with FHI-aims code at U = 0 eV are calculated by performing single point calculations with FHI-aims code (red) and VASP (green) and *(ii)* optimised structure with VASP code at U = 0 eV by using single point calculations with FHI-aims (black) and VASP (blue) shown in **Figure 8.3**.

	Plot Legend		**Trendline**		
	Structure	Single-point	*a*	*b* (eV)	R^2
Red	FHI-aims (U=0)	FHI-aims (each *U*)	0.103	2.510	0.989
Green	FHI-aims (U=0)	VASP (each *U*)	0.075	2.510	0.999
Black	VASP (U=0)	FHI-aims (each *U*)	0.106	1.980	0.984
Blue	VASP (U=0)	VASP (each *U*)	0.080	2.450	0.998

The change in the energy gap with increasing U is consistent, regardless of the atomic structure, as revealed by the slopes (*a*-values) of the red and black trendlines, presented in **Table 8.1**; i.e. the 0.5 eV offset is maintained over the range of *U*-values. This result is interesting because, as discussed, both FHI-aims and VASP predict similar structures, *vis* length and width, at the PW91 (U=0) level. However, small differences in the atomic structures yield appreciable differences in the energy gaps computed with the NAO basis set, while no differences were shown with the PW basis set. This highlights that, to avoid misunderstanding interpretations in the analysis of the electronic properties, structural

relaxation is crucial when using the NAO basis set. It appears that the impact of U is greater with NAO, related to the localised projector functions.[41]

It is also interesting to compare NAO and PW results when these calculations are performed on the same starting structure. For the FHI-aims relaxed structure, the energy gaps predicted by NAO (red) and PW (green) calculations are in agreement for small *U*-values, but the differences in the predicted gaps increase with increasing U. This is reflected in the slopes (*a*-values) of the trendlines fitted to the NAO (red) and PW (green) data, which are 0.103 and 0.075, respectively (see **Table 8.1**). In this case, the energy gap varies to a greater extent in the NAO calculations, which consistently predict larger gaps with respect to the PW calculations. Conversely, for the VASP relaxed structure, the energy gaps predicted by NAO (black) and PW (blue) differ over the entire range of considered *U*-values. For U = 0 eV, the PW-computed energy gap is larger than that computed with NAO by ~0.5 eV, but this difference decreases with increasing U, in accordance with the larger slope for the NAO data (0.106), with respect to that of the PW data (0.080). These results suggest that the differences observed in the computed Kohn-Sham energy gaps are not attributable to differences in the atomic structure, but rather to differences in the implementation of DFT+U for the NAO or PW basis set.

Finally, we note that each of the computational set-ups, with the exception of NAO calculations on the VASP relaxed structure (black), predict similar energy gaps of ~2.5 eV for U = 0 eV. For these three set-ups, the differences in the computed energy gaps are reasonable, i.e. within 0.15 eV, for *U*-values up to 4 eV. For U > 4 eV, the NAO basis set promotes a larger energy gap with respect to the PW basis set.

The data obtained from the calculations described in scenarios *(iii)* and *(iv)*, above, are presented in **Figure 8.4** and **Table 8.2**. We first look at the computed energy gaps for the

structures optimised at each *U*-value in FHI-aims (red) and VASP (blue). The energy gaps computed with the NAO basis set increase from 2.5 eV to 3.8 eV as U increases from 0 eV to 10 eV. This monotonic increase with U is expected and is corroborated in the trendline data, shown in **Table 8.2**.

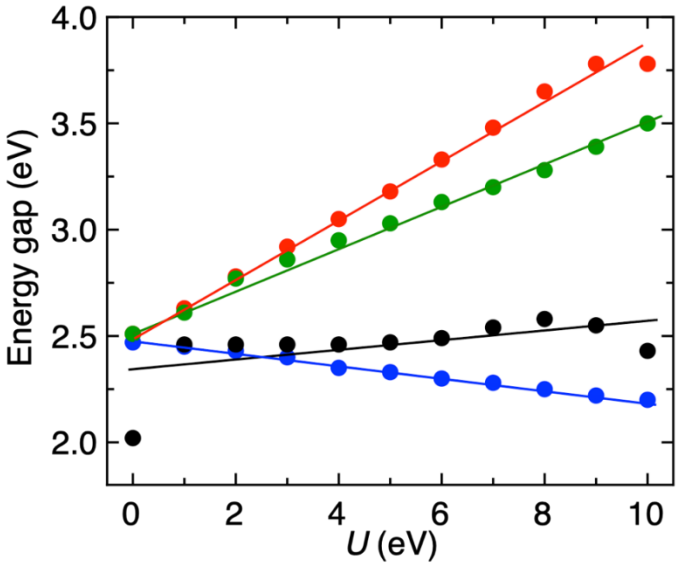

Figure 8.4 Variation of the energy gap with the parameter of U for: (scenario *(iii)*) the fully optimised $(TiO_2)_{35}$ anatase NP with the FHI-aims code (red) and VASP code (blue) and (scenario *(iv)*) single-point calculations in VASP (green) on the FHI-aims relaxed structure for each U and single-point calculations in FHI-aims (black) on the VASP-relaxed structure at each U. Details of the linear fit ($E_{gap} = aU + b$) data for each trend-line are listed in **Table 8.2**.

Interestingly, the opposite trend is observed for the energy gaps computed for the structures that were fully relaxed at each U with the PW basis set: in this case, the energy gaps decrease monotonically with increasing U. As seen in our discussion of **Figure 8.3**, increasing the *U*-value in a PW calculation on a fixed structure yields a larger energy gap. Thus, here we must attribute the decrease in the energy gaps to effects arising from the structural optimisation at each U. This result is surprising, not only because it is unexpected, but also because the changes in the PW-computed atomic structures over the

range of *U*-values are modest (see **Figure 8.2**), yet the impact on the electronic structure is significant, with states in the gap attributed to the presence of the low coordinated O atoms (see **Figure 8.5**). In fact, for the VASP-relaxed PW91 (U=0) structure, a single-point PW calculation with U = 4 eV yields an energy gap of 2.76 eV whereas for the fully relaxed structure at U = 4 eV, the energy gap is 2.35 eV. In other words, the emergence of the gap states occurs at lower U values in the PW calculations. This is clearly seen in the results in **Figure 8.5**, corresponding to the VASP and FHI-aims calculations for U = 2 and 6 eV, respectively.

Table 8.2 Linear fit ($E_{gap} = aU + b$) data for *(iii)* the fully optimised $(TiO_2)_{35}$ anatase NP with the FHI-aims code (red) and VASP code (blue) and *(iv)* single-point calculations in VASP (green) on the FHI-aims relaxed structure for each U and single-point calculations in FHI-aims (black) on the VASP-relaxed structure at each U shown in **Figure 8.4**.

	Plot Legend		**Trendline**		
	Structure	Single-point	*a*	*b* (eV)	R^2
Red	FHI-aims (each *U*)	-	0.136	2.520	0.993
Green	FHI-aims (each *U*)	VASP (each *U*)	0.095	2.550	0.994
Black	VASP (each *U*)	FHI-aims (each *U*)	0.027	2.310	0.358
Blue	VASP (each *U*)	-	-0.028	2.450	0.994

Performing a single-point PW calculation on the FHI-aims relaxed structures at each *U*-value produces the energy gaps represented with the green data points in **Figure 8.4**. Here we see that the data points agree with those computed with the NAO basis set (red) within 0.1 eV, up to U = 4 eV, after which the differences increase. This is in agreement with the trendline data listed in **Table 8.2**; the slopes for the NAO (red) and PW (green) basis sets are 0.136 and 0.095, respectively. Importantly, single-point PW calculations on the FHI-aims relaxed structures, at each U, predict an increase in energy gap with increasing

U. This further confirms that the decreasing trend in energy gaps for the VASP-relaxed structures arises from structural effects.

The energy gaps computed with single-point NAO calculations on the VASP-relaxed structures, at each U, are shown with the black data points in **Figure 8.4**. An outlier in this data is the energy gap computed for U = 0 eV, which is 2.02 eV. This value has been checked and the presence of an error in the calculation can be ruled out. Note, in addition, that the main effect of this calculation comes from the structural relaxation performed with VASP. Interestingly, for U = 1-10 eV, the computed energy gaps are consistently ~2.5-2.6 eV and this data shows no discernible increasing or decreasing trend. Unlike the case of U = 0 eV, the structural effect induced by a previous relaxation with VASP is coupled to the U implementation as implemented in FHI-aims. As seen in our discussion of single-point NAO calculations on both the FHI-aims and VASP PW91 (U=0) relaxed structures, the predicted energy gaps increase monotonically with increasing U. Once again, this suggests that subtleties in the structural optimisation within the PW implementation of DFT+U, probably linked to the low coordinated O atoms at the NP edge, produce these effects in the electronic structure.

For the NAO calculations, consistent with the linear trends for the red data reported in the legends of **Figure**s **8.3** and **8.4**, the relaxation at each U value has a negligible effect, as expected, on the fitting offset with respect to the calculation at the PW91 (U=0) structure. However, the fully relaxed calculations result in changes in the fitting slope. Thus, the opening of the energy gap is more pronounced for the fully optimised structures when employing the NAO basis.

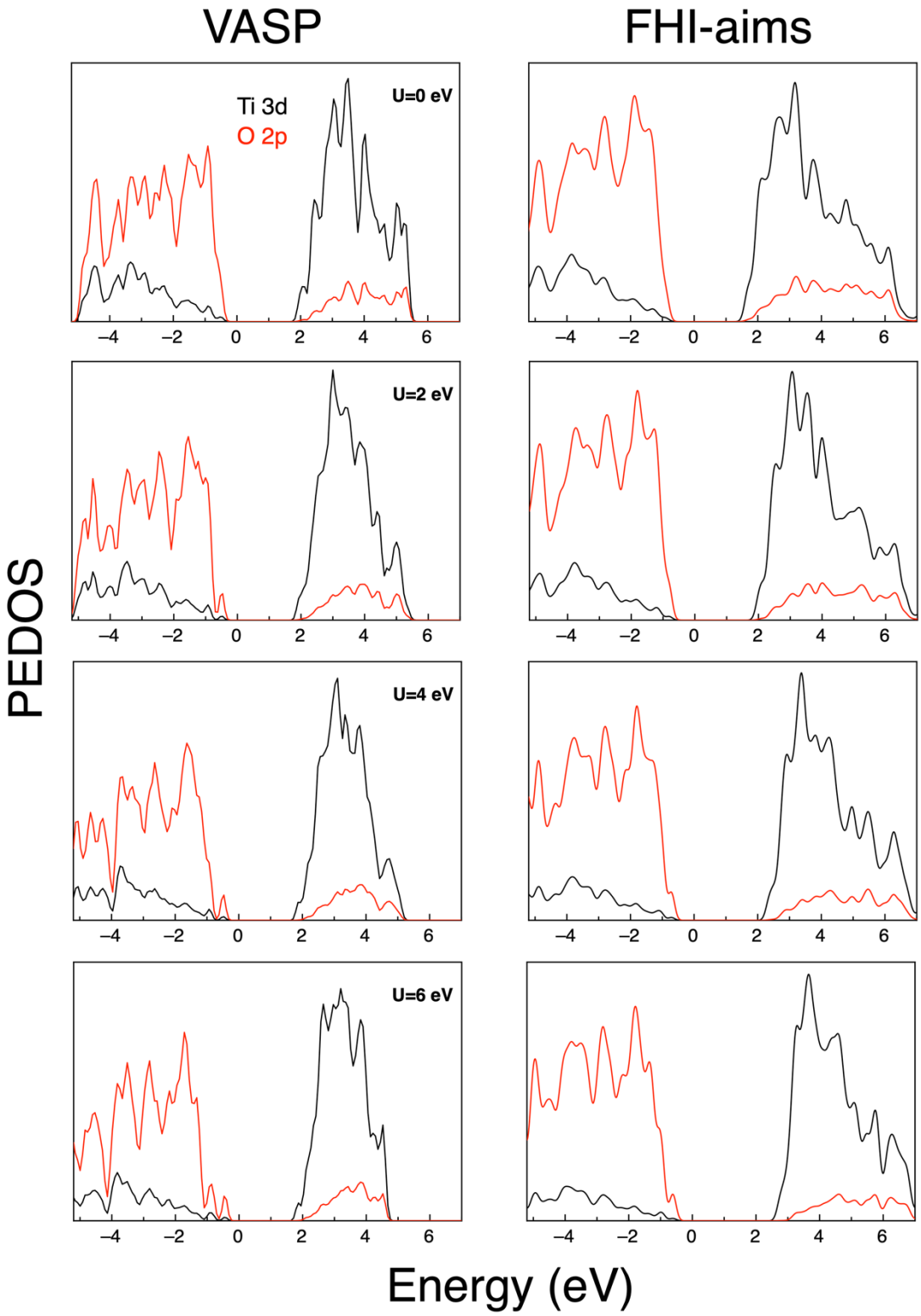

Figure 8.5 Projected electronic density of states (PEDOS) of the full relaxed $(TiO_2)_{35}$ NP using PW and NAO basis sets for *U*=0, 2, 4, and 6 eV.

This latter situation, where the NP structure is fully relaxed at each U in each code, is the most reasonable scenario to analyse the different behaviour observed between basis sets because artefacts due to the use of a structure not optimised within the method/basis set are ruled out. First of all, the energy gaps between the PW and NAO basis set are shifted by 0.25 eV (see **Figure 8.3**), which can be attributed to a different treatment of the effect of the core electrons and also relativistic effects.[69-70] The former are included explicitly in the calculations with the NAO basis set, whereas they are included through a frozen orbital type approach through the PAW in the calculations with the PW basis. Similarly, the relativistic effects are included explicitly at the ZORA level with the NOA basis and implicitly through the PAW description of the core electrons in the PW calculations. In principle, the most accurate results are obtained from the all-electron basis set implemented in FHI-aims. The most relevant results are found in the variation of the energy gap in response to increasing U. These are depicted in **Figure 8.4** and the trends (**Table 8.2**) are reflected in the linear fittings, with slopes of 0.136 and -0.028 for NAO and PW basis set, respectively. This result clearly shows the effect of U on the resulting energy gap does not only depend on the numerical value of this parameter but also on the projection of the Kohn-Sham states to determine the occupation numbers that enter the +U correction and the structural optimisation, which, in turn, depend on the basis set used. Thus, the +U part of the exchange-correlation potential severely depends on the DFT code, as already shown by Kick *et al.* for some systems.[Error! Bookmark not defined.]

To clarify this issue, we comment on how results from the PW91+U approaches used in the present work can compare to those corresponding to synthetised bipyramidal TiO_2 NPs containing almost 90% of (101) facets that morphologically match quite well with the $(TiO_2)_{35}$ NP model depicted in **Figure 8.1**. UV-Vis diffuse reflectance spectroscopy reported an energy gap of ca. 3.2 eV.[71] To reproduce this result using PW91+U requires

a U value between 4 and 5 eV for the NAO basis set. No *U*-value can reproduce this energy gap for the optimised structures with a PW basis set; however, U = 8-9 eV, implemented with a single-point PW calculation on the PW91 (U=0) structure does reproduce the experiments. Therefore, the DFT+U implementation in FHI-aims entails much lower values of U to reproduce results obtained with other codes such as VASP. This is attributed to the strongly localised character of the atomic NAO Hubbard projectors. In short, to achieve a given band gap, the value of U that is required is much lower with the NAO basis set compared to the PW basis set. In addition, we compare the experiments[Error! Bookmark not defined.] with the hybrid PBEx (12.5 % Fock exchange) density functional on the $(TiO_2)_{35}$ NP. FHI-aims and VASP yields energy gaps of 3.81[Error! Bookmark not defined.] and 3.71 eV, respectively. Not surprisingly, these values exceed the experimental evidences due to the quantum confinement effect.[Error! Bookmark not defined.]

Finally, to confirm that the present findings are not specific to the $(TiO_2)_{35}$ nanoparticle, we consider the anatase bulk phase and explore the transferability of U for calculations with PAW or NAO basis for a particular geometry. Hence, structural optimisations of the anatase bulk phase were first performed by using PW basis set and an energy gap of 3.17 eV, close to the experimental value, was achieved for U = 8 eV. Next, this structure was considered in NAO single point calculations to determine the U value that reproduces the energy gap and this was U = 6.5 eV. This confirms that the U value fitted to reproduce an experimental or hybrid functional calculated value using a given DFT code cannot be transferred to another code as it depends on the basis set used and on the method employed to define the corresponding projectors. Thus, for each materials system and DFT code, one should recompute suitable values for U through making initial benchmarks.

8.4 Conclusions

The effect of the DFT+U method on the structural and electronic properties of the $(TiO_2)_{35}$ NP is systematically investigated by two different basis sets, namely, plane-waves (PWs) and numerical atomic orbitals (NAOs), along with different approaches for the implementation of +U value. In the absence of U, PW and NAO calculations report the same structure and, consequently, the structural variations observed by its inclusion are due to the different implementation of U based on a simplified rotationally invariant approach and a linear combination of the NAO basis functions, respectively. Interestingly, the analysis of the energy gap reveals that a certain U value can reproduce the experimental value, however, it depends on the basis set and on the employed U parameter. Therefore, the transfer of U values between codes is not to be recommended and requires initial benchmarks for the property of interest as a reference to find the appropriate value. This study clearly shows that the DFT+U implementation in a localised basis set code such as FHI-aims entails much lower values of U to reproduce results obtained with a plane wave basis set code such as VASP.

8.5 Chapter References

1. Morales-García, Á.; Rhatigan, S.; Nolan, M.; Illas, F., On the use of DFT+U to describe the electronic structure of TiO_2 nanoparticles: $(TiO_2)_{35}$ as a case study. *The Journal of Chemical Physics* **2020,** *152* (24), 244107.
2. Ohno, T.; Sarukawa, K.; Tokieda, K.; Matsumura, M., Morphology of a TiO_2 Photocatalyst (Degussa, P-25) Consisting of Anatase and Rutile Crystalline Phases. *Journal of Catalysis* **2001,** *203* (1), 82-86.
3. Fujishima, A.; Rao, T. N.; Tryk, D. A., Titanium dioxide photocatalysis. *Journal of Photochemistry and Photobiology C: Photochemistry Reviews* **2000,** *1* (1), 1-21.
4. Fujishima, A.; Rao, T. N.; Tryk, D. A., TiO_2 photocatalysts and diamond electrodes. *Electrochimica Acta* **2000,** *45* (28), 4683-4690.
5. Hashimoto, K.; Irie, H.; Fujishima, A., TiO_2 Photocatalysis: A Historical Overview and Future Prospects. *Japanese Journal of Applied Physics* **2005,** *44* (12), 8269-8285.
6. Gao, M.; Zhu, L.; Ong, W. L.; Wang, J.; Ho, G. W., Structural design of TiO_2-based photocatalyst for H_2 production and degradation applications. *Catalysis Science & Technology* **2015,** *5* (10), 4703-4726.
7. Naldoni, A.; Altomare, M.; Zoppellaro, G.; Liu, N.; Kment, Š.; Zbořil, R.; Schmuki, P., Photocatalysis with Reduced TiO_2: From Black TiO_2 to Cocatalyst-Free Hydrogen Production. *ACS Catalysis* **2019,** *9* (1), 345-364.
8. Cho, D.; Ko, K. C.; Lamiel-García, O.; Bromley, S. T.; Lee, J. Y.; Illas, F., Effect of Size and Structure on the Ground-State and Excited-State Electronic Structure of TiO_2 Nanoparticles. *Journal of Chemical Theory and Computation* **2016,** *12* (8), 3751-3763.
9. Chen, X.; Liu, L.; Yu, P. Y.; Mao, S. S., Increasing Solar Absorption for Photocatalysis with Black Hydrogenated Titanium Dioxide Nanocrystals. *Science* **2011,** *331* (6018), 746-750.
10. Chen, X.; Li, C.; Grätzel, M.; Kostecki, R.; Mao, S. S., Nanomaterials for renewable energy production and storage. *Chemical Society Reviews* **2012,** *41* (23), 7909-7937.
11. Chen, X.; Mao, S. S., Titanium Dioxide Nanomaterials: Synthesis, Properties, Modifications, and Applications. *Chemical Reviews* **2007,** *107* (7), 2891-2959.
12. Selli, D.; Fazio, G.; Di Valentin, C., Using Density Functional Theory to Model Realistic TiO_2 Nanoparticles, Their Photoactivation and Interaction with Water. *Catalysts* **2017,** *7*.
13. Morales-García, Á.; Macià Escatllar, A.; Illas, F.; Bromley, S. T., Understanding the interplay between size, morphology and energy gap in photoactive TiO_2 nanoparticles. *Nanoscale* **2019,** *11* (18), 9032-9041.
14. Clot, E., Synergy between experiment and theory. *Dalton Transactions* **2014,** *43* (29), 11092-11092.
15. Kohn, W.; Sham, L. J., Self-Consistent Equations Including Exchange and Correlation Effects. *Physical Review* **1965,** *140* (4A), A1133-A1138.
16. Hohenberg, P.; Kohn, W., Inhomogeneous Electron Gas. *Physical Review* **1964,** *136* (3B), B864-B871.
17. Burke, K., Perspective on density functional theory. *The Journal of Chemical Physics* **2012,** *136* (15), 150901.
18. Lejaeghere, K.; Bihlmayer, G.; Björkman, T.; Blaha, P.; Blügel, S.; Blum, V.; Caliste, D.; Castelli, I. E.; Clark, S. J.; Dal Corso, A.; de Gironcoli, S.; Deutsch, T.;

Dewhurst, J. K.; Di Marco, I.; Draxl, C.; Dułak, M.; Eriksson, O.; Flores-Livas, J. A.; Garrity, K. F.; Genovese, L.; Giannozzi, P.; Giantomassi, M.; Goedecker, S.; Gonze, X.; Grånäs, O.; Gross, E. K. U.; Gulans, A.; Gygi, F.; Hamann, D. R.; Hasnip, P. J.; Holzwarth, N. A. W.; Iuşan, D.; Jochym, D. B.; Jollet, F.; Jones, D.; Kresse, G.; Koepernik, K.; Küçükbenli, E.; Kvashnin, Y. O.; Locht, I. L. M.; Lubeck, S.; Marsman, M.; Marzari, N.; Nitzsche, U.; Nordström, L.; Ozaki, T.; Paulatto, L.; Pickard, C. J.; Poelmans, W.; Probert, M. I. J.; Refson, K.; Richter, M.; Rignanese, G.-M.; Saha, S.; Scheffler, M.; Schlipf, M.; Schwarz, K.; Sharma, S.; Tavazza, F.; Thunström, P.; Tkatchenko, A.; Torrent, M.; Vanderbilt, D.; van Setten, M. J.; Van Speybroeck, V.; Wills, J. M.; Yates, J. R.; Zhang, G.-X.; Cottenier, S., Reproducibility in density functional theory calculations of solids. *Science* **2016,** *351* (6280), aad3000.

19. de P. R. Moreira, I.; Illas, F.; Martin, R. L., Effect of Fock exchange on the electronic structure and magnetic coupling in NiO. *Physical Review B* **2002,** *65* (15), 155102.

20. Wang, C. S.; Pickett, W. E., Density-Functional Theory of Excitation Spectra of Semiconductors: Application to Si. *Physical Review Letters* **1983,** *51* (7), 597-600.

21. Sham, L. J.; Schlüter, M., Density-Functional Theory of the Energy Gap. *Physical Review Letters* **1983,** *51* (20), 1888-1891.

22. Mori-Sánchez, P.; Cohen, A. J., The derivative discontinuity of the exchange–correlation functional. *Physical Chemistry Chemical Physics* **2014,** *16* (28), 14378-14387.

23. Mori-Sánchez, P.; Cohen, A. J.; Yang, W., Localization and Delocalization Errors in Density Functional Theory and Implications for Band-Gap Prediction. *Physical Review Letters* **2008,** *100* (14), 146401.

24. Becke, A. D., Density-functional thermochemistry. III. The role of exact exchange. *The Journal of Chemical Physics* **1993,** *98* (7), 5648-5652.

25. Muscat, J.; Wander, A.; Harrison, N. M., On the prediction of band gaps from hybrid functional theory. *Chemical Physics Letters* **2001,** *342* (3), 397-401.

26. Hubbard, J., Electron correlations in narrow energy bands. *Proc. R. Soc. London, Ser. A* **1963,** *276*, 238.

27. Anisimov, V. I.; Zaanen, J.; Andersen, O. K., Band theory and Mott insulators: Hubbard U instead of Stoner I. *Physical Review B* **1991,** *44* (3), 943-954.

28. Dudarev, S. L.; Botton, G. A.; Savrasov, S. Y.; Humphreys, C. J.; Sutton, A. P., Electron-energy-loss spectra and the structural stability of nickel oxide: An LSDA+U study. *Physical Review B* **1998,** *57* (3), 1505-1509.

29. Portillo-Vélez, N. S.; Olvera-Neria, O.; Hernández-Pérez, I.; Rubio-Ponce, A., *Surf. Sci.* **2013,** *616*, 115.

30. Curnan, M. T.; Kitchin, J. R., Investigating the Energetic Ordering of Stable and Metastable TiO2 Polymorphs Using DFT+U and Hybrid Functionals. *J. Phys. Chem. C* **2015,** *119*, 21060.

31. Wang, L.; Maxich, T.; Ceder, G., *Phys. Rev. B* **2006,** *73*, 195107.

32. Cococcioni, M.; de Gironcoli, S., Linear response approach to the calculation of the effective interaction parameters in the LDA+U method. *Phys. Rev. B* **2005,** *71*, 035105.

33. Loschen, C.; Carrasco, J.; Neyman, K. M.; Illas, F., First-principles LDA+U and GGA+U study of cerium oxides: Dependence on the effective U parameter. *Physical Review B* **2007,** *75* (3), 035115.

34. Arroyo-de Dompablo, M. E.; Morales-García, A.; Taravillo, M., DFT+U calculations of crystal lattice, electronic structure, and phase stability under pressure of TiO_2 polymorphs. *J. Chem. Phys.* **2011,** *135*, 054503.

35. Hu, Z.; Metiu, H., Choice of U for DFT+U Calculations for Titanium Oxides. *J. Phys. Chem. C* **2011,** *115*, 5841.
36. Deskins, N. A.; Dupuis, M., Electron transport via polaron hopping in bulk TiO_2: A density functional theory characterization. *Phys. Rev. B* **2007,** *75*, 195212.
37. Persson, C.; Ferreira da Silva, A., Strong polaronic effects on rutile TiO_2 electronic band edges. *Applied Physics Letters* **2005,** *86* (23), 231912.
38. Finazzi, E.; Di Valentin, C.; Pacchioni, G.; Selloni, A., Excess electron states in reduced bulk anatase TiO2: Comparison of standard GGA, GGA+U, and hybrid DFT calculations. *J. Chem. Phys.* **2008,** *129*, 154113.
39. Morgan, B. J.; Watson, G. W., Intrinsic n-type Defect Formation in TiO_2: A Comparison of Rutile and Anatase from GGA+U Calculations. *The Journal of Physical Chemistry C* **2010,** *114* (5), 2321-2328.
40. Barcaro, G.; Thomas, I. O.; Fortunelli, A., Validation of density-functional versus density-functional+U approaches for oxide ultrathin films. *J. Chem. Phys.* **2010,** *132*, 124703.
41. Himmetoglu, B.; Floris, A.; de Gironcoli, S.; Cococcioni, M., Hubbard-corrected DFT energy functionals: The LDA+U description of correlated systems. *Int. J. Quantum Chem.* **2014,** *114*, 14.
42. Kick, M.; Reuter, K.; Oberhofer, H., Intricacies of DFT+U, Not Only in a Numeric Atom Centered Orbital Framework. *J. Chem. Theory Comput.* **2019,** *15*, 170.
43. Lamiel-Garcia, O.; Ko, K. C.; Lee, J. Y.; Bromley, S. T.; Illas, F., When Anatase Nanoparticles Become Bulklike: Properties of Realistic TiO_2 Nanoparticles in the 1–6 nm Size Range from All Electron Relativistic Density Functional Theory Based Calculations. *Journal of Chemical Theory and Computation* **2017,** *13* (4), 1785-1793.
44. Nam, Y.; Lim, J. H.; Ko, K. C.; Lee, J. Y., Photocatalytic activity of TiO_2 nanoparticles: a theoretical aspect. *Journal of Materials Chemistry A* **2019,** *7* (23), 13833-13859.
45. Nunzi, F.; Agrawal, S.; Selloni, A.; De Angelis, F., Structural and Electronic Properties of Photoexcited TiO_2 Nanoparticles from First Principles. *Journal of Chemical Theory and Computation* **2015,** *11* (2), 635-645.
46. Kim, S.; Ko, K. C.; Lee, J. Y.; Illas, F., Single oxygen vacancies of $(TiO_2)_{35}$ as a prototype reduced nanoparticle: implication for photocatalytic activity. *Physical Chemistry Chemical Physics* **2016,** *18* (34), 23755-23762.
47. Qu, Z.-w.; Kroes, G.-J., Theoretical Study of the Electronic Structure and Stability of Titanium Dioxide Clusters $(TiO_2)_n$ with n = 1−9. *The Journal of Physical Chemistry B* **2006,** *110* (18), 8998-9007.
48. Weng, M.-H.; Chen, C.; Ju, S.-P., A First-Principle Study on Size-Dependent Thermodynamic Properties of Small TiO_2 Nanoclusters. *Chinese Journal of Catalysis* **2009,** *30* (5), 384-390.
49. Morita, K.; Yasuoka, K., Density functional theory study of atomic and electronic properties of defects in reduced anatase TiO_2 nanocrystals. *AIP Advances* **2018,** *8* (3), 035119.
50. Morales-García, Á.; Valero, R.; Illas, F., Performance of the G0W0 Method in Predicting the Electronic Gap of TiO_2 Nanoparticles. *Journal of Chemical Theory and Computation* **2017,** *13* (8), 3746-3753.
51. Morales-García, Á.; Valero, R.; Illas, F., Electronic Properties of Realistic Anatase TiO_2 Nanoparticles from G0W0 Calculations on a Gaussian and Plane Waves Scheme. *Journal of Chemical Theory and Computation* **2019,** *15* (9), 5024-5030.

52. Valero, R.; Morales-García, Á.; Illas, F., Theoretical Modeling of Electronic Excitations of Gas-Phase and Solvated TiO_2 Nanoclusters and Nanoparticles of Interest in Photocatalysis. *Journal of Chemical Theory and Computation* **2018,** *14* (8), 4391-4404.
53. Morales-García, Á.; Valero, R.; Illas, F., Reliable and computationally affordable prediction of the energy gap of $(TiO_2)_n$ ($10 \leq n \leq 563$) nanoparticles from density functional theory. *Physical Chemistry Chemical Physics* **2018,** *20* (28), 18907-18911.
54. Wulff, G., XXV. Zur Frage der Geschwindigkeit des Wachsthums und der Auflösung der Krystallflächen. *Zeitschrift für Kristallographie - Crystalline Materials* **1901,** *34* (1), 449.
55. Pigeot-Rémy, S.; Dufour, F.; Herissan, A.; Ruaux, V.; Maugé, F.; Hazime, R.; Foronato, C.; Guillard, C.; Chaneac, C.; Durupthy, O.; Colbeau-Justin, C.; Cassaignon, S., Bipyramidal anatase TiO_2 nanoparticles, a highly efficient photocatalyst? Towards a better understanding of the reactivity. *Applied Catalysis B: Environmental* **2017,** *203*, 324-334.
56. Kresse, G.; Hafner, J., *Ab initio* molecular-dynamics simulation of the liquid-metal-amorphous-semiconductor transition in germanium. *Physical Review B* **1994,** *49* (20), 14251-14269.
57. Furthmüller, J.; Hafner, J.; Kresse, G., Dimer reconstruction and electronic surface states on clean and hydrogenated diamond (100) surfaces. *Physical Review B* **1996,** *53* (11), 7334-7351.
58. Blum, V.; Gehrke, R.; Hanke, F.; Havu, P.; Havu, V.; Ren, X.; Reuter, K.; Scheffler, M., Ab initio molecular simulations with numeric atom-centered orbitals. *Computer Physics Communications* **2009,** *180* (11), 2175-2196.
59. Perdew, J. P.; Burke, K.; Ernzerhof, M., Generalized gradient approximation made simple. *Physical Review Letters* **1996,** *77* (18), 3865-3868.
60. Blöchl, P. E., Projector augmented-wave method. *Physical Review B* **1994,** *50* (24), 17953-17979.
61. Kresse, G.; Joubert, D., From ultrasoft pseudopotentials to the projector augmented-wave method. *Physical Review B* **1999,** *59* (3), 1758-1775.
62. van Lenthe, E.; van Leeuwen, R.; Baerends, E. J.; Snijders, J. G., Relativistic regular two-component Hamiltonians. *International Journal of Quantum Chemistry* **1996,** *57* (3), 281-293.
63. Chan, M.; Ceder, G., Efficient band gap prediction for solids. *Physical review letters* **2010,** *105* (19), 196403.
64. Chang, C.; Pelissier, M.; Durand, P., Regular Two-Component Pauli-Like Effective Hamiltonians in Dirac Theory. *Phys. Scr.* **1986,** *34*, 394.
65. Amtout, A.; Leonelli, R., Optical properties of rutile near its fundamental band gap. *Phys. Rev. B* **1995,** *51*, 6842.
66. Kowalczyk, S. P.; McFeely, F. R.; Ley, L.; Gritsyna, V. T.; Shirley, D. A., The electronic structure of $SrTiO_3$ and some simple related oxides (MgO, Al_2O_3, SrO, TiO_2). *Solid State Commun.* **1977,** *23*, 161.
67. Scanlon, D. O.; Dunnill, C. W.; Buckeridge, J.; Shevlin, S. A.; Logsdail, A. J.; Woodley, S. M.; Catlow, C. R. A.; Powell, M. J.; Palgrave, R. G.; Parkin, I. P.; Watson, G. W.; Keal, T. W.; Sherwood, P.; Walsh, A.; Sokol, A. A., Band alignment of rutile and anatase TiO_2. *Nature Materials* **2013,** *12*, 798.
68. Ko, K. C.; Lamiel-García, O.; Lee, J. Y.; Illas, F., Performance of a modified hybrid functional in the simultaneous description of stoichiometric and reduced TiO_2 polymorphs. *Physical Chemistry Chemical Physics* **2016,** *18* (17), 12357-12367.
69. Bachelet, G. B.; Christensen, N. E., Relativistic and core-relaxation effects on the energy bands of gallium arsenide and germanium. *Phys. Rev. B* **1985,** *31*, 879.

70. Sadigh, B.; Kutepov, A.; Landa, A.; Söderlind, P., Assessing Relativistic Effects and Electron Correlation in the Actinide Metals Th to Pu. *Appl. Sci.* **2019,** *9*, 5020.
71. D'Arienzo, M.; Dozzi, M. V.; Redaelli, M.; Di Credico, B.; Morazzoni, F.; Scotti, R.; Polizzi, S., Crystal Surfaces and Fate of Photogenerated Defects in Shape-Controlled Anatase Nanocrystals: Drawing Useful Relations to Improve the H_2 Yield in Methanol Photosteam Reforming. *J. Phys. Chem. C* **2015,** *119*, 12385.

9 Outlook and Perspectives

9.1 Perspectives

The preceding chapters have explored the modification of TiO_2 *via* doping and surface modification strategies with a focus on their use for water splitting. Our studies focus on the material properties that are relevant to the photocatalytic activity. These properties include: light absorption, oxygen vacancy formation, photoexcited charge separation and localisation, and the interaction of feedstock species at active sites of the catalyst surface. Our approach is based on DFT calculations and involves the computation of material descriptors, which represent a set of key performance indicators and facilitate evaluation and comparison of candidate photocatalyst materials. In addition, we have collaborated with experimental colleagues on a number of these studies as this is crucial to establish a bidirectional means of refining and optimising computational models and materials preparation.

Chapter 4, detailed the results of combined experimental and computational studies of Cu-, Mo-, and In-doped TiO_2. Doping is perhaps the most widely studied approach to altering the material properties of TiO_2 and is often implemented as a means to modulate the light absorption properties of the titania host and induce visible light absorption. While dopant-derived states can promote absorption of longer wavelengths of light, this does not always correlate with enhanced photocatalytic activity as these mid-gap states can act as charge recombination centres. Indeed, while Cu-doping yielded a small red shift in light absorption, it had a detrimental effect on the photocatalytic activity, as Cu^{1+}/Cu^{2+}-derived defect states acted as traps for photoexcited charges.

Our experimental collaborators paid particular attention to the impact of doping on the anatase-to-rutile phase transition (ART) temperature. Preserving the more photocatalytically active anatase phase under high temperature conditions is an important industrial concern. The results of **Chapter 4** showed that the ART was suppressed and the anatase content of the doped samples was retained at temperatures up to 650, 750 and 800 °C for Cu-, Mo-, and In-doped TiO_2, respectively. As oxygen vacancies are implicated in the ART, our computational models included an examination of the impact of doping on the formation of oxygen vacancies. For both Cu and In dopants in TiO_2, oxygen vacancies form spontaneously as the mechanism to ensure charge balance after substitution of Ti with the lower-valent dopants. The reducing oxygen vacancies also had moderate formation energies, relative to undoped TiO_2. For Mo-doped TiO_2, the vacancy formation energies were comparable to those computed for the un-doped system. Thus, the role of the dopants in the ART cannot be elucidated simply by the thermodynamics of oxygen vacancy formation and more complex models, involving kinetics and beyond the scope of this thesis, would be required.

Mo-doped TiO_2, calcined at 750 °C and with mixed rutile and anatase phases, performed better in the removal of bacteria from wastewater than un-doped anatase TiO_2. In-doped TiO_2, with 2% In, calcined at 700 °C and with mixed rutile and anatase phases, exhibited a photocatalytic activity comparable to that of un-modified anatase. Mo- and In-doping can be considered as approaches to preserve the anatase content of TiO_2 at higher preparation temperatures, while maintaining or enhancing the photocatalytic activity. Thus, Mo and In are effective dopants for the fabrication of thermally stable anatase TiO_2 with photocatalytic activity.

In **Chapters 5**, **6**, and **7** we examined the photocatalytic properties of titania surfaces modified with nanoclusters of other materials. It is clear from these studies that surface

modification is a viable strategy to impart properties important for photocatalytic applications. By rational selection of materials, and with control over the size and dispersion of the modifiers, these properties can include a red shift in light absorption, promotion of charge separation and enhanced reducibility, leading to a higher abundance of active oxygen vacancy sites. We considered metal oxide and metal chalcogenide modification for the promotion of the OER and HER, respectively.

Metal oxide modifiers, which are reducible with moderate energy costs, provide low coordinated ions, oxygen vacancies, reduced cations and interfacial sites with which feedstock species, such as H_2O, can interact. Metal chalcogenides have emerged as potential catalyst materials for the HER, with activities approaching that of the benchmark Pt catalyst. Interfacing nanoclustered chalcogenides with TiO_2 can combine the desirable properties of titania with intrinsically active sites for HER.

The computational approaches applied in this thesis, which are based on calculations of material descriptors, can be implemented as a means to assess the candidacy of novel photocatalytic materials. Moreover, these models can be built upon, through complementary computational approaches and machine learning techniques, as will be discussed in **Section 9.3**.

9.2 Outlook

9.2.1 OER catalysts

In **Chapters 5** and **6**, we examined titania surfaces modified with nanoclusters of CeO_2 and MnO_x and analysis included the adsorption of water molecules at the reduced composite surfaces. CeO_2-modified rutile (110) exhibited an off-stoichiometric ground

state and moderate energy costs to produce reducing oxygen vacancies. As a result, oxygen vacancies and reduced Ce^{3+} ions will likely be present under photocatalytic operating conditions. In this study, we examined water adsorption at cluster sites of the reduced CeO_x-TiO_2 composite surfaces, which was favourable and led to spontaneous dissociation to hydroxyls.

Subsequent work on CeO_x-modified TiO_2 as part of the H2020 M-ERA.net project RATOCAT has investigated, *via* computation and experiment, the mechanism by which CeO_x can be deposited on titania surface using ALD.[1] Future work can assess the water oxidation activity of CeO_x-TiO_2 composites, which can be complemented by simulations. Further computational models can expand on the results presented in **Chapters 5** and **6** and investigate additional adsorption sites at the nanocluster-surface interface and compute the free energies of reaction steps in the water oxidation pathway.

MnO_x-modified TiO_2, with hydroxyls present on the surface, also exhibited an off-stoichiometric ground state with moderate energy inputs required to produce reducing oxygen vacancies. Thus, the oxygen vacancies and reduced Mn^{2+} and Ti^{3+} ions will be present at the MnO_x-TiO_2 catalyst surface. The water adsorption mode at MnO_x-TiO_2 depended on the stoichiometry: for the off-stoichiometric ground state surface, water adsorbed in molecular form, while water spontaneously dissociated at the reduced surfaces.

These computational results indicate that MnO_x-modification of TiO_2 surfaces is a promising strategy to develop an active OER catalyst. An experimental characterisation of MnO_x-modified TiO_2 would help to refine the computational models and OER activity measurements will confirm or refute our computational results. Ongoing computational work is investigating the water oxidation pathway at sites of MnO_x-modified anatase

(101) and rutile (110), both with and without surface hydroxylation. The MnO_x clusters modifying the hydroxylated titania surfaces were described in detail in **Chapter 5**; the oxidised surfaces, modified with MnO_x, are shown in **Figure 9.1**. The modified anatase surface has an off-stoichiometric ground state, with a single oxygen vacancy forming spontaneously, and a moderate energy input of +1.71 eV is required for formation of a second, reducing oxygen vacancy. Conversely, the modified rutile surface is stoichiometric in the ground state and a single, reducing oxygen vacancy requires an energy input of +0.50 eV.

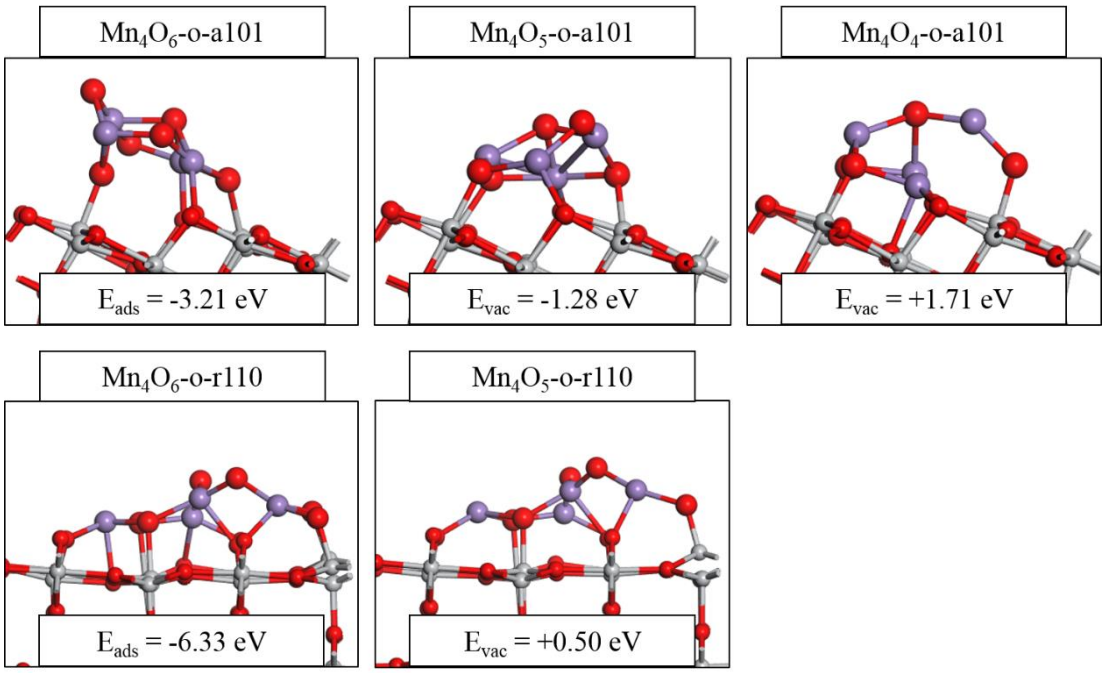

Figure 9.1 Top row: TiO_2 anatase (101) surface, modified with Mn_4O_6 for the stoichiometric case, the ground state with one oxygen vacancy, and the reduced state with two oxygen vacancies. Bottom row: TiO_2 rutile (110) surface, modified with Mn_4O_6 for the stoichiometric ground state and the reduced state with a single oxygen vacancy. The colour scheme is consistent with that in **Chapters 5** and **6.**

For both Mn_4O_6-o-a101 and Mn_4O_6-o-r110, each of the Mn ions are in the +3 oxidation state, as evidenced by computed Bader charges of 11.2-11.4 electrons and spin magnetisations of 3.7-3.9 μ_B. The computed spin magnetisations correspond to the $3d^4$

configuration of the Mn^{3+} ion. After formation of a single oxygen vacancy, two Mn ions are reduced to Mn^{2+}, in each case. This is confirmed by Bader charges of 11.5-11.6 electrons and spin magnetisations of 4.4-4.6 μ_B. Upon formation of the second, reducing oxygen vacancy, to produce Mn_4O_4-o-a101, each of the Mn ions are reduced to Mn^{2+}, with Bader charges of 11.6-11.7 electrons and spin magnetisations of 4.5-4.6 μ_B. This mix of oxidation states will have implications for the surface reactivity.

Some preliminary results for the water oxidation pathway at MnO_x-modified rutile (110) are included in **Table 9.1**. These results are for a single water molecule using models of the ground state and reduced state of MnO_x at the oxidised (o-r110) and hydroxylated (oh-r110) surfaces. This model, based on four proton-coupled electron transfer (PCET) steps, was described in **Chapter 2** and applied in **Chapter 6** for water oxidation at AEO-TiO_2. Similar analysis is ongoing for MnO_x-modified anatase (101) surfaces.

Table 9.1 Computed free energies of water oxidation steps for water adsorption at sites of MnO_x-modified O-r110 and OH-r110. GS = ground state; RS = reduced state.

Surface	**GS**	**RS**	**Surface**	**GS**	**RS**
O-r110	**Mn_4O_6**	**Mn_4O_5**	**OH-r110**	**Mn_4O_5**	**Mn_4O_4**
	ΔG (eV)	**ΔG (eV)**		**ΔG (eV)**	**ΔG (eV)**
Step A	1.1	0.85	**Step A**	1.06	0.12
Step B	2.12	1.95	**Step B**	1.94	0.70
Step C	1.56	1.07	**Step C**	0.92	1.58
Step D	0.13	1.05	**Step D**	0.99	2.53
Sum	4.92	4.92	**Sum**	4.92	4.92

For the ground state, Mn_4O_6-o-r110, and reduced state, Mn_4O_5-o-r110, the highest energy step is step B, which is dehydrogenation of a surface bound hydroxyl. The step requires energy inputs of 2.12 and 1.95 eV for the ground and reduced states, respectively. These values suggest that overpotentials of 0.89 and 0.72 V are required for the water oxidation reaction to proceed. Similarly, for the ground state of the modified, hydroxylated surface,

Mn_4O_5-oh-r110, step B is the highest energy step and requires an input of 1.94 eV, corresponding to an overpotential of 0.71 V. For the reduced state, Mn_4O_4-oh-r110, step D, which is the release of O_2 from the active site, is the rate-limiting step and has a computed free energy of 2.53 eV. This suggests that, for the MnO_x-modified, hydroxylated rutile surface, the interaction with water will result in the surface cycling between the ground state and reduced state. However, further calculations, involving additional water adsorptions and various adsorption sites, are required before predictions regarding the OER activity of MnO_x-TiO_2 can be made.

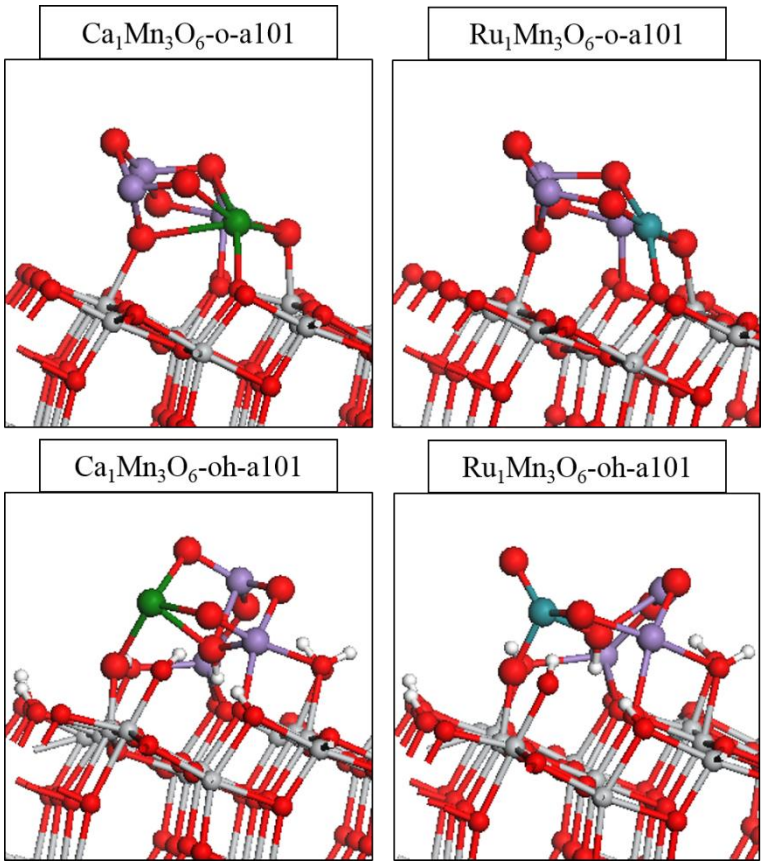

Figure 9.2 Relaxed atomic structure of $CaMn_3O_6$ and $RuMn_3O_6$ modifying the oxidised (top row) and hydroxylated (bottom row) anatase (101) surfaces. Ca is represented by a green sphere and Ru by a blue sphere.

We have also adapted models of MnO_x-TiO_2 to include calcium (Ca) and ruthenium (Ru) ions. In these models, the oxidised and hydroxylated titania surfaces are modified with

nanoclusters of compositions $CaMn_3O_6$ and $RuMn_3O_6$. The relaxed structures of these models are presented in **Figures 9.2** and **9.3**, for modified anatase (101) and rutile (110), respectively.

The goal with these models will be to perform the same analysis as described in **Chapters 5** and **6**. This will include computations of oxygen vacancy formation energies, PEDOS plots, oxidation states, and the photoexcitation model to examine charge separation and localisation. Finally, the free energies of the PCET steps of the water oxidation pathway will be computed; this will provide insight into the impact of the inclusion of Ca and Ru on the OER activity of MnO_x-modified TiO_2.

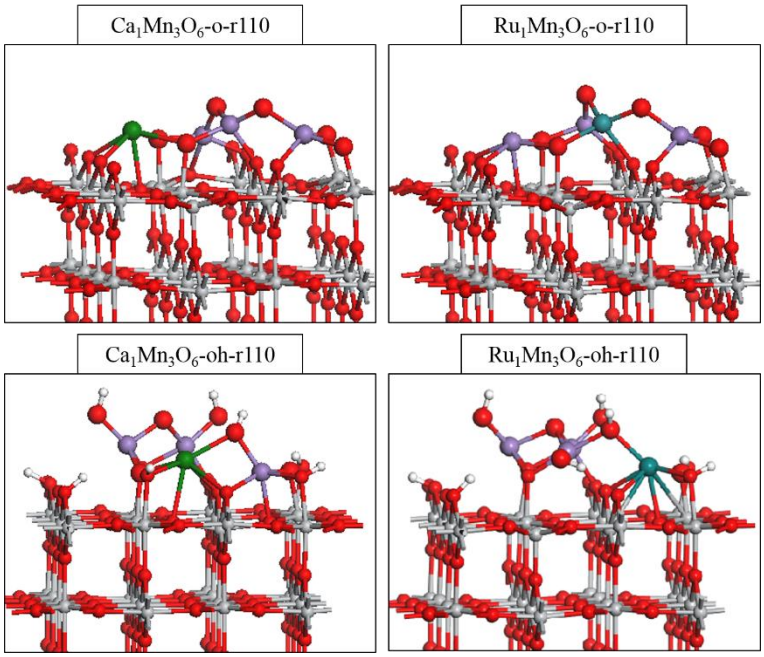

Figure 9.3 Relaxed atomic structure of $CaMn_3O_6$ and $RuMn_3O_6$ modifying the oxidised (top row) and hydroxylated (bottom row) rutile (110) surfaces. Ca is represented by a green sphere and Ru by a blue sphere.

9.2.2 HER catalysts

In **Chapter 7**, the rutile (110) surface was modified with metal chalcogenide nanoclusters as a means to promote the HER activity. The metal chalcogenide clusters were of composition Sn_4S_4, Sn_4Se_4, Zn_4S_4 and Zn_4Se_4 and we found that the sulphide modifiers were more promising candidates for the promotion of the HER, due to optimal free energies of H adsorption. As discussed in detail in **Chapter 3**, there are a wealth of sulphide and selenide materials that can be interfaced with metal oxide catalysts to produce bifunctional composite catalysts for water splitting. In this endeavour, computational models provide a means for the efficient screening of materials.

Metal Phosphides are another group of non-oxide materials that are seeing significant interest in HER. Similar to chalcogenide catalysts based on NiMo, Mo_2C and MoS_2, phosphide materials are HDS catalysts and are therefore potentially active for HER. Among phosphides, Ni_2P, CoP, Fe_2P and MoP and ternaries have been studied as HDS catalysts.[2-5]

Ongoing computational work, similar to that described in **Chapter 7**, involves the modification of TiO_2 rutile (110) with nanoclusters of composition Co_6P_3 and Ni_6P_3. The relaxed atomic structures for these composite surfaces, and the corresponding PEDOS plots, are shown in **Figure 9.4**. The adsorption energies indicate that the modifiers are strongly anchored at the rutile surface through the formation of interfacial metal-oxygen bonds. The PEDOS shows that these phosphide modifiers have a considerable effect on the band gap; Co and Ni 3*d*-states push the VBM of the titania support to higher energies. However, the extent of the impact on the energy gap is not discernible at this level of the theory (DFT+U) and Hybrid DFT calculations are necessary to yield a more quantitative picture.

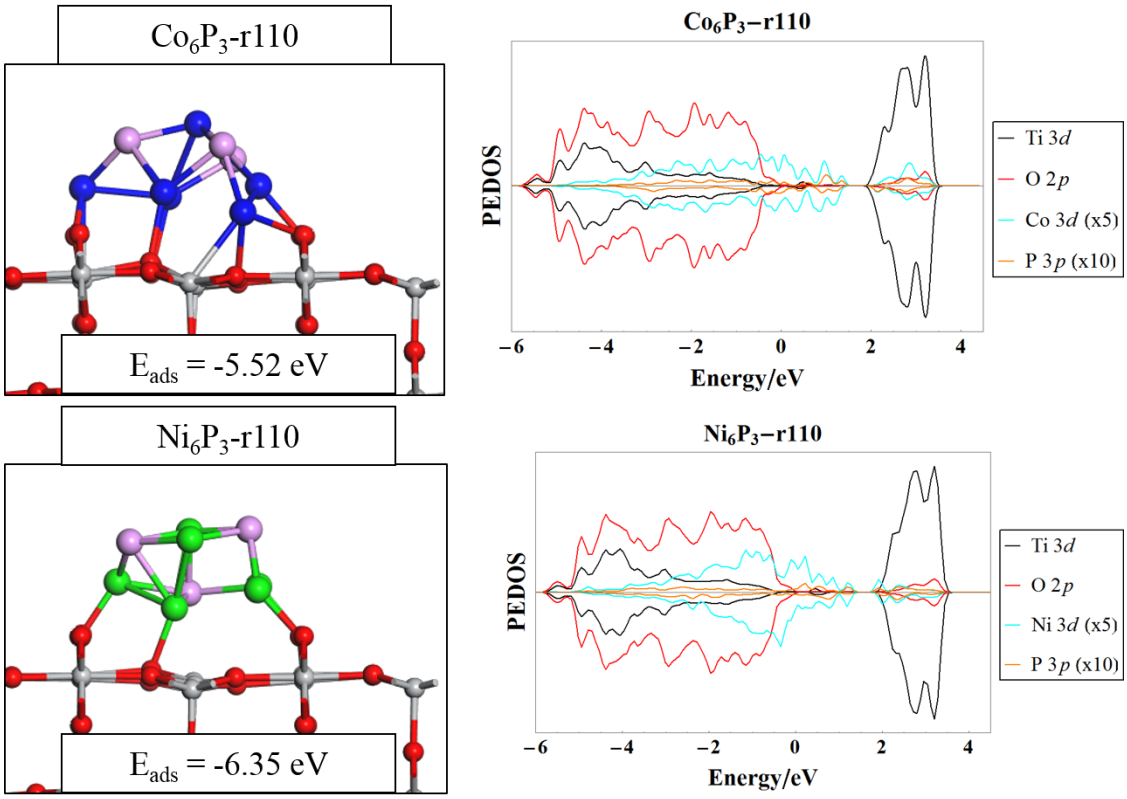

Figure 9.4 Relaxed atomic structures and computed PEDOS plots for Co_6P_3- and Ni_6P_3-modified rutile (110). Co, Ni and P are represented by blue, green and pink spheres, respectively.

Further work on these composite surfaces will include application of the model for photoexcitation to elucidate the impact of modification on charge carrier separation and localisation. Computations of the free energies of H adsorption at sites of the nanocluster modifiers and rutile surface over a range of H coverages are ongoing. Both metal and phosphorous sites of the nanoclusters and bridging oxygen sites of the support are considered for H adsorption.

9.3 Accelerating Materials Discovery

9.3.1 In situ and Operando Measurements

As mentioned in **Chapter 3**, care must be taken with the application and interpretation of computational models. Describing the complexity of the catalyst surface and its environment represents a considerable challenge for first principles simulations. The relevance of computational results depends on the accuracy with which the models approximate the real system. Moreover, the nature of the catalyst surface is dependent on its environment [6-7] and *ex situ* characterisation can fall short in the description of crucial surface features that emerge during operation.

For example, an X-ray absorption fine structure (XAFS) spectroscopic study of a PtO/TiO_2 catalyst during water splitting revealed differences in the catalyst structure between the *ex situ* and operating conditions.[8] Having identified PtO as the active site, the authors reported an increased Pt-O bond length, from 2.07 to 2.13 Å, and a decrease in the coordination number, from 4 to 2.5, for the catalyst *in operando*, relative to the catalyst *ex situ*, both before and after use.

The changes induced during operation can be significant, leading to the assertion from some authors that the term "pre-catalyst" is more appropriate when referring to the *ex situ* materials.[9-10] Despite this, it is often assumed that catalysts are stable under HER operating conditions and that *in situ* and *operando* analyses are more pertinent under harsh OER conditions.[7] While this assumption can be true, it should of course be the subject of rigorous testing. Deng and co-workers used *operando* Raman spectroscopy to confirm the consensus that S atoms are the active sites in the HER catalysis at amorphous MoS_x.[11] In addition, spatially resolved, *operando* measurements performed with scanning

electrochemical cell microscopy (SECCM) indicate increased HER activity at edge sites of MoS_2.[12-14]

Favaro and co-workers performed *operando* XPS to gain an understanding of the OER mechanism at a CoO_x catalyst.[15] The catalyst consisted of interfaced Co_3O_4 and $Co(OH)_2$ phases on a Si support. Under applied anodic potentials, these phases underwent partial and complete conversion to CoO(OH), prior to catalysis. *Operando* XPS measurements revealed highly active Co^{4+} centres under catalytic conditions. Oakton and colleagues studied IrO_2-TiO_2 as an electrocatalyst for the OER using *ex situ* and *operando* measurements.[16] The authors attributed the high OER activity to the presence of surface hydroxyls on IrO_2, which convert to oxo species under OER conditions. The results indicated that the OER mechanism on IrO_2-TiO_2 was the same as that on IrO_2, and the enhanced activity and stability of the composite catalyst was attributed to the stabilisation of small IrO_2 clusters on TiO_2.

Zhang *et al* used post-catalysis analysis of Co_2P and reported that the composition of the electrode surface was largely unchanged in acidic conditions but degraded to hydroxides in alkaline conditions.[17] However, *in situ* X-ray absorption spectroscopy (XAS) measurements suggest that metallic cobalt is the active component for HER.[18] Starting from amorphous metallic Co nanoparticles in pH 7 potassium phosphate solution, the authors found that the metal/phosphate ratio varied with changes in the cathodic potential. Saadi *et al* used *operando* spectroscopic techniques to show that the active component in HER at CoP films in acidic conditions consisted of an amorphous material with Co in a near-zerovalent state and P in a reduced state.[19] Moreover, the authors reported considerable differences in the composition of the catalyst between *ex situ* and *operando* characterisation.

Zhu *et al* used a combination of *operando* measurements, such as *in situ* XAS, Raman spectroscopy, and liquid-phase transmission electron microscopy (LP-TEM) to elucidate the nature of active sites of P-doped $CoSe_2$ in alkaline media under HER conditions.[9] The authors found that P-substitution facilitated the formation of defects, which exposed active, metallic Co sites for the HER.

Besides determining the true nature of the catalyst, *operando* can be used to gain greater insight into the reaction pathway. Wang *et al* used *operando* nuclear magnetic resonance (NMR) spectroscopy to elucidate the mechanism for the HER at anatase TiO_2 decorated with Pd nanoparticles.[20] Their study, which was supported by DFT calculations, yielded a detailed description of the key proton transfer steps involved in the HER, using methanol as a sacrificial hole scavenger.

In situ and *operando* spectroscopies continue to gain considerable traction in the study of catalysis and developments in this area have been the subject of recent reviews.[6-7] These considerations should serve to embolden rather than dishearten. As the tools at our disposal increase the breadth of our understanding, so too will they inform refined computational models and fabrication methods for the rational design of new photocatalyst materials.

9.3.2 Solvent

While free energy calculations are the workhorse of computational materials discovery, with demonstrable efficacy, there are efforts to bridge the gap between simple surface, vapour-phase models and the finite-temperature catalyst-solvent interface.[21-22]

There are various strategies to account for the solvent and its role in the chemistry at the catalyst surface. The solvent can be incorporated implicitly, where the solvent is treated

in an average way and described as a continuous medium, or explicitly, where the molecules that constitute the solvent are included in the computation.[23]

Explicit solvation models can range in complexity from single to multiple layers of molecules at the catalyst surface.[24-26] Ping and co-workers examined the impact of water on the band positions of some common photocatalyst materials.[24] They compared results among approaches including an explicit, single water layer, continuum solvation models (CSMs), and combinations of the two. The authors reported that, while CSMs were sufficient to account for the solvation shift in the band energies of hydrophobic surfaces, the inclusion of an explicit water layer was necessary to describe the stronger interactions at hydrophilic surfaces.

Skúlason and colleagues implemented a water bilayer in their model of the HER at Pt (111).[25] By varying the number of H atoms in the bilayer, the authors could examine the effect of the electrode potential on the activation energies in the HER. This is because the H atoms were solvated in the bilayer – the protons remained in the bilayer while the electrons moved to the catalyst surface. In this way, their model described the Helmholtz double layer.

The treatment of such systems with DFT can be used to determine the effect of the solvent on the binding energies of reaction intermediates. However, DFT is a 0 K theory, and so cannot describe the temperature-dependent effects of a liquid solvent. Thus, an approach to modelling the solvent at finite temperatures is to implement molecular dynamics (MD). Classical MD simulations can be used to obtain an array of local minima in the solvent configuration, which are subsequently treated with DFT.[23] In classical MD, quantum effects and electronic degrees of freedom are neglected and molecule positions are

determined by solving Newton's equations of motion. This necessitates implementation of force fields, which must be parametrised for the system under study.[27-28]

Another approach to modelling finite temperature solvents, explicitly, is *ab initio* MD (AIMD). AIMD differs from classical MD in that it is based on quantum, rather than classical, mechanics.[29] Kronberg and colleagues compared AIMD with NEB in their study of the Volmer-Heyrovsky mechanism for the HER at an N-doped carbon nanotube.[30] The authors reported substantial discrepancies between the activation and reaction energies computed with the two methods and highlighted the importance of explicitly including interfacial dynamics when studying the HER at the catalyst-electrolyte interface. Cheng and coworkers used AIMD to examine the role of charge trapping during deprotonation of a surface-bound hydroxyl at rutile TiO_2 (110).[31] Gono *et al* found that the explicit inclusion of water molecules in their models affected the overpotential for water oxidation at rutile TiO_2 by up to 0.5 V.[26]

Van den Bossche and coworkers approximated the solvent by a polarisable dielectric continuum in their study of the HER at Pt surfaces.[32] The authors maintained a constant electrode potential by varying the concentration of counterions in the electrolyte in response to changes in the number of electrons during the reaction. The results of this implicit approach compared favourably with the more rigorous and computationally expensive "extrapolation" approach.[33-34]

Chang *et al* used both implicit and explicit solvent models to examine the HER at sub-nm Au-Ag clusters.[35] In their implicit model, the authors computed the solvation energy of the nanoclusters and thereby adjusted the electron affinity to account for the water environment. The explicit model implemented AIMD to test the catalyst stability and introduce thermal effects.

9.3.3 Other Computational Approaches

Despite these advances in computational techniques to model the catalyst-electrolyte interface, descriptor-based approaches remain at the forefront of computation-driven design of new photocatalyst materials. Expanding on this theme and going beyond the usual application of DFT calculations to the OER and HER, machine learning approaches are being investigated. In machine learning, the algorithm is trained on a known data set related to the catalytic descriptor of interest and the resulting machine learning function is then used to explore a wide range of potential materials at much lower cost than a full DFT-level simulation.

In one example of this, Jäger and colleagues adopted a machine learning approach[36] in which they constructed a large data set of hydrogen adsorption energies on various sites of nanoclusters of MoS_2 and $Au_{40}Cu_{40}$, **Figure 9.5.a**. This data set was characterised by structural descriptors and used to train a model to predict the adsorption energy for an arbitrary site based on its description. The goal of this study was to establish how many data points were required to interpolate the potential energy surface and predict the hydrogen adsorption energy, ΔE_H, to an accuracy of 0.1 eV. Data sets consisted of 10,000 single-point DFT calculations of ΔE_H and comparisons were made between a number of structural descriptors: atom-centered symmetry functions (ACSF)[37]; many-body tensor representation (MBTR)[38]; and smooth overlap of atomic positions (SOAP)[39-40]. The authors concluded that each of the aforementioned descriptors performed satisfactorily well, provided they were given a training set of sufficient size, which is a key consideration in developing ML models.

Another computational descriptor that can be used to assess the active sites of a catalyst surface is the Fermi softness, S_F, which was introduced in **Chapter 3**.[41] This descriptor

finds its analogue in frontier molecular orbital (FMO) theory[42] which describes the spatial distribution of active sites of a molecule. Huang *et al* benchmarked this descriptor in a study of transition metal surfaces before examining active sites of a one-dimensional MoS_2 edge.[41] Based on analysis of $S_F(r)$, **Figure 9.5.b**, and subsequently confirmed by NEB calculations, the authors identified a subtlety in the reactivity at the MoS_2 edge: an anisotropy exists which promotes the HER at intra-S-dimer bridge sites, relative to inter-S-dimer bridge sites.

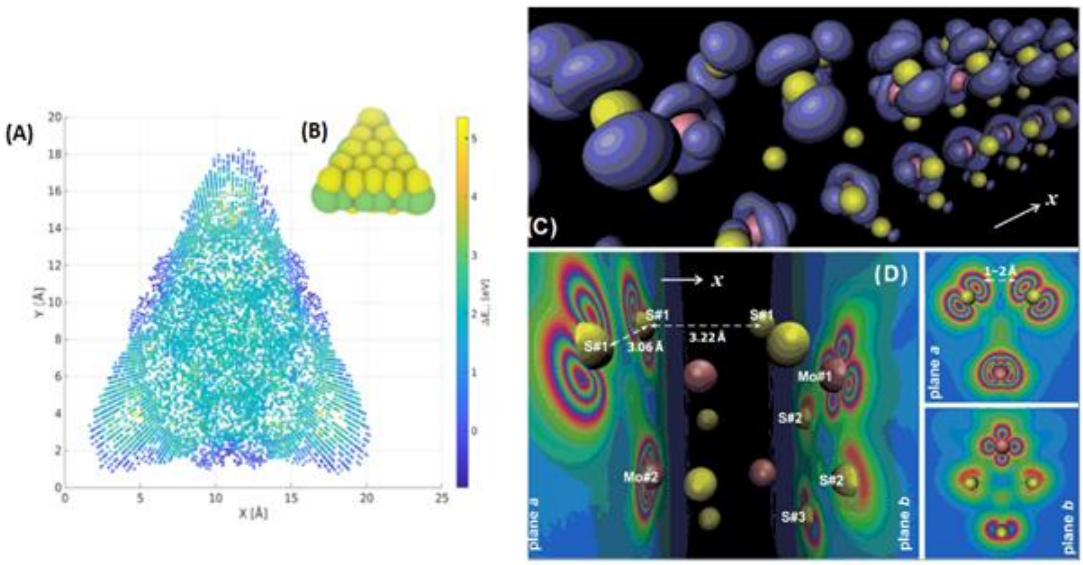

Figure 9.5 (a) Hydrogen position scan on the surface of a triangular-shaped MoS_2 cluster. The inset (**b**) shows the geometry of the MoS_2 cluster. From ref. [36] **(c)** A 3D view of the calculated $S_F(r)$ isosurface (blue, on which S_F=55 /keV/Å^3) at the MoS_2 edge. **(d)** The $S_F(r)$ is projected onto two planes, which are normal to the x-direction. From ref.[41].

Ran and colleagues established a relationship between the HER activity and bond electronegativity in a study of TMDs.[43] Citing a trial-and-error approach in existing endeavours to activating and optimizing catalysts for HER, the authors implemented a high-throughput first-principles strategy to identify a universal design principle. The study began with 2H-MoS_2 doped with other TMs and examined H adsorption at S-sites neighbouring the TM-dopant. The authors presented a formula that describes the

characteristic S-H bonding electron number, based on the local properties of the active site. The descriptor, Ψ, takes into account bond electronegativity, coordination numbers, and valence electrons, and was used to predict potential HER catalysts with high activities; although experimental confirmation is required to confirm the validity of such predictions.

9.4 Chapter References

1. Liu, J.; Saedy, S.; Verma, R.; van Ommen, J. R.; Nolan, M., Atomic Layer Deposition of CeOx Nanoclusters on TiO2. 2020. https://doi.org/10.26434/chemrxiv.12320855.v1
2. Oyama, S. T.; Wang, X.; Lee, Y. K.; Chun, W. J., Active phase of Ni_2P/SiO_2 in hydroprocessing reactions. *Journal of Catalysis* **2004,** *221* (2), 263-273.
3. Senevirathne, K.; Burns, A. W.; Bussell, M. E.; Brock, S. L., Synthesis and Characterization of Discrete Nickel Phosphide Nanoparticles: Effect of Surface Ligation Chemistry on Catalytic Hydrodesulfurization of Thiophene. *Advanced Functional Materials* **2007,** *17* (18), 3933-3939.
4. Oyama, S. T., Novel catalysts for advanced hydroprocessing: transition metal phosphides. *Journal of Catalysis* **2003,** *216* (1), 343-352.
5. Oyama, S. T.; Gott, T.; Zhao, H.; Lee, Y.-K., Transition metal phosphide hydroprocessing catalysts: A review. *Catalysis Today* **2009,** *143* (1), 94-107.
6. Föttinger, K.; Rupprechter, G., In Situ Spectroscopy of Complex Surface Reactions on Supported Pd–Zn, Pd–Ga, and Pd(Pt)–Cu Nanoparticles. *Accounts of Chemical Research* **2014,** *47* (10), 3071-3079.
7. Zhu, Y.; Wang, J.; Chu, H.; Chu, Y.-C.; Chen, H. M., In Situ/Operando Studies for Designing Next-Generation Electrocatalysts. *ACS Energy Letters* **2020,** *5* (4), 1281-1291.
8. Li, Y. H.; Li, C.; Yang, H. G., Quantitative analysis of the PtO structure during photocatalytic water splitting by operando XAFS. *Journal of Materials Chemistry A* **2017,** *5* (39), 20631-20634.
9. Zhu, Y.; Chen, H.-C.; Hsu, C.-S.; Lin, T.-S.; Chang, C.-J.; Chang, S.-C.; Tsai, L.-D.; Chen, H. M., Operando Unraveling of the Structural and Chemical Stability of P-Substituted $CoSe_2$ Electrocatalysts toward Hydrogen and Oxygen Evolution Reactions in Alkaline Electrolyte. *ACS Energy Letters* **2019,** *4* (4), 987-994.
10. Wygant, B. R.; Kawashima, K.; Mullins, C. B., Catalyst or Precatalyst? The Effect of Oxidation on Transition Metal Carbide, Pnictide, and Chalcogenide Oxygen Evolution Catalysts. *ACS Energy Letters* **2018,** *3* (12), 2956-2966.
11. Deng, Y.; Ting, L. R. L.; Neo, P. H. L.; Zhang, Y.-J.; Peterson, A. A.; Yeo, B. S., Operando Raman Spectroscopy of Amorphous Molybdenum Sulfide (MoS_x) during the Electrochemical Hydrogen Evolution Reaction: Identification of Sulfur Atoms as Catalytically Active Sites for H+ Reduction. *ACS Catalysis* **2016,** *6* (11), 7790-7798.
12. Daviddi, E.; Gonos, K. L.; Colburn, A. W.; Bentley, C. L.; Unwin, P. R., Scanning Electrochemical Cell Microscopy (SECCM) Chronopotentiometry: Development and Applications in Electroanalysis and Electrocatalysis. *Analytical Chemistry* **2019,** *91* (14), 9229-9237.
13. Bentley, C. L.; Kang, M.; Maddar, F. M.; Li, F.; Walker, M.; Zhang, J.; Unwin, P. R., Electrochemical maps and movies of the hydrogen evolution reaction on natural crystals of molybdenite (MoS_2): basal vs. edge plane activity. *Chemical Science* **2017,** *8* (9), 6583-6593.
14. Bentley, C. L.; Kang, M.; Unwin, P. R., Nanoscale Structure Dynamics within Electrocatalytic Materials. *Journal of the American Chemical Society* **2017,** *139* (46), 16813-16821.
15. Favaro, M.; Yang, J.; Nappini, S.; Magnano, E.; Toma, F. M.; Crumlin, E. J.; Yano, J.; Sharp, I. D., Understanding the Oxygen Evolution Reaction Mechanism on

CoO_x using Operando Ambient-Pressure X-ray Photoelectron Spectroscopy. *Journal of the American Chemical Society* **2017,** *139* (26), 8960-8970.
16. Oakton, E.; Lebedev, D.; Povia, M.; Abbott, D. F.; Fabbri, E.; Fedorov, A.; Nachtegaal, M.; Copéret, C.; Schmidt, T. J., IrO_2-TiO_2: A High-Surface-Area, Active, and Stable Electrocatalyst for the Oxygen Evolution Reaction. *ACS Catalysis* **2017,** *7* (4), 2346-2352.
17. Zhang, Y.; Gao, L.; Hensen, E. J. M.; Hofmann, J. P., Evaluating the Stability of Co_2P Electrocatalysts in the Hydrogen Evolution Reaction for Both Acidic and Alkaline Electrolytes. *ACS Energy Letters* **2018,** *3* (6), 1360-1365.
18. Lassalle-Kaiser, B.; Zitolo, A.; Fonda, E.; Robert, M.; Anxolabéhère-Mallart, E., In Situ Observation of the Formation and Structure of Hydrogen-Evolving Amorphous Cobalt Electrocatalysts. *ACS Energy Letters* **2017,** *2* (11), 2545-2551.
19. Saadi, F. H.; Carim, A. I.; Drisdell, W. S.; Gul, S.; Baricuatro, J. H.; Yano, J.; Soriaga, M. P.; Lewis, N. S., Operando Spectroscopic Analysis of CoP Films Electrocatalyzing the Hydrogen-Evolution Reaction. *Journal of the American Chemical Society* **2017,** *139* (37), 12927-12930.
20. Wang, X. L.; Liu, W.; Yu, Y.-Y.; Song, Y.; Fang, W. Q.; Wei, D.; Gong, X.-Q.; Yao, Y.-F.; Yang, H. G., Operando NMR spectroscopic analysis of proton transfer in heterogeneous photocatalytic reactions. *Nature Communications* **2016,** *7* (1), 11918.
21. Quesne, M. G.; Silveri, F.; de Leeuw, N. H.; Catlow, C. R. A., Advances in Sustainable Catalysis: A Computational Perspective. *Frontiers in chemistry* **2019,** *7*, 182-182.
22. Pérez, A. E.; Ribadeneira, R., Modeling with DFT and Chemical Descriptors Approach for the Development of Catalytic Alloys for PEMFCs. In *Density Functional Theory*, Glossman-Mitnik, D., Ed. IntechOpen: 2018.
23. Saleheen, M.; Heyden, A., Liquid-Phase Modeling in Heterogeneous Catalysis. *ACS Catalysis* **2018,** *8* (3), 2188-2194.
24. Ping, Y.; Sundararaman, R.; Goddard Iii, W. A., Solvation effects on the band edge positions of photocatalysts from first principles. *Physical Chemistry Chemical Physics* **2015,** *17* (45), 30499-30509.
25. Skúlason, E.; Karlberg, G. S.; Rossmeisl, J.; Bligaard, T.; Greeley, J.; Jónsson, H.; Nørskov, J. K., Density functional theory calculations for the hydrogen evolution reaction in an electrochemical double layer on the Pt(111) electrode. *Physical Chemistry Chemical Physics* **2007,** *9* (25), 3241-3250.
26. Gono, P.; Ambrosio, F.; Pasquarello, A., Effect of the Solvent on the Oxygen Evolution Reaction at the TiO_2–Water Interface. *The Journal of Physical Chemistry C* **2019,** *123* (30), 18467-18474.
27. Hawlitzky, M.; Horbach, J.; Ispas, S.; Krack, M.; Binder, K., Comparative classical and 'ab initio' molecular dynamics study of molten and glassy germanium dioxide. *Journal of Physics: Condensed Matter* **2008,** *20* (28), 285106.
28. Zhang, J.; Xu, F.; Hong, Y.; Xiong, Q.; Pan, J., A comprehensive review on the molecular dynamics simulation of the novel thermal properties of graphene. *RSC Advances* **2015,** *5* (109), 89415-89426.
29. Paquet, E.; Viktor, H. L., Computational Methods for Ab Initio Molecular Dynamics. *Advances in Chemistry* **2018,** *2018*, 9839641.
30. Kronberg, R.; Lappalainen, H.; Laasonen, K., Revisiting the Volmer–Heyrovský mechanism of hydrogen evolution on a nitrogen doped carbon nanotube: constrained molecular dynamics versus the nudged elastic band method. *Physical Chemistry Chemical Physics* **2020**.

31. Cheng, J.; VandeVondele, J.; Sprik, M., Identifying Trapped Electronic Holes at the Aqueous TiO_2 Interface. *The Journal of Physical Chemistry C* **2014,** *118* (10), 5437-5444.
32. Van den Bossche, M.; Skúlason, E.; Rose-Petruck, C.; Jónsson, H., Assessment of Constant-Potential Implicit Solvation Calculations of Electrochemical Energy Barriers for H2 Evolution on Pt. *The Journal of Physical Chemistry C* **2019,** *123* (7), 4116-4124.
33. Rossmeisl, J.; Skúlason, E.; Björketun, M. E.; Tripkovic, V.; Nørskov, J. K., Modeling the electrified solid–liquid interface. *Chemical Physics Letters* **2008,** *466* (1), 68-71.
34. Skúlason, E.; Tripkovic, V.; Björketun, M. E.; Gudmundsdóttir, S.; Karlberg, G.; Rossmeisl, J.; Bligaard, T.; Jónsson, H.; Nørskov, J. K., Modeling the Electrochemical Hydrogen Oxidation and Evolution Reactions on the Basis of Density Functional Theory Calculations. *The Journal of Physical Chemistry C* **2010,** *114* (42), 18182-18197.
35. Chang, L.; Cheng, D.; Sementa, L.; Fortunelli, A., Hydrogen evolution reaction (HER) on Au@Ag ultrananoclusters as electro-catalysts. *Nanoscale* **2018,** *10* (37), 17730-17737.
36. Jäger, M. O. J.; Morooka, E. V.; Federici Canova, F.; Himanen, L.; Foster, A. S., Machine learning hydrogen adsorption on nanoclusters through structural descriptors. *npj Computational Materials* **2018,** *4* (1), 37.
37. Rupp, M.; Tkatchenko, A.; Müller, K.-R.; von Lilienfeld, O. A., Fast and Accurate Modeling of Molecular Atomization Energies with Machine Learning. *Physical Review Letters* **2012,** *108* (5), 058301.
38. A Huo, H.; A Rupp, M., Unified Representation of Molecules and Crystals for Machine Learning. *Preprint at https://arxiv.org/pdf/1704.06439.pdf*. **2017**.
39. De, S.; Bartók, A. P.; Csányi, G.; Ceriotti, M., Comparing molecules and solids across structural and alchemical space. *Physical Chemistry Chemical Physics* **2016,** *18* (20), 13754-13769.
40. Bartók, A. P.; Kondor, R.; Csányi, G., On representing chemical environments. *Physical Review B* **2013,** *87* (18), 184115.
41. Huang, B.; Xiao, L.; Lu, J.; Zhuang, L., Spatially Resolved Quantification of the Surface Reactivity of Solid Catalysts. *Angewandte Chemie International Edition* **2016,** *55* (21), 6239-6243.
42. Fukui, K., Role of Frontier Orbitals in Chemical Reactions. *Science* **1982,** *218* (4574), 747-754.
43. Ran, N.; Qiu, W.; Song, E.; Wang, Y.; Zhao, X.; Liu, Z.; Liu, J., Bond Electronegativity as Hydrogen Evolution Reaction Catalyst Descriptor for Transition Metal (TM = Mo, W) Dichalcogenides. *Chemistry of Materials* **2020,** *32* (3), 1224-1234.

Appendix A: Materials and Methods

All preparation of materials and experimental characterisation were carried out by experimental collaborators and the details contained in this Appendix are included for completeness.

A.1 Cu-doped TiO_2

This section contains the materials and methods relevant to **Section 4.2**:

"Effect of Cu Doping on the Anatase-to-Rutile Phase Transition in TiO_2 Photocatalysts: Theory and Experiments"

Chemicals & Reagents

Titanium tetraisopropoxide (97%), copper sulphate pentahydrate (≥98.0%) and isopropanol (≥99.5%) were purchased from Sigma-Aldrich and were used without further treatment. 1,4-dioxane was purchased from Merck.

Preparation of TiO_2

46.16mL of titanium isopropoxide (TTIP) was added to 200 mL of isopropanol (IPA). This solution was stirred for 15 min. To this solution 200 mL of deionised water was added. This mixture was stirred for another 30 min. The resulting gel was dried in the oven set at 100°C for 12 hrs. The resulting powder was annealed at 400, 500, 600, 650, 700 and 800 °C, at a ramp rate of 10 °C/min and held at the target temperature for 2 hrs.

Preparation of copper doped materials

For a 2% copper sample, 45.24 mL of TTIP was added to 200 mL of IPA and was stirred for 15 min (Solution A). 0.8705 g of copper sulphate ($CuSO_4$) was added to 200 mL of deionised water, this was stirred for 15 min (Solution B). Solution B was added to Solution A and this was stirred for 30 min. The resulting gel was dried in the oven at 100 °C for 12 hrs. The resulting powder was annealed at 400, 500, 600, 650, 700 and 800 °C, at a ramp rate of 10 °C/min and was held for 2 hrs. This method was repeated for the 4% and 8% copper samples by altering the amount of TTIP and $CuSO_4$ (4% - 44.32 mL and 1.7375 g; 8% - 42.47 mL and 3.5075 g).

Characterisation

All samples were analysed with X-ray Diffraction (XRD). The diffractograms were produced using a Siemens D500 X-ray powder diffractometer, using Cu Kα radiation (λ= 0.15418 nm). The diffraction range examined was between 2θ=10°-80°. To determine the fraction of rutile in the samples, the Spurr equation was used (eq. A.1).[1]

$$F_R = \frac{1}{1 + 0.8[\frac{I_A(101)}{I_R(110)]}} \qquad \text{A.1}$$

where F_R is the quantity of rutile in mixed sample and $I_A(101)$ and $I_R(110)$ are the intensities of the main anatase and rutile peaks.

The crystallinity of the samples were calculated using the XRD spectra and the Scherrer equation (eq. A.2).[2]

$$\Phi = \frac{K\lambda}{\beta \cos\theta} \qquad \text{A.2}$$

where Φ is the crystallite size, K is the shape factor, λ is the X-ray wavelength, β is the full line width at the half-maximum height of the main intensity peak and θ is the Bragg angle.

The Horiba Jobin Yvan LabRAM HR 800 with a grating of 300 gr/mm was used for Raman analysis. A 660 nm solid state diode laser standard bandwidth version with double edge filter upgrade was the laser used. The acquisition time was 3 seconds. When focusing onto the sample a (× 50) lens was used.

A ThermoFisher Scientific Instruments (East Grinstead, UK) K-Alpha$^+$ spectrometer was utilised in obtaining XPS spectra, with a monochromatic Al Kα X-ray source (hν = 1486.6 eV) and ~400 μm radius was used as an x-ray spot. The survey spectra and a high-resolution core level spectrum for all elements was obtained using a Pass Energy of 200 eV and 50 eV, respectively. The C 1*s* peak (285) was used as a charge reference to account for charging effects during acquisition. The non-linear (Shirley) background was removed from the high resolution, core level spectra before calculating the quantitative surface chemical analyses. The manufacturer's Avantage software was used, which incorporates the appropriate sensitivity factors and corrects for the electron energy analyser transmission function.

The surface morphology of the samples was analysed using the Siemens TM1000 Scanning Electron Microscopy with Energy Dispersive X-Ray Analyser (SEM-EDX).

To determine the surface area of the samples the Brunauer– Emmett–Teller method (BET) was used. The samples were first degassed for an hour at 300 °C. The adsorption isotherms were acquired at -196.15 °C.

The following analyses were made according to the standard methods for the examination of water and wastewater (APHA 2005). Total organic carbon (TOC) was measured by

the combustion-infrared method using a multi N/C® 3100 TOC/TN analyser (Analytik Jena AG, Jena, Germany), which performed the catalytic combustion on cerium oxide at 850 °C.

1,4-Dioxane was quantified using gas−liquid chromatography (GLC) on a 7980A instrument (Agilent Technologies Inc., Palo Alto, CA), equipped with a flame ionisation detector. The temperatures of the injector and the detector were 310 and 280 °C, respectively. Samples (2 µL) were injected using the pulsed-split mode (split ratio 5:1) and analysed in a TRB-FFAP (Teknokroma, Sant Cugat del Vallès, Spain) fused silica column (30 m x 0.25 mm internal diameter x 0.25 µm film thickness) with He (43 psi) as carrier gas, and the following temperature programme: 80-240 °C at a 15 °C/min ramp rate, after a 9 min initial hold. Peaks were identified according to relative retention time figures provided by commercial standards. Quantification was performed according to peak area, corrected with the response factors calculated for each compound using 1-butanol (60 ppm) as internal standard, and the GC-ChemStation software Rev.B.04.02 (96) from Agilent.

Photocatalysis

Experiments were performed with a synthetic solution of 1,4-dioxane (75 mg/L) that was kept stirred during the experiment using a magnetic device. The corresponding doped-TiO_2 catalyst was added to the suspension with a concentration of 1 g/L. The photocatalytic reaction was performed for duration of 240 minutes. Samples were withdrawn from the solution every 30 min. The source of UV light was a solar simulator supplied by Newport (Irvine, USA) equipped with a Xenon lamp (300 W). A correction filter (ASTM E490-73a) provides the simulated solar spectrum under ideal conditions. A total photon flux of $6.8 \cdot 10^{19}$ photon$\cdot s^{-1}$ was calculated to flow inside the photochemical

reactor, as described by Liang et al. (2011). Light intensity between 200 to 400 nm resulted of 150 $W \cdot m^{-2}$ at 3 cm from the light source, which was the distance between the sample surface and the lamp. Light intensity was recorded using a radiometer (UV-Elektronik, UV-VIS Radiometer RM-21, Ettlingen, Germany).

The light intensity recorded on the irradiated liquid surface in Wm^{-2} ($Js^{-1}m^{-2}$) was converted to kJ/L, taking into account the volume of the solution (50 mL) and the irradiated surface (0.0104 cm^{-2}) in order to normalise the data. Blank experiments either performed without adding the catalyst, without switching the UV lamp on, or using no dopant concentration were performed. All experiments were repeated three times.

A.2 Mo-doped TiO_2

This section contains materials and methods relevant to **Section 4.3**:

"Mo doped TiO_2: impact on oxygen vacancies, anatase phase stability and photocatalytic activity"

Analytical grade chemicals were used in this study. All the chemicals were used as received without further purification.

Synthesis of Mo-TiO_2

In a typical procedure to prepare 0.5 mol. % Mo-TiO_2, titanium isopropoxide (TTIP; 41.81 ml) was mixed with isopropanol (200 ml) under stirring for 15 min, denoted as solution A. In the meantime, solution B was prepared by mixing 0.1225 g of ammonium molybdate tetrahydrate ($(NH_4)_6Mo_7O_{24}.4H_2O$) in 200 ml of double distilled water under vigorous stirring for 15 min. Afterwards, solution B was added drop by drop into solution A to initiate the hydrolysis process under stirring for 30 min. The resultant, milky white solution was dried at 100 °C for 24 h. The amorphous powders were then calcined at various temperatures (500, 600, 700, 750, and 800 °C) in a muffle furnace with a heating rate of 10 °C/min for 2 h. In a similar fashion, 1, 1.5 and 2 mol. % of Mo-TiO_2 samples were also synthesised. Pure TiO_2 (0 mol. % Mo-TiO_2) was synthesised by the same procedure without addition of any Mo precursor.

Photocatalytic wastewater disinfection

The photocatalytic activity of Mo-TiO_2 (0.1 g/L) was assessed by the disinfection of microbes in wastewater (secondary effluent of an urban wastewater (WW) treatment plant, Medinaceli, Soria, Spain) under LED light irradiation with different UVA wavelengths. The characteristics of effluent were determined by the standard method of

wastewater analysis. The parameters such as pH, conductivity, total volatile solids (TVS), total suspended solids (TSS), chemical oxygen demand (COD), and microbial count (*Escherichia coli*, non coliforms and other coliforms) were measured. Two parallel lines of 10 UVA LED lights (Seoul Viosys, Republic of Korea) of particular wavelength (385 and 395 nm), which were widely scattered to equally cover the reactor surface, provided the irradiation source. 250 mA of current intensity was used in each LED light setup. This was equivalent to consuming 8.38 W and 8.25 W of electrical power by the 385 nm and 395 nm LED lights, respectively. The lamp was located at a distance of 4.5 cm from the water surface. Under this experimental condition, the actual irradiated power was determined by potassium ferrioxalate actinometry method [3-4].The results showed that 1682.8 ± 77.1 and 1607.7 ± 56.1 μmol m^{-2} s^{-1} of photons emitted from the 385 and 395 nm LED lights, respectively. All the materials used in this experiment were previously sterilised in an autoclave at 100 ºC and 1.5 bar for 40 min. 100 ml of WW was treated in each trial in a glass reactor. 1.0 ml of aliquot was withdrawn from the photo-reactor at regular time intervals (such as 4, 8, 15, 30, 45, and 60 min) to measure the existence of bacteria, in terms of colony-forming units (CFU), by ISO 9308-1:2014 method [5].

At first, 0.5 mL of the WW sample was mixed with 0.5 mL of saline water (0.9 g L^{-1} NaCl in distilled water). Then the samples were filtrated through 0.45 μm white-gridded mixed cellulose ester filter (GN-6 Metricel®, Pall, New York, USA) in a laminar flow hood to avoid external contamination. Chromocult® agar plates (Millipore, Merck, Darmstadt, Germany) were used as the media to grow the bacterial colonies. CFUs were enumerated after incubating the plates at 36 ± 2 ºC for 21-24 h. There are three types of colonies may be identified to grow on Chromocult® agar plates such as *Escherichia coli* (dark-blue to violet colour); other coliforms, namely: *Enterobacter aerogenes*, *Citrobacter freundii*,

(pink to red colour); and some non-coliform bacteria, namely: *Enterococcus faecalis*, *Pseudomonas aeruginosa* (colourless).

Characterisation

ART of Mo-TiO_2 was investigated with the help of X-ray diffraction (XRD) and Raman spectroscopy. The crystallinity and phase changes were studied through XRD (Siemens D500) using Cu Kα radiation (λ= 0.15418 nm) in the 2θ range of 10 °- 80 °. Spurr equation (eq. A.1) was applied to determine the anatase and rutile phase composition.

The Scherrer equation was used to determine the average crystallite size. Raman spectra of Mo-TiO_2 samples were measured for an acquisition period of 3 s with a grating of 300 gr/mm. The surface chemical composition, and the bonding interactions of Mo-TiO_2 were analysed using X-ray photoelectron spectroscopy (XPS) with K-Alpha$^+$ spectrometer. Photoluminescence (PL) analysis was recorded to study the effect of Mo doping on the lifetime of charge carriers (excitation wavelength of 350 nm).

A.3 In-doped TiO_2

This section contains materials and methods relevant to **Section 4.4**:

"In-doped TiO_2 photocatalysts with high temperature anatase stability"

All the materials used were of analytical grade and they were used as received without further purification. Double distilled water was used in the experiments.

Synthesis of indium doped TiO_2 (In-TiO_2)

2 mol. % In-TiO_2 was synthesised through a sol-gel technique as follows: In a typical experiment, 38 ml of titanium isopropoxide (TTIP) was taken in 200 ml of isopropanol and the mixture was stirred for 15 min at RTP (solution A). 0.786 g of indium nitrate ($In(NO_3)_3.xH_2O$) was dissolved separately in 200 ml of double distilled water (solution B) at RTP. Then, solution B was added drop wisely into solution A under constant stirring for 30 min. The resulting gel was dried in an oven at 100 °C for 24 h. Afterwards, the powders were calcined in a muffle furnace at various temperatures (500, 600, 700, 750, 800, 850 and 900 °C) at a ramp rate of 10 °C/min for 2 h. The samples were synthesised using various mol. % of In. The as-synthesised samples such as such as 0, 2, 4, 8 and 16 mol. % In-TiO_2 were labelled as TiIn-0, TiIn-2, TiIn-4, TiIn-8 and TiIn-16, respectively. Pure TiO_2 was synthesised using the same procedure without the addition of In precursor.

Characterisation

ART and the TiO_2 crystalline phases were studied with the help of X-ray diffraction (XRD) using Cu Kα radiation (λ= 0.15418 nm) in the 2θ range of 10 °- 80 ° in a Siemens D500 XRD instrument. The percentages of TiO_2 anatase and rutile were calculated using the Spurr equation (eq. A.1)[6-7]:

The average crystallite size was determined using the Scherrer equation [8-9]. ART was also analyzed *via* Raman spectroscopy (Horiba Jobin Yvan LabRAM HR 800) with a grating of 300 gr/mm. The acquisition time of Raman analysis was 3 seconds. The oxidation state of elements and the bonding interactions of In-TiO_2 were examined by an X-ray photoelectron spectroscopy (XPS; ThermoFisher Scientific Instruments (East Grinstead, UK) with K-Alpha$^+$ spectrometer). The charge carrier recombination process was studied in terms of photoluminescence (PL) spectroscopy with an excitation wavelength of 350 nm. The photocatalytic activity (0.5 g/L) was evaluated using 0.5 g/L of nanoparticles for hydrogen (H_2) production in a 230 ml stainless steel reactor with a quartz window. The experiments were carried out using 115 ml of double distilled water under simulated solar light irradiation (300 W ozone free Xe lamp). Glycerol (10 %) was used as a sacrificial agent. H_2 gas was analysed through an Agilent gas chromatography (GC) with thermal conductivity detector (TCD) and flame ionisation detector (FID). Carboxen-1000 packed column was used in the GC.

A.4 hBN-modified TiO_2

This section contains materials and methods relevant to **Section 5.3**:

"Modification of TiO_2 with hBN: High Temperature Anatase Phase Stabilisation and Photocatalytic Degradation of 1, 4-Dioxane"

Materials

The chemicals used in this study were titanium tetraisopropoxide (97%), boron nitride and isopropanol (≥99.5%), all of them purchased from Sigma-Aldrich and used without any treatment. 1,4-dioxane (>99%) was purchase from Merck.

Preparation of Nanomaterials

TiO_2 was modified with BN at five different concentrations (0, 2, 4, 8 and 16% BN-TiO_2). For the 2 mol. % sample, 55.4 mL of TTIP was added to 200 mL of IPA and was stirred for 15 min (Solution A). 0.0948 g BN was added to 200 mL of deionized water, this was stirred for 15 min (Solution B). Solution B was added to Solution A and this was stirred for 30 min. The resulting sol-gel was dried in the oven at 100 °C for 12 hrs. The resulting powder was annealed at 500, 600, 650 and 700 °C at a ramp rate of 10 °C/min and was held for 2 hrs. This method was repeated for the 0, 4, 8 and 16% BN samples by changing the volume of TTIP and grams of BN (0% - 56.6 mL and 0 g; 4% - 54.2 mL and 0.1897 g; 8% - 52.2 mL and 0.3793 g; 16% - 47.6 mL and 0.7587 g).

Characterisation of Nanomaterials

A Siemens D500 X-ray powder diffractometer was used for the XRD characterization, using Cu Kα radiation (λ = 0.15418 nm). The diffraction range examined was between 2θ=10°-80°. To determine the fraction of rutile in the samples, the Spurr equation was

used (eq. A.1).[1] XRD data were also used for determining the size of the crystalline structures in each sample; this was determined using the Scherrer equation (eq. A.2).[2]

The Horiba Jobin Yvan LabRAM HR 800 with a grating of 300 gr/mm was used for Raman analysis. A 660 nm solid state diode laser standard bandwidth version with double edge filter upgrade was the laser used. The acquisition time was 3 seconds. When focusing onto the sample, a (× 50) lens was used.

A ThermoFisher Scientific Instruments (East Grinstead, UK) K-Alpha$^+$ spectrometer was employed for the XPS analysis of samples. A monochromatic Al Kα X-ray source (hν = 1486.6 eV) with a spot radius of ~400 μm was used to obtain the XPS spectra. A Pass Energy of 200 eV was used for acquiring survey spectra, while a Pass Energy of 50 eV was employed for producing core level spectra with high resolution for all elements. C 1*s* (285 eV) was used as a reference peak to correct for charging effects during acquisition. After accounting for the removal of a non-linear (Shirley) background, the core level spectra were used in calculating the quantitative surface chemical composition. To correct for electron energy analyser transmission function and integrate the applicable sensitivity factors, the manufacturers software (Avantage) was used.

Measurements of 1,4-dioxane were performed by a gas liquid chromatography-flame ionization detector (GLC-FID) (Agilent 7980A, Palo Alto, CA). Samples of 2 μL were injected with a split ratio of 5:1 at 310 ºC and analysed in a Teknokroma capillary column TRB-FFAP 30 m × 0.25 mm ID × 0.25 μm film thickness (Teknokroma, Spain). Carrier gas was He, 43 psi. After 9 min initial hold, the temperature was increased at 15 °C/min from 80 °C to 240 °C. A FID detector was used, detection temperature was 280ºC. GC-ChemStation software Rev.B.04.02 (96) from Agilent was used for quantification based on corrected peak areas. 60 ppm of 1-butanol was used as internal standard.

Photocatalysis

Photocatalytic analysis was performed using a total volume of 50 mL of synthetic solution, which was comprised of 1,4-dioxane (100 $mg \cdot L^{-1}$) dissolved in deionized water and TiO_2 catalyst (1 $g \cdot L^{-1}$). The concentration of 1,4-dioxane is similar or even lower than the concentration that may be found in industrial wastewater. [10-11] A sample was taken every 30 min, with a total reaction time of 240 min. There were three types of control experiments preformed: (1) without presence of UV radiation, (2) without any photocatalyst present, and (3) with photocatalyst not containing BN. All experiments were repeated in triplicate.

A solar simulator equipped with a 300W Xenon lamp (from Newport, USA) was used as UV light source. An ASTM E490-73a correction filter was used to obtain the solar spectrum. A total photon flux of 6.8×10^{19} photon$\cdot s^{-1}$ was calculated to flow inside the photochemical reactor using the methodology described by Liang et al. (2011). Light intensity between 315 to 400 nm resulted of 50 $W \cdot m^{-2}$ at 3 cm from the light source on a total surface of 0.0104 cm^{-2}. A UV-VIS Radiometer RM-21 (Elektronik, Germany) was used to record the light intensity

A.5 References

1. Spurr, R. A.; Myers, H., Quantitative analysis of anatase-rutile mixtures with an X-ray diffractometer. *Analytical Chemistry* **1957,** *29* (5), 760-762.
2. Scherrer, P., Bestimmung der Grösse und der inneren Struktur von Kolloidteilchen mittels Röntgenstrahlen. *Nachrichten von der Gesellschaft der Wissenschaften zu Göttingen, mathematisch-physikalische Klasse* **1918,** *1918*, 98-100.
3. Hatchard, C.; Parker, C. A., A new sensitive chemical actinometer-II. Potassium ferrioxalate as a standard chemical actinometer. *Proceedings of the Royal Society of London. Series A. Mathematical and Physical Sciences* **1956,** *235* (1203), 518-536.
4. Montalti, M.; Credi, A.; Prodi, L.; Gandolfi, M. T., *Handbook of photochemistry*. CRC press: 2006.
5. Lange, B.; Strathmann, M.; Oßmer, R., Performance validation of chromogenic coliform agar for the enumeration of Escherichia coli and coliform bacteria. *Letters in applied microbiology* **2013,** *57* (6), 547-553.
6. Byrne, C.; Fagan, R.; Hinder, S.; McCormack, D. E.; Pillai, S. C., New approach of modifying the anatase to rutile transition temperature in TiO_2 photocatalysts. *RSC Advances* **2016,** *6* (97), 95232-95238.
7. Ilie, A. G.; Scarisoreanu, M.; Dutu, E.; Dumitrache, F.; Banici, A.-M.; Fleaca, C. T.; Vasile, E.; Mihailescu, I., Study of phase development and thermal stability in as synthesized TiO_2 nanoparticles by laser pyrolysis: ethylene uptake and oxygen enrichment. *Applied Surface Science* **2018,** *427*, 798-806.
8. Boningari, T.; Inturi, S. N. R.; Suidan, M.; Smirniotis, P. G., Novel one-step synthesis of nitrogen-doped TiO_2 by flame aerosol technique for visible-light photocatalysis: Effect of synthesis parameters and secondary nitrogen (N) source. *Chemical Engineering Journal* **2018,** *350*, 324-334.
9. Vignesh, K.; Suganthi, A.; Rajarajan, M.; Sakthivadivel, R., Visible light assisted photodecolorization of eosin-Y in aqueous solution using hesperidin modified TiO_2 nanoparticles. *Applied Surface Science* **2012,** *258* (10), 4592-4600.
10. Barndõk, H.; Blanco, L.; Hermosilla, D.; Blanco, Á., Heterogeneous photo-Fenton processes using zero valent iron microspheres for the treatment of wastewaters contaminated with 1, 4-dioxane. *Chemical Engineering Journal* **2016,** *284*, 112-121.
11. Barndõk, H.; Hermosilla, D.; Han, C.; Dionysiou, D. D.; Negro, C.; Blanco, Á., Degradation of 1, 4-dioxane from industrial wastewater by solar photocatalysis using immobilized NF-TiO_2 composite with monodisperse TiO_2 nanoparticles. *Applied Catalysis B: Environmental* **2016,** *180*, 44-52.

Appendix B: Supplementary Material

B.1 MgO- and SnO-modified TiO_2

This section contains supplementary material relevant to **Section 5.2**:

"Impact of surface hydroxylation in MgO-/SnO-nanocluster modified TiO_2 anatase (101) composites on visible light absorption, charge separation and reducibility"

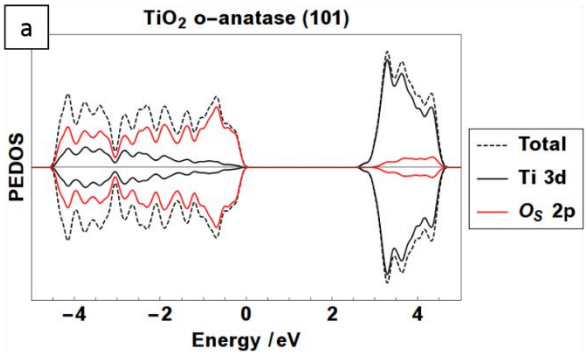

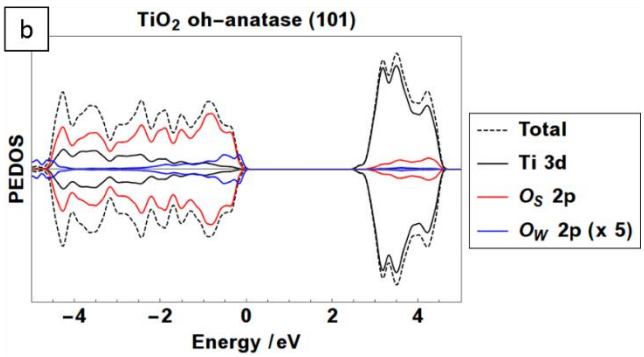

Figure B.1.1 PEDOS for **(a)** bare and **(b)** hydroxylated anatase (101).

Spin density plots for photoexcited model applied o-anatase and oh-anatase (101) are shown in **Figure B.1.2**. For o-anatase (101) (**Figure B.1.2.a**) the electron localises at a Ti_{6f} atom of the surface which is rendered five-fold coordinated through the breaking of a bond with one of the oxygen sites (O_{2f}) over which the hole is distributed. For the oh-

anatase (101) surface (**Figure B.1.2.b**) the electron localises at a Ti_{5f} site while the hole is distributed over an O_W site and an O_{3f} site in the surface.

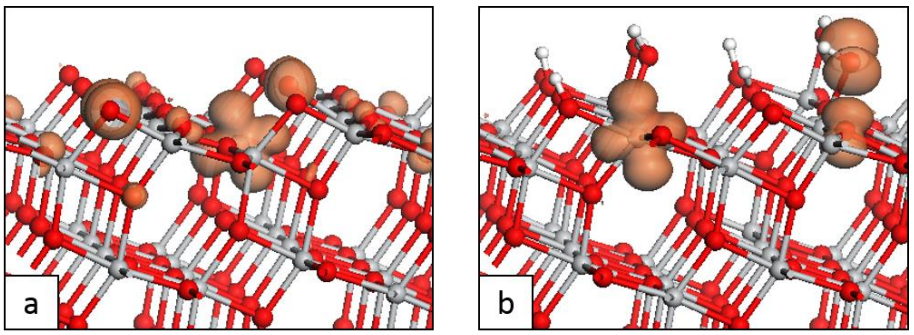

Figure B.1.2 Excess spin density plots for **(a)** bare and **(b)** hydroxylated anatase (101).

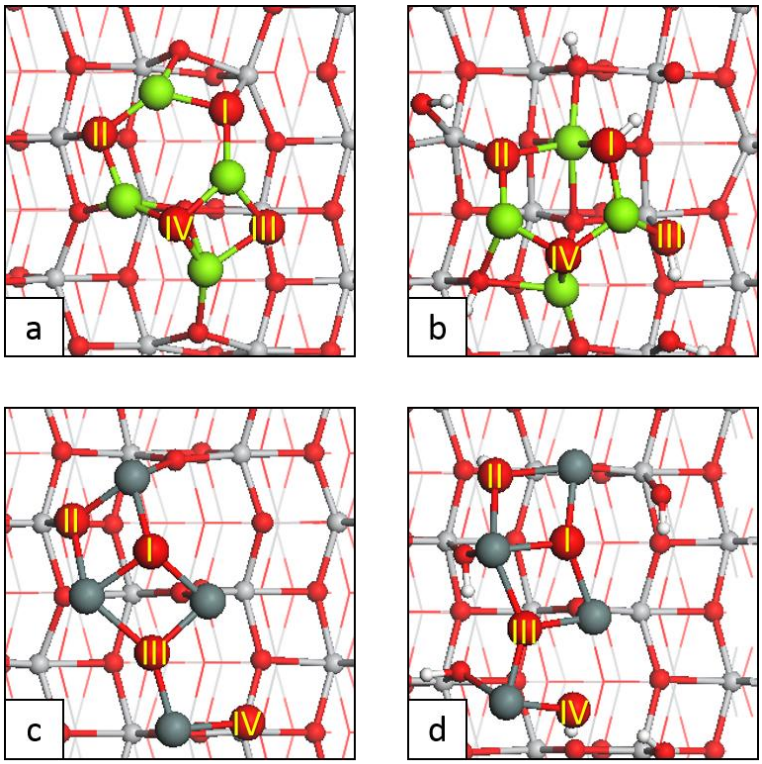

Figure B.1.3 Oxygen atoms in the nanocluster are labelled using roman numerals from I - IV for **(a)** Mg_4O_4-o-anatase (101), **(b)** Mg_4O_4-oh-anatase (101), **(c)** Sn_4O_4-o-anatase (101) and **(d)** Sn_4O_4-o-anatase (101).

The images in **Figure B.1.3** represent the labelling scheme used in the calculations of the most stable nanocluster sites for the formation of an oxygen vacancy. Each oxygen site

of the supported nanoclusters is labelled with a Roman numeral (I-IV) according to their order in the input file (POSCAR).

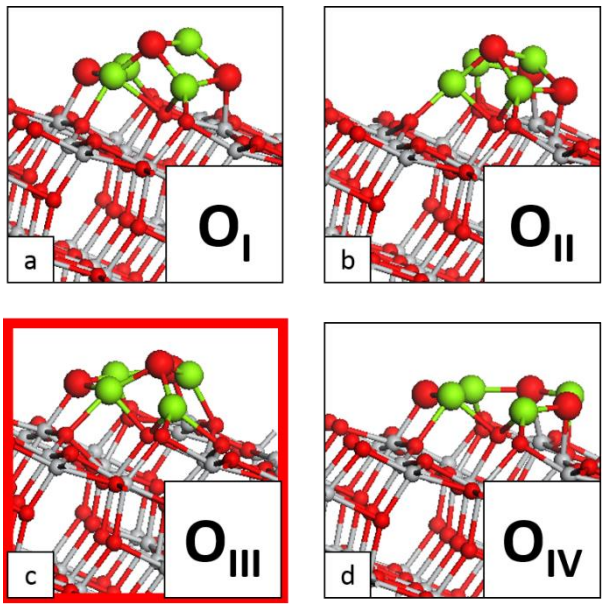

Figure B.1.4 Relaxed atomic structures for Mg_4O_4-o-anatase (101) with one oxygen vacancy. The most stable structure is highlighted in red. The labelling in the inset of each panel corresponds with the labelling in **Figure B.1.3**. Red border = most stable site.

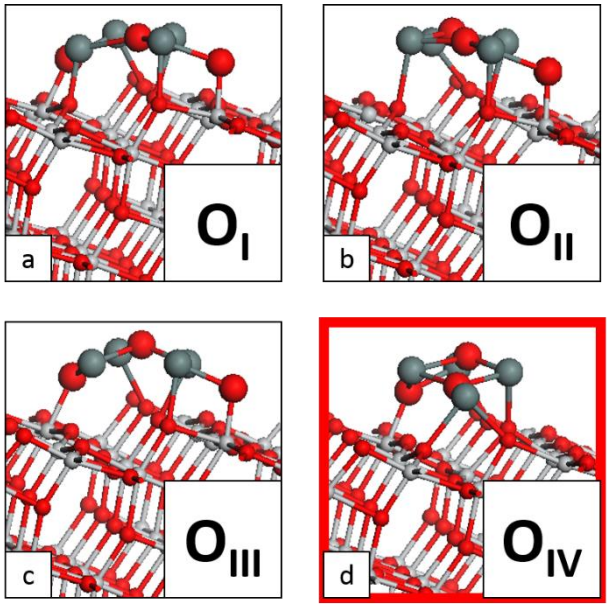

Figure B.1.5 Relaxed atomic structures for Mg_4O_4-o-anatase (101) with one oxygen vacancy. The most stable structure is highlighted in red. The labelling in the inset of each panel corresponds with the labelling in **Figure B.1.3**. Red border = most stable site.

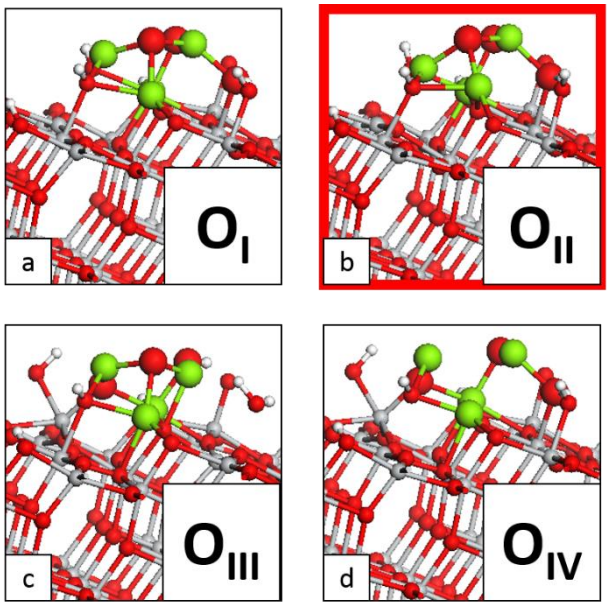

Figure B.1.6 Relaxed atomic structures for Mg_4O_4-oh-anatase (101) with one oxygen vacancy. The most stable structure is highlighted in red. The labelling in the inset of each panel corresponds with the labelling in **Figure B.1.3**. Red border = most stable site.

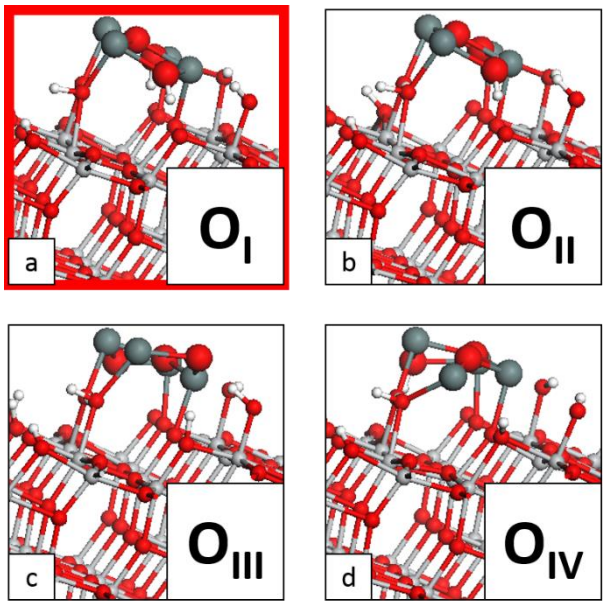

Figure B.1.7 Relaxed atomic structures for Sn_4O_4-oh-anatase (101) with one oxygen vacancy. The most stable structure is highlighted in red. The labelling in the inset of each panel corresponds with the labelling in **Figure B.1.3**. Red border = most stable site.

Table B.1.1 Computed oxygen vacancy formation energies for Mg_4O_4 and Sn_4O_4 modified o-anatase and oh-anatase (101). The most stable vacancy sites are highlighted in bold.

Structure	Vacancy site	E^{vac} (eV)
Mg_4O_4-**o**-anatase(101)	**O_I**	3.31
	O_{II}	4.97
	O_{III}	**2.82**
	O_{IV}	3.69
Mg_4O_4-**oh**-anatase (101)	**O_I**	**0.67**
	O_{II}	**0.61**
	O_{III}	3.90
	O_{IV}	5.38
Sn_4O_4-**o**-anatase (101)	**O_I**	3.47
	O_{II}	3.88
	O_{III}	2.83
	O_{IV}	**1.82**
Sn_4O_4-**oh**-anatase (101)	**O_I**	**1.59**
	O_{II}	2.57
	O_{III}	3.27
	O_{IV}	2.88

B.2 hBN-modified TiO_2

This section contains supplementary material relevant to **Section 5.3**:

"Modification of TiO_2 with hBN: High Temperature Anatase Phase Stabilisation and Photocatalytic Degradation of 1, 4-Dioxane"

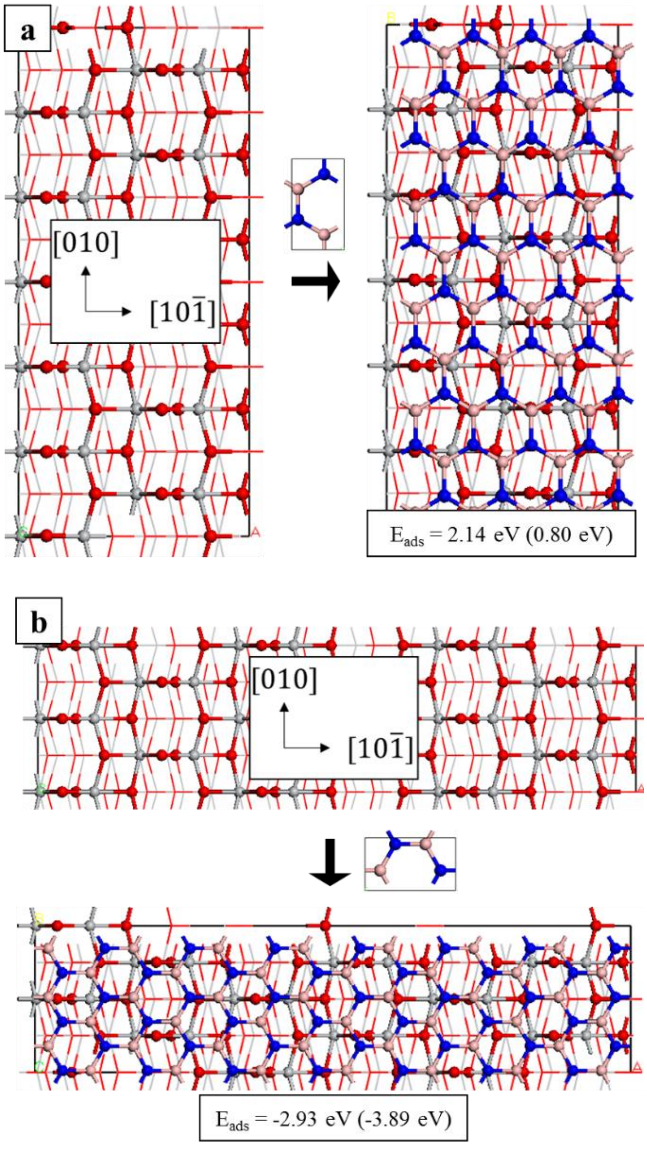

Figure B.2.1 Construction of two BN-TiO_2 interface models. In panel **(a)** the long axis of the BN layer unit cell is parallel to the [010] direction. In panel **(b)** the short axis of the BN layer unit cell is parallel to [010]. The adsorption energies are computed within the DFT-D2 (vdW-DF) framework. In this and subsequent figures, grey spheres represent Ti, red for O, blue for N and pink for B.

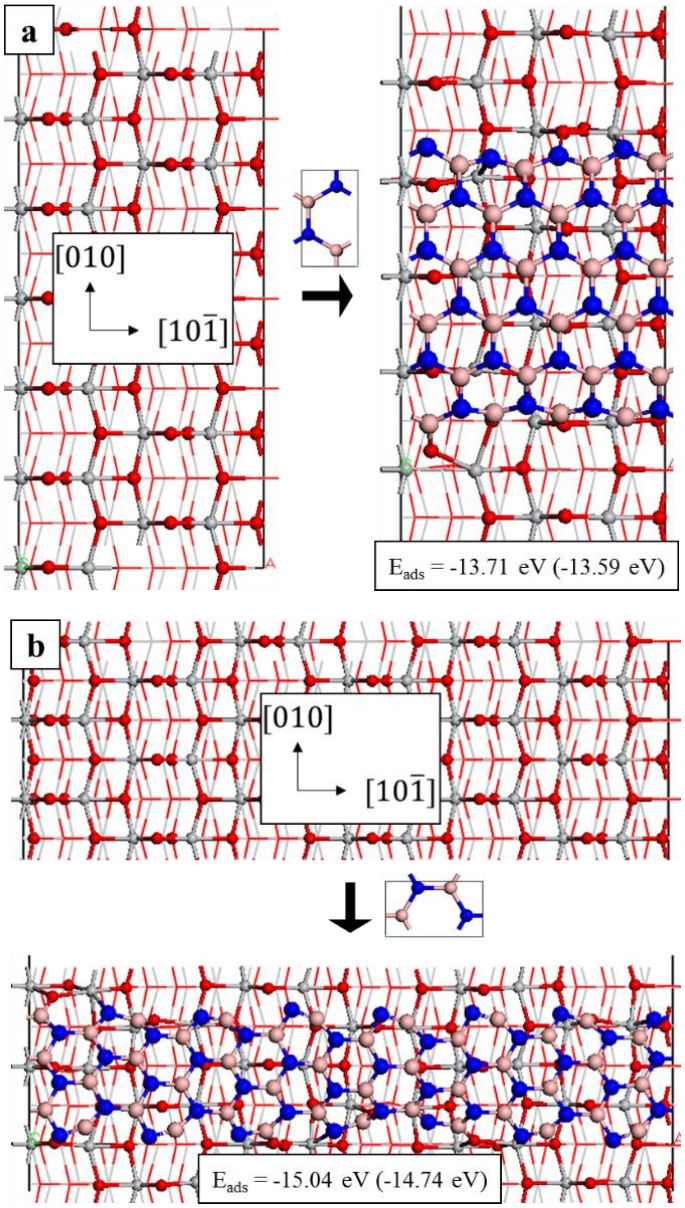

Figure B.2.2 Construction of the two ribbon models which are presented in the main text. Panel **(a)** shows the $(BN)_{24}$-a101 model where the short axis of the BN unit cell is parallel to $[10\bar{1}]$. Panel **(b)** shows the $(BN)_{42}$-a101 model in which the long axis of the BN unit cell is parallel to $[10\bar{1}]$. In both models the ribbons are periodic along $[10\bar{1}]$. The adsorption energies are computed within the DFT-D2 (vdW-DF) framework.

BN-modified anatase TiO_2 is modelled as one, two and three *h*BN rings in intimate contact with the anatase (101) surface, denoted 1-$(BN)_3$-a101, 2-$(BN)_3$-a101 and 3-$(BN)_3$-a101. The adsorption energies are calculated using:

$$E_{ads} = E(x\text{-}(\mathrm{BN})_3\text{-a101}) - E(\mathrm{a101}) - xE((\mathrm{BN})_3) \qquad \text{B.2.1}$$

where $E(x\text{-}(\mathrm{BN})_3\text{-a101})$ is the total energy of the modified surface, x is the number of BN rings, $E(\mathrm{a101})$ is the total energy of the unmodified surface and $E((\mathrm{BN})_3)$ is the energy of a single BN ring in the gas phase.

Two additional models consist of *h*BN ribbons, of compositions $(\mathrm{BN})_{24}$ and $(\mathrm{BN})_{42}$, at the anatase (101) surface. These models are denoted $(\mathrm{BN})_{24}$-a101 and $(\mathrm{BN})_{42}$-a101 and more details about their construction are provided provded below. In each model the *h*BN layer is continuous at the periodic boundary along $[10\bar{1}]$, but discontinuous along [010] due to a mismatch between the lattice parameters of the *h*BN layer and the anatase (101) surface. Thus, the *h*BN layers resemble 1D periodic ribbons. For $(\mathrm{BN})_{24}$-a101, one edge is terminated by B ions and the other by N ions and these edges are separated by 12 Å across the periodic boundary along [010]. For $(\mathrm{BN})_{42}$-a101, the ribbon edges are terminated by alternating B and N ions, with these edges separated by 5.5 Å across the periodic boundary along [010]. For these ribbon models, the adsorption energy is computed as:

$$E_{ads} = E((\mathrm{BN})_{\mathrm{x}}\text{-a101}) - E(\mathrm{a101}) - E((\mathrm{BN})_{\mathrm{x}}) \qquad \text{B.2.2}$$

where x denotes the number of BN units per ribbon.

Comparisons are made between the DFT-D2[1] and vdW-DF[2-3] approaches to account for vdW interactions. In general, these approaches yielded qualitatively consistent results. Quantitative differences only arose in computed adsorption energies and interfacial bond lengths while computed density of states and charge localisation were not affected by choice of approach. Throughout the text, the results relevant to the DFT-D2 set-up will be presented in detail, with reference made to those computed within vdW-DF where appropriate.

Figure B.2.1 shows two models of extended *h*BN monolayers at the anatase (101) surface. The model in **Figure B.2.1.a** is comprised of a (1×6) expansion of the (101)

anatase surface with a (4×5) BN layer. In this configuration strain on the BN unit cell is 2.5% along the short axis (parallel to $[10\bar{1}]$) and 4.5% along the long axis (parallel to $[010]$). The model shown in **B.2.1.b** is constructed of a (3×2) expansion of anatase (101) interfaced with a (7×3) BN layer. In this model the strain on the BN layer 1% along the short axis (parallel to $[010]$) and 2% along the long axis (parallel to $[10\bar{1}]$).

The adsorption energies indicate that for the model shown in **Figure B.2.1.a**, the BN-surface interaction is not favourable, likely due to the strain on the BN lattice. Conversely, the interaction between the surface and BN layer in the model shown in **Figure B.2.1.a** is favourable; the strain on the BN monolayer is this model is more moderate.

In each case the adsorption energies computed with the vdW-DF scheme are more stable than those computed with DFT-D2. For both models, the gap between the anatase surface and the BN layer is computed as 2.6 (2.7) Å for DFT-D2 (vdW-DF).

Figure B.2.2, in combination with **Figure B.2.1**, provides further insight into the construction of the ribbon models denoted $(BN)_{24}$-a101 and $(BN)_{42}$-a101 in the main text. For $(BN)_{24}$-a101, shown in **Figure B.2.2.a**, one edge of the ribbon is terminated by N ions and the other by B ions. The ribbon is periodic along $[10\bar{1}]$ with a strain of 2.5% for the BN lattice along this direction. For $(BN)_{42}$-a101, shown in **Figure B.2.2.b**, both edges of the ribbon are terminated by alternating B and N ions. In this model the ribbon is periodic also along $[10\bar{1}]$ with a strain of 2% for the BN lattice along this direction.

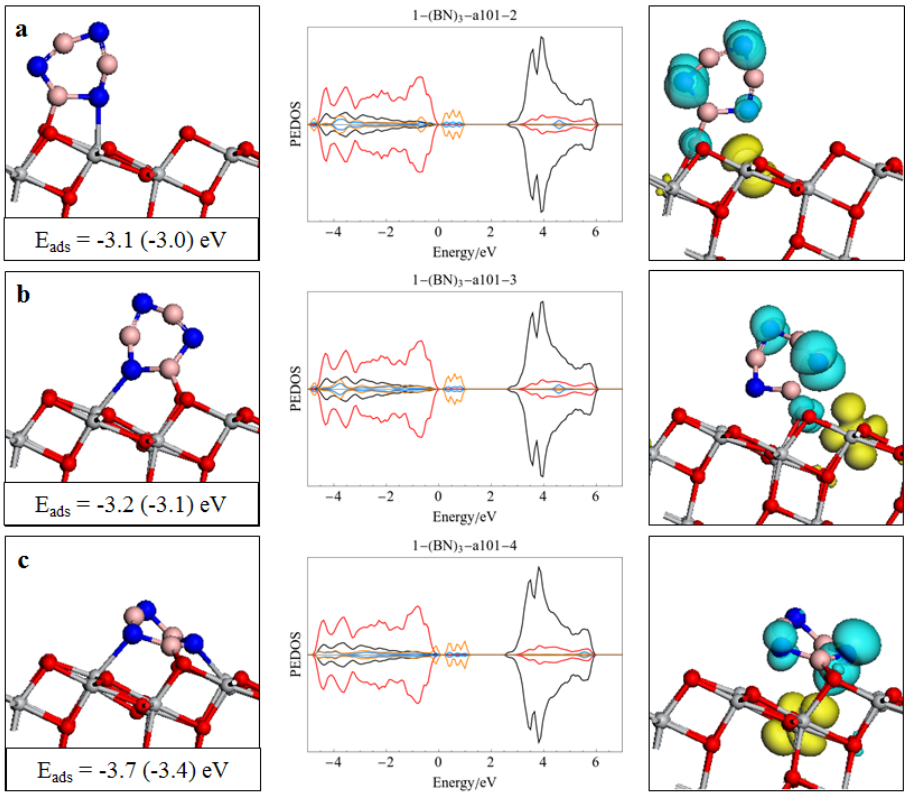

Figure B.2.3 Alternative geometries for a single *h*BN ring adsorbed at the anatase (101) surface. Panels on the left show the relaxed geometry in the ground state, the centre panels show the computed DOS for each geometry and the panels on the right show charge localisation after imposition of the triplet electronic state in the photoexcitation model. The spin density isosurfaces are yellow for electrons and blue for holes and enclose spin densities of up to 0.02 eV/Å^3. The adsorption energies are computed within the DFT-D2 (vdW-DF) framework.

In addition to the models presented in the main text, alternative geometries of one and two *h*BN rings at the anatase (101) surface were considered. These geometries are presented in the left hand panels of **Figures B.2.3** and **B.2.4** and are less stable than those reported in the main text. What is important is that the electronic structure and interfacial charge transfer are unaffected by the precise orientation of the modifiers at the anatase surface. For the DOS plots, shown in the middle panels of **Figures B.2.3** and **B.2.4**, the features which emerge in the band gap due to modification are qualitatively consistent. The N-*p* peaks which emerge above the VBM of the titania host are shifted depending on

the specific orientation of the *h*BN rings at the surface but the overall impact of modification is that mid gap states are introduced which will facillitate electron transfer from these filled states to the Ti-dominated conduction band. Based on these results, we predict a red shift in the light absorption edge. Further evidence for the direction of charge transfer at the interface is provided by the photoexcitation model (see right hand panels of **Figures B.2.3** and **B.2.4**). The electron localises at a surface Ti site, reducing Ti to Ti^{3+}, and the hole state localises at low-coordinated N-sites of the modifiers and this behaviour is unaffected by the details of the surface geometry.

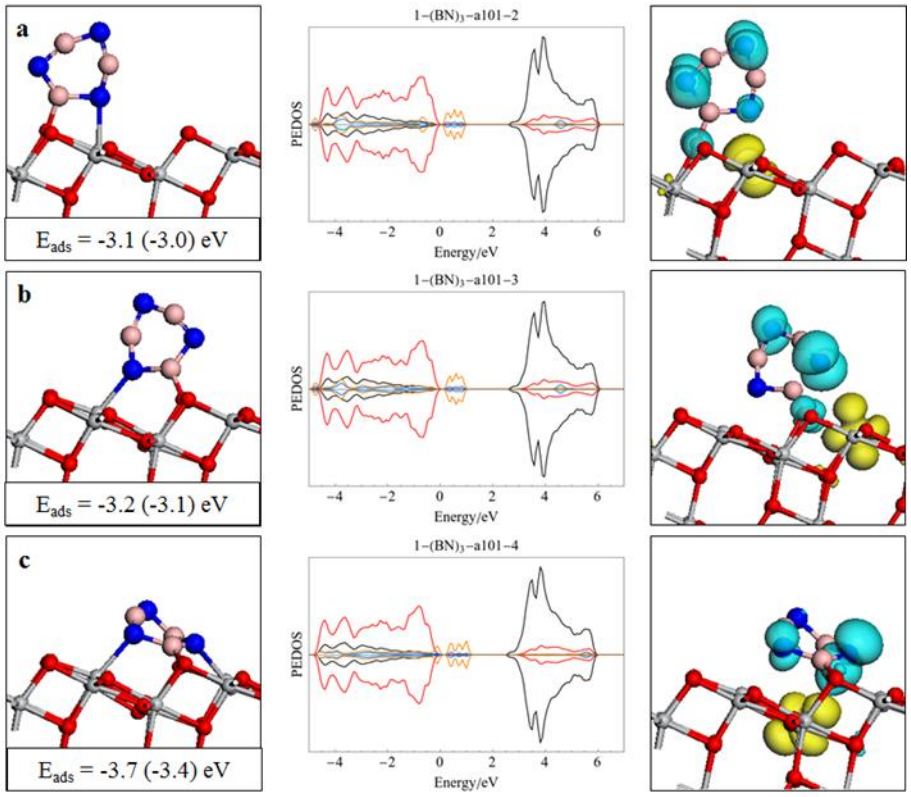

Figure B.2.4 Alternative geometries for two *h*BN rings adsorbed at the anatase (101) surface. Panels on the left show the relaxed geometry in the ground state, the centre panels show the computed DOS for each geometry and the panels on the right show charge localisation after imposition of the triplet electronic state in the photoexcitation model. The spin density isosurfaces are yellow for electrons and blue for holes and enclose spin densities of up to 0.02 eV/Å^3. The adsorption energies are computed within the DFT-D2 framework.

B.3 CeO_x-modified TiO_2

This section contains supplementary material relevant to **Section 5.4**:

"CO_2 and Water Activation on Ceria Nanocluster Modified TiO_2 Rutile (110)"

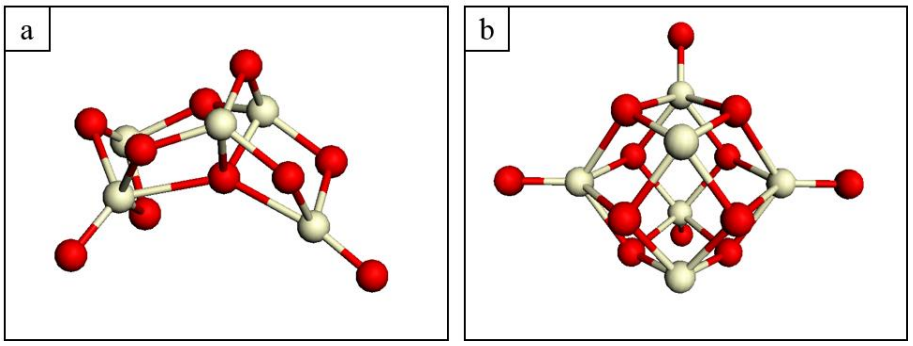

Figure B.3.1 Relaxed atomic structures of stoichiometric gas phase nanoclusters, **(a)** Ce_5O_{10} and **(b)** Ce_6O_{12}.

The nanocluster modifiers, of compositions Ce_5O_{10} and Ce_6O_{12}, shown in **Figure B.3.1**, were relaxed in the gas phase within the same computational setup described in **Chapter 2** for the study in **Section 5.4**, with no constraints on the ionic positions. These geometries are typical of the non-bulk-like structure found for this size of (predominantly) ionic oxide nanoclusters.

These ceria nanoclusters were adsorbed at the rutile (110) surface in different configurations and each of these were relaxed, as described in previous work.[4-10] The most stable $(CeO_2)_n$-rutile-(110) heterostructures were used in subsequent calculations. Although there are many possible adsorption structures of the nanoclusters on the rutile (110) surface, with a range of adsorption energies, we find that once the nanoclusters are adsorbed in stable configurations, the trends in key properties, such as band gap reduction, are unaffected.[10] We use representative CeO_x-rutile-(110) composites to examine the impact of modification on the photocatalytic properties and the interaction of CO_2 and

water, and expect little significant effect due to the precise structure of the composite surface.

Table B.3.1 Computed oxygen vacancy formation energies for each O site of the supported ceria nanoclusters. The most stable vacancy sites are highlighted in bold. Values in brackets were computed with aspherical gradient corrections.

Ce_5O_{10}-rutile-(110)		**Ce_5O_9-rutile-(110)**	
O site	**E_{vac} (eV)**	**O site**	**E_{vac} (eV)**
1	1.35	1	2.96
2	2.03	2	2.95
3	1.38	3	1.86
4	1.67	4	2.03
5	2.38	5	2.38
6	**0.18 (0.02)**	6	2.30
7	1.93	**7**	**1.44 (1.33)**
8	1.53	8	1.76
9	1.56	9	2.35
10	1.65		

Ce_6O_{12}-rutile-(110)		**Ce_6O_{11}-rutile-(110)**		**Ce_6O_{10}-rutile-(110)**	
O site	**E_{vac} (eV)**	**O site**	**E_{vac} (eV)**	**O site**	**E_{vac} (eV)**
1	1.91	1	1.56	1	2.15
2	1.68	2	1.49	2	2.97
3	-0.10	**3**	**-0.16 (-0.62)**	3	3.35
4	1.68	4	1.60	4	1.98
5	1.26	5	1.03	5	2.60
6	1.62	6	1.72	6	2.02
7	0.58	7	1.56	7	2.68
8	2.81	8	2.49	8	2.89
9	3.09	9	2.01	**9**	**0.30 (0.31)**
10	0.29	10	0.14	10	5.04
11	**-0.46 (-0.26)**	11	2.40		
12	2.70				

Table B.3.2 Ce-O distances and coordination for each of the Ce ions in the supported nanoclusters in the stoichiometric, ground state and reduced state. Reduced Ce^{3+} ions are highlighted in bold.

Stoichiometry	Ion	Coord	Ce-O distances (Å)					
Ce_5O_{10}	Ce_I	5	2.42	2.24	2.19	2.17	2.14	
	Ce_{II}	5	2.38	2.31	2.31	2.17	2.15	
	Ce_{III}	4	2.29	2.12	2.11	2.08		
	Ce_{IV}	5	2.44	2.29	2.24	2.16	2.15	
	Ce_V	4	2.24	2.15	2.13	2.08		
Ce_5O_9	**Ce_I**	6	2.59	2.57	2.54	2.45	2.33	2.31
	Ce_{II}	5	2.42	2.35	2.31	2.14	2.13	
	Ce_{III}	4	2.34	2.15	2.14	2.01		
	Ce_{IV}	5	2.60	2.42	2.40	2.29	2.25	
	Ce_V	4	2.25	2.14	2.12	2.08		
Ce_5O_8	**Ce_I**	5	2.57	2.56	2.40	2.29	2.22	
	Ce_{II}	5	2.54	2.53	2.38	2.31	2.25	
	Ce_{III}	4	2.34	2.13	2.09	2.07		
	Ce_{IV}	4	2.47	2.43	2.33	2.17		
	Ce_V	3	2.24	2.17	2.16			
Stoichiometry	**Ion**	**Coord**	**Ce-O distances (Å)**					
Ce_6O_{12}	Ce_I	5	2.46	2.41	2.39	2.38	1.86	
	Ce_{II}	5	2.52	2.37	2.36	2.35	1.86	
	Ce_{III}	4	2.19	2.19	2.13	2.07		
	Ce_{IV}	5	2.35	2.22	2.20	2.20	2.15	
	Ce_V	6	2.45	2.41	2.37	2.24	2.24	2.2
	Ce_{VI}	5	2.57	2.54	2.42	2.33	1.85	
Ce_6O_{10}	**Ce_I**	4	2.35	2.32	2.26	2.23		
	Ce_{II}	5	2.49	2.36	2.36	2.34	1.88	
	Ce_{III}	4	2.35	2.32	2.26	2.23		
	Ce_{IV}	5	2.48	2.36	2.31	2.30	2.28	
	Ce_V	6	2.48	2.48	2.45	2.21	2.16	2.16
	Ce_{VI}	6	2.58	2.58	2.55	2.36	2.36	2.31

Ce_6O_9	**Ce_I**	4	2.31	2.29	2.28	2.26		
	Ce_{II}	4	2.32	2.28	2.28	2.25		
	Ce_{III}	4	2.29	2.29	2.29	2.29		
	Ce_{IV}	5	2.48	2.41	2.34	2.28	2.28	
	Ce_V	6	2.57	2.56	2.51	2.34	2.33	2.32
	Ce_{VI}	6	2.60	2.58	2.56	2.37	2.33	2.32

Light Absorption Properties

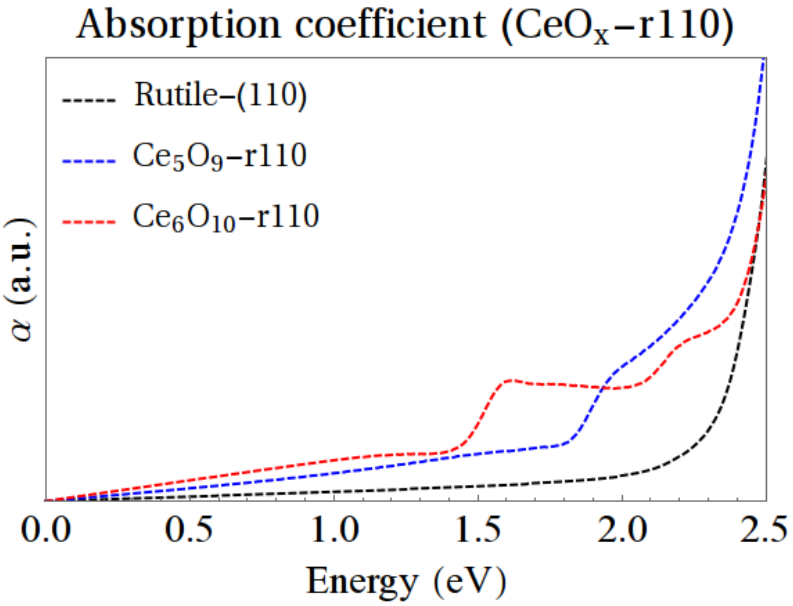

Figure B.3.2 Computed absorption spectra for unmodified rutile (110), and the ground state heterostructures, Ce_5O_9- and Ce_6O_{10}-rutile-(110).

To complement our analysis of the DOS plots and their implications for the light absorption properties of the modified surfaces we compute the real and imaginary parts, ϵ_1 and ϵ_2, of the frequency dependent dielectric function. From this we calculate the extinction coefficient, κ, *via*:

$$\kappa = \sqrt{\frac{\sqrt{\epsilon_1^2 + \epsilon_2^2} - \epsilon_1^2}{2}}$$

and from κ, we compute the absorption coefficient:

$$\alpha = \frac{2\omega\kappa}{c}$$

where ω and c are the angular frequency and speed of light in vacuum respectively.

The computed absorption spectra for the bare rutile (110) surface and the ground states heterostructures, Ce_5O_9- and Ce_6O_{10}-rutile-(110), are shown in **Figure B.3.2**. We observe the onset of light absorption at lower energies for the ceria-modified rutile structures; optical gaps are ~2.2 eV for unmodified rutile (110) and for Ce_5O_9- and Ce_6O_{10}-rutile-(110), the optical gaps are ~1.8 eV and ~1.4 eV respectively. This agrees with trends observed in the DOS plots (**Figure 5.4.3** of **Section 5.4**). For Ce_5O_9-rutile-(110) (**Figure 5.4.3.b**), occupied states, due to Ce^{3+} ions, in the band gap are responsible for the red shift in the absorption edge. For Ce_6O_{10}-rutile-(110) (**Figure 5.4.3.e**), a combination of occupied Ce^{3+}-derived states and O_C *2p* states contribute to the observed red shift. The reduced optical gap computed for Ce_6O_{10}-rutile-(110) relative to Ce_5O_{10}-rutile-(110) can be understood in regarding the insets of **Figures 5.4.3.b** and **5.4.3.e**; for the larger nanocluster-surface composite, the occupied Ce *4f* states lie higher in energy and closer to the conduction band of the TiO_2 support.

Photoexcitation Model

For the photoexcited model applied to the Ce_6O_{10}-rutile-(110) composite, shown in **Figure B.3.3**, there are five unpaired electrons; four are due to the formation of two neutral oxygen vacancies and are localized at Ce_I, Ce_{III}, Ce_{IV} and Ce_V (compare with **Figure 5.4.2.c** of **Section 5.4**). The fifth photoexcited electron localizes at Ce_V; Ce_V maintains a six-fold coordination, and the Ce-O distances increase by up to 10% relative

to their values in the ground state. In the Ce_6O_{10}-rutile-(110) system the hole localizes at a singly coordinated terminal oxygen site; the Ce-O distance increases from 1.9 Å in the ground state to 2.3 Å after excitation. Hole localization is accompanied by a change in the computed Bader charge of the oxygen by 0.4 electrons, from 7.1 to 6.7 electrons. A spin magnetization of 0.78 μ_B was computed for the singly terminated oxygen site at which the hole localizes in Ce_6O_{10}-rutile-(110).

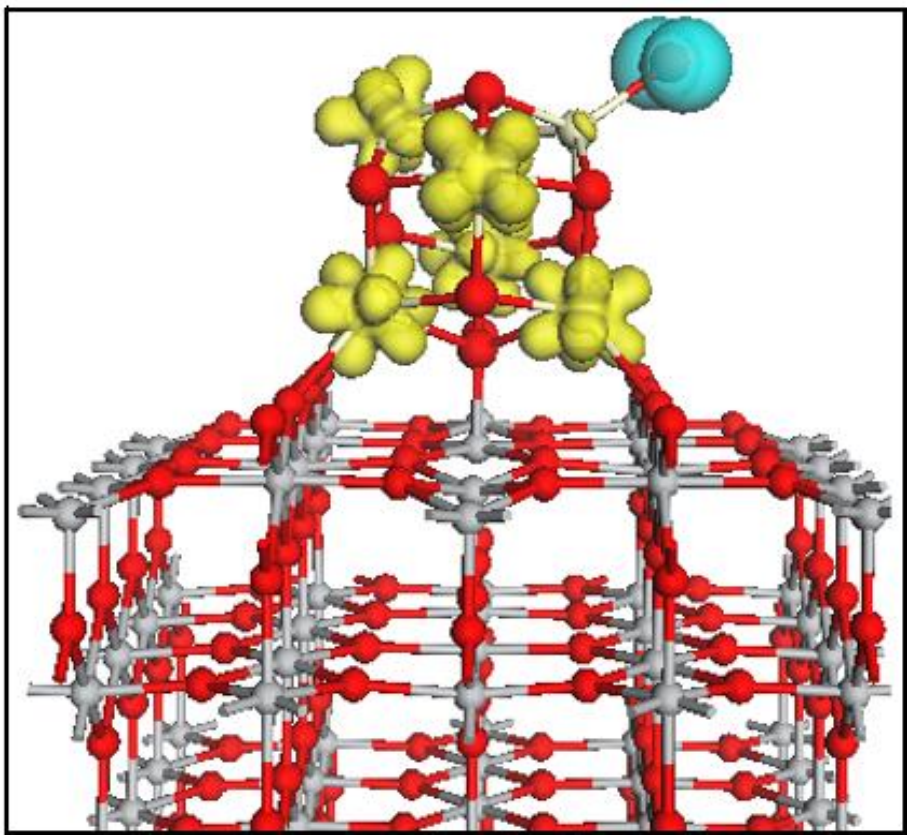

Figure B.3.3 Spin density plots for the photoexcited electron and hole in Ce_6O_{10}-rutile-(110). The spin density isosurfaces are yellow for electrons and blue for holes and enclose spin densities of up to 0.02 eV/**Å^3.**

H_2O adsorption

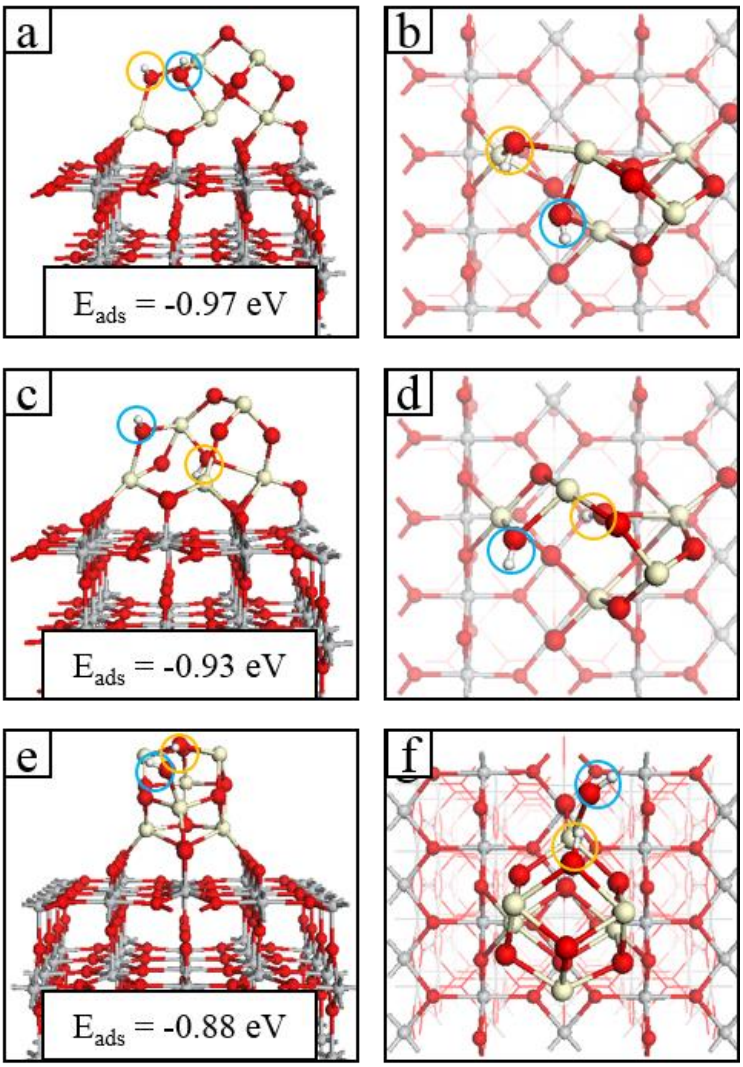

Figure B.3.4 Additional stable configurations of H_2O adsorbed at **(a)**, **(b)**, **(c)** and **(d)** Ce_5O_8-rutile-(110) and **(e)** and **(f)** Ce_6O_9-rutile-(110). Panels on the left show side views, panels on the right show top views. Insets of panels on the left show the adsorption energies. Colour code: Ti, grey; O, red; Ce, cream; H, white.

Figure B.3.5 shows the PEDOS of the H_2O molecule and reduced Ce_6O_9-rutile-(110) composites in the non-interacting case (H_2O + surface) and after dissociative adsorption (H_2O-surface). In the non-interacting cases (**Figure B.3.5.a**), the water-derived O_W *2p* states are well defined peaks at energies of -3.9 eV and -2.0 eV relative to the VBM (0 eV) of the TiO_2 support. For the interacting cases (**Figure B.3.5.b**) the O_W *2p*-derived states overlap the O_C *2p*-derived states near the VBM of the titania host.

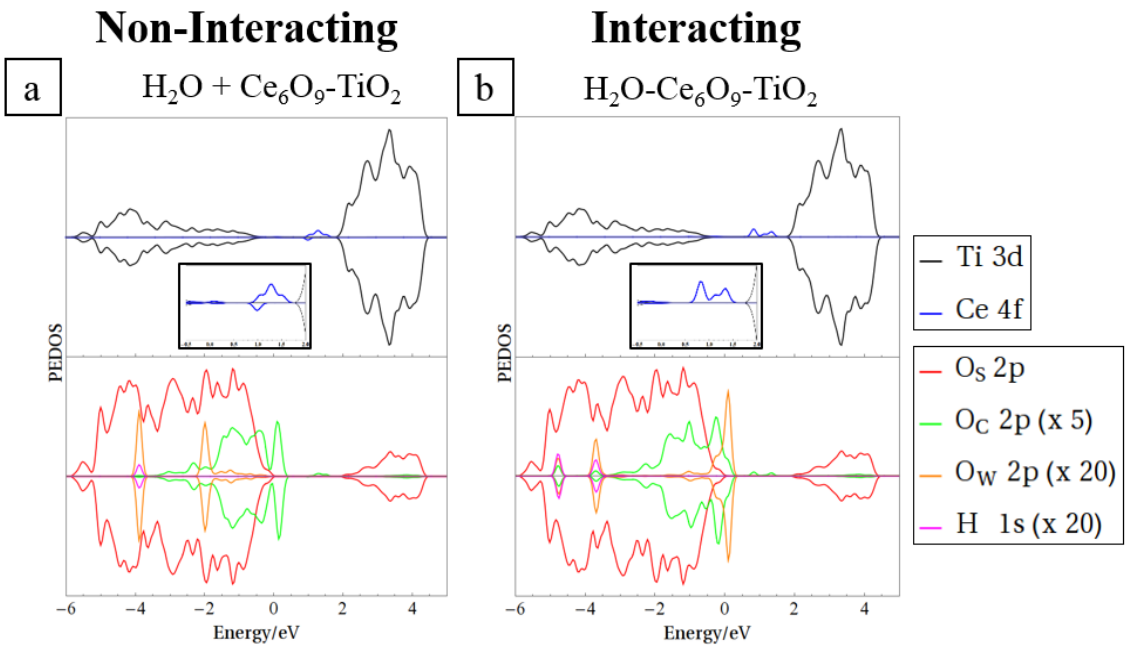

Figure B.3.5 Spin polarized projected electron density of states (PEDOS) for **(a)** H_2O + Ce_6O_9-rutile-(110) (non-interacting) and **(b)** H_2O-Ce_6O_9-rutile-(110) (interacting). The top half of each panel displays Ti *3d*- and Ce *4f*-derived states. Bottom halves of the panels display contributions to the DOS from surface (O_S), nanocluster (O_C) and water (O_W) oxygen *2p*-derived states and H *1s* states. Insets in the top panels show the mid-gap Ce-derived states in the range -0.5 eV – 2.0 eV.

The differences in the adsorption geometries, and perhaps the underlying mechanisms driving dissociation, are reflected in the behaviour of the O_W *2p*-derived states after adsorption. For dissociated water on the Ce_6O_9-rutile-(110) surface, a sharp O_W *2p*-derived peak lies above the VBM because the OH group is terminal, coordinating to a single Ce site. For adsorption at the Ce_5O_8-rutile-(110) composite (see **Figure 5.4.6** of **Section 5.4**), the O_W *2p* states broaden and lie below the VBM, overlapping with O_C derived states, as in this instance the OH groups each bridge two Ce sites of the nanocluster. Comparing **Figures 5.4.6.a** and **5.4.6.b**, the O_W-derived states are shifted to lower energies upon dissociative adsorption. This trend is not seen in comparing **Figures B.3.5.a** and **B.3.5.b** due to the aforementioned singly coordinated OH group which results from adsorption of H_2O at the Ce_6O_9-rutile-(110) surface.

B.4 MnO_x-modified TiO_2

This section contains supplementary material relevant to **Section 5.5**:

"Activation of water on MnO_x-nanocluster-modified rutile (110) and anatase (101) TiO_2 and the role of cation reduction"

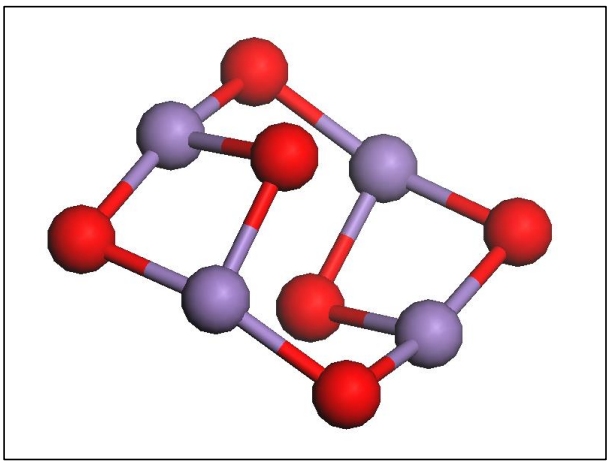

Figure B.4.1 Relaxed atomic structure of the stoichiometric gas phase Mn_4O_6 nanocluster.

The Mn_4O_6 nanocluster modifier shown in **Figure B.4.1**, was relaxed in the gas phase within the same computational setup described in the **Chapter 2**, with no constraints on the ionic positions.

The nanocluster was then adsorbed at the hydroxylated rutile (110) and anatase (101) surfaces in different configurations and each of these were relaxed, as described in previous work.[4-10] The most stable Mn_4O_6-OH-r110 and Mn_4O_6-OH-a101 heterostructures were used in the subsequent calculations. Although there are many possible adsorption structures of the nanoclusters on the titania surfaces, with a range of adsorption energies, we find that once the nanoclusters are adsorbed in stable configurations, the trends in key properties, such as band gap reduction are unaffected.[7]

Reduction via Oxygen Vacancy Formation

The structures shown in **Figure B.4.2**, their formation energies and distribution of ions should be compared with those shown in **Figure 5.5.1** of **Chapter 5**. For the configurations with one O_V, the structures described in the main text are more stable by ~0.9 eV than those shown in **Figure B.4.2.a** and **B.4.2.b**. For the configurations with two O_V the formation energies are comparable and one would expect that Mn and Ti ions are present in a variety of oxidation states at the MnO_x-modified titania surfaces.

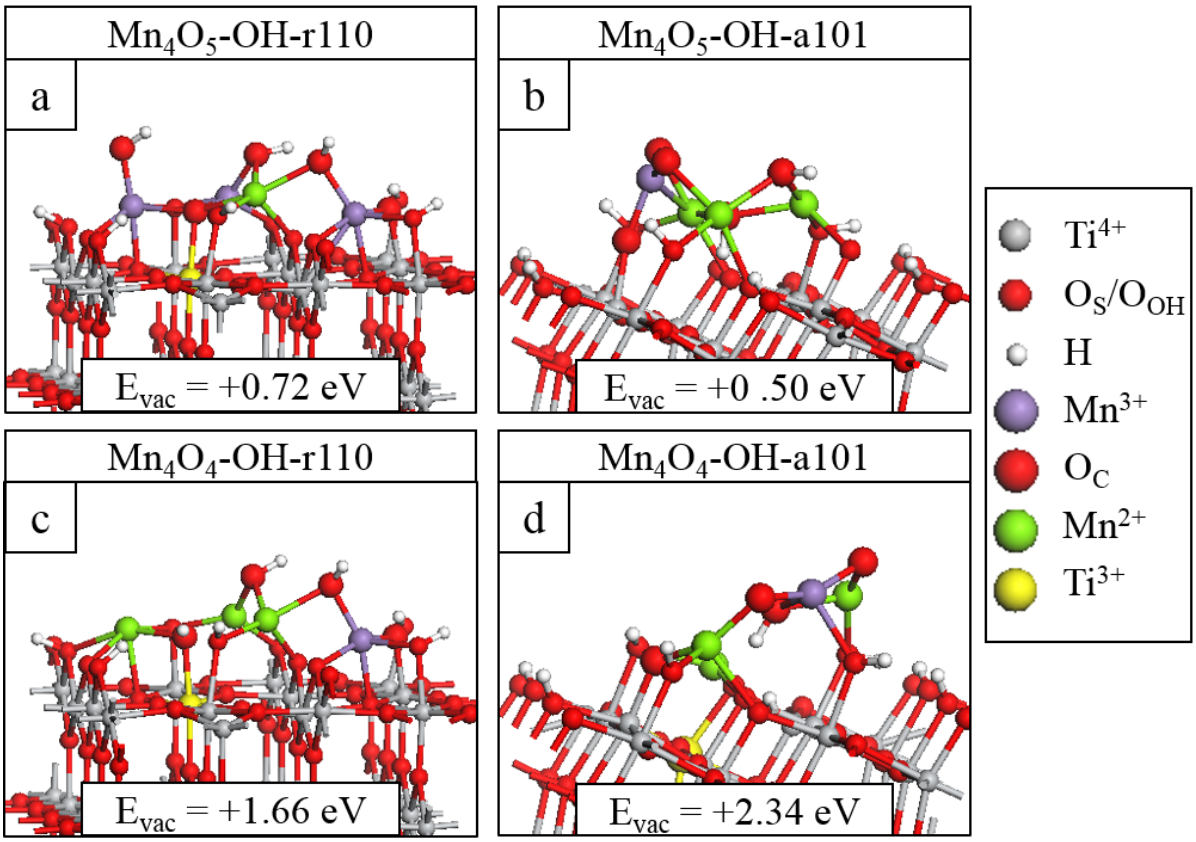

Figure B.4.2 Relaxed atomic structures of additional configurations of MnO_x-modified titania surfaces with oxygen vacancies. **(a)** Mn_4O_5-OH-r110, **(b)** Mn_4O_5-OH-a101, **(c)** Mn_4O_4-OH-r110 and **(d)** Mn_4O_4-OH-a101. The formation energies are computed relative to the most stable structure with one less O_V.

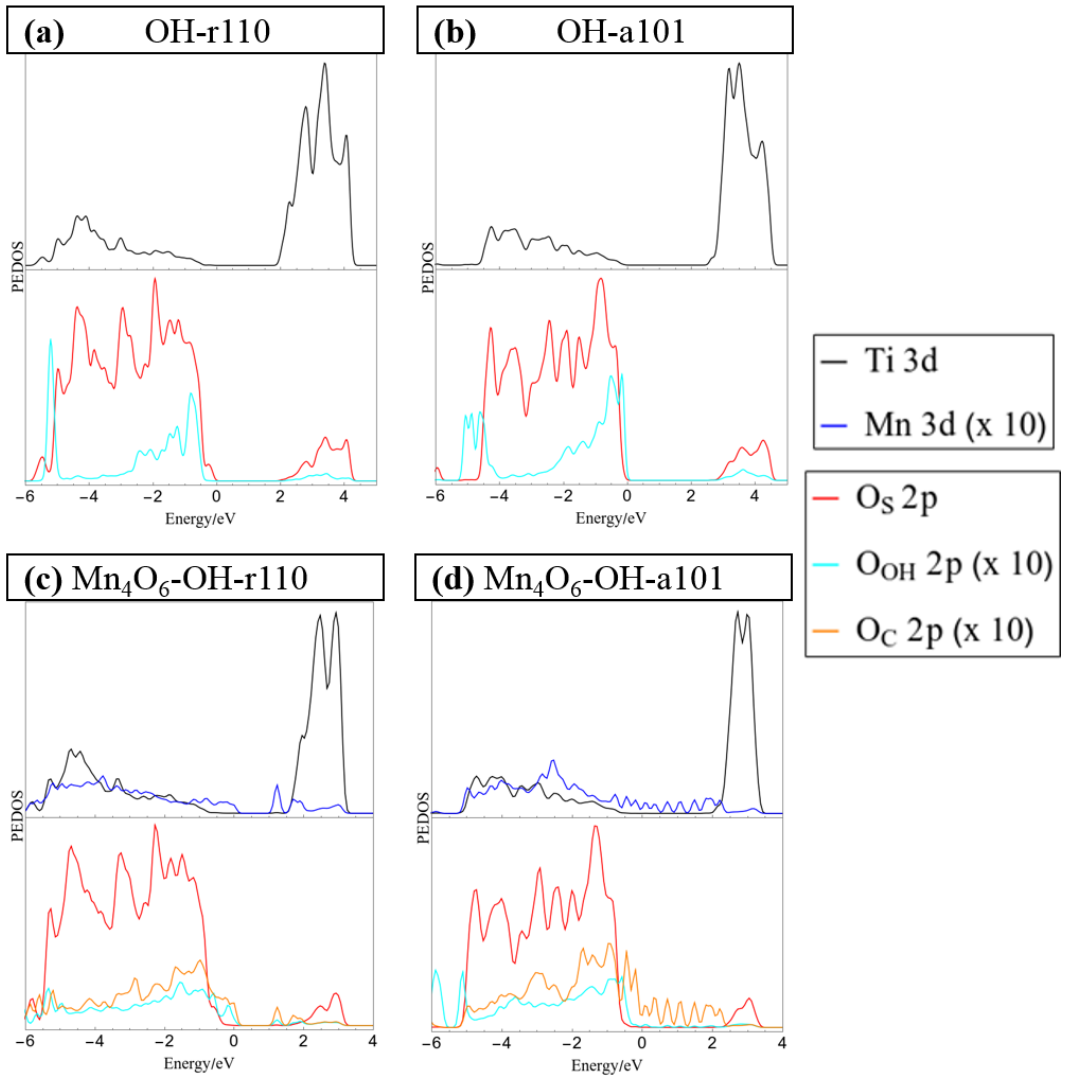

Figure B.4.3 Computed DOS plots for unmodified, hydroxylated rutile (110) and anatase (101), and the stoichiometric Mn_4O_6-OH-r110 and Mn_4O_6-OH-a101 composites.

From **Figure B.4.3.a**, we can see that for unmodified rutile (110) that the presence of hydroxyls has no impact on the bandgap; the highest occupied hydroxyl-derived states lie lower in energy than the VBM of the rutile (110) surface. For unmodified anatase (101), the hydroxyl-derived states overlap the O 2p states of the surface at the valence band edge. From these plots we can conclude that the computed bandgaps are *ca.* 2 eV and 2.7 eV for hydroxylated rutile (110) and anatase (101), respectively; this agrees with analysis of the photoexcited model applied to these systems and described in the main text.

For Mn_4O_6-OH-r110, shown in **Figure B.4.3.c**, nanocluster derived states extend to 0.3 eV above the VBM of the rutile (110) surface. Unoccupied Mn 3d-derived states also emerge in the titania band gap at 0.4 eV below the CBM. For Mn_4O_6-OH-a101, the modifier-derived states span the titania bandgap. However, these systems favours non-stoichiometry as O_V form spontaneously and so are present in the ground state as Mn_4O_5-OH-r110 and Mn_4O_5-OH-a101 (see **Section 5.5**). We may conclude that these computed DOS do not represent a physical system and they have been included here for completeness.

Water adsorption

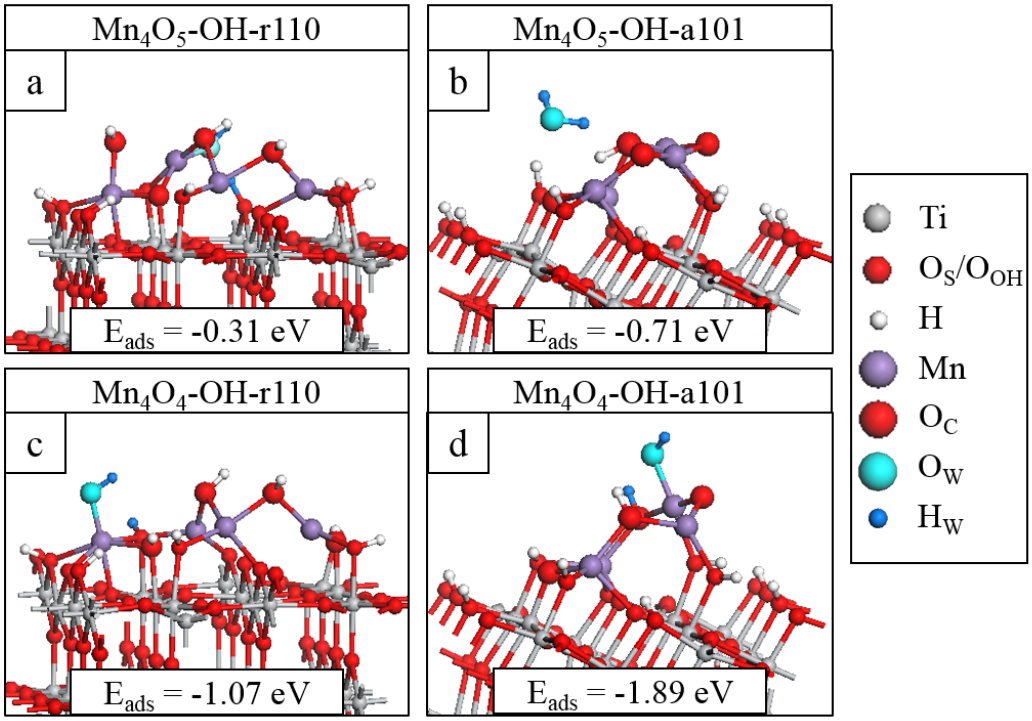

Figure B.4.4 Relaxed atomic structures for stable configurations of H_2O adsorbed at **(a)** Mn_4O_5-OH-r110, **(b)** Mn_4O_5-OH-a101, **(c)** Mn_4O_4-OH-r110 and **(d)** Mn_4O_4-OH-a101. Atomic species are distinguished by colour according to the legend on the right hand side.

Figure B.4.4 displays additional stable configuration for water molecules adsorbed at the off-stoichiometric Mn_2O_x-modified titania surfaces. For the structures with a single O_V, water only adsorbed at the vacancy site and did so both molecularly and dissociatively for Mn_4O_5OH-r110 and only molecularly for Mn_4O_5OH-a101. The final relaxed geometry and adsorption energy differed depending on the initial adsorption set-up and the most stable configurations are described in the main text. For the modified surfaces with two O_V, water adsorption was favourable at multiple sites and led to spontaneous dissociation. The interaction is strongest for water adsorbed at Mn_4O_4-OH-a101; computed adsorption energies were in the range of -2.0 eV to -1.3 eV.

B.5 Water Oxidation Steps at AEO-modified TiO_2

This section contains supplementary material relevant to **Section 6.3**:

"Surface modification of Rutile TiO_2 with Alkaline-Earth Oxide Nanoclusters for Enhanced Oxygen Evolution"

Methodology

Catalyst characterisation

BET surface area measurements were carried out by N_2 adsorption at 77 K using a Micromeritics 2000 instrument.

X-ray diffraction (XRD) patterns were obtained using a Siemens D-501 diffractometer with Ni filter and graphite monochromator. The X-ray source was Cu Kα radiation. From the line broadening of corresponding XRD peaks, we have calculated the mean crystallite size according to the Scherrer equation.

Micro-Raman measurements were performed using a Lab-RAM Jobin Yvon spectrometer equipped with a microscope. Laser radiation (λ = 532 nm) was used as the excitation source at 5 mW. All measurements were recorded under the same conditions (2 s of integration time and 30 accumulations) using a 100x magnification objective and a 125 mm pinhole.

Diffuse reflectance spectra were obtained on a UV–vis scanning spectrophotometer Shimadzu AV2101, equipped with an integrating sphere, using $BaSO_4$ as reference. UV-vis spectra were performed in the diffuse reflectance mode (R) and transformed to a magnitude proportional to the extinction coefficient (K) through the Kubelka-Munk function, $F(R_\infty)$. For the sake of comparison, all spectra were arbitrarily normalised in

intensity to 1. Band gap values were obtained from the plot of the modified Kubelka-Munk function $(F(R_{\infty})E)^{1/2}$ versus the energy of the absorbed light, E.

To investigate the recombination of photogenerated electrons/holes in the photocatalysts, the photoluminescence (PL) emission spectra of the samples were recorded. Room temperature PL emission spectra of the catalysts were recorded in a Horiba Jobin-Yvon Fluorolog3 spectrofluorometer operating in the front face mode with a xenon lamp at the excitation wavelength of 320 nm.

XPS data were recorded on pellets, 0.5 mm thick, prepared by slightly pressing the powdered materials, which were outgassed in the prechamber of the instrument at room temperature up to a pressure below $2 \cdot 10^{-8}$ torr to remove chemisorbed water from their surfaces. Spectra were recorded using a Leybold-Heraeus LHS-10 spectrometer, working with constant pass energy of 50 eV. The spectrometer main chamber, working at a pressure $<2 \cdot 10^{-9}$ Torr, is equipped with an EA-200 MCD hemispherical electron analyser with a dual X-ray source working with Al Kα ($h\nu$ = 1486.6 eV) at 120 W and 30 mA. The C 1s signal (284.6 eV) was used as the internal energy reference in all the experiments.

Field emission scanning electron microscopy (FE-SEM) was performed using a Hitachi S 4800 microscope. The samples were dispersed in ethanol using an ultrasonicator and dropped on a carbon grid.

Photocatalytic runs

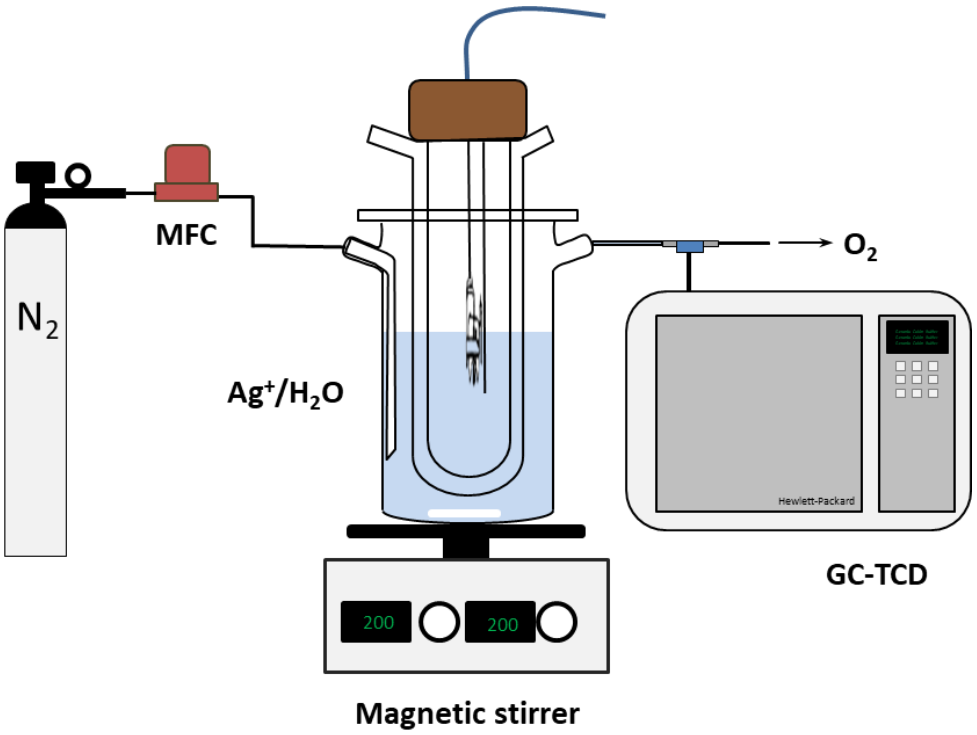

Figure B.5.1 Schematic of photocatalytic flow-reactor used for oxygen production rate.

Results

Alternative adsorption geometries for $Mg_{12}O_{12}$ and $Ca_{12}O_{12}$ at rutile (110)

In **Figure B.5.2** we can see that adsorption of the stable $Mg_{12}O_{12}$ gas-phase nanocluster at the surface (**Figure B.5.2.a**) is the least favourable configuration of those shown. More stable adsorption geometries were found when beginning from the adsorption of three 4-unit clusters, as shown in **Figures B.5.2.b**, **S4.c** and **B.5.2.d**. This facilitates the formation of more interfacial bonds between the nanocluster and the rutile (110) surface. The most stable of these is shown in **Figure B.5.2.d** in which the clusters aggregate at the surface to form a single, contiguous cluster. A similar trend was observed among the adsorption geometries of $Ca_{12}O_{12}$ at the rutile (110) surface (see **Figure B.5.3**).

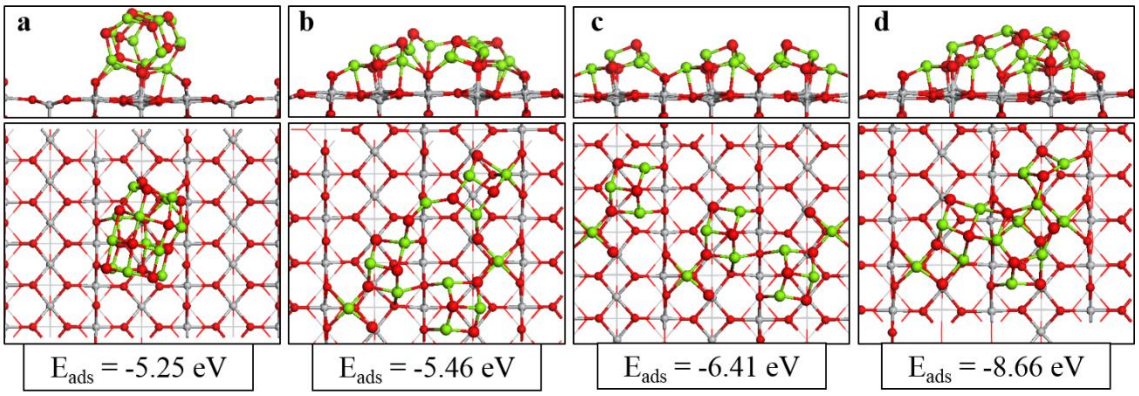

Figure B.5.2 Alternative geometries for $Mg_{12}O_{12}$ adsorbed at the rutile (110) surface. The adsorption energies are included. Ti are represented by grey spheres.

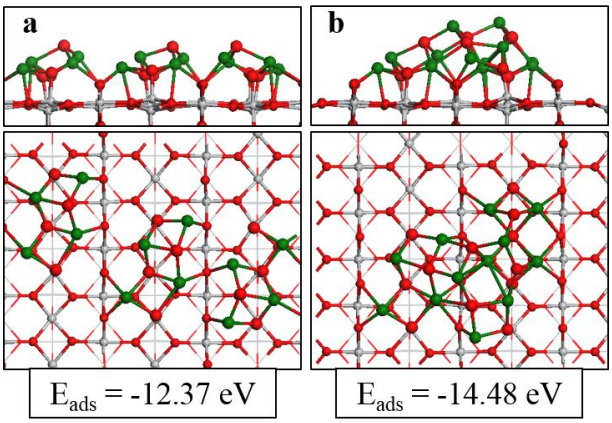

Figure B.5.3 Alternative geometries for $Ca_{12}O_{12}$ adsorbed at the rutile (110) surface. The adsorption energies are included.

As stated in **Chapter** 6, we do not attempt to find the structure that represents the global energy minimum. Of the different configurations examined in the current work, we perform analysis on those which are most stable. However, while these are representative structures and not the most stable ground state of all possible configurations, we find that the properties we investigate do not depend on the precise details of the NC-surface structure. Thus, we may investigate the photocatalytic properties of the composite surfaces without being overly concerned about the exact geometry of the heterostructure.

To further illustrate this point, we performed some calculations on a less favourable configuration for $Mg_{12}O_{12}$, shown in **Figure B.5.2.a**. The results of this analysis are presented in **Figure B.5.4** and **Table B.5.1**, and show qualitatively similar behaviour, independent of the geometry. In **Figure B.5.4**, we see that when the photoexcitation model is applied, the electron consistently localises at a subsurface Ti site and the hole localises at O sites of the modifier. The values in **Table B.5.1**, indicate that the energies computed in the photoexcitation model differ only quantitatively. Similarly, the free energies ΔG of the initial PCET step A follow similar trends for both the stoichiometric and reduced surfaces. The largest difference is seen in the computed oxygen vacancy formation energy; the value for E_{vac} is lower for the less stable structure, as expected.

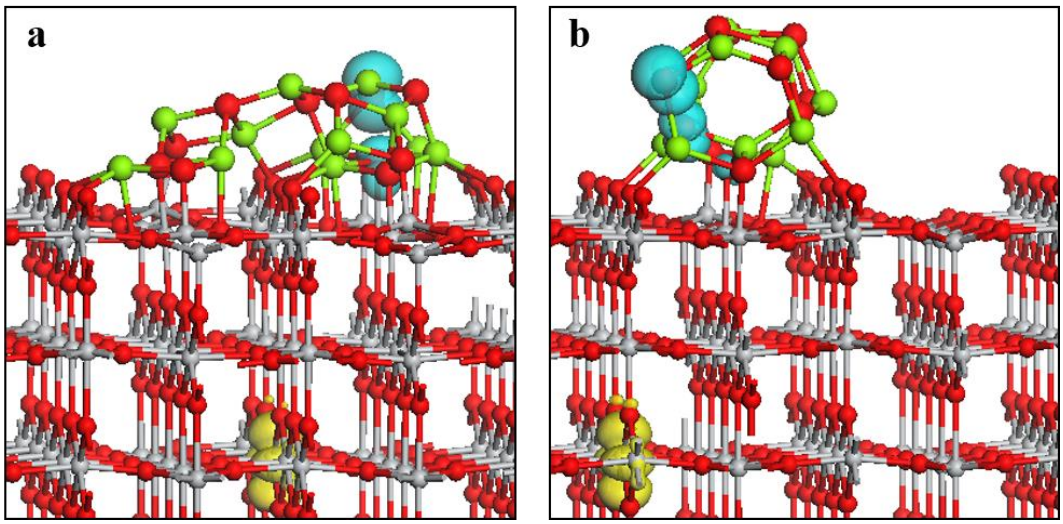

Figure B.5.4 Comparison of photoexcitation model applied to two configurations of $Mg_{12}O_{12}$ adsorbed at the rutile (110) surface. Localisation of electron and holes is indicated by yellow and blue isosurfaces, respectively, which enclose spin densities up to 0.02 eV/Å^3.

Table B.5.1 Comparison of selected energies computed for two configurations of the $Mg_{12}O_{12}$ cluster at the rutile (110) surface. The structure labelled A is the most stable of the geometries investigated in the current work and is shown in **Figure B.5.2.d**. The structure labelled B is less stable and is shown in **Figure B.5.2.a**.

Structure:	**Energy (eV)**	**A (Fig. B.5.2.a)**	**B (Fig. B.5.2.a)**
Stoichiometric	$\mathbf{E^{vertical}}$	1.98	1.93
	$\mathbf{E^{st}}$	0.62	0.72
	$\mathbf{E^{relax}}$	1.36	1.21
	ΔG(A1)	-0.47	-0.87
	ΔG(A2)	1.73	2.41
	ΔG(A)	1.26	1.54
Reduced	$\mathbf{E_{vac}}$	2.58	1.97
	ΔG(A1)	-0.50	-1.18
	ΔG(A2)	0.56	0.09
	ΔG(A)	0.06	-0.09

Table B.5.2 Computed oxygen vacancy formation energies. Each site of the AEO-modifiers was considered for the formation of a neutral oxygen vacancy formation. The most stable sites are highlighted in bold. (*) signifies a calculation that is not fully converged.

Mg_4O_4-r110		**Mg_8O_8-r110**		**$Mg_{12}O_{12}$-r110**	
Site	**E_{vac} (eV)**	**Site**	**E_{vac} (eV)**	**Site**	**E_{vac} (eV)**
1	**1.90**	**1**	**2.33**	1	4.85
2	3.35	2	3.21	2	3.81
3	2.40	3	2.69	3	3.05
4	1.93	4	2.79	**4**	**2.58**
		5	4.87	5	4.95
		6	4.35	6	3.20
		7	4.32	7	*6.10
		8	2.46	8	*6.15
				9	2.58
				10	3.54
				11	*4.34
				12	*5.61
Ca_4O_4-r110		**Ca_8O_8-r110**		**$Ca_{12}O_{12}$-r110**	
Site	**E_{vac} (eV)**	**Site**	**E_{vac} (eV)**	**Site**	**E_{vac} (eV)**
1	2.01	1	1.94	1	*4.78
2	3.32	2	1.95	2	*4.09
3	2.90	3	3.45	3	3.45
4	**1.56**	4	3.46	**4**	**2.23**
		5	2.39	5	5.14
		6	2.39	6	3.12
		7	**1.88**	7	3.52
		8	1.88	8	*4.43
				9	3.24
				10	3.68
				11	*4.68
				12	*5.64

Projected Electronic Density of States (PEDOS) for bare rutile.

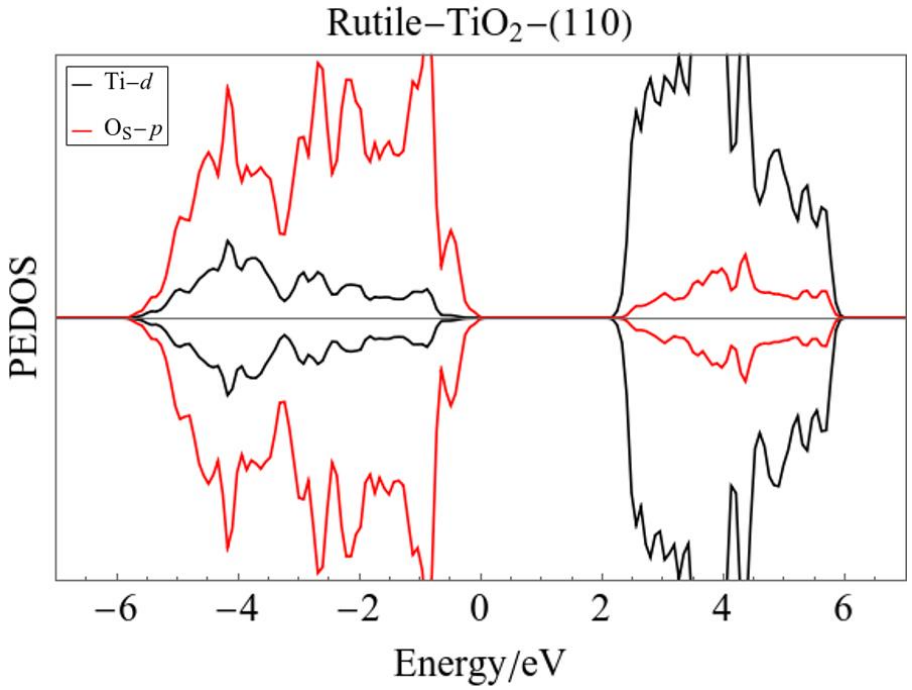

Figure B.5.5 Computed PEDOS for the bare TiO_2 rutile (110) surface. The computed energy gap is 2.16 eV.

Water Oxidation at TiO_2 rutile (110)

Table B.5.3 presents the results of the water oxidation applied to the bare rutile (110) surface. These results were obtained from a model which was constructed based on the work of Valdés *et al*.[11] and the values from their work are included for comparison.

Table B.5.3 Free energies for the water oxidation PCET steps proceeding at the bare rutile (110) surface. These results were obtained with standard DFT and DFT+U. The results from the work of Valdés *et al*.[11] are included for reference.

Step	DFT	DFT+U	Valdes *et al*[11]
A	2.42	2.19	2.20
B	1.34	1.48	1.47
C	1.31	1.21	1.55
D	-0.15	0.05	-0.30

Water Oxidation at AEO-modified TiO_2 rutile (110)

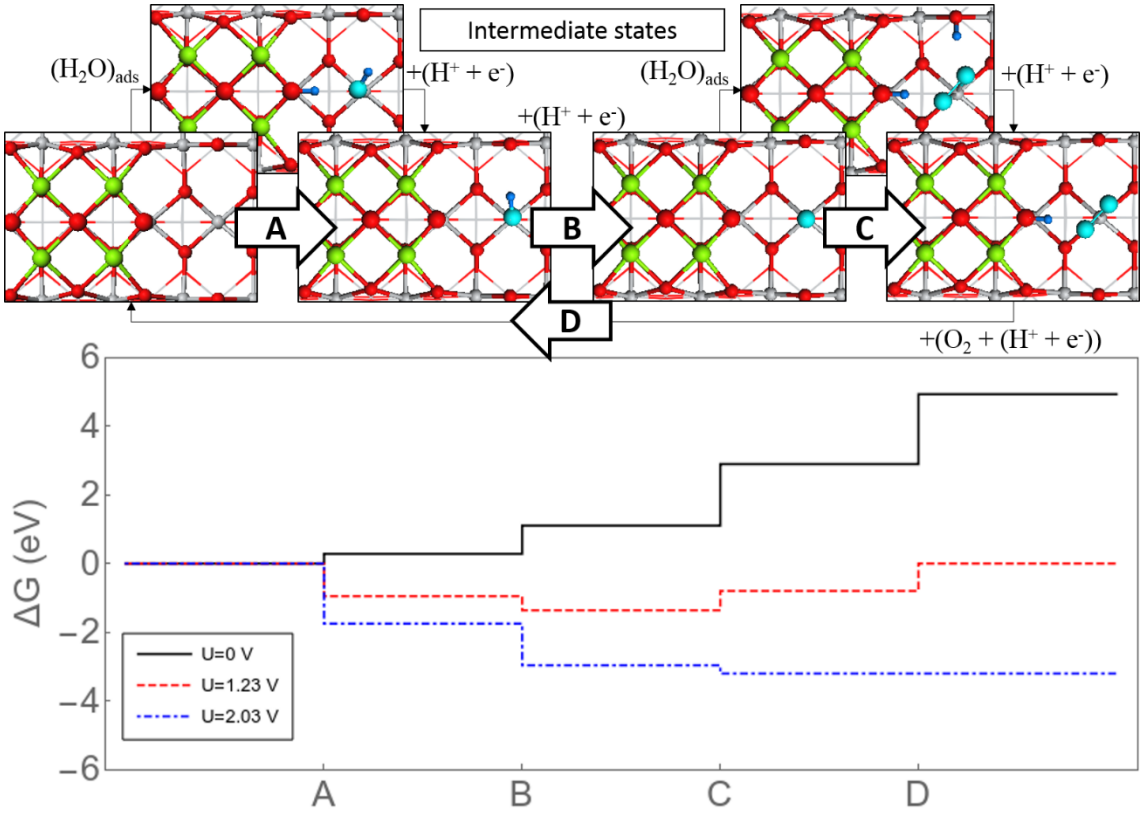

Figure B.5.6 Reaction pathway for water oxidation starting from dissociative water adsorption at an interfacial site of the reduced Mg_4O_3-r110 composite surface. The free energy profile of the pathway is shown for overpotentials U = 0, 1.23 and 2.03 eV. At the equilibrium potential, U = 1.23 V, steps B and C are uphill and at U = 2.03 eV all reaction steps are downhill in free energy.

For the water oxidation pathway proceeding at the interfacial site of reduced Mg_4O_3-r110, the intermediates and free energy profile are shown in **Figure B.5.6**. In sub-step A1, as described previously, the water derived hydroxyl group is singly bound to a Ti site of rutile (110), causing the Ti ion to migrate out from the surface by 0.5 Å. A second hydroxyl is formed after migration of the second H ion to an O_C site. The first dehydrogenation, described by sub-step A2, is most favourable at the cluster-bound hydroxyl and leaves the terminal hydroxyl group bound to Ti at the surface. After the second dehydrogenation (step B), the water-derived O ion remains singly bound at this

Ti site. Sub-step C1 involves the adsorption of a second water molecule which interacts with the terminal O ion. After relaxation, an O_2 group is bound to Ti and two hydroxyls form when the H ions migrate to an O_C site and a bridging O_S site. It is this latter hydroxyl from which dehydrogenation is most favourable (sub-step C2). Finally, the surface-bound O_2 group and the cluster-bound H atom desorb to restore the catalyst to its initial state, Mg_4O_3-r110. The free energy profile in **Figure B.5.6** shows that at the equilibrium potential of 1.23 V, steps C and D are uphill. At a potential bias of 2.03 V each reaction step is downhill and this corresponds to an overpotential of 0.80 V.

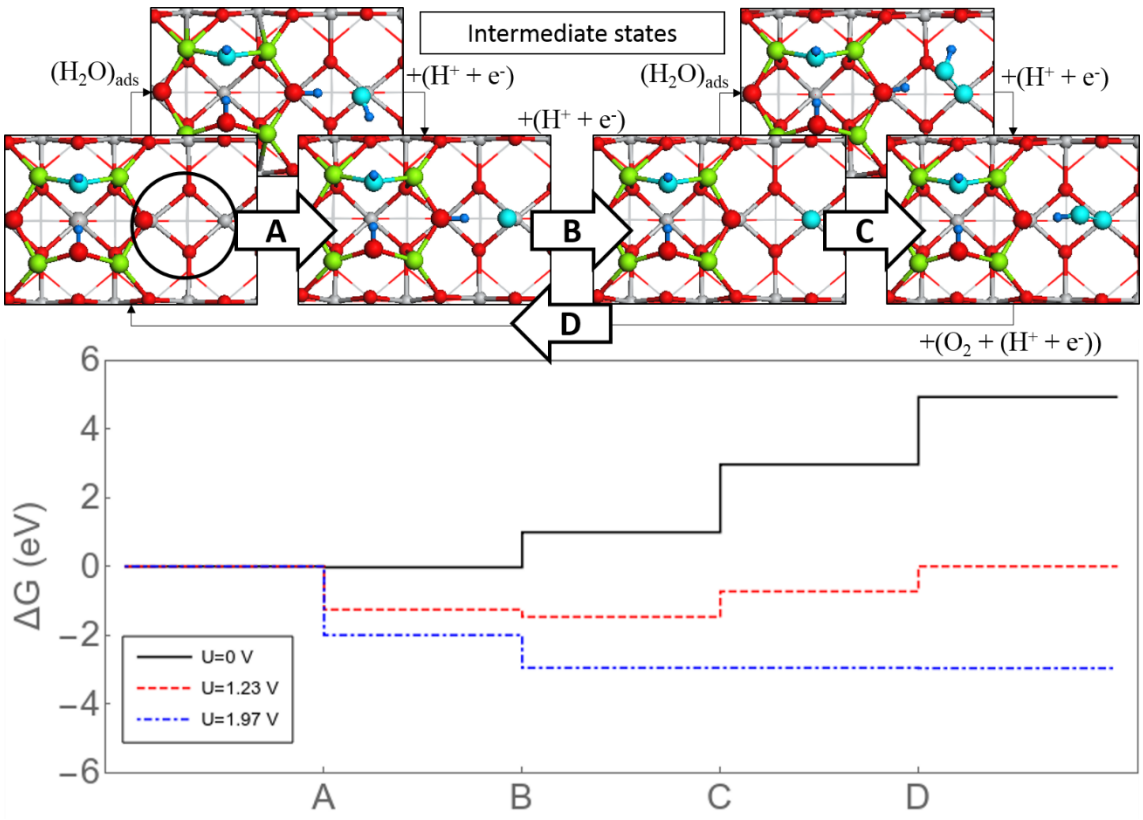

Figure B.5.7 Reaction pathway for water oxidation starting from dissociative water adsorption at an interfacial site of the reduced Mg_4O_3-r110 composite surface, after hydroxylation of the cluster. The free energy profile of the pathway is shown for overpotentials U = 0, 1.23 and 1.97 eV. At the equilibrium potential, U = 1.23 V, steps B and C are uphill and at U = 1.97 eV all reaction steps are downhill in free energy. The reaction site is highlighted with the black circle in the panel on the left.

For the OER proceeding at an interfacial site of the reduced Mg_4O_3-r110 composite surface, after hydroxylation of the cluster (**Figure B.5.7**), the first dehydrogenation is most favourable from the terminal hydroxyl group and leaves a *O species bound at the rutile (110) surface. After step B the terminal *O species remains at the surface. After the water adsorption described by sub-step C1, an *OOH species is bound to the surface Ti site and a second hydroxyl forms due to migration of the H atom to an O_C site. In sub-step C2, dehydrogenation occurs from the cluster and leaves an *OOH species bound at the Ti site. In step D, an O_2 molecule evolves with the release of the cluster-bound H atom.

B.6 References

1. Grimme, S., Semiempirical GGA-type density functional constructed with a long-range dispersion correction. *J. Comput. Chem.* **2006,** *27* (15), 1787-1799.
2. Klimeš, J.; Bowler, D. R.; Michaelides, A., Chemical accuracy for the van der Waals density functional. *J. Phys.: Condens. Matter* **2009,** *22* (2), 022201.
3. Klimeš, J.; Bowler, D. R.; Michaelides, A., Van der Waals density functionals applied to solids. *Phys. Rev. B.* **2011,** *83* (19), 195131.
4. Fronzi, M.; Nolan, M., Surface Modification of Perfect and Hydroxylated TiO_2 Rutile (110) and Anatase (101) with Chromium Oxide Nanoclusters. *ACS Omega* **2017,** *2* (10), 6795-6808.
5. Nolan, M.; Iwaszuk, A.; Lucid, A. K.; Carey, J. J.; Fronzi, M., Design of novel visible light active photocatalyst materials: surface modified TiO_2. *Advanced Materials* **2016,** *28* (27), 5425-5446.
6. Iwaszuk, A.; Nolan, M., Reactivity of sub 1 nm supported clusters: $(TiO_2)_n$ clusters supported on rutile TiO_2 (110). *Physical Chemistry Chemical Physics* **2011,** *13* (11), 4963-4973.
7. Lucid, A.; Iwaszuk, A.; Nolan, M., A first principles investigation of Bi2O3-modified TiO2 for visible light Activated photocatalysis: The role of TiO_2 crystal form and the Bi^{3+} stereochemical lone pair. *Materials Science in Semiconductor Processing* **2014,** *25*, 59-67.
8. Iwaszuk, A.; Mulheran, P. A.; Nolan, M., TiO_2 nanocluster modified-rutile TiO_2 photocatalyst: a first principles investigation. *J. Mater. Chem. A* **2013,** *1* (7), 2515-2525.
9. Fronzi, M.; Iwaszuk, A.; Lucid, A.; Nolan, M., Metal oxide nanocluster-modified TiO 2 as solar activated photocatalyst materials. *Journal of Physics: Condensed Matter* **2016,** *28* (7), 074006.
10. Fronzi, M.; Daly, W.; Nolan, M., Reactivity of metal oxide nanocluster modified rutile and anatase TiO_2: Oxygen vacancy formation and CO_2 interaction. *Applied Catalysis A:* **2016,** *521*, 240-249.
11. Valdés, Á.; Qu, Z. W.; Kroes, G. J.; Rossmeisl, J.; Nørskov, J. K., Oxidation and Photo-Oxidation of Water on TiO_2 Surface. *The Journal of Physical Chemistry C* **2008,** *112* (26), 9872-9879.